Civil Engineering ETDs

Engineering ETDs

7-12-2014

On Dynamic Modulus of Asphalt Concrete for Moisture Damage

Mekdim Weldegiorgis

Follow this and additional works at: https://digitalrepository.unm.edu/ce_etds

Mekdim T. Weldegiorgis
Candidate

Civil Engineering
Department

This dissertation is approved, and it is acceptable in quality and form for publication:

Approved by the Dissertation Committee:

Dr. Rafiqul A. Tarefder, Chairperson

Dr. Arup K. Maji

Dr. Mahmoud R. Taha

Dr. Tariq Khraishi

ON DYNAMIC MODULUS OF ASPHALT CONCRETE
FOR
MOISTURE DAMAGE

BY

MEKDIM T. WELDEGIORGIS

B. Sc., Civil Engineering, Arbaminch Water Technology Institute,2003
M.Sc., Civil Engineering (Road and Transportation), Addis Ababa University, 2007

DISSERTATION

Submitted in Partial Fulfillment of the
Requirements for the Degree of

Doctor of Philosophy

Engineering

The University of New Mexico
Albuquerque, New Mexico

May, 2014

DEDICATION

This dissertation is dedicated to my mother, Alemtsehay K. Ali, my Father, Teshome

Weldegiorgis and my sisters Engidawork T. Weldegiorgis and Million T. Weldegiorgis.

iii

ACKNOWLEDGMENTS

On Dynamic Modulus of Asphalt Concrete for Moisture Damage

BY

MEKDIM T. WELDEGIORGIS

B. Sc. in Civil Engineering, Arbaminch Water Technology Institute.
Arbaminch, Ethiopia, 2003

M.Sc. in Civil Engineering (Road and Transportation) Addis Ababa University.
Addis Ababa, Ethiopia, 2007

Ph.D. in Engineering, University of New Mexico.
Albuquerque, USA, 2014

ABSTSRACT

Dynamic modulus (E^*) test has gained substantial acceptance in recent years for evaluating Hot Mix Asphalt (HMA) rutting and fatigue cracking performances. Indeed, the recently developed Mechanistic Empirical Pavement Design Guide (MEPDG) uses E^* data for stress and strain calculation, and E^*-based models for prediction fatigue and rutting performances of a HMA pavement. Unfortunately, neither HMA mix design method nor the MEPDG uses E^* value to evaluate moisture damage characteristics of HMA pavements. In fact, moisture damage is a very complex problem, and there exists no models for inclusion in the MEPDG for predicting moisture damage performance of HMA pavements. Rather, moisture damage performance of HMA is evaluated during the mix design state using the AASHTO T 283 test. According to AASHTO T 283 method, indirect tensile strength ratio of wet to dry samples is used as an indicator of moisture

damage performance of a HMA mix. The AASHTO T 283 is a simple method, but it is not very reliable. In some cases, it gives false negative and positive values about the moisture damage characteristic of an HMA sample. To this end, this study attempts to study moisture damage in Asphalt Concrete (AC) sample by determining the loss in dynamic modulus (E*) value based on continuum damage mechanics. The loss in E* is evaluated by calculating the ratio of wet E* to dry E* (DMR).

In this study, *E** testing is performed on five different asphalt mixtures. Three of the asphalt mixtures are plant produced Superpave mixes, and the other two are laboratory prepared HMA mix. The plant produced mixes include SP-II mix with asphalt binder's Performance Grade (PG) PG 64-22, SP-III mix with PG 70-22, and SP-IV mix with PG 70-22. The laboratory mixes are SP-III mix with PG 64-22, and SP-II with binder PG 70-22. The *E** test is conducted at five temperatures (-10, 4, 21, 37, 54 °C) and six frequencies (25, 10, 5, 1, 0.5, 0.1 Hz). The resulting *E** data are used to generate time-temperature mastercurves. Also, the laboratory *E** data is fitted to several models such as the viscosity (η) -based Witczak model, the dynamic shear modulus (*G**) -based Witczak models, and the Hirsch model. However, all models are found to underpredict the laboratory *E** values. Therefore, the η-based Witczak model is modified to improve *E** prediction accuracy in this study and *E** ratios are used for evaluating moisture damage in AC.

As mentioned above, the most common test method for evaluating moisture damage susceptibility of HMA mix is the AASHTO T 283. According to the AASHTO T 283, a

dry asphalt concrete sample is vacuum saturated and then subjected to one cycle of freezing and thawing. However, one cycle of freeze-thaw does not simulate moisture condition resulting from repeated pore water pressure buildup and scouring cycles that occur when vehicle tires pass over a saturated pavement. Recently, Moisture Induced Sensitivity Tester (MIST) equipment can apply repeated pore pressure cycles inside an AC sample in the laboratory. Therefore, MIST device is employed in this study to cause damage in AC samples. Moisture damage resulting from MIST conditioning is then evaluated using the Dynamic Modulus Ratio (DMR) of wet to dry samples. MIST conditioning is performed at three different pressures (40, 55, 70 psi), three temperatures (40, 50, 60 ºC) and three different numbers of cycles (3500, 7000 and 10,500). MIST conditioning is found to decrease the E^* value of asphalt concrete indicating the presence of moisture damage. The average DMR is observed to decrease from 1.0 to 0.85, 0.46 and 0.56 for MIST conditioning at 3500, 7000 and 10500 cycles, respectively. When the MIST conditioning temperature is increased to 40, 50 and 60 ºC, the average DMR decreases from 1.0 to 0.90, 0.82 and 0.76, respectively. The DMR at 276, 376 and 483 kPa MIST conditioning pressures are determined to be 1.0, 0.91 and 0.72, respectively. Therefore, moisture damage increases with an increase in number of cycles, temperatures and pressures. However, it is shown that temperature affects moisture damage less significantly than the number of cycles and pressures in a MIST device. Therefore, number of traffic and magnitude of traffic loading should be considered carefully to design moisture damage free pavements.

Based on the E* test results, it is observed that DMR increases with an increase in loading frequency. Considering the variation of DMR with $E*$ testing temperature and frequency, two different surface models to correlate DMR with MIST parameters are developed using four dimensional second order polynomial functions. The coefficient of determination of $R^2 = 0.969$ and $R^2 = 0.839$ for the MIST-Cycle and MIST-Pressure models represent a good model fitting.

It is evident from the above paragraph that the MIST pressure causes significant moisture damages inside an AC sample. Repeated increase and decrease of pore pressure in MIST may have some scouring or washing effects, which is further examined in this study through a leaching test. Leaching of asphalt binder elements resulting from MIST moisture conditioning is examined using three tests: Inductively Coupled Plasma Mass Spectrometry (ICP-MS), Inductively Coupled Plasma Optical Emission Spectroscopy (ICP-OES) and Ion Chromatography (IC) tests. ICP-MS tests show an increase in the concentration of vanadium from 0.1 to 7.59 ppb, 0.1 to 5.40 ppb and 0.1 to 8.39 ppb in the De-Ionized (DI) water for 3500, 7000 and 10500 MIST conditioning cycles, respectively. When tested in normal tap water, the concentration of vanadium is found to increase from 5.12 ppb to 10.7, 9.12 and 9.72 ppb for conditioning at 40, 55 and 70 psi pressures, respectively. ICP-OES test reveals 13%, 10% and 10% increase in the concentration of sulfur for conditioning at 3500 cycles at 40, 55 and 70 psi, respectively. At 40 psi pressure, the increase in the concentration of sulfur in DI water is found to be 1162%, 973% and 2718% for 3500, 7000 and 10500 conditioning cycles, respectively. The IC test shows 245%, 198% and 698% increase in the concentration of sulfate for

viii

3500, 7000, and 10500 conditioning cycles, respectively. This confirms that MIST conditioning washes away some chemical elements of asphalt binder in addition to weakening and causing damage in AC by pore water pressure.

TABLE OF CONTENTS

xiv

LIST OF FIGURES

xviii

LIST OF TABLES

Chapter 1

Introduction

⌣⌣

1.1. General

Dynamic modulus is one of the most important material characterization parameter among the design inputs in MEPDG (ARA Inc. 2004). Dynamic modulus is used in MEPDG to determine the stress state of AC and the empirical relationships for predicting pavement distresses use dynamic modulus as an input variable. Hence, dynamic modulus is very important for material characterization in both state of the art asphalt mix design and pavement design procedures. Therefore, using a single E^* value it is possible to provide guarantee to the performance of Superpave volumetric mixes and predict pavement structural response for design. This brings significant benefits to the state highway agencies because only one test parameter and/or test method is required for both pavement response (rutting and fatigue cracking) prediction and asphalt volumetric mixture design. The present study attempts to use E^* for predicting moisture damage, which has not been addressed by MEPDG yet.

There has been a long history of the use of E^* parameter by many researchers such as: Shook et al., 1969; Kallas, 1970; Bohn et al., 1970; Cragg and Pell, 1971; Yeager and Wood, 1975; Majidzadeh et al., 1979; Akhter and Witczak, 1985; Miller et al., 1983; Witczak and Fonseca, 1996. In the past, E^* was used by researchers, but use of E^* as a fundamental martial property in design of pavements in state highway departments is quite new and recent. Moreover, the use of E^* for moisture damage characterization of

1

AC is an even newer concept. To this end, dynamic modulus tests are performed on New Mexico Department of Transportation (NMDOT) mixes. Generated E^* data is used for evaluating the accuracy of available dynamic modulus prediction models and then for moisture damage analysis.

Problem Statement Related to Hypothesis 1

The performance of viscosity (η) -based Witczak model for predicting dynamic modulus of asphalt concrete has been evaluated by many researchers: Clyne et al. (2003) implemented the η-based Witczak model to predict E^* mastercurves for Minnesota department of transportation mixes. The results indicated that η-based Witczak model always under predicted measured E^* values of all mixes. The extent to which the model under predicted was also found to be different for different mixes. Christensen et al. (2003) also reported that the use of η-based Witczak predictive equation produced slightly less values than test results at higher modulus values. Birgisson et al. (2005) found predicted E^* values to be largely dependent on the binder viscosity-temperature relationship. In their study, it is reported that the use slope (A) and intercept (*VTS*) values of viscosity-temperature relationship proposed for mix/laydown condition by Witczak and Fonseca (1996) result in an over prediction of measured E^* values. Kim et al. (2005) also investigated the accuracy of the η-based Witczak predictive model by calculating the percent of error at each frequency and temperature combination and then averaging for different frequencies at the same temperature. The findings implied that the η-based Witczak equation predicts better at cooler temperatures than at warmer temperatures. Schwartz (2005) employed sensitivity and validation analysis to evaluate the accuracy of η-based Witczak predictive equation and concluded that the η-based Witczak model

produces reasonable estimates in some cases and underpredict measured values at its worst performance. Moreover, they have also found the model to lack in predicting the performance variation of different mixes under varying design conditions. Tran and Hall (2005) used the coefficient of determination test statistic to evaluate how well the η-based Witczak predictive equation estimates the measured E^* and concluded that Witczak predictive equation have good correlation to the measured E^* values. However, close observation of measured and predicted results indicated a tendency to underpredict E^* values. Mohammad et al. (2005) investigated the accuracy of η-based Witczak model utilizing E^* data collected at the Federal Highway Administration (FHWA) mobile laboratory and the Louisiana Transportation Research Center (LTRC) laboratory. They also found that predicted E^* values are on the average 75% of measured E^* values. Dongré et al. (2005) implemented the η-based Witczak model for original, Rolling Thin Film Oven (RTFO) and Pressure Aging Vessel (PAV) aged binder cases. It is reported in their study that the η-based Witczak model produces unreasonable estimates for modulus below 700 MPa (100,000 psi) and underpredicts measured E^* for air void and binder content higher than the mix design. Dongré et al. (2005) have also recommended to improve the sensitivity of η-based Witczak model to volumetric variables, such as the percentage of voids in mineral aggregate (VMA), the percentage of voids filled with asphalt (VFA), asphalt concrete percentage (AC), and Percentage of air voids by volume of mix (*Va*). To this end, this study attempts to modify the η-based Witczak model in order to improve its prediction accuracy for New Mexico mixes.

Problem Statement Related to Hypothesis 2

The suitability of using dynamic modulus has not been tried for determining moisture-induced damage either by MEPDG or by asphalt mix designs. MEPDG currently does not include any model for predicting moisture-induced damage of asphalt pavement. Rather, moisture-induced damage of asphalt concrete is addressed during the mix design stage. Mix moisture damage is evaluated through a ratio of the indirect tensile strength of a set of wet samples to that of a set of dry samples, which is based on continuum damage mechanics. There is a need for evaluating whether dynamic modulus can characterize moisture damage in a wet conditioned asphalt concrete sample. In addition, a moisture damage model based on dynamic modulus can bridge the gap between the current practice of asphalt mix design and pavement design. Such a model or correlation between pavement moisture damage and contributing factors such as temperature, pressure, number of load cycles is a long due to the pavement community.

Nationally, significant attempts have been made for determining the dynamic modulus of asphalt mixes in an effort to establish MEPDG inputs. However, dynamic modulus has not been used for determining moisture damage in wet conditioned asphalt samples over a wide range of *E** testing temperatures and moisture conditioning parameters. Solaimanian et al. 2007 have investigated moisture damage of AC using dynamic modulus test at room temperature. They conducted dynamic modulus test on moisture conditioned and dry conditioned samples at 25°C. The test temperature of 25°C was chosen considering that dynamic modulus test results show lesser variability at this temperature. Moisture conditioning was performed using an environmental conditioning system (ECS) that runs warm water at a temperature of 60°C through the specimen. *E**

4

tests were conducted using a haversine load. The conditioning temperature of 60°C was chosen to bring asphalt samples close to the field pavement temperatures and to accomplish accelerated moisture damage. The conditioning procedure is believed to partially simulate wet pavement traffic loading. Another work conducted by Nadkarni et al. (2009) investigated moisture damage of AC using dynamic modulus testing at room temperature. Nadkarni et al. (2009) investigated the possibility of using dynamic modulus in place of indirect tensile strength (ITS) test in AASHTO T 283 and found that dynamic modulus can replace the ITS test. However, in both of these studies the effects of moisture conditioning on dynamic modulus of AC at temperatures other than 25°C were not investigated. Moreover, the change in moisture-induced damage of AC with varying pavement temperatures, cycles of traffic loads, and tire pressures were not investigated. It is believed that the effect of pavement temperatures, cycles of traffic loads and tire pressures on moisture induced damage of AC can be studied by quantifying the change in dynamic modulus for a range of moisture conditioning temperatures, pressures, and cycles. Therefore, in this study it is proposed to conduct dynamic modulus testing of dry and moisture conditioned AC over a wide range of conditioning temperatures, pressure magnitude, and cycles to determine how these factors affect the wet to dry dynamic modulus of AC.

In this study, moisture damage is determined as a loss of E* in asphalt concrete. Moisture damage is believed to be caused by caused by loss in mechanical interlock, change in interfacial energy or chemical reactions that result in degradation of adhesive bond between an aggregate and the binder film. Primary contributors to loss in mechanical interlock are detachment, film rapture, pore pressure, and hydraulic scouring (Yilmaz and

5

Sargin 2012). When a newly constructed pavement is exposed to traffic loading and moisture simultaneously, high pore water pressure builds up, which ruptures asphalt film resulting in water infiltration to aggregate surface and ultimately stripping. In addition, water is pushed and pulled out of the asphalt layer whenever a vehicle tire passes over saturated pavement surface, which results in hydraulic scouring (leaching) of asphalt binder (Karlson 2005; Shah 2003). Traditional AASHTO T283 wet conditioning process lacks to capture the dynamic moisture damage resulting from leaching and film rupture because the AASHTO T283 test standard subjects asphalt samples only to one cycle of freeze-thaw and no pressurization and dynamic movement of water is induced during moisture conditioning. Recently, moisture-induced Sensitivity Tester (MIST) equipment is developed for moisture conditioning of AC by simulating pore pressure, film rupture and hydraulic scouring. Moreover, using MIST it is possible to conduct moisture conditioning at different temperatures, pressures and number of cycles. Therefore, MIST can be used for moisture (or wet) conditioning of samples at different combination of temperature, pressure, and loading cycles, and then dynamic modulus test can be performed on the wet and dry conditioned samples to investigate moisture damage resulting from pore pressure, film rupture and leaching.

1.2. Research Hypotheses

Hypothesis one
Previous studies indicate that the prediction accuracy of viscosity based Witczak model is not good. However, the underlying cause for the poor performance of the model is not known yet. It is hypothesized that optimizing the mix and binder input variables can

6

reveal the fundamental causes for the poor performance of viscosity based Witczak model and it is possible to develop a model by modifying the viscosity based Witczak model to improve the prediction accuracy.

Hypothesis two

Moisture conditioning temperature, pressure, and number of cycles are believed to affect the amount of moisture-induced damage occurring in an asphalt concrete sample. However, how and to what extent they affect moisture damage are not known. It is hypothesized that moisture-induced damage due to various conditioning temperatures, pressures and number of cycles can be quantified through laboratory dynamic modulus testing of dry and MIST conditioned asphalt concrete samples. Specifically, moisture-induced damage resulting from various MIST conditioning temperature, pressure and number of cycles can be quantified using dynamic modulus ratio (DMR) of wet to dry samples.

1.3. Objectives

The primary objectives of this study are to:

- Apply Witczak and Hirsh models to predict the dynamic modulus from mix information and determine prediction accuracy. Improve the prediction accuracy of viscosity based Witczak model by developing a modified version of the model.

- Utilize MIST conditioning coupled with dynamic modulus testing to investigate moisture damage due to pore water pressure and leaching for different combinations of moisture conditioning temperatures, pressures, and loading cycles. Conduct dynamic modulus test on three plant produced and two laboratory

7

produced NMDOT asphalt mixes. Develop models relating moisture damage in dynamic modulus with MIST conditioning cycle and pressure

1.4. Dissertation Organization

This dissertation comprises of nine chapters. Chapter 1 describes the need for the research and specific objectives. Chapter 2 provides literature review on dynamic modulus testing and currently available moisture conditioning methods. Chapter 3 presents dynamic modulus experimental program and test results, a description of asphalt material used for testing, dynamic modulus specimen fabrication procedure and dynamic modulus testing equipment. Chapter 4 presents independent assurance test results and associated statistical analysis. Chapter 5 presents the application of viscosity based Witczak model, Dynamic shear modulus based Witczak model and Hirsh model, respectively. In addition, a discussion on the predictive errors and their effects on pavement performance and a modified E^* model with emphasis on mix properties are also included. Chapter 6 presents detailed investigation of physical and chemical changes resulting from MIST conditioning and quantifying the effect of different MIST conditioning parameters on dynamic modulus. In Chapter 7, conclusions from this research and future research recommendations are given.

8

<div align="center">

Chapter 2

Literature Review

</div>

2.1. Dynamic Modulus

Dynamic modulus testing involves application of an oscillatory force (stress) to a material and measuring the resulting displacement (strain). In purely elastic materials, the stress and strain occur in phase, so that the response of one occurs simultaneously with the other. In purely viscous materials, there is a phase difference between stress and strain, where strain lags stress by 90 degree phase lag. In viscoelastic materials, the behavior is somewhere in between that of purely viscous and purely elastic materials, exhibiting some phase lag less than that for purely viscous materials. Stress and strain in a viscoelastic material can be represented using Equation (2.1) and (2.2) (Meyers and Chawla 1999):

Strain:

$$\varepsilon = \varepsilon_o \sin(t\omega + \delta) \tag{2.1}$$

Stress:

$$\sigma = \sigma_o \sin(t\omega) \tag{2.2}$$

where ω is frequency of strain oscillation; t is time and δ is phase lag between stress and strain.

Dynamic modulus is the property of viscoelastic materials. For linear viscoelastic material, the dynamic modulus is defined mathematically as the ratio of peak dynamic stress (σ_o) and the peak recoverable axial strain (ε_o), which is shown Equation (2.3) (Tashman 2004).

$$|E^*| = \frac{\sigma_0}{\varepsilon_0} \qquad (2.3)$$

where $|E^*|$ is dynamic modulus, σ_o is peak dynamic stress and ε_o is peak recoverable axial strain.

For mechanistic empirical pavement design guide (MEPDG), dynamic modulus is used as the stiffness parameter. The MEPDG incorporates this important material characteristic by developing master curve of asphalt mix. There are three input hierarchies in the MEPDG. Predictive equations are used to estimate the dynamic modulus at Level-3 MEPDG input hierarchy and no laboratory E^* testing is required. For Level 2 MEPDG input hierarchy predictive equations are again used to estimate E^* of asphalt mixes but laboratory test data is required for asphalt binder input variable. For, Level 1 MEPDG input hierarchy laboratory E^* test results and laboratory G^* test results of asphalt binder are required (Cross et al. 2009, Kim 2009).

2.2. Factors Affecting Dynamic Modulus of Asphalt Concrete

- Rate of loading

The stiffness of asphalt concrete gets higher as the rate of loading increases (Kim, 2009).

- Temperature

The stiffness of asphalt concrete decreases as the temperature increases (Kim, 2009).

- Age

Asphalt aging results in an increase of the stiffness however the brittle fracture susceptibility also increases with aging (Kim, 2009).

- Moisture

The effect of moisture and temperature on the stiffness; of asphalt concrete is similar. Both high moisture and high temperature result in plastic flow which is accompanied with decrease in the stiffness (Kim, 2009).

- Modulus of binder

Dynamic modulus of asphalt concrete has a direct relationship with modulus of binder. In a study conducted by Shu and Huang (2008) the dynamic modulus of asphalt concrete is shown to increase with increasing binder modulus.

- Modulus of aggregate

Dynamic modulus of asphalt concrete is found to have a direct relationship with aggregate modulus. In the investigation of Shu and Huang (2008), it was observed that the value of dynamic modulus continually increased with increasing binder modulus however the dynamic modulus is found to reduce beyond a thresh hold aggregate modulus of 5000MPa. This is taken by the authors to show the dynamic modulus of asphalt concrete is governed by the modulus of the binder.

11

- Asphalt content

The dynamic modulus of asphalt concrete is found to decrease with increasing binder content. The underlying cause of this phenomenon might be the increasing lubrication effect as the binder content increases leading to over lubrication. This indicates that lower level the asphalt content is one effective way of increasing the dynamic modulus (Shu and Huang 2008)

- Air voids

Shu and Huang (2008) and Kim (2009) observed that higher air void content leads to lower value in the dynamic modulus. In addition to the amount of air voids, the size and distribution of air voids also have significant effect on the dynamic modulus. Kim (2009) described the effect of small well-dispersed air voids in the mix as "micro crack arresters". Well-dispersed air voids provide enough volume for the asphalt to expand into at high temperatures but too much air will accelerate the growth of micro cracks and provides suitable access for both air and water into the interior sections of asphalt concrete layer acting as a catalyst for aging and moisture damage. On the other hand, too little air will cause bleeding and promote large plastic deformations.

2.3. Dynamic Modulus Test Methods

There are several methods to determine the dynamic modulus of a martial. These methods vary based on test control methods and test load application. The test control types can be classified in to two as: stress controlled and strain controlled. In stress controlled test a specified load is applied and resulting displacements are measured. In

stain controlled tests, precise strain amount is applied onto specimens and stress is measured. The types of loads that can be applied include axial forces, torsion and shear. In addition the testing procedure can be classified as temperature sweep, frequency sweep, or stress amplitude sweep. In the temperature sweep testes, the dynamic modulus is measured by changing the sample temperature and keeping the test frequency constant. For frequency sweep tests, the temperature is kept constant and loading frequency is varied. Stress sweep testing procedure is performed by gradually increasing the loading amplitude (Menard 1999).

Dynamic modulus test on asphalt concrete has been conducted in both stress and stain (displacement) controlled test modes and by applying axial and shear modes of loading. However, the American Association of State Highway and Transportation Officials (AASHTO) adopted the provisional test standard in TP-62, which is a uniaxial stress controlled dynamic testing procedure. Now, this test is fully developed AASHTO T 342.

2.3.1. AASHTO TP62 - Standard Method of Test for Determining Dynamic Modulus of Hot-Mix Asphalt Concrete Mixtures

The AASHTO TP 62 test standard is a stress controlled dynamic modulus testing procedure. The total test series recommended in this test standard consists of testing at five different temperatures which are -10, 4.4, 21.1, 37.8, and 54.4 ºC (14, 40, 70, 100, and 130 ºF) and six loading frequencies (0.1, 0.5, 1.0, 5, 10, and 25 Hz) at each temperature.

13

2.3.2. ASTM D3479-79 - Standard Test Method for Dynamic Modulus of Asphalt mixtures

This test method was adopted as a standard by the American Society of Testing and Materials (ASTM) in 1979. It is a stress controlled testing, in which the stress is kept constant throughout the testing frequency. The total test serious is a temperature sweep of 41, 77 and 104 ºF (5, 25, and 40 ºC) and loading frequencies of 1, 4, and 16 Hz for each temperature. Uniaxial compressive haversine load between 0 and 241 kPa is applied in the test series. The stress level is decreased as the temperature is increased to avoid damaging the specimen and to keep the specimen in the linear viscoelastic range.

2.3.3. Confined Dynamic Modulus Testing Protocol

Confined dynamic modulus test follows the same test procedure as that of AASHTO TP 62. The only difference is the application of confinement pressure. Typical confining pressures applied are on the order of 138 kPa and 206 kPa. Due to the additional complexity of testing, confined dynamic modulus tests are difficult to perform than unconfined dynamic modulus tests. Confined dynamic modulus test is found to be better to categorize and contrast the field performance of dense- graded, gap- graded and open- graded mixtures (Sotil et al. 2004, Sotil 2003 and Pellinen 2001).

Sotil et al. (2004) conducted confined dynamic modulus tests and found that the unconfined and confined dynamic modulus test results have a linear relationship with the applied bulk stress and were almost parallel regardless of the confinement level. Seo et al. (2007) also compared the dynamic moduli determined from unconfined and confined axial compression tests on specific mixture and determined that the effect of confinement

is significant at a high temperature and/or low loading frequency. They showed that as the temperature increases or loading frequency decreases, the asphalt binder becomes softer and the effect of confinement on the aggregate structure becomes more significant which makes the asphalt–aggregate mixture more resistant to stress and, thus, resulting in a greater dynamic modulus for the triaxial test than the uniaxial test. In addition, they have found that the effect of confinement is greater for the mix that has larger aggregate particles.

2.3.4. Simplified Dynamic Modulus Testing Protocol

The AASHTO TP62 test procedure requires testing at least two replicate specimens at five temperatures 14°F, 40°F, 70°F, 100°F, and 130°F (−10°C, 4.4°C, 21.1°C, 37.8°C, and 54.4°C) and. and six loading rates of 25, 10, 5, 1.0, 0.5, and 0.1 Hz. Bonaquist and Christensen (2005) observed that there is a large amount of overlap in the measured data from this test method that is not needed for the development of the master curve. With that drive, they have come up with an alternative testing protocol which requires testing at only three temperatures 40°F, 70°F, and 115°F (4.4°C, 21.1°C, and 46.1°C), and four rates of loading 10, 1, 0.1, and 0.01 Hz. The master curve obtained from this procedure was also shown to be comparable with that of the standard test. For mastercurve development, the maximum dynamic modulus of AC is estimated using the Hirsch model. Using maximum binder modulus in the Hirsch model the range for maximum mixture modulus is estimated to be from about 3,000,000 psi (20.6 GPa) for mixtures with very high void in mineral aggregate (VMA) and low voids filled with asphalt (VFA) to about 3,800,000 (26.2 GPa) for mixtures with low VMA and high VFA.

15

2.3.5. Dynamic Shear Modulus (*G**) test / Simple shear (SST) test

The SHRP research program developed shear frequency sweep test and it is performed using the simple shear tester (SST). "The test protocol was first introduced as SHRP Designation M-003: Standard Method of Test for Determining the Shear Stiffness Behavior of Modified and Unmodified Hot Mix Asphalt with Superpave Shear Test Device. Later the test protocol was adopted by the American Association of State Highway and Transportation Officials (AASHTO) as a Provisional Standard TP7-94 (Kim 2009).

The SST test is conducted by applying a shear load to a specimen with a diameter of 150 mm and 50 mm height. The specimen is glued on top and bottom to platens and shearing action is applied from the bottom. The test is stain controlled with a maximum applied stress of 100 micro stains. The test temperatures are 4, 20 and 40°C. At each temperature a sinusoidal shear stain is applied with maximum frequency of 10 Hz and minimum frequency of 0.1 Hz. while the shear strain is applied sufficient compressive or tensile load is also applied to keep the specimen height constant (Kim 2009).

2.3.6. Resilient Modulus Test in Indirect Tensile test mode

Kim et al (2009) derived a relationship to determine uniaxial dynamic modulus data from repeated resilient modulus test in an indirect tensile mode. The main motivation for this work is the luck of field cores meeting sample size requirements for dynamic modulus test. The AASHTO TP-62 test procedure for dynamic modulus test requires a sample with 150mm height. This is often impossible to get from field coring since most pavements are constructed with less thickness. This greatly reduces the use of dynamic

16

modulus testing for investigating pavement condition. However, with the linear viscoelastic solution derived by Kim et al (2009), it is possible to conduct the IDT test and derive dynamic modulus data.

2.3.7. Hollow cylinder tensile test (HCT)

Buttlar et al. (2002) explored the feasibility of using the HCT to obtain the dynamic modulus of asphalt concrete and found that the HCT device related well with dynamic modulus measurements obtained with uniaxial compression testing apparatus at 0°C and 20°C. In addition, the Witczak dynamic modulus predictive equation results are found to be in reasonably accurate agreement with the test results of the HCT. The Hollow cylinder tester (HCT) is developed with a desire to have an alternative test for the indirect tensile test (IDT). The test is conducted by applying pressure to the internal wall of a hollow cylindrical specimen using flexible membrane. The applied pressure produces hoop stress on the wall of hallow cylindrical specimen. By implementing closed form solutions for thick walled cylinders the tensile strength and creep compliance are calculated from the raw measurements. The stain is either measured by the use stain gauges or directly calculated from the volume change of the cavity. The specimen size is 115mm height by 150mm outside diameter and 106mm inside diameter.

2.4. Moisture Damage Test Methods

Several test methods are available to quantify moisture damages in asphalt concrete. These methods can be qualitative or quantitative tests. Qualitative tests include boiling water test, freeze-thaw pedestal test, quick bottle test and rolling bottle test while quantitative tests include immersion compression test, indirect tensile test, marshall

17

immersion test, double punch test and resilient modulus test. Moisture sensitivity tests can also be conducted on loose and compacted samples. Loose mix moisture sensitivity testes include methylene blue test, film stripping test, static immersion, dynamic immersion test, chemical immersion test, surface reaction test, quick bottle test, boiling water test, rolling bottle test, net adsorption test, surface energy and pneumatic pull-off test. Some of the moisture sensitivity testes on compacted samples are moisture vapor sensitivity test, immersion compression test, marshall immersion test, freeze-thaw pedestal test, original lottman indirect tensile test, modified lottman indirect tensile test, tunicliff-root test, environmental conditioning system with resilient modulus test, hamburg wheel tracking test, asphalt pavement analyzer and multiple freeze-thaw (Solaimanian et al. 2003).

2.4.1. Immersion-Compression Test

Immersion-compression test is adopted as ASTM D1075 and AASHTO T165. In this test one group of dry and one group of wet samples are used. The wet samples are immersed for 4 days at 49 °C (120 °F). Alternatively, a quick test can be done by immersing for 24 hr. at 60 °C (140 °F). Compressive strength test is done for specific deformation rate and temperature. The average strength of conditioned sample with dry sample is used as an indicator of moisture sensitivity in the mix (Solaimanian et al. 2003, ASTM D1075, AASHTO T165-2006).

2.4.2. Moisture Vapor Susceptibility

Moisture vapor susceptibility test is done on two specimens prepared in stainless steel mold by kneading compactor. The compacted surface of each specimen is covered with

18

aluminum seal cap. The sample is then placed in to 60°C temperature water for 75 hours. After conditioning the sample is tested in Hveem stabilometer (Solaimanian et al. 2003).

2.4.3. Lottman Indirect Tension Test

In this procedure samples are separated in to dry and wet groups. Sample size is 100 mm (4 in) diameter and 63.5mm (2.5 in) thick. The sample is initially vacuum saturated by applying 660 mm mercury (26 in mercury) vacuum pressure for 30 min and is kept at atmospheric pressure for the next 30 min. Afterwards, accelerated freeze–thaw saturation is done by putting the sample into water bath of -18°C (0°F) for 15 hr followed by 60°C (140°F) for 24 hr. then the sample is tested for tensile resilient modulus or indirect tensile test at 13°C (55°F) with 1.7 mm/min (0.065 in/min) loading rate or at 23°C (73°F) with 3.8 mm/min (0.150 in/min) loading rate. The sensitivity of moisture is measured by determining the strength ratio of wet and dry. This test is adopted as AASHTO T283 with some modification. The first difference between the original and modified Lottman test is the vacuum saturation is continued until the saturation level reaches to 70% to 80% range. The second difference is the loading rate and the testing temperature. The modified test requires 1.7 mm/min (0.065 in/min) loading rate for 13°C (55°F) or 50.8 mm/min (2 in/min) loading rate for 25°C (77°F). Higher loading rate and temperature is selected to conduct the test using Marshall Stability tester (Solaimanian et al. 2003, AASHTO T283-2007).

2.4.4. Modified Texas Freeze–Thaw Pedestal Test

This test is performed on compacted specimen with 41 mm (1.6 in) diameter and 19 mm (0.75 in) thickness. The asphalt mixes for this test are limited to contain aggregates

19

passing 0.85mm (#20) sieve and retained on 0.5 mm (#35) sieve to minimize test result variation due to aggregate size variability. For moisture conditioning, samples are first submerged for 3 days at room temperature in distilled water. Then, the samples are exposed to thermal cycles of 15 hr freezing at -12°C (10°F) and 9 hr thawing at 49°C (120°F) until visible cracks are detected (Solaimanian et al. 2003).

2.4.5. Environmental Conditioning System (ECS)

The ECS is developed to simulate actual field temperature, moisture and traffic loading conditions in the laboratory. Samples with 102±4 mm diameter and 102±4 mm thickness and 7.5±0.5% air void are recommended to be used for ECS conditioning. To evaluate the moisture susceptibility of the compacted sample, first, Resilient Modulus (MR) test is performed on a dry sample with haversine wave loading (loading period = 0.1 sec and rest period = 0.9 sec). After measuring the dry MR, the sample is then saturated using three cycles of pulling of distilled water through the sample at 60 °C for 6 h followed by 25 °C distilled water for 2 h. then, the wet MR is determined. If the ratio of conditioned sample MR is less than 70% of unconditioned sample MR, the sample is deemed moisture susceptible (Solaimanian et al. 2003).

Recently, NCHRP project 9-34 compared moisture sensitivity test results from the use of ASTM D4867, AASHTO T-283 and dynamic modulus coupled with environmental conditioning system (ECS). The results showed superior reproducibility for ECS/dynamic modulus method compared with ASTM D4867 and AASHTO T-283. However, ECS/dynamic modulus test method still takes a long time (more than 18 h) to complete moisture conditioning (Solaimanian et al. 2007).

From the literature review presented above, it is clear that there are several methods to quantify the moisture sensitivity of asphalt concrete and all methods including ECS/dynamic modulus take a long time reaching up to days to complete moisture conditioning. Moreover, in all cases the dynamic pour water pressure cycles created by passing vehicle tires is not captured. The experimental program undertaken in the present study attempts to address these shortcomings by combining the dynamic modulus testing with Moisture Induced Sensitivity Tester (MIST).

2.4.6. Moisture Induced Sensitivity Tester (MIST)

Moisture Induced Sensitivity Tester (MIST) applies repeated pore water pressure stressing to a compacter asphalt concrete sample (InstroTek, Inc, 2012). Many researchers have described pore pressure as one of the mechanisms for stripping in asphalt concrete (Karlson 2005, Shah 2003, Tarrer and Wagh 1991, Parker 1989, Birgisson and Massad 2005, Kutay and Aydilek 2007, Yilmaz and Sebnem 2012, Jiang et al. 2012).

Theoretically, stripping can be a result of mechanical interlock detachment, chemical reaction or interfacial energy incompatibility processes. Among the three theoretical explanations, pore pressure build up contributes to stripping primary through mechanical process. The process by which pore pressure cycles result in degradation of pavements in the field is due to the compaction of asphalt concrete with traffic loading, which results in pore pressure build up when the pavement is saturated. Stripping due to pore pressure cycles mostly affects newly constructed pavements since during construction new pavements are compacted to an air void content higher than design specification with the

21

assumption that initial traffic loading will bring the air void level to design specified values. However, when the pavement gets saturated during this period, some of the moisture will be trapped in the voids and more compaction will result in an increase of pore pressure. In the event, high pore pressure occurs; the thin asphalt film ruptures and allows water to infiltrate to the aggregate surface resulting in stripping (Yilmaz and Sebnem 2012).

MIST simulates the cycles of pore pressure build up by increasing and decreasing the pressure in a cylindrical chamber filled with water, in which the asphalt sample is kept. Figure 2.1 (a) shows a photographic view of asphalt concrete sample placement in the MIST chamber and Figure 2.1 (b) depicts the mechanism used to simulate the effect of pore pressure on asphalt concrete using the MIST equipment. The pressure inside the chamber is increased and decreased by inflating and deflating the diaphragm using a hydraulic pump and piston mechanism at the bottom of the chamber. When the diaphragm is inflated, the Solenoid valve gets closed and the entire chamber pressure is increased. To let air bubbles leave the chamber, the Solenoid valve opens when pressure is released. During pressurizing two phenomena occur. One, water is pushed into the compacted asphalt sample and some part of the entrapped air is displaced. Second, part of the entrapped air is compressed. Then, during depressurizing, the compressed air expands and pushes some of the water out of the voids. This leads to an increase of pressure in the pores, gradual displacement of entrapped air in the pores and scouring of asphalt. Thus, the MIST simulates the action of an automobile tire in creating pore water pressure build up and scouring in field pavements (InstroTek, Inc, 2012).

(a) Photographic View
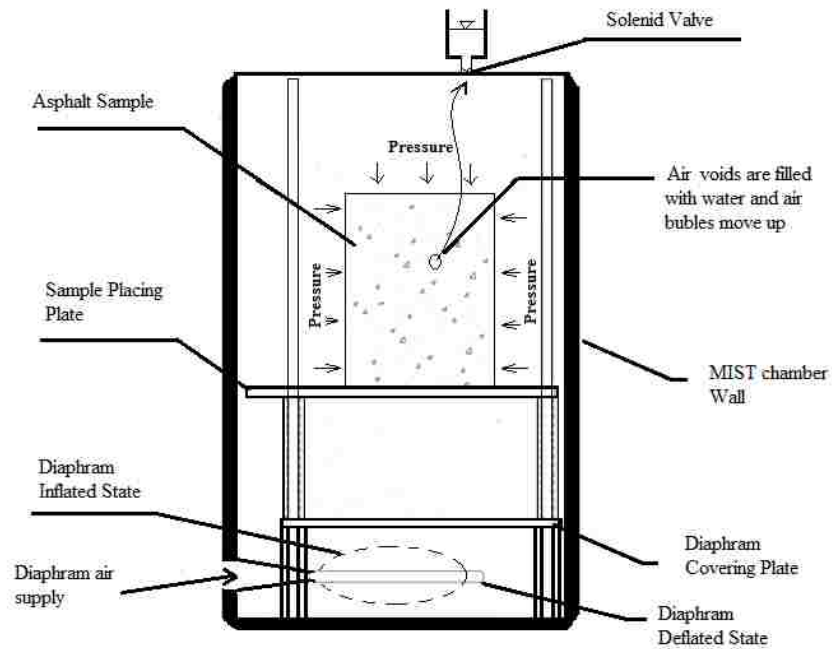
(b) Conditioning Mechanism

Figure 2.1 Moisture Induced Sensitivity Tester (MIST)

23

Chapter 3

Dynamic Modulus Testing for New Mexico Asphalt Mixes

3.1. Introduction

This chapter is dedicated to martial description, sample preparation, and dynamic modus testing of New Mexico asphalt mixes. In this study the dynamic modulus testing is used to characterize the mechanical properties of asphalt concrete in the linear viscoelastic range. Dynamic modulus is a well-used material property for viscoelastic material; however its use in the asphalt industry is relatively new. The provisional standard TP-62 "Standard Method of Test for Determining Dynamic Modulus of Hot-Mix Asphalt Concrete Mixtures" from the American Association of State Highway and Transportation Officials (AASHTO) was used as a guide to conduct the tests.

3.2. Objective

The objectives of this study are to:

- determine dynamic modulus values for New Mexico asphalt mixes
- develop mastercurves for New Mexico Asphalt mixes

3.3. Test matrix

Table 3.1 presents the test matrix adopted for dry conditioned dynamic modulus (E^*) testing. For this study, E^* test is performed on specimens prepared from five different asphalt mixtures. Three of the asphalt mixtures are plant mixed Superpave mixes and the

24

other two are laboratory prepared mixtures. The plant mixes are SP-II mix with binder grade PG 64-22, SP-III asphalt mix with PG 70-22 and SP-IV mix with binder grade PG 70-22, while the laboratory mixes are SP-III mix with PG 64-22 and SP-II with binder PG 70-22. *E** testing is performed at five temperatures (14, 40, 70, 100, 130 °F) and six frequencies (25, 10, 5, 1, 0.5, 0.1 Hz). This gives a total of 30 dynamic modulus test results per specimen. For each mix type six replicate samples are tested.

3.4. Dynamic Modulus Testing System

Figure 3.1 presents GCTS ATM-025 Servo-Hydraulic testing system available in the pavement laboratory of the University of New Mexico. The equipment is capable of producing controlled haversine compressive loading up to 100 Hz frequency. The top actuator has a dynamic load capacity of 25 kN and a stock of the top actuator 100 mm. The system is also equipped with an environmental chamber capable of controlling temperature over the range of -30 °C to +150 °C. The system has its own air conditioning unit and the temperature in the chamber can be controlled with an accuracy of ± 0.5 °C. The GCTS ATM-025 is controlled with a digital servo controller SCON-2000. The SCON-2000 is capable of controlling even when the interface computer is shut down. It has a capacity of controlling up 24 sensors. The control system has a maximum of 6Hz loop rate and 300 kHz conversion rate between channels. For dynamic modulus testing top actuator is connected with a load cell that is capable of measuring loads up to 25kN with a resolution of 5N.

25

3.5. Mix collection and Sample Fabrication

3.5.1. Mix Collection

With aim of collecting Superpave HMA mixes that are widely used in the design and construction of roads in the state of New Mexico, Superpave HMA mixes are collected from an actual construction site in cooperation with the New Mexico Department of Transportation research bureau.

SP-III and SP-II Superpave asphalt mixes sampling was conducted from the Materials Plant for Tramway Blvd to Benallio road reconstruction project. The Project is widening of I-25 from two to three lanes each way from Tramway Boulevard on Albuquerque's north side to the southern exit at Bernalillo with a total length of 7.7 miles. These mixes are prepared in the mixing pant and sampling was performed from windrows of the actual pavement construction as per the requirements of AASHTO T-168. SP-IV mix is collected at a later date from a commercial mix at Lafarge Mix plant in Albuquerque.

In addition to the mix collection virgin aggregates, binders and recycled asphalt samples are also collected. The aggregates source for SP-II and SP-III mixes is the Santo Domingo Pit located in Sandoval County and for SP-IV mix a combination of pits in Bernalillo County are utilized. Sampling of these aggregates is done according to AASHTO T-2. The main source of Recycled Asphalt Concrete (RAP) for SP-II and SP-III mixes is milling from the old I-25 road. Sampling of RAP is also done according to AASHTO T-2 from the RAP pile present in the mix plant. Binder samples for the two binder grades PG 70-22 and PG 64-22 are also collected.

3.5.2. Sieve Analysis Test (AASHTO T-27)

Aggregate distribution of the SP-II, SP-III and SP-IV mix aggregates is studied as per the requirements of AASHTO T-27. Samples are obtained by burning off respective SP-II, SP-III and SP-IV asphalt mix samples. The results are plotted in 0.45 powers Gradation Chart as presented in Figure 3.2.

3.5.3. Asphalt content (AASHTO T-308)

Asphalt content test for all plant mixes is also conducted as per the requirements AASHTO T-308. The average asphalt content was found to be 4.61% for SP-III plant mix, 4.42% for SP-II plant mix and 6.27% for SP-IV mix. Table 3.2 shows asphalt content test results.

3.5.4. Theoretical Maximum Gravity (G_{mm}) (AASHTO-T-209)

The theoretical maximum specific gravity of the mixes is determined using mass determination in air method outlined in AASHTO T-209. Testing Apparatus used for this test include: vacuum Pump, Balance, Vacuum flask, Vacuum gauge, water bath and drying oven. The volumetric flask is standardized over the range of water bath temperatures likely to be encountered and a water bath with temperature control is used to keep the water at constant temperature. A number of replicate tests were conducted to check for operator precision and the average result is also compared with data provided in the specification sheet. The results were found acceptable both for single operator precision as well as multi laboratory precision. Table 3.3 provides theoretical maximum gravity test results for the five types of asphalt mixtures used in this study.

27

3.5.5. Sample Compaction (AASHTO T-312)

Superpave Gyratory Compactor (SGC) is used to compact samples as per the recommendations of AASHTO T-312 and current mix design methods. Figure 3.3 shows the gyrator compactor used to compact asphalt mixtures. The SGC is a preferred method of compaction for dynamic modulus sample preparation since it is the best available laboratory compaction method to produce samples with similar characteristics as in the field.

The pine Gyratory compaction machine is used to compact a 150mm diameter and 170 mm height sample. The compaction temperature used to achieve a viscosity of 280±30 is selected according to the binder grade used and the handling temperature shown in Table 3.4. Several trial gyratory specimens are prepared with the aim of achieving 5.5±0.5% air void for the inside core. The compaction is controlled using minimum height of 170mm (6.7in) and the maximum number of gyrations equal to 160. Compacting the 170mm x 150mm sample at 10.5% air void is found to give the desired air void for the inside core. The sample used for compaction is about 6500gm. Compacted samples are cooled off and left for about 16hrs to gain strength.

3.5.6. Coring and Trimming

A 100 mm (4 in) diameter sample is cores out of the 150mm diameter gyratory compaction sample using the GCTS coring machine. Figure 3.4 shows the coring machine with an illustrative cored specimen. The coring machine is water cooled and it is fit with diamond edged drilling barrels for drilling out 100 mm (4 in) diameter test specimens. The coring rate is pressure controlled and the drilling motor is electric

28

controlled. The drilling motor has a 1.5HP and adjustable spindle speeds. The ends of the cored 100 mm (4 in) diameter samples are then trimmed off using a diamond cutting edge wet saw. Figure 3.5 shows the diamond cutting edge wet saw that is used to cut specimens. The saw system is equipped with 3HP electric motor, diamond edge cutting blade, pressure controlled automatic feed and a specimen holding setup. It is also completely covered in a rectangular hood for safety.

3.5.7. Bulk Specific Gravity (G_{mb}) (AASHTO T-166)

Bulk specific gravity is determined for all samples according to the AASHTO T-166. Bulk specific gravity and theoretical maximum gravity are required to determine the air void of compacted asphalt mixtures. The bulk specific gravity of each sample used for dynamic modulus testing is presented in Table 3.5.

3.5.8. Percent Air Void Determination (Volumetric calculation)

To determine the air voids in the sample theoretical maximum gravity (G_{mm}) and Bulk Specific gravity (G_{mb}) of the samples are utilized as using the air void relation given in Equation (3.1). Sample air voids (%Av) of all samples used for dynamic modulus test are provided in Table 3.6.

$$\%A_v = \left(1 - \frac{G_{mb}}{G_{mm}}\right) * 100 \tag{3.1}$$

3.5.9. Air Void Uniformity Check

The air voids of three samples are checked for uniformity. The air voids of the top and bottom section are compared with the middle section air void to determine the

29

significance of the difference. The test results and statistical analysis calculations are presented in Table 3.7. As can be seen from the analysis the air voids of the top and bottom sections are not significantly different from the middle section. This indicates that the cored sample has uniform air void distribution throughout.

3.5.10. Fixing Loading Buttons

LVDT mounting buttons are then glued to the specimen meeting all air void and sample geometry requirements. Five minute epoxy is used to fix the LVDT mounting buttons on to specimens. The gauge length is maintained to be 100mm (50mm away from the mid height of the specimen on each side) using the automatic positioning fixture shown in Figure 3.6. This helps to maintain consistent position for all LVDTs on the specimen.

3.5.11. E^* Test Specimen Geometric Requirements

The samples prepared for dynamic modulus should meet geometry requirements in addition to the desired air void. Geometric parameters mentioned to be checked for specific requirements in the AASHTO TP-62 provisional standard are sample diameter, height, end perpendicularity and waviness.

The diameters of each specimen at the middle, top and bottom sections along two axes 90 degree apart are recorded. The means and standard deviations are calculated and compared with the AASHTO TP 62-07 requirements; which states that the average of recorded diameters should be between 100 and 104 mm. In addition, the standard deviation for the average should not be greater than 2.5mm.

30

The ends of all samples are checked for perpendicularity and waviness requirements right before testing as well. Perpendicularity is checked at two perpendicular axes of both top and bottom ends by using the rock flatness gauge shown in Figure 3.7. Waviness is checked by using a straightedge and feeler gauge shown in Figure 3.8. The AASHTO recommended tolerance for waviness is 0.05 mm across three axes 120 degrees apart. Moreover, the specimen end should not depart from perpendicular by more than 1.0°.

3.6. Test Setup

Different test setup techniques have been used in the past and currently the use of spring loaded LVDTs are recommended in the AASHTO TP-62. AASHTO TP-62 recommends to measure deformation at a minimum of two locations 180° apart and by increasing the LVDTs to three locations located 120° apart the required number of replicates for testing can be reduced. For testing in this study two spring loaded LVDTs are used. The deformation range of these LVDTs is ± 0.5mm and the resolution is 0.0025mm. Figure 3.9 shows the specimen set up with two LVDTs mounted 180º apart.

End treatments are used instead of capping between specimen ends and platens. Even though, capping is recommended in the ASTM test standard for dynamic modulus, Witczak et al. (2000) recommends avoiding capping and using friction-reducing treatments between the specimen ends and the platens. Recommended end treatments in the AASHTO TP-62 provisional test standard is to use a sandwich of two 0.5-mm-thick latex sheets separated with silicone or vacuum grease.

31

3.7. Test Procedure

First Axial LVDTs are attached to the specimen and adjusted to extend up to at least the middle of the linear range to make sure that enough of the range is available for the accumulation of compressive permanent deformation. Then specimen is conditioned to reach to the desired temperature. This is achieved by keeping the specimen in the environmental chamber and allowing it to equilibrate to the specified testing temperature. A dummy specimen with a thermocouple mounted at the center is also used to monitor the specimen temperature. Minimum recommended temperature equilibrating time in the AASHTO standard is also strictly followed.

The specimen is centered with the hydraulic load actuator visually in order to avoid eccentric loading and then a contact load equal to 5 percent of the dynamic load is applied. Then eccentricity is checked at the conditioning stage by applying 50 percent of the required load and observing the response from the LVDTs. The position of the specimen is moved and adjusted very carefully to balance the LVDT measurements. Then, once the deformations are uniform, the full haversine loading is applied to the specimen. The full dynamic load is adjusted to produce axial strains of about 55 microstrains. The AASHTO recommended stain range is between 50 and 150 microstrain. The testing dynamic load increases as the stiffness increases which in turn increases as the temperature decreases. The general range recommended for the entire dynamic modulus test over all temperatures is between 15 and 2800 kPa (2 and 400 psi).

Two minute rest period between frequencies in the frequency sweep is applied during testing. This is mainly because the controller used cannot produce continuous frequency

sweeps and each frequency is programmed separately in such a manner that there will be some lag time or rest period between each frequency. According to kim et al (2009), even though applying rest period helps to prevent specimen from heating up too much during cyclic testing the application of rest period allows some of the transient strains to recover during testing which may have some effect on the measured modulus values and selection of suitable data analysis methods.

Dynamic modulus testing is conducted at -10, 4, 20, 40, and 54 °C (14, 40, 70, 100 and 130°F). at each temperature a frequency sweep test of 0.1, 0.5, 1.0, 5, 10, and 25 Hz is applied. Testing is conducted starting at the lowest temperature. Within each temperature testing is conducted staring at the highest frequency and proceeding to the lowest frequency. Therefore, the last frequency and temperature combination is the highest temperature with the lowest frequency.

3.8. Test results and Analysis

3.8.1. Raw Data

The data collected using the SCON 2000 data acquisition system are the time, axial force and the displacements of the linear variable differential transducers (LVDT). Even though the system is capable of collecting and storing the entire set of test, to reduce load on the system and increase efficiency, the stored data is only for the last five cycles. Therefore, time is the time period from the last to five cycles to the end of the testing time for each frequency. The axial force is the vertical load applied on the specimen. This is measured using the attached load cell. The displacements of the two LVDTs is recorded and stored separately. However, for the calculation of strain the average of the

33

two is taken. The axial gage length of the LVDTs is100 mm and two LVDTs are mounted on a specimen surface. Actual stress under which the specimen is exposed to for each test condition is calculated dividing the axial force by the calculated area of the specimen. In same fashion, the displacements from the LVDTs are divided by the axial gage length to get the actual axial strain. Figure 3.10 is typical stress and strain versus time plots on a GCTS CATS software interface.

Dynamic modulus values are calculated by determining the stress amplitude and strain amplitude from the sinusoidal curves. The phase angle is determined by determining the difference of the phase angles of the strain and stress sinusoidal curves.

- The peak stress (σ_o) is defined as:

$$\sigma_o = \frac{\bar{P}}{A} \tag{3.2}$$

$where$: $\bar{P}$ is average of the last five load amplitudes; A is area of the specimen

- Recoverable axial strain (ε_o) is defined as :

$$\varepsilon_o = \frac{\bar{\Delta}}{GL} \tag{3.3}$$

$where$: $\bar{\Delta}$ is average of the last five deformation amplitudes; GL is gauge length

- Dynamic Modulus $|E^*|$ is defined as:

34

$$|E^*| = \frac{\sigma_o}{\varepsilon_o} \tag{3.4}$$

- Phase angle (ϕ) is defined as:

$$\phi = \frac{t_i}{t_p} * 360 \tag{3.5}$$

$where$: t_i is average lag between a cycle of stress and strain (sec); t_p is average time for stress cycle (sec).

3.8.2. Dynamic Modulus Data Analysis and Presentation

Dynamic modulus data can be presented with Isothermal and Isochronal curves, mastercurves. Isothermal and Isochronal curves are important to check the trends of the data and identify errors readily. The mastercurve is a representation of dynamic modulus data in one smooth curve in frequency/time domain by using time temperature superposition principle (TTSP).

By applying TTSP dynamic modulus data at different temperatures are moved horizontally on the loading time or frequency scale to produce one smooth curve dependent only on loading frequency or time. The amount by which dynamic modulus data is shifted to fit in a smooth curve at a reference temperature is referred to as shift factor *a(T)*. Shifting is achieved by dividing the loading time by the shift factor to get the reduced time as shown Equation (3.6) in the time domain or multiplying the loading

35

frequency by the shift factor to get the reduced frequency as shown in Equation (3.8) in the frequency domain. The smooth curve that is developed by shifting the dynamic modulus data is referred to as master curve. The master curve can be developed for any reference temperature chosen arbitrarily. At the reference temperature the shift factor is one or its logarithm is zero. The use of TTSP to develop master curve have two advantages: the first and foremost is it reduces the three dimensional data (dynamic modulus, loading time/frequency and temperature) in to two dimensional data by eliminating the temperature variable. This makes it easy to compare test results conducted at different conditions. The other advantage is the possibility of interpolation to get intermediate data within the test data range (Kim 2009).

$$t_r = \frac{t}{a(T)} \tag{3.6}$$

$$\log(t_r) = \log(t) - \log[a(T)] \tag{3.7}$$

$$f_r = f * a(T) \tag{3.8}$$

$$\log(f_r) = \log(f) + \log[a(T)] \tag{3.9}$$

3.8.3. Shift Factor Functions

Different shift factor functions have been used to fit the shift factors trend. The Arrhenius equation, the Williams, Landel, and Ferry (WLF) equation, Modified Kaelble equation and Second degree polynomial have shown good performance to implement the time temperature principle for both asphalt binders and asphalt concrete test data (Kim 2009).

- Arrhenius equation

The Arrhenius equation is represented by the following equation. Different values ranging from $44kJ/mol$ to $205kJ/mol$ are reported in the literature for the activation energy of asphalt binders. C is also reported to have values of $10920K$, $13060K$ and $7680K$ (Rowe and Sharrock 2010).

$$\log a_t = C\left(\frac{1}{T} - \frac{1}{T_{ref}}\right) = \frac{E_a}{2.203 * R}\left(\frac{1}{T} - \frac{1}{T_{ref}}\right) \qquad (3.10)$$

where C is a material constant (K); E_a is the activation energy (J/mol); R is the ideal gas constant ($8.314 \frac{J}{mol} * K$) ; T is the experimental temperature (K); T_{ref} is the reference temperature and the value 2.303 is the natural logarithm of the number 10.

- Williams, Landel, and Ferry (WLF) equation

Rowe and Sharrock (2010) recommend using the WLF equation near the glassy temperature(T_g) of the material. The WLF equation is given in the following equation:

$$\log a_t = \frac{-C_1(T - T_{ref})}{C_2 + (T - T_{ref})} \qquad (3.11)$$

$where$: C_1 and C_2 are constants that depend on the material properties and reference temperature.

37

- Modified Kaelble equation

Rowe and Sharrock (2010) developed an alternative equation to fit shift factors. The function they developed is termed as the modified kaelbel equation and is given as follows:

$$\log a_T = -C_1 * \left(\frac{(T - T_d)}{C_2 + |T - T_d|} - \frac{\left(T_{ref} - T_d\right)}{C_2 + \left|T_{ref} - T_d\right|} \right) \tag{3.12}$$

- Second degree polynomial

Another function that is available for fitting the shift factor data is a second degree polynomial as given in the following equation;

$$\log a_T = aT^2 + bT + c \tag{3.13}$$

3.8.4. Master Curve Fitting

The function that is predominantly used for developing mastercurve for dynamic modulus data covering a wide range of temperatures is the sigmoid function. The sigmoidal function is given in Equation (3.14). Parameter γ in the equation indicates the steepness of the function (that is how fast the modulus is changing from the minimum value to the maximum) and parameter β shows the horizontal position at which the rate of change of modulus changes form positive to negative. The parameter δ on the other hand is associated with the minimum value of asphalt mix modulus which is caused by high temperatures. At high temperatures the modulus of the binder becomes insignificant and aggregate interlock starts to play a significant role in the compressive stiffness. This

38

behavior of asphalt mix is captured by the parameter δ. The highest mix modulus which is associated with binder modulus at very low temperature is represented in the sigmoidal function by the sum of parameters δ and α, $\delta + \alpha$. This highest modulus is also referred to as glassy modulus (Kim 2009).

$$\log(|E^*|) = \delta + \frac{\alpha}{1 + e^{\beta - \gamma \log(t_r)}} \tag{3.14}$$

where $|E^*|$ is dynamic modulus; t_r is reduced frequency; δ is minimum modulus value; α is span of modulus values; β, γ are shape parameters.

There are different methods that can be used to fit the sigmoidal function to shifted dynamic modulus data. Witczak and sotil (2004) have investigated a variety of methods and recommended to optimize all four parameters of the sigmoidal function together with the three coefficients of the polynomial shift factor function. This method is only dependent on dynamic modulus experiment and the form of the shift function is not forced to the mastercurve. The sigmoidal function of the mastercurve can be fitted using solver function in the Excel spreadsheets program.

- Experimental E^* Master Curve fitting steps

The following procedure adopted from Witczak and Sotil (2004) is used to develop the master curve. All calculations can be performed using MS excel spread sheet.

Step 1: Determine the Logarithm of test frequency and dynamic modulus

39

Step 2: Choose the reference temperature. For example 21 °C reference temperature can be chosen.

Step 3: Give initial estimate of shift factors for each temperature case and program excel with if statement to change the values for each temperature in the iteration process. Dynamic modulus test in this study is conducted at five temperatures, -10° C, 4° C, 21° C, 37° C, 54° C. The following equations used in the MS-excel program.

$$a(t) = \frac{f_T}{f_{T_o}} \tag{3.15}$$

$$f_r = f_T = a(t) * f_{T_o} \tag{3.16}$$

$$log(f_r) = log\{a(t)\} + log(f_{T_o}) \tag{3.17}$$

Step 4: Choose initial values for the master curve parameters. A symmetrical sigmoid function is chosen for the mastercurve fitting in this study and initial value of one is used for the parameters α, β, γ and δ.

$$\log(|E^*|) = \delta + \frac{\alpha}{1 + e^{\beta + \gamma \log(fr)}} \tag{3.18}$$

Step 5: Calculate the coefficient of determination. To evaluate the goodness of fit for the iteration results of the solver function it is required to minimize the sum of error squared values and the final result goodness of fit can be evaluated by the coefficient of determination given in the following equation.

$$R^2 = 1 - \frac{SS_{err}}{SS_{tot}} = \frac{\sum_i^n (y_i - \bar{y})^2}{\sum_i^n (y_i - f_i)^2} \qquad (3.19)$$

where R^2 = Coefficient of determination; y_i = Data set has values; f_i = Modelled value;

$\bar{y} = \frac{\sum_i^n y_i}{n}$

3.9. Dynamic Modulus Results for SPIII with PG 70-22 (Plant Mix)

The dynamic modulus test result on six samples prepared from SP-III mix with binder grade of PG 70-22 is presented in tabular and graphic form in Appendix A. A summarized depiction of all data represented by mastercurves developed for each test is shown in Figure 3.11. The test results from the six samples were averaged and Figure 3.12 and Figure 3.13 are isothermal and isochronal plot of the average data respectively. As can be seen from the Isothermal and isochronal Curves the trend of dynamic modulus is found to be decreasing with increasing temperature and increasing with increasing frequency. Then, the master curve is developed for the average of all test results and presented in Figure 3.14. Experimental fitting of the sigmoid function has shown very good fit to the shifted data. Polynomial function is used to fit the shift factor results and it is shown in Figure 3.15.

3.10. Dynamic Modulus Results of SPIII Mix with PG 64-22 (Laboratory Mix)

Dynamic modulus tests were also conducted on specimens compacted from laboratory prepared SP-III hot mix asphalt mixes. For this mix the aggregate gradation is kept the same as SP-III plant mix and the binder grade is changed to PG 64-22. Dynamic modulus tests are conducted on six specimens prepared from this mix and all the results are given

41

in Appendix B. Mastercurves of all six specimens is summarized in Figure 3.16. the results are averaged and the tends of dynamic modulus with temperature and frequency are analyzed using isothermal and isochronal plots as presented in Figure 3.17 and Figure 3.18 respectively. The averaged results showed trends that are similar with the previous SP-III Plant mix. The dynamic modulus reduced as temperature is increased and increased with increasing loading frequency. The mastercurve for this mix is presented in Figure 3.19 and polynomial shift factor fit plot in Figure 3.20.

3.11. Dynamic Modulus Results of SPII Mix with PG 64-22 (Plant Mix)

The dynamic modulus test results on six specimens of plant mixed SP-II HMA with binder grade of PG 64-22 is presented in tabular and graphic form in Appendix C. the summery of all test results is given in master curve format in Figure 3.21. The trend analysis is done using Isothermal and Isochronal plots as presented in Figure 3.22 and Figure 3.23 respectively. The dynamic moduli tend with respect to temperature as well as with respect to frequency are found to agree with previous results from literature. Dynamic modulus curve fit and associated shift factor fit equations are developed and the respective plots are shown in Figure 3.24 and Figure 3.25.

3.12. Dynamic Modulus Results of SPII Mix with PG 70-22 (Laboratory Mix)

Another SP-II mix was also prepared in the laboratory with binder grade PG 70-22. Dynamic modulus test results on six specimens are presented in tabular and graphic form in Appendix D. Individual mastercurves developed for each sample tested from this mix are presented in a single plot in Figure 3.26. Isothermal and isochronal plots were developed to check tends with respect to temperature and frequency. As can be seen form

42

Figure 3.27 and Figure 3.28, the dynamic modulus showed a decreasing tend with temperature and increasing trend with increasing frequency. The dynamic modulus mastercurve is developed and presented in Figure 3.29 and the associated shift factor tend line is followed in Figure 3.30.

3.13. Dynamic Modulus Results of SPIV Mix with PG 70-22 (Commercial Mix)

Dynamic modulus tests on six specimens were conducted for the SP-IV mix with binder grade of PG 70-22. The test results for all tests are presented in tabular and graphic form in Appendix E. A summarized depiction of all data represented by mastercurves developed for each test is shown in Figure 3.31. The test results from the four samples were averaged and Figure 3.32 is an Isothermal representation of the average data and Figure 3.33 is isochronal plot of the average data. As can be seen from the Isothermal and isochronal Curves the trend of dynamic modulus trend is found to be decreasing with increasing temperature and increasing with increasing frequency. The master curve is developed for the average of all test results and presented in Figure 3.34. Experimental fitting of the sigmoid function has shown very good fit to the shifted data. Polynomial function is used to fit the shift factor results and it is shown in Figure 3.35.

3.14. Comparison of SP-II, SPIII and SP-IV dynamic modulus data

The average dynamic modulus master curves of all plant and laboratory produced mixes is presented in one plot in Figure 3.36. The plot shows that the average mastercurve of SP-II and SP-III mixes, regardless of plant or laboratory produced are found to be close to each other and the SP-IV mix exhibited lower dynamic modulus than all other mixes at lower reduced frequencies (which represents intermediate and high temperatures). The

43

average mastercurve for SP-II mix with PG 64-22 is found to have greatest stiffness over the entire frequency and temperature range and the SP-III mix is intermediate between SP-II and SP-IV mixes.

3.15. Conclusions

The study presented in this chapter can be summarized as follows:

- The dynamic modulus test results increase with increasing loading frequency and decrease with increasing temperature for all mixes as presented the isothermal plots.

- The effect of change in loading frequency becomes more significant with increasing temperature for all mixes as presented by the isochronal plots.

- The sigmoidal function used to fit the mastercurve is found to provide a very good fit to the laboratory testing data.

- Visual observations of dynamic modulus mastercurve plots shows that SPII mixes have higher dynamic modulus than SPIII mixes. SP-IV mix exhibits lowest dynamic modulus.

44

Table 3.1: Test Matrix for Dynamic Modulus

Test Matrix Parameters	HMA Mixture Type				
	SP-II plant	SP-III plant	SP-II lab	SP-III lab	SP-IV plant
PG Binder Grade	PG 64-22	PG 70-22	PG 70-22	PG 64-22	PG 70-22
Test Frequency (Hz)	25, 10, 5, 1, 0.5, 0.1				
Corresponding Cycle to Test Frequency	200, 200, 100, 20, 15, 15				
Test Temperature (°C)	-10, 4, 21, 37, 54				
Required Number of replicate samples	Six	Six	Six	Six	Six

45

Table 3.2: Asphalt Content Test Results

Mix type	Sample wt. (gm)	Wight loss (gm)	Percent Loss (%)	Calibrated Asphalt Content (%)	Average AC (%)
SP-II	1649	92.7	5.62	4.42	
SP-II	1720	97.4	5.66	4.46	4.42
SP-II	1530	85.2	5.57	4.37	
SP-III	1306	75.3	5.77	4.57	
SP-III	1423	85	5.97	4.77	4.61
SP-III	1329	75.6	5.69	4.49	
SP-IV	1917	121	6.92	6.31	
SP-IV	1959	120	6.23	6.13	6.27
SP-IV	1902	121	6.03	6.36	

Table 3.3: Theoretical Maximum Specific Gravity Test

Mix type	Sample No.	G_{mm}	Average G_{mm}
SP-II with PG 64-22	1	2.445	2.439
	2	2.432	
SP-II with PG 70-22	1	2.416	
	2	2.422	2.437
	3	2.453	
SP-III with PG 70-22	1	2.430	
	2	2.431	
	3	2.422	2.431
	4	2.439	
SP-III with PG 64-22	1	2.400	
	2	2.429	
	3	2.428	2.417
	4	2.421	
	5	2.412	
SP-IV with PG 70-22	1	2.386	
	2	2.377	2.383
	3	2.386	

Table 3.4: Recommended Handling Temperatures

Superpave Mix Design	SP-II	SP-III	SP-IV
Binder Grade	PG 64-22	PG 70-22	PG 70-22
RAP content (%)	15	15	15
Mixing Temperature ($^\circ$F)	311	339	318
Molding Temperature ($^\circ$F)	289	312	295
Lay down Temperature ($^\circ$F)	289 +/- 22	312 +/- 22	295 +/- 22
Lab Compaction Temperature ($^\circ$F)	289 +/- 4	312 +/- 4	295 +/- 4

Table 3.5: Bulk Specific Gravity Test

Sample No.	Mix type	Wt. in air (gm)	Wt. in water (gm)	Wt. Surface Dry (gm)	Water absorbed (%)	Gmb
1		2760.8	1578.6	2772.4	0.972	2.313
2		2772.4	1573.9	2774.5	0.175	2.309
3	SP-II with PG 64-22	2752.2	1562	2758.7	0.543	2.300
4		2759.2	1572.8	2763.5	0.361	2.317
5		2688.7	1532.5	2693.4	0.405	2.316
6		2780.2	1573.6	2786.3	0.503	2.293
1		2680.9	1523	2701.3	1.731	2.275
2		2656.6	1501.7	2673.1	1.409	2.268
3	SP-II with PG 70-22	2701.0	1540	2729.1	2.363	2.271
4		2731.1	1559.1	2759.1	2.333	2.276
5		2742.9	1557.7	2756.9	1.167	2.287
6		2710	1529.6	2717.5	0.631	2.281
1		2787.7	1577.9	2794	0.518	2.292
2		2777.7	1575.9	2794	1.338	2.280
3	SP-III with PG 70-22	2820.2	1606.8	2828.3	0.663	2.309
4		2737.8	1542.7	2745.3	0.624	2.277
5		2737.6	1546.7	2741	0.285	2.292
6		2791.2	1569.4	2795.9	0.383	2.276
1		2766	1569.6	2775.9	0.821	2.293
2		2752.5	1565.6	2760.7	0.686	2.303
3	SP-III with PG 64-22	2732.5	1555.6	2740.7	0.692	2.306
4		2734.8	1560.4	2751.9	1.435	2.295
5		2705.8	1545.4	2725.8	1.694	2.292
6		2756.8	1575.3	2772.5	1.311	2.303
1		2684.5	1503	2697.5	1.088	2.247
2		2723.6	1518.3	2729.8	0.512	2.248
3	SP-IV with PG 70-22	2716.6	1527.3	2726.9	0.859	2.265
4		2732.1	1533.3	2739.9	0.646	2.264
5		2639	1471	2647	0.680	2.244
6		2698.4	1512.2	2705.7	0.612	2.261

49

Table 3.6: Percentage Air Voids Test

Sample No.	Mix type	Air Void (%)
1		5.2
2		5.3
3	SP-II with PG 64-22	5.7
4		5.0
5		5.0
6		6.0
1		5.7
2		6.0
3	SP-II with PG 70-22	5.9
4		5.7
5		5.2
6		5.5
1		5.2
2		5.7
3	SP-III with PG 70-22	5.0
4		5.8
5		5.2
6		5.8
1		6.0
2		5.6
3	SP-III with PG 64-22	5.5
4		5.9
5		6.0
6		5.6
1		5.8
2		5.8
3	SP-IV with PG 70-22	5.1
4		5.1
5		5.9
6		5.1

Table 3.7: Air Void Uniformity Check

Sample No	Mix type	Core No	Wt. in air (gm)	Wt. in water (gm)	Wt. Surface Dry (gm)	Water absorbed (%)	G_{mb}	G_{mm}	Air void (%)
26	SPIII	Top section	824.6	467.4	827.3	0.750	2.291	2.43	5.712
		Middle section	947.9	537.1	949.3	0.340	2.300	2.43	5.366
		Bottom section	818.4	461.9	823.6	1.438	2.263	2.43	6.887
24	SPIII	Top section	909.2	512.5	910.5	0.327	2.284	2.43	5.991
		Middle section	819.6	465.8	821.5	0.534	2.304	2.43	5.177
		Bottom section	868.3	495.5	871.3	0.798	2.311	2.43	4.916
8	SPIII	Top section	857.7	481.1	860.4	0.712	2.261	2.43	6.944
		Middle section	849.6	478.5	851.5	0.509	2.278	2.43	6.266
		Bottom section	866.5	489.3	868.8	0.606	2.283	2.43	6.038
						mean Top section	2.279		6.216
						mean Middle section	2.294		5.603
						mean Bottom section	2.285		5.947
						variance Top section	0.000		0.417
						variance Middle section	0.000		0.338
						variance Bottom section	0.001		0.977
		mean of top section is equal to mean of middle section test statistic < 2.78, means they are equal					1.221		1.221
		mean of bottom section is equal to mean of middle section test statistic < 2.78, means they are equal					0.520		0.520

51
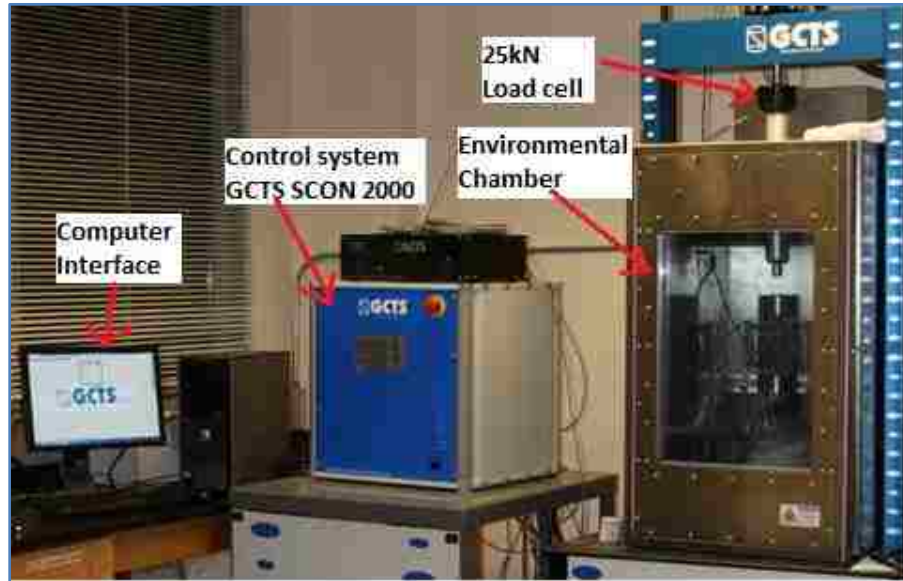
Figure 3.1: Servo-Hydraulic Testing System
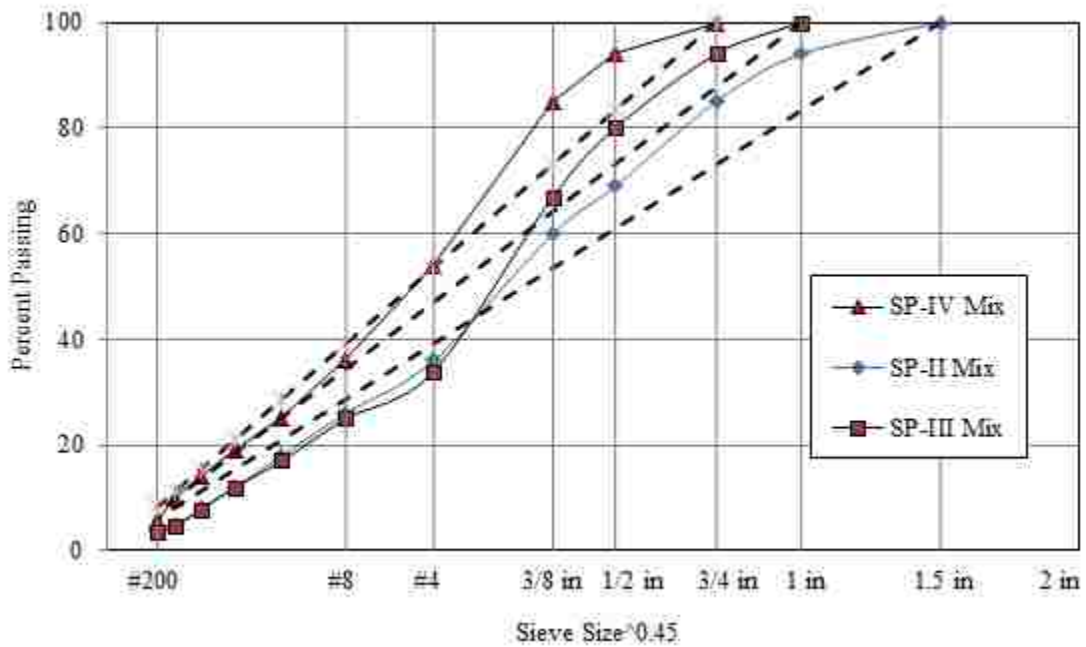
Figure 3.2: Sieve analysis for SP-II and SP-III mixes

52
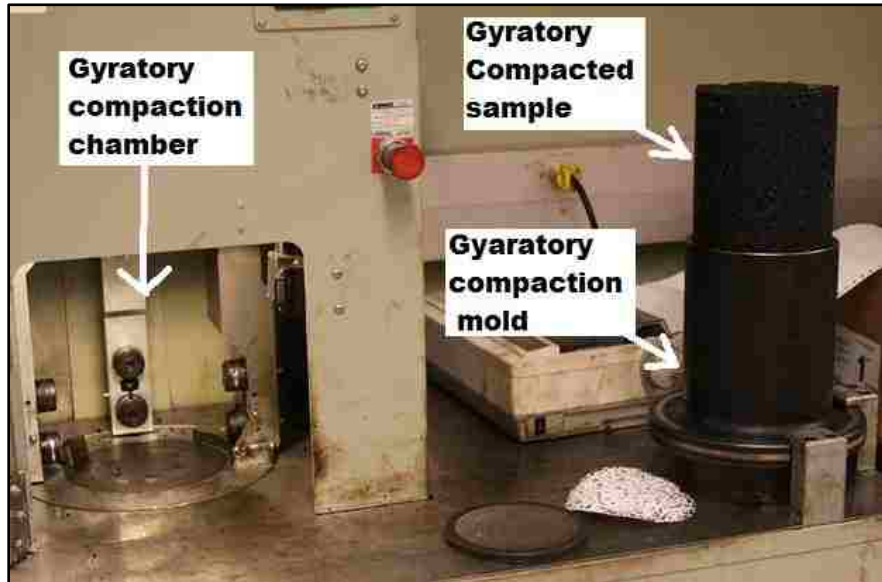
Figure 3.3: Gyratory Compactor
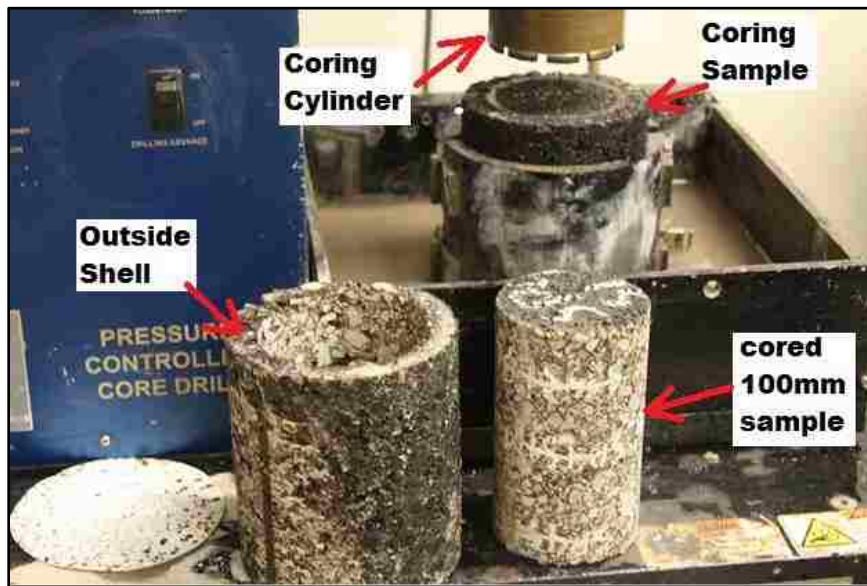
Figure 3.4: Asphalt Coring Machine

53
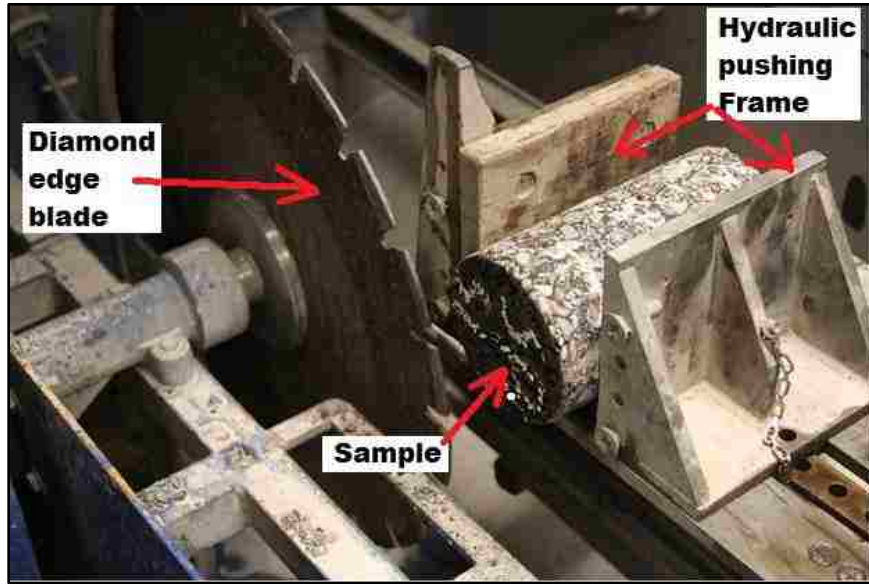
Figure 3.5: Lab Specimen Saw

Figure 3.6: Automatic Positioning Fixture
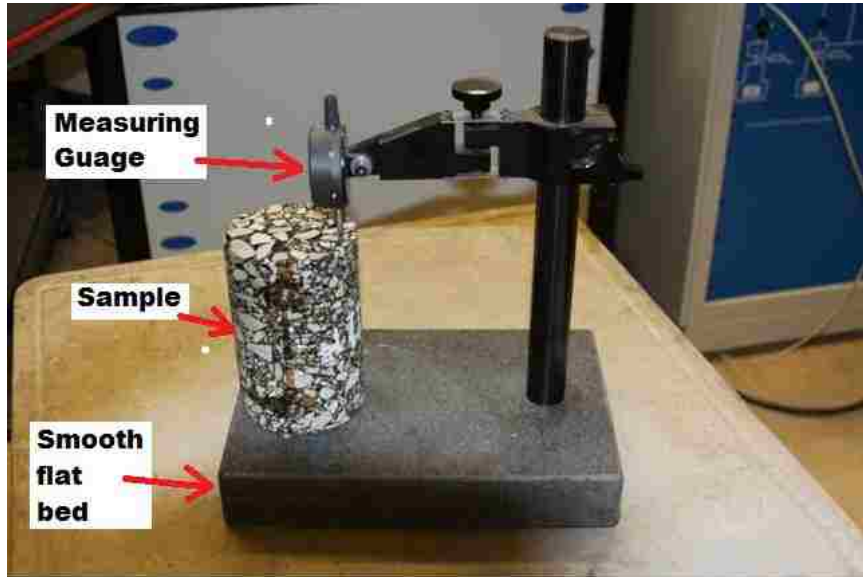
Figure 3.7: Rock Flatness Gauge
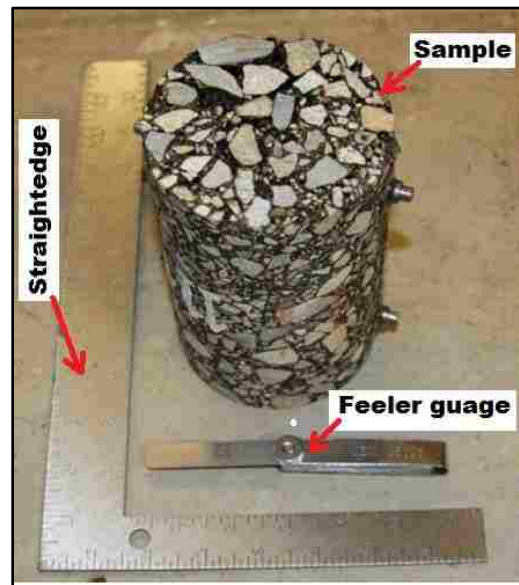
Figure 3.8: straightedge and feeler gauge for Waviness check
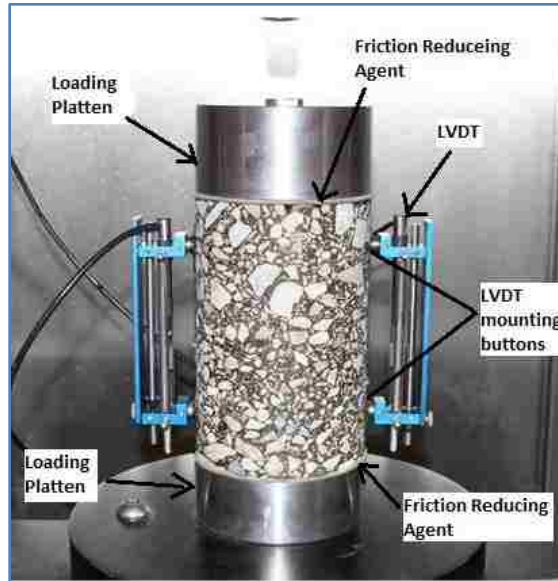
Figure 3.9: Linear Variable Differential Transformers (LVDTs) Mounted On Specimen
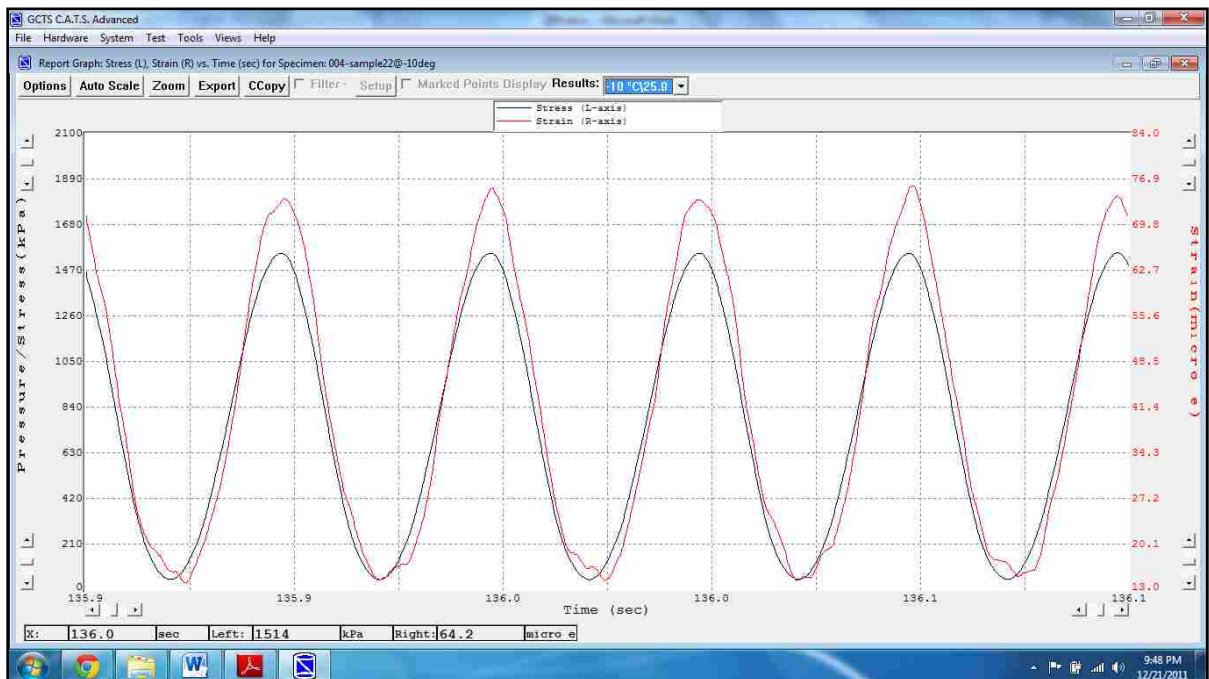
Figure 3.10: Typical stress, strain vs. Time Plot at Temperature (-10°C)

56
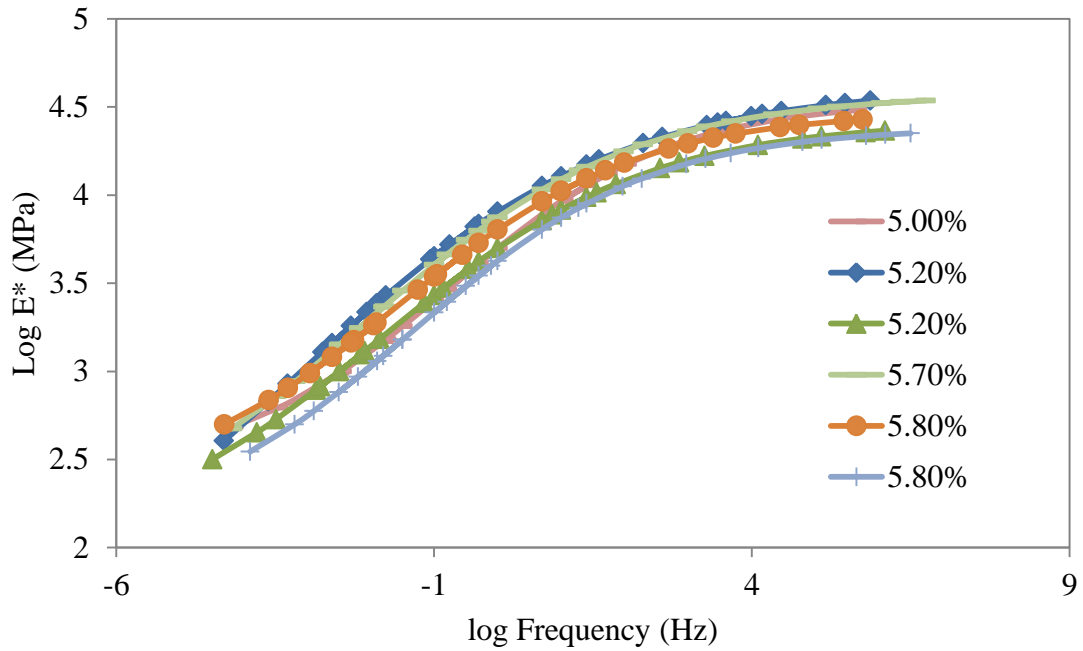
Figure 3.11: Comparison Master Curves with %AV for SP-III with PG 70-22
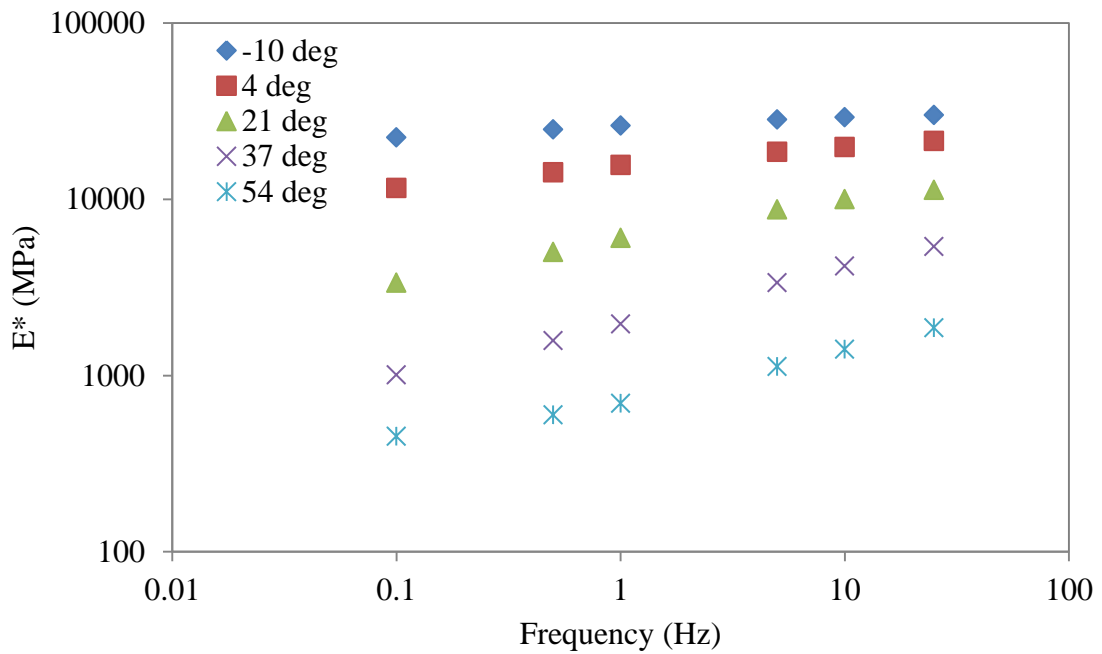
Figure 3.12: Isothermal Plot for Average of SP-III, PG 70-22

57
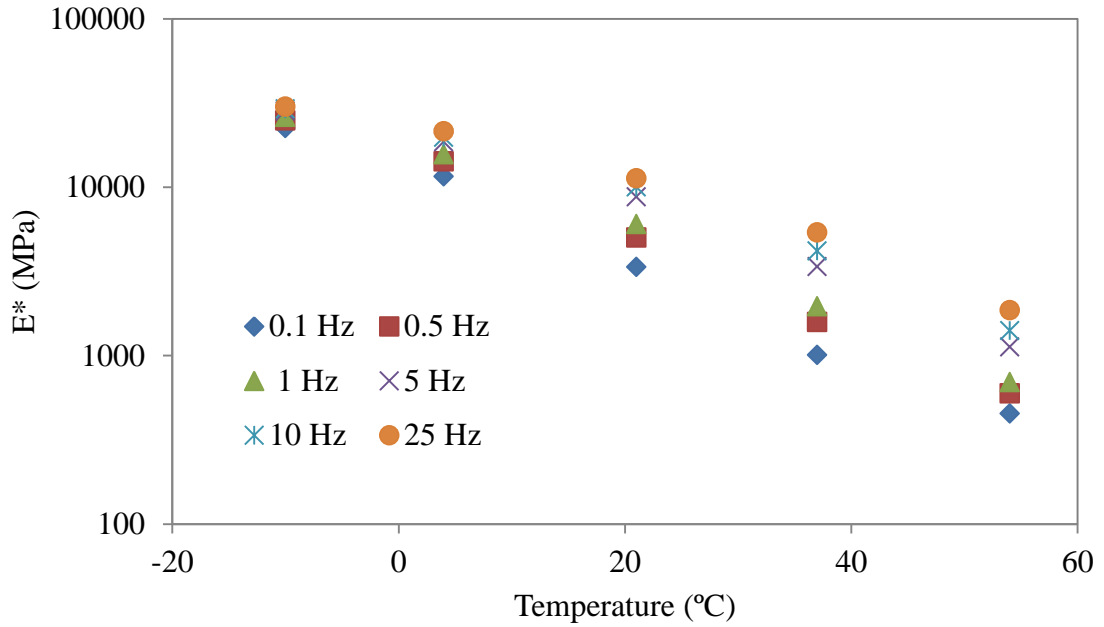
Figure 3.13: Isochronal Plot for Average of SP-III, PG 70-22

$$log(|E^*|) = 2.07 + 2.43/(1 + e^{(-0.85 - 0.49\, log(fr))})$$
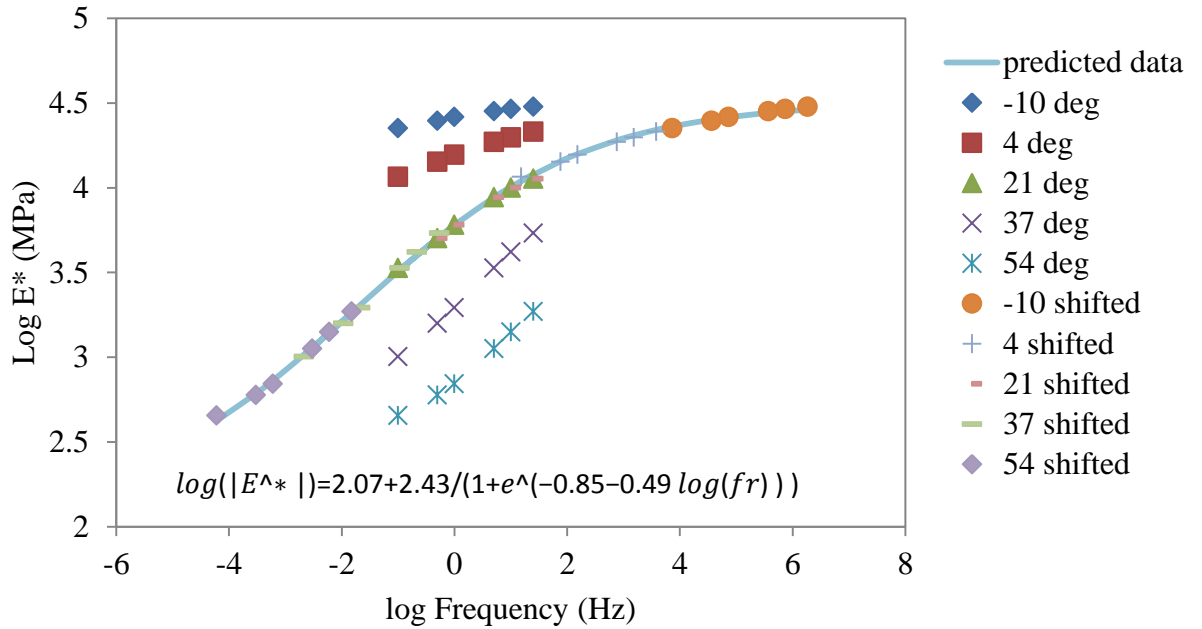
Figure 3.14: Master Curve for Average of SP-III, PG 70-22

58
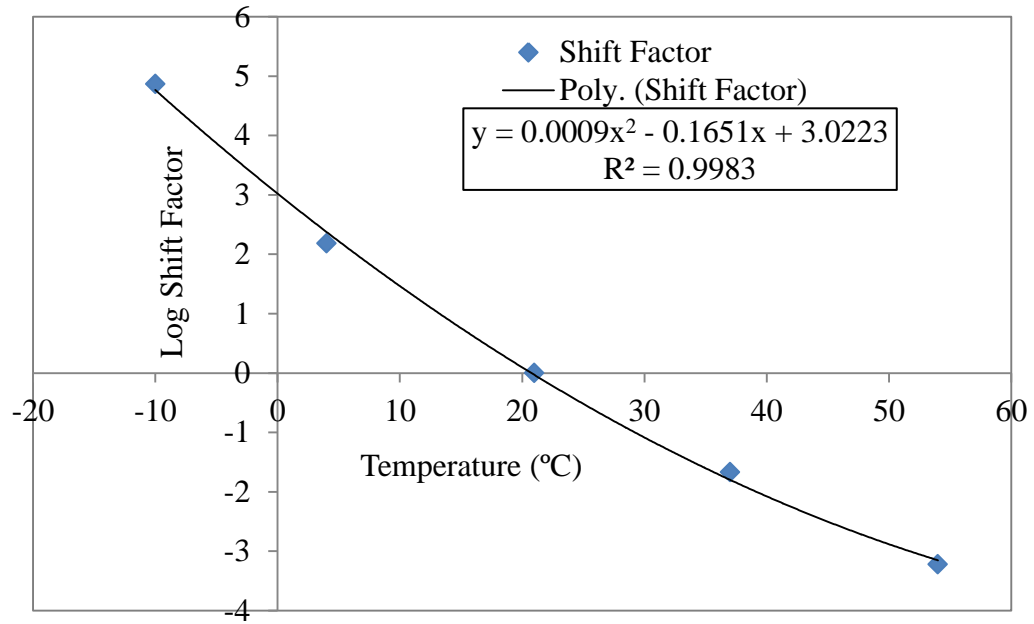
Figure 3.15: Shift Factor for Average of SP-III, PG 70-22
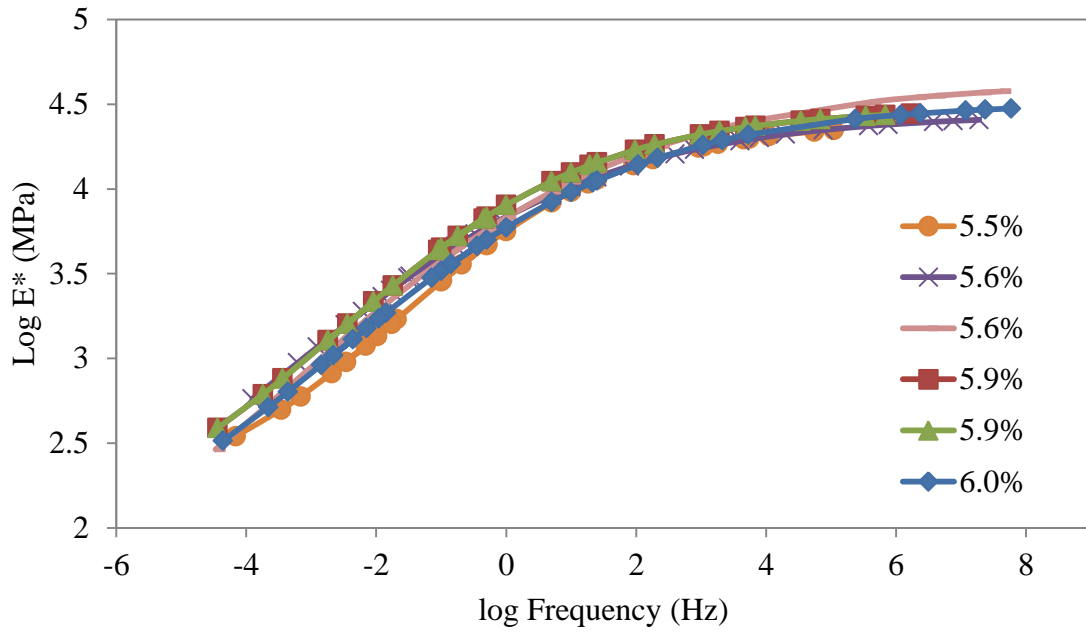
Figure 3.16: Comparison Master Curves for SP-III, PG 64-22 Test Results
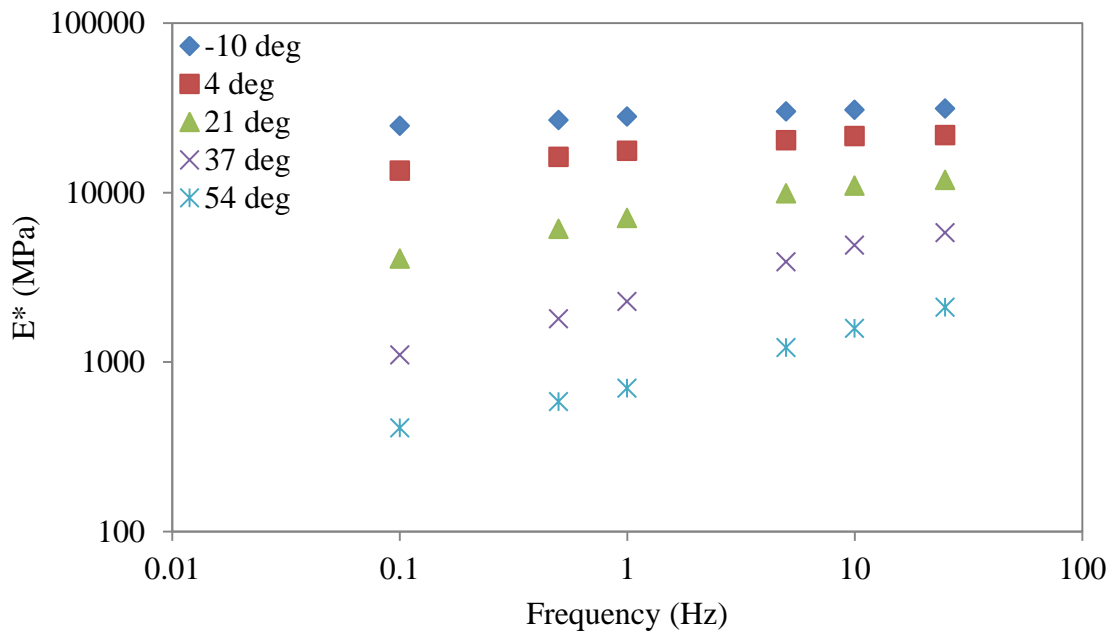
Figure 3.17: Isothermal Plot for Average of SP-III, PG 64-22

60
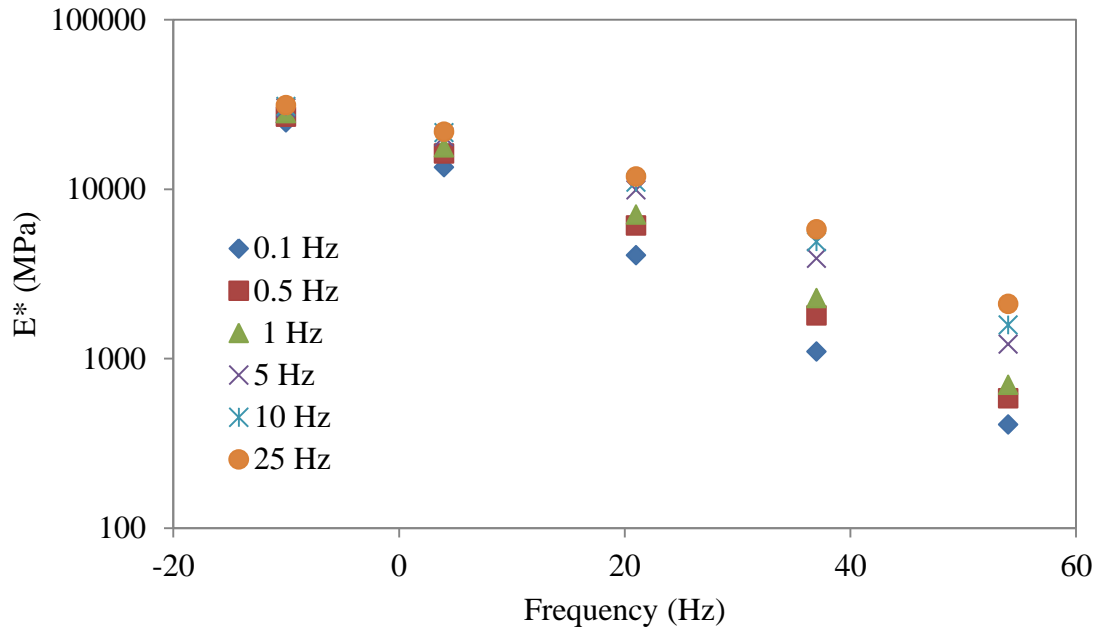
Figure 3.18: Isochronal Plot for Average of SP-III, PG 64-22

$$log(|E^*|)=1.65+2.87/(1+e^{(-1.19-0.44\,log(fr))}$$
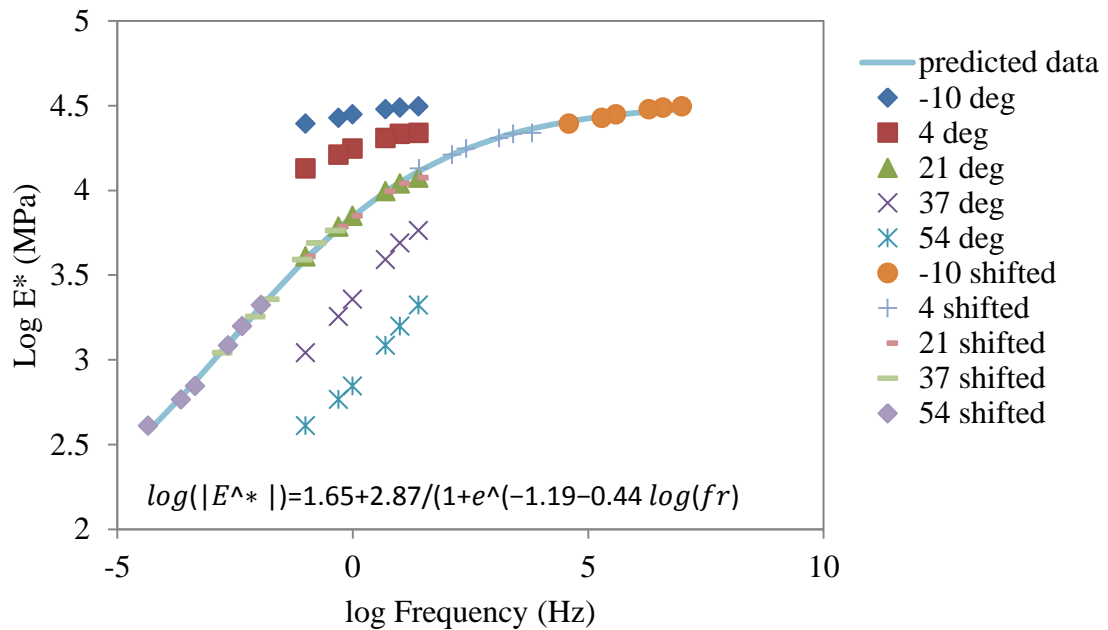
Figure 3.19: Master Curve for Average of SP-III, PG 64-22

61
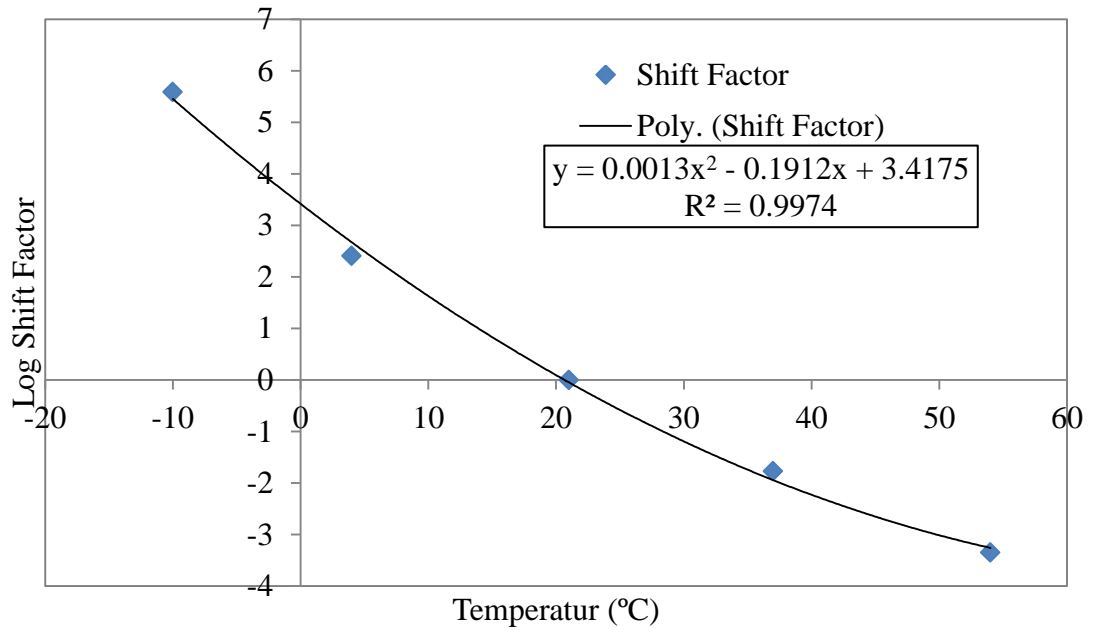
Figure 3.20: Shift Factor for Average of SP-III, PG 64-22
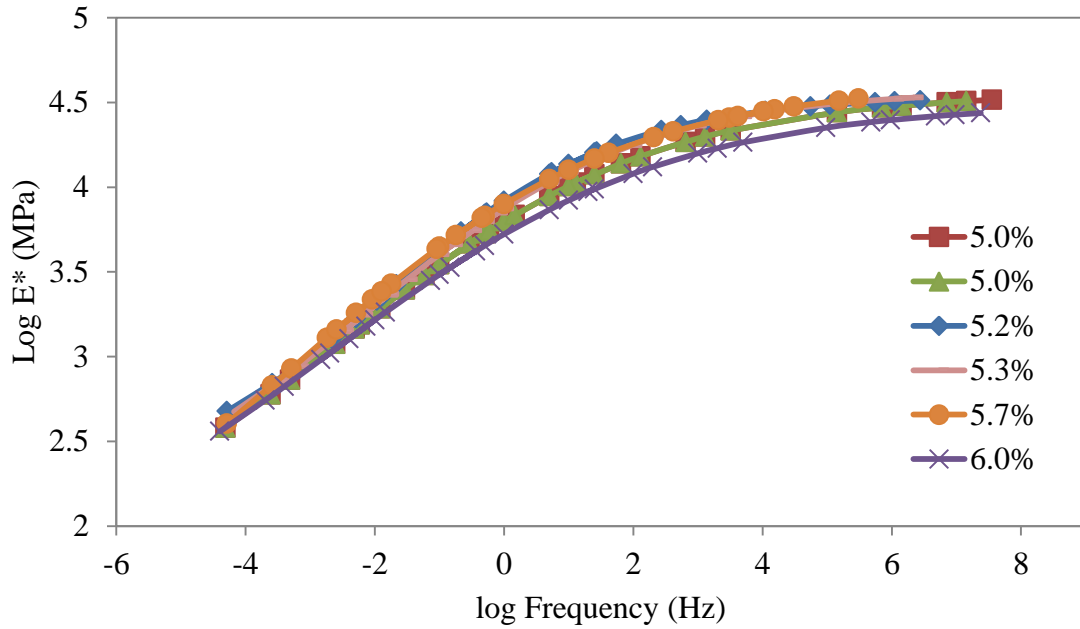
Figure 3.21: Comparison Master Curves for SP-II, PG 64-22 Test Results
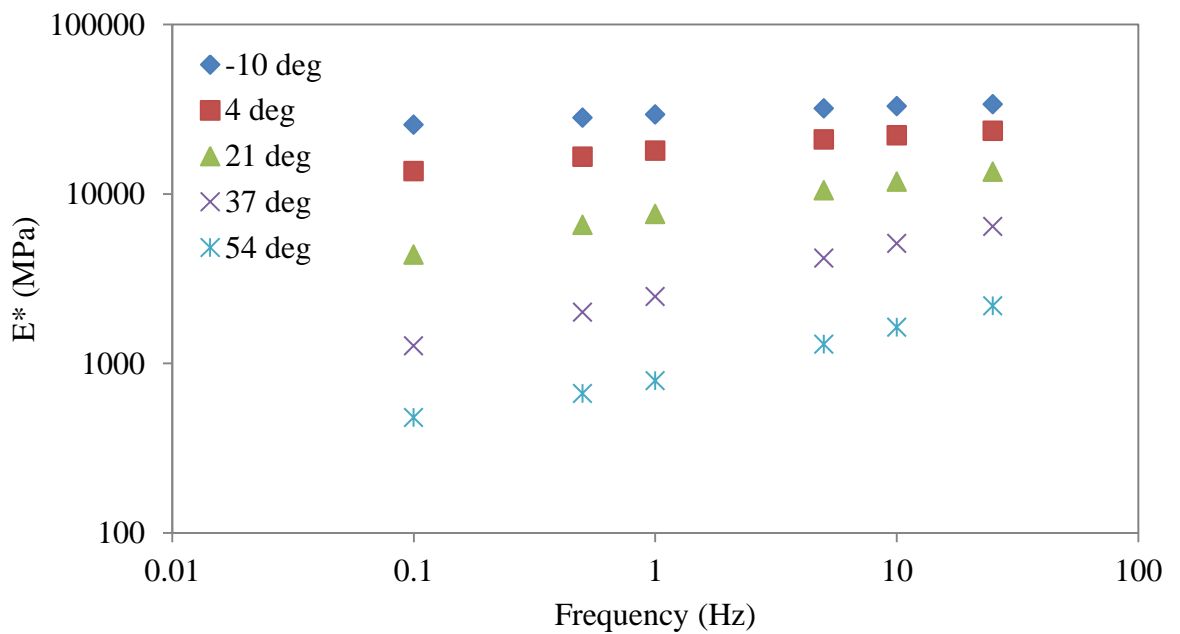
Figure 3.22: Isothermal Plot for Average of SP-II, PG 64-22

63
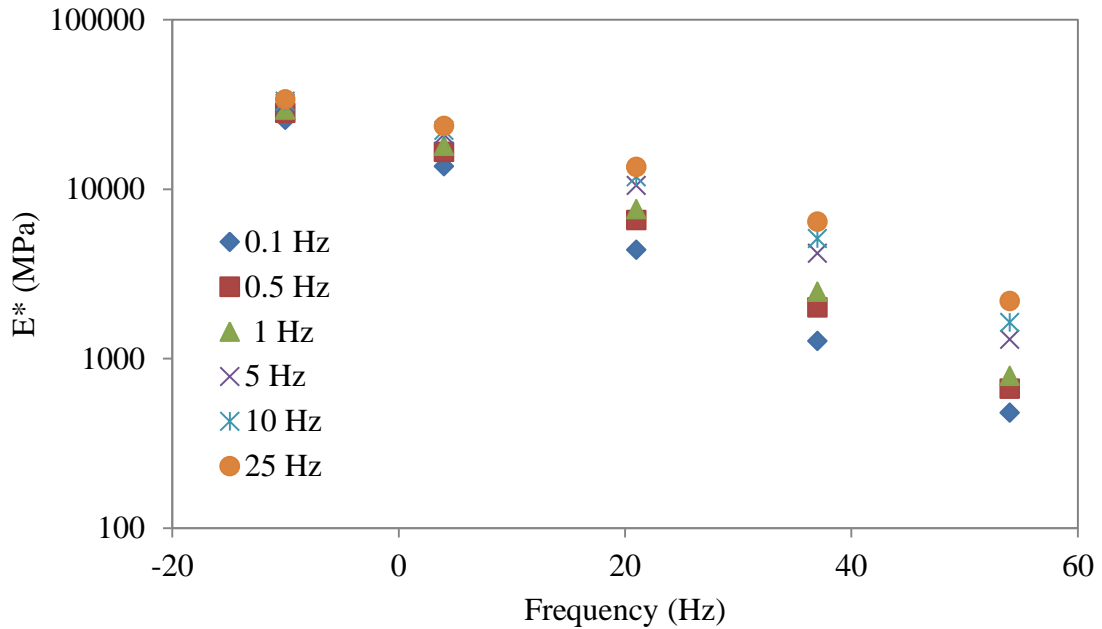
Figure 3.23: Isochronal Plot for Average of SP-II, PG 64-22

$$log(|E^* |)=1.90+2.66/(1+e^{\wedge}(-1.07-0.45 \, log(fr)))$$
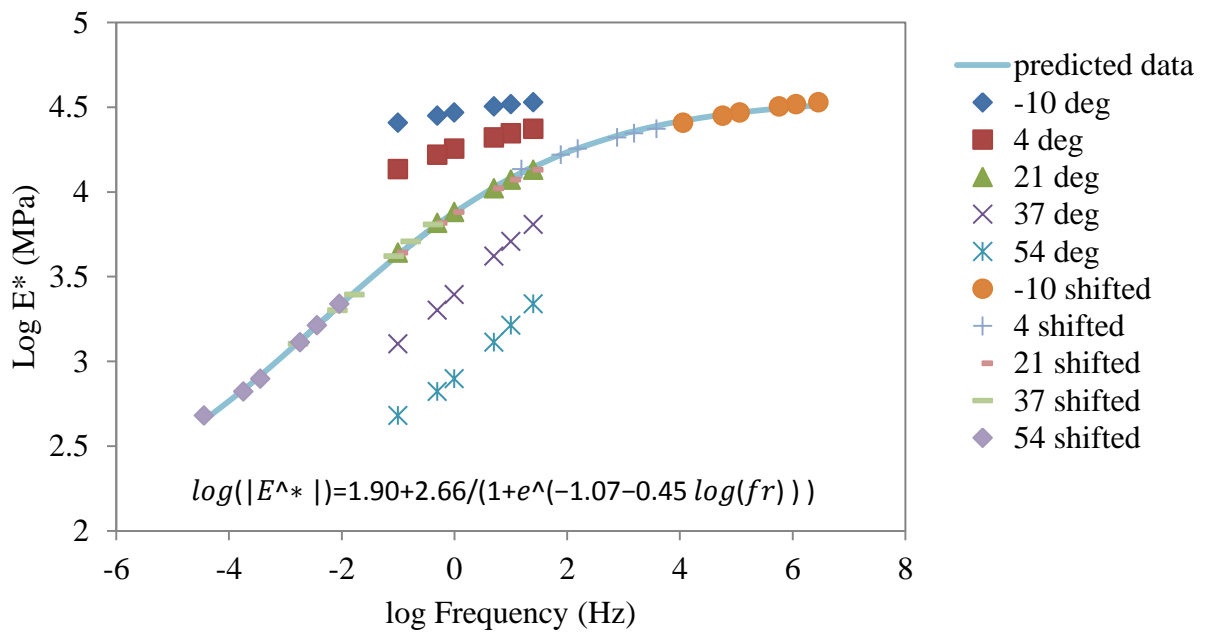
Figure 3.24: Master Curve for Average of SP-II, PG 64-22

64
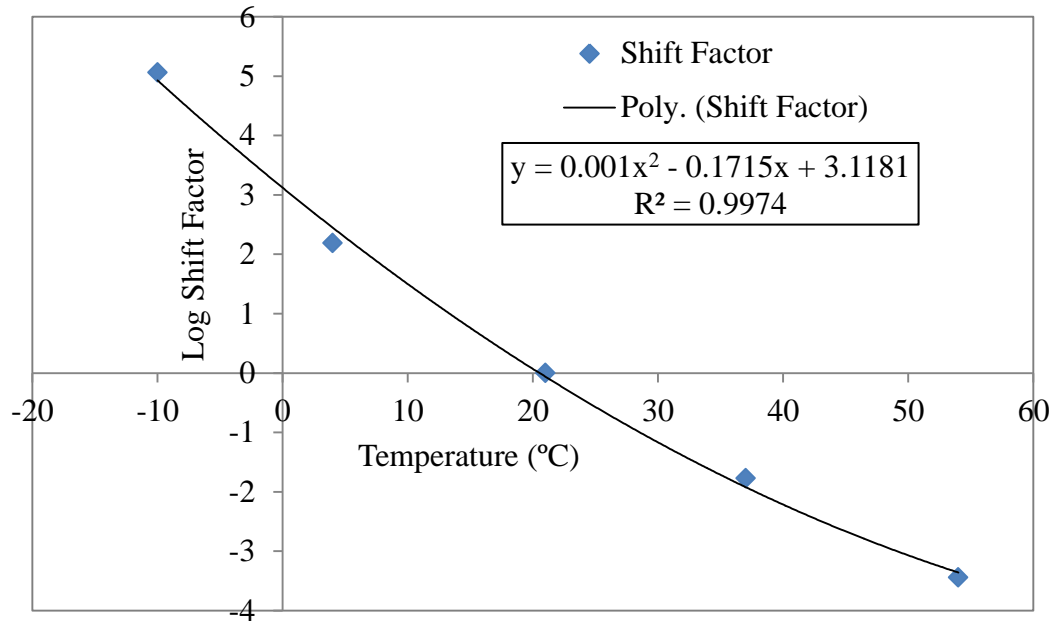
Figure 3.25: Shift Factor for Average of SP-II, PG 64-22

65
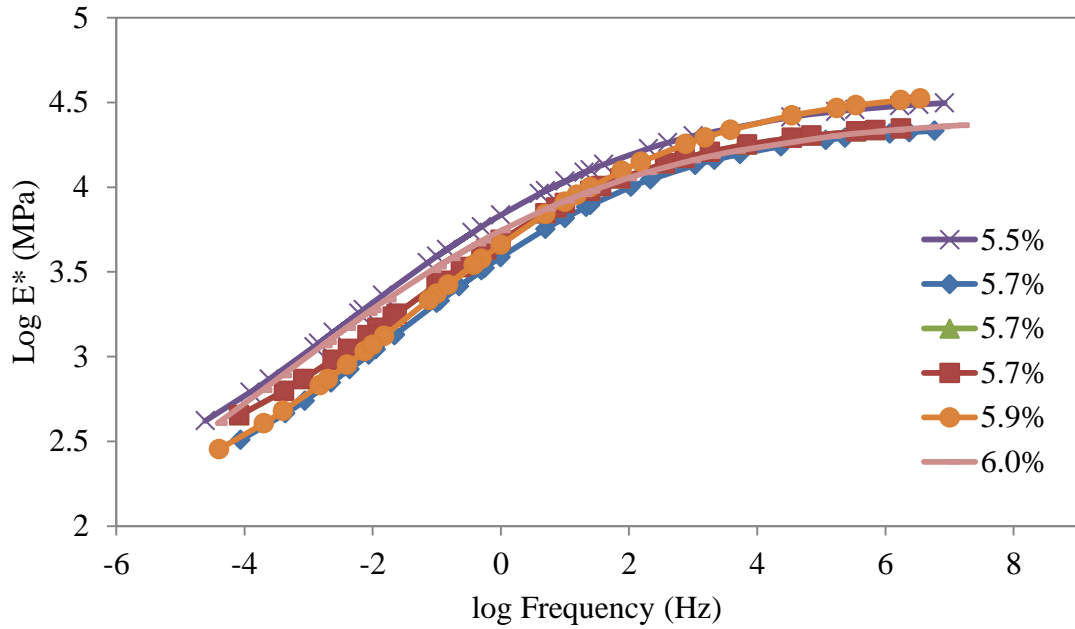
Figure 3.26: Comparison Master Curves for SP-II, PG 70-22 Test Results
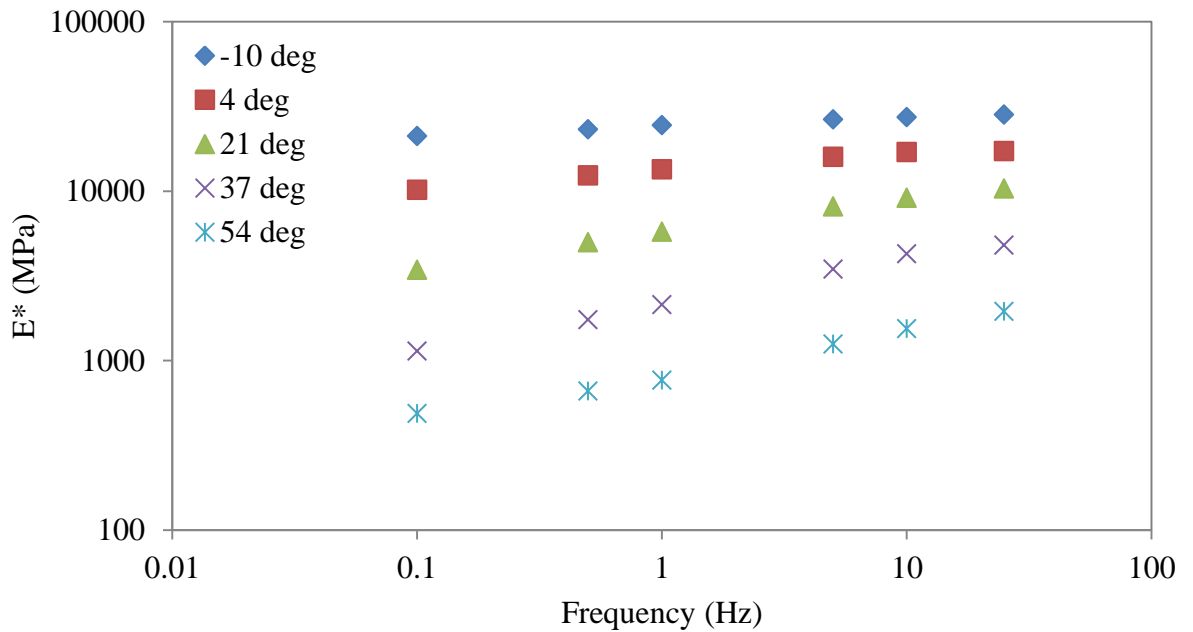
Figure 3.27: Isothermal Plot for Average of SP-II, PG 70-22

66
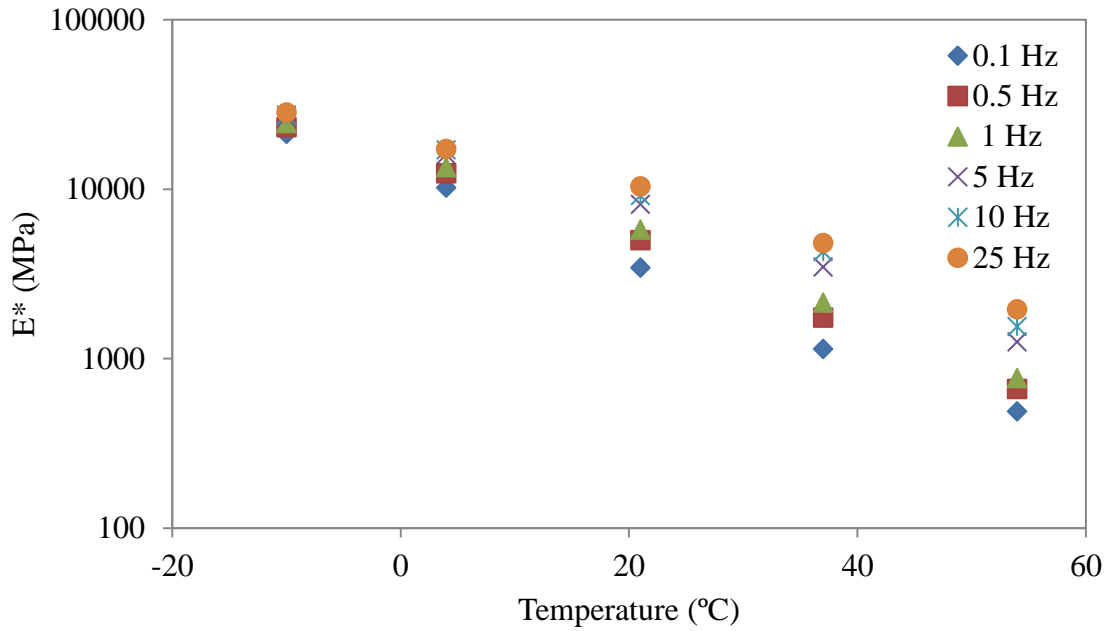
Figure 3.28: Isochronal Plot for Average of SP-II, PG 70-22

$$log(|E^*|) = 1.81 + 2.69/(1 + e^{(-0.99 - 0.41\, log(fr))})$$
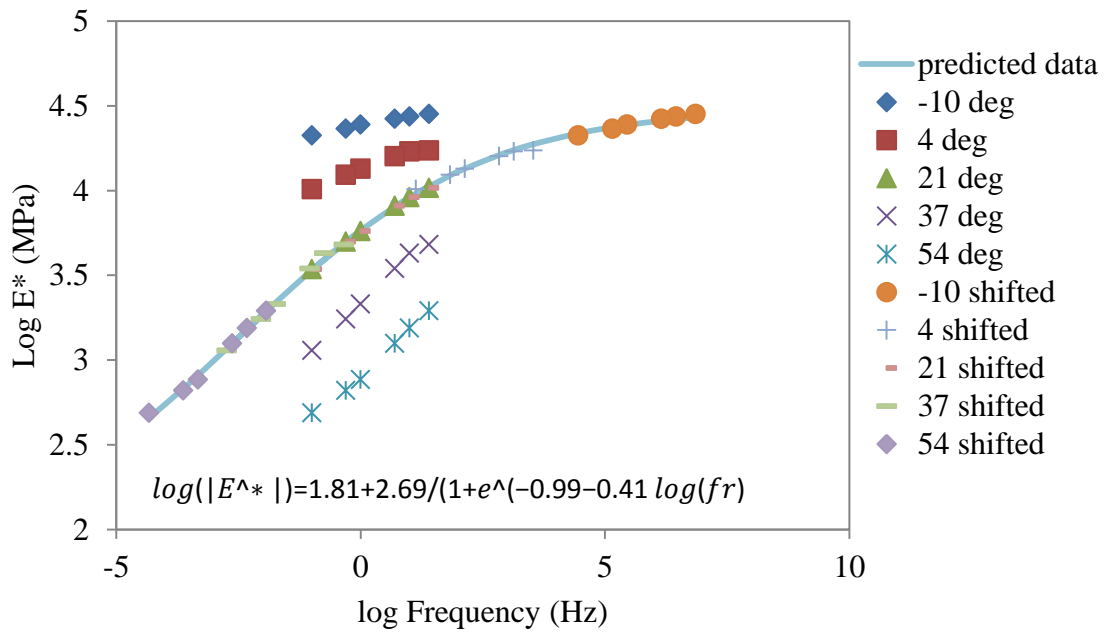
Figure 3.29: Master Curve for Average of SP-II, PG 70-22

67
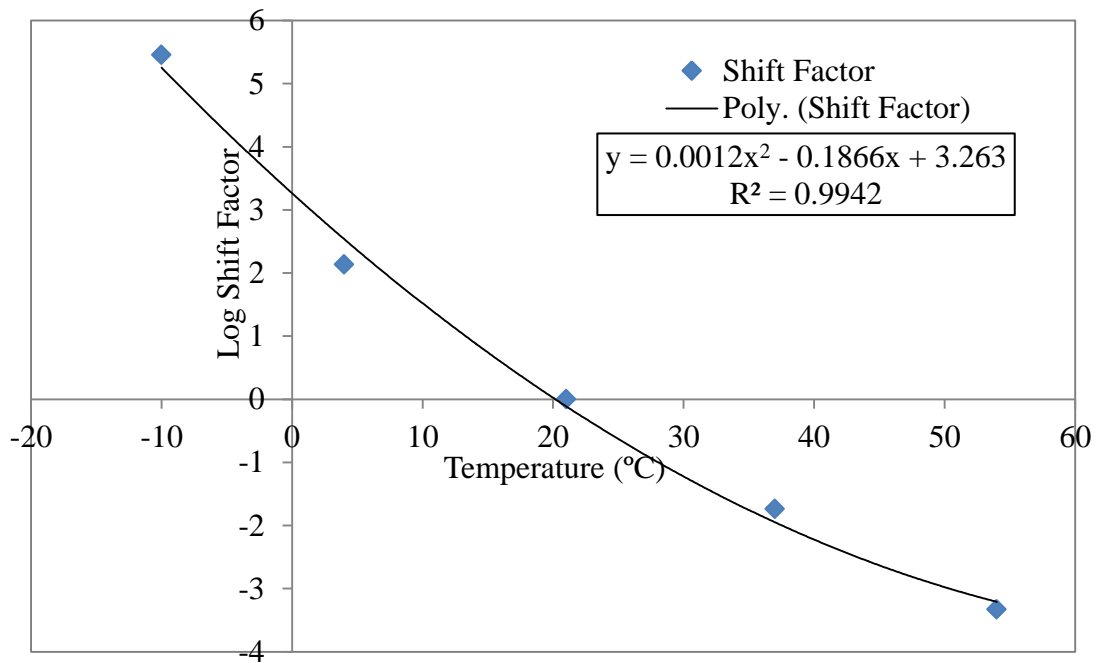
Figure 3.30: Shift Factor for Average of SP-II, PG 70-22

68
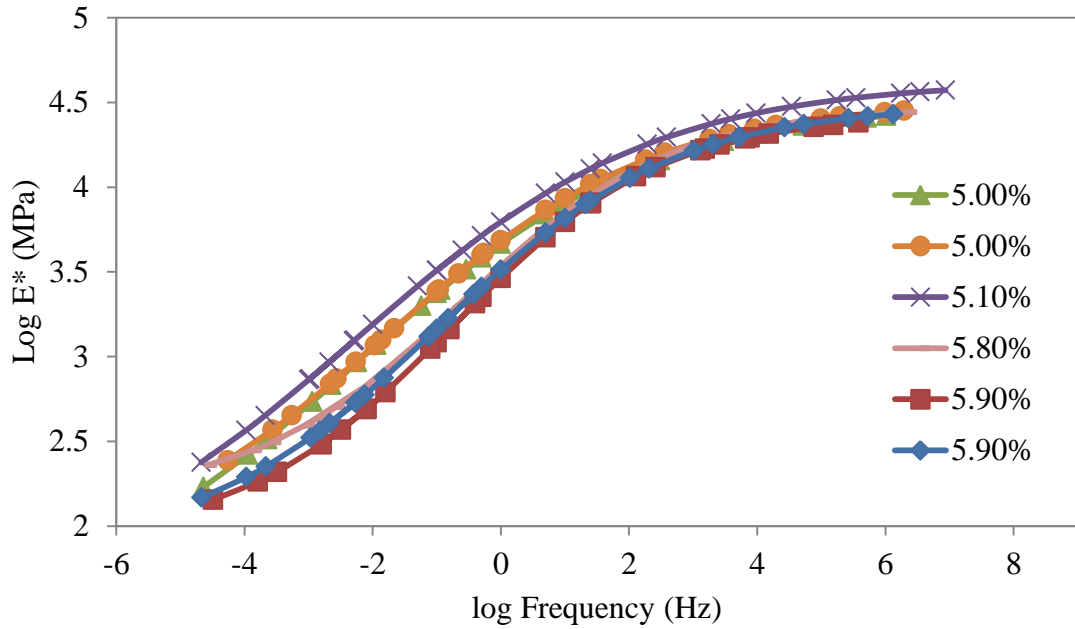
Figure 3.31: Comparison of Master Curves for SP-IV, PG 70-22 Test Results
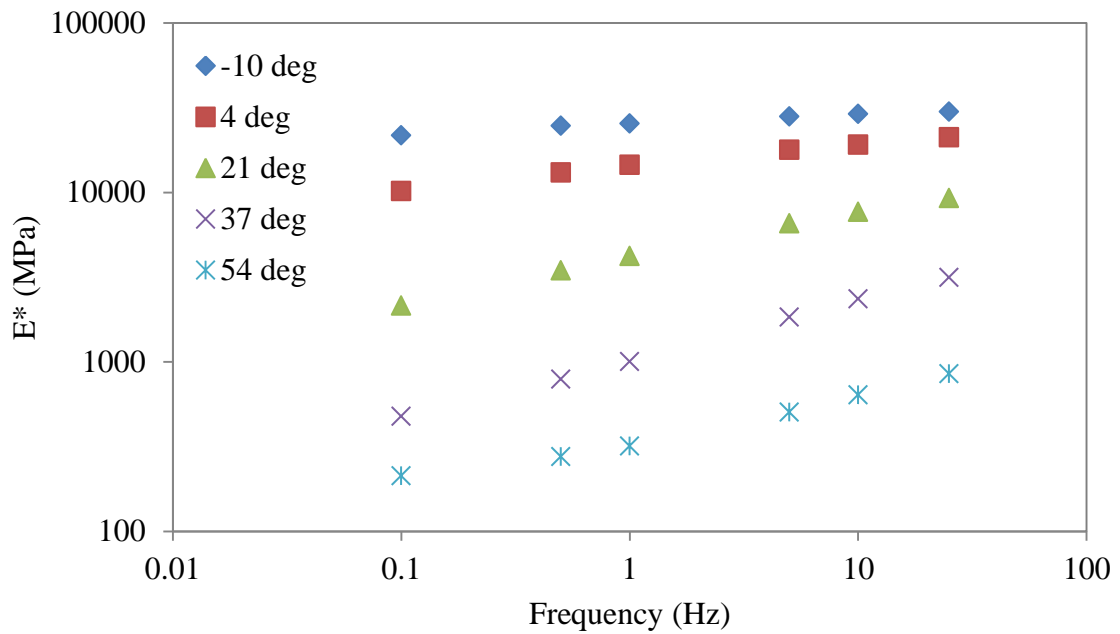
Figure 3.32: Isothermal Plot for Average of SP-IV, PG 70-22

69
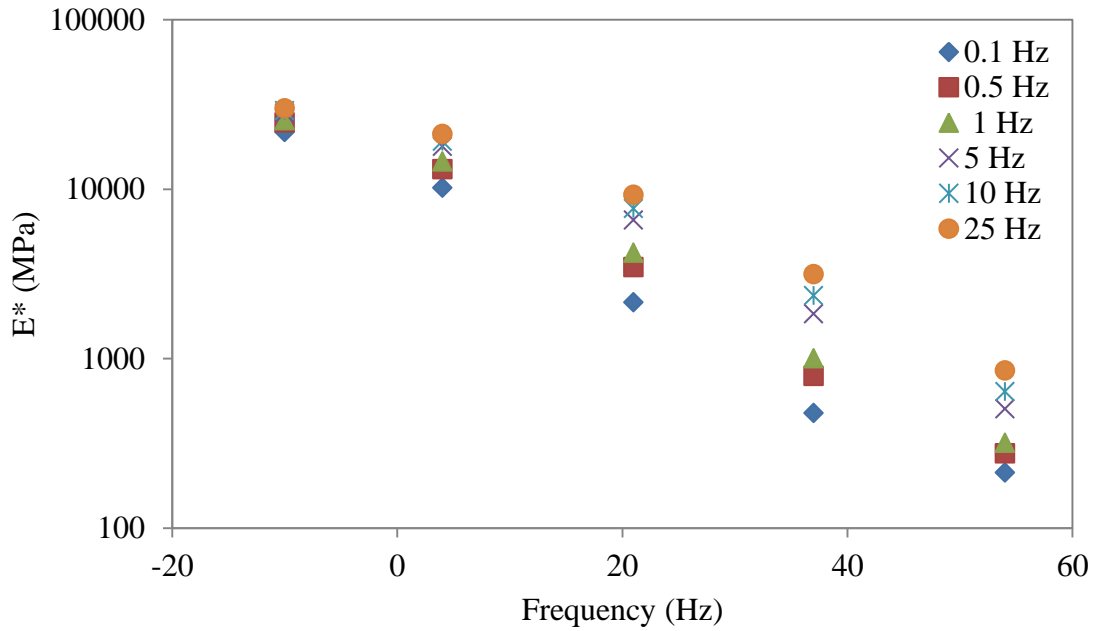
Figure 3.33: Isochronal Plot for Average of SP-IV, PG 70-22

$$log(|E^*|)=1.84+2.67/(1+e^{(-0.70-0.50\,log(fr)})$$
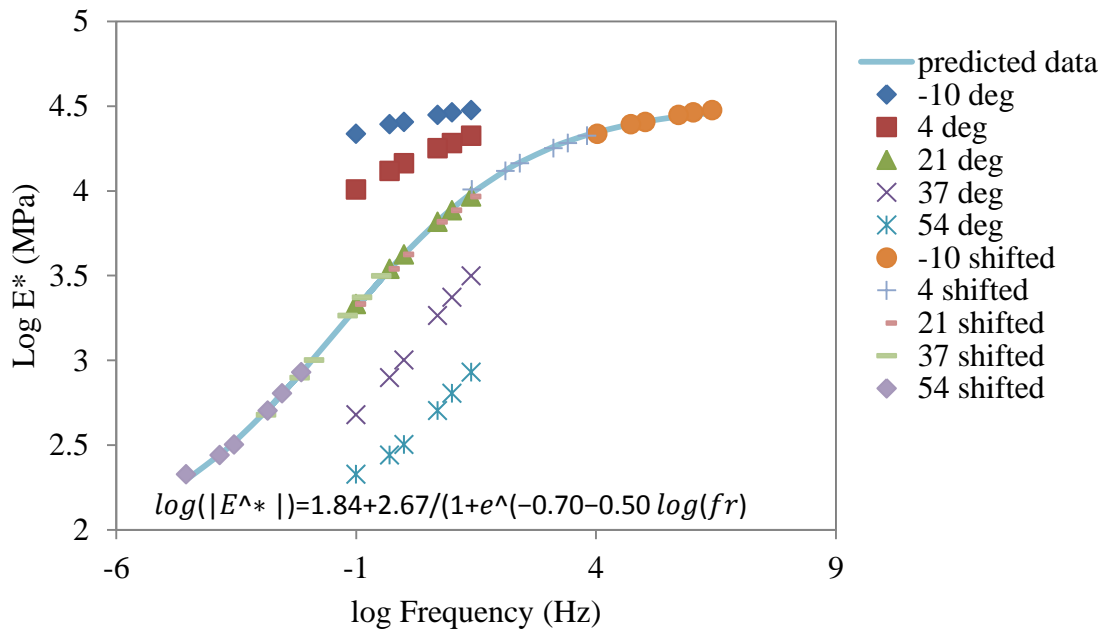
Figure 3.34: Master Curve for Average of SP-IV, PG 70-22

70
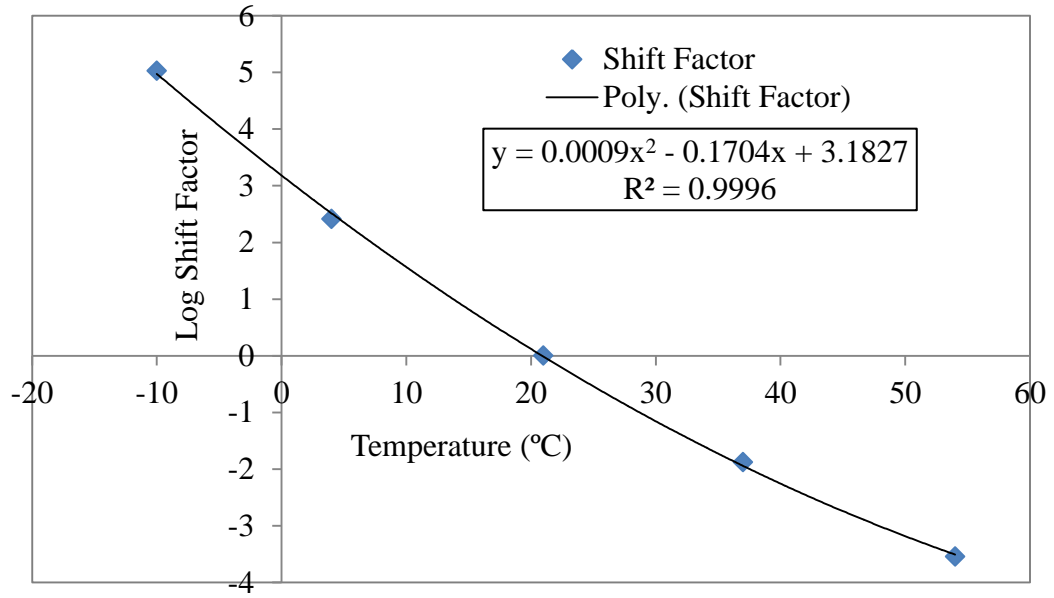
Figure 3.35: Shift Factor for Average of SP-IV, PG 70-22
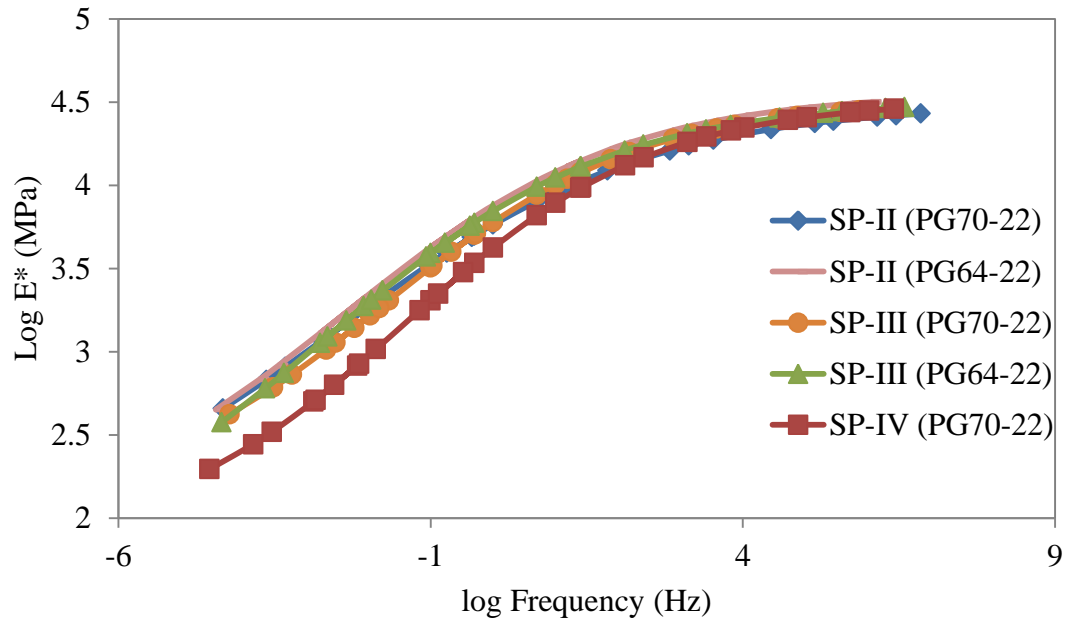
Figure 3.36: Comparison Master Curves for SP-II, SP-III and SP-IV Test Results

Precision of Dynamic Modulus Values

4.1. Introduction

Typical *E**-testing is conducted over a five temperatures and six loading frequencies resulting in a large amount of data per test. Test results may vary and independent assurance (IA) testing can help understand the precision of test results and identify probable causes of variations.

To date, a limited number of studies have been conducted to establish the precision statement for *E**-testing. Phase VI of NCHRP Project 9-29, conducted by Bonaquist in 2011 (Bonaquist 2011), is the most recent study on the precision of *E**-testing. The study presented the precision statement for *E**-tests conducted with the Asphalt Mixture Performance Tester (AMPT). Precision statements were developed following the recommendation of ASTM test standard E69-2012. Eight laboratories participated in conducting the *E**-testing. All *E**-testing in the laboratories was performed following the recommendation of AASHTO TP 79 (2009). Specimens were prepared from loose asphalt mix at each of the eight laboratories as per the recommendation of AASHTO PP 60 (2009). To investigate the significance of variation on *E**-test results from sample preparation at different laboratories; supplementary samples were prepared at a single laboratory and distributed for testing. *E**-testing was conducted on three replicate samples at 7% air void at each laboratory and the test temperatures were limited to 4, 20 and 40 ºC. Consistency analysis performed on all samples indicated very good

73

consistency at 95% confidence. The critical within-laboratory consistency statistic (*k*-statistic) was determined to be 3.3 and 3.1 for samples from loose mix and prefabricated samples respectively. The critical interlaboratory consistency statistic (*h*-statistic), on the other hand, was found to be 1.2 and 2.1 for samples from loose mix and prefabricated samples respectively. The trend of coefficient of variation (COV) was also investigated and a maximum of 35% COV was observed, but most COVs were found to be below 15% for both sample preparation conditions.

Repeatability of *E**-test was found to be affected by the Nominal Maximum Aggregate Size (NMAS) and stiffness of the mix. It was found that the repeatability COV for *E**-test worsened as the NMAS decreased and the stiffness increased. Reproducibility of *E**-test results, on the other hand, were found to be affected only by stiffness of the mix. Reproducibility was found to improve with an increase in stiffness (dynamic modulus) of the asphalt concrete (AC). Bonaquist (2011) developed the relationship between repeatability and reproducibility with mix stiffness and NMAS, which are presented in Equation (4.1) and Equation (4.2). The repeatability COV was found to be around 7% at higher stiffness values and as the stiffness decreased, the repeatability COV increased reaching a value of 24%. The reproducibility COV for the *E**-testing was found to be approximately 10% at high stiffness conditions and as the stiffness decreased, the reproducibility COV increased to values as high as 47% (Bonaquist 2011).

$$s_r\% = \left[29.8e^{(0.014*NMAS)}\right] * |E^*|^{-\left[0.189e^{(0.012*NMAS)}\right]} \tag{4.1}$$

where $s_r\%$ is repeatability COV for $|E^*|$, %; NMAS is nominal maximum aggregate size, mm, and $|E^*|$ is average dynamic modulus, MPa.

74

$$s_R\% = 223.81 * |E^*|^{-[0.312]} \qquad (4.2)$$

where $s_R\%$ is reproducibility COV for $|E^*|$, %, and $|E^*|$ is average dynamic modulus, MPa.

Bennert and Williams (2009) at Center for Advanced Infrastructure & Transportation (CAIT) preformed another study on the precision of E^*-testing. The study was part of the E^*-testing research performed for New Jersey Department of Transportation (NJDOT). Seven laboratories participated by conducting E^*-testing following the recommendations of AASHTO TP 62-07 (2007). The round-robin testing program was performed on two Superpave mixes fabricated using binder grade PG 64-22. E^*-testing was conducted on three replicate samples for each mix at the standard five temperatures and six testing frequencies. Then, test data was evaluated and precision statements were developed following the ASTM test standard E691(2012) procedure. COV determined for the E^*-data of all laboratories over all temperatures and frequencies ranged from 7.7% to 43.5% with an average of 25.7%. However, COV determined for each laboratory separately averaged to 11.9%. Precision statements were developed using percentage precision statistics, one-sigma limit in present (1s%) and two-sigma limit in percent (D2s%). The 1s% was determined to be 13.03% and 26.89% for single operator and multi-laboratory precision, respectively, while the D2s% were determined to be 36.47% and 75.3% for single operator and multi-laboratory precision respectively. Moreover, E^*-variability was found to increase with increasing testing frequency (Bennert and Williams 2009).

As of this writing, only these two studies on the precision of E^*-testing were found. There is a wide variation between the precision statements of the two studies, which

75

indicates the need for more precision studies on E^*-testing. To this end, this study evaluates the precision of E^*-testing conducted on typical New Mexico asphalt mixes through an Independent Assurance (IA) testing program.

4.2. Objective

Specific objectives of this study are to:

- Evaluate the precision and accuracy of E^*-testing conducted for New Mexico mixes through IA testing

- Conduct statistical analysis to determine the precision and accuracy of the E^*-testing program. Statistical analysis include k-statistic, h-statistic, one-way analysis of variance (ANOVA), repeatability and reproducibility analysis

4.3. Methodology

In this study, the precision and accuracy of E^*-testing are evaluated using an IA testing program. Figure 4.1 presents pictorial illustration of the concepts of precision and accuracy. When the data points of each laboratory are very much dispersed as shown in Figure 4.1 (c) and (d), it indicates low precision with in each laboratory. When the total data points form two laboratories are very much dispersed away from the lime of equality as shown in Figure 4.1 (a) and (d), it indicates low accuracy of test data from each laboratory. Therefore, test data collected from two laboratories is accurate and precise if the data variability with in each laboratory is small and the total data from each laboratory is found to very close to the line of equality as shown in Figure 4.1 (c). Therefore, precision is defined as the closeness of the E^*-test results in one laboratory

and accuracy is defined as the closeness of test results from different laboratories. To determine the precision and accuracy of test results in this study, statistical analysis is performed. Statistical analyses performed for precision study are *k*-statistic and repeatability analyses while the accuracy of the testing program is evaluated through *h*-statistic, ANOVA and reproducibility analyses.

Within-laboratory consistency statistic (*k*-statistic) is defined as the ratio of the standard deviation in one laboratory to the average standard deviation of all laboratories (ASTM E691 2012). In this study the *k*-statistic is used to compare test variability within each laboratory.

Between-laboratory consistency statistic (*h*-statistic) is defined as the ratio of the deviation of one laboratory average from the average of all laboratories to the standard deviation of the averages of each laboratory (ASTM E691 2012). In this study, the *h*-statistic is used to show how the average *E**-test results from the two laboratories compare with each other.

ANOVA is a statistical tool used to evaluate the difference between two averages and the variation in the process of collection of data for each average (Kottegoda 2008). In this study, ANOVA analysis is used to evaluate the variance between the two laboratories to determine if there is a significant difference in the testing procedure adopted by each laboratory.

Repeatability is defined as closeness of the test results from a single laboratory using one test procedure on one specific material by a single operator using the same test machine (ASTM E691 2012). The repeatability study is conducted to evaluate the variation of test

77

results in a single laboratory to establish a repeatability limit for a test procedure. In this study, repeatability limits established by both Bonaquist (2011) and Bennert and Williams (2009) are compared with the *E**-test data ranges of each laboratory.

Reproducibility is defined as the closeness of test results conducted at different laboratories using one test procedure on a single material by different operators and test machines (ASTM E691 2012). Reproducibility limits determined by Bonaquist (2011) and Bennert and Williams (2009) are utilized to evaluate the accuracy of *E**-testing in this study.

4.4. *E**-Test Matrix

Extensive *E**-testing was conducted in UNM Pavement Laboratory and the IA *E** was conducted in AMEC Environment & Infrastructure, Inc. (AMEC). IA testing was performed on a minimum of two specimens for each mix. All samples for IA testing were prepared in the UNM laboratory and shipped to the AMEC laboratory for testing. Design test matrix for the study is shown in Table 4.1.

All Five Superpave asphalt mixes were used in this study, which are designated as SP-II (PG 64-22), SP-II (PG 70-22), SP-III (PG 64-22), SP-III (PG 70-22) and SP-IV (PG 70-22). The designations of mixes were based on the maximum nominal aggregate size and binder grade utilized. For example, the maximum aggregate size and binder PG-grade for SP-II (PG 64-22) mix is 25 mm and PG 64-22 while the maximum aggregate size of SP-III (PG 70-22) mix is 19 mm mixed with a binder grade of PG 70-22. The NMAS for SP-IV mixes is 12.5 mm. All asphalt mixes contain recycled asphalt pavement. Three of the mixes were collected from an actual mixing plant and the other two mixes were produced

78

in UNM's laboratory using the same gradation of mixes but changing binder grades. The five mixes utilized in this study with their respective descriptions are presented below:

- SP-II (PG 64-22) Superpave mix with NMAS of 25 mm and binder grade of PG 64-22 binder (Plant mix)

- SP-II (PG 70-22) Superpave mix with NMAS of 25 mm and binder grade of PG 70-22 binder (Laboratory mix)

- SP-III (PG 64-22) Superpave mix with NMAS of 19 mm and binder grade of PG 64-22 binder (Plant mix)

- SP-III (PG 70-22) Superpave mix with NMAS of 19 mm and binder grade of PG 70-22 binder (Laboratory mix)

- SP-IV (PG 70-22) Superpave mix with NMAS of 12.5 mm and binder grade of PG 70-22 binder (Plant mix)

4.5. Results and Discussion

Dynamic modulus test results from AMEC laboratories were analyzed and dynamic modulus mastercurves are also developed for each sample. Appendix F provides the results. To determine whether there was significant variation between UNM and AMEC E^*-results, statistical analysis was conducted. To match the number of specimens for the analysis, two samples having the closest air voids to samples used for IA testing are utilized. Analysis of data collected from each laboratory was performed using E^*-trend plots, COV plots, within-laboratory consistency (k-statistic) plots, between-laboratory (h-statistic) plots, one-way ANOVA, and repeatability and reproducibility analyses.

4.5.1. *E**-Trend Plots

Figure 4.2(a) to Figure 4.2(e) presents *E**-trend plots as a function of temperature and frequency for test results of the five mixes. The trend plot for all samples tested in both laboratories shows that the dynamic moduli are similar for all samples tested in both laboratories, indicating that temperature and frequency effects are similar in both laboratories for all mixes tested. The UNM average and AMEC average *E**-data overlap for all five test temperatures and six test frequencies suggesting the data obtained from the two laboratories is very similar.

4.5.2. Coefficient of Variation (COV) Plots

The COV is defined as the ratio of standard deviation to the average expressed in percentage as shown in Equation (4.3) (ASTM C670 2010).

$$COV = \frac{\sigma}{\mu} * 100 \tag{4.3}$$

where COV is COV (%), σ is standard deviation, μ is average.

The COVs for UNM laboratory and AMCE laboratory test data are computed for all testing temperature and frequency combinations. The results are presented in a graphical format in Figure 4.3(a) to Figure 4.3(e). Comparison of the COV plots from the two laboratories show that the COV values of both laboratories are relatively similar. The average and range of COV values determined for each mix type are as follows:

80

- Figure 4.3 (a): SP-II (PG 64-22) – COV range 0% – 22 % with an average of 13 % for UNM laboratory and range 1% – 27 % with an average of 16 % for AMEC laboratory

- Figure 4.3 (b): SP-II (PG 70-22) – COV range 0% – 24 % with an average of 12 % for UNM laboratory and range 0% – 21 % with an average of 8 % for AMEC laboratory

- Figure 4.3 (c): SP-III (PG 64-22) – COV range 0% – 22 % with an average of 10 % for UNM laboratory and range 8% – 37 % with an average of 20 % for AMEC laboratory

- Figure 4.3 (d): SP-III (PG 70-22) – COV range 0% – 17 % with an average of 6 % for UNM laboratory and range 9% – 30 % with an average of 16 % for AMEC laboratory

- Figure 4.3 (e): SP-IV (PG 70-22) – COV range 1% – 38 % with an average of 9 % for UNM laboratory and range 0% – 29 % with an average of 9 % for AMEC laboratory

Over all, COV values computed for UNM laboratory are relatively smaller than COV values determined for AMEC laboratory. An average COV value computed for E^*-results of all mixes at UNM laboratory is found to be 10% while the corresponding average COV value determined for AMEC laboratory is 14%. This might suggest that there is some variability in the testing process adopted by these laboratories and further analysis.

81

4.5.3. Within-Laboratory Consistency k-statistic Plots

The *k*-statistic is computed using Equation (4.4) (ASTM E691 2012).

$$k = \frac{s}{\sqrt{\sum_1^P \frac{S^2}{P}}} \tag{4.4}$$

where*: k* is within-laboratory consistency statistic, *s* is within-laboratory standard deviation, and *p* is number of laboratories in the interlaboratory study.

The within-laboratory consistency statistic, *k*, is an indicator of the variability in one laboratory as compared to the combined variability in all laboratories. *k*-statistic always assumes a positive value. A value of 1.0 for *k*-statistic indicates the average within-laboratory variability of both laboratories. When the computed *k*-statistic for a specific laboratory is less than 1.0, it indicates that the within-laboratory variability for that laboratory is less than the average variability of all laboratories in the study. Similarly, *k*-statistic greater than 1.0 indicates that within-laboratory variability for that laboratory is more than the average within-laboratory variability of both laboratories involved.

Figure 4.4(a) to Figure 4.4(e) presents a graphical presentation of the *k*-statistic computed for UNM and AMEC laboratories by mix type. Comparison of *k*-statistic plots from the two laboratories shows that the within-laboratory variability of both laboratories is relatively similar. The average and range of *k*-statistic values determined for each mix type are as follows:

- Figure 4.4(a): SP-II (PG 64-22) – *k*-statistic range 0 − 1.4 with an average of 0.9 for UNM laboratory and range 0.1 − 1.4 with an average of 0.9 for AMEC laboratory

- Figure 4.4 (b): SP-II (PG 70-22) – *k*-statistic range 0 − 1.4 with an average of 1 for UNM laboratory and range 0.1 − 1.4 with an average of 0.9 for AMEC laboratory

- Figure 4.4 (c): SP-III (PG 64-22) – *k*-statistic range 0 − 1.0 with an average of 0.5 for UNM laboratory and range 1 − 1.4 with an average of 1.3 for AMEC laboratory

- Figure 4.4 (d): SP-III (PG 70-22) – *k*-statistic range 0 − 1.1 with an average of 0.4 for UNM laboratory and range 0.9 − 1.4 with an average of 1.3 for AMEC laboratory

- Figure 4.4 (e): SP-IV (PG 70-22) – *k*-statistic range 0.2 − 1.4 with an average of 1.0 for UNM laboratory and range 0.1 − 1.4 with an average of 0.8 for AMEC laboratory

The average *k*-statistic value computed for UNM's laboratory was found to be 0.8 while the corresponding average *k*-statistic value determined for AMEC's laboratory was 1.0. This indicates that the within-laboratory variability from both laboratories is very similar. The fact that both values are very close to 1.0 indicates that testing conducted in both laboratories is precise.

4.5.4. Between-Laboratory Consistency h-statistic Plots

The *h*-statistic is computed using Equation (4.5) given below (ASTM E691 2012).

83

$$h = \frac{\bar{x} - \bar{\bar{X}}}{\sqrt{\Sigma_1^P \frac{(\bar{x} - \bar{X})^2}{(p-1)}}} \tag{4.5}$$

where h is between-laboratory consistency statistic; $\bar{x}$ is laboratory average, $\bar{\bar{X}}$ is average of the laboratory averages, and p is number of laboratories in the interlaboratory study.

The between-laboratory consistency statistic, h-statistic, is used to compare average test results of a specific laboratory with the overall average test results of all laboratories involved in the interlaboratory study. The overall average test results from all laboratories in the study are represented by h-statistic equal to "0.0". For averages of individual laboratories, the h-statistic can assume positive and negative values. Positive h-statistic indicates that the average values of that particular laboratory are higher than the overall average while a negative value for h statistic correspondingly indicates an average value less than the overall average of all laboratories (ASTM E691 2012, Sholar et.al. 2001).

Figure 4.5(a-e) presents the h-statistic for both UNM and AMEC laboratories for all mixes tested in this study. Comparison of h-statistic plots from the two laboratories suggests that the E^*-results from both laboratories are relatively similar with average UNM laboratory results being less than corresponding values obtained from AMEC. The average and range of h-statistic values determined for each mix type are as follows:

- Figure 4.5 (a): SP-II (PG 64-22) – h-statistic range -0.71 – 0.71 with an average of 0.28 for UNM laboratory and range -0.71 – 0.71 with an average of 0.28 for AMEC laboratory

84

- Figure 4.5 (b): SP-II (PG 70-22) – *h*-statistic range -0.71 – 0.71 with an average of -0.66 for UNM laboratory and range -0.71 – 0.71 with an average of 0.66 for AMEC laboratory

- Figure 4.5 (c): SP-III (PG 64-22) – *h*-statistic range -0.71 – 0.71 with an average of -0.66 for UNM laboratory and range -0.71 – 0.71 with an average of 0.66 for AMEC laboratory

- Figure 4.5 (d): SP-III (PG 70-22) – *h*-statistic range -0.71 – 0.71 with an average of -0.52 for UNM laboratory and range -0.71 – 0.71 with an average of 0.52 for AMEC laboratory

- Figure 4.5 (e): SP-IV (PG 70-22) – *h*-statistic range -0.71 – 0.71 with an average of 0.05 for UNM laboratory and range -0.71 – 0.71 with an average of -0.05 for AMEC laboratory

The average *h*-statistic values computed for UNM laboratory was found to be -0.3 while the corresponding average *h*-statistic value determined for AMEC laboratory was 0.3. This indicates that the averages of both laboratories are close to the overall average and the accuracy of testing in both laboratories is good.

4.5.5. Mastercurve Comparison

The E^*-data collected for each sample at different temperatures and frequencies is converted into a mastercurve for the purpose of comparing the E^*-data at a reference temperature of 21 ºC. The sigmoidal function shown in Equation (4.6) is used to fit the individual E^*-data to the mastercurve.

85

$$\log(|E^*|) = \delta + \frac{\alpha}{1+e^{\beta-\gamma\log(f_r)}} \tag{4.6}$$

where: δ is the minimum value of $|E^*|$; $\delta + \alpha$ is the maximum value of $|E^*|$; β, γ are parameters describing the shape of the sigmoidal function; f_r is reduced frequency of loading at reference temperature.

Figure 4.6(a-e) presents the *E**-mastercurves developed for all samples tested from each mix. It can be observed from Figure 4.6 that the trend of mastercurves for all samples is very similar within each mix. Comparison of *E**-values from different samples at each reduced frequency might indicate some variation, however, the difference between the *E**-mastercurves does not look significant from the visual inspection.

4.5.6. One-way ANOVA Analysis

One-way ANOVA is conducted to test the equality of means of *E**-data collected from the two laboratories. One-way ANOVA analysis is performed for each temperature and frequency combination cases of all mixes at a 5% significance level. The null and alternative hypotheses are formulated as follows:

Null hypothesis: - The mean *E** computed from UNM laboratory is the same as the mean *E** determined from AMEC laboratory (i.e. the variance caused by testing at the two different laboratories is insignificant), as in Equation (4.7).

$$\mu_{|E^*_{UNM}|} = \mu_{|E^*_{AMEC}|} \tag{4.7}$$

Alternative Hypothesis: - *E**-test results from UNM and AMEC laboratories have different means, as in Equation (4.8).

$$\mu_{|E^*_{UNM}|} \neq \mu_{|E^*_{AMEC}|} \tag{4.8}$$

Significance Level: - A significance level of 0.05 is selected for this study. (i.e., the probability of being wrong to reject the null hypothesis is 5 %.)

Test Statistic: - The test statistic for ANOVA analysis is F-statistic. The F-statistic for each temperature and frequency combination is calculated and presented in Table 4.2. The F-critical value is found to be 18.5.

If the F-statistic $\geq$ F-critical, then we will reject the null hypothesis.

If the F-statistic $<$ F -critical, then we do not reject the null hypothesis.

P-value: - the P-value represents the probability of obtaining an F-statistic value that is equal or more assuming the null hypothesis is true. Computed P-values for each test temperature and frequency combinations for each mix are presented in Table 4.2.

If the P-value $<$ 0.05, then we will reject the null hypothesis.

If the P-value $\geq$ 0.05, then we do not reject the null hypothesis.

From Table 4.2, it can be seen that the F-statistic is always below the F-critical value. Considering the fact that all F-statistic data is well below the F-critical value, the null hypothesis is accepted leading to the conclusion that the means of the *E**-data collected from the UNM and AMEC laboratories is the same. On the same note, the P-values are always well above the critical value of 5% which dictates to accept the null hypothesis. The F-test and P-value analysis both confirm the equality of the *E**-results from the two

87

laboratories, which indicates that variance caused by conducting the tests at AMEC and UNM laboratories is insignificant.

4.5.7. Repeatability Analysis

The repeatability limit for E^*-test results is the maximum acceptable range between replicate test results in a single laboratory. It is determined by multiplying the repeatability COV with the appropriate factor dependent on the number of test results (ASTM C670 2010). Bonaquist (2011) determined the repeatability COVs to be dependent on NMAS and E^*-values of the mix. Bonaquist (2011) also found that E^*-testing at low temperatures shows less variability with a repeatability COV close to 7%. As the stiffness of AC decreases, however, the repeatability COV increases exponentially. Bennert and Williams (2009), on the other hand, developed general precision statements, which are not a function of any mix variables. They determined the COV for repeatability to be 13.03%. The multiplying factor for two replicate samples is $2\sqrt{2}$. The average and maximum range values are determined for each mix type as follows:

- SP-II (PG 64-22) – maximum range 31 with an average of 19 for UNM laboratory and range 27 with an average of 16 for AMEC laboratory
- SP-II (PG 70-22) – maximum range 33 with an average of 17 for UNM laboratory and range 29 with an average of 12 for AMEC laboratory
- SP-III (PG 64-22) – maximum range 31 with an average of 13 for UNM laboratory and range 53 with an average of 28 for AMEC laboratory

88

- SP-III (PG 70-22) – maximum range 24 with an average of 8 for UNM laboratory and range 43 with an average of 23 for AMEC laboratory

- SP-IV (PG 70-22) – maximum range 53 with an average of 12 for UNM laboratory and range 40 with an average of 12 for AMEC laboratory

Repeatability analysis results are presented in Figure 4.7(a) to Figure 4.7(e). Acceptable ranges for repeatability along with computed ranges of E^*-test data for each mix tested in UNM and AMCE are presented. It can be observed that the acceptable ranges (d2s% limits) determined using the functions developed by Bonaquist (2011) are lower than the d2s% limits specified by Bennert and Williams (2009). Moreover, for all mixtures tested in this study, the *computed E^*-ranges* are found to be below the Bennert and Williams (2009) limit and in most cases higher than Bonaquist (2011) limits. This indicates acceptable repeatability of E^*-testing in UNM and AMEC laboratories.

4.5.8. Reproducibility Analysis

The reproducibility limit is the maximum allowable difference between the averages of test results obtained from the different laboratories. The reproducibility limit is also calculated by multiplying the reproducibility COV with an appropriate factor from Table 1 of ASTM C670 (2010) and dividing it by the square root of the number of samples used to calculate the averages (ASTM C670). Bonaquist (2011) determined the reproducibility COVs to be dependent on E^*-values of the mix and found that the reproducibility COV is close to 10% for E^*-testing at low temperatures and as the stiffness of AC decreases, the reproducibility COV increases. Bennert and Williams (2009), on the other hand, determined reproducibility COV to be 26.89%. The multiplication factor for two replicate

89

tests is determined to be 2. The average and maximum range values for UNM and AMEC test results are determined for each mix type as follows:

- Figure 4.8 (a): SP-II (PG 64-22) – maximum range 28 with an average of 10

- Figure 4.8 (b): SP-II (PG 70-22) – maximum range 44 with an average of 25

- Figure 4.8 (c): SP-III (PG 64-22) – maximum range 24 with an average of 13

- Figure 4.8 (d): SP-III (PG 70-22) – maximum range 29 with an average of 16

- Figure 4.8 (e): SP-IV (PG 70-22) – maximum range 43 with an average of 15

Reproducibility analysis for UNM and AMEC test results is presented in Figure 4.8(a) to Figure 4.8(e). Reproducibility limits using the functions developed by Bonaquist (2011) and general limits provided by Bennert and Williams (2009) are presented along with the range for averages of UNM and AMEC E^*-results. Similar to the repeatability analysis, the limits for reproducibility computed using Bonaquist (2011) are less than the reproducibility limits provided by Bennert and Williams (2009). In addition, it can be observed from Figure. 8(a-e) that the reproducibility statistic computed for the two laboratories is, in most cases, below d2s% limits specified by both round-robin studies. This indicates acceptable reproducibility of E^*-results between UNM and AMEC laboratories.

4.6. Conclusions

This study is conducted to determine the precision of E^*-testing preformed in UNM pavement laboratory through IA testing. The results from both laboratories were investigated through statistical analysis. In addition, repeatability and reproducibility

analysis was performed based on previous round-robin studies conducted in the past. From this study, the following conclusions can be made:

- COV plots indicate that the results from UNM and AMEC laboratories are very similar.

- Within-laboratory consistency (k-statistic) plots suggest that the within-laboratory variability from UNM and AMEC laboratories are close to each other, indicating good precision of testing in each laboratory.

- Between-laboratory consistency (h-statistic) plots suggest that the average E^*-value determined from UNM and the average E^*-value determined from AMEC laboratory testing are close to each other indicating good accuracy.

- One-way ANOVA analysis was performed for each temperature and frequency testing condition. The results indicate no significant difference in the means as well as the variances for testing at UNM and AMEC laboratories, which indicates good accuracy of testing in both laboratories.

- Repeatability analysis of selected test results indicate acceptable repeatability of E^*-testing in UNM and AMEC laboratories. This indicates good precision testing in both laboratories.

- Reproducibility analysis of selected test results indicate acceptable reproducibility of E^*-testing in UNM and AMEC laboratories, which indicates good accuracy of test results.

- IA testing is a good and economical way to evaluate the accuracy and precision of E^*-testing of a specific laboratory.

91

Table 4.1: Test Matrix for Dynamic Modulus

Laboratories	Asphalt Mixes	Replicate Samples	Test Frequency (Hz)	Test Temperature (°C)
(Two)	(Five)	(two)	(six)	(five)
UNM-Lab	SP-II (PG 64-22)		25	-10
AMEC-Lab	SP-II (PG 70-22)		10	4
	SP-III (PG 64-22)		5	21
	SP-III (PG 70-22)		1	37
	SP-IV (PG 70-22)		0.5	54
			0.1	

Table 4.2: ANOVA Analysis Results

Temp.	FrEquation	SP-2 (PG64-22)		SP-2 (PG70-22)		SP-3 (PG64-22)		SP-3 (PG70-22)		SP-4 (PG70-22)	
(°C)	(Hz)	F-stat	P-value	F-stat	P-value	F-stat	P-value	F-stat	P-value	F-stat	P-value
-10	25	2.902	0.231	0.001	0.976	0.176	0.716	4.730	0.162	0.033	0.873
	10	3.729	0.193	0.001	0.982	0.208	0.693	7.680	0.109	0.087	0.795
	5	3.534	0.201	0.009	0.933	0.207	0.694	6.784	0.121	0.110	0.771
	1	4.255	0.175	0.009	0.933	0.131	0.752	4.259	0.175	0.166	0.723
	0.5	4.270	0.175	0.020	0.900	0.261	0.660	4.266	0.175	0.189	0.706
	0.1	3.765	0.192	0.010	0.929	0.162	0.726	3.047	0.223	0.230	0.679
4	25	0.218	0.687	3.640	0.197	0.552	0.535	6.208	0.130	14.995	0.061
	10	0.181	0.712	6.334	0.128	0.338	0.620	8.053	0.105	12.953	0.069
	5	0.194	0.703	6.283	0.129	0.321	0.628	8.731	0.098	13.130	0.068
	1	0.110	0.772	6.523	0.125	0.218	0.686	7.694	0.109	8.060	0.105
	0.5	0.052	0.840	5.210	0.150	0.273	0.654	7.637	0.110	9.717	0.089
	0.1	0.013	0.919	5.247	0.149	0.191	0.705	3.854	0.189	9.126	0.094
21	25	0.053	0.839	0.012	0.923	2.696	0.242	1.761	0.316	3.818	0.190
	10	0.004	0.953	0.092	0.790	1.600	0.333	1.505	0.345	4.586	0.166
	5	0.018	0.907	0.171	0.719	1.424	0.355	1.580	0.336	11.382	0.078
	1	0.102	0.780	0.013	0.918	1.666	0.326	1.685	0.324	0.062	0.826
	0.5	0.085	0.798	0.043	0.855	1.039	0.415	1.709	0.321	0.027	0.886
	0.1	0.118	0.764	0.041	0.858	1.465	0.350	1.319	0.370	0.025	0.888
37	25	0.387	0.597	0.012	0.923	0.691	0.493	0.448	0.572	0.010	0.930
	10	0.157	0.730	5.160	0.151	0.306	0.636	0.308	0.635	0.020	0.900
	5	0.111	0.771	3.587	0.199	0.989	0.425	0.253	0.665	8.974	0.096
	1	0.018	0.907	6.134	0.132	1.095	0.405	0.136	0.748	8.874	0.097
	0.5	0.073	0.813	6.537	0.125	0.887	0.446	0.012	0.923	3.173	0.217
	0.1	0.184	0.710	12.232	0.073	0.548	0.536	0.008	0.936	0.438	0.576
54	25	1.300	0.372	0.452	0.571	7.812	0.108	0.236	0.675	0.191	0.705
	10	0.718	0.486	0.016	0.911	4.848	0.159	0.000	0.987	5.124	0.152
	5	0.581	0.525	0.001	0.983	5.820	0.137	0.004	0.955	0.730	0.483
	1	0.013	0.918	0.112	0.769	2.102	0.284	0.302	0.638	0.888	0.445
	0.5	0.087	0.795	0.741	0.480	0.925	0.438	0.887	0.446	1.339	0.367
	0.1	0.789	0.468	3.498	0.202	0.078	0.806	0.620	0.513	1.649	0.328

93
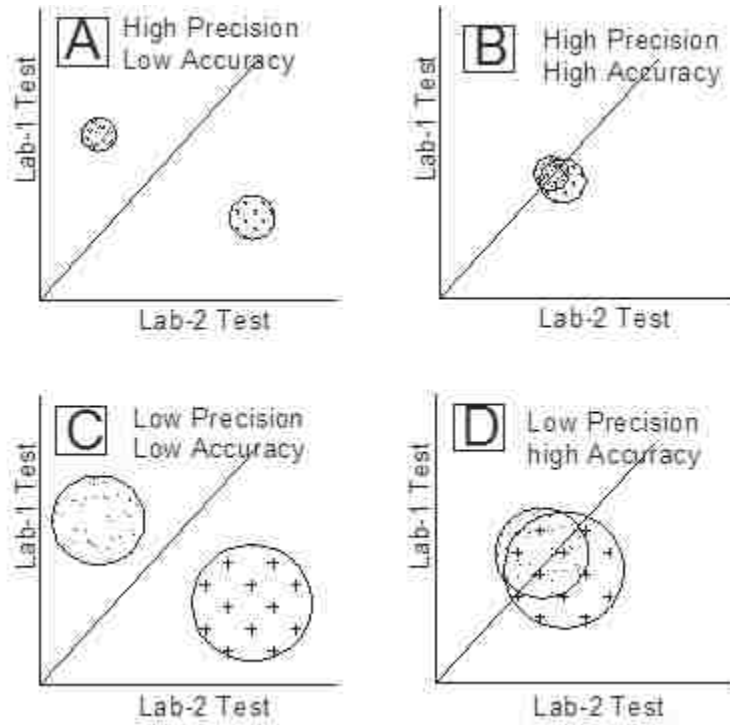
Figure 4.1: Concepts of Precision and Accuracy.

94
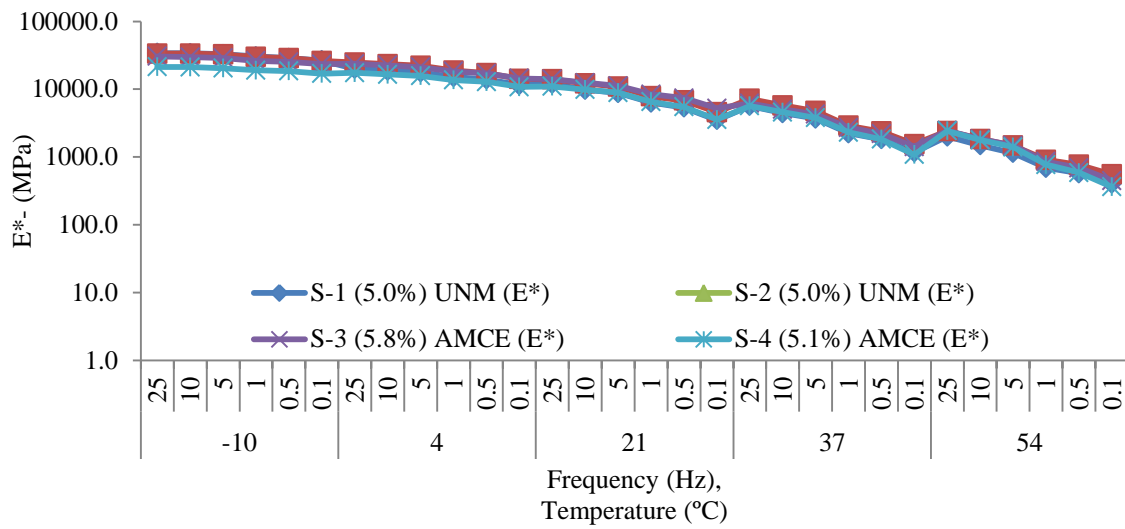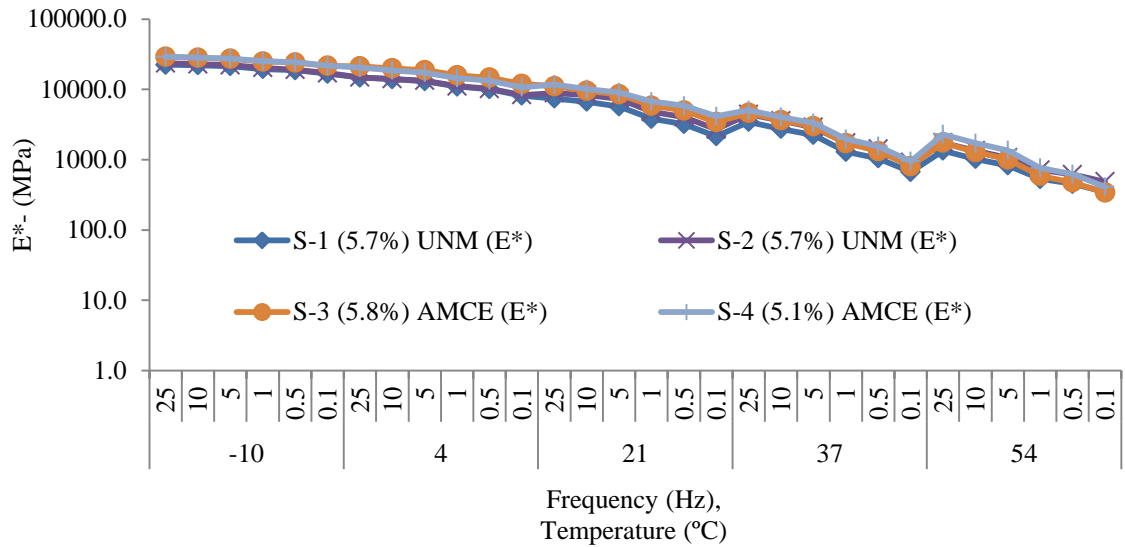
(a) SP-II with PG 64-22

(b) SP-II with PG 70-22

Figure 4.2 (a-b) E^*-Trend Plots as a Function of Frequency and Temperature.
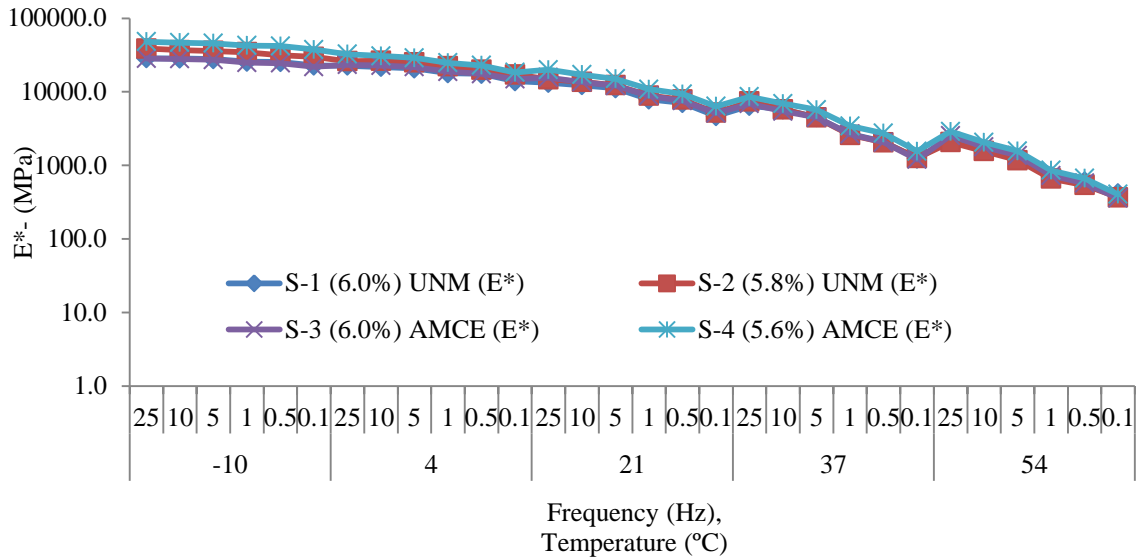
(c) SP-III with PG 64-22
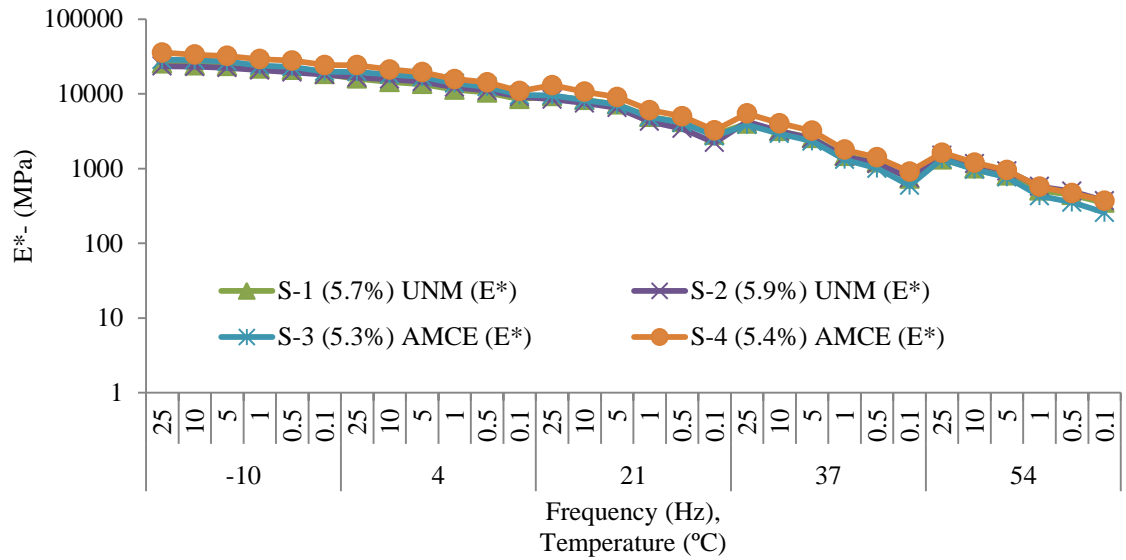
(d) SP-III with PG 70-22

Figure 4.2 (c-d) E^*- Trend Plots as a Function of Frequency and Temperature.

96
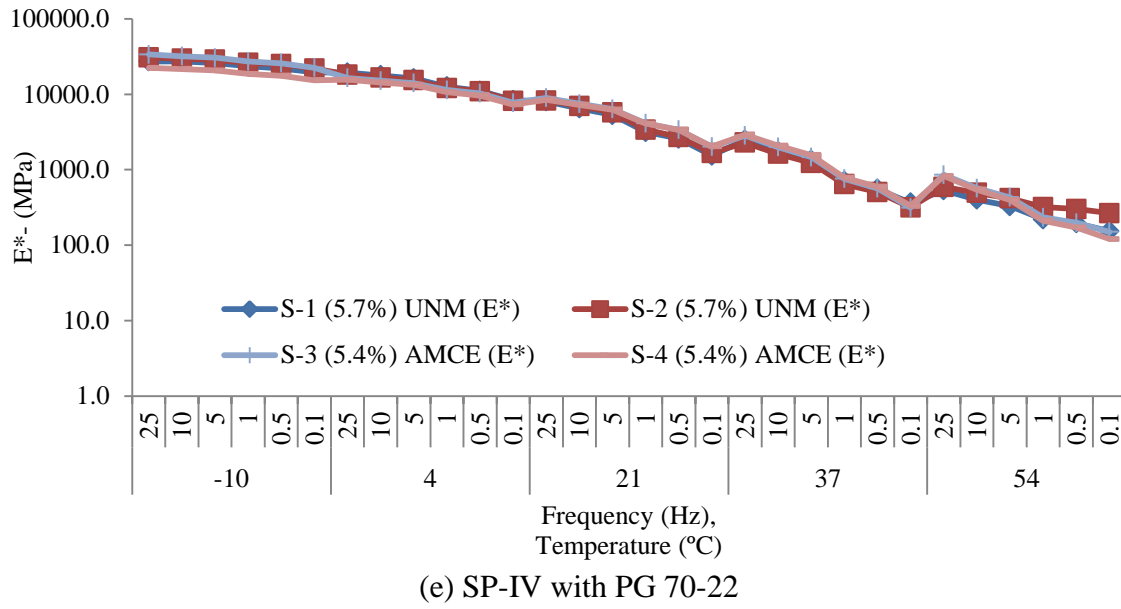
Figure 4.2 (a-e) *E**- Trend Plots as a Function of Frequency and Temperature.
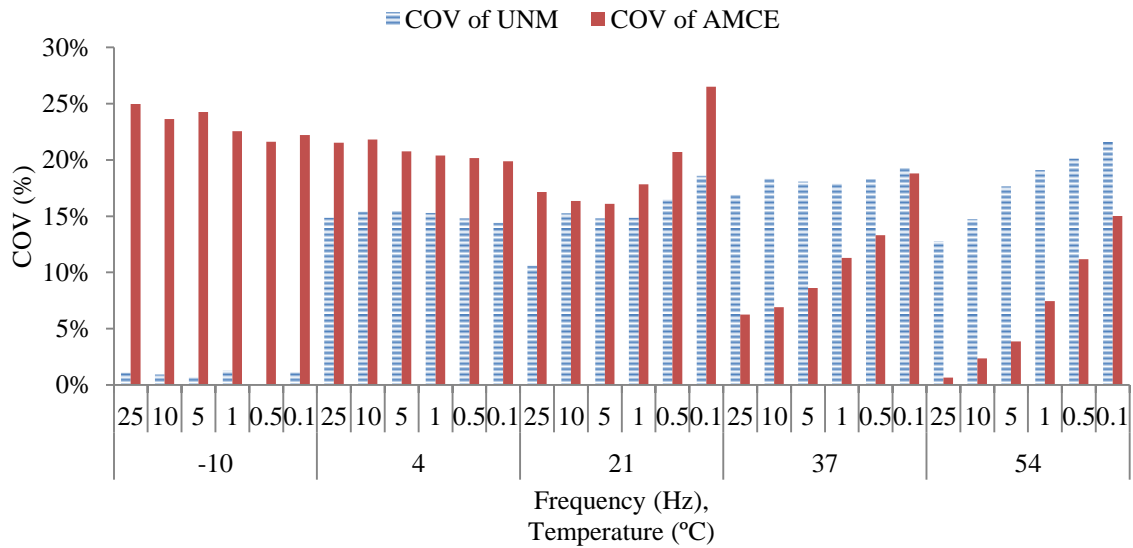
(a) SP-II with PG 64-22
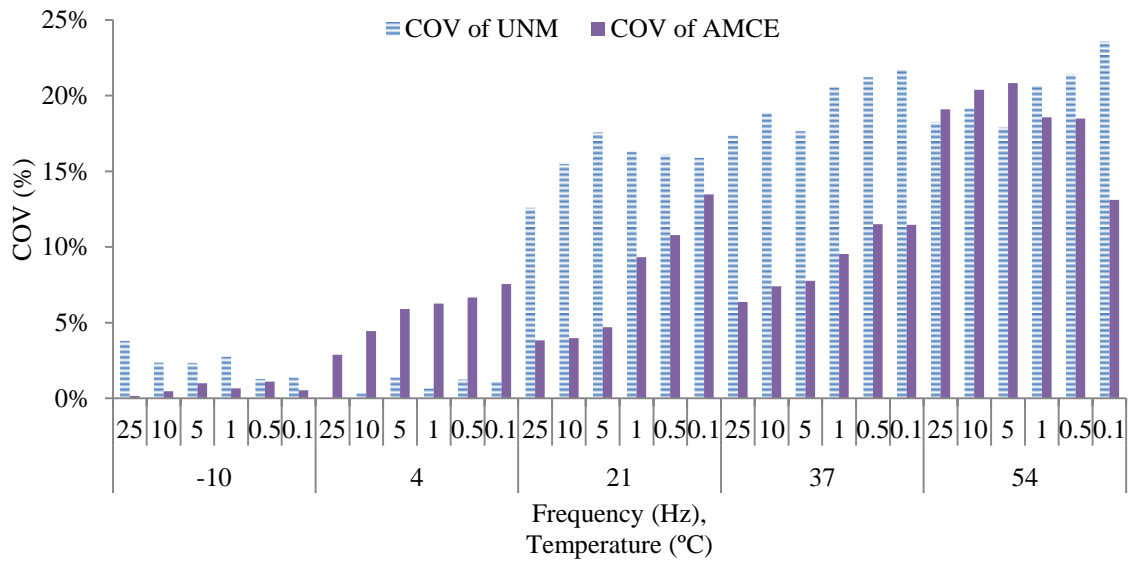
(b) SP-II with PG 70-22

Figure 4.3 (a-b) Coefficient of Variation (COV) Plots.
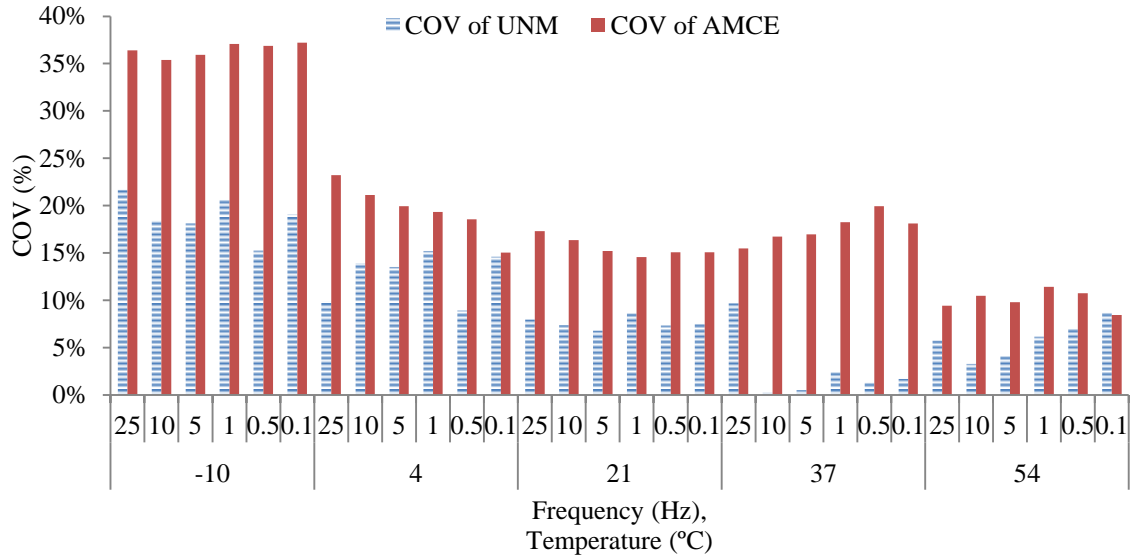
(c) SP-III with PG 64-22
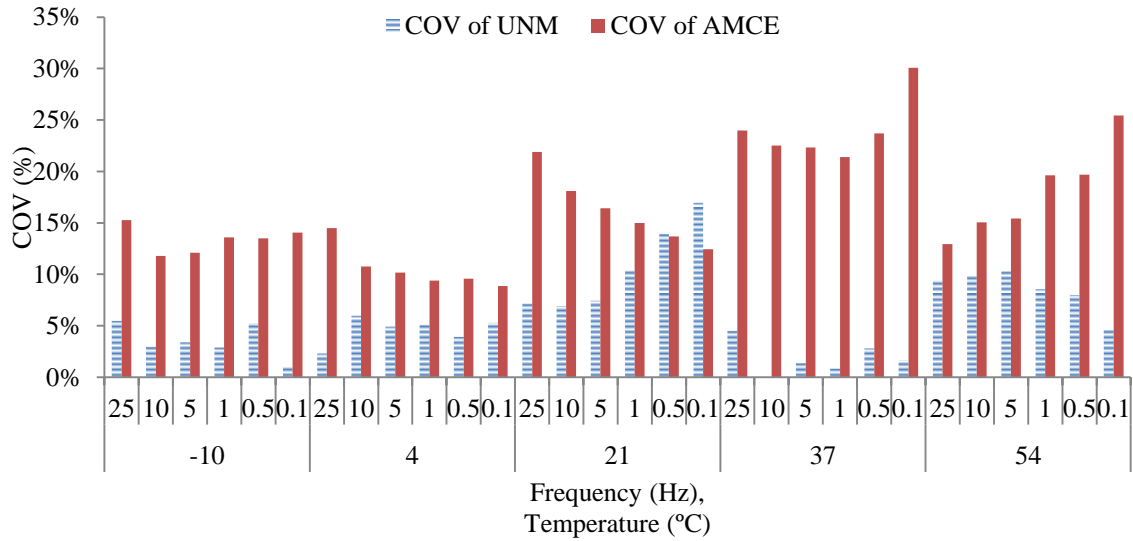
(d) SP-III with PG 70-22
Figure 4.3 (c-d) Coefficient of Variation (COV) Plots.

99
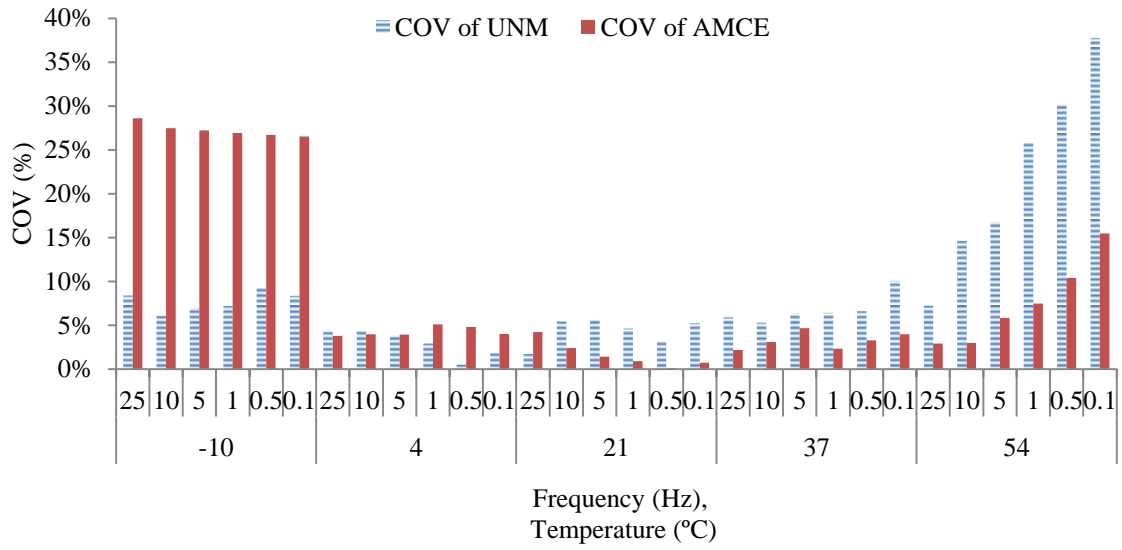
(e) SP-IV with PG 70-22

Figure 4.3 (a-e) Coefficient of Variation (COV) Plots.
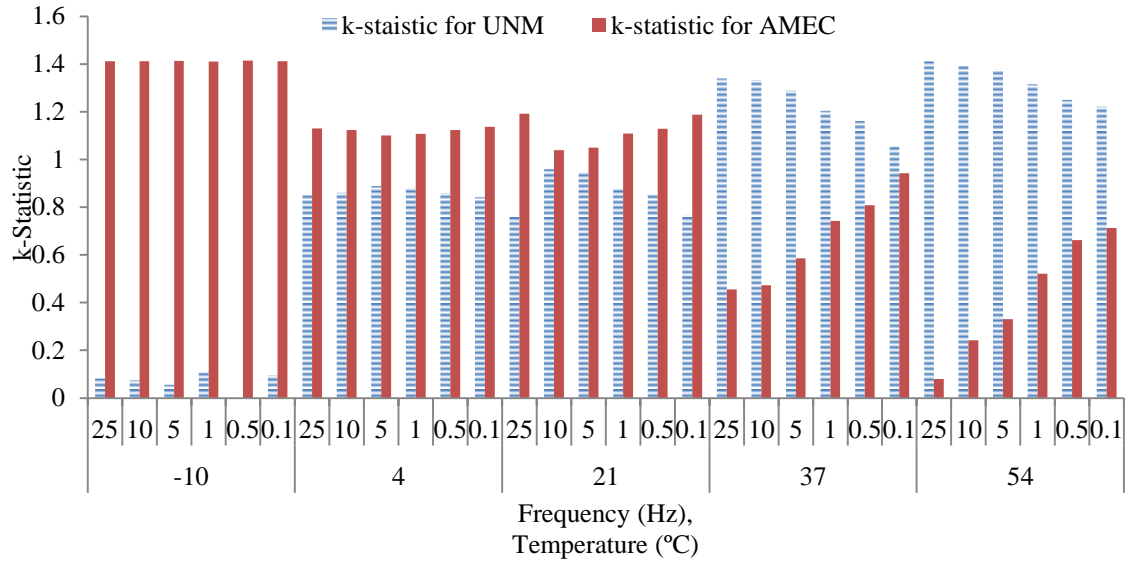
(a) SP-II with PG 64-22
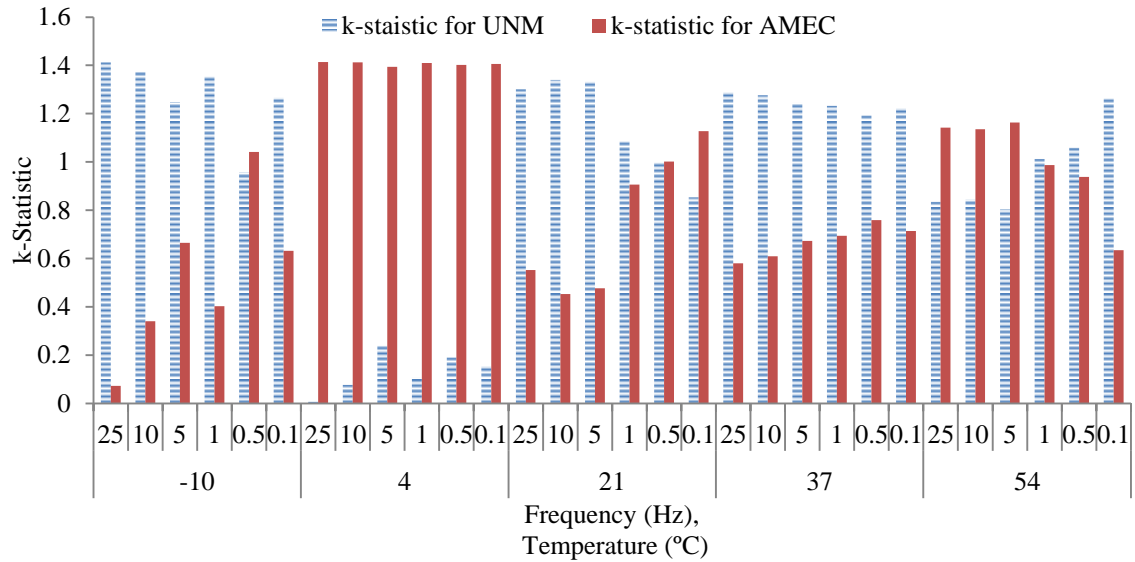
(b) SP-II with PG 70-22

Figure 4.4 (a-b) Within-Laboratory Consistency (*k*-Statistic) Plots.
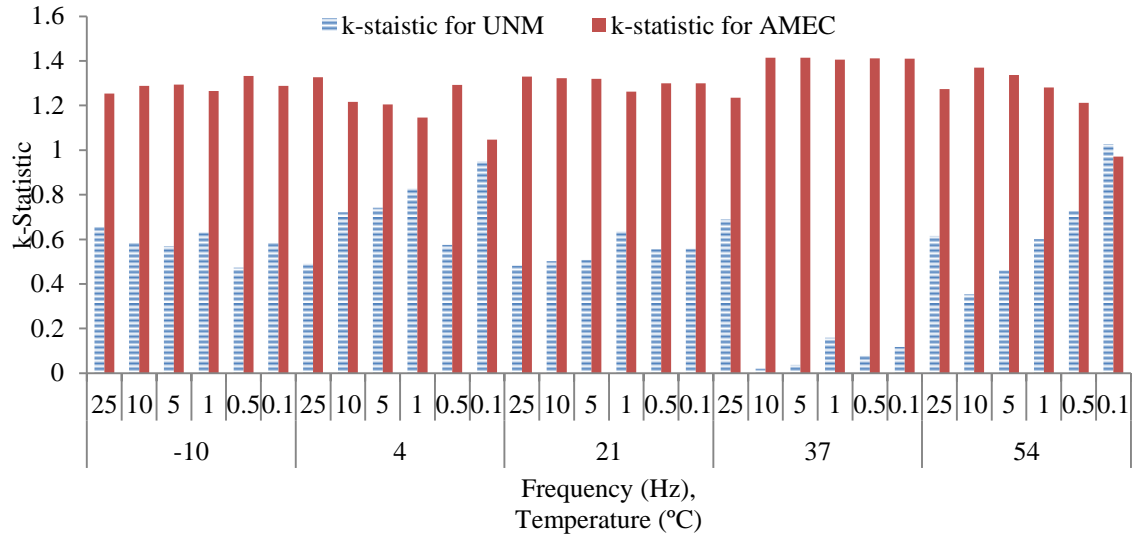
(c) SP-III with PG 64-22
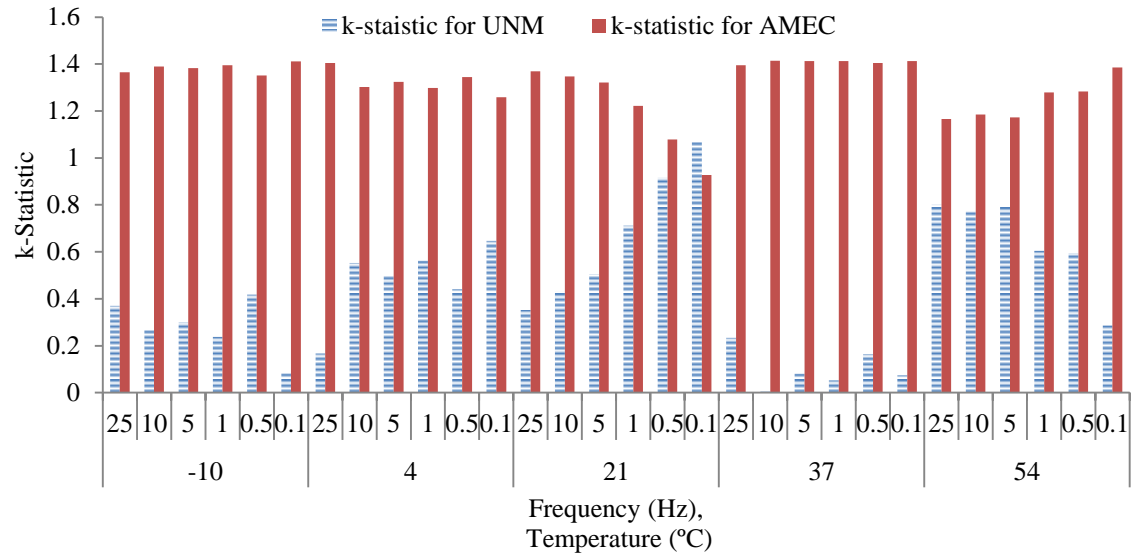
(d) SP-III with PG 70-22

Figure 4.4 (c-d) Within-Laboratory Consistency (*k*-Statistic) Plots.

(e) SP-IV with PG 70-22
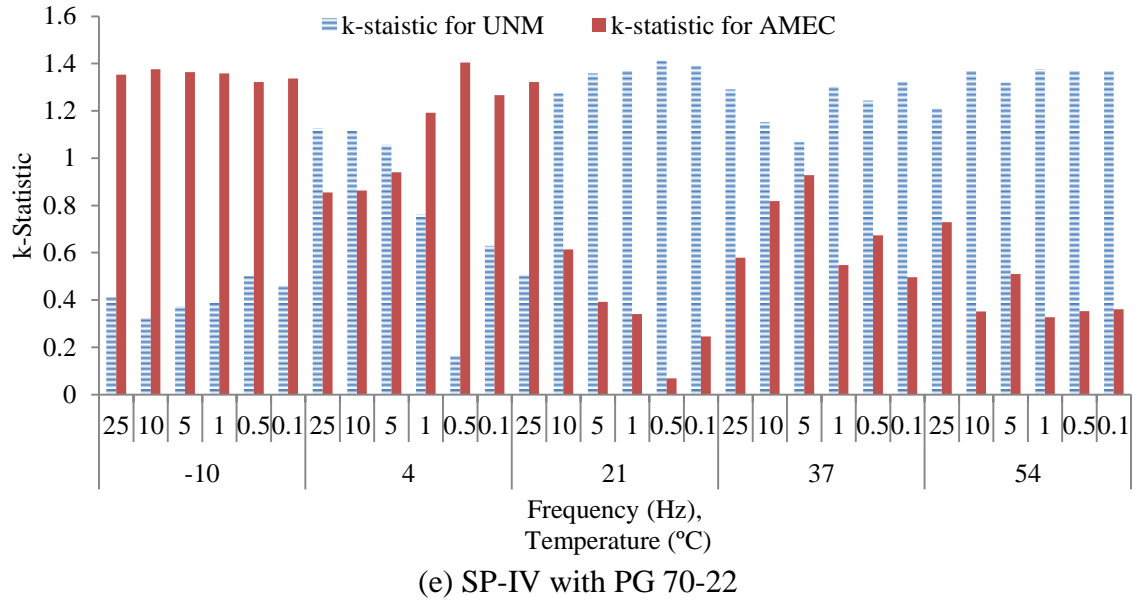
Figure 4.4 (a-e) Within-Laboratory Consistency (*k*-Statistic) Plots.

103
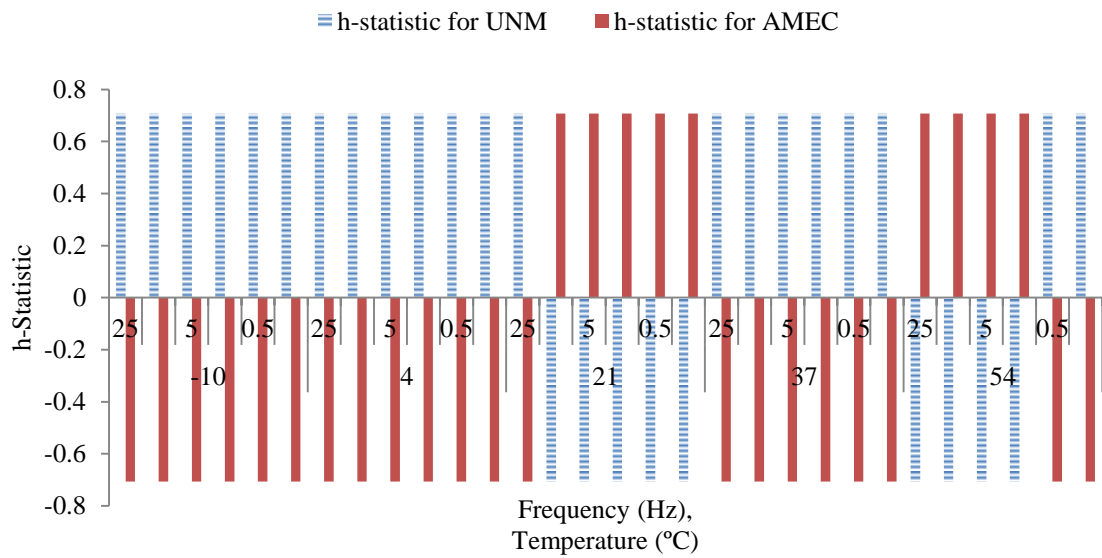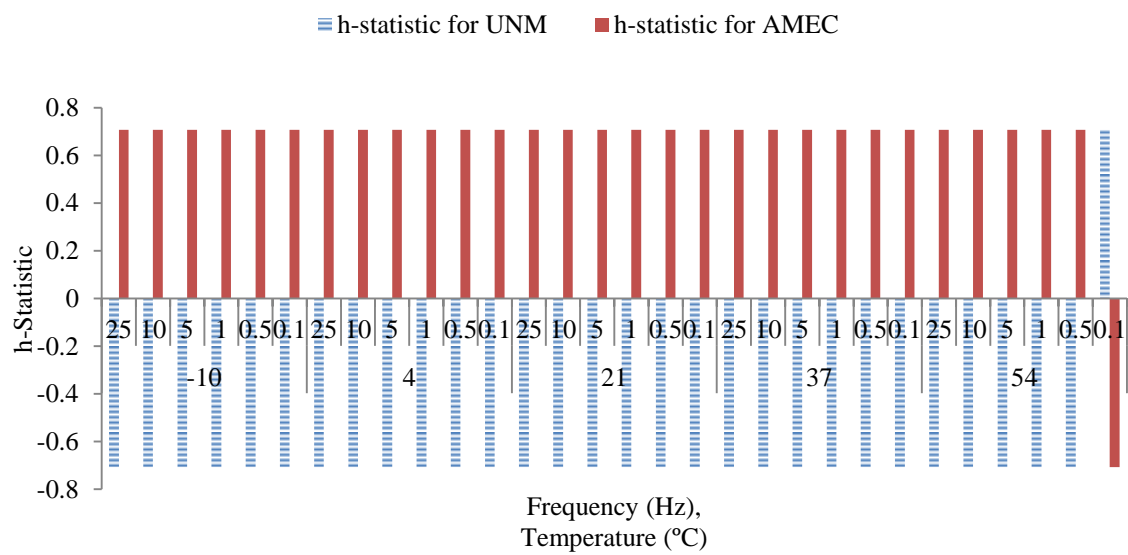
(a) SP-II with PG 64-22

(b) SP-II with PG 70-22

Figure 4.5 (a-b) Between Laboratories *h*-statistic Plots.

■ h-statistic for UNM   ■ h-statistic for AMEC

(c) SP-III with PG 64-22

■ h-statistic for UNM   ■ h-statistic for AMEC
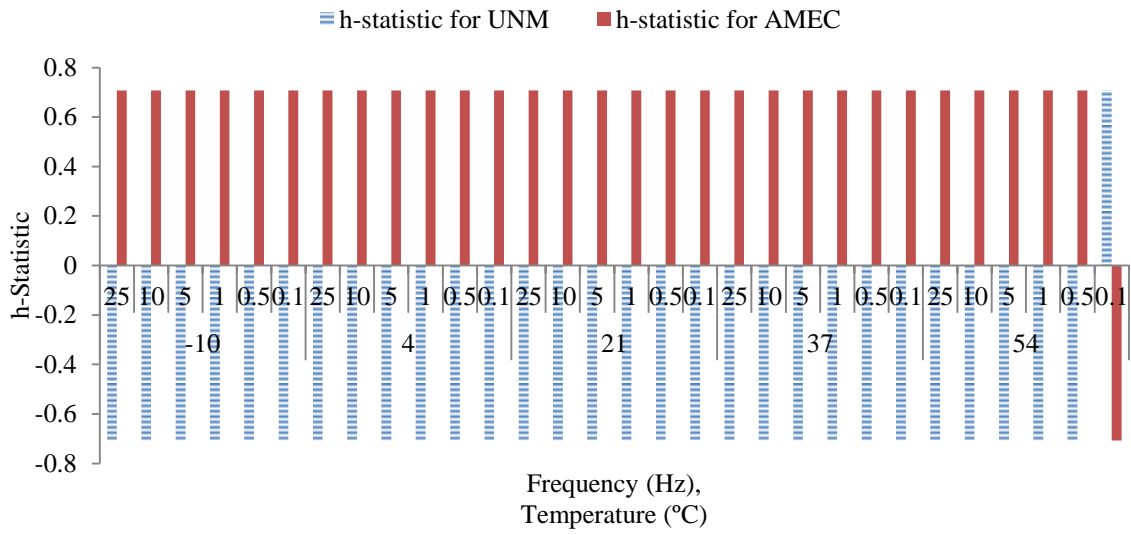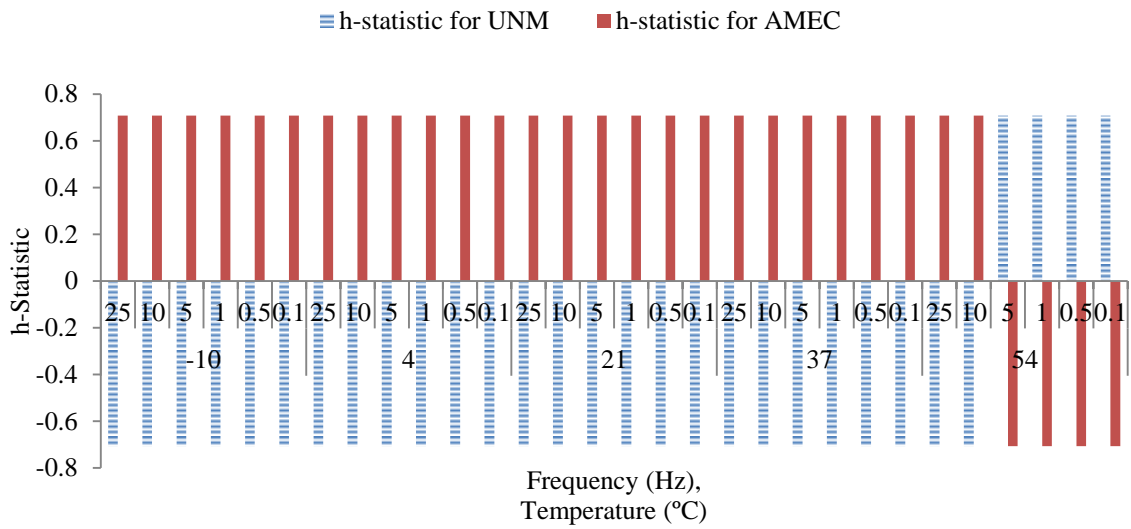
(d) SP-III with PG 70-22

Figure 4.5 (c-d) Between Laboratories *h*-statistic Plots.

105
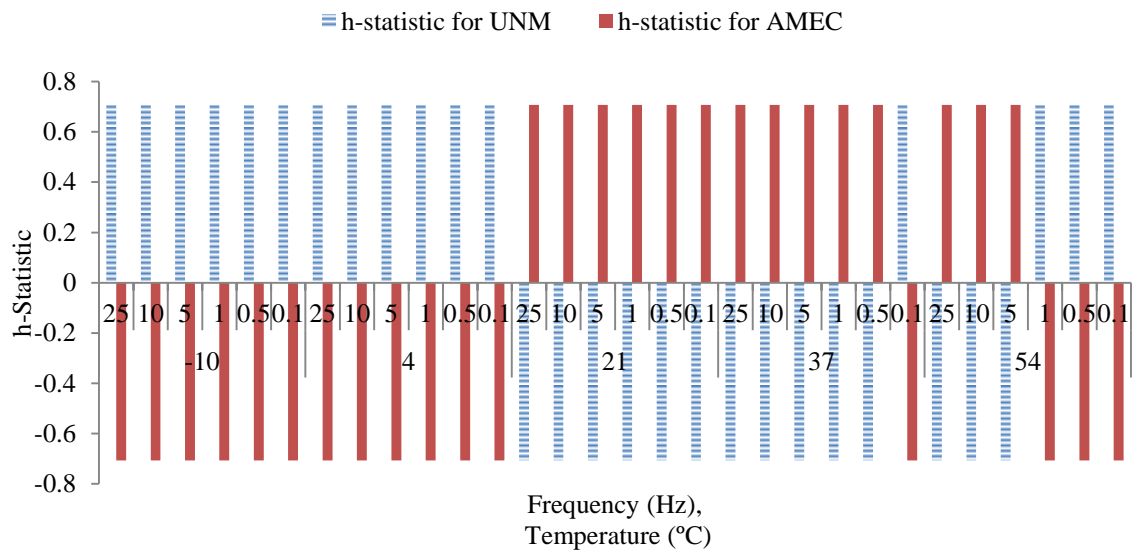
(e) SP-IV with PG 70-22

Figure 4.5 (a-e) Between Laboratories *h*-statistic Plots.

106
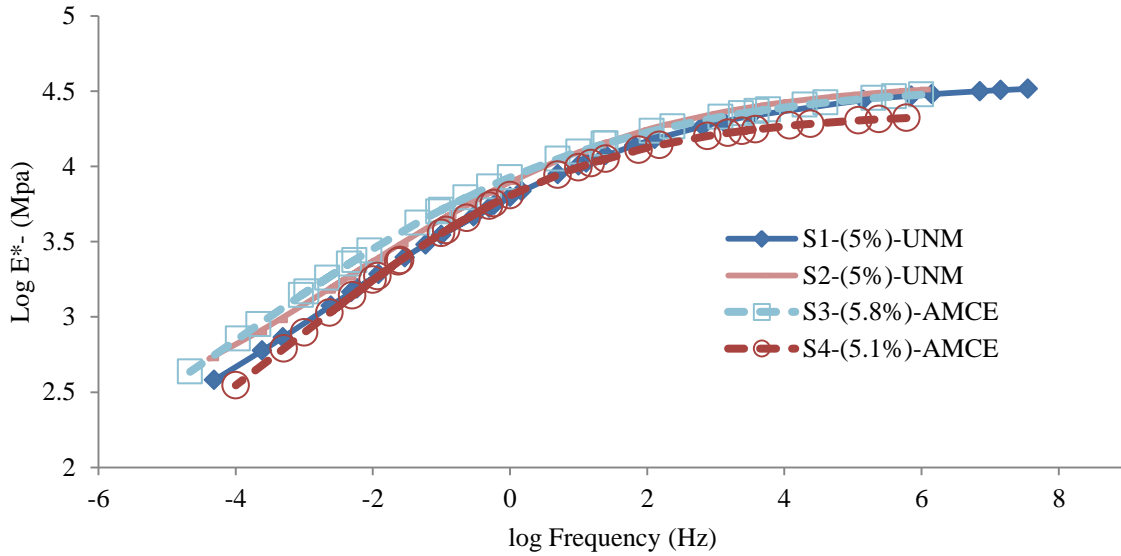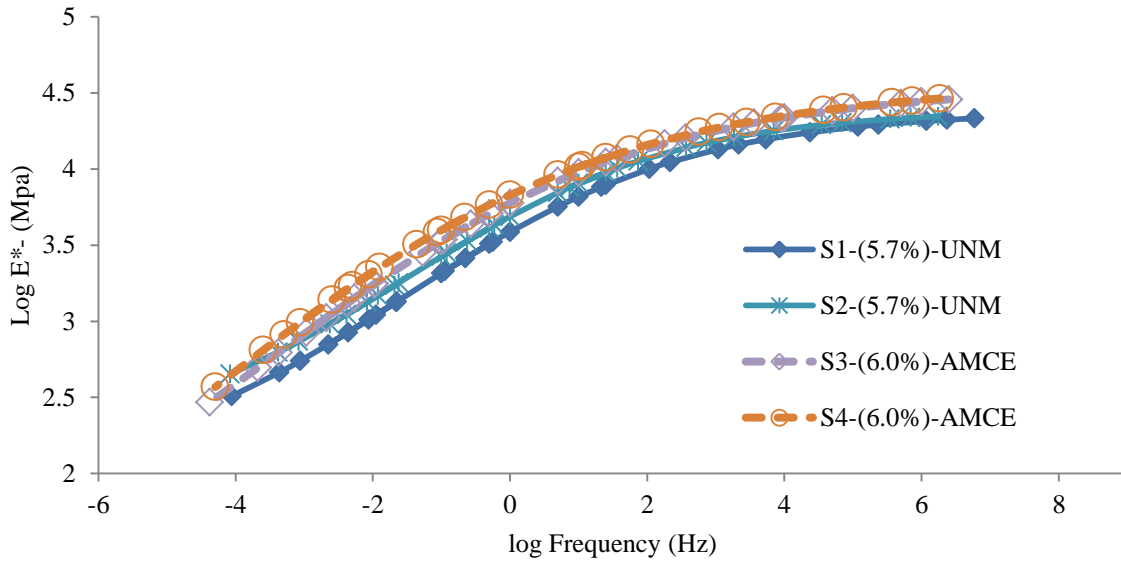
(a) SP-II with PG 64-22

(b) SP-II with PG 70-22

Figure 4.6 (a-b) Mastercurve Plots.

107
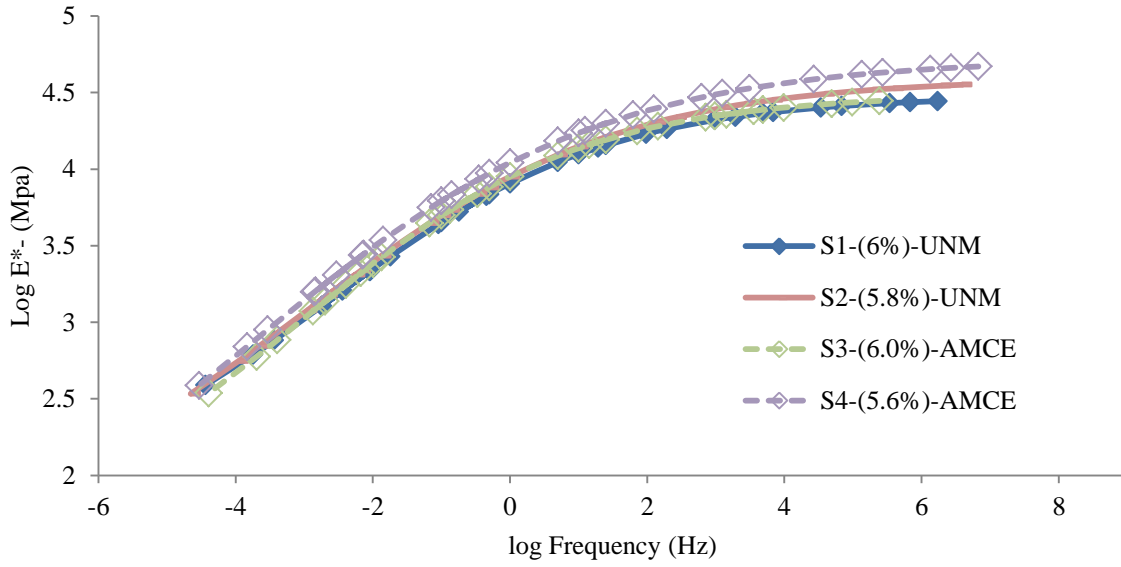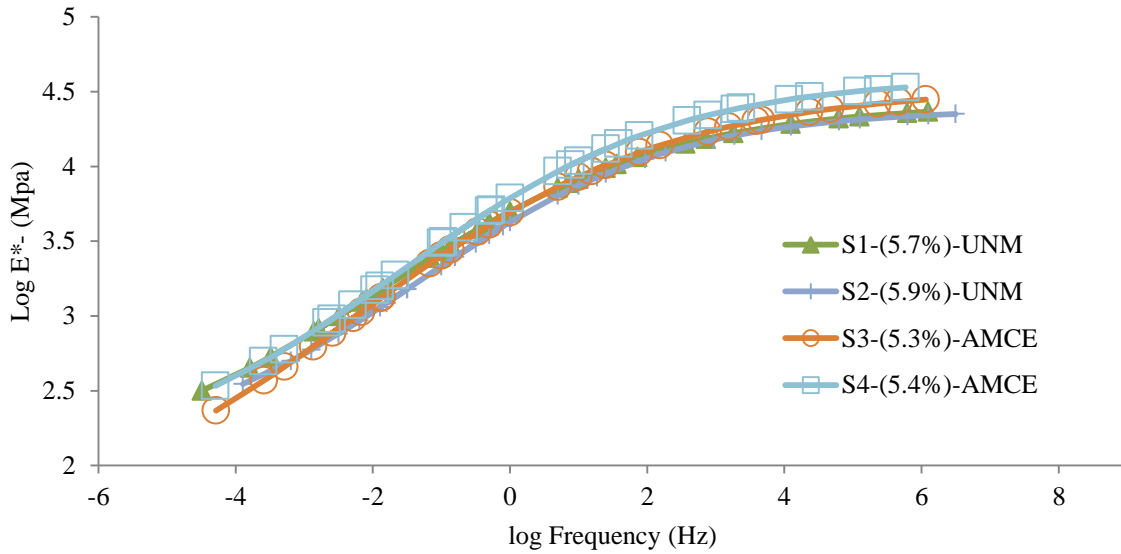
(c) SP-III with PG 64-22

(d) SP-III with PG 70-22

Figure 4.6 (c-d) Mastercurve Plots.
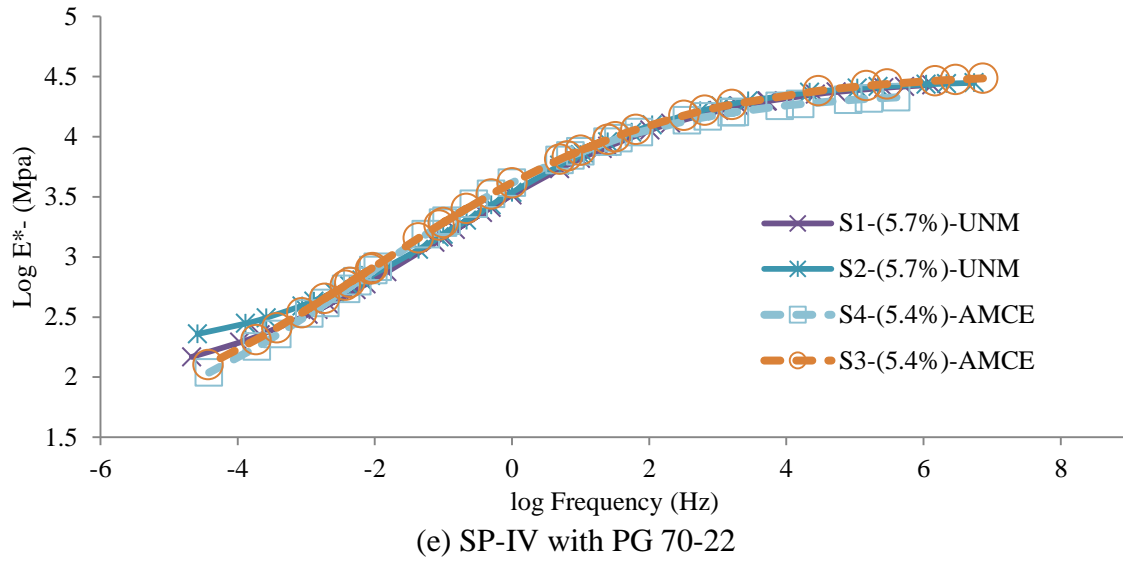
(e) SP-IV with PG 70-22

Figure 4.6 (a-e) Mastercurve Plots.
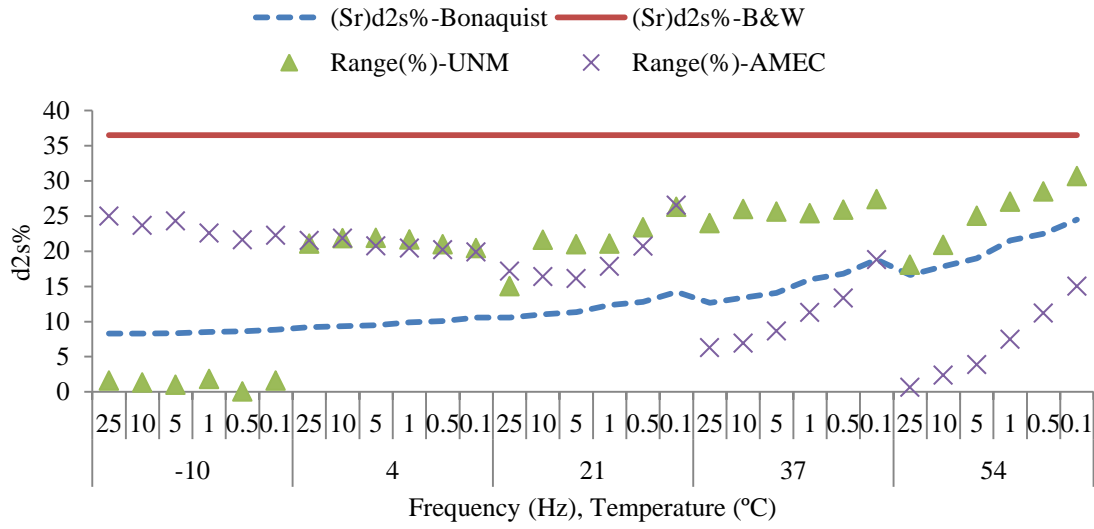
(a) SP-II with PG 64-22
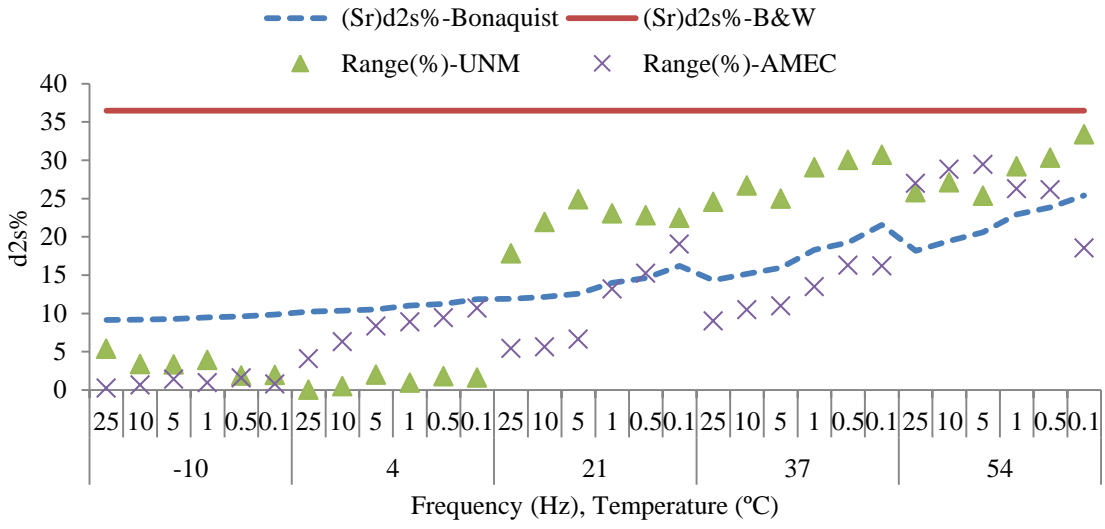
(b) SP-II with PG 70-22

Figure 4.7 (a-b) Repeatability Analysis of E^*-Results From UNM and AMEC Laboratories.

(c) SP-III with PG 64-22
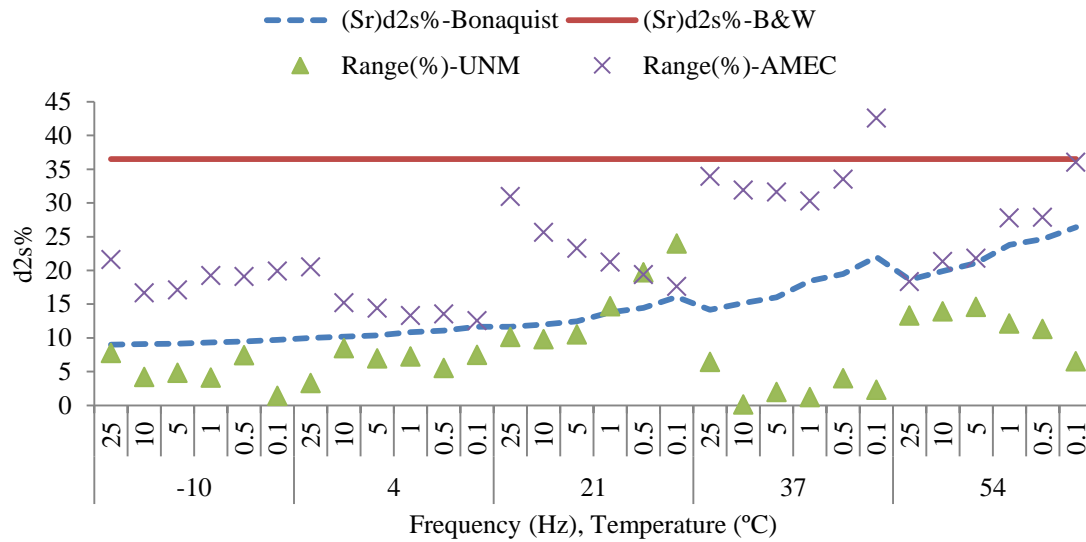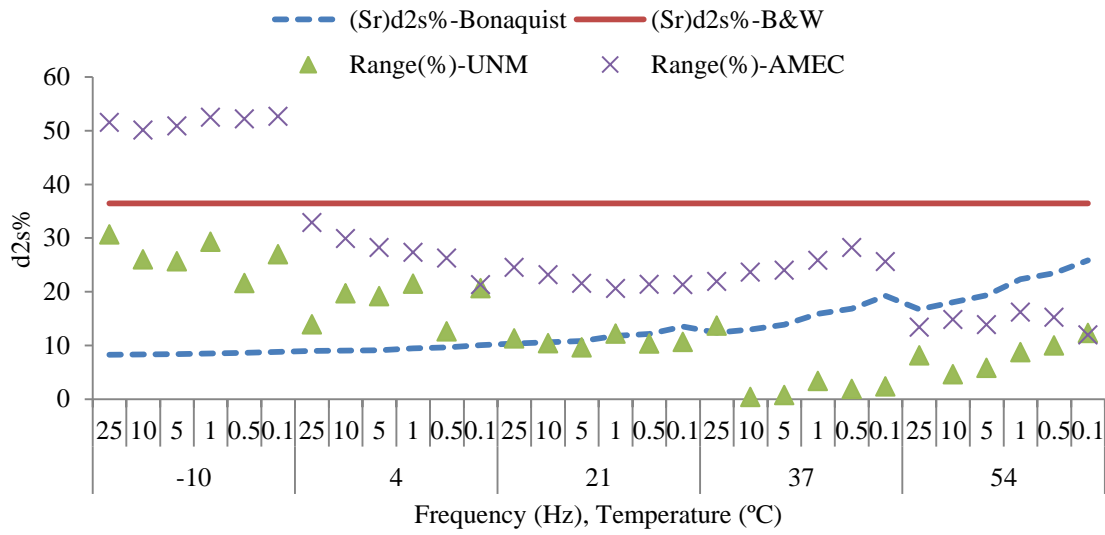
(d) SP-III with PG 70-22

Figure 4.7 (c-d) Repeatability Analysis of *E**-Results From UNM and AMEC Laboratories.
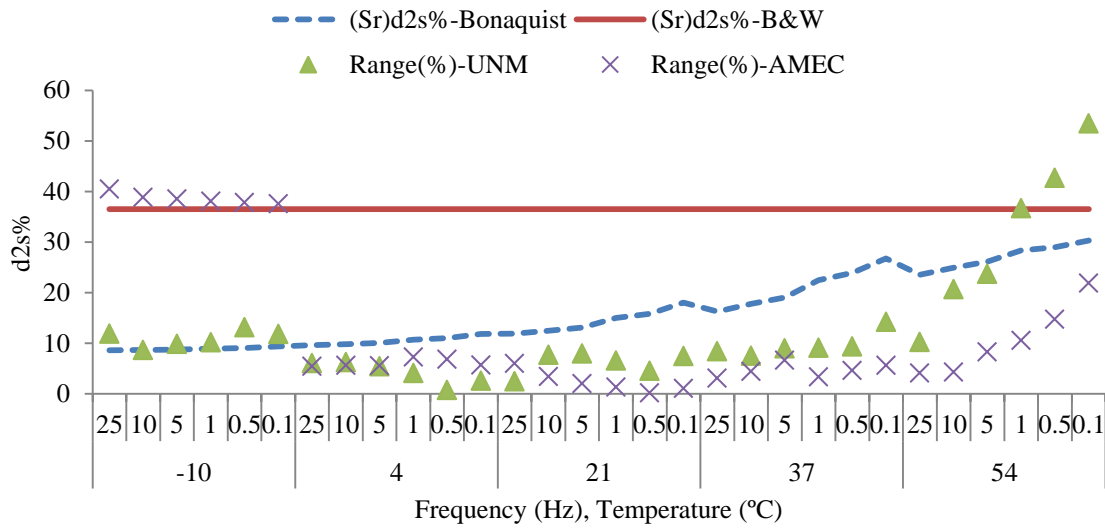
(e) SP-IV with PG 70-22

Figure 4.7 (a-e) Repeatability Analysis of *E**-Results From UNM and AMEC Laboratories.
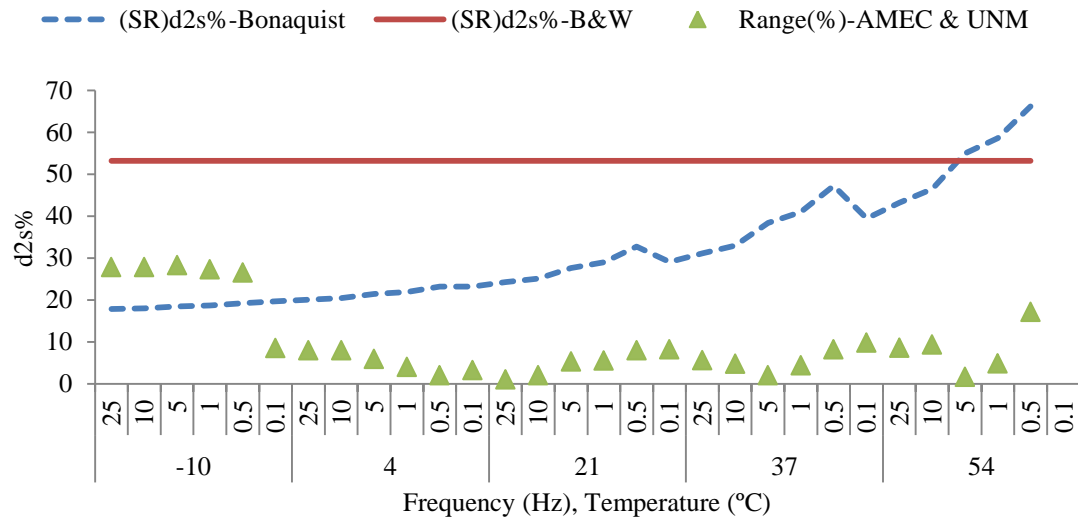
(a) SP-II with PG 64-22
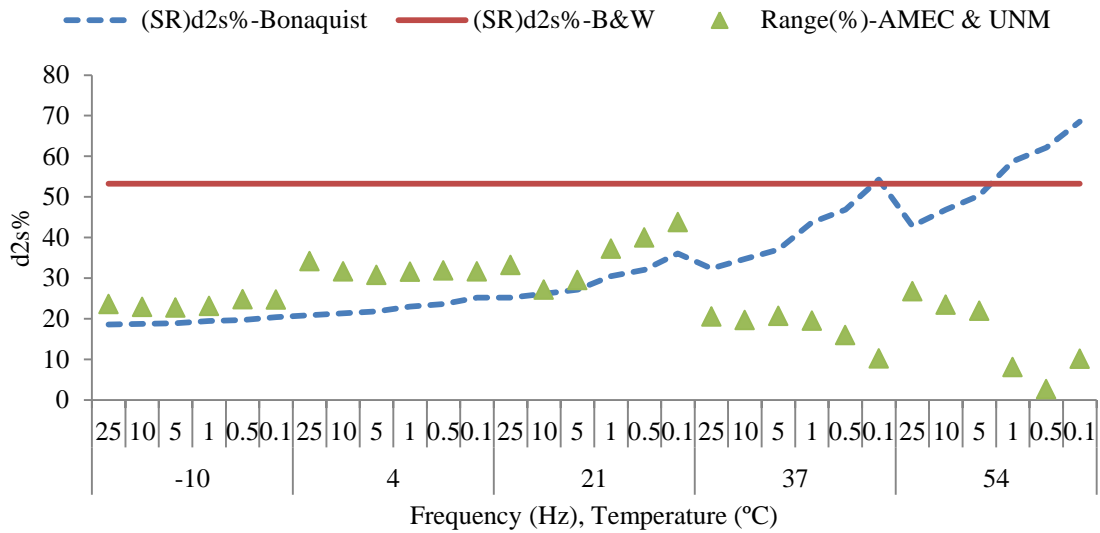
(b) SP-II with PG 70-22

Figure 4.8 (a-b) Reproducibility Analysis of *E**-Results From UNM and AMEC Laboratories.
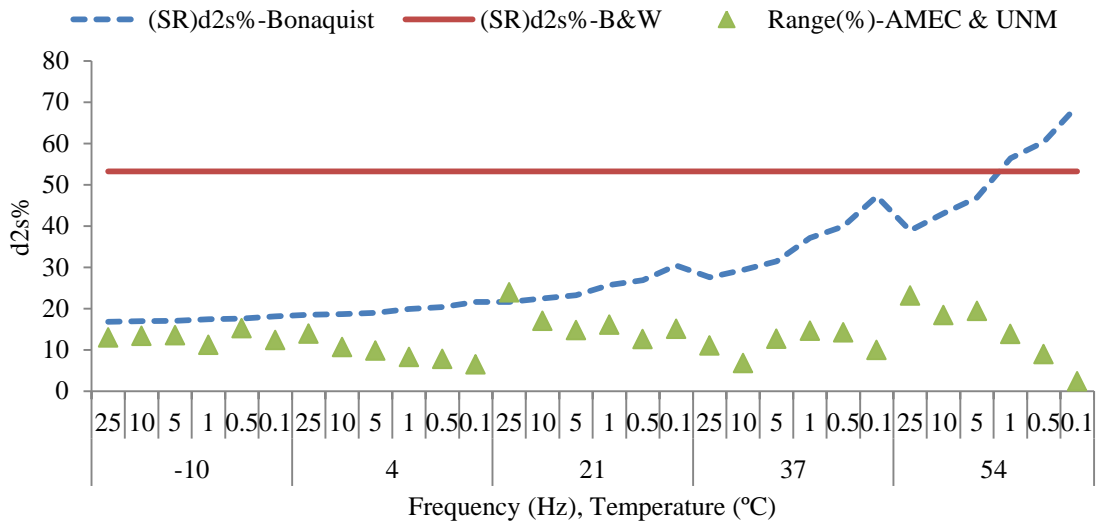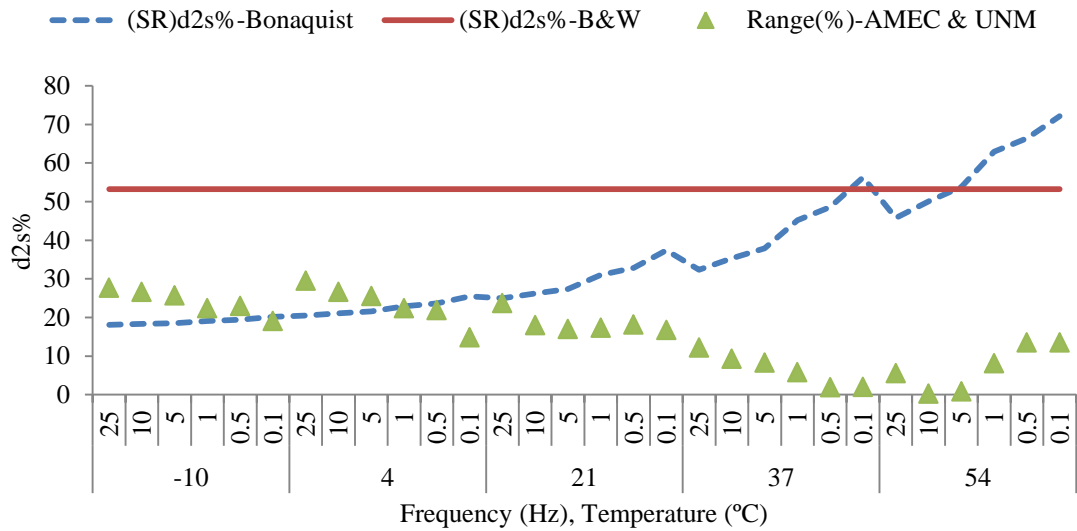
(c) SP-III with PG 64-22

(d) SP-III with PG 70-22

Figure 4.8 (c-d) Reproducibility Analysis of *E**-Results From UNM and AMEC
Laboratories.

114
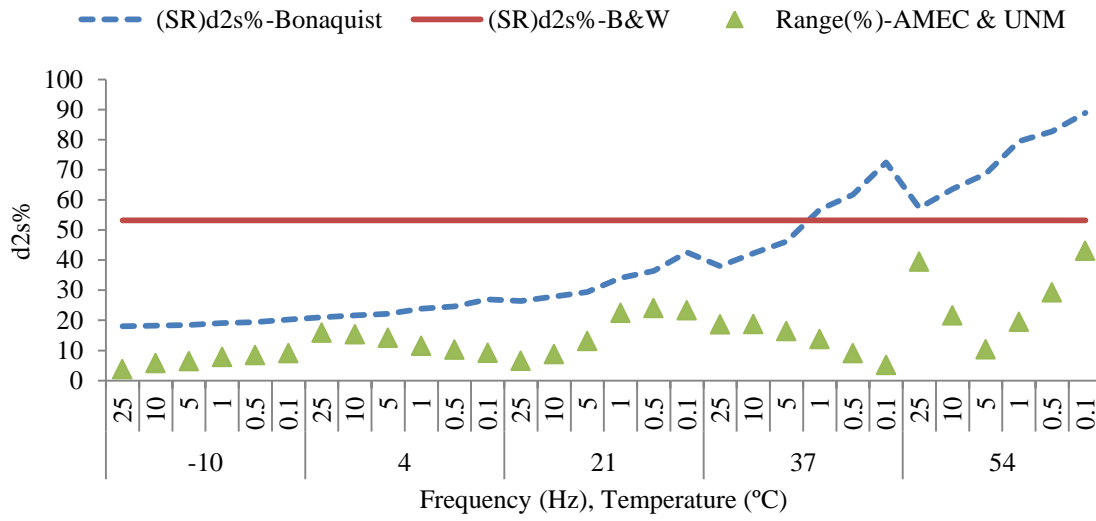
(e) SP-IV with PG 70-22

Figure 4.8 (a-e) Reproducibility Analysis of E^*-Results From UNM and AMEC Laboratories.

Chapter 5

Modeling of Dynamic Modulus

5.1. Introduction

In this chapter the accuracies of viscosity based Witczak model, dynamic shear modulus based Witczak model and Hirsch model are examined for predicting measured dynamic modulus values of typical New Mexico asphalt concrete. Moreover, the viscosity based model is also modified by giving more emphasis on mix volumetrics and introducing a modified version of aggregate contact factor developed by for Hisch model. The model modification is based on the hypothesis that dynamic modulus is mostly influenced by mastic and mix volumetrics.

5.2. Objective

Specific objectives of this study are to:

- Apply viscosity based Witczak model for predicting measured dynamic modulus values of typical New Mexico Mixes

- Apply dynamic shear modulus based Witczak model for predicting measured dynamic modulus values of typical New Mexico Mixes

- Apply Hirsch model for predicting measured dynamic modulus values of typical New Mexico Mixes

- Modify the viscosity based Witczak model by giving more emphasis on mix volumetric properties

116

5.3. Analysis Method

The viscosity based Witczak model is implemented in the following two different ways:

- By using the default A and *VTS* values provided in MEPDG (method implemented in Level 3 input hierarchy of MEPDG)

- By determining the *G** and phase angle of binder through a temperature sweep test, determining the A and *VTS* relationship for the binder and utilizing that for the model (method implemented in Level 2 input hierarchy of MEPDG)

The dynamic shear modulus based Witczak model is implemented in the following three in three different ways:

- By using the default A and *VTS* values provided in MEPDG (method implemented in Level 3 input hierarchy of MEPDG).

- By determining the $G^*{}_b$ and δ_b of binder through a temperature sweep test for a single frequency and determining the A and *VTS* relationship for the binder to be utilized for the model (method implemented in Level 2 input hierarchy of MEPDG).

- Conducting temperature and frequency weep $G^*{}_b$ testing and developing the mastercurve for $G^*{}_b$ and δ_b for the model prediction.

It is possible to implement the Hirsh model in different ways based on how the binder *G** data is obtained and utilized.

- First, default A and *VTS* values are used to estimate the *G** of the binder using the temperature susceptibly model developed by Bari (2005).

117

- Second actual the *G** test is conducted at seven different temperatures (40, 55, 70, 85, 100, 115, 130 ℉) and 10 rad/sec to determine the actual A and *VTS* values for the binders being used and then the *G** of the binder is estimated by using the temperature susceptibly model developed by Bari (2005).

- Third, the *G** mastercurves are utilized to estimate the *G** values corresponding to the *E** values at the same reduced frequency.

The viscosity based Witczak model is modified after the inputs are maneuvered to determine if it is possible to obtain accurate prediction of laboratory dynamic modulus data and subsequent determination of inputs that will produce better predictions.

5.4. Viscosity Based Witczak Model

The Viscosity based Witczak model is the primary dynamic modulus prediction model in MEPDG. The viscosity based Witczak model, presented in Equation (5.1), uses viscosity of binders as the main input parameter to capture the effect of binders. For developing this model 2750 dynamic modulus measurements from 205 different asphalt mixtures were tested in the laboratories of the Asphalt Institute, the University of Maryland, and the Federal Highway Administration. According to the developers, the model can predict the dynamic modulus of mixtures using both modified and conventional asphalt cements (ARA, Inc. 2004).

$$\log|E^*| \tag{5.1}$$

$$= -1.249937 + 0.029232\rho_{200} - 0.001767(\rho_{200})^2 - 0.002841\rho_4$$

$$- 0.058097V_a - 0.802208\left(\frac{V_{beff}}{V_{beff} + V_a}\right)$$

$$+ \frac{3.871977 - 0.0021\rho_4 + 0.003958\rho_{38} - 0.000017(\rho_{38})^2 + 0.00547\rho_{34}}{1 + e^{(-603313 - 0.313351\log(f) - 0.393532\log(\eta))}}$$

where: $|E^*|$ is dynamic modulus, 10^5 psi; η is bitumen viscosity, 10^6 Poise; f is loading frequency, Hz; V_a is air void content, %; V_{beff} is effective bitumen content, % by volume; ρ_{34} is cumulative % retained on the 19-mm (3/4-in.) sieve; ρ_{38} is cumulative % retained on the 9.5-mm (3/8-in.) sieve; ρ_4 is cumulative % retained on the 4.76-mm (No. 4) sieve; ρ_{200} is % passing the 0.075-mm (No. 200) sieve.

5.5. Dynamic Shear Modulus Based Witczak Predictive Model

The dynamic shear modulus based Witczak model is the most advanced dynamic modulus prediction model in MEPDG. It is possible to utilize this model in the Level 2 and 3 design hierarchies of MEPDG. This model uses dynamic shear modulus test results as an input parameter instead of viscosity. The model was also developed with larger database of dynamic modulus. 7400 data points from 346 HMA mixtures were used to develop this revised version of the Witczak *E** predictive model (Bari 2005).

119

$$log|E^*| = -0.349 +$$

(5.2)

$$\left\{ 0.754(|G_b^*|^{-0.0052}) * \begin{pmatrix} 6.65 - 0.032\rho_{200} + 0.0027(\rho_{200})^2 - 0.011\rho_4 \\ -0.0001(\rho_4)^2 + 0.006\rho_{38} - 0.00014(\rho_{38})^2 \\ -0.08V_a - 1.06\left(\dfrac{V_{beff}}{V_{beff}+V_a}\right) \end{pmatrix} \right\} +$$

$$\left\{ \dfrac{2.558 + 0.032V_a + 0.713\left(\dfrac{V_{beff}}{V_{beff}+V_a}\right) + 0.0124\rho_{38} +}{1 + e^{(-0.7814 - 0.5785\,log|G^*|_b - 0.8834\,log(\delta_b))}} \right\}$$

where: $|E^*|$ is dynamic modulus, psi; ρ_{200} is % (by weight of total aggregate) passing the 0.075-mm (No. 200) sieve; ρ_4 is cumulative % (by weight) retained on the 4.76-mm (No. 4) sieve; ρ_{34} is cumulative % (by weight) retained on the 19-mm (3/4-in.) sieve; ρ_{38} is cumulative % (by weight) retained on the 9.5-mm (3/8-in.) sieve; V_a is air void content (by volume of the mix), %; V_{beff} is effective binder content (by volume of the mix), %; $|G^*|_b$ is dynamic shear modulus of binder, psi; δ_b is phase angle of binder associated with $|G^*|_b$ degree.

5.6. Hirsch Model

The Hirsch model is the other well accepted dynamic modulus prediction model developed by Christensen et al. (2003). The Hirsch model is not adopted in the MEPDG design software, however, it has been used quite frequently for predicting dynamic modulus. The Hirsh model is different from Witczak model because it is based on rule of the mixtures for composite materials. Various forms of the mixture rule model were

120

developed and the best model given in Equation (5.3) is selected. The Hirsch model was calibrated using dynamic modulus database developed by compiling E^* test results from Advanced Asphalt Technologists (AAC) and Arizona State university (ASU). The database included a total of 206 dynamic modulus measurements from 18 different mixtures (Christensen et al. 2003).

$$|E^*| = P_c \left[4{,}200{,}000 * \left(1 - \frac{VMA}{100} \right) + 3|G^*| \left(\frac{VFA * VMA}{10{,}000} \right) \right] \tag{5.3}$$

$$+ (1 + P_c) \left[\frac{1 - \frac{VMA}{100}}{4{,}200{,}000} + \frac{VMA}{VFA * 3 * |G^*|} \right]^{-1}$$

$$P_c = \frac{\left(20 + \frac{VFA * 3 * |G_b^*|}{VMA} \right)^{0.58}}{650 + \left(\frac{VFA * 3 * |G_b^*|}{VMA} \right)^{0.58}} \tag{5.4}$$

$$\phi = -21(\log P_c)^2 - 55 \log P_c \tag{5.5}$$

where: $|E^*|$ is dynamic modulus, psi; $|G_b^*|$ is binder dynamic modulus, psi; VMA is voids in the mineral aggregate, %; VFA is voids filled with asphalt, %; P_c is aggregate contact factor.

121

5.7. Application of Viscosity (η) based Witczak Model using Default *A* and *VTS* values

In this section the viscosity (η) based Witczak model is implemented using Microsoft excel to predict dynamic modulus mastercurves developed for the five mixes tested in this study. Default MEPDG A and *VTS* values are used in the temperature susceptibility relationship, given below in Equation (5.6), to estimate the viscosity of each binder used. The default A and *VTS* values for PG 70-22 are 10.299 and -3.426 respectively and for PG 64-22 are A=10.98 and *VTS*=-3.68 (ARA, Inc. 2004).

$$\log\log\eta = A + VTS \log T_R \qquad (5.6)$$

where: η is viscosity (cP); T_R is temperature (Rankine); A and *VTS* are regression intercept and regression slope of viscosity temperature susceptibility relationship.

Mastercurves are developed using predicted and measured data for the five mixes (SP-III-PG-64-22 (lab mix), SP-II-PG-70-22 (lab mix), SP-III-PG-70-22 (plant mix), SP-II-PG-64-22 (plant mix) and SP-IV-PG-70-22(plant mix)) and the results are presented in Figure 5.1 (a-e). The mastercurves developed using η-based Witczak model are found to underpredict mastercurves developed form measured data for all mixes except for the SP-IV mix. A scatter plot of raw η-based Witczak model E^*prediction results in comparison with the measured E^*data for all mixes tested in this study is presented in Figure 5.2. The result shows that η-based Witczak model predicts the E^*test results of SP-IV mix with good accuracy but underpredicts $E^*$of all other four mixes.

122

To quantitatively evaluate the accuracy of the η-based Witczak model, the percent difference between predicted and tested data (the difference between the measured and predicted E^* divided by the measured E^*) at each frequency and temperature are calculated. Then the average percent difference at each temperature is determined and tabulated in Table 5.1. Moreover, the trend of calculated percent of error with respect to temperature is presented in Figure 5.3(a) and the trend with respect to frequency is presented in Figure 5.3(b). Line representing the zero percent error for perfect prediction is shown in both figures. Positive sign of error indicates over prediction and negative sign indicates under prediction. It can be observed that the percent error of predicted E^* is minimum for the cold temperature and increases with increasing temperature. However, no apparent trend is observed with respect to test frequency.

5.8. Level-3 E^* Mastercurve prediction in MEPDG

For Level-3 input hierarchy MEPDG utilizes the viscosity (η) based Witczak model to predict the E^* of asphalt mixes. At Level-3 input hierarchy no laboratory E^* or binder viscosity test is required. Binder viscosity is determined using predetermined default A and *VTS* values specified based on previous test results. Mix data that are required for Level-3 MEPDG model prediction are: air void content (V_a) in %, effective bitumen content (V_{beff}) in % by volume, cumulative % retained on the 19 mm (3/4 in) sieve (ρ_{34}), cumulative % retained on the 9.5 mm (3/8 in) sieve (ρ_{38}), cumulative % retained on the 4.76 mm (No. 4) sieve (ρ_4) and % passing the 0.075 mm (No. 200) sieve (ρ_{200}) which are basically the inputs for viscosity (η) based Witczak model (ARA, Inc. 2004).

123

MEPDG software is run to develop mastercurves for the SP-II, SP-III and SP-IV plant mixes tested this study. Figure 5.4 (a-c) present a comparison of Level-3 mastercurves developed using MEPDG software and laboratory test mastercurves. The results from the analysis show that the MEPDG software outputs are exactly the same as the excel calculations. The SP-II and SP-III mastercurves are under predicted while relatively better prediction accuracy is observed for SP-IV mix.

5.9. Application of Viscosity (η) Based Witczak Model using Actual *A* and *VTS* values

The A and *VTS* values for the binders are determined by conducting dynamic shear, G^*, test on the binders and converting the results to viscosity using Equation (5.7) and then using Equation (5.6) for the viscosity data. For this purpose, the dynamic shear modulus test is conducted for binder grades PG 70-22 and PG 64-22. These binders are used for SP-II, SP-III and SP-IV mixes. For both binder grades dynamic shear modulus test is conducted on three replicate samples at seven different temperatures (40, 55, 70, 85, 100, 115, 130 ºF). These test temperature are selected based on MEPDG level two input requirements.

Table 5.2 present numeric dynamic shear modulus, G^*, and phase angle, δ, test results for binder grade PG 64-22 and PG 70-22. It can be observed that G^* values decrease with increasing temperature while phase angle increases with increasing test temperature which confirms the rationality of the test results. The trends of dynamic shear modulus, G^*, and phase angle, δ, for PG 64-22 and PG 70-22 are presented pictorially in Figure 5.5 (a), (b) and Figure 5.6 (a), (b) respectively. Then, the A and *VTS* relationships

are developed and presented for PG 64-22 and PG 70-22 in Figure 5.5 (c) and Figure 5.6 (c) respectively.

$$\eta = \frac{G^*}{10}\left(\frac{1}{\sin\delta}\right)^{4.8628} \qquad (5.7)$$

where: G^* is binder shear modulus (Pa), δ is binder phase angle (deg), η is viscosity (cP)

Then theses A and *VTS* values are used in the η-based Witczak model to predict dynamic modulus for the five mixes tested in this study. A scatter plot of raw η-based Witczak model E^* prediction results in comparison with the measured E^* data for all mixes is presented in Figure 5.7. The result shows that η-based Witczak model still underpredicts E^* of all other five mixes.

5.10. Level-2 E^* Mastercurve Prediction in MEPDG

The viscosity (η) based Witczak model is still the primary model to predict the E^* of asphalt mixes at the Level-2 input hierarchy of MEPDG. However, dynamic shear modulus, G^*, and phase angle, δ, test results are required to determine the binder viscosity. Binder viscosity is determined using the G^* conversion and the temperature susceptibility relationships provided in Equation (5.7) and Equation (5.6). The A and *VTS* values determined by MEPDG software were compared with the values determined in this study and the results are found to match perfectly. Mix data that are required for Level-2 MEPDG model prediction are exactly the same as Level-3 input hierarchy (ARA, Inc. 2004). Then, MEPDG software is run using the binder and mix data inputs to develop mastercurves for the SP-II, SP-III and SP-IV plant mixes at Level-2 input

hierarchy and the results are presented in Figure 5.8 (a-c). The results from the analysis show that the MEPDG software outputs are exactly the same as the excel calculations and the MEPDG mastercurves under predicted all mixes.

5.11. Application of G* Based Witczak Model Using Default A and VTS Values of MEPDG

In this section the G^*-based Witczak model is implemented to predict dynamic modulus mastercurves developed for the five mixes tested in this study. For this model, the temperature susceptibility relationship, given in Equation (5.6), has been improved to consider loading frequency in addition to temperature as shown in Equation (5.8), (5.9) and (5.10) (Bari, 2005). Specific viscosity values for each binder grade are determined for each test temperature and frequency combination which are in turn used to determine the dynamic shear modulus, G^*_b, and phase angle, δ_b, of the binders. Equation (5.11) and Equation (5.12) are the relationships developed by Bari (2005) for predicting the dynamic shear modulus, G^*_b, and phase angle, δ_b from binder viscosity. The default A and *VTS* values given in MEPDG are used to estimate the viscosity of each binder used. The default A and *VTS* values for PG 70-22 are 10.299 and -3.426, respectively, and for PG 64-22 are A=10.98 and *VTS*=-3.68 (ARA, Inc. 2004).

$$log \, log \, \eta_{f,T} = A' + VTS' \, log \, T_R \tag{5.8}$$

$$A' = 0.9699 f_s^{-0.0527} * A \tag{5.9}$$

$$VTS' = 0.9668 f_s^{-0.0575} * VTS \tag{5.10}$$

126

$$|G^*|_b = 0.0051 f_s \eta_{f,T} (\sin \delta_b)^{7.1542 - 0.4929 f_s + 0.0211 f_s^2} \tag{5.11}$$

$$\delta_b = 90 + (-7.3146 - 2.6162 VTS') * \log(f_s * \eta_{f,T}) \tag{5.12}$$
$$+ (0.1124 + 0.2029 VTS') * \log(f_s * \eta_{f,T})^2$$

where: $\eta_{f,T}$ is viscosity as a function of both temperature and frequency (cP); T_R is temperature (Rankine); A and VTS are regression intercept and regression slope of viscosity temperature susceptibility relationship; A' and VTS' are A and VTS values adjusted for frequency. f_s is loading frequency in similar mode as for DSR testing (Hz); $|G^*|_b$ is dynamic shear modulus (Pa), δ_b phase angle (deg).

Figure 5.9 presents a scatter plot of raw G^*-based Witczak model E^* prediction results in comparison with the measured E^* data for all asphalt mixes (SP-III-PG-64-22 (lab mix), SP-II-PG-70-22 (lab mix), SP-III-PG-70-22 (plant mix), SP-II-PG-64-22 (plant mix) and SP-IV-PG-70-22(plant mix)) tested in this study. The result show that G^*-based Witczak model predicts the E^* test results of SP-IV mix with better accuracy than the rest of mixes. For all asphalt mixes the predicted data is higher than measured E^* at low temperatures and at high and intermediate temperatures measured E^* are under predicted with the G^*-based Witczak model.

To quantitatively evaluate the accuracy of the G^*-based Witczak model the percent difference between predicted and tested data (the difference between the measured and predicted E^* divided by the measured E^*) at each frequency and temperature are calculated. The average percent difference between predicted and tested data at each temperature is tabulated in Table 5.3. Moreover, the trend of calculated percent error with

127

respect to temperature is presented in Figure 5.10 (a) and the trend with respect to frequency is presented in Figure 5.10 (b). Line of zero percent error for perfect prediction is shown in both figures. Positive sign of error indicates over prediction and negative sign indicates under prediction. It can be observed form Figure 5.10 (a) that the percent error of predicted E^* at cold temperatures indicate significant over prediction. Minimum percent errors are observed at 21 ºC and as the temperature increases the percent errors go further below zero indicating under prediction of measured E^* data. The trend of percent errors with respect to frequency, Figure 5.10 (b), shows a decrease in the range of percent error with increasing test frequency, which indicates an improvement in precision of predicted E^* with increasing test frequency.

5.12.   Application of G* Based Model Using Actual A and VTS Values of MEPDG

Dynamic shear,G^*, test is conducted on three replicate samples of PG 70-22 and PG 64-22 at different seven temperatures (40, 55, 70, 85, 100, 115, 130 ºF) and 10 rsd/sec. The same test results and A and *VTS* calculations are utilized for G^*-based Witczak model instead of the default values provided in MEPDG guide. The actual *A* and *VTS* values are determined to be 7.7598 and -2.5142 for PG 70-22 respectively and for PG 64-22 are *A*=8.052 and *VTS*=-2.6173.

A scatter plot of raw G^*-based Witczak model E^* prediction results using actual *A* and *VTS* results in comparison with the measured E^* data for all mixes is presented in Figure 5.11. The result show a significant improvement in the prediction accuracy of the G^*-based Witczak model, especially at cold temperatures, compared with the prediction using default *A* and *VTS* values. However, as the $|E^*|$ value decreases the G^*-based

Witczak model is still under predicting measured |E*| of all five asphalt mixes. The average percent difference between predicted and tested data at each temperature is tabulated in Table 5.4. Comparing the results in Table 5.4 with those in Table 5.3, clearly shows the improvement in prediction accuracy of the G^*-based Witczak model at cold temperatures. However, at intermediate and high temperatures the prediction accuracy the G^*-based Witczak model does not show any improvement due to the use of actual A and VTS values and it still underpredicts the measured E^*.

Figure 5.12 (a) presents the trend of calculated percent error with respect to temperature. It can be observed that the percent error of predicted E^* at -10 ºC is positive which indicate over prediction. Moreover, the range of percent prediction is very wide which indicates luck of precision. As the temperature increases, however, the range of percent error decreases indicating an improvement in the prediction precision. Yet, even if there is an increase in precision, the model is significantly underpredicting measured E^* at high and intermediate temperatures.

 The trend with respect to frequency is presented in Figure 5.12 (b). Most of the percent errors are below the zero percent error for perfect prediction, which clearly shows the under perceive tendency of the model. However, similar to the results observed by using default A and VTS values, the range of percent error is found to decrease with increasing test frequency, which indicates an improvement in precision of predicted E^* with increasing test frequency.

5.13.   Application of G*-based model by using |G*| and δ Mastercurves

In this section dynamic shear modulus, G^*, and phase angle, δ, mastercurves are used to generate G^*_b and δ_b inputs for the G^*-based Witczak model. Frequency sweep tests of dynamic shear modulus over a wide temperature and frequency range are conducted for developing dynamic shear modulus mastercurves. G^*- Mastercurves characterize binder rheological properties over a wide range of frequencies at a specific reduced temperature. This makes G^*- mastercurves very attractive to estimate binder G^* and δ values at any temperature and frequency point of interest. Therefore, in this study, G^* and δ – mastercurves are developed at the same reference temperature at which E^*- mastercurves are developed and G^*_b and δ_b values corresponding to the reduced frequency of mix dynamic modulus are determined.

DSR test is conducted to determine dynamic shear modulus, G^* and phase angle, δ, for the two types of binders used in the asphalt mixes in this study. DSR test is conducted at seven test temperatures and 15 frequencies for each temperature. The seven testing temperatures are 130, 115, 100, 85, 70, 55, and 50°F. Two different sample sizes were used for conducting these tests. 25mm diameter samples are tested at 130 and 115 °F. However, torsion force required to maintain a measurable strain level of a 25mm sample at lower temperatures exceeds the machine capacity. Therefore, the 8mm diameter sample size is used to conduct DSR testing 100, 85, 70, 55 and 50°F.

The DSR test is conducted in a stain controlled fashion. That is shear stress is measured while applying a preselected strain level. Appropriate strain level is selected to produce measureable strain amount according to the DSR compliance while taking in to

130

consideration the maximum stress that can be applied by the machine. Therefore, the testing strain level is selected in such a way that it is large enough to be measured by the equipment and small enough so that the stress capacity of the machine is not exceeded. The applied strain level for the 8mm and 25mm sample is 1.0%.

DSR Test data of dynamic shear modulus, $|G^*|$, and phase angle, δ, is provided in Appendix G. The mastercurve for the DSR test results is developed using the time temperature superposition principle. The Modified Sigmoidal Model is found to be the best function for fitting the shifted G^*- data to a mastercurve (Yusoff et al, 2010). The modified sigmoidal function is given in Equation (5.13). Mastercurves for phase angle are also developed using the parameters determined for the $|G^*|$ mastercurves. Equation (5.14) provides the mathematical relationship used for phase angle mastercurves (Chailleux et al. 2006). Figure 5.13 and Figure 5.14 present the G^* and δ – mastercurves developed for both binder grades, PG 64-22 and PG 70-22, used in this study. The mastercurve parameters for both binders are also given in Table 5.5.

$$\log(|G^*|) = \delta + \frac{\max - \delta}{1 + e^{\beta + \gamma \log(f_r)}} \tag{5.13}$$

$$\varphi = \frac{\pi}{2} * \frac{d\log|G^*|}{d\log(f_r)} = \frac{\pi}{2} * \alpha\gamma * \frac{e^{\beta + \gamma \log(f_r)}}{(1 + e^{\beta + \gamma \log(f_r)})^2} \tag{5.14}$$

where G^* = dynamic modulus; δ = the minimum value of E^*; max= the maximum value of G^* which is taken as 1.0Gpa; β and γ are parameters that describe the shape of the sigmoidal function, f_r is reduced frequency of loading at a reference temperature.

131

Figure 5.15 (a) is a scatter plot for G*-based Witczak model prediction using G^* and Phase angle mastercurves for SP-II, SP-III and SP-IV mixes. In all cases G*-based Witczak model is found to under predict measured dynamic modulus here as well. Figure 5.15 (b) presents the percent difference between the predicted and test data over the entire reduced frequency range. The percent difference between predicted and measured dynamic modulus for all mixtures is found to be very close to 80% over the entire reduced frequency range. Applying 80% shift factor on the Witczak predicted results produced a good estimation of test results.

5.14. Application of Hirsch Model using Default A and VTS Values of MEPDG

The MEPDG default *A* and *VTS* values are used in Equation (5.6) through Equation (5.10) to determine temperature and frequency dependent viscosity for each binder. The default *A* and *VTS* values for PG 70-22 are 10.299 and -3.426 respectively and for PG 64-22 are *A*=10.98 and *VTS*=-3.68 (ARA, Inc. 2004). Then, the dynamic shear modulus, $G^*{}_b$, of the binders are determined using Equation (5.11) for each temperature and frequency combination. Finally, the dynamic moduli of each mix at each test temperature and frequency combination are estimated using the Hirsh model.

Figure 5.16 presents a scatter plot of Hirsh model E^* prediction results in comparison with the measured E^* data for all asphalt mixes tested in this study. The result show that Hirsh model underpredicts the E^* test results for all mixes at high and intermediate temperatures and over predicts for low temperature. The best prediction is observed for 4 ℃. Moreover, a clear bias for high temperature prediction is observed for all asphalt mixes.

Table 5.6 presents the average percent difference between predicted and tested data at each temperature. It can be observed that at -10 ℃ the model is over predicting the measured E^* by about 100% for all mixes and as the test temperature increases the model under predicts test results with increasing trend form 50% to 70%.

Figure 5.17 (a) presents the trend of all percent difference between predicted and tested data with temperature. The %error for -10 ℃ is positive and ranges form 50-100% and as the temperature increases the model underpredicts the measured E^*. The % error is closest to zero (percent error for perfect prediction) at 4 ℃. The range of the error is also observed to decrease with increasing temperature. This indicates that the model is more precise at higher temperatures but the accuracy of the prediction is questionable.

Figure 5.17 (b) presents the trend of calculated percent error with respect frequency. The range of % error is observed to be from -100 to 150 % for all mixes. The maximum range is observed at the lowest test frequency and as the test frequency increases the range is observed to decrease. This indicates an increase in the precision of the model with increasing frequency.

5.15. Application of Hirsch Model using Actual A and VTS Determined through DSR Testing

To determine actual *A* and *VTS* values for the binders, *G** test is conducted at seven different temperatures (40, 55, 70, 85, 100, 115, 130 ℉) at a frequency of 10 rad/sec. the *G** data is converted to viscosity using Equation (5.7). Then, the relationship between viscosity and temperature is determined by plotting the logarithm of the logarithm of viscosity with respect to temperature in Rankin unit and fitting the linear regression line.

133

This process provided the actual *A* and *VTS* values for the binders used in this study. The *A* and *VTS* values for PG 70-22 are determined are to be 7.759 and -2.514 respectively and for PG 64-22 are *A*=8.052 and *VTS*=-2.617. Following this, the dynamic shear modulus, G^*_b, of the binders are determined using Equation (5.11) for each temperature and frequency combination. Finally, the dynamic moduli of each mix at each test temperature and frequency combination are estimated using the Hirsh model.

Figure 5.18 presents a scatter plot of Hirsh model E^* prediction results using actual *A* and *VTS* values. The Hirsh model is found to under predict measured E^* in this case as well. The E^* predictions are very close to the line of equality at -10 ºC and at 4 ºC and higher the Hirsch model is observed to under predict measured E^*. The bias at high temperature prediction is still observed but the use of actual *A* and *VTS* values have improved the results.

Table 5.7 presents the average percent difference between predicted and tested data at each temperature for the case of using actual *A* and *VTS* values. There is a clear improvement in the accuracy of the predictions at -10 ºC resulting from the use of laboratory determined *A* and *VTS* values. However, the average percent difference remained very similar at intermediate and high temperature predictions.

Figure 5.19 (a) presents the trend of all percent difference between predicted and tested data with temperature. The prediction at all temperatures is observed to under predict measured E^*. The %error for -10 ºC ranges from -50 to 0%. The trend of calculated percent error with respect to frequency is presented in Figure 5.19 (b). Similar to the previous case, the maximum range for % error is observed at the lowest test frequency

134

and as the test frequency increases the range is observed to decrease. This indicates an increase in the precision of the model with increasing frequency.

5.16. Application of Hirsh Model by using G^* and δ Mastercurves

For this method the E^* mastercurves at reference temperature of 21 ℃ is performed by using G^* and δ mastercurves at a reference temperature of 21 ℃ in the Hirsch model. Therefore, G^* and δ – mastercurves replace the use of any type of model to predict G^*_b and $δ_b$ for use in the Hirsh model. The same G^* and δ – mastercurves developed for the case of G^*-based Witczak model are utilized here as well.

Figure 5.20 (a) presents the scatter plot for the predicted and measured E^* values. The Hirsch model is still under predicting measured E^* values but the accuracy of the prediction is observed to be significantly improved. The bias at high temperature however, still remains. Figure 5.20 (b) presents the percent difference between the predicted and test data over the entire reduced frequency range at a reference temperature of 21 ℃. The percent difference between predicted and measured dynamic modulus is observed to decrease with increasing frequency.

5.17. Maneuvering MEPDG inputs for Level-3 E^* Mastercurve Predictions

In this section of the study the MEPDG mix input variables (air void content (V_a) in %, effective bitumen content (V_{beff}) in % by volume, cumulative % retained on the 19 mm (3/4 in) sieve (ρ_{34}), cumulative % retained on the 9.5 mm (3/8 in) sieve (ρ_{38}), cumulative % retained on the 4.76 mm (No. 4) sieve (ρ_4) and % passing the 0.075 mm (No. 200) sieve (ρ_{200})) are optimized to minimize the error of predicted mastercurves

135

and produce exact prediction of laboratory dynamic modulus tests results in level-3 input hierarchy. In other words, a solution for laboratory mastercurves are searched by changing mix input variables.

Optimization of mix input variables are performed by minimizing the sum of squared differences between predicted and test dynamic modulus values. To produce physically realistic optimized asphalt mix input data for Level-3 input hierarchy the following constraints are applied:

- All input values are physical quantities; therefore, the minimum value they can logically hold is zero.

- All input values are expressed in percentage; therefore, the maximum value they can hold is 100.

- The aggregate input values, cumulative % retained on the 19 mm (3/4 in) sieve (ρ_{34}), cumulative % retained on the 9.5 mm (3/8 in) sieve (ρ_{38}), cumulative % retained on the 4.76 mm (No. 4) sieve (ρ_4) are hierarchically related. Therefore, for physically logical results $\rho_{34} \leq \rho_{38} \leq \rho_4 \leq 100$.

- The model has air void content (V_a) in % and effective bitumen content (V_{beff}) in % by volume sum as a denominator, therefore, $V_a + V_{beff} > 0$.

Figure 5.21 (a-c) show a comparison of MEPDG Level-3 prediction of $|E^*|$ mastercurves using optimized input data and $|E^*|$ mastercurves developed from the actual $|E^*|$ test results for SP-II, SP-III and SP-IV plant mixes. The mastercurve plots show remarkable improvement of MEPDG Level-3 prediction when the optimized mix input values are used.

136

Original mix input values determined through laboratory test and optimized input values determined using Excel solver functions are presented in Table 5.8. The lab original values are actual laboratory test results while optimized values are obtained after minimizing the error between laboratory E^* test results and model predicted E^* values. Comparison of the optimized input data with original input values shows that the mix aggregate distribution variables, ρ_{34}, ρ_{38} and ρ_4, are zero and the change in V_a, V_{beff} and ρ_{200} values are not very large. Therefore, the course aggregate influence on accuracy of η-based Witczak model is minimal and variables ρ_{34}, ρ_{38} and ρ_4 can be eliminated without causing significant problems on model performance. Based on this finding it is valid to make a hypothesis that dynamic modulus of asphalt concrete is influenced significantly by mastic properties and mix volumetrics, which indicates that the η-based Witczak model can be modified by eliminating course aggregate variables and predominantly using mix volumetric variables.

5.18. Modification of Viscosity Based Witczak Model by Giving Emphasis to Mix Volumetrics

The η-based Witczak model has been found to underpredict the laboratory measured E^* for typical NMDOT mixes. Additionally, the performance evaluation of the η-based Witczak model by numerous researchers also indicated the need for refining. Based on the findings of input optimization performed above, a modified version for η-based Witczak model is developed by eliminating the aggregate size variables and giving emphasis to mix volumetric indicators. For modification of this model the E^* database

developed by Bari (2005) is utilized. Bari's E^* database includes 7400 sets of E^* data from 346 asphalt mixes.

Main assumptions for the modification the η-based Witczak model are:

- E^* of asphalt concrete is predominantly influenced by mix volumetric and mastic properties.

- The effect of aggregate distribution on E^* can be captured by introducing aggregate contact factor which is dependent on mix volumetrics and viscosity of mastic in the mix.

- The viscosity of binder can be accurately modeled using the viscosity temperature susceptibility liner regression model, Equation (5.6), having intercept and regression slope of A and *VTS*.

Similar to the η-based Witczak model nonlinear regression analysis using the generalized reduced gradient optimization approach in Microsoft Excel's Solver is utilized for optimization. The sigmoidal function form as used for the η-based Witczak is kept unchanged in the modification of the η-based Witczak model considering its proven performance in precious model developments. Therefore, the four sigmoidal function parameters α, β, γ and δ are utilized in the modification. The dependent variable is also kept as $\log|E^*|$ with a unit of pound per square inch (psi).

The η-based Witczak model has four sub models based on the four sigmoidal function parameters α, β, γ and δ. The δ –model in the η-based Witczak predictive equation is given by Equation (5.15) (ARA, Inc. 2004). The modified δ –model given by Equation (5.16) eliminates the course aggregate variable (ρ_4) and introduces a new aggregate contact factor (P_c) given by Equation (5.17) is introduced. P_c is a modified version of the

138

aggregate contact factor in the Hirsh model (Christensen et al. 2003). The regression

constants in the P_c (P_0, P_1 and P_2) are calibrated along the other regression constants of

the modified model.

$$\delta = 3.750063 + 0.02932\rho_{200} - 0.001767(\rho_{200})^2 - 0.002841\rho_4 \tag{5.15}$$

$$- 0.058097V_a - 0.802208\left(\frac{V_{beff}}{V_{beff}+V_a}\right)$$

$$\delta = a + b.\rho_{200} + c.(\rho_{200})^2 + d.\rho_4 + e.V_a + e.\left(\frac{V_{beff}}{V_{beff}+V_a}\right) + f.P_c \tag{5.16}$$

$$P_c = \frac{\left[P_o + \eta * \left(\frac{VFA}{VMA}\right)\right]^{P_1}}{P_2 + \left[\eta * \left(\frac{VFA}{VMA}\right)\right]^{P_1}} \tag{5.17}$$

$$VFA = \frac{V_{beff}}{V_{beff}+V_a} * 100 \tag{5.18}$$

$$VMA = \frac{Vol_{air}+Vol_{eff\ asphlt}}{Vol_{bulk}} * 100 = V_{beff}(\%)+V_a(\%) \tag{5.19}$$

where: VFA is % voids filled with asphalt, VMA is % voids in mineral aggregate, η is

bitumen viscosity, 10^6 Poise; V_a is air void content, %; V_{beff} is effective bitumen content,

% by volume; ρ_4 is cumulative % retained on the 4.76-mm (No. 4) sieve; ρ_{200} is %

passing the 0.075-mm (No. 200) sieve, P_c is aggregate contact factor,

$a, b, c, d, e, f, P_o, P_1, P_2$ are regression constants to be determined with the modification.

The α –model in the η-based Witczak predictive equation is given by Equation (5.20)

(ARA, Inc. 2004). Similar to the δ –model the course aggregate variables ρ_4, ρ_{38} and

ρ_{34} are removed and replaced with P_c and VMA and the resulting form of the α –model

for the modified model is given by Equation (5.21).

139

$$\alpha = 3.871977 - 0.0021\rho_4 + 0.003958\rho_{38} - 0.000017(\rho_{38})^2 \qquad (5.20)$$

$$+ 0.00547\rho_{34}$$

$$\alpha = g + h.P_c + i.(VMA) \qquad (5.21)$$

where ρ_{34} is cumulative % retained on the 19-mm (3/4-in.) sieve; ρ_{38} is cumulative % retained on the 9.5-mm (3/8-in.) sieve; ρ_4 is cumulative % retained on the 4.76-mm (No. 4) sieve; VMA is % voids in mineral aggregate, P_c is aggregate contact factor, g, h, i regression constants to be determined with the modification.

The exponential part of the sigmoidal function $(\beta + \gamma \log(f))$ is modeled by Equation (5.22) in the η-based Witczak predictive equation ARA, Inc. (2004). Similar functional form and variables are also used in the modified model as well. The exponent term in the modified model is given by Equation (5.23).

$$\beta + \gamma \log(f) = -603313 - 0.313351 \log(f) - 0.393532 \log(\eta) \qquad (5.22)$$

$$\beta + \gamma \log(f) = j + k.\log(f) + l.\log(\eta) \qquad (5.23)$$

The model optimization is performed using the Generalized Reduced Gradient (GRG nonlinear) algorism in the solver function of Microsoft Excel. The GRG nonlinear algorism is run with a convergence criterion of 0.0001. Initial starting values for recalibrating the model were chosen to avoid non-convergent solutions.

The modification is performed by determining the difference between the observed $\log|E^*|$ and predicted $\log|E^*|$ and minimizing the sum of the squared differences by optimizing the regression constants using the GRG nonlinear algorism in the solver function of Microsoft Excel. As mentioned earlier, the E^* database developed by Bari (2005) is utilized for modification. The data base includes 7400 sets of $|E^*|$ data from

346 asphalt mixes. The modified model is presented in Equation (5.24) and Equation (5.25).

$$log|E^*| = 5.603 + 0.06045\rho_{200} - 0.00419(\rho_{200})^2 - 0.0847V_a \tag{5.24}$$

$$- 1.602\left(\frac{V_{beff}}{V_{beff}+V_a}\right)$$

$$- 0.0816P_c + \frac{-0.00896 + 2.1496P_c + 0.0185VMA}{1 + e^{-0.1765 - 0.6729log(\eta) - 0.39985\,log(f)}}$$

$$P_c = \frac{\left[107.566 + \eta*\left(\frac{VFA}{VMA}\right)\right]^{0.0364}}{0.00008075 + \left[\eta*\left(\frac{VFA}{VMA}\right)\right]^{0.0364}} \tag{5.25}$$

where: $|E^*|$ is dynamic modulus, 10^5psi; VFA is % voids filled with asphalt, VMA is % voids in mineral aggregate, η is bitumen viscosity, 10^6 Poise; V_a is air void content, %; V_{beff} is effective bitumen content, % by volume; ρ_4 is cumulative % retained on the 4.76-mm (No. 4) sieve; ρ_{200} is % passing the 0.075-mm (No. 200) sieve, P_c is aggregate contact factor.

Figure 5.22 (a) and (b) provided a scatter plot of all 7400 data points in logarithmic scale and in in arithmetic scale respectively. The measured $log|E^*|$ is the abscissa and the predicted $log|E^*|$ is the ordinate for both Figure 5.22 (a) and (b). For an ideally perfect perdition all points in the scatter plots should lie on the line of equality. It can be observed from Figure 5.22 (a) that the scatter pots are closely populated along the line of equality for both models in the logarithmic scale, which shows a good prediction power of both models in the logarithmic scale. However, comparison of the scatter produced from the two models indicates that the η-based Witczak model tends to underpredict the measured E^* more than the new modified model. Moreover, it is clearly visible that

141

equality line passes right through the middle of the new modified model scatter plot but the center of scatter plot for the η-based Witczak model is slightly below the line of equality. The arithmetic plot, Figure 5.22 (b), on the other hand, presents a scatter plot of observed $|E^*|$ on the abscissa verses predicted E^* for both models. The arithmetic plot indicates that the predictions from both models decrease with increasing E^*. However, in the arithmetic sale also, the η-based Witczak model tends to underpredict the measured $|E^*|$ more than the new modified model. This indicates that the modified model has superior power than the η-based Witczak model.

5.19. Performance Evaluation using Goodness of Fit Statistic

The goodness of fit of the new modified model is evaluated by calculating the coefficient of determination using Equation (5.26). The coefficient of determination for the new modified model is determined both in the logarithm and arithmetic scale. For the arithmetic scale, observed and predicted $|E^*|$ values in 10^5 Psi are used and for logarithmic scale observed and predicted $\log|E^*|$ values in Psi are used. Table 5.9 presents the statistics for the newly modified model. The evaluation based on coefficient of determination shows that the new modified model have excellent prediction power with $R^2 = 0.89$ in logarithmic scale. Great correlation is also found in the arithmetic scale as well, with $R^2 = 0.76$. Goodness of fit for the η-based Witczak model is determined to be 0.71 and 0.52 in logarithmic and arithmetic scales respectively. this clearly indicates the superior performance of the new modified model over the η-based Witczak model in predicting the 7400 data points populated by Bari (2005).

142

$$R^2 = 1 - \frac{n-p}{n-1} \cdot \left(\frac{S_e}{S_y}\right)^2 \qquad (5.26)$$

where: n is number of data points, p is number of regression constants, $n - p$ is degrees of freedom, S_e is standard error of estimate, S_y is standard deviation

5.19.1. Validation of Modified η-Based Model

The validation the new modified model is performed by using laboratory E^* data collected by testing NMDOT SP-II-PG 70-22 (lab mix), SP-II-PG 64-22 (plant mix), SP-III-PG 70-22 (plant mix) and SP-III-PG 64-22 (lab mix) asphalt mixes. Figure 5.23 shows the scatter plots for the new modified model predicted E^* data. By Comparing Figure 5.23 and Figure 5.2, it clear that the new modified model is performing much better than the η -based Witczak model. The most noticeable improvement is the prediction accuracy for high temperature dynamic modulus. The average percent error of prediction for the new calibrated model at each temperature is also tabulated in Table 5.10. In addition, the difference in the absolute % error (|% error of Witczak model| − |% error of new model|) is shown in brackets. Positive values indicate improvement of prediction by the new model and negative values indicate the reverse. The results in Table 5.10 show remarkable improvement.

The trend of calculated percent of error with respect to temperature is presented in Figure 5.24 (a) and the trend with respect to frequency is presented in Figure 5.24 (b). The percent error of predicted E^* is found to be much closer to the zero line for all temperatures and the trend is not as obvious for Witczak model and no apparent trend is also observed with respect to test frequency.

143

As described above, the aggregate size distribution and binder grades of SP-II and SP-III mixes are different. Moreover, Both SP-II and SP-III mixes are prepared using two binder grades (PG 64-22 and PG 70-22). However, the performance of the new modified model has improved in all cases and the predictions are with very good accuracy. This indicates the robust performance of the new modified model and its capability to take care of aggregate sizes variation as well as binder grade variation.

5.19.2. Frequency Distribution of Residuals

The dynamic modulus of asphalt concrete is assumed to be normally distributed in the η-based Witczak model, therefore the same assumption is adopted for the modified model as well. The normality of the new modified model is checked by plotting a histogram of the residuals. For the normality assumption to be valid, the plot of the residuals should be similar to the normal distribution plot centered at zero (Bari 2005 and Montgomery 2001).

Figure 5.25 (a) shows the frequency distribution of the residuals of E^* in logarithmic scale (predicted $\log|E^*|$ - observed $\log|E^*|$) for the new modified model. The distribution of residuals in logarithmic scale looks very much like a normal distribution. The average and standard deviation is found to be 0.00 and 0.22 respectively.

Figure 5.25 (b) shows the frequency distribution of the residuals of E^* in arithmetic scale (predicted $|E^*|$ - observed $|E^*|$). The average of the residuals for the new modified model is $1.151*10^5$ Psi and the standard deviation is equal to $7.114*10^5$ Psi. The range and standard deviation of the base laboratory E^* data is found to be $0.10*10^5$-$86.45*10^5$ Psi and $14.59*10^5$ psi respectively. Compared with variation observed in the base laboratory

144

$|E^*|$ data, the mean and standard deviation of the residuals are very small. Moreover, Bari (2005) also indicated that it is impossible to find a mean value of zero for the residuals in arithmetic scale since base laboratory E^* follow a logarithmic model. Therefore, the new modified model is an accurate predictive model that is normally distributed in both arithmetic and logarithmic scale.

5.20. Model Sensitivity Analysis

Sensitivity analysis is crucial for evaluation of new models since unrealistic model structure can result in unreasonable predictions even if the model calibration shows very good coefficient determination. For the new modified model to pass sensitivity test, the predicted dynamic modulus values must follow reasonably well the trend of laboratory measured E^* data while one selected input variable is being varied (Bari 2005). In this study, the new modified model is developed based on the argument that mix volumetric properties (VMA, VFA) and aggregate contact variable are crucial in the model performance. As shown above all these variables are a function of % air voids and effective binder content therefore sensitively analysis is performed for these two input variables. In addition, sensitivity analysis of the model to percent of fines is also included.

The procedure adopted by Bari (2005) is followed in performing the sensitivity analysis. First, the maximum, minimum and average values of the input variables at -10, 21 and 54 ºC are summarized only for 10 Hz frequency. This allowed grasping the variability of each input. Then, the range of each selected variable is divided in to five subdivisions and for each sub division the input variables and the laboratory measured dynamic modulus

145

values are averaged. For the sensitivity analysis, the average input values in each subdivision are used to predict the average dynamic modulus. It is important to note that the average value of all other variables is used in predicting the dynamic modulus and only the selected input variable is varied according to the subdivisions and corresponding average dynamic modulus of the subdivision are compared with the predicted data.

5.20.1. Model Sensitivity to V_a

The average air void values of all subdivisions of V_a and corresponding observed dynamic modulus values at -10, 21 and 54 ºC are calculated for 10 Hz frequency. Then the New modified model is utilized to predict the dynamic modulus at each subdivision. The trend of both predicted and measured dynamic moduli with increasing air void is presented in Figure 5.26 (a). The trend of predicted data is following the measured data closely which indicates the accurate prediction capability of the new modified model.

5.20.2. Model Sensitivity to V_{eff}

Effective binder content is used in the new modified model in combination with percent air voids to capture the effect of mixture density as explained in Bari (2005) and in combination with viscosity and percent air void to reflect the increasing effect of aggregate contact friction with increasing temperature as explained in Christensen et al. (2003). Average incremental values of effective binder content are calculated from each subdivision at -10, 21 and 54 ºC for 10 Hz frequency with corresponding average measured dynamic modulus. Dynamic moduli are also predicted using the new predicted model for each increment of effective binder. The trend of both predicted and measured dynamic moduli with increasing effective binder content is presented in Figure 5.26 (b).

146

The trend of predicted data is following the measured data closely which indicates the accurate prediction capability of the new modified model.

5.20.3. Model Sensitivity to ρ_{200}

The binding material in asphalt concrete is not pure asphalt; rather it is a mixture of asphalt binder with passing #200 sieve fines (% ρ_{200}). Average %ρ_{200} values are also calculated for each subdivision with respective average measured dynamic modulus values at -10, 21 and 54 ℃ for 10 Hz frequency. Predicted dynamic moduli are determined for each subdivision using the new modified model and the trend of predicted and measured dynamic moduli values are presented in Figure 5.26 (c). The trend of predicted data is following the measured data closely which indicates the accurate prediction capability of the new modified model.

5.21. Conclusions

In this study, the viscosity based Witczak model, the G^*-based Witczak model and the Hirsch model are applied for predicting measured dynamic modulus values of typical New Mexico Mixes and a new modified viscosity based Witczak model is developed by giving more emphasis on mix volumetric properties. From this study, the following conclusions can be dawn:

- The viscosity based Witczak model is applied by using the default *A* and *VTS* values and the predicted dynamic modulus values are found to be less than the measured dynamic modulus values for all SP-III and SP-II mixes. However,

147

better agreement is obtained between predicted and laboratory mastercurves for SP-IV mix.

- The application of viscosity based Witczak model using actual *A* and *VTS* valued determined using DSR test results is found to underpredict the dynamic modulus results of all typical NMDOT mixes.

- Mastercurve prediction at both Level-3 and Level-2 input hierarchy using viscosity based Witczak model in MEPDG are found to under predict the dynamic modulus of SP-III and SP-II mixes. However, better agreement is obtained between predicted and laboratory mastercurves for SP-IV mix.

- The percent error of prediction for viscosity based Witczak model is found to be minimum at the cold temperature and showed an increasing trend with increasing temperature. However, no apparent trend is observed with respect to test frequency.

- The use of G^*-based Witczak model with MEPDG default binder properties indicated that the model underpredicts the dynamic modulus of NMDOT mixes

- G^*-based Witczak model application using laboratory determined binder properties have shown improvement in the prediction accuracy, however, the model is found to underpredict measured dynamic modulus of NMDOT mixes in this case as well.

- The Hirsch model is found to under predict measured dynamic modulus values regardless of model predicted or laboratory determined $|G^*|_b$ and δ_b are used. However, the accuracy of the model predictions has increased when laboratory

148

determined G^* values are used. Moreover the Hirsch model is found be biased at high temperatures.

- It is found that, by optimizing the mix variable values, it is possible to improve the viscosity based Witczak model prediction significantly and optimized solution showed that the course aggregate variables in the viscosity based model can be eliminated without huge change in the mastic and binder input variable values. This indicate the low significance of course aggregate variables(ρ_{34}, ρ_{38} and ρ_4) on the model prediction accuracy.

- *A* new dynamic modulus predictive model has been developed by eliminating the course aggregate variables in the viscosity based Witczak model and keeping the sigmoidal mathematical structure and introducing a modified aggregate contact factor from Hirsh model.

- The new dynamic modulus model showed significant improvement in predicting the dynamic modulus of typical NMDOT mixes.

- Sensitivity analysis of the new model showed the prediction of the model is rational to variations of air void, effective binder and percentage of fine aggregates.

- The New modified viscosity based model has showed significant improvement in prediction accuracy over the viscosity based Witczak model.

149

Table 5.1: Average Percent Difference between Witczak predicted and tested *E** data

Temperature (ºC)	SP-III With PG 64-22 (lab mix)	SP-II With PG-70-22 (lab mix)	SP-III With PG-70-22 (plant mix)	SP-II With PG-64-22 (plant mix)	SP-III With PG-70-22 (plant mix)
-10	-14%	3%	-25%	-14%	-16%
4	-28%	1%	-38%	-28%	-20%
21	-49%	-24%	-54%	-49%	-9%
37	-59%	-37%	-61%	-59%	17%
54	-61%	-45%	-62%	-61%	27%

Table 5.2: DSR test Results for PG 64-22 and PG 70-22

Binder	Temp. (°C)	Complex Modulus, |G*| (Kpa)			Phase Angle ,δ (Deg)			Avg. |G*| (Kpa)	Avg. δ (Deg)
		Test-1	Test-2	Test-3	Test1	Test2	Test3		
PG 64-22	4.4	12100	12100	12000	56.5	56.5	56	12066.7	56.3
	12.8	5380	5020	5230	58.8	59.7	58.5	5210.0	59.0
	21.1	1800	1760	1820	61.6	62.2	61.3	1793.3	61.7
	29.4	547	541	571	64.8	65.3	64.3	553.0	64.8
	37.8	155	150	165	68.8	69.4	68.3	156.7	68.8
	46.1	43.9	41.9	46.9	73.5	74.1	73.2	44.2	73.6
	54.4	13.1	12.3	14.2	78.9	78.9	78.3	13.2	78.7
PG 70-22	4.4	9430	8840	9140	57.7	58.2	57.6	9136.7	57.8
	12.8	3050	2970	3050	60.2	60.4	60	3023.3	60.2
	21.1	939	910	962	62.2	62.3	61.9	937.0	62.1
	29.4	276	266	281	63.8	63.9	63.5	274.3	63.7
	37.8	81.2	78.7	84.3	65	65.1	64.8	81.4	65.0
	46.1	26.6	25.8	27.5	65.9	66	65.8	26.6	65.9
	54.4	9.98	9.67	10.3	67.1	67.2	67.1	10.0	67.1

Table 5.3: Average Percent Difference between *G**-Based Witczak Predicted and
Measured *E** Data Using Default *A* and *VTS* Values

Temperature (ºC)	SP-III-PG-64-22 (lab mix)	SP-II-PG-70-22 (lab mix)	SP-III-PG-70-22 (plant mix)	SP-II-PG-64-22 (plant mix)	SP-III-PG-70-22 (plant mix)
-10	113%	76%	133%	117%	74%
4	98%	30%	94%	54%	57%
21	-24%	-55%	-21%	-46%	-13%
37	-57%	-73%	-53%	-69%	-25%
54	-57%	-66%	-51%	-61%	-4%

Table 5.4: Average Percent Difference between *G**-Based Witczak predicted and Tested
E* Data Using Actual *A* and *VTS* Values

Temperature (ºC)	SP-III-PG-64-22 (lab mix)	SP-II-PG-70-22 (lab mix)	SP-III-PG-70-22 (plant mix)	SP-II-PG-64-22 (plant mix)	SP-III-PG-70-22 (plant mix)
-10	2%	4%	10%	26%	-15%
4	-38%	-41%	-41%	-31%	-50%
21	-66%	-69%	-65%	-63%	-59%
37	-68%	-70%	-64%	-65%	-40%
54	-56%	-56%	-50%	-49%	-3%

Table 5.5: Mastercurve Parameters for Binders (Ref. Temp = 21 ºc)

Asphalt mix	Master curve parameters			
	max	β	δ	γ
PG 70-22	9	-1.27	-1.27	-1.27
PG 64-22	9	-0.73	-0.26	-0.32

Table 5.6: Average Percent Difference between Hirsch Predicted and Measured *E** Data
Using Default *A* and *VTS* Values

Temperature (ºC)	SP-III-PG-64-22 (lab mix)	SP-II-PG-70-22 (lab mix)	SP-III-PG-70-22 (plant mix)	SP-II-PG-64-22 (plant mix)	SP-III-PG-70-22 (plant mix)
-10	129%	84%	123%	102%	134%
4	41%	-7%	19%	-4%	26%
21	-45%	-68%	-49%	-65%	-32%
37	-74%	-83%	-74%	-82%	-53%
54	-70%	-73%	-68%	-70%	-30%

151

Table 5.7: Average Percent Difference between Hirsch Predicted and Tested *E** Data Using Actual *A* and *VTS* Values

Temperature (°c)	SP-III-PG-64-22 (Lab Mix)	SP-II-PG-70-22 (Lab Mix)	SP-III-PG-70-22 (Plant Mix)	SP-II-PG-64-22 (Plant Mix)	SP-III-PG-70-22 (Plant Mix)
-10	-26%	-29%	-31%	-26%	-31%
4	-54%	-54%	-61%	-53%	-59%
21	-81%	-81%	-82%	-80%	-75%
37	-83%	-84%	-83%	-83%	-67%
54	-72%	-72%	-69%	-69%	-34%

Table 5.8: Original and Optimized Mix Variables for MEPDG Level-3 Analysis

Mix Type	Mix Variables	LAB Original	LEVEL-3 Optimized Values
SP-II	VA (%)	5.5	0.00026036
	Vbeff (%)	8.78	0.00402348
	P34 (%)	6	0
	P38 (%)	33	0
	P4 (%)	66	0
	P200 (%)	3.4	4.2263935
SP-III	VA (%)	5.5	0.0001
	Vbeff (%)	9.42	0.00047256
	P34 (%)	15	0
	P38 (%)	40	0
	P4 (%)	64	0
	P200 (%)	3.4	4.82795556
SP-IV	VA (%)	5.5	18.8964269
	Vbeff (%)	10.02	0
	P34 (%)	0	0
	P38 (%)	10	0
	P4 (%)	45	0
	P200 (%)	5.7	8.29808601

Table 5.9: Goodness of Fit of the Modified η-based Model

Model	New Modified Model		η-based Witczak model	
parameter	Logarithmic Scale	Arithmetic Scale	Logarithmic Scale	Arithmetic Scale
Data points	7400	7400	7400	7400
No. of Mixes	346	346	346	346
S_e	0.22	7.20	0.36	10.07
S_y	0.66	14.59	0.66	14.59
S_e/S_y	0.33	0.49	0.54	0.69
R^2	0.89	0.76	0.71	0.52

Table 5.10: Average Percent Difference between Witczak predicted and tested E^* data

Temperature (ºC)	SP-III PG-64-22 (lab mix)		SP-II PG-70-22 (lab mix)		SP-III PG-70-22 (plant mix)		SP-II PG-64-22 (plant mix)	
-10	7%	(+7%)	-11%	(-8%)	-3%	(22%)	-9%	(5%)
4	32%	(-5%)	1%	(0%)	15%	(23%)	1%	(27%)
21	30%	(19%)	-11%	(13%)	20%	(34%)	-7%	(42%)
37	21%	(38%)	-20%	(17%)	21%	(40%)	-16%	(43%)
54	6%	(55%)	-22%	(23%)	10%	(52%)	-19%	(42%)

153
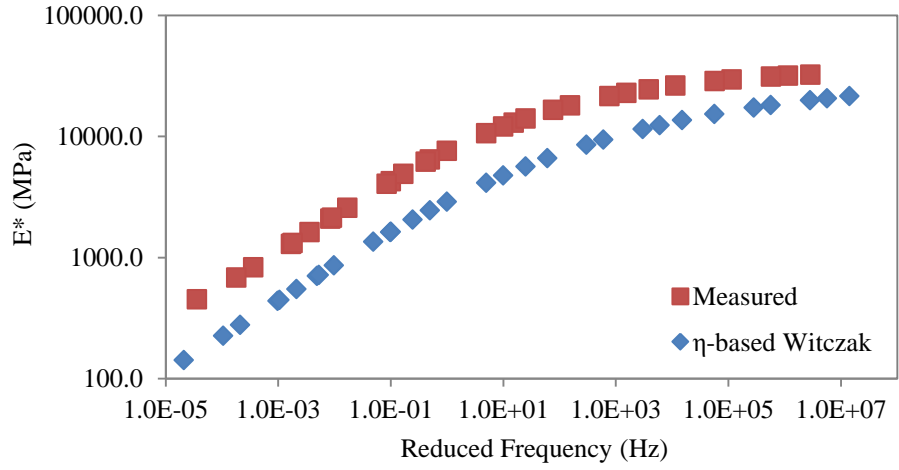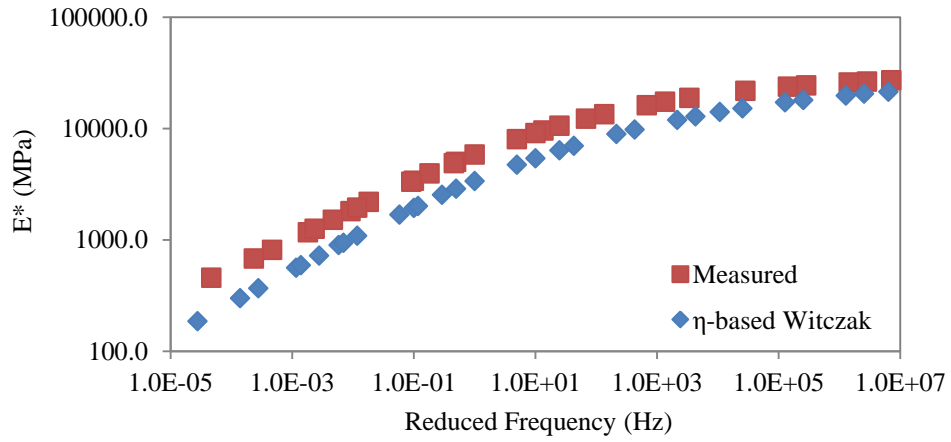
(a) SP-II plant

(b) SP-II Lab
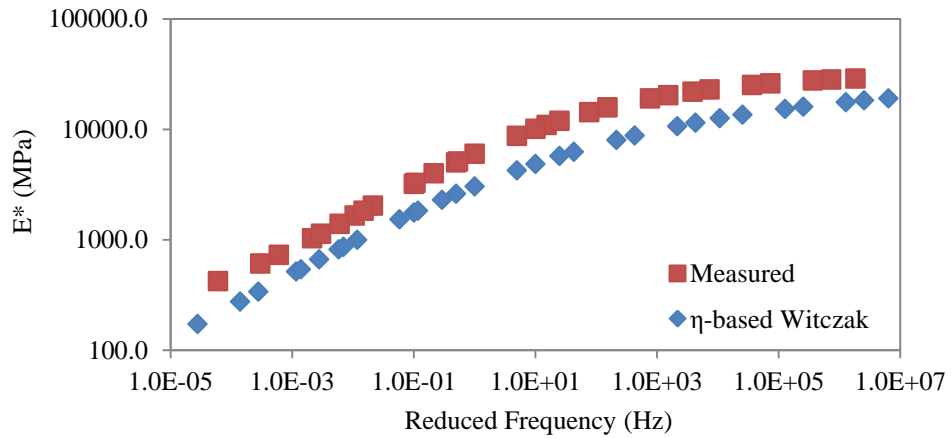
(c) SP-III plant

Figure 5.1(a-c): $\boldsymbol{\eta}$-based Witczak model predicted vs. Laboratory Measured $|\boldsymbol{E}^*|$

154
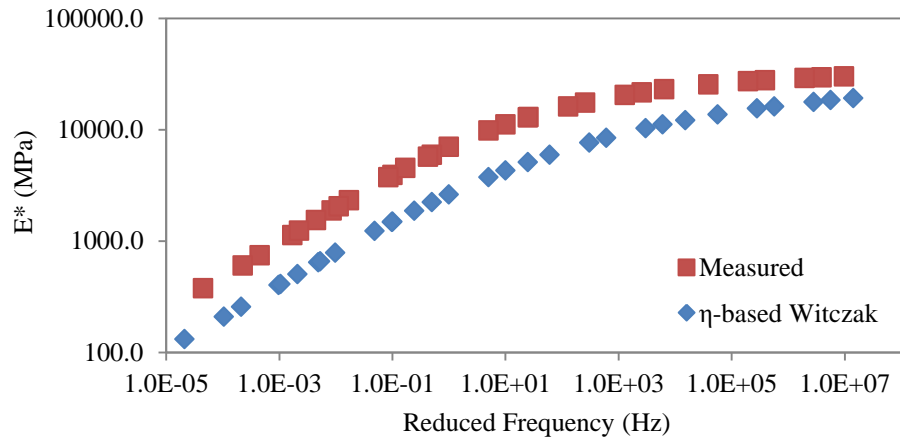
(d) SP-III lab
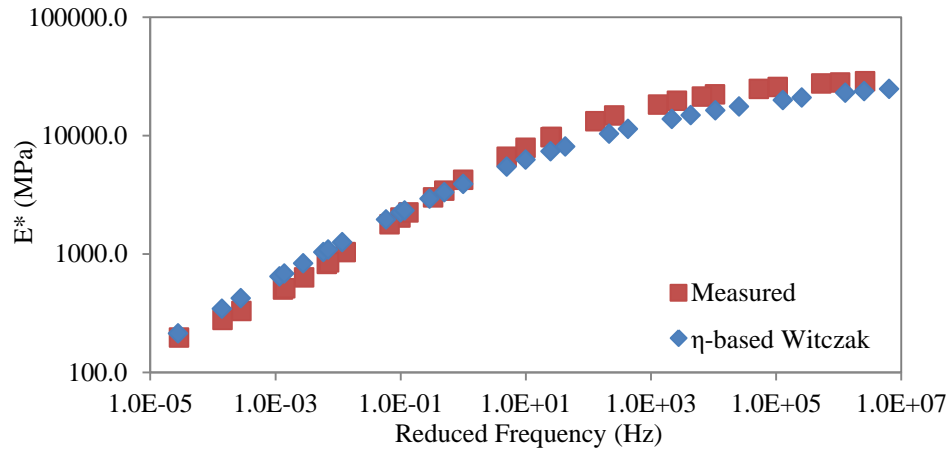
(e) SP-IV plant

Figure 5.1(a-e): $\boldsymbol{\eta}$-based Witczak model predicted vs. Laboratory Measured $|\boldsymbol{E}^*|$

155
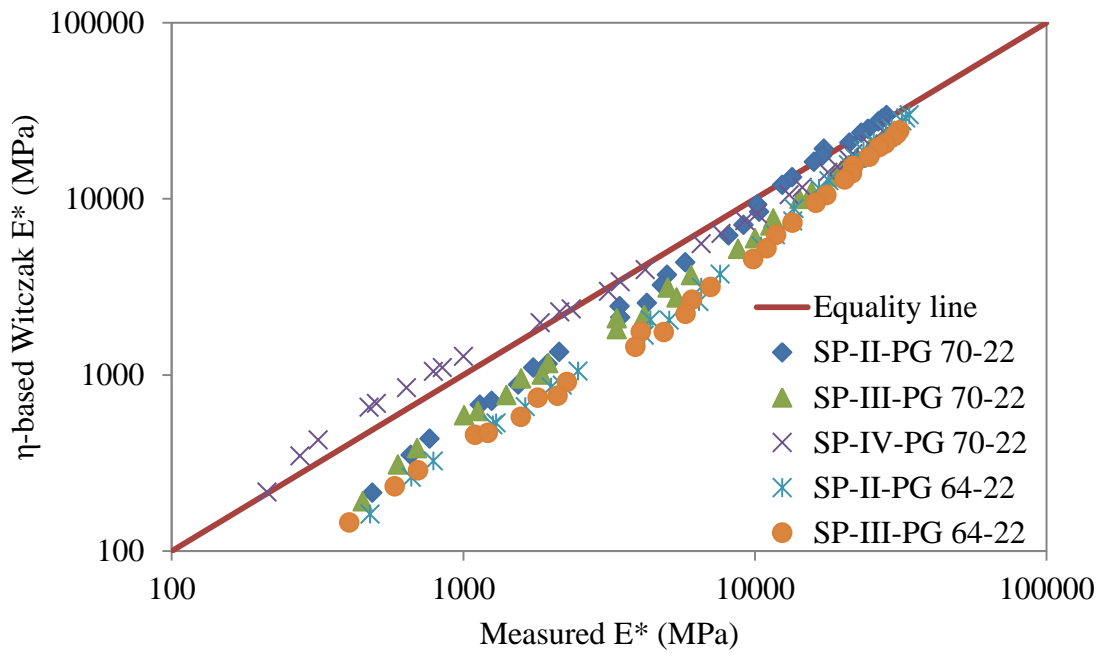
Figure 5.2: Scatter Plot for η-Based Witczak Model Predicted Vs. Laboratory Measured $|E^*|$ Data
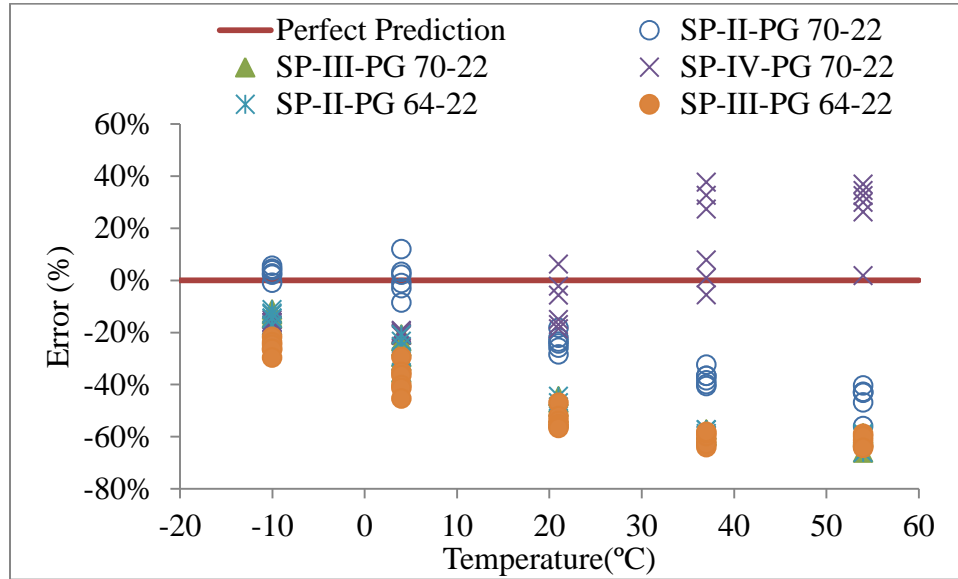
(a) Prediction error trend with temperature
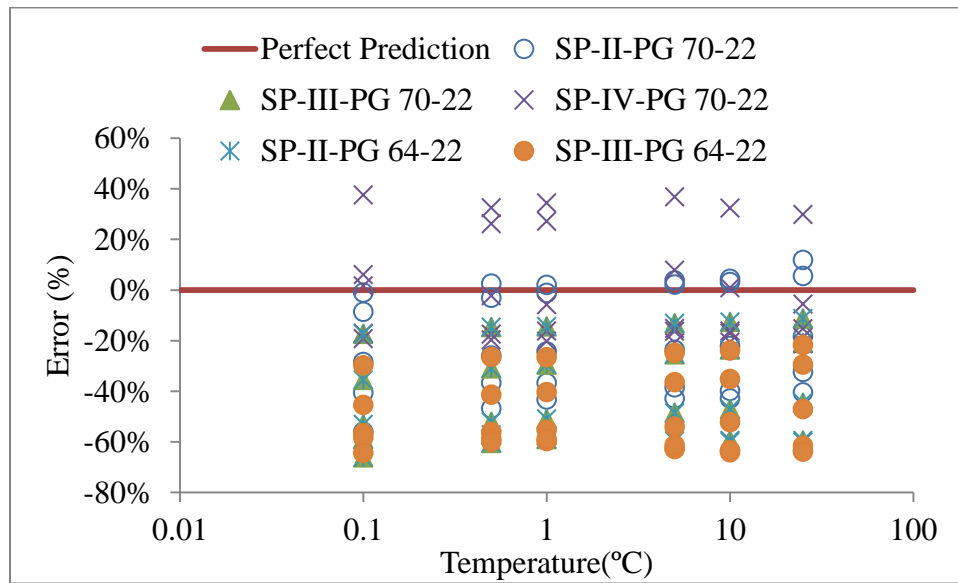
(b) Prediction error trend with frequency

Figure 5.3: Trend of Prediction % Error For η-Based Witczak Model

157
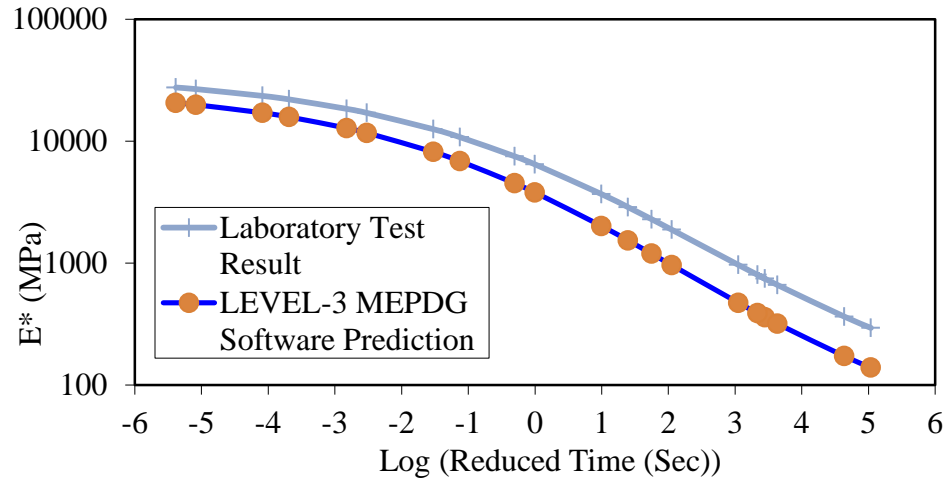
(a) SP-III mix
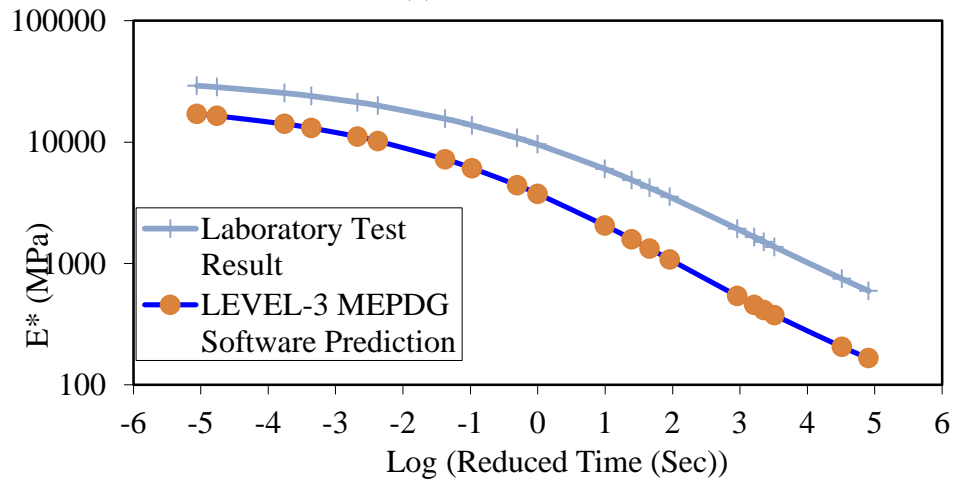
(b) SP-II mix
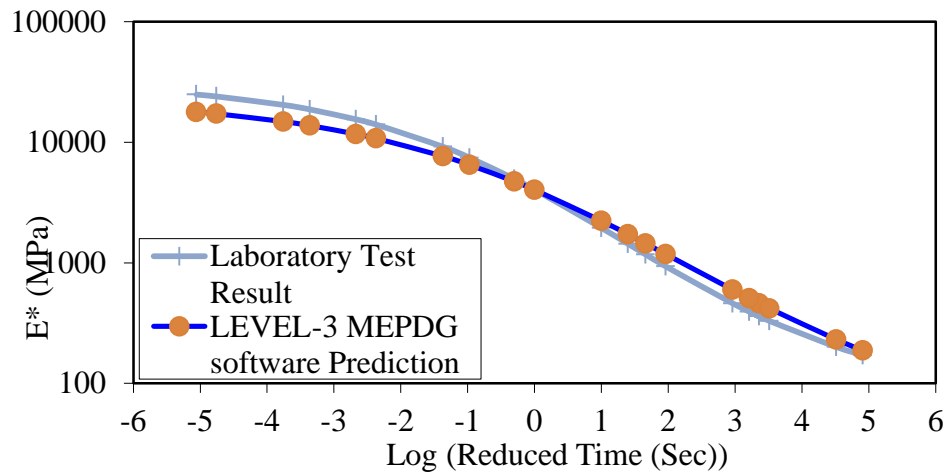
(c) SP-IV mix

Figure 5.4: MEPDG Level-3 Mastercurve Prediction vs. Mastercurve Developed for Laboratory $|E^*|$ Test Results

(a) *G** test results

(b) Phase angle test results

$$y = -2.6173x + 8.052$$
$$R^2 = 0.9825$$
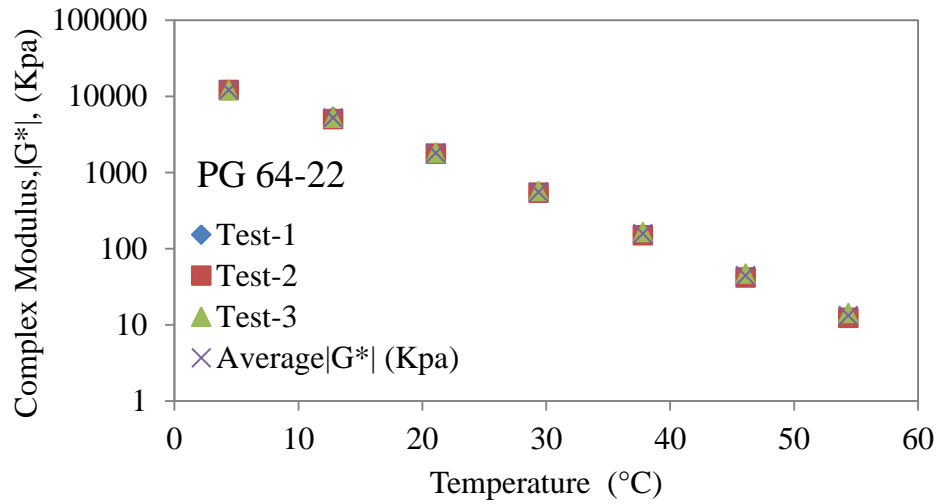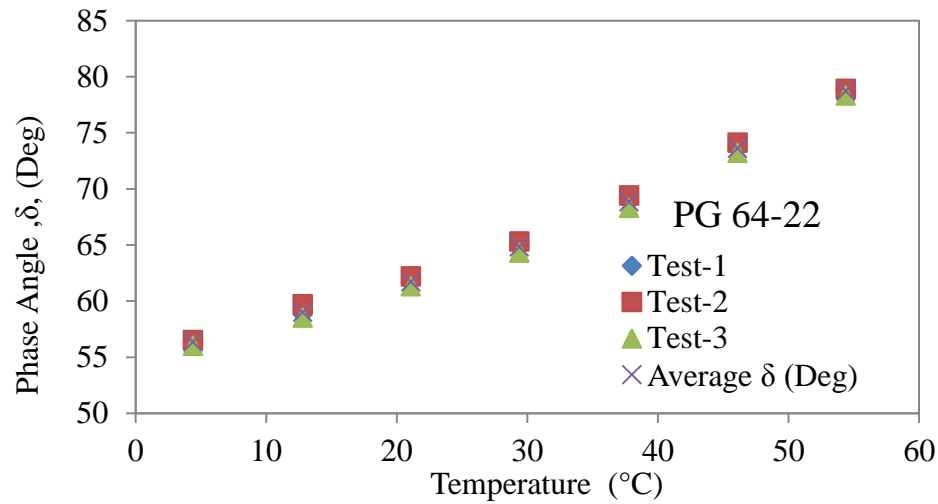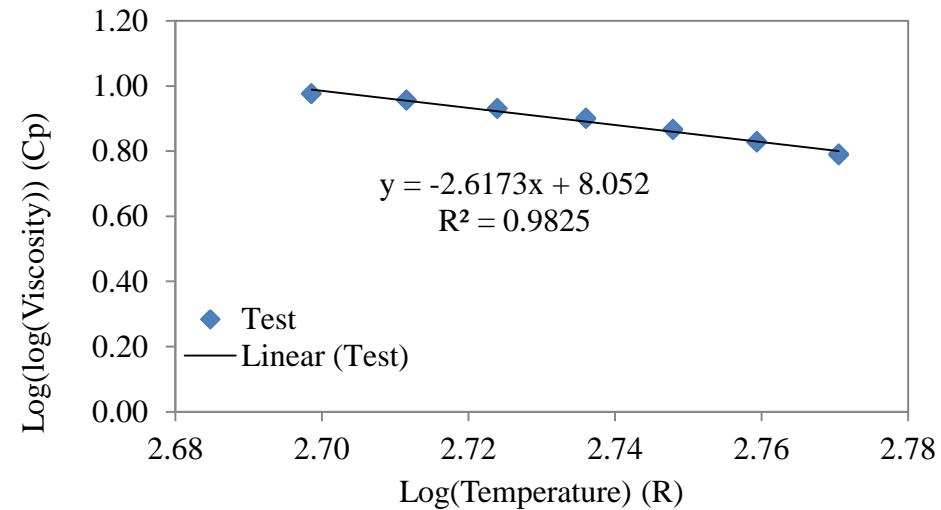
(c) *A* and *VTS* relationship

Figure 5.5: DSR Test Results and *A* and *VTS* Relationship for PG 64-22

159

(a) *G** test results

(b) Phase angle test results

$$y = -2.5142x + 7.7598$$
$$R^2 = 0.9964$$
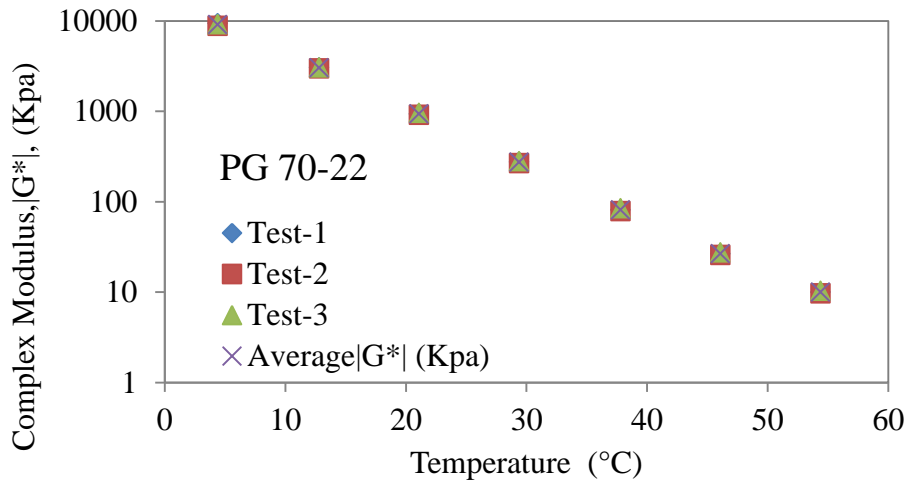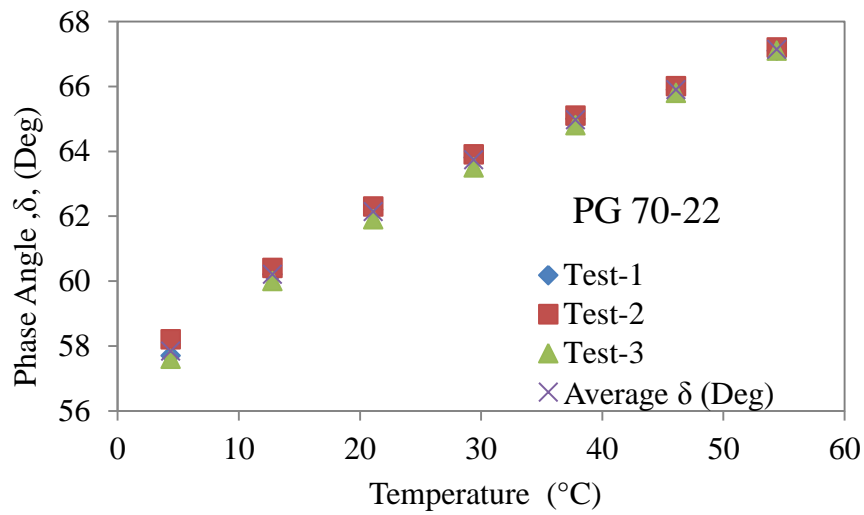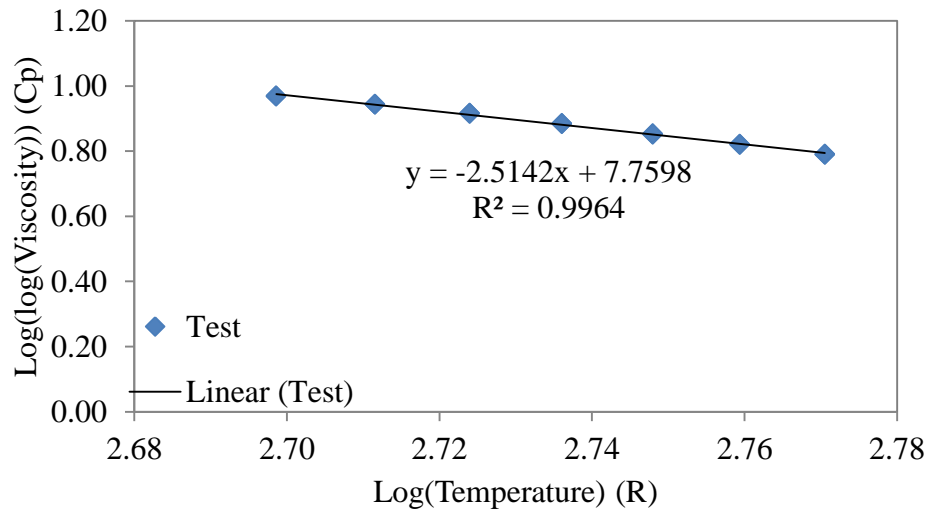
(c) A and *VTS* relationship

Figure 5.6: DSR Test Results and *A* and *VTS* Relationship for PG 70-22

160
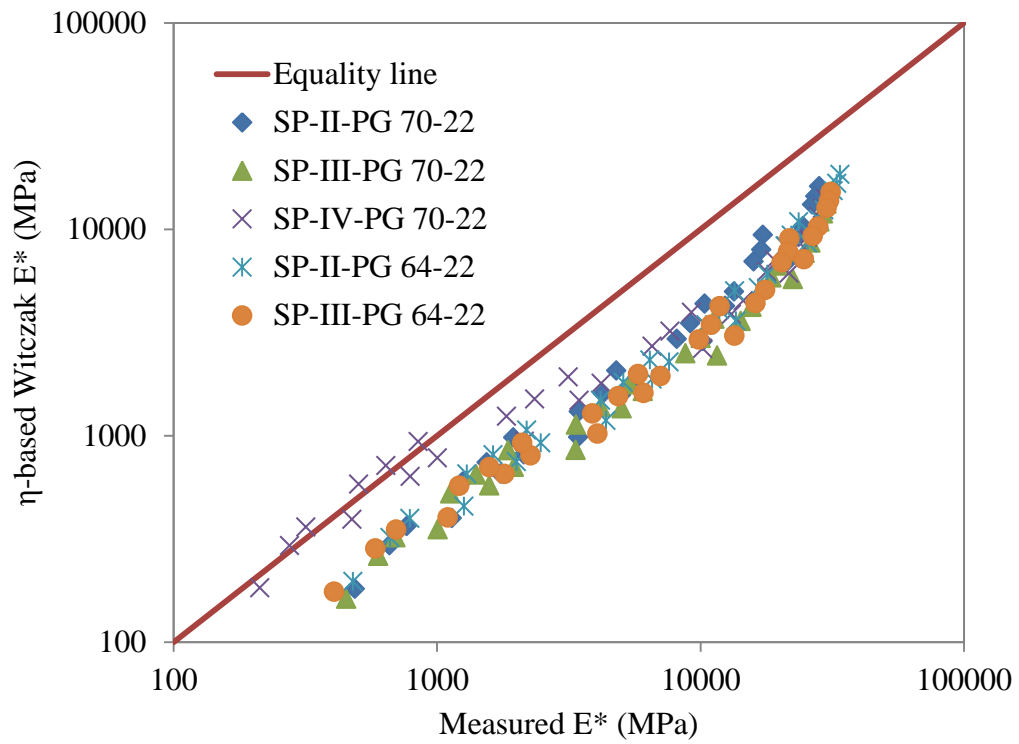
Figure 5.7: Scatter Plot for η-Based Witczak Model Prediction Using Actual *A* And *VTS* Developed Through Laboratory DSR Test

161
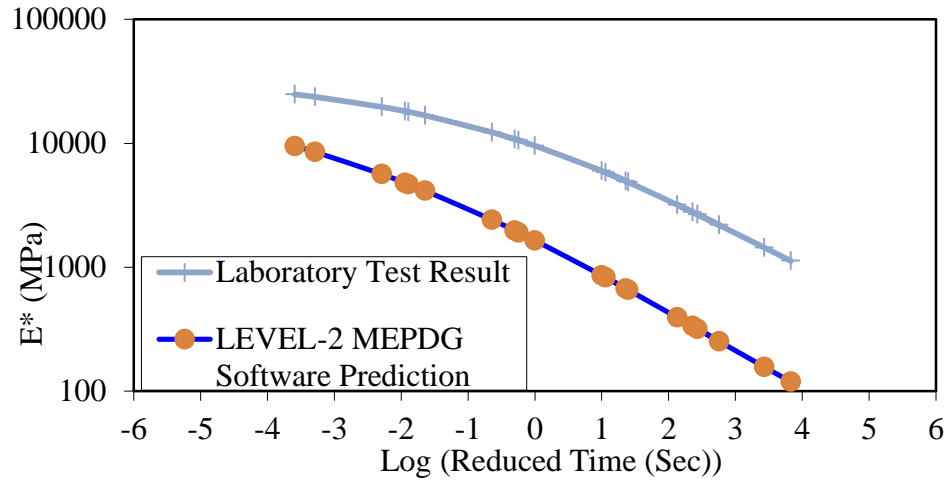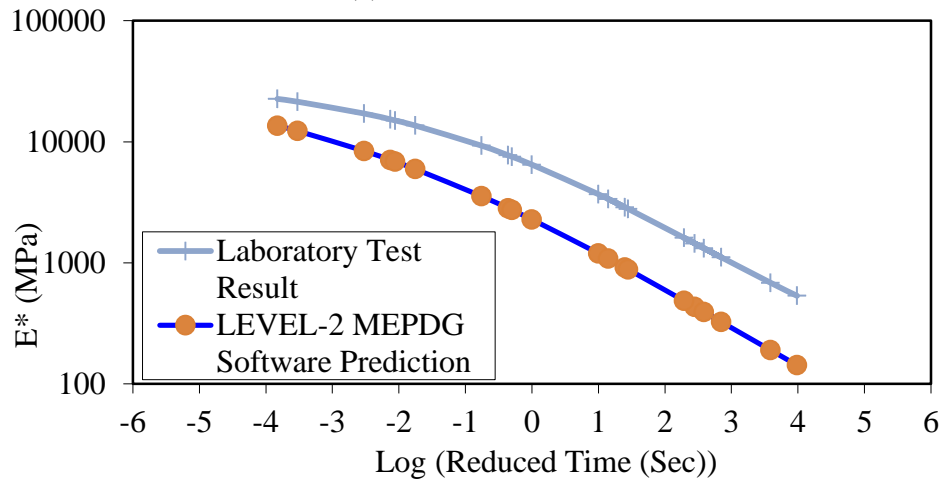
(a) SP-III Plant Mix

(b) SP-II Plant Mix
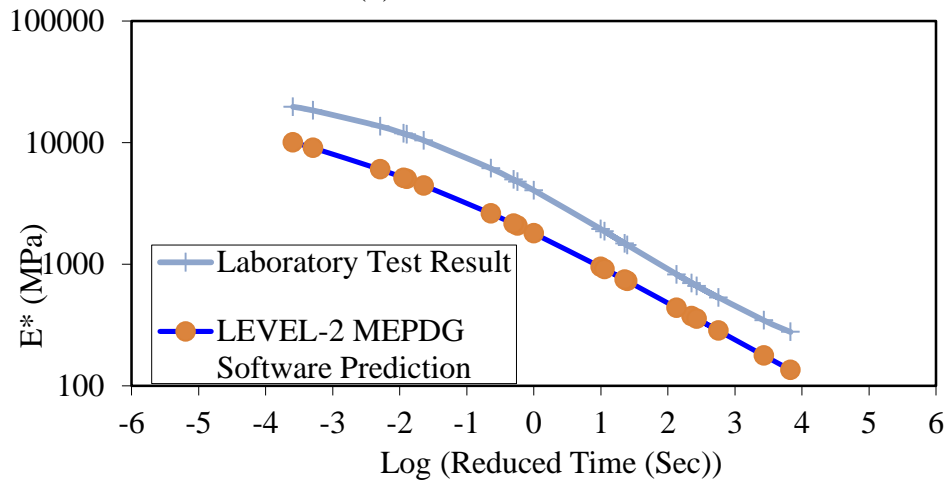
(c) SP-IV Plant Mix

Figure 5.8: MEPDG Level-2 Mastercurve Prediction vs. Mastercurve Developed for Laboratory $|E^*|$ Test Results

162
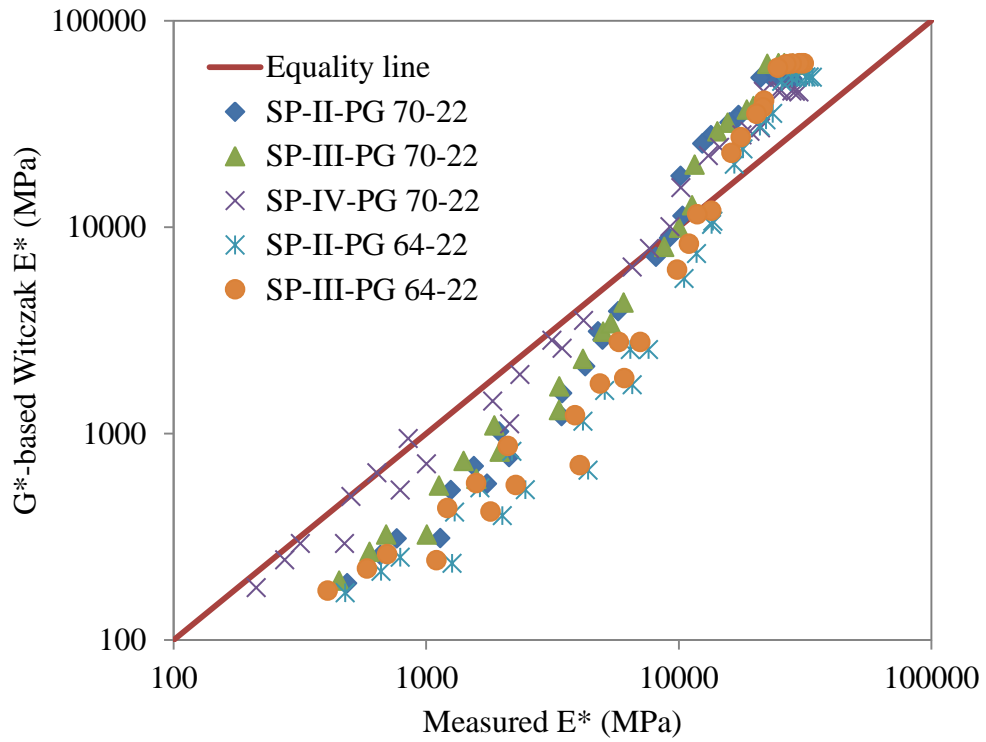
Figure 5.9: Scatter Plot for **G***-Based Witczak Model Prediction Using Default *A* and *VTS* Values From MEPDG.
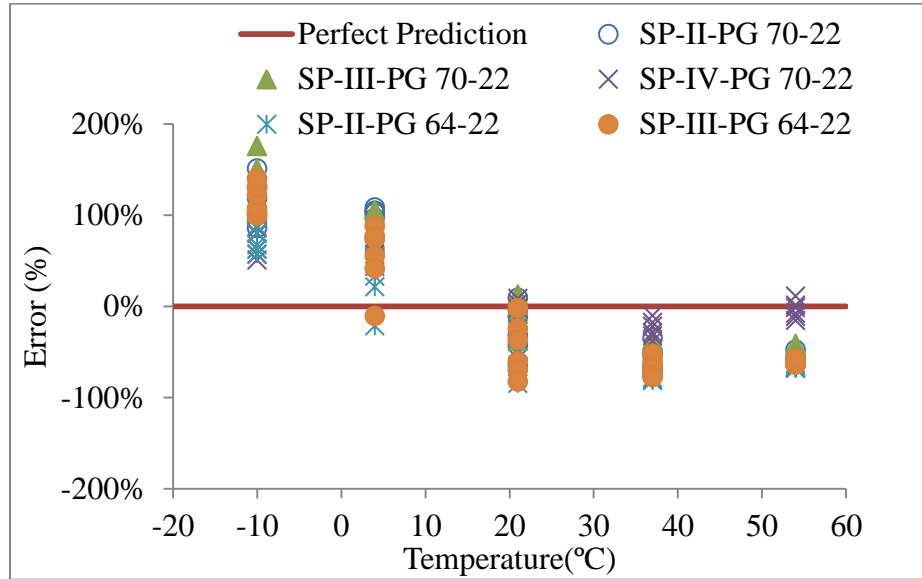
(a) Prediction error trend with temperature
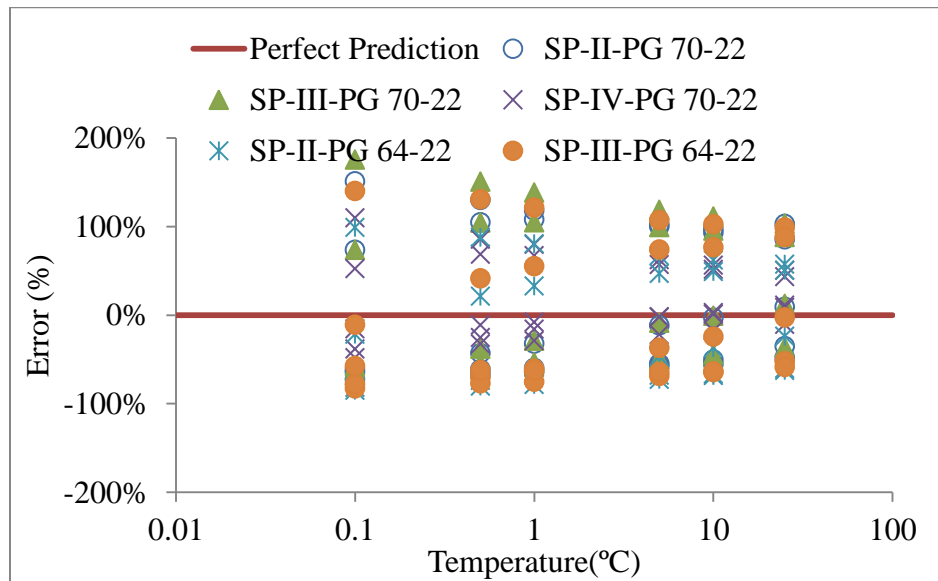
(b) Prediction error trend with frequency

Figure 5.10: Trend of Prediction % error for G^*-based Witczak model using default A and VTS values from MEPDG.

164
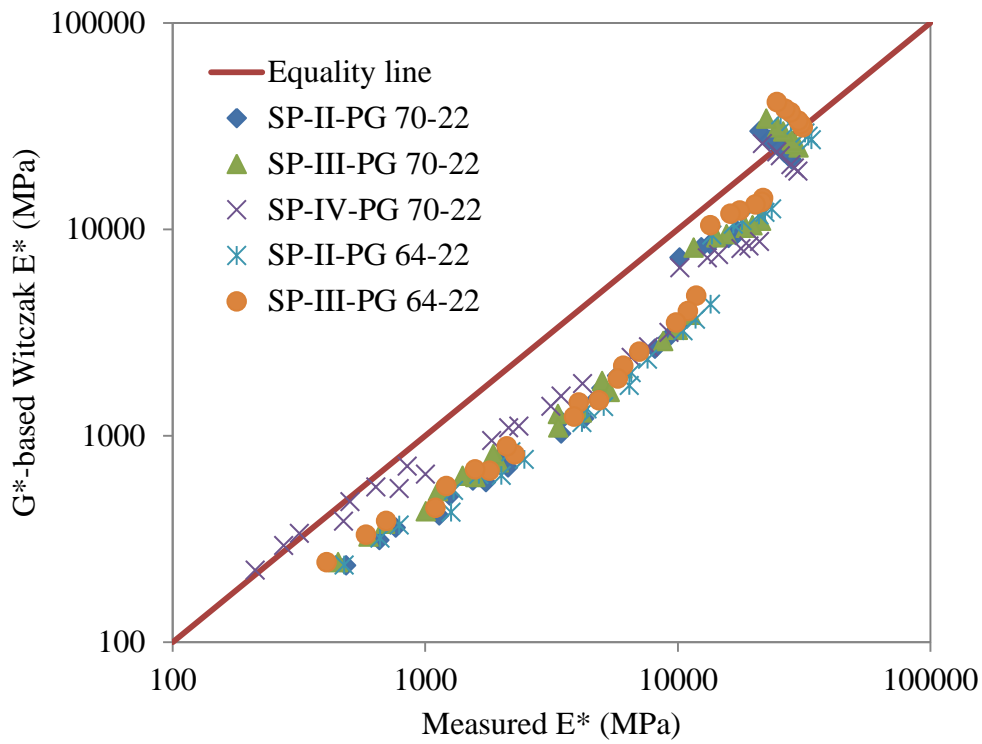
Figure 5.11: Scatter Plot For G^*-Based Witczak Model Prediction Using Actual A and *VTS* Values Determined From Laboratory DSR Test.
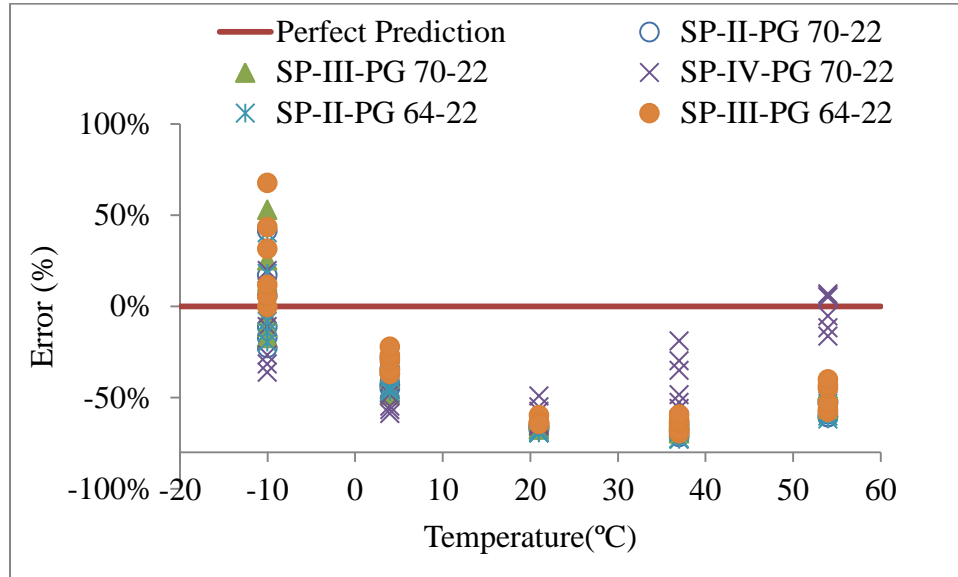
(a) Prediction Error Trend With Temperature
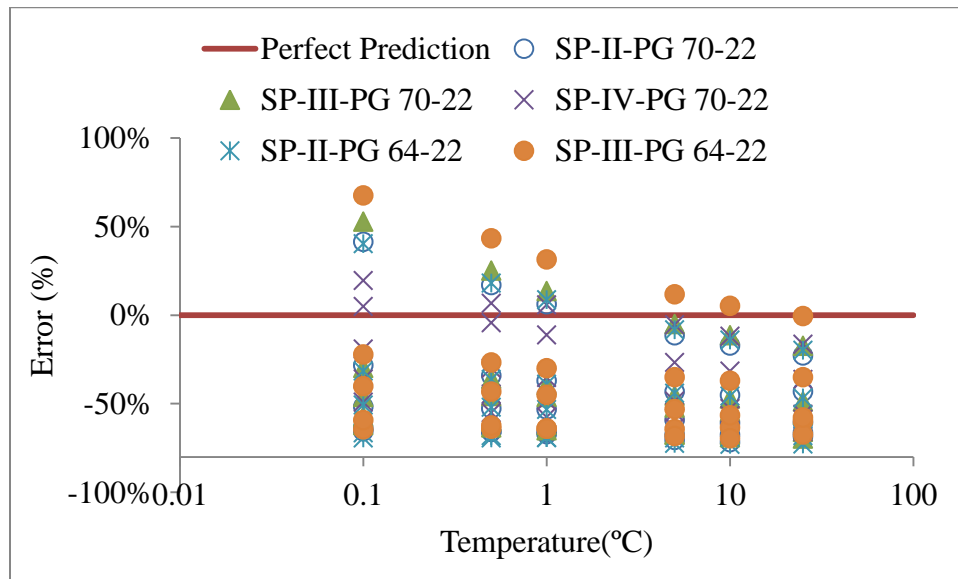
(b) Prediction Error Trend With Frequency

Figure 5.12: Trend of Prediction % Error for G^*-Based Witczak Model Using Default A and VTS Values from MEPDG

166
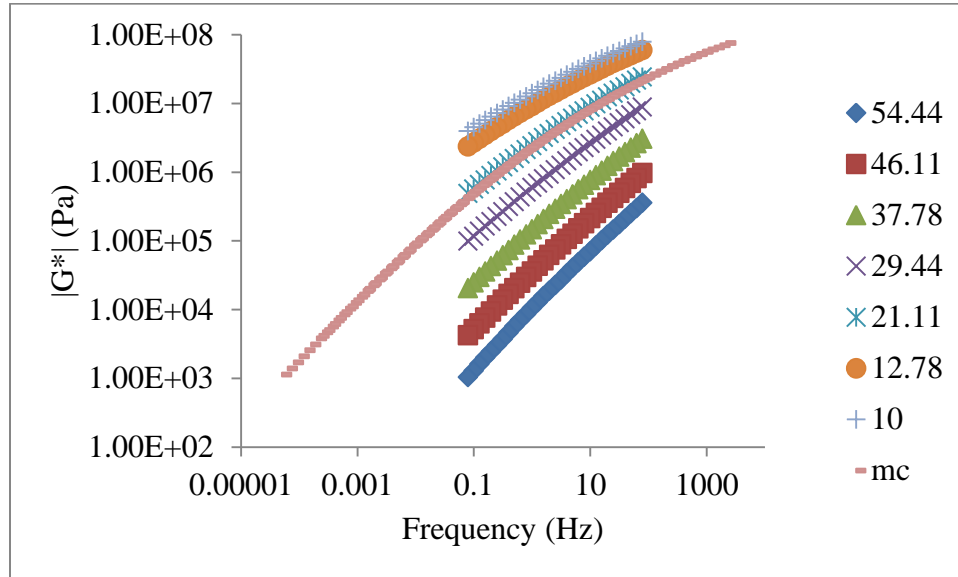
(a) *G* Mastercurve for PG 64-22*
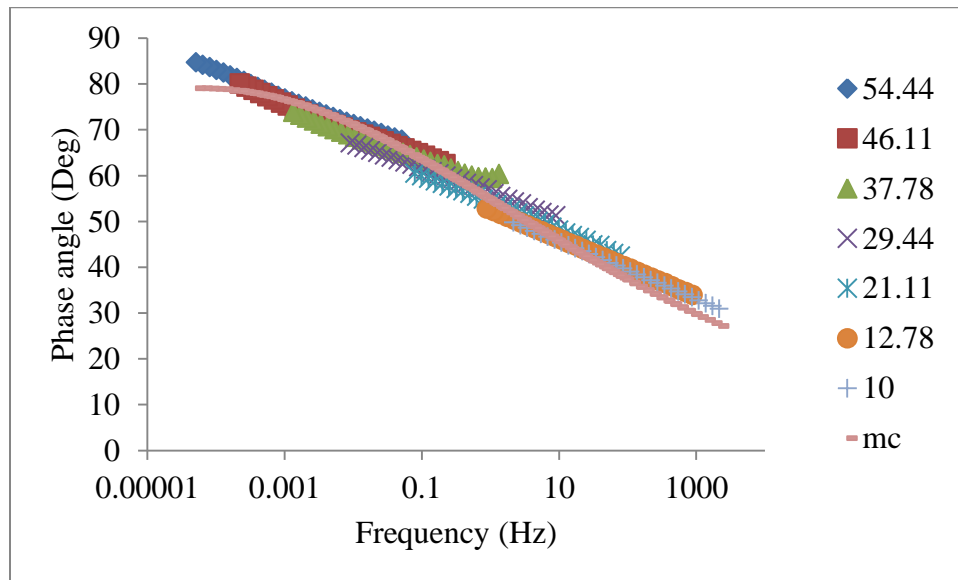
(b) Phase Angle Mastercurve for PG 64-22

Figure 5.13: *G* and Phase Angle Mastercurves For PG 64-22*

167

www.manaraa.com
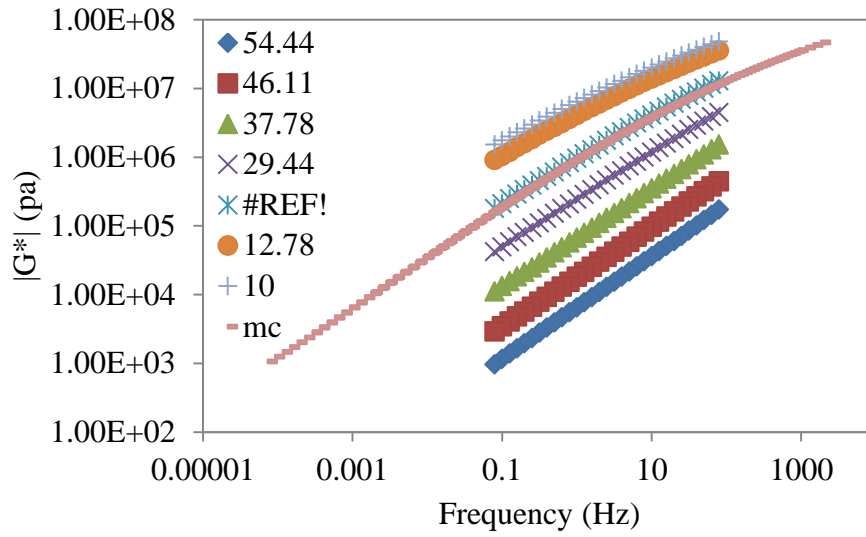
(a) *G** mastercurve for PG 70-22
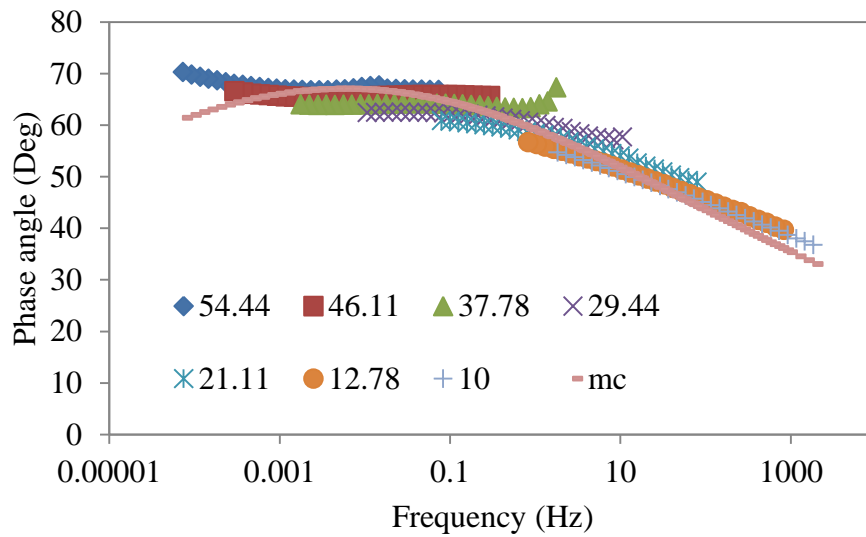
(b) Phase angle mastercurve for PG 70-22

Figure 5.14: *G** and Phase angle mastercurves for PG 70-22
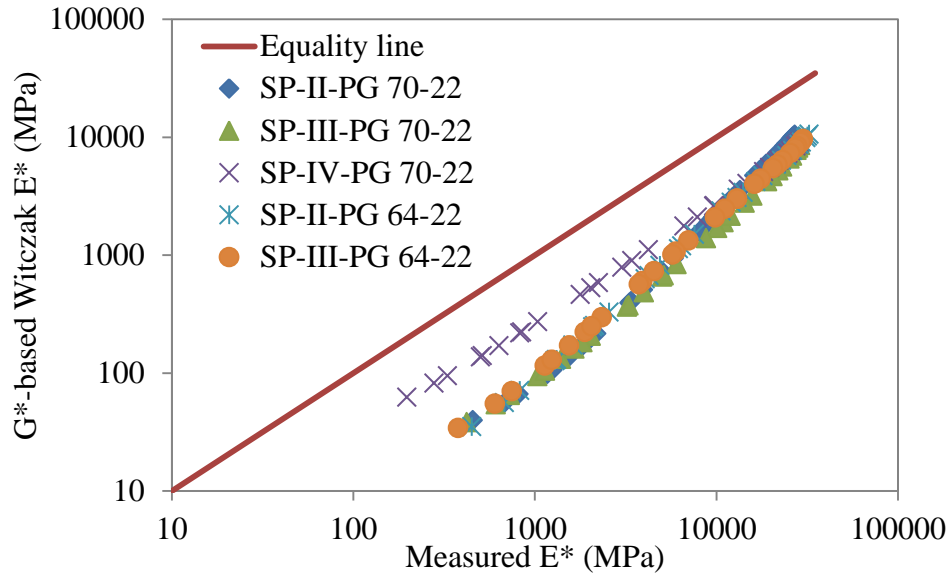
168

(a) scatter plot for G*-based Witczak model prediction
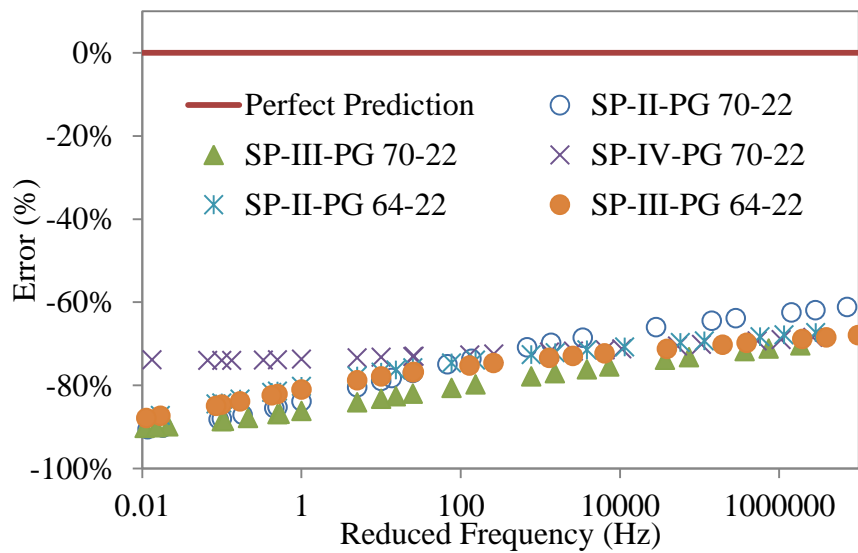
(b) Prediction error trend with frequency at 21ºC

Figure 5.15: Scatter Plot for G*-Based Witczak Model Prediction Using $G*$ and Phase Angle Mastercurves.
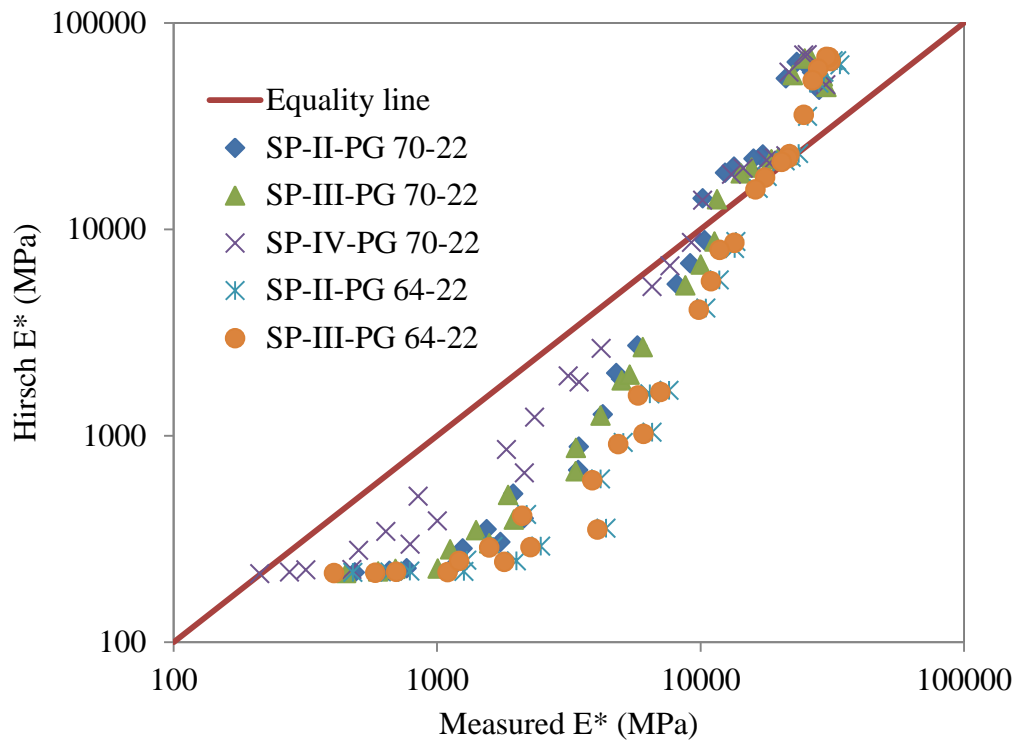
Figure 5.16: Scatter Plot for Hirsch Model Prediction Using Default *A* And *VTS* Values
From MEPDG.
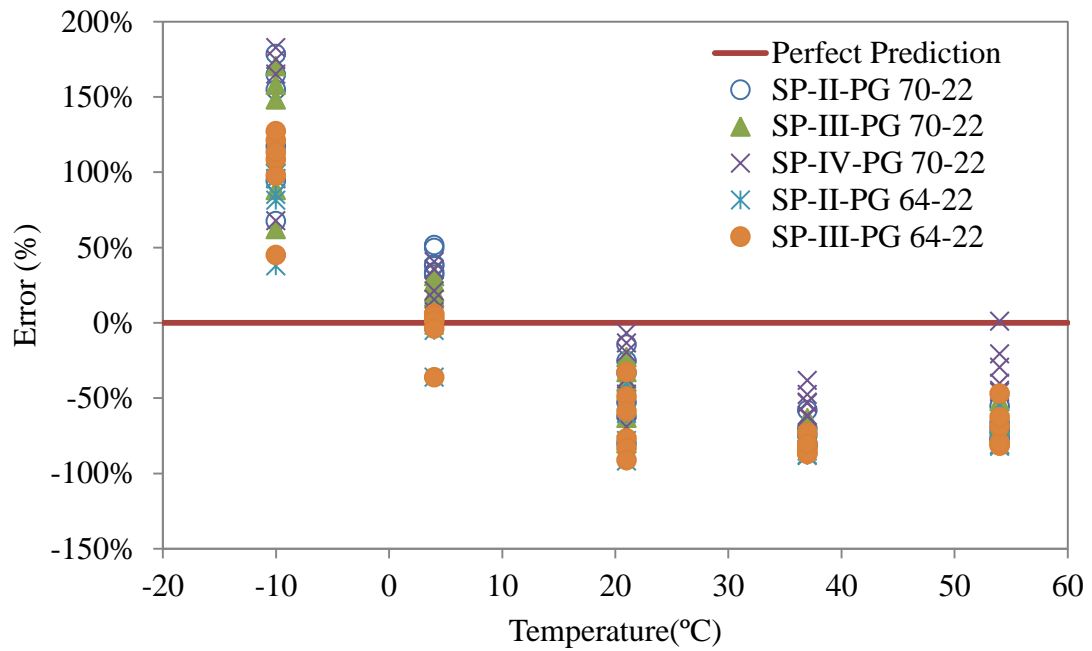
(a) Prediction Error Trend With Temperature
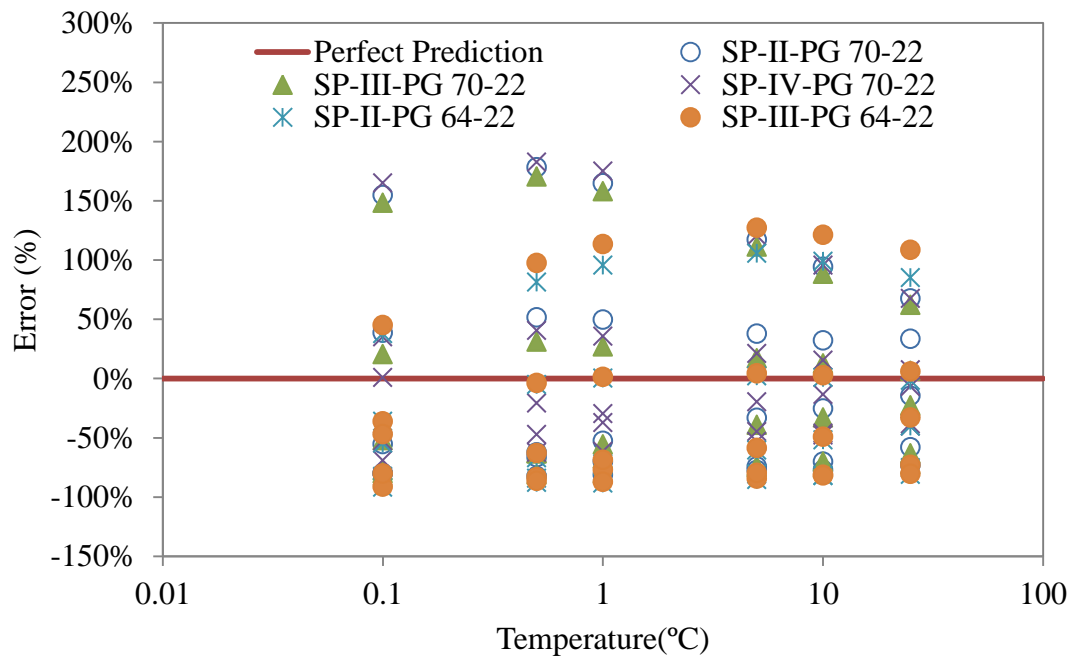
(b) Prediction Error Trend With Frequency

Figure 5.17: Trend of Prediction % Error for Hirsch Model Using Default *A* And *VTS* Values From MEPDG.

171
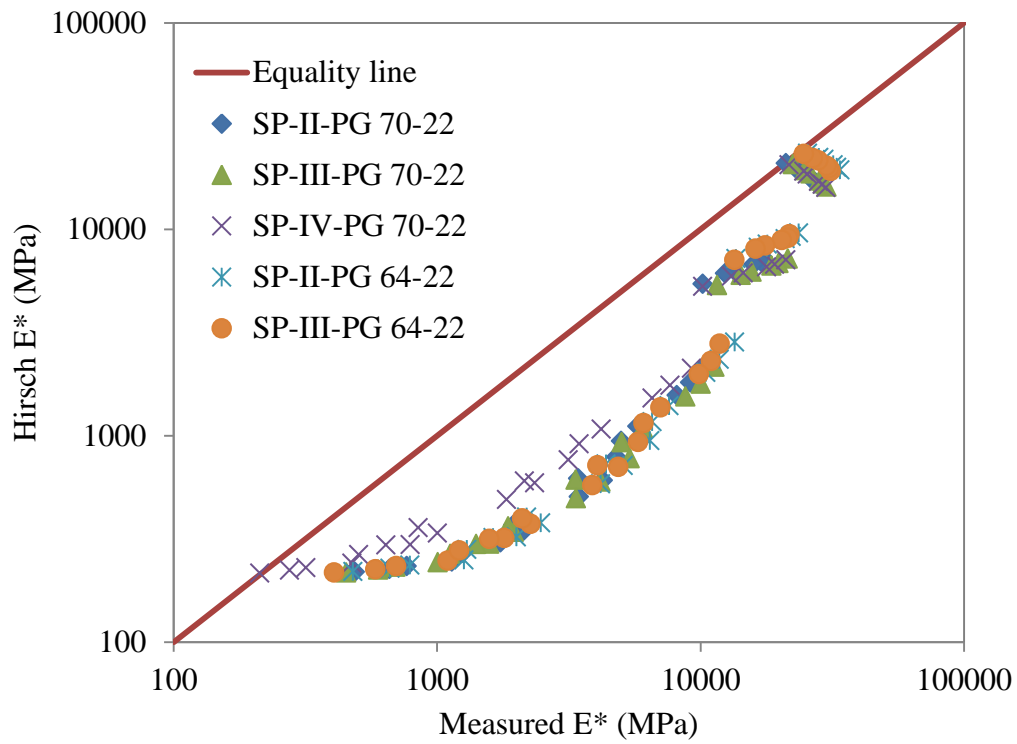
Figure 5.18: scatter plot for Hirsch model prediction using actual *A* and *VTS* values determined from laboratory DSR test.
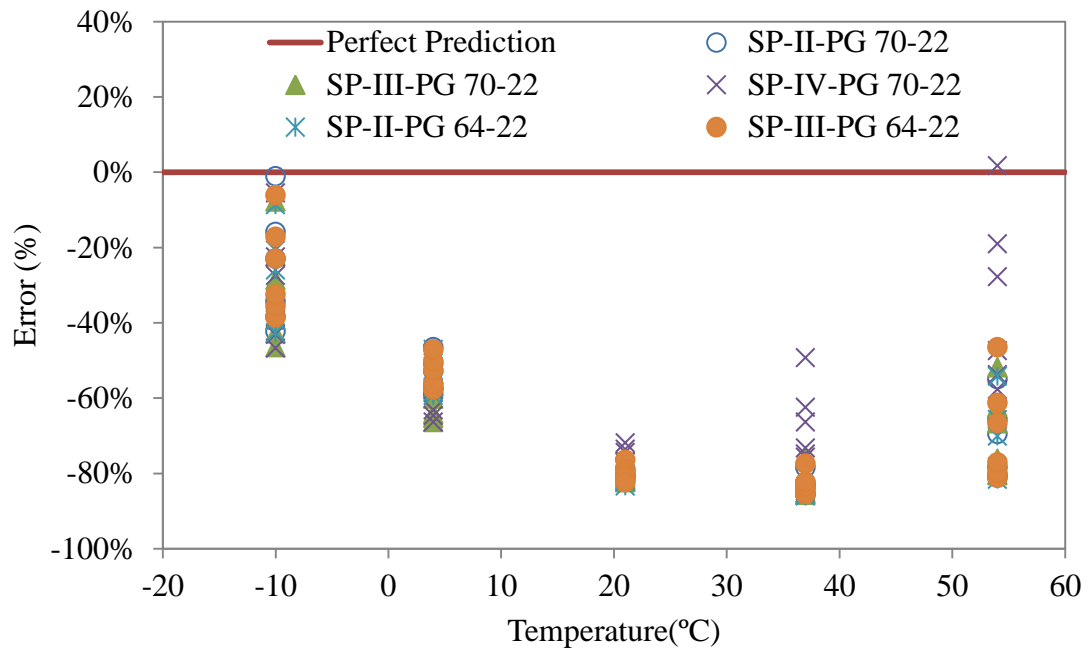
(a) Prediction error trend with temperature
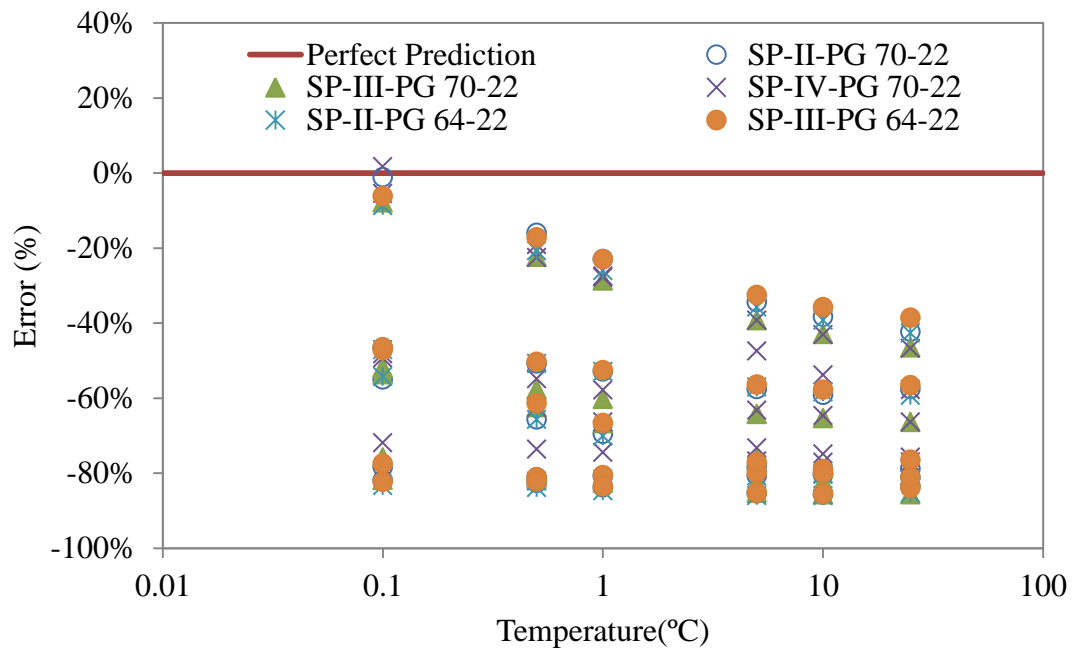
(b) Prediction error trend with frequency

Figure 5.19: Trend of Prediction % Error for Hirsch Model Using Default *A* and *VTS* Values From MEPDG

173
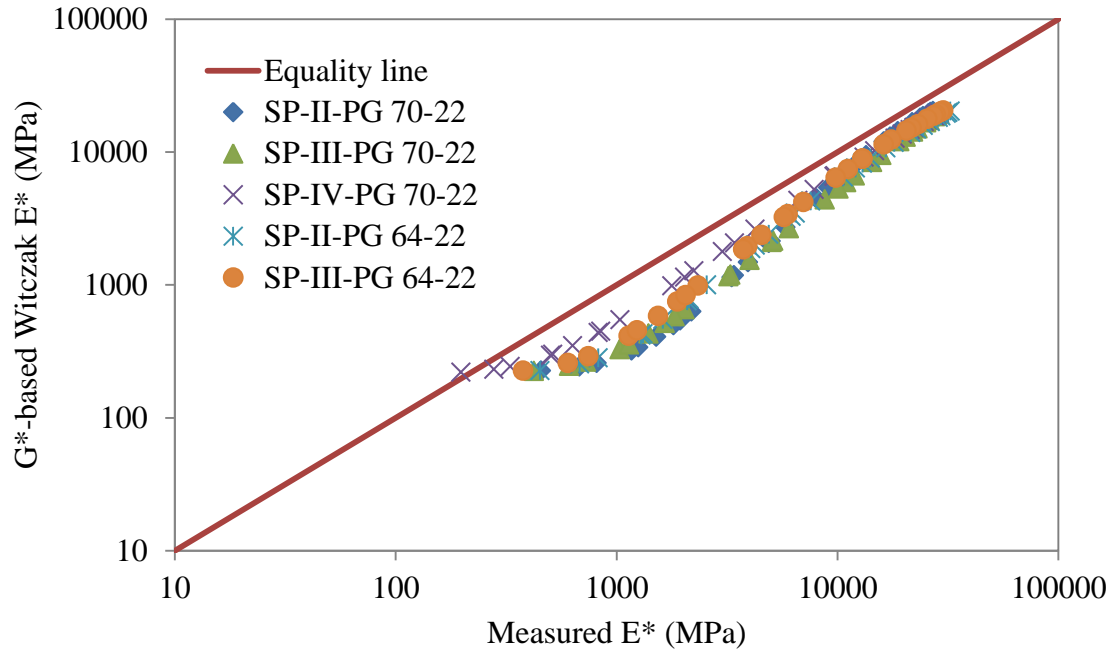
(a) scatter plot for Hirsch model prediction
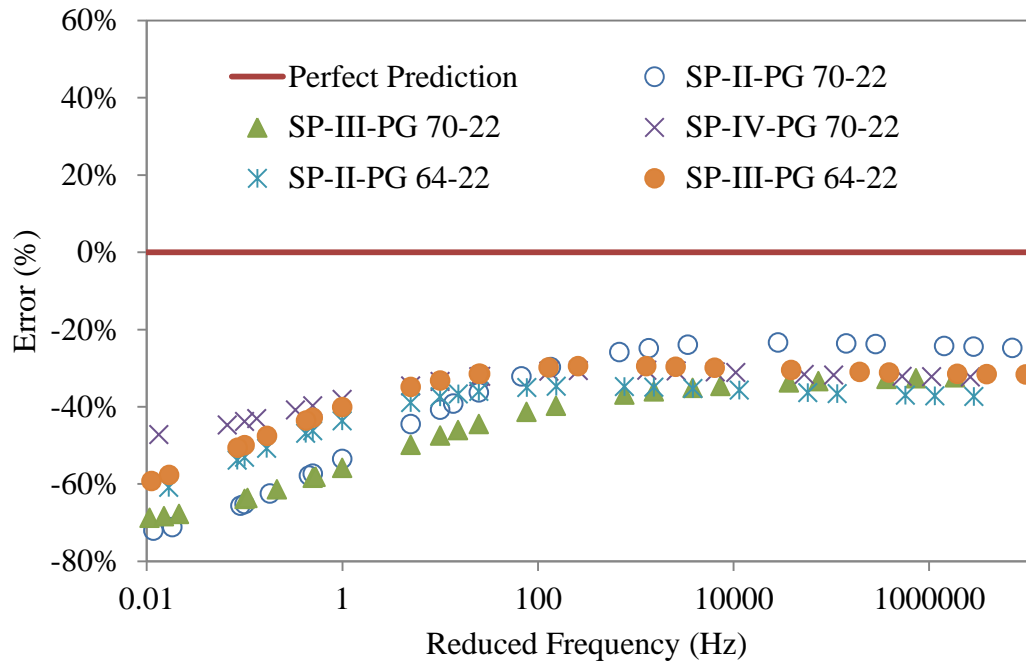
(b) Prediction error trend with frequency at 21℃

Figure 5.20: Scatter plot for Hirsch model prediction using $G*$ and Phase angle mastercurves
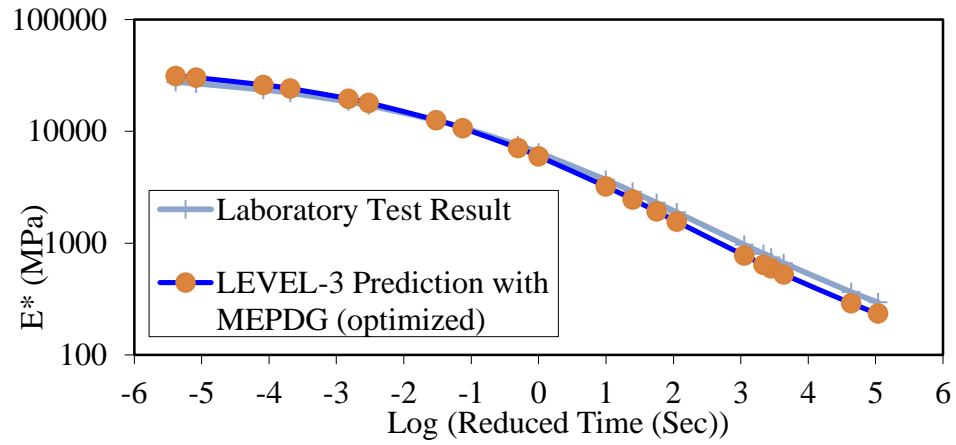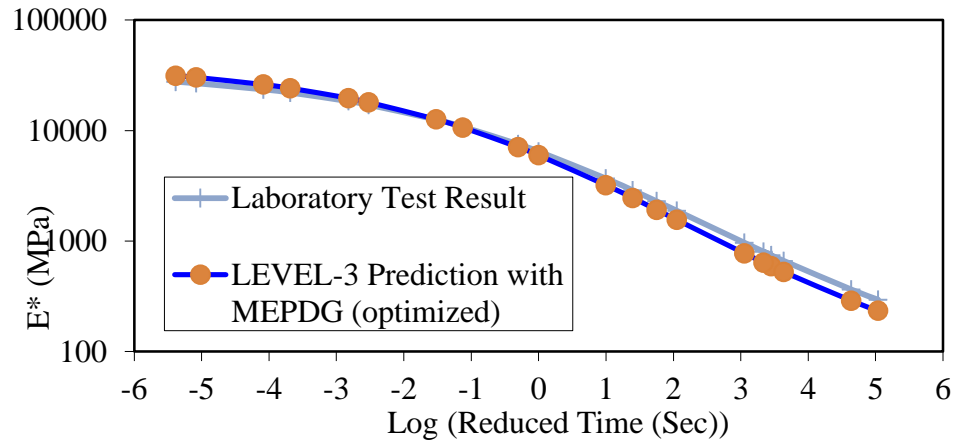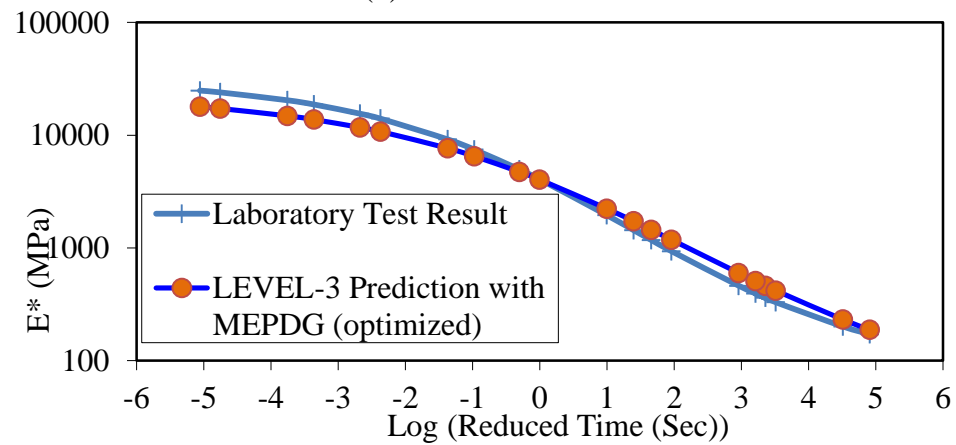
Figure 5.21: MEPDG Level-3 Mastercurve Predictions Using Optimized Mix Data Vs. Mastercurve Developed for Laboratory $|E^*|$ Test Results.
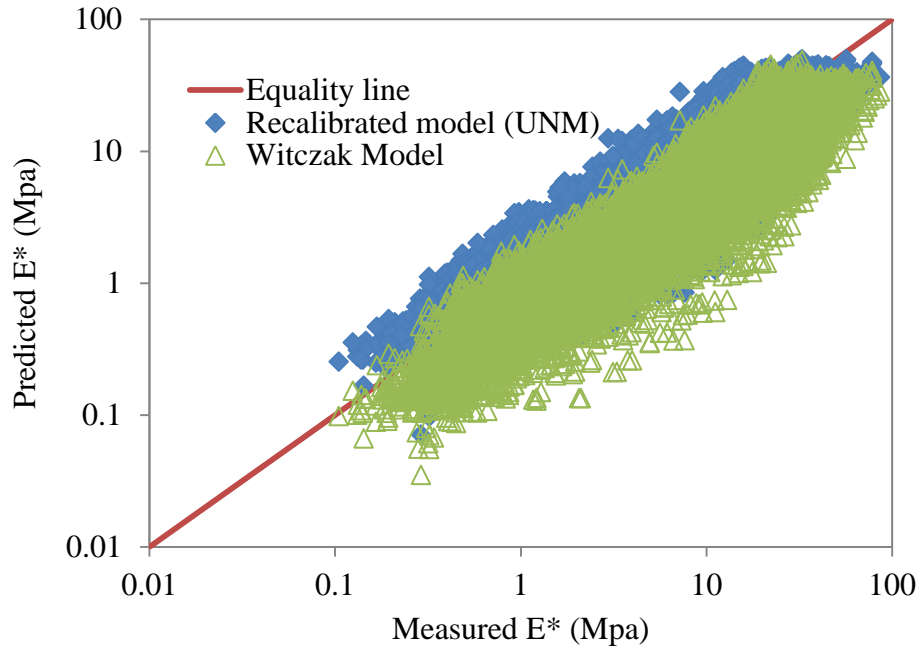
(a) Predicted Vs. Measured Scatter Plot (Logarithmic Scale)
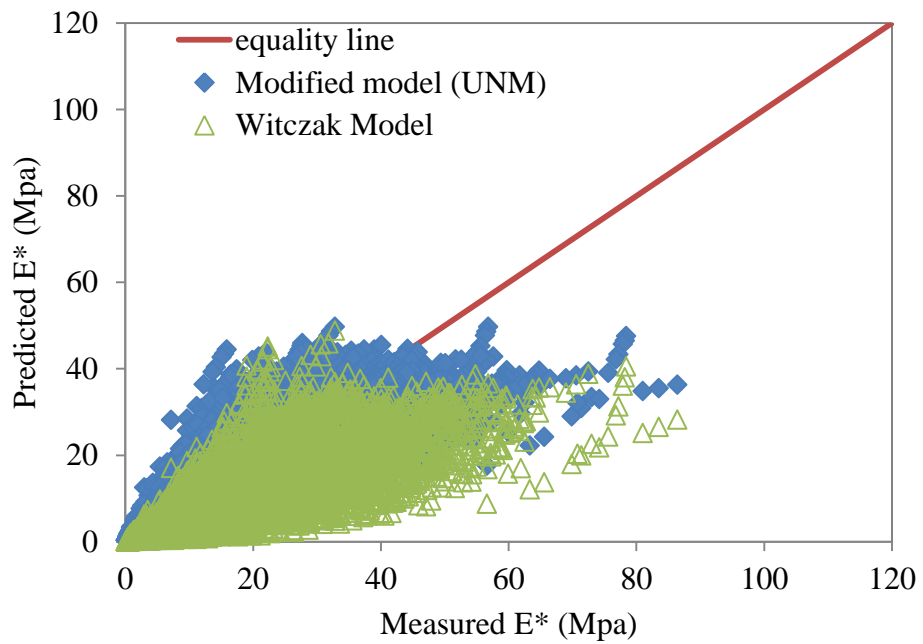
(b) Predicted Vs. Measured Scatter Plot (Arithmetic Scale)

Figure 5.22: Predicted Vs. Measured Scatter Plot

176
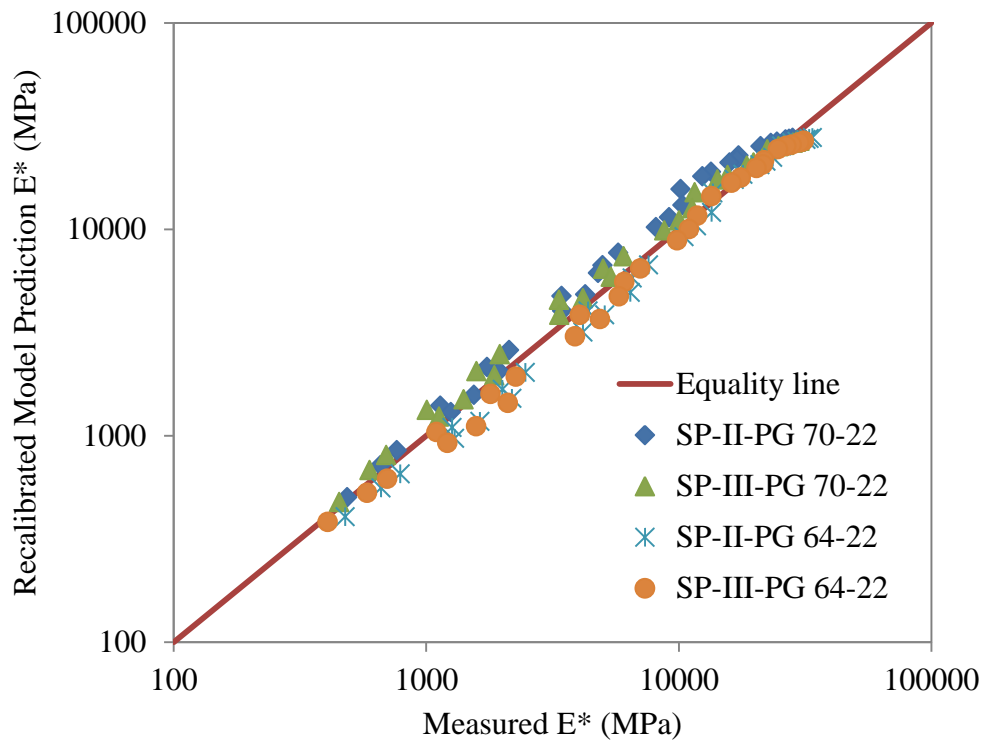
Figure 5.23: Scatter Plot for New Modified Model
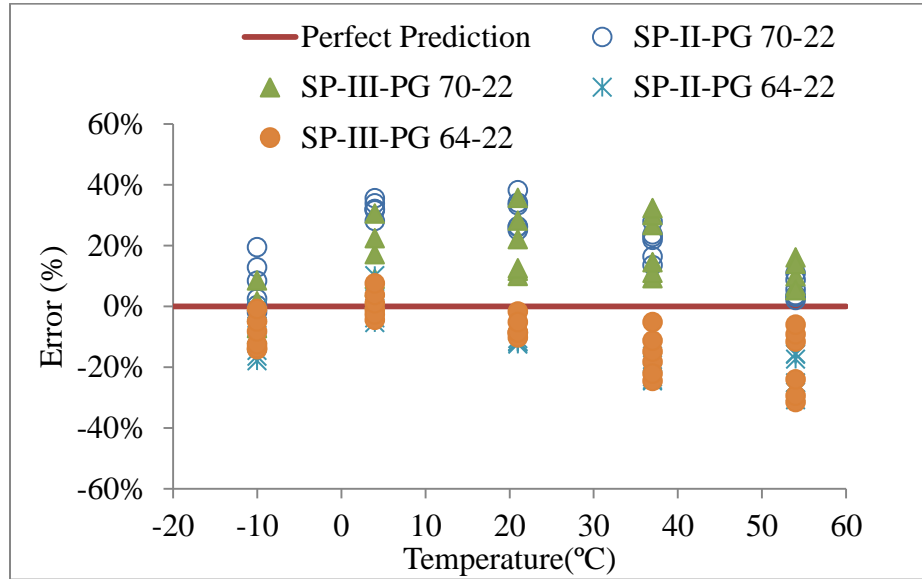
(a) Prediction Error Trend With Temperature
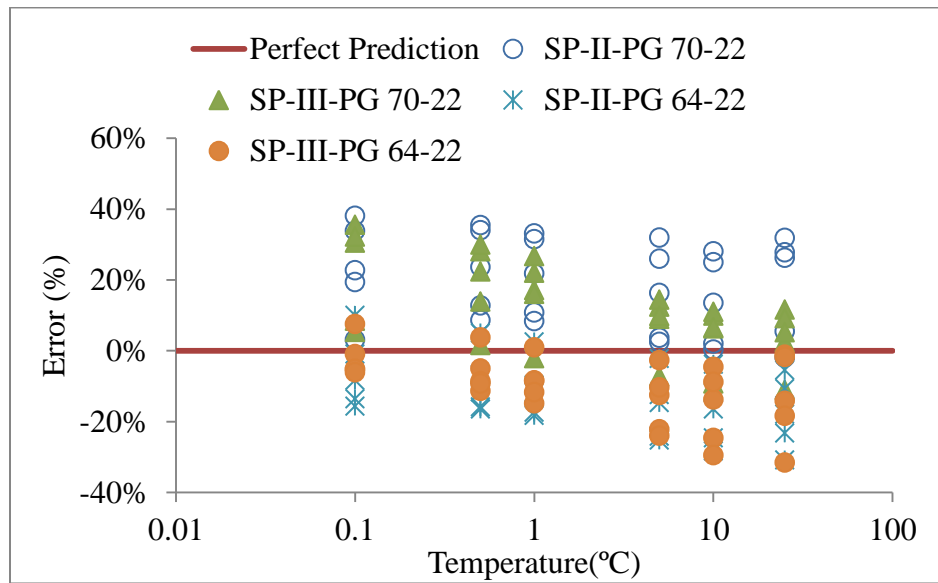
(b) Prediction Error Trend With Frequency

Figure 5.24: Trend of Prediction % Errors for New Modified Model

178
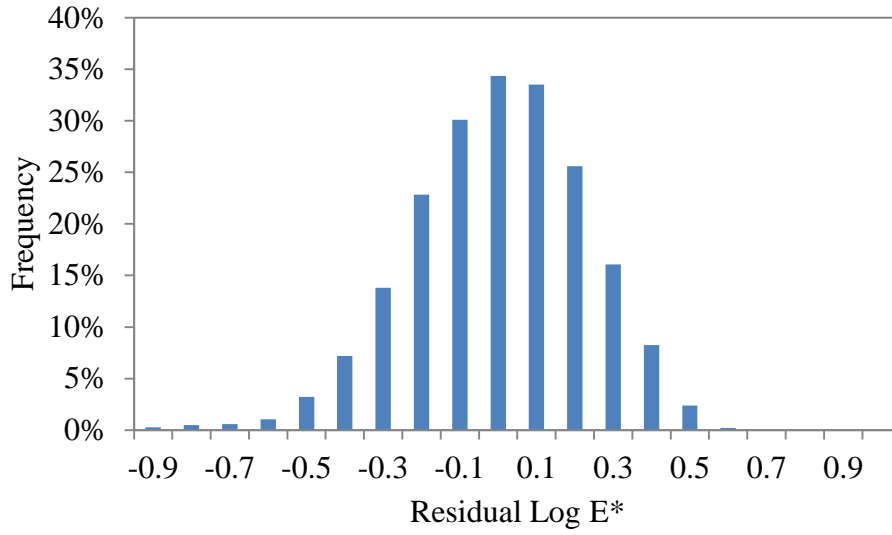
(a) Logarithmic Scale
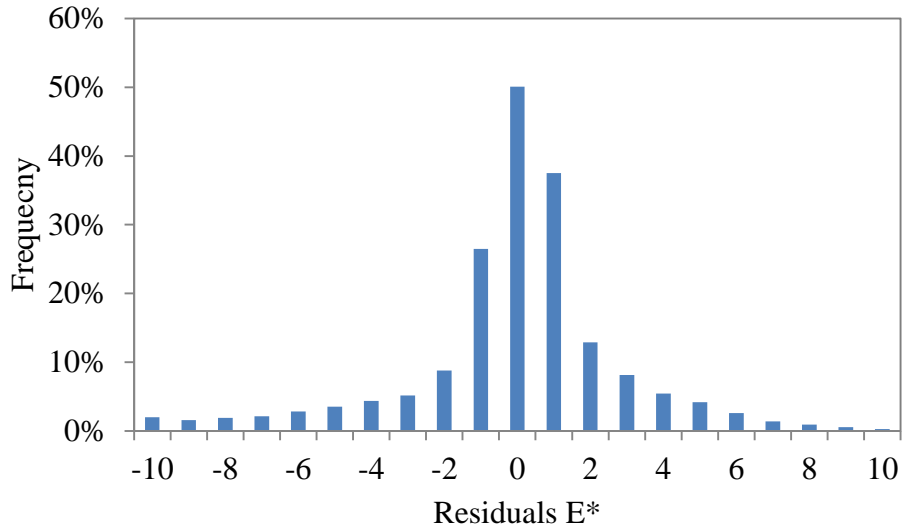
(b) Arithmetic Scale

Figure 5.25: Frequency Distribution of E^* Residuals

179
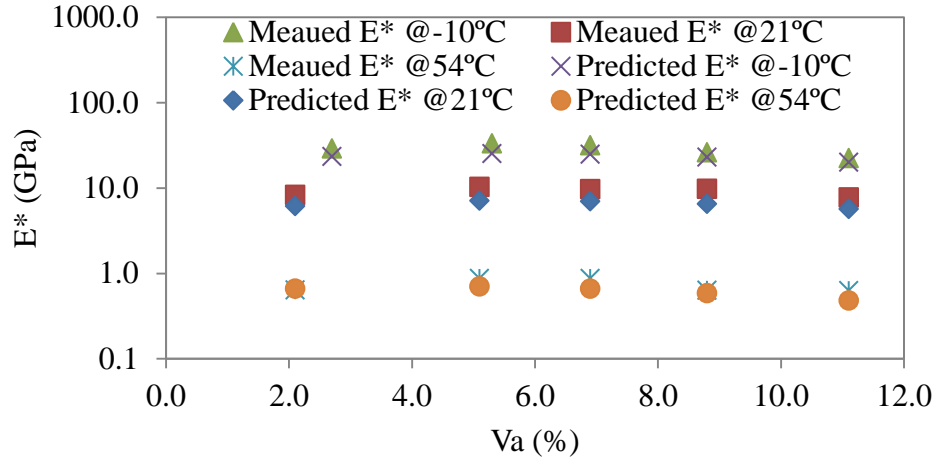
(a) Sensitivity to Mix Air Void
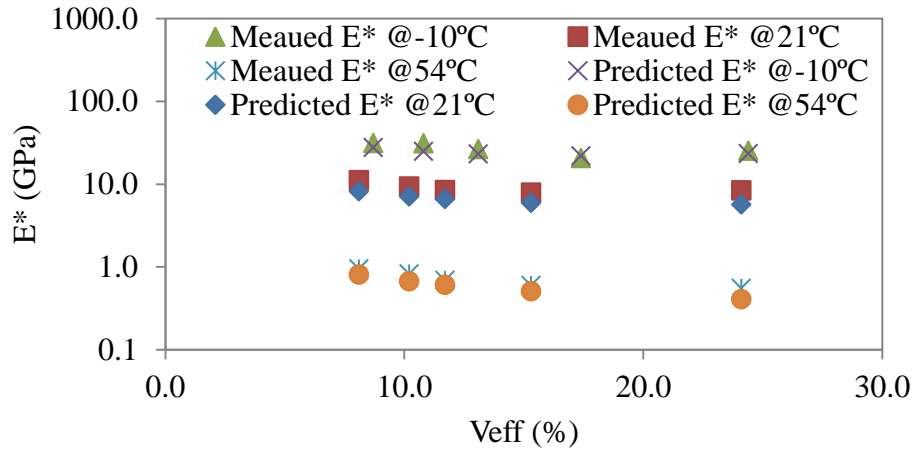
(b) Sensitivity to Mix Effective Binder Content
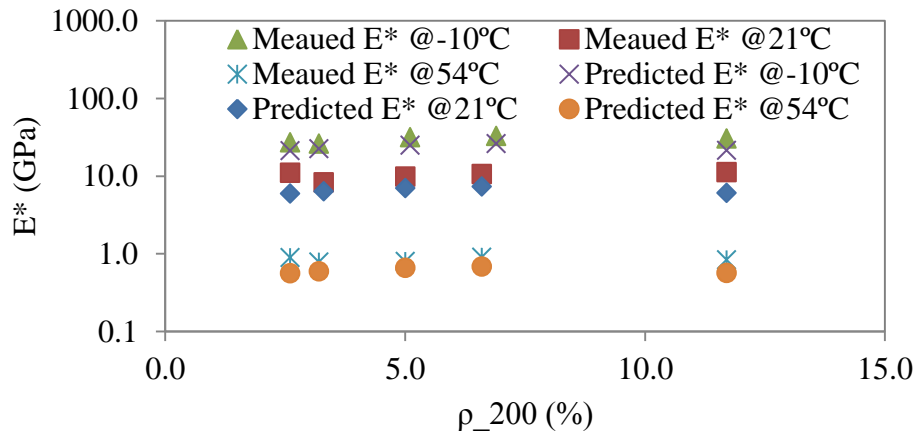
(c) Sensitivity to Percentage of Fines In The Mix
Figure 5.26: Sensitivity Analysis for the New Modified Model

180

Chapter 6
Assessment of Moisture Damage Using MIST Conditioning Coupled with Dynamic Modulus

----

6.1. Introduction

A Moisture Induced Sensitivity Tester (MIST) was recently purchased for the Pavement Laboratory at UNM. According to its developer, InstroTek Inc., MIST can simulate the action of traffic on wet pavement for the purpose of evaluating the resistance of an asphalt mix to stripping and moisture damage (InstroTek 2012). When a vehicle tire rolls over a saturated pavement all water accessible pores get stressed and high pore pressure occurs then the stress gets reduced when the tire rolls away. This creates pore water pressure, pore saturation and draining cycles in the asphalt pavement. MIST replicates this condition by putting on and taking away high pressure from compacted samples of Hot Mix Asphalt (HMA) (InstroTek 2012).

The modified Lottman or AASHTO T283 (AASHTO T283 2007) test method is currently used for evaluation of moisture damage potential of Superpave mixes. The conditioning process for this test is performed by saturating the compacted HMA samples using a vacuum pump and then subjecting it to accelerated freeze-thaw conditioning cycles for approximately 24 hours. Next, the conditioned sample is tested for indirect tensile strength. The tensile strength of the conditioned samples is compared to tensile strengths of a set of unconditioned samples for the same mixture. A minimum tensile strength ratio (TSR) of 75 to 80 percent is generally specified by state agencies as the passing limit for a moisture damage resistant mixture. Therefore, the moisture

181

conditioning process used in the AASHTO T283 does not replicate the dynamics of pore pressure and scouring created in the field by vehicle tires passing over wet pavement.

On the other hand, the National Cooperative Highway Research Program (NCHRP) completed a research project tilted Superpave support and performance models management which is often referred to as NCHRP Project 9-19. This project focused on filling the gap of the Superpave mix design procedure by developing mechanical tests to evaluate mix performance as part of the mix design procedure (Witczak 2005, Witczak et al. 2002, Witczak 2007). Three main tests considered in the research project are Dynamic Modulus, Flow Number and Flow Time. Among these tests, the Dynamic Modulus test is the most widely accepted procedure. In addition, the 2002 NCHRP Project 01-37A has developed the current state of the art Mechanistic-Empirical pavement design guide that takes dynamic modulus (E^*) as a primary material property of asphalt mixes.

In this study, MIST conditioning method is combined with dynamic modulus test for evaluating moisture sensitivity of asphalt concrete. This method affords to investigate moisture damage resulting from pore water pressure, pore saturation and draining cycles. The current and most widely used moisture damage test, AASHTO T283, induces damage through a freeze and thaw process and do not give insight on moisture damage resulting from pore water pressure, pore saturation and draining cycles. Thus, the use of E^* and MIST conditioning to investigate moisture damage is a positive step towards understanding asphalt moisture damage.

6.2. Materials

MIST conditioning and E^* testing was conducted on three typical Superpave (SP) asphalt mixes of New Mexico Department of Transportation (NMDOT). These typical NMDOT asphalt mixes are designated as SP-II, SP-III and SP-IV mixes. The Nominal Maximum Aggregate Size (NMAS) for SP-II, SP-III and SP-IV mixes are 25 mm, 19 mm and 12 mm respectively. The performance grade (PG) of binder used for mixing all of the SP-II, SP-III and SP-IV mixes is PG 70-22. All these three mixes contain about 15% Recycled Asphalt Pavement (RAP) materials.

6.3. Test Matrix

Table 6.1 shows the test matrix designed for this study. The test matrix is divided in to three testing sections with the aim to determine the effect of MIST pressure, temperature and number of cycle variation on E^*. SP-II mix with PG 70-22, SP-III with PG 70-22 and SP-IV with PG 70-22 are used to study the effect of MIST pressure, cycle and temperature respectively. Samples were conditioned in two ways: dry and MIST conditioning. E^* test is conducted on six replicate samples to establish base E^* values for the dry condition. Then, other two replicate samples are MIST conditioned and E^* testing is performed at 4, 37 and 54 ºC.

6.4. Dry Condition E^* Test Results

The dynamic modulus test was conducted at six different frequencies (25, 10, 5, 1, 0.5, 0.1 Hz) and five distinct temperatures (-10, 4, 21, 37, 54 °C) for the dry samples. The recommended numbers of the loading cycles (200, 200, 100, 20, 15, and 15)

183

corresponding to the six test frequencies (25, 10, 5, 1, 0.5, 0.1 Hz) were applied as per the AASHTO TP 62 requirement and an average of the last five cycles was used for the dynamic modulus calculation. The dynamic modulus test on each sample produced thirty data points or modulus values for different combinations of temperature and frequency.

The time-temperature superposition principle was used to plot these thirty data points by a single curve, which is known as a dynamic modulus mastercurve. Laboratory E^* mastercurves for each asphalt mix (SP with II-PG 70-22, SP-III with PG-70-22, and SP-IV with PG 70-22) are developed using the procedure outlined by Witczak and Sotil (2004) and are presented in Figure 6.1. The sigmoidal function is used to fit the individual dynamic modulus data to the mastercurve at a reference temperature of 21 °C.

All calculations to develop the master curve were performed using Microsoft Excel spread sheet. The fitting values for the sigmoid function parameters, $α, β, γ$ and $δ$, are presented in Table 6.2. The maximum $δ$ value is observed for SP-III with PG 70-22 mix indicating this mix is the most suitable for slow moving traffic. SP-III with PG 70-22 mix is also found to have the maximum $δ + α$ value, which makes it the best mix for fast moving traffic. The $γ$ values indicate the rate of change of modulus with frequency. That is the E^* of the mix is more stable with smaller $γ$ values and is expected to perform better with regards to temperature fluctuation. Therefore, SP-II with PG70-22 mix is expected to be most stable for temperature fluctuation.

6.5. MIST Conditioning

In the laboratory, MIST conditioning was performed first by placing the asphalt concrete sample in the MIST chamber and then completely filling the chamber with water. Then, the chamber was tightly secured with a Stainless steel cover that is equipped with a Solenoid valve to release air bubbles. Bolts strong enough to withstand at least 300 kPa were used to secure the Stainless steel cover. Following that, the temperature of the specimen and water in the chamber was raised to specified temperature and required conditioning cycles were applied to each sample with a selected chamber pressure.

Initial MIST conditioning parameter (pressures, temperature, and number of cycles) values are selected based on the recommendations found in the MIST instrument application brief (InstroTek 2012) and ASTM test standard D7878/D7870M-13. The recommend conditioning pressures, temperature, and number of cycles are 275 kPa, 60 ºC and 3500 respectively. These values were selected based on the study conducted by InstroTek, Inc. comparing the MIST conditioning with the AASHTO T283 which determined that conditioning at the above recommended pressure, temperature and number of cycles produces a good indication to moisture damage susceptibility of asphalt mixes (InstroTek 2012). From actual field conditions point of view, a chamber pressure of 275 kPa is to the lower end of pressures exerted on pavement since normal recommended tire pressure for trucks ranges from 240 kPa to 550 kPa (Michelin America 2013). The 3500 MIST cycles are also representing the lower end of actual traffic loading since the Average Annual Daily Traffic (AADT) in most travelled highways of the United States are above 250,000 and the hourly traffic on this road is above 10,000 (FHWA 2013).

185

In this study, additional MIST conditioning parameters are used to study the effect of conditioning pressures, temperature, and number of cycles on E^*. MIST conditioning is performed at three different temperatures (40, 50 and 60 ℃) to investigate the effect temperature. SP-IV mix was used for temperature study. For pressure study, SP-II mix was used and MIST conditioning was performed at 276, 379 and 483 kPa. Finally, MIST conditioning is performed for 3500, 7000 and 10500 cycles on SP-III mix to investigate the effect of number of cycles. The total time for stabilizing the temperature and applying pressure cycles of 3500, 7000 and 10,500 was about 3.5, 7 and 10 hours respectively. MIST conditioned samples were then oven dried for dynamic modulus testing.

6.6. Visual Inspection of MIST Conditioned Samples

Figure 6.2 presents a visual comparison of MIST conditioned sample with dry sample. For the purpose of visual inspection, one dynamic modulus sample is cut into two parts and the first half is kept dry and the other half is conditioned with MIST. The samples are then split diametrically into two using an asphalt flow frame. Comparison of failure surfaces reveals more exposure of aggregate surfaces for MIST conditioned sample than for dry sample. This suggests a weakening of adhesion bond between the binder film and aggregate surface for MIST conditioned sample. Weakening of adhesion force between aggregate and binder film in MIST conditioned sample is caused by the rupturing of binder film on the aggregate surface which results moisture infiltration. In addition, a decreased shininess in the binder of the MIST sample is also observed as compared to the dry sample. This indicates the leaching of oily part of asphalt binder due to MIST conditioning.

186

6.7. Effect of MIST-Pressure

Figure 6.3 presents the effect of MIST conditioning pressure on E^* of asphalt concrete in a bar-chart format. Each bar represents the average E^* of two replicate samples. MIST conditioning is performed at pressures of 276, 379 and 483 kPa. All pressures are applied for 3500 cycles and the temperature of the sample is maintained at 60ºC.

Figure 6.3 (a), 7(b) and 7(c) present average E^* of MIST conditioned and unconditioned samples at the E^* testing temperatures of 4, 21 and 37 °C respectively. The E^* of samples conditioned at 276 kPa are observed to be slightly higher than E^* of unconditioned samples in most cases. However, mostly the difference between the E^*s are less than 5%, which suggests the variation is due to sample variation and is not caused by the MIST conditioning. This implies MIST conditioning at 276 kPa-3500 cycles-60 ºC setting do not cause significant moisture damage. The E^* of all samples conditioning with a pressure of 379 kPa are found to be less than the E^* of unconditioned (dry) samples. This implies an increasing damage with increasing MIST conditioning pressure. A maximum decrease in E^* equal to 18% is recorded at 21 ºC and 1 Hz for MIST conditioning at 376 kPa-3500 cycles-60 ºC setting. The E^* of samples conditioned at a pressure of 483 kPa are found to be significantly less than the E^* of dry samples. The decrease in dynamic modulus ranges from 10% to 40% for 483 kPa-3500 cycles-60 ºC, which confirms the increasing moisture damage with increasing MIST conditioning pressure.

Figure 6.3 (d) presents average E^* ratio (DMR) of MIST conditioned (wet) to unconditioned (dry) samples. Overall average is determined for all six E^* test frequencies

187

(0.1, 0.5, 1.0, 5.0, 10, 25 Hz) and three temperatures (4, 21 and 37 ºC) at each MIST conditioning pressure. The overall average E^* ratio at 276, 376 and 483 kPa MIST conditioning pressures are 1.0, 0.91 and 0.72 respectively. This clearly indicates increasing moisture damage with increasing MIST conditioning pressure.

6.8. Effect of MIST-Temperature

Figure 6.4 presents the effect of MIST conditioning temperature on E^* of asphalt concrete. Two replicate samples are conditioned for each temperature case therefore each bar represents the average E^* of the two replicate samples. MIST conditioning is performed at 40, 50 and 60 °C. MIST conditioning at all temperatures is performed by fixing the number of cycles to 3500 and the pressure at 276 kPa.

Figure 6.4 (a), 8(b) and 8(c) present average E^* of MIST conditioned and unconditioned samples at E^* testing temperatures of 4, 21 and 37 °C respectively. The E^* of MIST conditioned samples are found to be less than the E^* of dry samples in most cases. Samples that are MIST conditioned at 40 ºC show no significant change in E^* at the E^* test temperature of 4 ºC. However, at E^* test temperatures of 21 and 37 ºC the E^* of MIST conditioned samples is found to be 10% and 23% less than the E^* of dry samples. Averaged over all E^* test temperatures, the average decrease in E^* for MIST conditioning at 276 kPa-3500 cycles-40 ºC is found to be 10%. The E^* of all samples conditioned at a temperature of 50 ºC are also found to be less than the E^* of unconditioned (dry) samples. The average decease in E^* at the test temperatures of 4, 21 and 37 ºC are determined to be 24%, 12% and 18%. The overall average decrease in E^* for MIST conditioning at 276 kPa-3500 cycles-50 ºC is found to be 18%. This implies an

188

increasing damage with increasing MIST conditioning temperature. The E^* of samples conditioned at a MIST temperature of 60 ℃ are found to be significantly less than the E^* of dry samples at 21 and 37 ℃ test temperatures. However, at the E^* test temperature of 4 ℃, the E^* of conditioned samples are found to have no significant difference from the E^* of dry samples. The average decease in E^* at the test temperatures of 4, 21 and 37 ℃ are determined to be 0%, 33% and 44% respectively. The overall average decrease in E^* for MIST conditioning at 276 kPa-3500 cycles-60 ℃ is found to be 24% which confirms the increasing moisture damage with increasing MIST conditioning temperature.

Figure 6.4 (d) presents overall average E^* ratio (DMR) of MIST conditioned (wet) to unconditioned (dry) samples. Overall average is determined for all six E^* test frequencies (0.1, 0.5, 1.0, 5.0, 10, 25 Hz) and three temperatures (4, 21 and 37 ℃) at each MIST conditioning pressure. The overall average DMR at MIST conditioning temperatures of 40, 50 and 60 ℃ are determined to be 0.90, 0.82 and 0.76 respectively. This clearly indicates the increasing trend of moisture damage with increasing MIST conditioning temperature.

6.9. Effect of MIST-Cycle

Figure 6.5 presents the effect of MIST conditioning cycles on E^* of asphalt concrete. Two replicate samples are conditioned at 3500, 7000 and 10,500 MIST conditioning cycles therefore each bar represents the average E^* of the two replicate samples. MIST conditioning at all cycles are performed by fixing the temperature and pressure at 60℃ and 276 kPa respectively.

189

The E^* test results for samples conditioned with 3500, 7000 and 10,500 MIST conditioning cycles together with the E^* of unconditioned samples at E^* temperature of 4, 21 and 37 °C are presented in Figure 6.5 (a), 9(b) and 9(c) respectively. The E^* of MIST conditioned samples are found to be less than the E^* of dry samples at all E^* test frequency and temperature cases. Averaged over the six frequencies, for 3500 MIST conditioning cycles the E^* decreased by 19%, 13% and 13% at 4, 21 and 37 °C test temperatures. Averaged over all E^* test temperatures, the E^* samples with MIST conditioning at 276 kPa-3500 cycles-60 ℃ is found to decrease by 15%. The E^* of samples conditioned with 7000 MIST cycles deceased on the average by 45%, 55% and 61% for 4, 21 and 37 °C test temperatures. The overall average decrease in E^* for MIST conditioning at 276 kPa-7000 cycles-60 ℃ is found to be 54%. This implies an increasing damage with increasing number of MIST conditioning cycles. The E^* of samples conditioned for 10,500 MIST cycles are found to be slightly greater than the E^* of samples conditioned with 7000 MIST cycles. However, the difference is not significant and the probable cause is sample to sample variation. 39%, 43% and 49% reduction in E^* is observed for samples conditioned at 10,500 cycles at 4, 21 and 37 ℃ test temperatures respectively. The overall average decrease in the E^* of MIST conditioned samples at 276 kPa-10500 cycles-60 ℃ is found to be 44%.

Figure 6.5 (d) presents average DMR of MIST conditioned samples to dry samples. Overall average DMR is determined for all six E^* test frequencies (0.1, 0.5, 1.0, 5.0, 10, 25 Hz) and three temperatures (4, 21 and 37 ℃). The overall average DMR for 3500, 7000 and 10,500 MIST conditioning cycles are determined to be 0.85, 0.46 and 0.56

190

respectively. This clearly indicates the increasing trend of moisture damage with increasing MIST conditioning cycles.

6.10. Leaching Investigation Using Chemical Tests

MIST equipment simulates the leaching action that results from the pushing and pulling of water in the pores of the asphalt concrete whenever a vehicle tire passes over it. The pulling and pushing action is created in the MIST through the inflation and deflation the rubber membrane. When the rubber membrane is inflated, it increases the pressure of water in the MIST chamber and pushes water into the pores of the asphalt concrete sample, which leads to the partial displacement and compression of air in the pores. When the rubber membrane is deflated, the pressure in the MIST chamber is released and the compressed air in the pores expand partially pushing out the water forced into the pores during pressurization of the MIST chamber. This process induces leaching of asphalt that eventually leads to stripping. Hereafter, Inductively Coupled Plasma Mass Spectrometry (ICP-MS), Inductively Coupled Plasma Optical Emission Spectroscopy (ICP-OES) and Ion Chromatography (IC) tests are conducted to evaluate, if indeed MIST conditioning result in leaching.

6.10.1. Inductively Coupled Plasma Mass Spectrometry (ICP-MS) Test

ICP-MS test is performed by separating the complex sample to its constituent atomic composition and ionizing the atoms so that they can be detected. The ICP-MS is a coupling of Inductively Coupled Plasma (ICP) and mass spectrometer (MS). The ICP is used to energize the atoms into ions and the MS is used to separate and detect ions based on their mass to charge ratio (Tomas 2004).

191

In this study, ICP-MS is used to determine the presence of leached Nickel and Vanadium in the water used for MIST conditioning. Nickel and Vanadium are found in asphalt binder in 0.4-109 ppm and 4-1380 ppm concentrations respectively (Roberts 2009). The extent at which this metals would be present in the water used for MIST conditioning would be extremely low. However, ICP-MS is an excellent method for detecting the metals at extremely low detections limits. The ICP-MS can detect the presence of Nickel and vanadium at a concentration levels as low as 1 to 10 parts per trillion as shown in Figure 6.6(Tomas 2004).

Figure 6.7 shows the ICP-MS testing instrument available in the department of geology at the University of New Mexico. The instrument has three parts, which are the auto sampler, the ICP and the MS. The auto sampler is used to load samples automatically and it can accommodate 300 samples at a time. The ICP is used to atomize, Ionize and increase the energy level of the atoms to a plasma state and the MS is used to separate atoms of interest, detect and quantify the intensity of each atom. The MS of this particular instrument uses quadruple analyzer to separate atoms with specific mass to charge ratio.

A schematic for the ICP-MS operation mechanism is shown in Figure 6.8. First, the sample is injected into a nebulizer that has a piezo electric crystal which makes the sample aerosolize in an Argon gas. Then, the aerosolized sample is directed through induction coil which heats it up to a temperature of 6000-10000K at which point the sample is converted to a plasma state. The plasma is a combination free electron, ionized atoms of the sample and Argon gas. Then the plasma is injected into the MS instrument. In the MS instrument, the plasma is first passed through the sample and skimmer cones

192

which permits only some part of the ionized atoms and directs them to the lenses. The lenses in the MS focus and accelerate the beam of ions to the quadrupoles analyzer. In the quadruple analyzer the ratio of voltages is selected so that only the atoms with selected mass to charge ratio can travel through the entire length of the quadrupoles. At the selected voltage other atoms will have unstable trajectories and they will collide with the rods of the quadrupoles. At the end of the quadrupoles the detector will quantify the intensity of each atom with particular mass to charge ratio (Tomas 2004).

6.10.1.1.   ICP-MS Test Sample Preparation

The ICP-MS test is conducted on water sample extracted from the MIST chamber. Water samples are extracted from the MIST chamber after the 40, 55, and 70 psi MIST conditionings and 3500, 7000 and 10500 cycles of MIST conditionings. The MIST conditioning with different pressures is performed using tap water and MIST conditioning for the different cycles is performed using De-Ionized (DI) water.

The water samples are then filtered using a 0.45 µm filter paper to avoid clogging of the nebulizer and injector. Required sample size for one ICP-MS test is 2 milliliters. Out of the 2 milliliters, one milliliter is used to flash the tubes and the rest one milliliter is used for testing. Three replicate samples are tested for each cases of MIST conditioning pressures and number of cycles. In addition, four standard samples are prepared and tested for each metal type tested in this study. Standard sample with known concentrations of Nickel and Vanadium are prepared to develop the relationship between intensity of atoms reported form the MS with concentrations. These relationships are then used to determine the concentration of the metals in the samples.

193

6.10.1.2.   ICP-MS Test Results and Discussion

As mentioned earlier, ICP-MS tests were conducted to investigate leaching of Nickel and Vanadium from asphalt binder. ICP-MS runs for Nickel indicated no detection for all cases of MIST conditioning pressures and number of cycles. This might have occurred either because Nickel is not present in the binder at hand or Nickel is not being leached out of the binder. However, the results of Vanadium ICP-MS runs indicate leaching of Vanadium.

Figure 6.9 presents ICP-MS test results to detect the presence of vanadium in DI water before and after being used for MIST conditioning. The bar plots indict the concentration of vanadium in the DI water in parts per billion. The concentration of vanadium in DI water before MIST conditioning is very close to zero (0.1 ppb). However, the concentration of vanadium increased to 7.59, 5.40 and 8.39 ppb in the DI water after being used for 3500, 7000 and 10,500 MIST conditioning cycles. This increase in the concentration of vanadium clearly indicates the loss of vanadium from asphalt binder during MIST conditioning. The vanadium concentration indicates an increasing trend with increasing number of MIST conditioning cycles. However, the slope at which the concentration increases is very small since the vanadium concentration shoed a decrease from 7.59 ppb to 5.40 ppb and increased to 8.39 as the MIST conditioning cycles increased from 3500 to 10,500.

Figure 6.9 presents the ICP-MS test results for the three different MIST conditioning pressures. The concentration of vanadium for the base water sample was fond to be 5.12 ppb. However, the concentration of vanadium increased to 10.7, 9.12 and 9.72 ppb after

3500 MIST conditioning cycles of 40, 55 and 70 psi pressures, respectively, at 60 ºC. It can be observed that, the Vanadium concentration in the water sample has doubled after MIST conditioning. This confirms the leaching of asphalt binder in the process of MIST conditioning. A decreasing trend in the vanadium concentration is observed with the increase of MIST conditioning pressure. This suggests that the increase in the MIST conditioning pressure might not have significant effect on the extent of leaching but more testing is required to confirm this result.

In conclusion, ICP-MS test results showed an increased vanadium concentration in the conditioning water due to MIST conditioning. This is a clear indication of the leaching effect of MIST conditioning, which confirms that the mechanism of moisture damage induced by MIST conditioning includes erosion of binders in addition to the pore pressure build up.

6.10.2. Inductively Coupled Plasma Optical Emission Spectroscopy (ICP-OES) Test

The ICP-OES is a coupling of Inductively Couples Plasma (ICP) and Optical Emission spectrometer (OES). The ICP is used to convert the atoms into ions and elevate their energy level, while the OES is used to detect the intensity of the ions based on the weave length of the electromagnetic radiation they emit. The wave length of the electromagnetic radiation emitted by each element is distinct, which makes the basis for this test (Meyers 2000).

In this study, ICP-OES is used to determine the presence of leached sulfur in the water used for MIST conditioning. Sulfur makes 1 to 5 percent of asphalt binder (Roberts 2009). The ICP-OES can detect the presence of sulfur at a concentration levels as low as

1 to 10 parts per billion as shown in Figure 6.11. The very high detection limit of ICP-OES makes it very suitable for detection of sulfur in water used for MIST conditioning, since very low concentration is expected.

Figure 6.12 shows the ICP-OES testing instrument available in the department of geology at the University of New Mexico. The instrument has three parts, which are the auto sampler, the ICP and the OES. The auto sampler is used to load samples automatically and it can accommodate 300 samples at a time. The ICP is used to atomize, Ionize and increase the energy level of the atoms to a plasma state. The OES is used to disperse the electromagnetic waves into different wave lengths and determine the intensity.

A schematic for the ICP-OES operation is shown in Figure 6.13. Similar to the ICP-MS, the sample is injected into the ICP through the nebulizer and plasma is developed which emit electromagnetic radiation. The electromagnetic radiation is directed into the OES. The OES is composed of a series of lenses that focus the radiation to an optical grating. The optical grating disperses the radiation into different beams depending on the wave lengths. The dispersed beams are directed to the optical spectrometer which detects the different wave lengths. Then, intensity of the wave length associated to sulfur (180.669 nano-meters) is measured and the concentration of sulfur is determined based on the intensity- concentration correlation developed using standard samples.

6.10.2.1.   ICP-OES Test Sample Preparation

The ICP-OES test is conducted on water sample extracted from the MIST chamber. Water samples are extracted from the MIST chamber after the 40, 55, and 70 psi MIST conditionings and 3500, 7000 and 10500 cycles of MIST conditionings. The MIST

196

conditioning with different pressures is performed using tap water and MIST conditioning for the different cycles is performed using De-Ionized (DI) water. In addition, four standard samples with known concentrations of sulfur are prepared to develop the relationship between the intensity of electromagnetic wave reported from the OES with concentrations. For each MIST conditioning scenario, three replicate samples are tested. Before loading to the auto sampler, the water samples are filtered using a 0.45 µm filter paper to avoid clogging of the nebulizer and injector of the ICP-OES equipment. The auto sampler takes two milliliter samples and loads it to the nebulizer. Out of the 2 milliliter sample one milliliter is used to flash the tubes of the ICP and the rest one milliliter is ignited into plasma state for testing.

6.10.2.2.   ICP-OES Test Results and Discussion

ICP-OES tests were conducted to investigate the leaching of Sulfur from asphalt binder. Figure 6.14 presents ICP-OES test results on tap water used for MIST conditioning at 40, 55 and 70 psi pressures. The average concentration of total sulfur in the water used for MIST conditioning is found to be 39.32, 38.34 and 38 milligrams per liter for 40, 55 and 70 psi MIST condition pressures respectively. The concentration of sulfur in the base tap water is found to be 34.94 milligrams per liter. This indicates 13%, 10% and 10% increase in the concentration of sulfur due to the MIST conditioning at 40, 55 and 70 psi respectively. Therefore, the ICP-OES test results show that Sulfur is being leached from asphalt binder due to the MIST conditioning at all pressure levels. However, the amount of sulfur leached form the asphalt binder is not found to increase with increasing conditioning pressure which suggests that the conditioning pressure might not be a significant contributor to the leaching of sulfur.

197

Figure 6.15 presents the ICP-OES test results on DI water used for MIST conditioning at 3500, 7000 and 10,500 cycles. The bar chart shows the smallest concentration of sulfur for the base DI water with a value of 0.079 milligrams per liter. The concentration of sulfur after 3500, 7000 and 10,500 MIST cycles are found to be 0.997, 0.848 and 2.226 milligrams per liter. The increase in the concentration of sulfur in DI water is found to be 1162%, 973% and 2718% due to 3500, 7000 and 10,500 cycles respectively. This indicates the significant leaching of sulfur due to MIST conditioning. Moreover, the concentration sulfur in the water used for 10,500 MIST conditioning cycles is found to be more than double the concentrations of sulfur found in the water used for 3500 and 7000 MIST conditioning cycles. This suggests that the number of MIST conditioning cycles has a significant effect on the amount of leaching of sulfur.

In conclusion, the ICP-OES test results showed an increased concentration of sulfur in the water used for MIST conditioning. In addition, the amount of leaching is found to increase very significantly with an increase in MIST conditioning cycles. This is a clear indication of the leaching effect of MIST conditioning, which indicates that the mechanism of moisture damage induced by MIST conditioning includes leaching of binders.

6.10.3. Ion Chromatography (IC) Test

Ion Chromatography (IC) tests are performed to determine the presence of Sulfate molecules in the MIST conditioning water. IC is capable of determining the presence of ions in parts per billion concentration levels. This makes IC very convenient to determine

198

the change in the Sulfate concentration of MIST conditioning water with increasing number of cycles and varying conditioning pressures.

The ICS-1100 ion chromatography system shown in Figure 6.16 is used in this study. The chromatographic separation of the sample into its chemical constituents takes place in the IC column. In the IC column, ions with stronger charge are attracted strongly to the stationary part of the column; therefore they are retained longer in the column. Ions with lesser charge however, are attracted less therefore; they are pushed through the column faster. In this manner, the different chemical constituents of the mix are separated depending on their relative affinity to the stationary part of the column. After departing the IC column the ions are passed through the suppresser to the conductivity detector. The main role of the suppresser is to suppress the conductivity of the sodium carbonate so that the conductivity of the ions can be measured clearly. Time of arrival and conductivity of each ion are recorded and analyzed using custom software. Analysis output of the ICS 1100 for a standard sample containing Fluoride, Chloride, Nitrite, Bromide, Nitrate and Sulfate is shown in Figure 6.17. The time at which peaks of conductivity occur provide qualitative data about the different ions present in the sample. The area under each peak is used for quantitative determination of concentration of each ion. Several standard samples with varying concentrations are tested to establish the correlation between the areas under the conductivity curves and ion concentration. This correlation curve is used to determine the concentration of sulfate in the test samples.

199

6.10.3.1.   IC Sample Preparation

DI Water samples for the IC test are extracted from the MIST chamber after 3500, 7000 and 10500 cycles of MIST conditionings. The samples are then filtered using a 0.45 µm filter paper to avoid clogging of the injector. Then samples are diluted in a sodium carbonate solution eluent and placed into the auto sampler. The sample size required to conduct one run of IC test is 2 milliliters. Out of the 2 milliliter samples loaded by the auto sampler one milliliter is used to flash the tubes and the rest one milliliter is used for testing. In this study, three replicate runs are performed for each conditioning cycle cases and the average is reported.

6.10.3.2.   IC-Test Results and Discussion

Figure 6.18 presents IC separation test results on DI water used for MIST conditioning at 3500, 7000 and 10,500 cycles. A clear increase in the sulfate concentration is observed for the DI water after MIST conditioning. The concentration of sulfate in the base sample is determined to be 0.77 milligrams per liter. The average concentration of sulfate is found to be 2.64, 2.28 and 6.13 milligrams per liter in the DI water used for MIST conditioning at 3500, 7000 and 10,500 cycles respectively. These results indicate a 245%, 198% and 698% increase in the concentration of sulfate due to the MIST conditioning at 3500, 7000 and 10,500 cycles respectively. This confirms that Sulfur is being leached from asphalt binder due to the MIST conditioning. The concentration of sulfate in the water used for 10,500 MIST conditioning cycles is found to be 2.3 and 2.6 times the concentrations of sulfate found in the water used for 3500 and 7000 MIST conditioning

200

cycles respectively. This clearly indicates the increase in the leaching of asphalt with increasing MIST conditioning cycles.

In conclusion, the IC separation test results also showed an increase in the concentration of sulfur in the water used for MIST conditioning. In addition, the amount of leaching is found to increase with an increase in MIST condition cycles. This confirms that leaching is one of the mechanisms through which moisture damage is induced by MIST.

6.11. Model Development

Here after, models are developed to capture the effect of MIST conditioning cycles and pressures on dynamic modulus. These models can be used to represent degradation asphalt concrete due to moisture pore pressure build-up and leaching as traffic loading cycles with various tire pressures are applied on saturated pavements.

Two models are developed using a four dimensional polynomial function to capture effect of MIST-cycles and MIST-pressures. Four dimensional polynomial functions are selected to capture the variability of observed DMR values with E^* test temperature and frequency for each MIST-conditioning cycles and pressures.

The polynomial function that is calibrated to model DMR surfaces is shown in Equation (6.1).

$$DMR(x, y, z) = C + \alpha_1 z + \alpha_2 z^2 + \alpha_3 y + \alpha_4 yz + \alpha_5 yz^2 + \alpha_6 y^2 + \qquad (6.1)$$

$$\alpha_7 y^2 z + \alpha_8 y^2 z^2 + \alpha_9 x + x * (\alpha_{10} z + \alpha_{11} z^2 + \alpha_{12} y + \alpha_{13} yz + \alpha_{14} yz^2 +$$

$$\alpha_{15} y^2 + \alpha_{16} y^2 z + \alpha_{17} y^2 z^2) + \alpha_{18} x^2 + x^2 * (\alpha_{19} z + \alpha_{20} z^2 + \alpha_{21} y +$$

$$\alpha_{22} yz + \alpha_{23} yz^2 + \alpha_{24} y^2 + \alpha_{25} y^2 z + \alpha_{26} y^2 z^2)$$

where *DMR* is dynamic modulus ratio of wet conditioned and dry conditioned samples, *x* represents E^* test temperature, *y* represents E^* test frequency and z represents either MIST-cycles or MIST pressure and α_m are regression coefficients, where m ranges from 1 to 26, C is also a constant

The model developed for MIST- cycle and DMR is given in Equation (6.2).

$$DMR(x, y, z) = 1.478 - 0.246z + 0.016z^2 - 0.0103y + 0.004yz + \qquad (6.2)$$

$$-0.00029yz^2 + 0.0187x + x * (-0.00615z + 0.000396z^2 -$$

$$0.000081y + 6.389E - 06yz + 4.382E - 07yz^2)$$

where *DMR* is dynamic modulus ratio of wet conditioned and dry conditioned samples, *x* represents E^* test temperature, *y* represents E^* test frequency and z represents either MIST-cycles

The coefficient of determination (R^2) for the MIST- cycle and DMR model is determined to be 0.969 which indicates a very good goodness of fit to the laboratory data. Figure 6.19 (a) presents the trend of laboratory determined DMR with changing MIST-cycles, E^*-frequency and E^*-temperature and Figure 6.19 (b) presents the MIST- cycle and DMR model outputs. Comparison of the two plots indicates a very good match between the laboratory and model predicted DMR trends.

202

The model developed for MIST- pressure and DMR is given in Equation (6.3).

$$DMR(x, y, z) = \qquad (6.3)$$

$$0.894 + 0.152z + -0.0274z^2 + 0.0262y + -0.00859yz +$$

$$0.000736yz^2 + -0.0000457y^2 + -0.0319x + 0.00674xz + x^2 *$$

$$(0.000555z^2 + -0.000132y)$$

where *DMR* is dynamic modulus ratio of wet conditioned and dry conditioned samples, *x* represents *E** test temperature, *y* represents *E** test frequency and z represents either MIST-pressure

The coefficient of determination (R^2) for the MIST- pressure and DMR model is determined to be 0.839 which indicates a good goodness of fit to the laboratory data. Figure 6.20 (a) presents the trend of laboratory determined DMR with changing MIST-pressure, *E**-frequency and *E**-temperature and Figure 6.20 (b) presents the MIST-pressure and DMR model outputs. Comparison of the two plots indicates a good match between the laboratory and model predicted DMR trends.

These preliminary models indicate the great potential of MIST moisture conditioning for application in the design of pavements. However, MIST is only able to simulate the moisture damage arising from pore water pressure build-up and associated leaching due to passage of vehicle tires, which means other environmental factors like freeze-thaw cycles should not be forgotten in moisture damage evaluations. This means, moisture damage evaluation is a multi-phase problem that requires multiple types of tests and MIST is just one, which is very good for simulating pore water pressure and leaching effects in asphalt concrete.

203

6.12. Conclusions

In this study Moisture Induced Sensitivity Tester (MIST) is used for Moisture conditioning of asphalt samples and the induced damage is evaluated through visual inspection and dynamic modulus (E^*) testing. Inductively Coupled Plasma Mass Spectrometry (ICP-MS), Inductively Coupled Plasma Optical Emission Spectroscopy (ICP-OES) and Ion Chromatography (IC) tests are used to determine the extent of asphalt binder leaching. Form the results of this study it is possible to conclude that:

- MIST conditioning decreases the E^* of asphalt concrete indicating the presence of moisture damage.

- The amount of moisture damage (loss in E^*) increased significantly when the MIST conditioning number of cycles, pressures and temperatures are increased.

- ICP-MS test indicated an increased concentration of vanadium in the water used for MIST conditioning. ICP-OES test indicated an increased concentration of total sulfur in the water used for MIST conditioning. IC test indicated an increased concentration of total sulfate in the water used for MIST conditioning. These results indicate that an increase in the number of MIST conditioning cycles produces significant increase in leaching of binder.

- The effect of increasing MIST conditioning pressure on leaching of binders is investigated with ICP- MS and ICP-OES tests and the results indicated that the changes in pressure are not significantly affecting the leaching of asphalt binder.

204

Table 6.1 Test Matrix

Test Matrix Variables	Pressure Study Matrix	Cycles Study Matrix	Temperature Study Matrix
HMA Mixture Type	SP-II with PG 70-22	SP-III with PG 70-22	SP-IV with PG 70-22
Moisture conditions	Dry, MIST	Dry, MIST	Dry, MIST
MIST Pressure (kPa)	276, 379, 483	276	276
Number of MIST Cycles	3500	3500	3500, 7000, 10500
MIST Conditioning Temperature (°C)	60	40, 50, 60	60
Mechanical Test methods	Dynamic modulus	Dynamic modulus	Dynamic modulus
E^* Test Temperature (ºC)	4, 37, 54	4, 37, 54	4, 37, 54

Table 6.2 Mastercurve Parameters for Dynamic Modulus Test (ref. Temp = 21 ℃)

Asphalt mix	Master curve parameters			
	α	β	δ	γ
SP-II PG70-22	2.69	-0.99	1.81	-0.41
SP-III PG70-22	2.43	-0.85	2.07	-0.49
SP-IV PG70-22	2.67	-0.70	1.84	-0.50
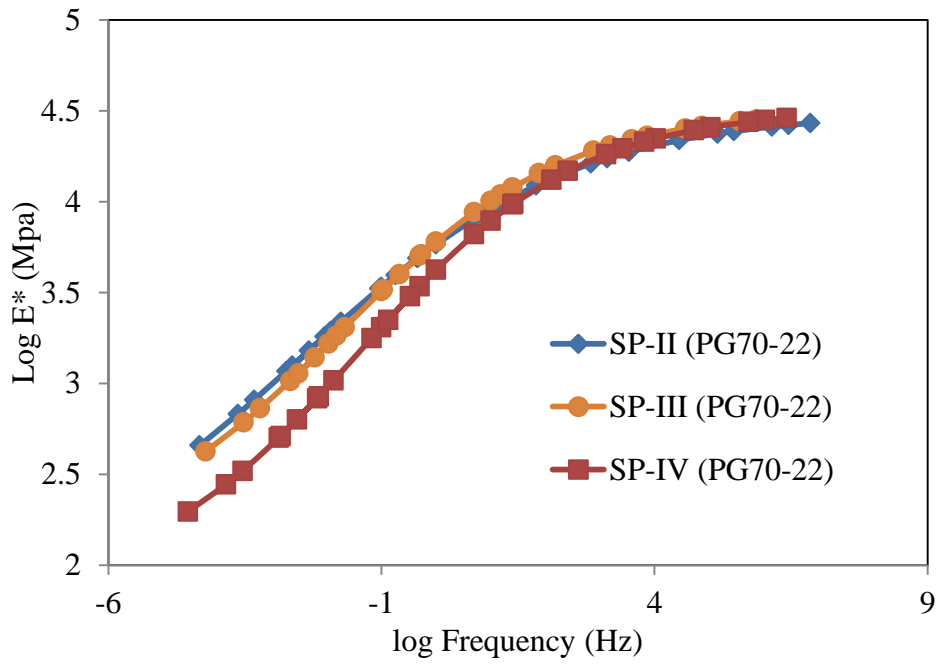
Figure 6.1 Mastercurves for laboratory $\mathbf{E}^*$ test results.

Dry sample → ⟵ MIST Conditioned sample

Figure 6.2 Photographic view of dry and MIST conditioned samples
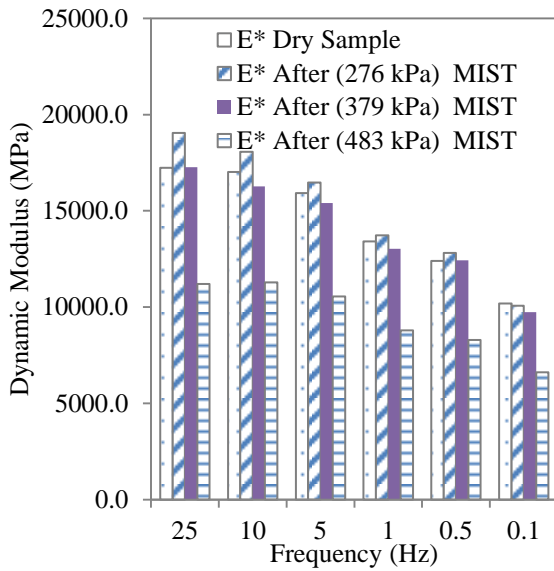
(a) Moisture Sensitivity at 4°C
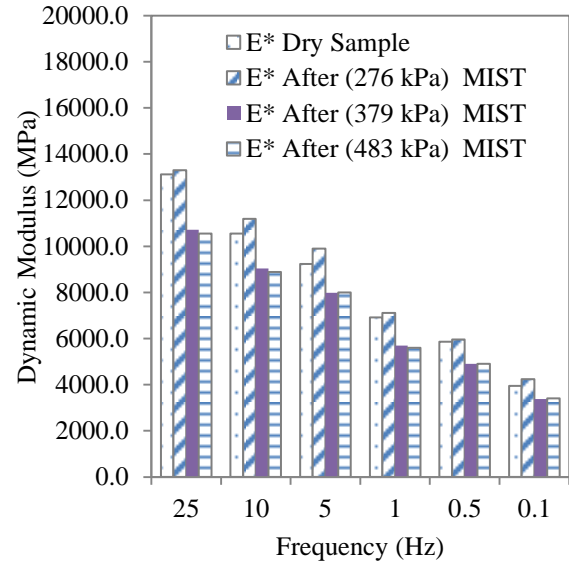
(b) Moisture Sensitivity at 21°C
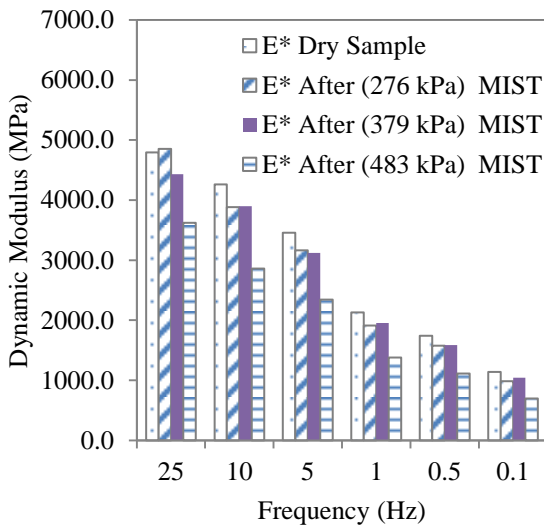
(c) Moisture Sensitivity at 37°C
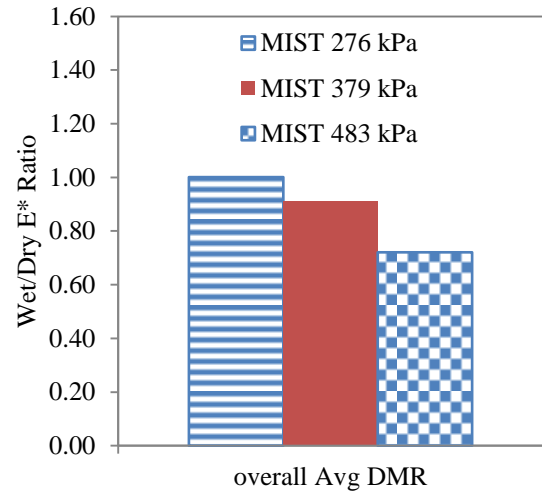
(d) DMR trend with MIST pressure

Figure 6.3 Effect of MIST conditioning pressure on E^*
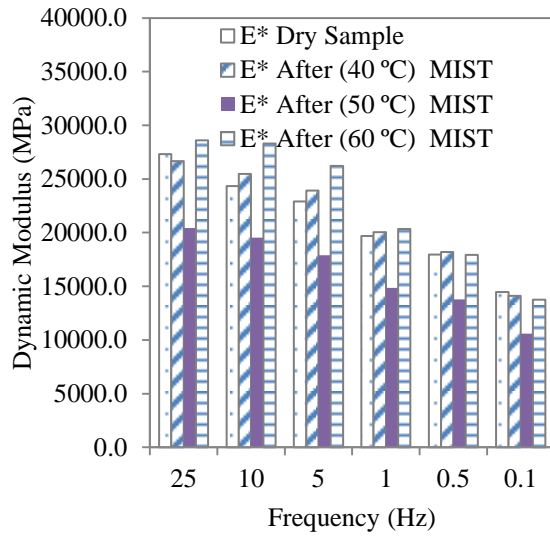
209

(a) Moisture Sensitivity at 4°C
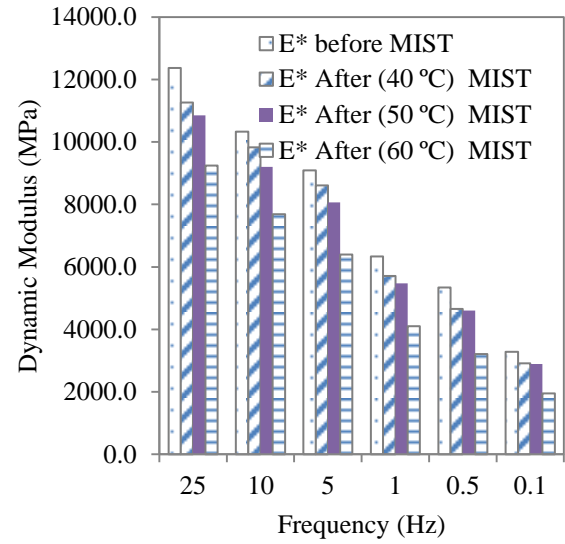
(b) Moisture Sensitivity at 21°C
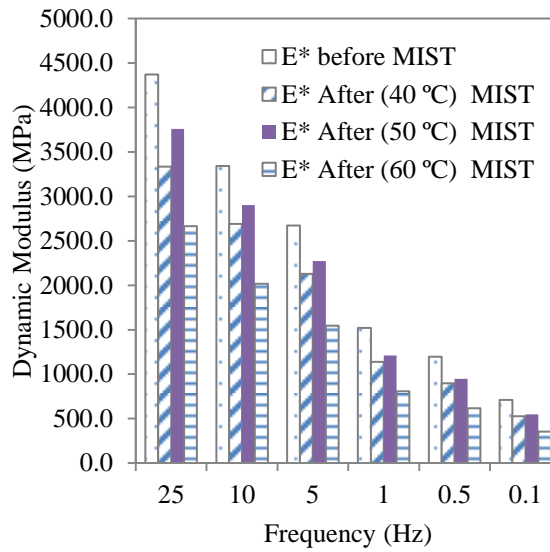
(c) Moisture Sensitivity at 37°C
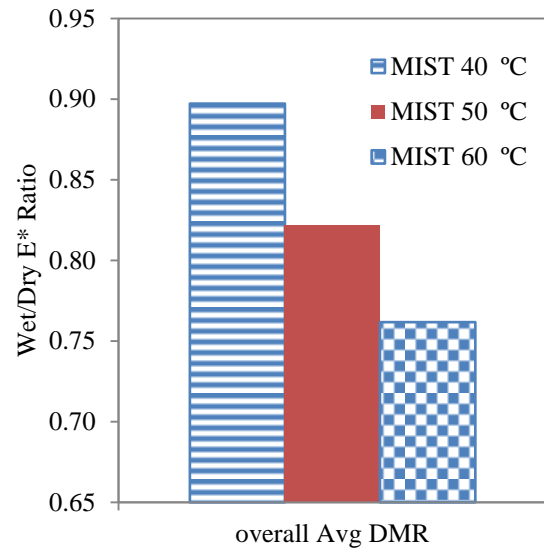
(d) DMR trend with MIST temperature

Figure 6.4 Effect of MIST conditioning temperature on E^*
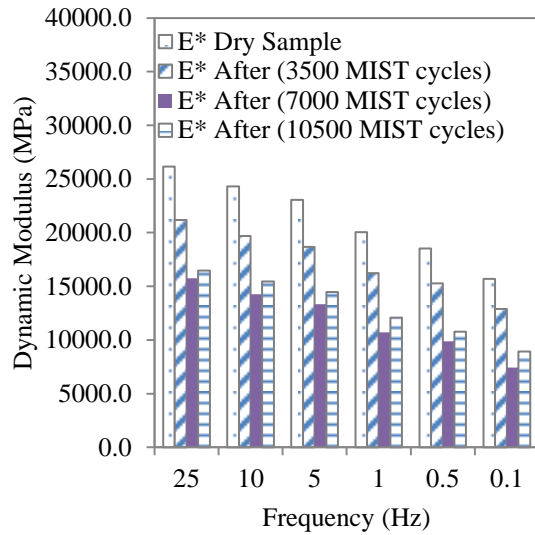
210

(a) Moisture Sensitivity at 4°C
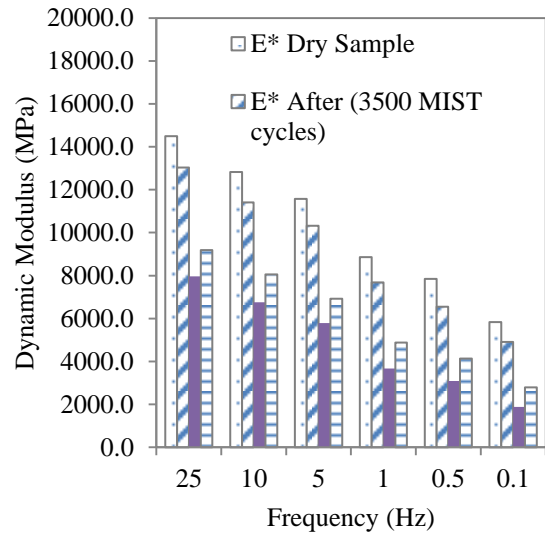
(b) Moisture Sensitivity at 21°C
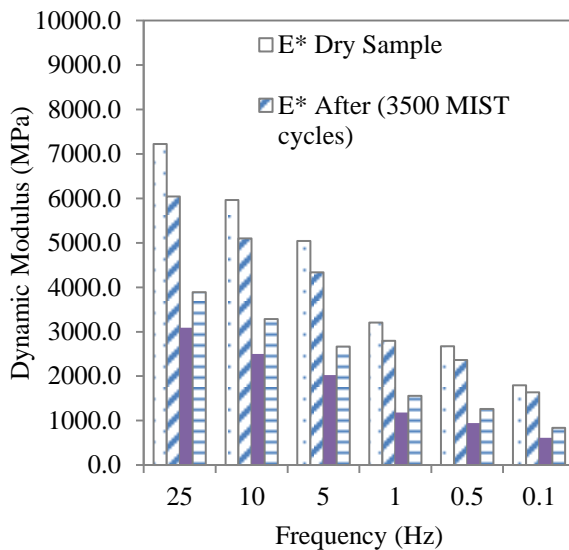
(c) Moisture Sensitivity at 37°C
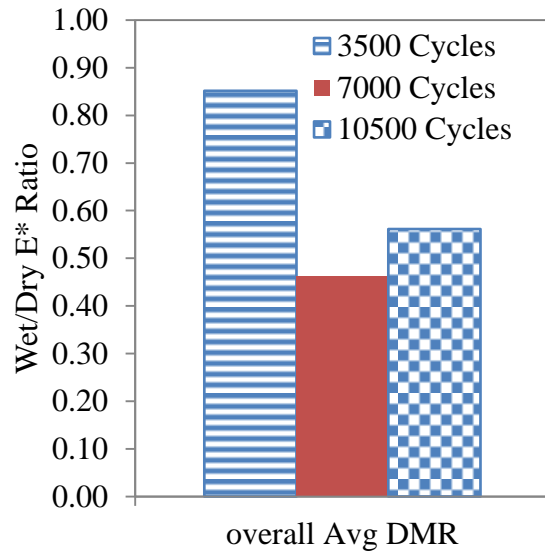
(d) DMR trend with MIST cycles

Figure 6.5 Effect of MIST conditioning cycle on *E**

211
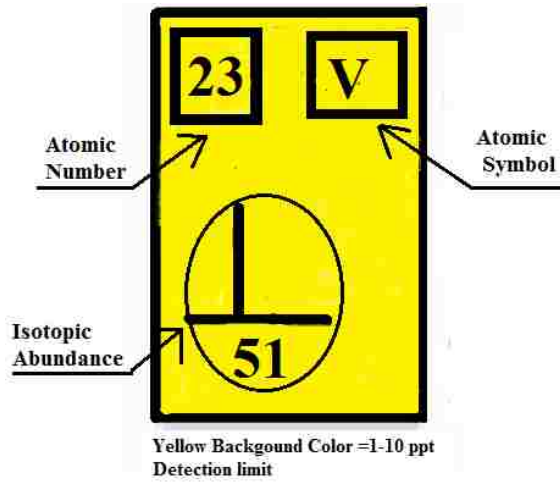
Figure 6.6 Approximate detection capabilities of quadruple ICP-MS.
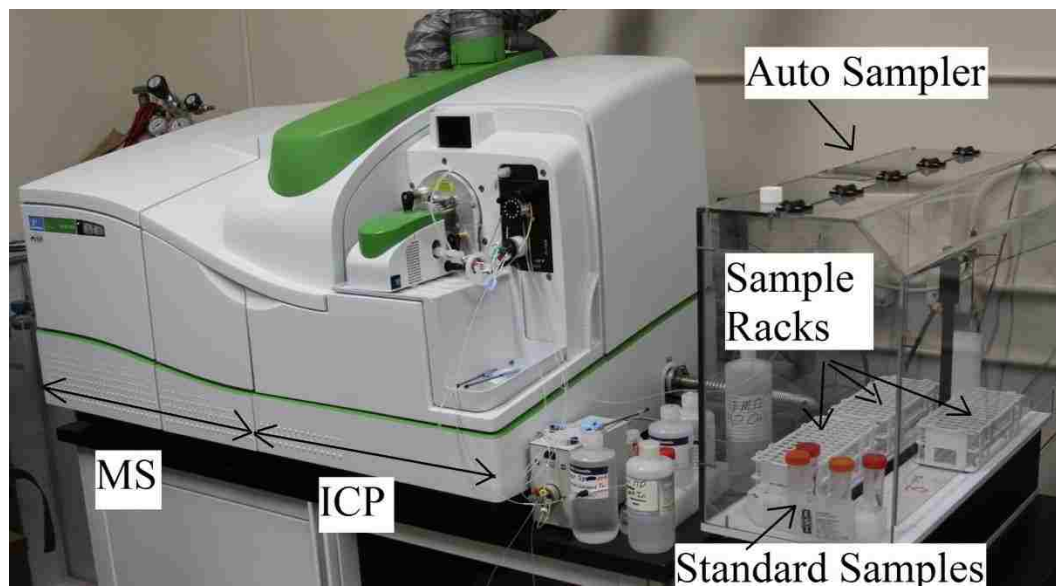
Figure 6.7 Photographic image of ICP-MS instrument
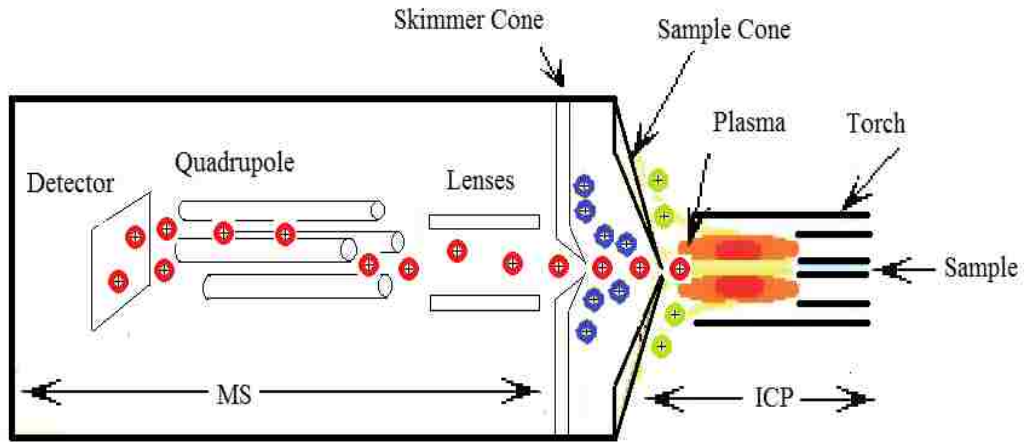
Figure 6.8 Schematics of ICP-MS
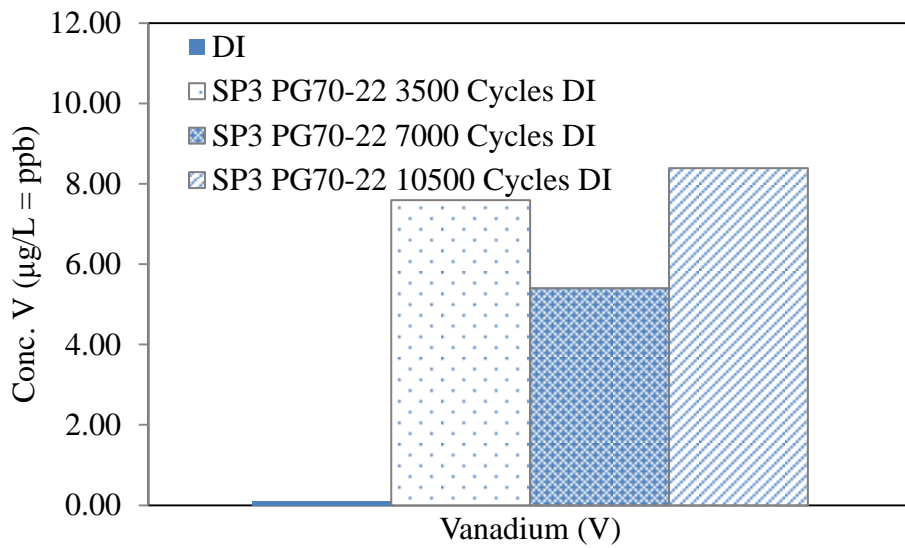
Figure 6.9 ICP-MS test results with varying MIST conditioning pressures

213
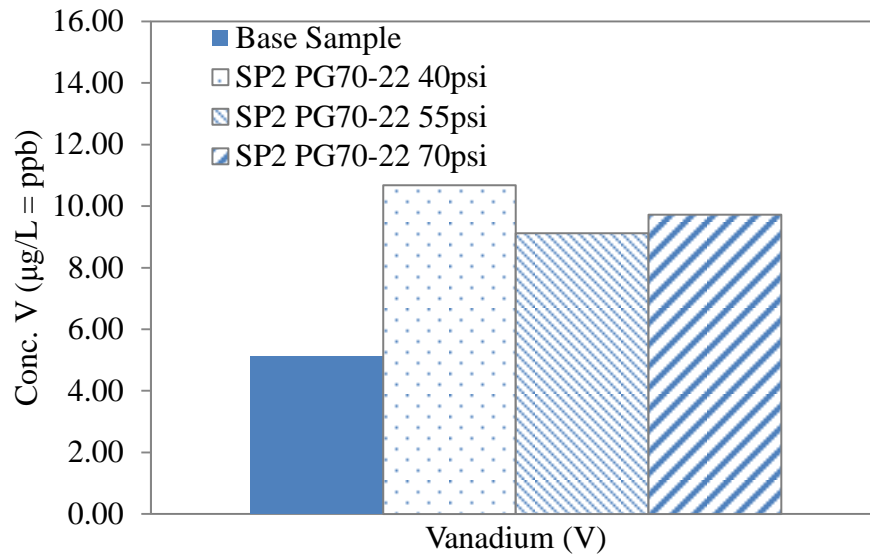
Figure 6.10 ICP-MS test results with varying MIST conditioning cycles
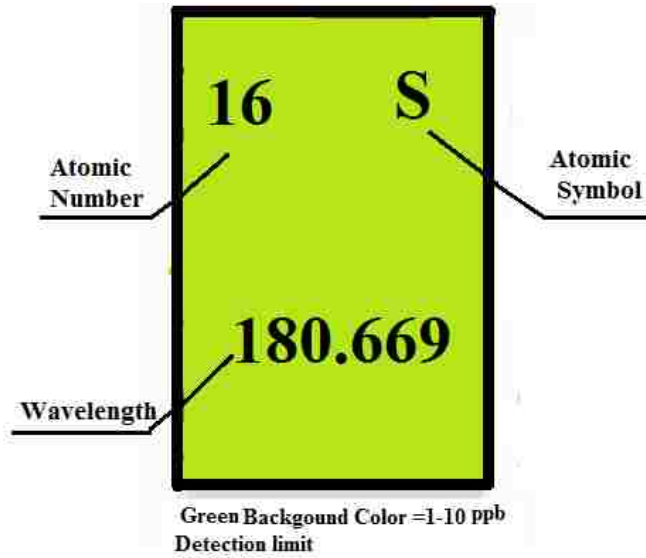
Figure 6.11 Approximate detection capabilities of ICP-OES. (Courtesy of TAL facility)
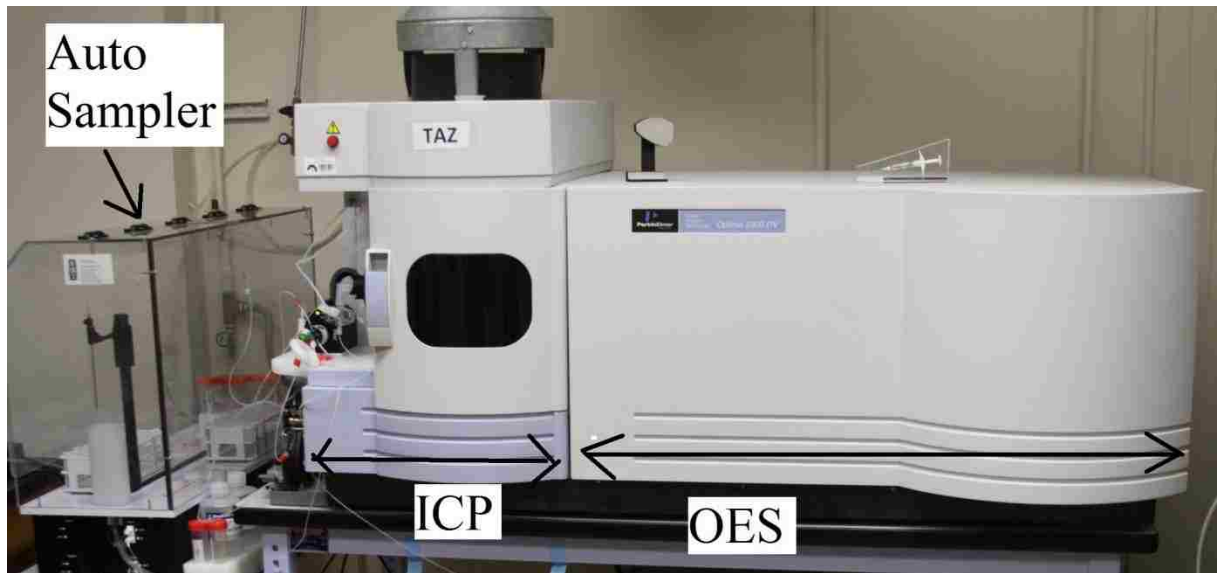
Figure 6.12 Photographic image of ICP-OES instrument
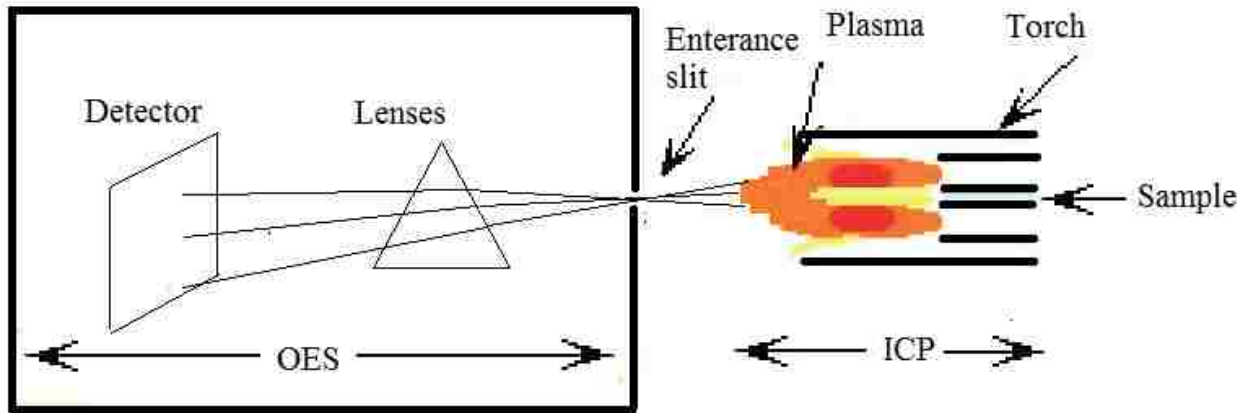
Figure 6.13 Schematics of ICP-OES
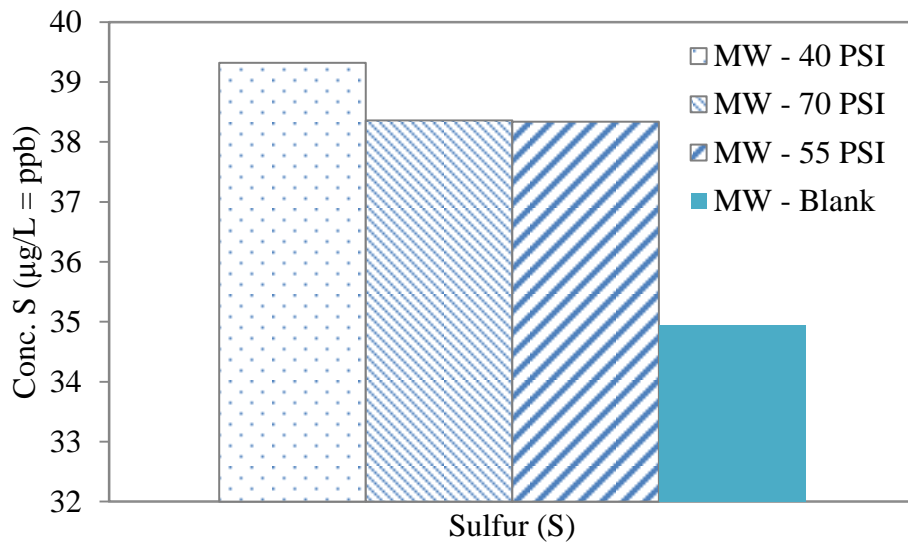
Figure 6.14 ICP-OES test results with varying MIST conditioning pressures
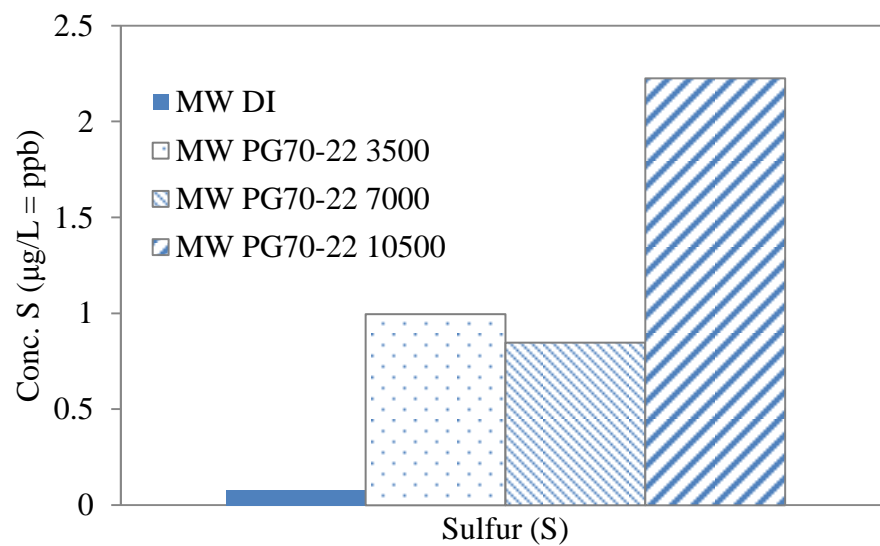
Figure 6.15 ICP-OES test results with varying MIST conditioning cycles
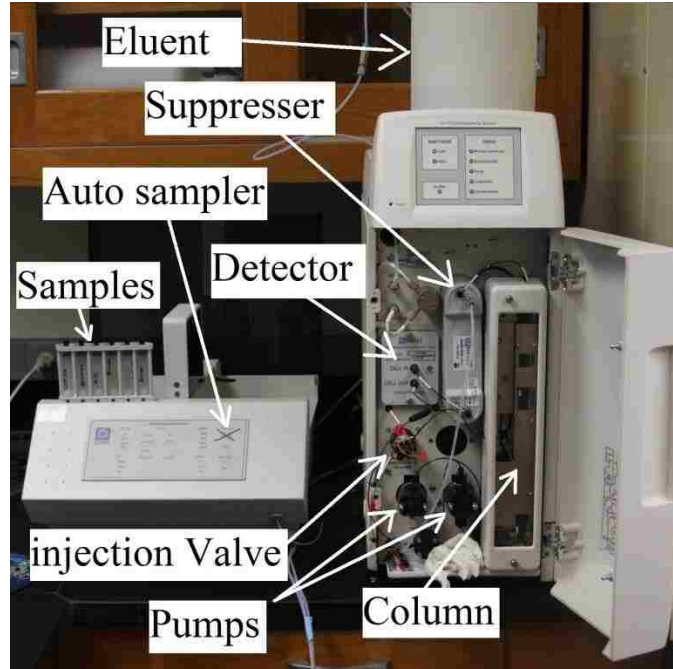
Figure 6.16 ICS-1100 ion chromatography system
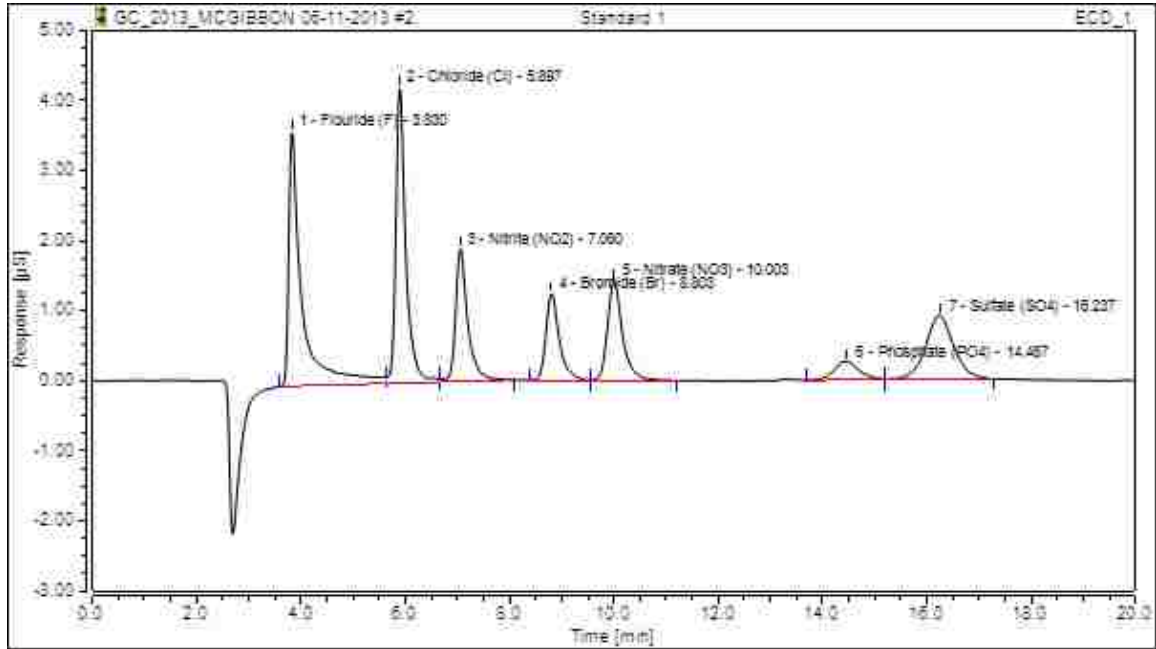
Figure 6.17 ICS-1100 ion chromatography systems
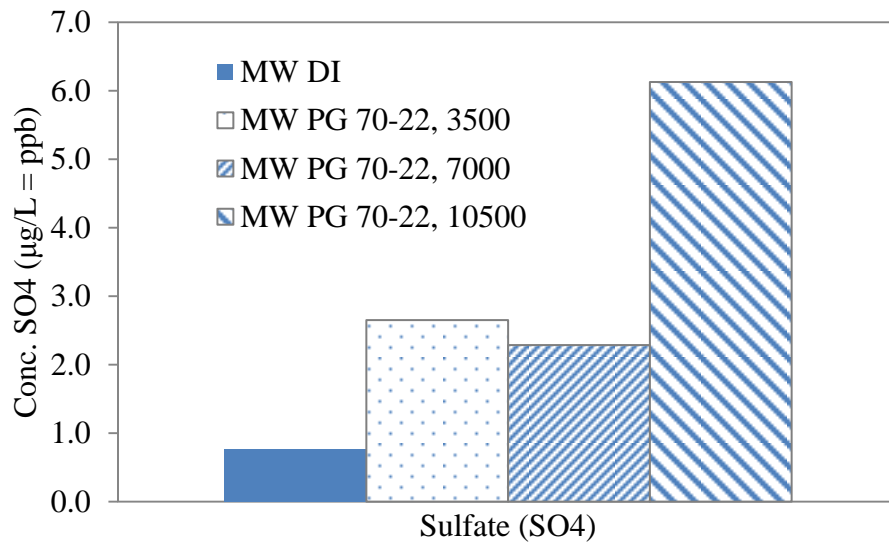
Figure 6.18 Sulfate concentrations variation for MIST conditioning water with cycles

219
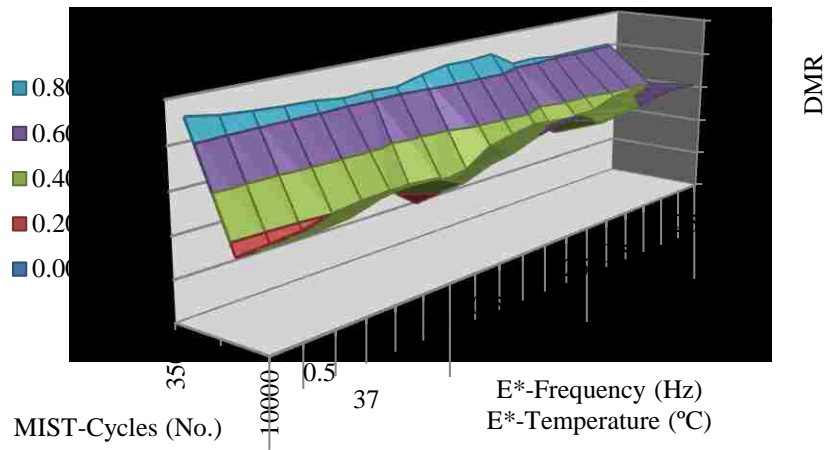
(a) Laboratory results
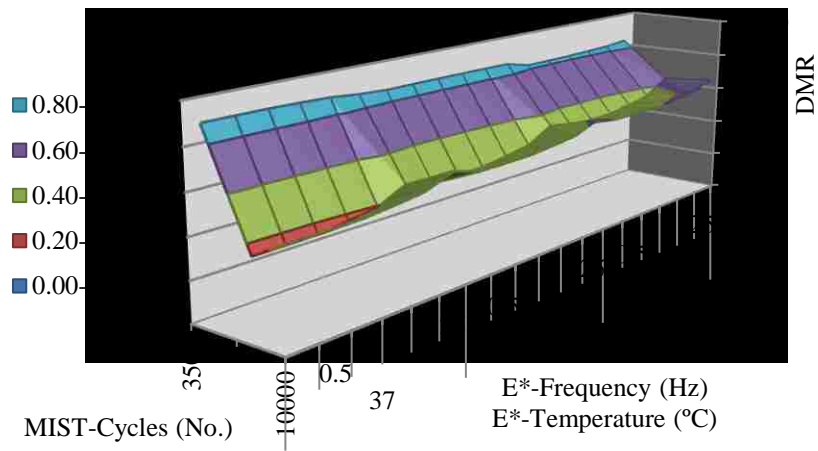
(b) Model output
Figure 6.19 Trend of DMR with changing MIST-cycles, E^*-Frequency and E^*-Temperature

220
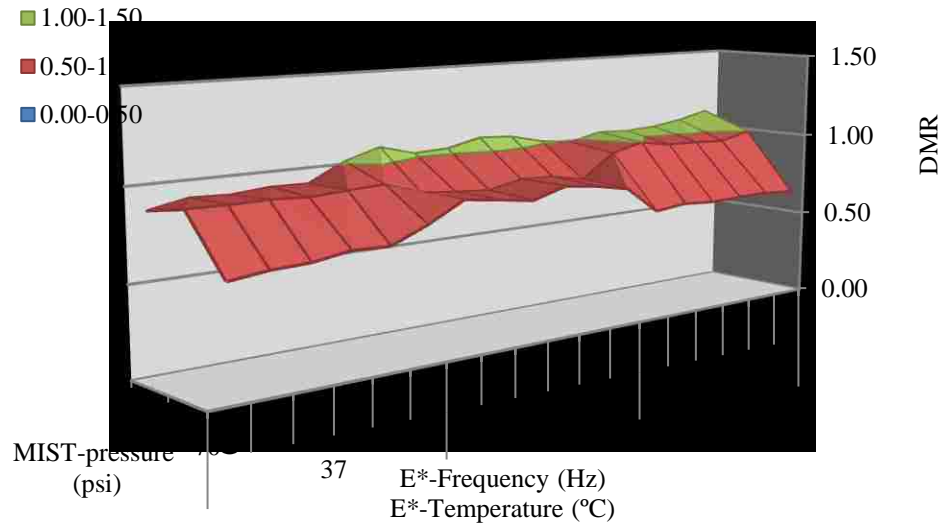
(a) Laboratory results
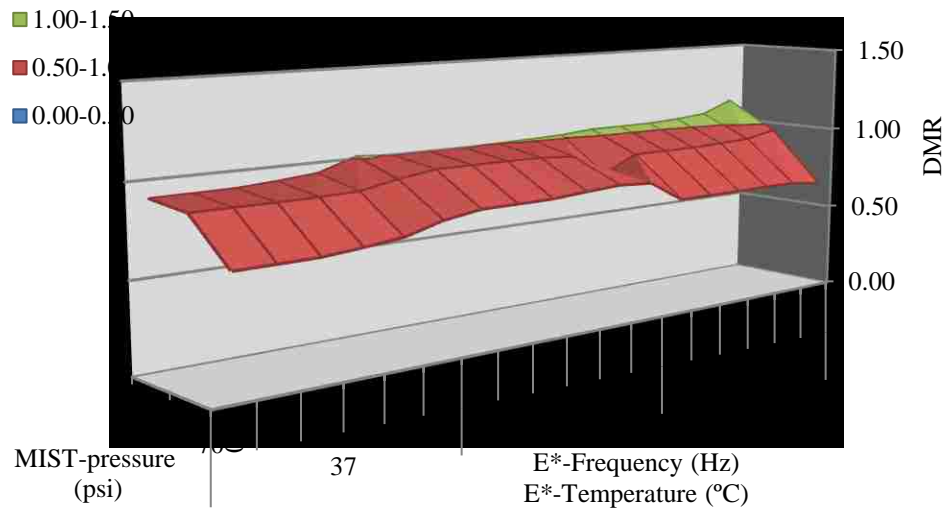
(b) Model output

Figure 6.20 Trend of DMR with changing MIST-pressure, *E**-Frequency and *E**-Temperature

Chapter 7

Conclusions and Recommendations

....

7.1. General

In this study laboratory dynamic modulus testing for five typical New Mexico asphalt mixes is performed and mastercurves are developed. Independence assurance testing is performed to assess the precision and accuracy of the test results. Then the viscosity based Witczak model, the dynamic modulus Witcak model and the Hirsh model are implemented and the accuracy of prediction is evaluated. Following which, the modified Witczak model is developed by giving more emphasis to mix volumetrics and mastic properties.

MIST moisture conditioning is coupled with dynamic modulus testing to investigate moisture damage due to pressure build-up and scouring. The pore water pressure build-up and scouring in asphalt concrete are further evaluated through visual investigation and chemical testing. Finally, the effects of MIST conditioning parameters on dynamic modulus are examined and models relating MIST conditioning cycles and pressures with dynamic modulus ratio are developed.

7.2. Conclusions

In this study, dynamic modulus testing was conducted on five mixes of NMDOT. The E^* data collected is found to have tends that are consistent with literature. To further check the accuracy and precision of the E^* data Independent assurance (IA) testing is

222

performed in collaboration with AMEC laboratories and the statistical analysis showed that the results are repeatable and reproducible. Furthermore, the viscosity based Witczak model, the G^*-based Witczak model, the Hirsch model for predicting laboratory test E^* test data are implemented and the E^* prediction accuracy of each model is evaluated. Based on this study the following conclusions are drawn:

- The viscosity based Witczak model, the G^*-based Witczak model, the Hirsch model are applied for predicting measured dynamic modulus values using default A and VTS values and actual A and VTS values determined using DSR test results and it is found that all models underpredict the dynamic modulus results of all typical NMDOT mixes. Moreover, the Hirsch model is found be biased at high temperatures.

- Optimizing the mix variable values showed that the course aggregate variables in the viscosity based model can be eliminated without significant change in the mastic and binder input variable values. This indicated the low significance of course aggregate variables (ρ_{34}, ρ_{38} and ρ_4) on the model prediction accuracy.

- Based on the above finding, a new dynamic modulus predictive model has been developed by eliminating the course aggregate variables in the viscosity based Witczak model and keeping the sigmoidal mathematical structure and introducing a modified aggregate contact factor from Hirsh model. The new dynamic modulus model showed significant improvement in predicting the dynamic modulus of typical NMDOT mixes. Sensitivity analysis of the new model also showed the E^* predictions of the model is rational to variations of air void, effective binder and percentage of fine aggregates.

223

To study moisture damage of AC resulting from repeated cycles of pore pressure and scouring actions, MIST is used for wet conditioning of samples. Then, moisture damage is evaluated through visual inspection and E^* testing. Further, the leaching of chemical elements of asphalt binder are quantified using ICP-MS, ICP-OES and IC tests. Based on the results, it is possible to conclude that:

- MIST conditioning decreases the E^* of asphalt concrete which shows significant structural degradation of AC moisture damage.

- ICP-MS, ICP-OES, and IC tests indicated an increased concentration of vanadium sulfur and sulfate in the water used for MIST conditioning respectively. This indicates that MIST conditioning induces leaching of binder in addition to the pore water pressure cycles. The effect of increasing MIST conditioning pressure on leaching of binders is investigated with ICP- MS and ICP-OES tests and the results indicated that the changes in pressure are not significantly affecting the leaching of asphalt binder. However, increase in the number of MIST conditioning cycles showed significant increase in leaching of binder, which indicates prolonged exposure of saturated pavements to traffic loading increases the scouring of binders from pavements.

7.3. Recommendations

The following future research recommendations are made:

- Both Viscosity and G^* based Witczak models are found to under predict the measured dynamic modulus valued of typical NMDOT mixes. Since these models are used in MEPDG for design purposes, it is recommended to investigate the effect of dynamic modulus prediction error on the pavement performance prediction in MEPDG rutting and fatigue models.

- The New revised model developed in this research has shown promising results in predicting measured dynamic modulus of NMDOT mixes. It is recommended to validate the accuracy of this model with further dynamic modulus test results in the future.

- MIST moisture damage models are developed based on limited data, extensive testing over wide verities of asphalt mixes is required to develop a generalized moisture damage model.

Reference

AASHTO T2 (2011). "Standard Practice for Sampling aggregates." AASHTO Standards.

AASHTO T165 (2006). "Standard Method of Test for Effect of Water on Compressive Strength of Compacted Bituminous Mixtures." American Association of State Highway and Transportation Officials (AASHTO) Standard Specifications. Washington, D.C.

AASHTO T166 (2009). "Standard Method of Test for Bulk Specific Gravity (Gmb) of Compacted Hot Mix Asphalt (HMA) Using Saturated Surface-Dry Specimens." AASHTO Guide, AASHTO, Washington, D.C.

AASHTO T168 (2011). "Standard Practice for Sampling Bituminous Paving Mixtures." AASHTO Guide, AASHTO, Washington, D.C.

AASHTO T209 (2007). "Theoretical Maximum Specific Gravity and Density of Bituminous Paving Mixtures." AASHTO Guide, AASHTO, Washington, D.C.

AASHTO T283 (2007). "Standard Method of Test for Resistance of Compacted Hot Mix Asphalt (HMA) to Moisture-Induced Damage." AASHTO Standard Specifications. AASHTO Guide, AASHTO, Washington, D.C.

AASHTO T308 (2011). "Determining The Asphalt Binder Content of Hot Mix Asphalt (HMA) By The Ignition Method." AASHTO Guide, AASHTO, Washington, D.C.

AASHTO T312 (2009). "Preparing and Determining Density of Hot Mix Asphalt (HMA) Specimens by Means of the Superpave Gyratory Compactor." AASHTO Guide, AASHTO, Washington, D.C.

AASHTO T342 (2011) "Standard Method of Test for Determining Dynamic Modulus of Hot Mix Asphalt." AASHTO Guide, AASHTO, Washington, D.C.

AASHTO TP4 (2011). "Gyratory Compaction" AASHTO Provisional Standards. AASHTO Guide, AASHTO, Washington, D.C.

AASHTO TP 62 (2005). "Standard Method of test for Determining the dynamic modulus of Hot-Mix Asphalt Concrete Mixtures." AASHTO Guide, AASHTO, Washington, D.C.

AASHTO TP79 (2009). "Determining the Dynamic Modulus and Flow Number for Hot Mix Asphalt (HMA) Using the Asphalt Mixture Performance Tester (AMPT)." AASHTO Guide, AASHTO, Washington, D.C.

AASHTO PP60 (2009). "Preparation of Cylindrical Performance Test Specimens Using the Superpave Gyratory Compactor (SGC)." AASHTO Standard Specifications. Washington, D.C.

Akhter, G.F. and M.W. Witczak. (1985) "Sensitivity of Flexible Pavement Performance to Bituminous Mix Properties." In Transportation Research Record: Journal of the Transportation Research Board, No. 1036, TRB, National Research Council, Washington, D.C.

227

Al-Swailmi, S., and Terrel, R. L. (1992). "Evaluation of Water Damage of Asphalt Concrete Mixtures Using the Environmental Conditioning System (ECS)." Journal of the Association of Asphalt Paving Technologists, Vol. 61, pp. 405-445.

ARA, Inc., ERES Consultants Division (2004). "Guide for Mechanistic-Empirical Design of New & Rehabilitated Pavement structures." NCHRP Project 1-37A, (Final Report) <http://onlinepubs.trb.org/onlinepubs/archive/mepdg/guide.htm> (July 19, 2013).

ASTM C670 (2010). "Standard Practice for Preparing Precision and Bias Statements for Test Methods for Construction Materials." American Society for Testing and Materials (ASTM) Standards. West Conshohocken, PA.

ASTM D1075 (2011). "Standard Test Method for Effect of Water on compressive strength of Compated bitumineius mixtures." ASTM Standards, ASTM International, West Conshohocken, PA.

ASTM D3497 (2003). "Standard Tests Method for Dynamic Modulus of Asphalt Mixtures." (Reapproved 2003). ASTM Standards, ASTM International, West Conshohocken, PA.

ASTM D4867/D4867M (2009). "Standard Test Method for Effect of Moisture on Asphalt Concrete Paving Mixtures." ASTM Standards, ASTM International, West Conshohocken, PA.

228

ASTM D7878/D7870M (2013). "Standard Practice for Moisture Conditioning Compacted Asphalt Mixture Specimens by Using Hydrostatic Pore Pressure." ASTM Standards, ASTM International, West Conshohocken, PA.

ASTM E691 (2012). "Standard Practice for Conducting an Interlaboratory Study to Determine the Precision of a Test Method." ASTM Standards. West Conshohocken, PA.

Bari, J. (2005). "Development of a New Revised Version of the Witczak E^* Predictive Models for Hot Mix Asphalt Mixtures." Ph.D. Dissertation, Arizona State University, Phoenix, AZ.

Bennert T. and Williams S. G. (2009). " Precision of AASHTO TP62-07 for use in mechanistic-empirical pavement design guide for flexible pavements." J. of the Transportation Research Board (TRB), 2127, 115–126.

Birgisson, B., Sholar, G., and Roque, R. (2005). "Evaluation of Predicted Dynamic Modulus for Florida Mixtures." 84th Annual Meeting of the Transportation Research Board, Paper No. 05-1309, Washington D.C.

Birgisson, B. and Massad, E. (2005). "Development and Evaluation of Test Methods to Evaluate Water Damage and Effectiveness of Antistrippling Agenets," Final Report, Florida Department of Transportation, Tallahassee, FL.

Bonaquist, R. (2011). "Precision of the Dynamic Modulus and Flow Number Tests Conducted with the Asphalt Mixture Performance Tester." NCHRP Report 702, TRB of the National Academies, Washington, D.C.

229

Bonaquist, R. and Christensen, D. W. (2005). "Practical Procedure for Developing Dynamic Modulus Master Curves for Pavement Structural Design." Transportation Research Record: Journal of the Transportation Research Board, No. 1929, Transportation Research Board of the National Academies, Washington, D.C., pp. 208–217.

Bohn, A.O., P. Ullidtz, and R. Stubstad. (1970). "The Dynamic Modulus of Asphalt Concrete Surfaces." Dansk Vejtidsskrift, Vol. 47.

Brown, R., Kandhal, P., and Zhang, J. (2001). "Performance Testing for Hot Mix Asphalt." NCAT Report No. 2001-05A, National Center for Asphalt Technology, Auburn, AL.

Buttlar W.G., Bauer J.M., Sherman D. S. (2002). "Dyanmic Modulus of Asphalt Concrete with Hollow Cylinder Tensile Tester". Transportation Research Records, 1789, Paper vol. 02-4112

Ceylan, H., Schwartz, C. W., Kim, S., and Gopalakrishnan, K. (2009). "Accuracy of Predictive Models for Dynamic Modulus of Hot-Mix Asphalt." Journal of Materials in Civil Engineering, Vol. 21, No. 6, 286-293

Chailleux, E., Ramond, G.,Roche, C. D. L. (2006), "A mathematical-based master-curve construction method applied to complex modulus of bituminous materials." Road Materials and Pavement Design, EATA, pages 75-92.

Christensen, Jr., D.W., Pellinen, T.K., and Bonaquist, R.F. (2003). "Hirsch Model for Estimating the Modulus of Asphalt Concrete," Journal of the Association of Asphalt Paving Technologists, 72, 97–121.

Christensen, D.W., Pellinen, T.K., and Bonaquist, R.F. (2003). "Hirsch Model for Estimating the Modulus of Asphalt Concrete." Journal of the Association of Asphalt Paving Technologists, Volume 72, Lexington, KY.

Clyne, T. R., Li, X., Marasteanu, M. O. and Skok, E. L. (2003). "Dynamic and Resilient Modulus of Mn/Dot Asphalt Mixtures", Final Report, Department of Civil Engineering, University of Minnesota, 500 Pillsbury Dr. S.E., Minneapolis, MN 55455-0116.

Cragg, R. and Pell, P.S. (1971) "The Dynamic Stiffness of Bituminous Road Materials," Journal of Association of Asphalt Paving Technologists, Vol. 40.

Clyne, T.R., Li, X., Marastenau, M.O., and Skok, E.L. (2003). "Dynamic and Resilient Modulus of Mn/DOT Asphalt Mixtures." Final Report MN/RC–2003-09. University of Minnesota, Minneapolis, MN.

Hossain, Z., Zaman, M., Doiron, C., Cross, S. (2011). "Development of Flexible Pavement Database for Local Calibration of MEPDG" Annual report for FY 2009 (ODOT SPR No. 2209 (job piece 01946(52)), Oklahoma Department of Transportation, 200 N.E. 21st Street, Oklahoma City, Oklahoma 73105.

231

Dongré, R., Myers, L., D'Angelo, J., Paugh, C., and Gudimettla, J. (2005). "Field Evaluation of Witczak and Hirsch Models for Predicting Dynamic Modulus of Hot-Mix Asphalt." Pre-Print of the Journal of the Association of Asphalt Paving Technologists, Volume 74.

Federal Highway Adminstartion (2013). "Most Travelled Urban Highways Average Annual Daily Traffic," http://www.fhwa.dot.gov/policyinformation/tables/02.pdf (August, 2013)

Garcia, G., and Thompson, M., (2007). "HMA dynamic modulus - Temperature relations" Research Report FHWA-ICT-07-006, Illinois Center for Transportation, Department of Civil and Environmental Engineering, University of Illinois, 205 North Mathews – MC-250 Urbana, IL 61801.

GCTS Testing Systems, (2013). "Servo-Hydraulic Asphalt Testing System (ATM-025)," http://www.gcts.com/?s=prod_ver&p=products&ID=46 (August, 2013)

Huang, Y. H. (2004). "Pavement Analysis and Design." Pearson Education, Inc., Upper Saddle River, New Jersey, 76-90

InstroTek, Inc. (2012). "The MIST." <http://instrotek.com/material-testing/laboratory-products/mist/#!prettyPhoto> (Jul. 12, 2012).

Jiang W. H., Zahang, X. N., Simulation, Z. Li., (2012). "Test of the Dynamic Water Pressure of Ashalt Concrete," Jourenal of Highway and Transportatiion Development. Vol. 7, pp. 23-27.

232

Kallas, B.F. (1970). "Dynamic Modulus of Asphalt Concrete in Tension and Tension-Compression," Journal of Association of Asphalt Paving Technologists, Vol. 39.

Karlson, T. K. (2005). "Evaluation of Cyclic Pore Pressure Induced Moisture Damage in Asphalt Pavement," Master of Science Thesis, University Of Florida.

Kim, R. Y., (2009). "Modelling of Asphalt Concrete" American society of Civil Engineers, 1801 Alexander bell Drive, Reston, VA, USA

Kim, Y.R., King, M., and Momen, M. (2005). "Typical Dynamic Moduli Values of Hot Mix Asphalt in North Carolina and Their Prediction." 84th Annual Meeting of the Transportation Research Board, Paper No. 05-2568, Washington D.C.

Kutay, M. E. and Aydilek, A. H. (2007). "Dynamic Effects on Moisture Transport In Asphalt Concrete," Journal of Transportation Engineering. Vol. 133, pp. 406-414.

Kottegoda, N. T. (2008). Applied statistics for civil and environmental engineers. Blackwell Pub., Malden, MA.

Lakes R. S. (2009). "Viscoelastic materials". Cambridge University Press. Avenue of Americas, NY, USA

Majidzadeh, K., S. Khedr, and M. El-Mojarrush. (1979). "Evaluation of Permanent Deformation in Asphalt Concrete Pavements." Transportation Research Record: Journal of the Transportation Research Board, No. 715, TRB, National Research Council, Washington, D.C.

McCrum, Buckley, and Bucknell (2003). "Principles of Polymer Engineering," 117-176.

233

Menard, Kevin P. (1999). "Dynamic Mechanical Analysis: A Practical Introduction" CRC Press

Meyers and Chawla (1999): "Mechanical Behavior of Materials," 98-103.

Meyers, R. A. (2000). "Encyclopedia of Analytical Chemistry" John Wiely & Sons Ltd, Chichester, West Sussex, UK , pp. 9468–9485.

Miller J.S., J. Uzan, and M.W. Witczak. (1983). "Modification of the Asphalt Institute Bituminous Mix Modulus Predictive Equation." Transportation Research Record: Journal of the Transportation Research Board, No. 911, TRB, National Research Council, Washington, D.C.

Mohammad, L.N., Wu, Z., Myers, L., Cooper, S., and Abadie, C. (2005). "A Practical Look at Simple Performance Tests: Louisiana's Experience." Journal of the Association of Asphalt Paving Technologists, Volume 74, 2005 (in press).

Montgomery, D. C. (2001). "Design and Analysis of Experiments." John Wiley and Sons, Inc. New York.

Michelin America, (2013). "Load and Inflation Tables." http://www.michelintruck.com/michelintruck/tires-retreads/load-inflation-tables.jsp (August, 2013)

Nadkarni A. A., Kaloush K. E., Zeiada W. A., Biligiri K. P. (2009). "Using Dynamic Modulus Test to Evaluate Moisture Susceptibility of Asphalt Mixtures."

Transportation Research Record: Journal of the Transportation Research Board, Vol. 2127, pp 29-35.

Pellinen, T. K. (2001). "Investigation of the use of Dynamic modulus as an indicator of Hot-Mix Asphalt performance." PhD. Dissertation, Arizona State University.

Parker, F., (1989). "A Field Study of Stripping Potential of Asphalt Concrete Mixtures," Final Report, The State of Alabama Highway Department, Montgomery, AL.

Portela, E. L., Coutinho, R. P., Junior, E. P., Holanda, Á. S. (2009), "Thermo-Mechanical Analysis of Asphalt Pavements." Federal University of Ceará – Department of Transportation Engineering Campus do Pici , Bl. 703, 60455-760, Fortaleza, Ceará, Brazil

Roberts, F. L., (2009). "Hot Mix Asphalt Materials, Mixture Design, and Construction" National Center for Asphalt Technology, Auburn, AL.

Rowe and Sharrock (2010). "Alternate Shift Factor Relationship for Describing the Temperature Dependency of the Visco-Elastic Behavior of Asphalt Materials". Journal of the Transportation Research Board, pp 125-135

Schwartz, C. W. (2005). "Evaluation of the Witczak Dynamic Modulus Prediction Model." 84th Annual Meeting of the Transportation Research Board, Paper No. 05-2112, Washington D.C.

Seo, Y., El-Haggan, O., King, M., Lee, S. J., and Kim, Y. R. (2007). "Air Void Models for the Dynamic Modulus, Fatigue Cracking, and Rutting of Asphalt Concrete." Journal of Materials in Civil Engineering, Vol. 19, No. 10.

Shah, B. D., (2003). "Evaluation of Moisture Damage within Asphalt Concrete Mixes," Master of Science Thesis, Texas A&M University.

Sholar, G. A., Musselman, J. A., Page, G. C., Upshaw, P. B., and Moseley, H. L. (2001). "Precision Statements for the Ignition Oven Using Plant-Produced Mix." Research Report- FL/DOT/SMO/01-445, Florida Department of Transportation, State Materials Office, Gainesville, FL.

Shook, J.F., Kallas B.F., and McLeod B.F., (1969). "Factors Influencing Dynamic Modulus of Asphalt Concrete," Journal of Association of Asphalt Paving Technologists, Vol. 38.

Solaimanian, M., Bonaquist, R. F., Tandon, V., (2007). "Improved Conditioning and Testing Procedures for HMA Moisture Susceptibility," NCHRP Report 589. TRB, Washington, D.C.

Solaimanian, M., Harvey, J., Tahmoressi, M., Tandon, V., (2003). "Test Methods to Predict Moisture Sensitivity of Hot-Mix Asphalt Pavements," TRB Report: Moisture Sensitivity of Asphalt Pavements. Topic 3. TRB National Seminar, San Diego, CA, February 4-6, PP. 77–113.

Sotil, A. (2003). "Material Characterization of Asphalt Rubber Mixtures Using the Dynamic Modulus Test. Master's thesis. Arizona State University, Tempe.

Sotil, A., Kaloush, K. E., and Witczak, M. W. (2004) "Reduced Confined Dynamic Modulus Testing Protocol for Asphalt Mixtures." Transportation Research Record: Journal of the Transportation Research Board, No. 1891, TRB, National Research Council, Washington, D.C., pp. 153–162.

Tashman, L. and Elangovan, M. A. (2004). "Dynamic Modulus Test − Laboratory Evaluation and Future Implementation in the State of Washington." Final research report, Washington State University (WSU), Transportation Research Center (TRAC), Pullman, WA 99164-2910.

Tran, N.H., and Hall, K.D. (2005). "Evaluating the Predictive Equation in Determining Dynamic Moduli of Typical Asphalt Mixtures Used in Arkansas." Pre-Print of the Journal of the Association of Asphalt Paving Technologists, Volume 74.

Tarrer, A.R. and Wagh, V., (1991). "The Effect of the Physical and Chemical Characteristics of the Aggregate on Bonding," SHRP Report, National Research Council, Washington, D.C.

Tomas, R., (2004). "Practical Guide to ICP-MS" Marcel Dekker, Inc., New York, NY.

Witczak, M.W. (2007). "Specification Criteria for Simple Performance Tests for Rutting." NCHRP Report 580, Transportation Research Board Washington, D.C.

Witczak, M.W. and Fonseca, O.A. (1996) "Revised Predictive Model for Dynamic Modulus of Asphalt Mixtures." Transportation Research Record: Journal of the Transportation Research Board, No. 1540, TRB, National Research Council, Washington, D.C.

Witczak, M. W., Bonaquist, R., Von Quintus, H., and Kaloush, K. (2000). "Specimen Geometry and Aggregate Size Effects in Uniaxial Compression and Constant Height Shear Test." Journal of the Association of Asphalt Paving Technologists, Vol. 69, 733–793.

Witczak M. W. and sotil A. (2004). "A Recommended Methodology for Developing Dynamic Modulus E^* Master Curves from Nonlinear Optimization". Arizona State University, Tempe.

Witczak M. W., Andrei D., Mirza W. (1999). "Development of the 2002 Guide for the Design of New and Rehabilitated Pavement Structures APPENDIX CC-4: Development of a Revised Predictive Model for the Dynamic (Complex) Modulus of Asphalt Mixtures". NCHRP 1-37 A, University of Maryland, College Park, MD 20740.

Witczak, M., (2005). "Simple performance tests: summary of recommended methods and database," NCHRP Report 547, TRB, Washington, D.C.

Witczak, M., Kaloush, K., Pellinen, T., Basyouny, M. El., Von Quintus, H., (2002), "Simple performance test for Superpave Mix Design," NCHRP Report 456, TRB, Washington, D.C.

Witczak, M., (2007). "Specification Criteria for Simple Performance tests for Rutting," NCHRP Report 580. TRB, Washington, D.C.

Yeager L.L. and L.E. Wood. (1975). "Recommended Procedure for Determining the Dynamic Modulus of Asphalt Mixtures." Transportation Research Record: Journal

of the Transportation Research Board, No. 549, TRB, National Research Council, Washington, D.C.

Yilmaz, A. and Sebnem, S., (2012). "Water Effect on Deteriorations of Asphalt Pavements," The Online Journal of Science and Technology. Vol. 2, pp. 1-6.

APPENDIX A

Dynamic Modulus Test Results for SP-III with PG 70-22 Binder

Table A.1: *E** test results for Sample 1 (SP-III with PG 70-22 binder)

Temperature	Frequency	Stress		Dynamic Modulus	Phase Angle		Strain			
		Amplitude (P-P)	SE			UC	(P-P) Recoverable	Permanent	SE	UC
(deg C)	(Hz)	(kPa)	(%)	(MPa)	(deg)	(deg)	(micro e)	(micro e)	(%)	(%)
-10	25	1899	7.7	33749.695	10.2	4.1	56.27	57.228	9.7	6.9
-10	10	1953	7	33554.328	5.7	0.6	58.203	20.955	7.9	11.6
-10	5	1948	5.9	32484.578	5.8	0.1	59.952	19.034	7	11.3
-10	1	1741	2.1	29745.029	7	0.9	58.53	20.474	4	12.9
-10	0.5	1611	1.3	28972.107	7.2	0.8	55.621	24.642	3.5	14.6
-10	0.1	1543	0.5	25734.52	7.5	0.2	59.949	47.949	3	12.4
4	25	1350	6.2	29351.537	14.2	0.1	46.002	80.698	9.3	25.4
4	10	1329	6.8	26583.441	10.9	1.4	50.001	50.655	7.4	26.8
4	5	1266	5.5	25116.166	10.7	1.7	50.419	50.954	6.6	26.5
4	1	1066	2	21178.668	12	2.2	50.354	51.283	5.3	25.7
4	0.5	980	1.2	19158.592	13.3	2.1	51.162	56.562	2.8	26.9
4	0.1	883	0.6	15886.74	15.9	1.7	55.574	91.716	3.4	23.1
21	25	878	6	14279.107	20.7	1.5	61.477	186.417	8.1	2.7
21	10	756	6.2	12464.3	18.9	3.3	60.652	147.93	6.9	3
21	5	657	5.1	10947.893	19.9	3.7	60.022	136.691	5.7	3
21	1	464	2.6	7958.353	23.5	4.6	58.252	113.201	4.8	8.8
21	0.5	405	1.8	6771	25.2	5.2	59.849	117.486	4	11.7
21	0.1	629	0.5	4841.598	26	3.3	129.913	348.54	4	1.5
37	25	424	6.5	6867.026	25.1	2.3	61.718	336.534	6.2	13.6
37	10	303	6.8	5362.621	25	3	56.435	358.401	5.7	17.3
37	5	251	4.6	4345.317	25.9	1.7	57.688	362.349	5.4	18
37	1	155	3.1	2582.42	29.4	2.1	60.071	333.565	3.8	14.5
37	0.5	127	2.2	2087.269	30.1	2.3	60.989	337.311	3.4	12.6
37	0.1	85	1.3	1320.332	29.1	2.3	64.249	381.253	3.8	11.6
54	25	205	6.1	2553.447	30	0.3	80.181	335.349	5.7	2.4
54	10	158	4.7	1859.337	28.5	0.8	84.837	398.812	3.8	2.1
54	5	127	4.6	1417.013	28.1	0.9	89.928	409.597	3.6	4.3
54	1	74	3.2	795.796	27.1	0.7	93.044	394.694	3.7	0.9
54	0.5	59	2.8	645.422	25.5	0.5	90.892	391.743	4.3	0.5
54	0.1	39	3	426.353	20.6	0	92.122	415.725	5.5	7.9

241

Figure A. 1: Master curve for Sample 1 (SP-III with PG 70-22 binder)

$$y = 0.0006x^2 - 0.15x + 2.9899$$
$$R^2 = 0.9985$$

Figure A. 2: Shift factor for Sample 1 (SP-III with PG 70-22 binder)

242

Table A.2: *E** test results for Sample 2 (SP-III with PG 70-22 binder)

| Temperature | Frequency | Stress | | Dynamic Modulus | Phase Angle | | Strain | | | |
| | | Amplitude (P-P) | SE | | | UC | (P-P) Recoverable | Permanent | SE | UC |
(deg C)	(Hz)	(kPa)	(%)	(MPa)	(deg)	(deg)	(micro e)	(micro e)	(%)	(%)
-10	25	2038.0	6.1	36369.1	7.3	2.0	56.0	61.2	10.4	7.1
-10	10	2067.0	6.1	35345.8	6.2	1.7	58.5	22.5	8.0	7.7
-10	5	2011.0	5.2	34335.3	6.1	1.8	58.6	25.6	6.7	7.7
-10	1	1804.0	1.5	32016.0	6.1	2.1	56.3	28.7	8.0	4.4
-10	0.5	1697.0	0.9	30246.1	8.0	2.2	56.1	30.4	4.3	3.2
-10	0.1	1543.0	0.5	27514.6	8.5	2.1	56.1	44.0	3.6	0.4
4	25	1521.0	6.3	24786.0	10.7	3.6	61.4	91.5	9.5	0.6
4	10	1490.0	6.5	23750.9	9.0	0.2	62.7	35.7	8.7	9.8
4	5	1420.0	5.2	22707.9	9.0	0.1	62.5	35.1	8.5	9.9
4	1	1201.0	1.7	19412.5	11.4	0.5	61.9	33.1	5.0	13.6
4	0.5	1103.0	1.0	17873.1	12.1	1.0	61.7	37.1	5.8	15.8
4	0.1	994.0	0.4	14309.3	15.3	0.2	69.4	82.4	3.9	17.2
21	25	855.0	7.3	12127.9	20.0	3.1	70.5	193.5	10.5	3.0
21	10	723.0	7.5	12137.9	17.5	0.3	59.5	161.3	7.7	28.9
21	5	626.0	6.8	10871.3	18.4	0.7	57.6	153.8	7.7	30.5
21	1	412.0	3.8	7686.1	23.0	0.4	53.6	124.5	4.2	30.6
21	0.5	348.0	2.5	6540.1	24.2	0.1	53.1	121.1	3.4	31.2
21	0.1	225.0	0.8	4174.9	27.3	0.2	53.9	154.9	3.1	32.1
37	25	485.0	8.9	7589.4	26.9	1.3	63.9	399.8	10.0	16.4
37	10	427.0	9.6	5981.9	26.5	2.2	71.3	498.9	7.8	22.8
37	5	364.0	9.1	4887.7	28.0	2.5	74.4	531.9	7.6	27.1
37	1	242.0	4.4	2706.5	31.0	2.2	89.2	514.2	6.7	36.7
37	0.5	200.0	3.2	2152.8	31.5	1.8	92.9	520.5	6.0	40.8
37	0.1	149.0	1.4	1343.0	30.3	0.5	110.7	606.6	5.7	44.2
54	25	137.0	9.1	2378.4	33.3	1.6	57.5	207.0	6.8	32.5
54	10	113.0	9.2	1770.0	30.2	1.1	64.0	262.8	6.0	25.5
54	5	97.0	8.7	1410.2	29.4	0.8	68.6	284.6	6.0	25.1
54	1	62.0	5.8	829.0	28.5	1.0	74.9	282.3	5.3	32.2
54	0.5	54.0	4.3	702.4	27.0	1.0	77.5	288.8	5.6	36.1
54	0.1	42.0	2.1	515.0	22.5	0.8	81.8	319.0	6.3	47.2

Figure A. 3: Master curve for Sample 2 (SP-III with PG 70-22 binder)

$$y = 0.0011x^2 - 0.1789x + 3.2715$$
$$R^2 = 0.9953$$
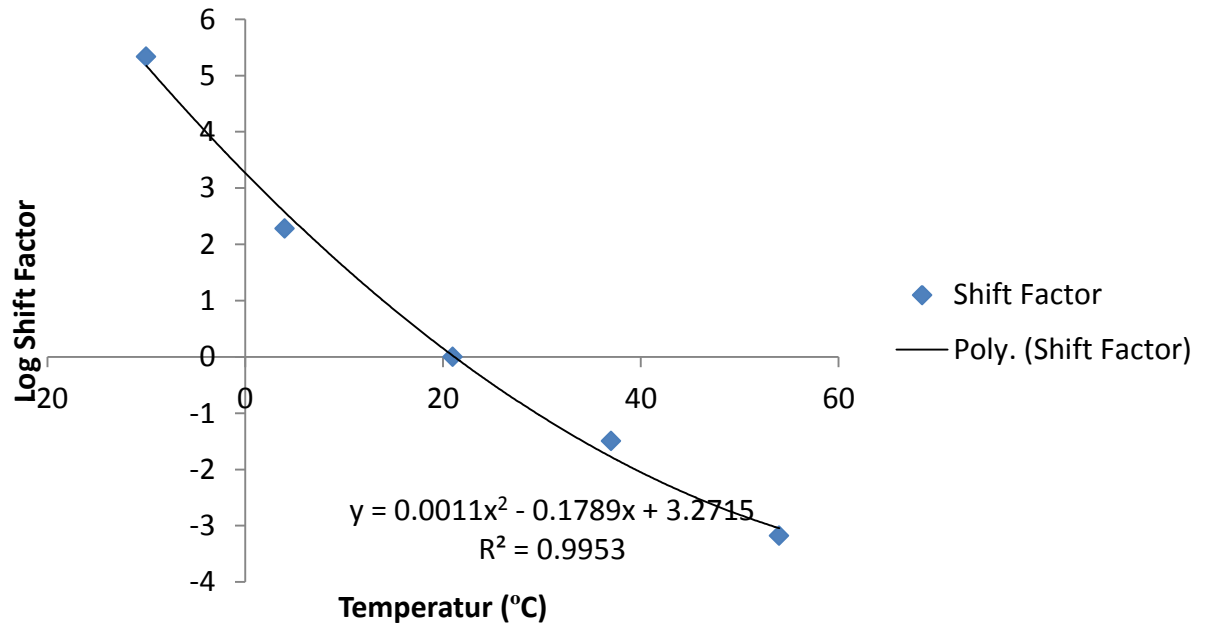
Figure A. 4: Shift factor for Sample 2 (SP-III with PG 70-22 binder)

244

Table A. 3: *E** test results for Sample 3 (SP-III with PG 70-22 binder)

Temperature	Frequency	Stress		Dynamic Modulus	Phase Angle		Strain			
		Amplitude (P-P)	SE			UC	(P-P) Recoverable	Permanent	SE	UC
(deg C)	(Hz)	(kPa)	(%)	(MPa)	(deg)	(deg)	(micro e)	(micro e)	(%)	(%)
-10	25	2049	6.8	32667.498	7	1	62.734	72.951	9.5	19.5
-10	10	1979	6.3	31308.1	6.6	0.6	63.2	18.07	8.3	18.3
-10	5	1908	5.1	30411.125	6.2	0	62.741	16.513	7.2	16.9
-10	1	1653	1.8	27615.971	6.4	0.1	59.846	15.778	5.8	13
-10	0.5	1571	1	26189.592	8.8	1.9	60.003	17.994	3.7	10.8
-10	0.1	1386	0.5	23250.439	9.1	1	59.618	33.955	4.4	7.9
4	25	1294	7.5	21708.938	10.7	3.4	59.621	131.618	9.8	3.9
4	10	1215	7.4	19684.326	11.4	0.7	61.746	76.446	7.4	6.4
4	5	1129	6.4	18147.914	12.2	0.8	62.188	75.79	6.2	5.4
4	1	886	2.8	14740.722	14.6	0.7	60.111	69.371	5.1	3.8
4	0.5	795	1.8	13102.343	16.6	2.3	60.662	74.204	4.3	0.8
4	0.1	608	0.9	10267.097	18.7	0.7	59.228	116.988	3.5	1.2
21	25	697	8	11424.726	17	6.6	60.965	240.313	11	20.4
21	10	574	8.3	9281.548	19.8	1.2	61.851	236.956	6.7	13.8
21	5	491	8.1	7974.197	21	1	61.521	233.081	6.6	13.3
21	1	310	5.4	5051.058	25.3	0.5	61.315	201.597	6.9	9.7
21	0.5	245	3.6	3978.456	26.6	1.9	61.697	195.752	5.2	10
21	0.1	158	1.5	2494.03	27.7	1.2	63.295	228.028	3.6	7.8
37	25	283	9.9	4857.816	27.8	4.2	58.202	168.393	8.1	9.2
37	10	225	9.3	3621.459	26.8	1.6	62.201	195.095	6.7	21.4
37	5	180	8.7	2896.652	26.9	1.7	62.259	202.194	6.4	23.6
37	1	114	5.8	1759.675	26.9	2.2	64.945	192.523	5.8	23.2
37	0.5	89	3.7	1441.959	26.2	2.2	62.038	193.184	5.5	23
37	0.1	61	1.5	986.215	24.6	1.3	61.874	217.7	7.7	22.4
54	25	102	9.7	1550.854	29.1	1.6	65.521	83.723	6.9	3.5
54	10	80	8.8	1201.377	26.6	2.3	66.285	111.038	5.7	8.6
54	5	64	8.1	973.169	25.4	2.5	66.066	118.016	5.5	2.1
54	1	44	5.6	685.538	23.4	3.5	64.2	114.045	5.1	4.5
54	0.5	40	4.1	613.822	22.4	3	64.429	115.623	5.8	6.7
54	0.1	38	2	511.312	19.8	3.4	74.378	136.762	7.3	12.3

245

Figure A. 5: Master curve for Sample 3 (SP-III with PG 70-22 binder)
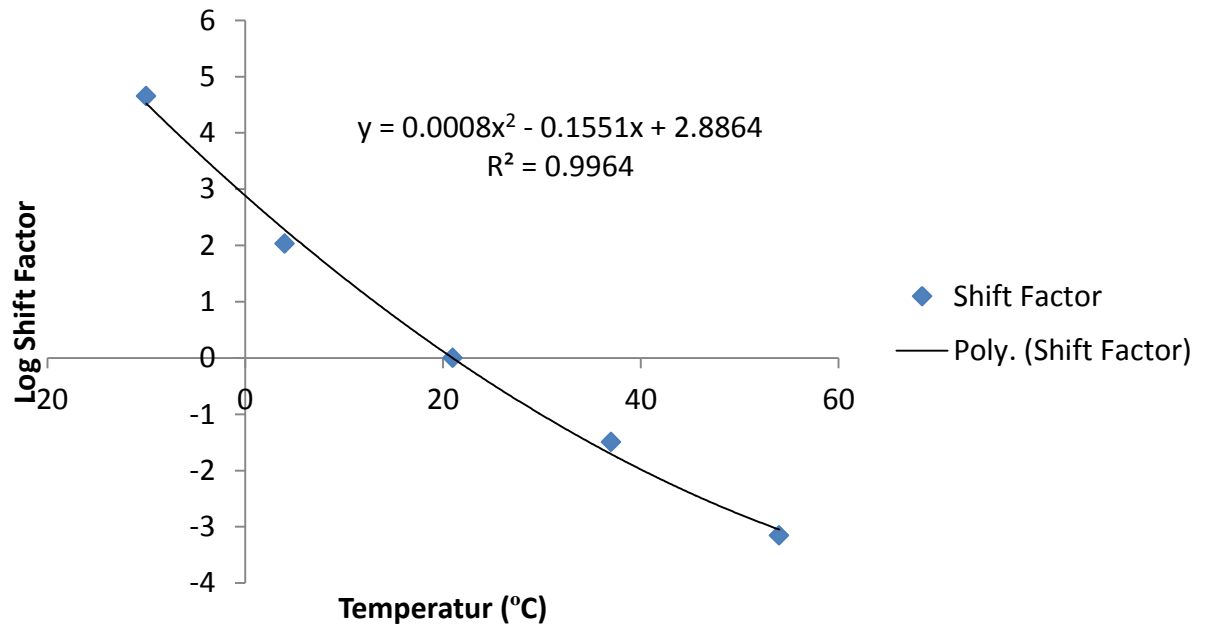
Figure A. 6: Shift factor for Sample 3 (SP-III with PG 70-22 binder)

Table A. 4: *E** test results for Sample 4 (SP-III with PG 70-22 binder)

Temperature	Frequency	Stress		Dynamic Modulus	Phase Angle		Strain			
		Amplitude (P-P)	SE			UC	(P-P) Recoverable	Permanent	SE	UC
(deg C)	(Hz)	(kPa)	(%)	(MPa)	(deg)	(deg)	(micro e)	(micro e)	(%)	(%)
-10	25	1682	6.3	29150.547	8.6	4.4	57.697	53.002	9.7	4.9
-10	10	1653	6.1	27856.824	7.6	2.1	59.332	12.374	8.9	1.9
-10	5	1610	4.9	27035.098	7.3	2.2	59.544	12.917	7.4	2
-10	1	1431	1.7	25229.08	8.3	2.3	56.739	11.417	6.1	4.8
-10	0.5	1392	1	23516.889	7.8	3.4	59.182	13.598	4.9	3.2
-10	0.1	1223	0.4	21690.828	9.3	2.8	56.405	26.508	4.7	6.8
4	25	1119	6.5	20288.385	12.2	8.2	55.164	45.561	9.7	3.3
4	10	1057	6.6	18643.26	12.7	3.9	56.677	2.701	9.2	0.2
4	5	989	5.4	17597.004	13	3.8	56.224	4.165	7.8	0.1
4	1	806	2.1	15001.527	15.8	4.4	53.741	3.156	6.2	1
4	0.5	739	1.3	13755.886	15.3	5.4	53.688	8.705	4.9	2.2
4	0.1	605	0.6	11377.559	18.5	3.8	53.216	38.133	5.4	6
21	25	664	6.3	12161.355	15.6	6.1	54.566	222.559	8.4	0.6
21	10	603	6.9	10465.024	17.9	1.4	57.588	231.192	6.5	7
21	5	518	5.6	9083.568	19.8	2.2	57.035	231.035	5.4	6.7
21	1	353	3.2	6414.058	25	3.2	55.075	203.765	4	3.8
21	0.5	294	2.1	5228.625	27.1	3.6	56.319	203.334	3.8	4.2
21	0.1	198	0.7	3592.041	27.8	2.5	55.073	241.806	3.7	8.3
37	25	423	6.7	4778.304	24.8	6.7	88.445	450.94	7	18.3
37	10	300	6.9	3759.005	26.1	2.1	79.864	471.986	4.5	11
37	5	249	4.5	2989.541	27	2	83.256	471.888	3.1	10.4
37	1	153	2.3	1782.164	29.6	2	86.067	435.573	3.6	7.7
37	0.5	126	1.5	1429.418	30.1	2.3	87.874	428.526	3.6	6.2
37	0.1	85	1	920.219	28.6	1.9	92.368	469.715	4.5	2.5
54	25	120	6.1	1868.617	31.8	0.5	64.402	191.509	5.8	16.4
54	10	95	6.2	1449.93	28.3	1.3	65.784	244.924	5.2	20.3
54	5	76	4	1208.933	27.1	0.9	62.681	259.605	5.1	20.9
54	1	48	4.5	775.469	26.6	1.9	61.715	256.523	6	22.9
54	0.5	42	4.4	684.54	24.7	2.1	60.869	265.624	6.4	26.9
54	0.1	32	4.9	540.118	20.9	2.6	59.3	291.875	8.1	35.5

247
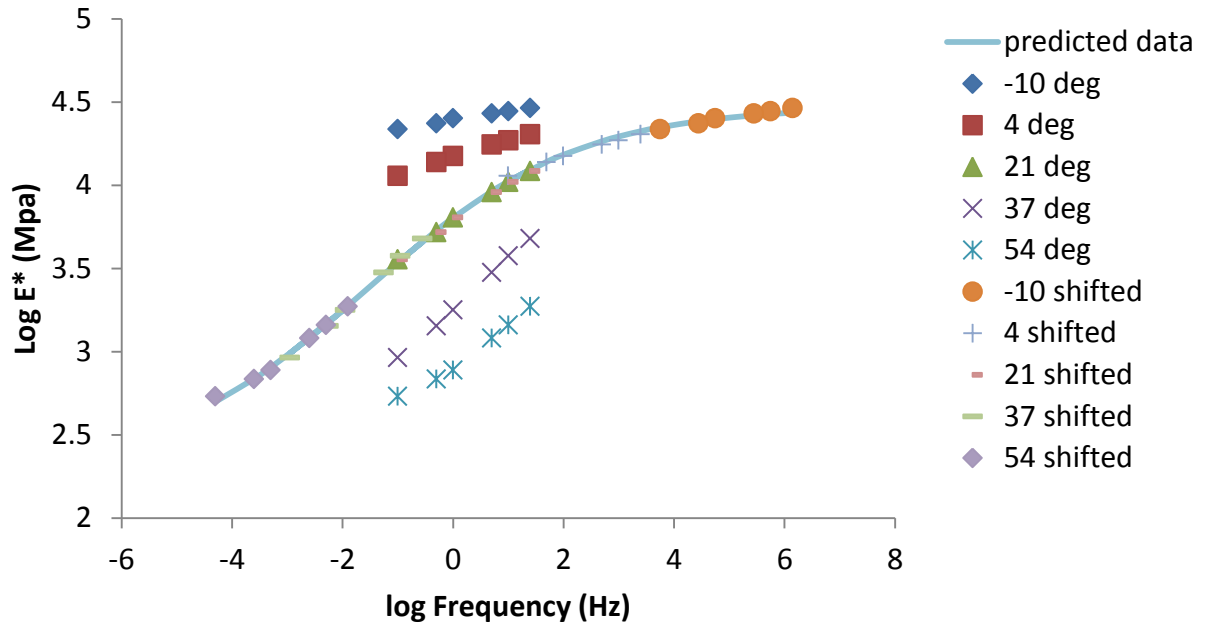
Figure A. 7: Master curve for Sample 4 (SP-III with PG 70-22 binder)

$y = 0.001x^2 - 0.166x + 2.8862$
$R^2 = 0.9975$

Figure A. 8: Shift factor for Sample 4 (SP-III with PG 70-22 binder)

248

Table A. 5: *E** test results for Sample 5 (SP-III with PG 70-22 binder)

Temperature	Frequency	Stress		Dynamic Modulus	Phase Angle		Strain			
		Amplitude (P-P)	SE			UC	(P-P) Recoverable	Permanent	SE	UC
(deg C)	(Hz)	(kPa)	(%)	(MPa)	(deg)	(deg)	(micro e)	(micro e)	(%)	(%)
-10	25	1494	6.4	25315.043	7.4	0.9	59.025	39.872	12	4.9
-10	10	1416	5.6	24060.75	5.6	0.2	58.851	8.067	9.8	4.7
-10	5	1372	3.7	23369.6	5.4	0.1	58.702	7.018	8.3	4.6
-10	1	1251	0.9	21594.982	6.2	0.2	57.938	8.517	5.5	4.4
-10	0.5	1197	0.6	20879.859	6.4	0.8	57.35	7.775	5.2	2.9
-10	0.1	1097	0.5	18319.586	7.6	0.2	59.897	23.579	4.7	4.8
4	25	914	6.3	15974.339	10.3	5.3	57.21	60.447	8.5	7.2
4	10	867	5.6	14368.625	10.1	0.5	60.358	52.587	9.1	6.7
4	5	823	4.1	13518.951	10.5	0.7	60.895	53.558	5.4	6.5
4	1	713	1.2	11344.43	12.1	0.3	62.886	51.313	3.2	5.4
4	0.5	623	0.9	10407.276	12.4	0.9	59.89	53.826	2.8	5.1
4	0.1	507	1.4	8478.356	15.9	0.3	59.839	91.809	3.1	1.1
21	25	490	6.5	9337.947	16.6	0.5	52.454	150.836	5.9	3.9
21	10	414	7.6	8265.17	16.4	0.5	50.11	167.021	5.6	5.2
21	5	356	6.9	7214.462	17.5	0.6	49.373	166.349	4.8	6.6
21	1	246	2.8	4920.59	20.7	1.3	50.089	149.907	3.1	9.5
21	0.5	206	1.9	4180.631	21.9	1.5	49.206	149.801	2.7	9.9
21	0.1	137	0.9	2827.762	23.9	1.4	48.58	180.482	2.9	10.4
37	25	219	5.4	3985.028	24.7	4.6	55.029	182.812	7.7	17.3
37	10	175	4	3164.449	24.5	0.2	55.332	199.029	5.8	19.1
37	5	147	3.8	2562.399	25.4	0.4	57.199	186.981	5.7	16.2
37	1	78	3.9	1472.059	28.8	1.3	52.757	140.493	6.8	24.2
37	0.5	87	4	1208.22	28.8	4.1	71.701	153.393	6.3	36.9
37	0.1	55	8.2	728.453	27.2	4.8	75.081	204.161	7.8	41.9
54	25	85	6.3	1314.608	29.5	1.2	64.726	202.678	6.1	5.2
54	10	69	5	1006.376	26.2	1.7	68.112	249.421	5.2	8.6
54	5	53	4.4	802.425	24.8	1.9	66.21	265.086	5.1	10.6
54	1	35	2.9	508.68	22	2.7	69.49	268.458	4.7	13.7
54	0.5	29	3	442.619	20.1	2.7	66.195	273.282	5.1	11.7
54	0.1	22	2.9	347.756	15.7	2.5	64.531	297.461	5.7	9.5

249
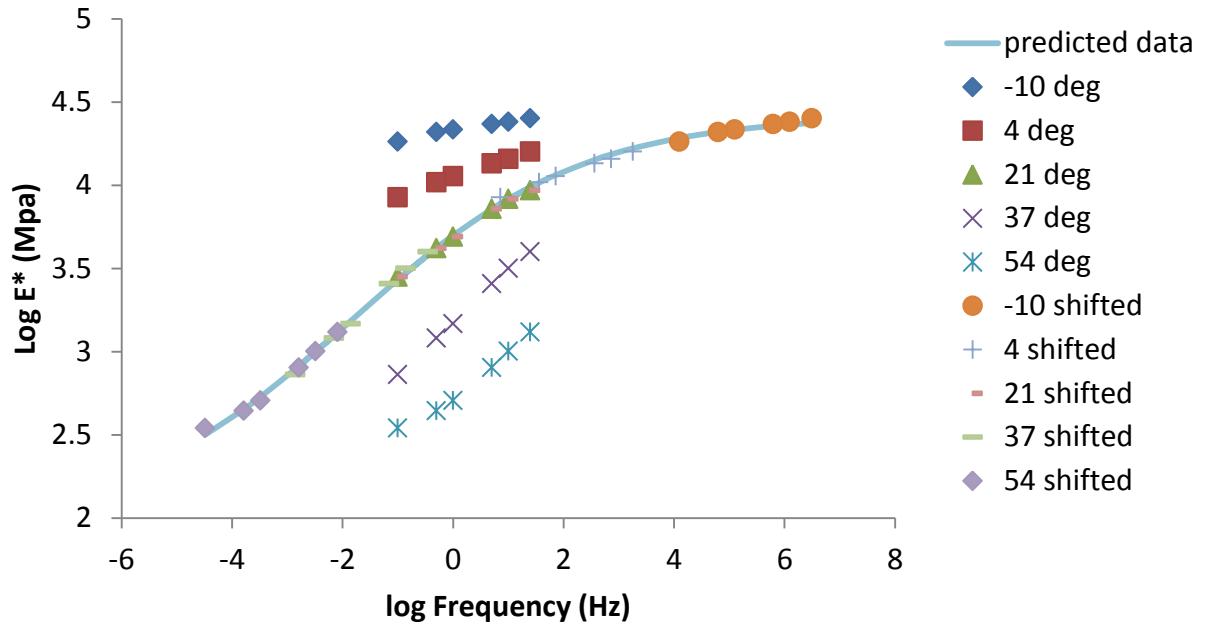
Figure A. 9: Master curve for Sample 5 (SP-III with PG 70-22 binder)

$$y = 0.001x^2 - 0.1749x + 3.0157$$
$$R^2 = 0.992$$

Figure A. 10: Shift factor for Sample 5 (SP-III with PG 70-22 binder)

250

Table A. 6: *E** test results for Sample 6 (SP-III with PG 70-22 binder)

Temperature	Frequency	Stress		Dynamic Modulus	Phase Angle		Strain			
		Amplitude (P-P)	SE			UC	(P-P) Recoverable	Permanent	SE	UC
(deg C)	(Hz)	(kPa)	(%)	(MPa)	(deg)	(deg)	(micro e)	(micro e)	(%)	(%)
-10	25	1332	6.2	23431.807	10.5	0	56.859	38.507	6.2	12.7
-10	10	1350	6.1	23077.113	7.9	0.9	58.484	2.989	5.7	12.7
-10	5	1330	5.1	22279.92	7.7	1.1	59.693	1.3	5.1	12.6
-10	1	1178	2	20731.375	8.5	1.2	56.84	0.988	3.7	10.4
-10	0.5	1087	1.2	19385.332	8.6	1.7	56.072	1.904	3.9	12.7
-10	0.1	1027	0.5	18065	9.3	1.3	56.861	13.22	3.9	11.4
4	25	1151	6.4	16503.855	13.5	3	69.717	101.957	6.3	40.3
4	10	1109	6.3	15632.985	11.4	3	70.955	51.629	5.7	41.4
4	5	1044	5.1	14492.424	12.4	3.3	72.034	48.558	5	41
4	1	838	2.1	12192.285	14.7	4.4	68.736	43.977	3.2	38.7
4	0.5	787	1.4	10998.2	15	5.4	71.518	49.394	3	39
4	0.1	634	0.6	9135.794	17.4	4.5	69.427	90.786	2.8	39.7
21	25	591	6.8	8439.486	19.3	1.3	70.074	207.386	7.2	17.5
21	10	537	7.3	7494.641	17	1	71.633	222.707	4.4	19
21	5	461	6.2	6494.875	18.3	0.8	70.994	216.123	4.6	19.3
21	1	299	3.4	4248.157	22.1	1.5	70.267	184.139	5.1	21.8
21	0.5	247	1.7	3431.381	24	1	71.892	177.453	3.4	19.4
21	0.1	158	0.7	2222.786	25.4	2.8	71.039	216.052	3.4	21.2
37	25	308	6.8	4248.188	25.4	1.7	72.595	245.525	5.4	18.1
37	10	249	5.5	3167.497	24.9	1	78.68	258.544	3.4	14.7
37	5	188	4.1	2512.946	26.4	1.7	74.825	250.028	2.6	14.5
37	1	103	2.1	1454.584	28.6	0.8	70.905	221.532	3.2	24.9
37	0.5	81	1.4	1161.21	28.7	0.4	70.178	219.39	3.4	29.6
37	0.1	49	1.6	745.322	27.1	0	65.909	245.547	3.7	38.6
54	25	121	7.1	1501.398	30.1	3.2	80.647	120.697	6.6	16.6
54	10	94	5.9	1156.913	27	2.4	81.46	155.73	5.9	11.9
54	5	77	5.8	928.563	25.6	2.7	82.397	157.843	5.4	10.4
54	1	49	4	574.108	23.2	2.5	84.768	155.05	5.2	8.8
54	0.5	43	4.1	495.56	20.9	2.4	85.784	161.4	6.9	8.1
54	0.1	32	4.9	371.193	17.3	2.4	84.903	192.221	6.9	3.4

251

Figure A. 11: Master curve for Sample 6 (SP-III with PG 70-22 binder)

$$y = 0.0012x^2 - 0.1737x + 3.1376$$
$$R^2 = 0.9978$$
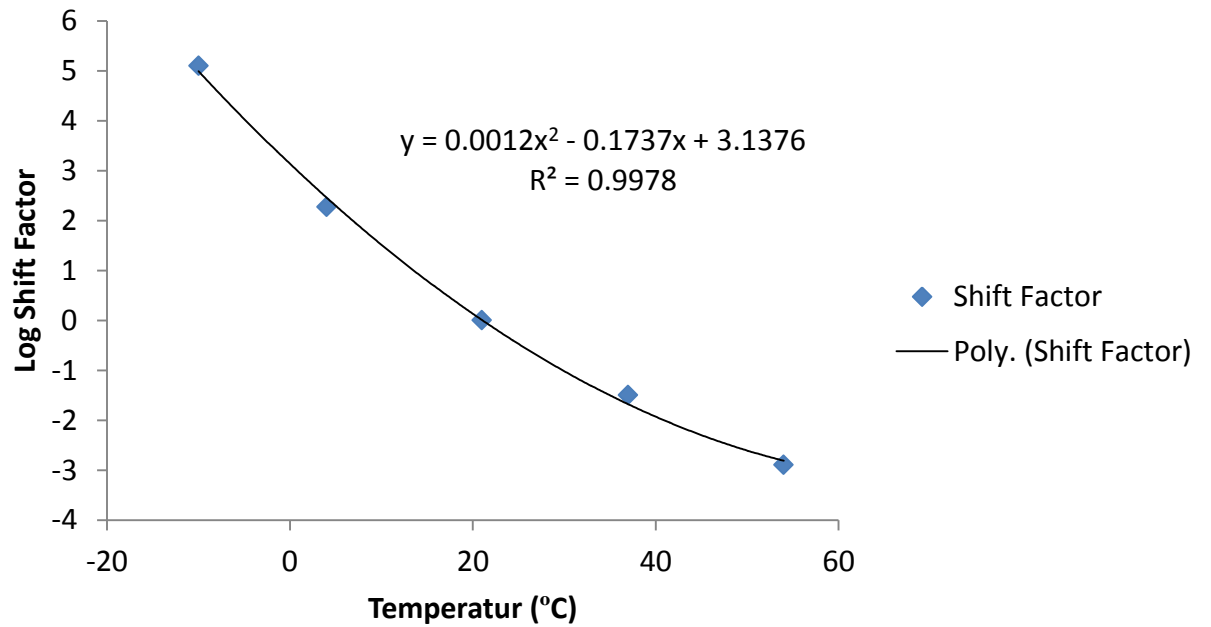
Figure A. 12: Shift factor for Sample 6 (SP-III with PG 70-22 binder)

252

APPENDIX B

Dynamic Modulus Test Results for SP-III with PG 64-22 Binder

Table B. 1: *E** test results for Sample 1 (SP-III with PG 64-22 binder)

Temperature	Frequency	Stress		Dynamic Modulus	Phase Angle		Strain			
		Amplitude (P-P)	SE			UC	(P-P) Recoverable	Permanent	SE	UC
(deg C)	(Hz)	(kPa)	(%)	(MPa)	(deg)	(deg)	(micro e)	(micro e)	(%)	(%)
-10	25	1692	5.4	31337.896	8.7	0	53.978	51.805	9	16.1
-10	10	1646	5.5	30917.109	6.3	1.7	53.232	16.918	6.8	18.4
-10	5	1599	4.4	30069.268	6.3	1.3	53.173	17.994	9.4	19.3
-10	1	1426	1.1	27965.736	7.4	3.1	51.005	19.13	6.4	18.6
-10	0.5	1387	0.6	27021.791	8.1	3.8	51.343	21.677	5.5	20.3
-10	0.1	1221	0.4	24568.281	8.3	1.9	49.689	34.553	6.3	20
4	25	1114	6.3	19062.848	15.7	0.4	58.43	69.156	9.9	8.1
4	10	1137	7	19328.514	9.1	0.5	58.829	46.958	8.2	8.1
4	5	1071	5.8	18027.525	9.7	0	59.402	49.703	6.6	5.5
4	1	874	2.1	15269.101	11.3	0.3	57.25	49.216	3.7	3.5
4	0.5	794	1.3	14043.222	12.1	1.2	56.574	54.39	2.6	2.4
4	0.1	642	0.7	11343.323	15.3	0.1	56.627	92.254	3.4	3.7
21	25	656	7.8	9663.283	21.5	2.2	67.886	303.004	13	17.7
21	10	580	8.3	9486.148	17.2	1.5	61.158	390.839	8.7	18.6
21	5	500	6.9	8529.991	18.5	1.2	58.575	442.694	7.2	15.7
21	1	347	3.8	6125.399	23.1	1.9	56.72	447.293	5.3	9.9
21	0.5	281	2	5094.076	25.2	1.4	55.103	472.697	5.5	1.6
21	0.1	192	0.9	3413.253	28	3.3	56.376	552.326	5.3	9.3
37	25	259	7.6	4714.375	34.1	7.9	54.851	347.461	11	17.5
37	10	227	7.4	3945.555	26.7	1.5	57.447	535.292	6.2	7.9
37	5	184	6.2	3177.973	27.7	2	57.814	610.915	5.2	8.2
37	1	108	2.9	1807.236	29.8	4.8	59.605	608.898	3.7	4.1
37	0.5	86	2.1	1431.4	29.6	5.4	59.951	626.89	3.7	9.7
37	0.1	52	1.6	851.621	27.3	6.2	60.775	676.02	2.9	23.7
54	25	106	6.5	1777.092	33.4	10.3	59.382	168.863	7.2	29.5
54	10	82	5.7	1315.882	30.6	3.2	62.524	267.143	5.8	19.9
54	5	65	4.7	1023.748	29.1	4.3	63.5	303.366	5.6	12.7
54	1	45	2.3	580.03	26.1	6.4	76.893	312.06	3.8	9.3
54	0.5	40	2.3	489.127	23.9	6.1	81.084	329.09	6	15.8
54	0.1	37	1.7	369.198	17.9	4.3	100.621	399.629	7.7	25.3

254

Figure B. 1: Master curve for Sample 1 (SP-III with PG 64-22 binder)

$y = 0.0017x^2 - 0.2211x + 3.7221$

$R^2 = 0.9918$

Figure B. 2: Shift factor for Sample 1 (SP-III with PG 64-22 binder)

255

Table B. 2: *E** test results for Sample 2 (SP-III with PG 64-22 binder)

Temperature	Frequency	Stress		Dynamic Modulus	Phase Angle		Strain			
		Amplitude (P-P)	SE			UC	(P-P) Recoverable	Permanent	SE	UC
(deg C)	(Hz)	(kPa)	(%)	(MPa)	(deg)	(deg)	(micro e)	(micro e)	(%)	(%)
-10	25	1684	6.1	39516.027	8.9	0.4	42.61	37.892	8.1	21.3
-10	10	1636	6.9	39410.977	5.5	0.4	41.512	11.03	7.6	23.2
-10	5	1589	5.1	38824.109	4.7	0.1	40.929	12.448	7.1	23.1
-10	1	1424	1.4	34941.195	7.1	0.8	40.746	13.37	5.5	24
-10	0.5	1387	0.8	34042.211	6.8	0	40.75	15.708	6.8	22.6
-10	0.1	1218	0.5	31414.158	7	0	38.766	23.558	6.7	24.9
4	25	1506	6.2	24130.764	12.2	2.7	62.427	93.1	8.9	21.6
4	10	1449	7.2	22428.479	9.3	0.1	64.608	44.845	8.5	12.9
4	5	1356	5.6	20991.328	9.7	0.5	64.589	45.512	6.4	13.2
4	1	1144	1.9	17791.613	11.2	0	64.308	45.277	4.5	13.2
4	0.5	1065	1.1	16397.324	12.3	0.5	64.972	51.53	3	10.1
4	0.1	838	0.5	13484.795	14.6	0.6	62.139	88.915	3.5	8.3
21	25	664	6.7	11463.028	22.7	6.9	57.959	210.758	11	23.7
21	10	578	6.9	11011.873	17.3	1	52.475	265.408	6.7	33.4
21	5	500	5.9	9854.926	17.9	0.6	50.765	299.03	6.4	33.5
21	1	348	3	7012.647	21.8	1.9	49.695	298.292	5.3	36.7
21	0.5	282	2	5800.085	24.3	0.4	48.667	317.822	5.1	36.5
21	0.1	194	0.7	3820.879	26.8	1.5	50.789	394.336	3.8	39
37	25	320	7.7	5212.354	31.8	14.9	61.46	363.564	15	30.3
37	10	275	6.6	4033.591	26.5	3.4	68.189	522.086	8.3	45.5
37	5	228	5.4	3302.319	27.8	3	68.925	588.309	7.8	45.2
37	1	135	2.5	1894.822	30.3	3.9	71.114	573.641	5.8	47.7
37	0.5	107	1.6	1494.127	30.6	3.7	71.339	585.409	4.9	49.3
37	0.1	65	1	898.829	28.8	2.3	71.922	625.897	4.8	53.6
54	25	112	7.1	1852.333	45.5	25.5	60.432	255.664	14	9.3
54	10	80	6.6	1358.079	32.2	7.3	59.113	348.747	8.9	19
54	5	61	5.3	1034.453	31.1	7.5	59.117	377.314	9.1	24.8
54	1	34	3.1	564.193	27.3	8.6	59.62	366.493	8.8	46.2
54	0.5	28	3.3	471.387	23.6	8.5	59.281	373.442	13	57.9
54	0.1	23	2.5	318.732	19	4.8	71.133	410.3	7.3	68.8

Figure B. 3: Master curve for sample 2 (SP-III with PG 64-22 binder)

$$y = 0.0018x^2 - 0.2306x + 3.8416$$
$$R^2 = 0.9912$$

Figure B. 4: Shift factor for sample 2 (SP-III with PG 64-22 binder)

257

Table B. 3: *E** test results for Sample 3 (SP-III with PG 64-22 binder)

Temperature	Frequency	Stress		Dynamic Modulus	Phase Angle		Strain			
		Amplitude (P-P)	SE			UC	(P-P) Recoverable	Permanent	SE	UC
(deg C)	(Hz)	(kPa)	(%)	(MPa)	(deg)	(deg)	(micro e)	(micro e)	(%)	(%)
-10	25	1429	6.8	24301.539	4.9	2.7	58.805	52.445	8.3	24.8
-10	10	1442	7.3	22754.941	5.4	0.7	63.351	20.351	8.5	18.8
-10	5	1408	5.8	22090.209	4.7	0.2	63.748	22.041	8.7	19.2
-10	1	1266	1.8	20305.637	4.8	0	62.338	22.718	5.6	18.3
-10	0.5	1189	1.1	19241.973	5.3	0.1	61.774	24.801	4.7	16.4
-10	0.1	1080	0.5	17721.838	7.8	0.9	60.927	41.729	6.1	18
4	25	953	8.1	18866.928	10.8	6.4	50.497	50.451	17	16.4
4	10	927	7.9	18478.998	10.4	1.5	50.186	40.853	12	25.8
4	5	882	6.7	17472.617	10.8	1.5	50.488	42.111	11	27.3
4	1	752	2.7	15062.924	12.4	0.9	49.931	41.418	9.4	24.9
4	0.5	691	1.7	13657.909	15.1	1.8	50.627	47.003	7.7	25
4	0.1	621	0.6	10957.547	17.4	2.4	56.712	89.554	6.7	22.5
21	25	857	7.8	10678.063	20.1	3	80.218	444.809	11	38.6
21	10	727	8.2	9272.583	18.4	0.8	78.391	466.628	8.6	24
21	5	630	7.6	8148.166	19.2	0.6	77.258	489.383	7.7	21.7
21	1	415	4.5	5614.063	24.4	0.9	73.875	457.89	4.6	18.6
21	0.5	349	3.2	4731.282	26.3	1.3	73.801	465.705	4	17.2
21	0.1	226	1.2	3025.313	28.6	1.9	74.771	530.577	3.2	17.7
37	25	254	9.9	4981.711	35.9	14.4	50.901	303.246	14	41.6
37	10	215	9.8	3732.825	28.4	3.1	57.608	369.513	8.5	21.2
37	5	186	9.2	2988.708	29.6	3.7	62.213	376.951	8.2	20.1
37	1	126	5.9	1644.457	32.4	4.2	76.579	344.634	6.4	20
37	0.5	106	4.2	1283.537	32.8	4.1	82.532	349.247	4.7	20.9
37	0.1	73	1.6	782.056	30.5	4.3	93.949	414.95	3.8	18.8
54	25	82	9.7	1578.961	33.7	2.5	51.729	119.921	8.5	0.3
54	10	67	8.6	1193.614	29.8	1.7	56.399	177.158	6.3	2.5
54	5	57	8.1	948.844	28.5	1.9	59.672	198.294	5.9	4
54	1	36	5.7	580.198	26.3	2.5	62.144	197.478	5	5.9
54	0.5	32	4.5	500.923	23.6	1.9	62.954	204.956	5	6.4
54	0.1	24	2	364.013	19.8	1.4	67.084	234.518	5.3	11.8

Figure B. 5: Master curve for sample 3 (SP-III with PG 64-22 binder)

$y = 0.0005x^2 - 0.1359x + 2.6849$

$R^2 = 0.9994$
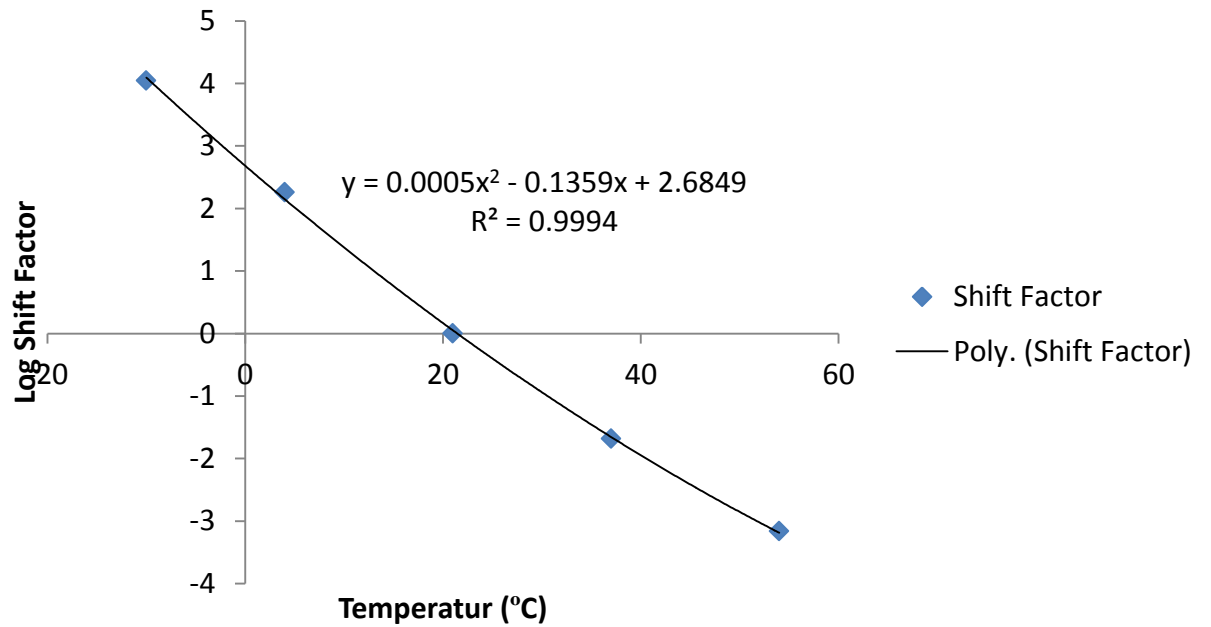
Figure B. 6: Shift factor for sample 3 (SP-III with PG 64-22 binder)

Table B. 4: *E** test results for Sample 4 (SP-III with PG 64-22 binder)

Temperature	Frequency	Stress		Dynamic Modulus	Phase Angle		Strain			
		Amplitude (P-P)	SE			UC	(P-P) Recoverable	Permanent	SE	UC
(deg C)	(Hz)	(kPa)	(%)	(MPa)	(deg)	(deg)	(micro e)	(micro e)	(%)	(%)
-10	25	2187	6.6	28456.047	5.5	0.5	76.859	62.24	8.3	20.1
-10	10	2177	6.4	28372.594	5.2	0.8	76.717	2.745	6.5	1.5
-10	5	2102	5.2	27799.273	4.8	0.7	75.63	4.019	6.1	1.4
-10	1	1878	1.8	25733.543	4.5	0.7	72.976	0.97	6.6	1.5
-10	0.5	1796	1	25433.66	6.7	1.3	70.598	2.879	9	0.8
-10	0.1	1681	0.4	22739.225	6.6	0.7	73.925	16.537	5.1	2.1
4	25	1520	7.8	22645.568	10.3	2.6	67.135	91.752	8.9	6.5
4	10	1481	8	21738.816	8	0.6	68.125	40.728	9.1	8.4
4	5	1418	6.8	20769.295	8.4	0.3	68.295	41.186	7	9.1
4	1	1207	3	17927.912	10.5	1	67.348	40.327	11	10.3
4	0.5	1106	1.9	17511.275	10.2	0.4	63.156	45.375	6.7	14
4	0.1	994	0.6	13964.575	12.4	0.6	71.148	83.804	4.7	13
21	25	863	8.9	13227.816	12.9	4.4	65.274	201.785	16	51.6
21	10	728	8.3	12289.354	15.3	0.2	59.264	186.334	7.3	25.4
21	5	629	7.7	11166.761	16	0.6	56.302	190.617	8.5	21.3
21	1	432	4.3	7879.575	19.8	0.9	54.794	168.735	5	13.2
21	0.5	381	2.8	7059.471	21.9	0.3	54.012	171.617	5.2	7.2
21	0.1	302	1.6	4674.593	24.2	0.4	64.687	249.973	4.6	2
37	25	375	9.3	6440.611	17.6	17.8	58.249	282.743	27	63.6
37	10	320	11	5783.175	24.4	0.4	55.292	393.382	8.9	35
37	5	273	8.4	4508.117	25.9	0.7	60.568	439.345	7.2	27.4
37	1	183	4.9	2673.577	29.5	0.8	68.273	425.222	4.7	24.1
37	0.5	151	3.3	2097.048	30	1.1	72.095	432.399	4.1	22.3
37	0.1	112	2	1232.507	28.9	1.5	90.821	509.339	4	20.2
54	25	138	9	2241.489	36.1	7.8	61.533	276.176	12	11.9
54	10	120	11	1633.508	32.6	3.8	73.189	435.834	8.7	26.5
54	5	96	9.8	1244.183	31.5	3.5	77.034	511.597	7.9	24.4
54	1	65	7	719.161	28.8	2.6	90.103	538.588	7.7	29.2
54	0.5	58	5.3	595.869	26.3	2.7	98.107	564.89	8	27
54	0.1	46	2.4	415.15	20.7	2.3	111.389	633.451	7.5	28.8

Figure B. 7: Master curve for sample 4 (SP-III with PG 64-22 binder)

$$y = 0.0008x^2 - 0.1624x + 3.0576$$
$$R^2 = 0.9991$$

Figure B. 8: Shift factor for sample 4 (SP-III with PG 64-22 binder)

Table B. 5: *E** test results for Sample 5 (SP-III with PG 64-22 binder)

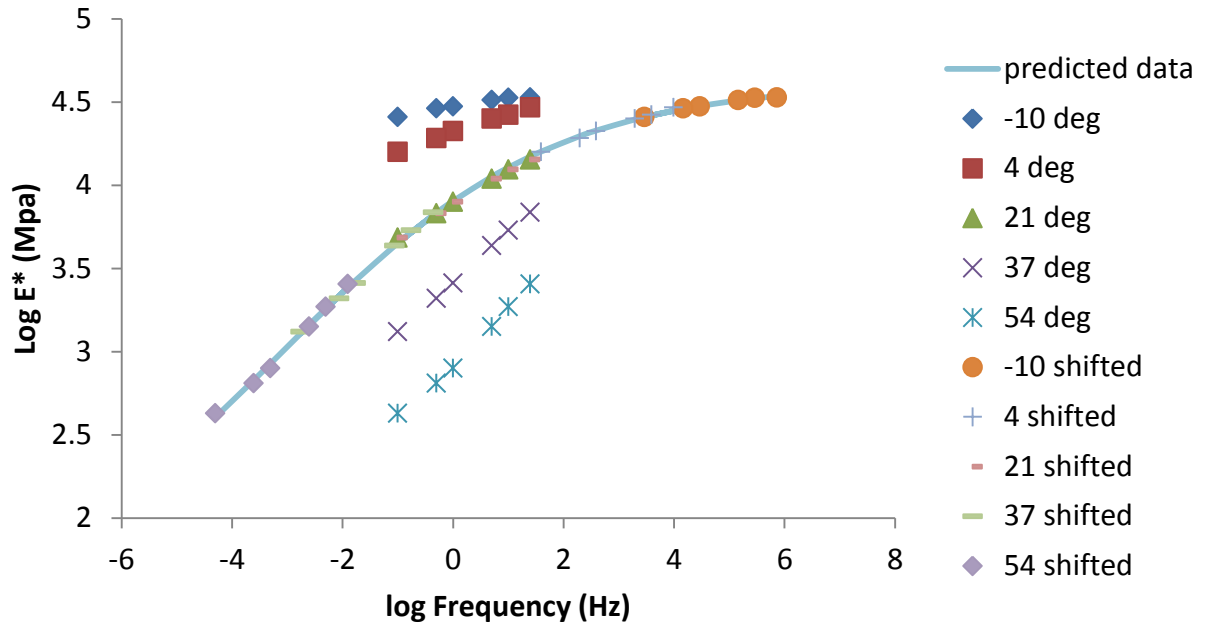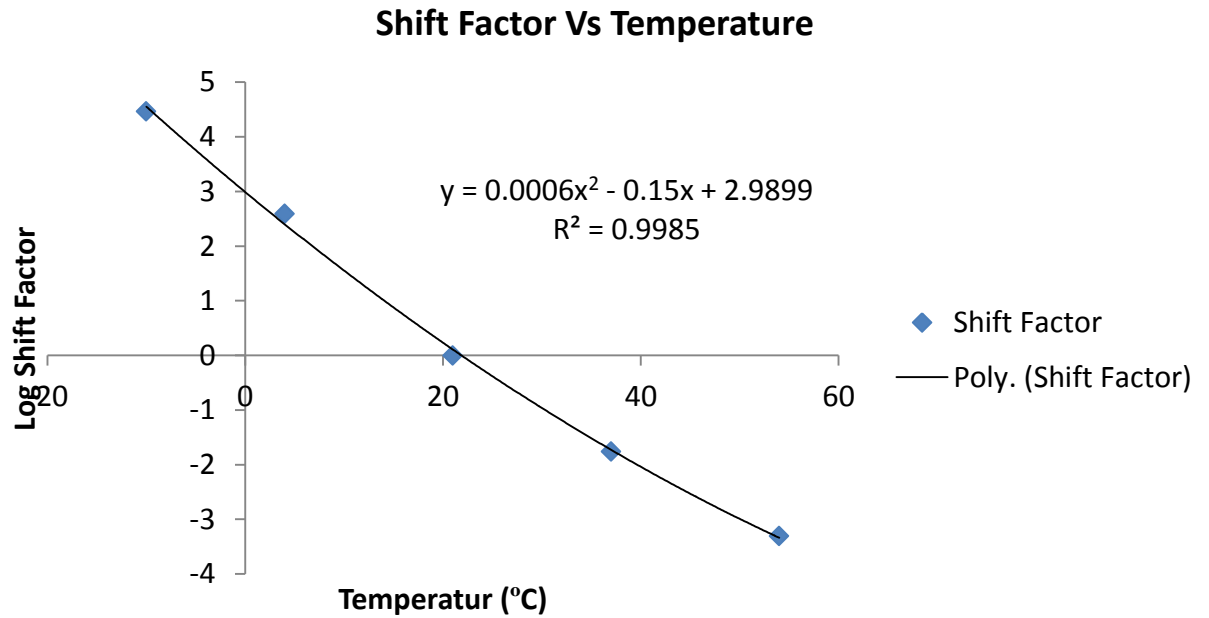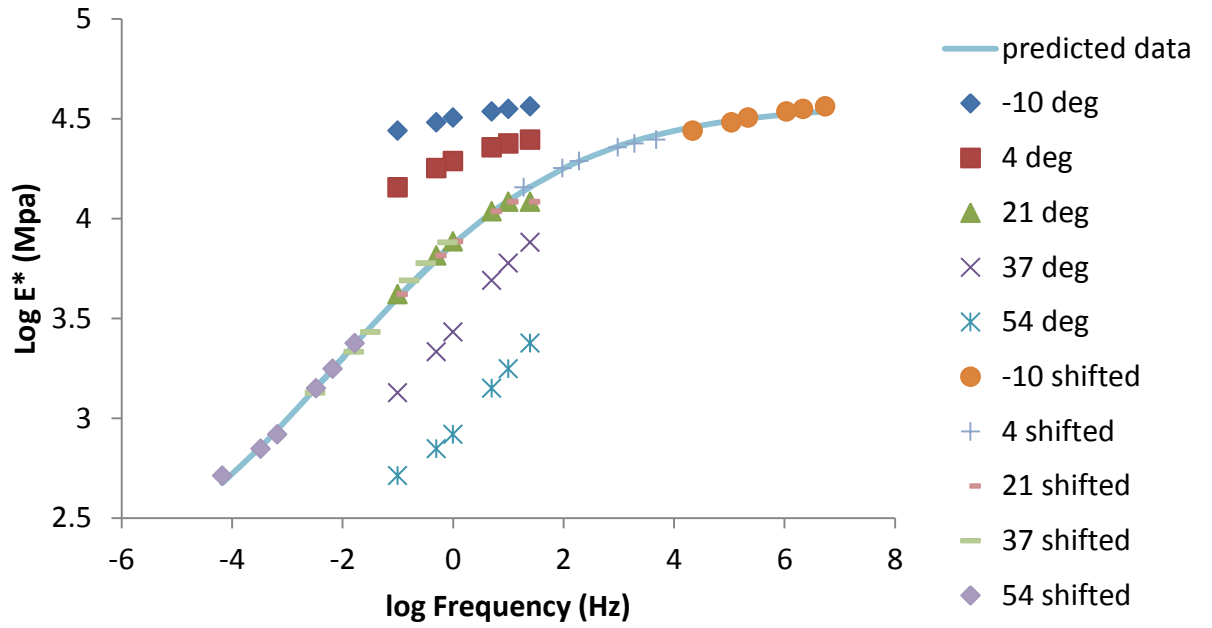| Temperature | Frequency | Stress | | Dynamic Modulus | Phase Angle | | Strain | | | |
		Amplitude (P-P)	SE			UC	(P-P) Recoverable	Permanent	SE	UC
(deg C)	(Hz)	(kPa)	(%)	(MPa)	(deg)	(deg)	(micro e)	(micro e)	(%)	(%)
-10	25	2192	6.4	38748.406	1.9	1.9	56.563	52.91	12	14.3
-10	10	2176	5.8	36853.953	4.4	0.4	59.036	9.812	9.2	19.8
-10	5	2097	4.7	35965.59	4.3	0.4	58.292	9.775	8.3	19.6
-10	1	1874	1.4	34554.699	2.6	1.9	54.238	8.273	10	23.7
-10	0.5	1794	0.8	31582.086	5.3	0.3	56.803	9.792	8.9	20.3
-10	0.1	1680	0.4	29829.203	7.3	1	56.322	16.376	11	23.6
4	25	1524	7.5	26037.035	8.9	0.4	58.539	73.61	8.4	3.3
4	10	1483	7.6	26481.822	8	0.2	56.007	33.148	9.3	2
4	5	1417	6.3	25162.861	7.6	0.5	56.331	32.932	7.7	2.6
4	1	1205	2.7	22245.033	8.6	0.2	54.156	32.577	8.6	4.3
4	0.5	1104	1.7	19868.914	10	0	55.565	36.347	5.4	3.1
4	0.1	994	0.6	17175.463	13.1	0.2	57.85	65.689	6.6	7
21	25	862	8.2	14808.646	14.3	1.5	58.219	172.062	8.3	19.7
21	10	722	8.6	13637.328	16.1	0.2	52.962	166.569	8.8	35.8
21	5	628	7.9	12292.71	16.9	0.1	51.053	170.177	7.9	35.8
21	1	432	4.5	8902.611	21	0.2	48.521	158.188	5.1	35.6
21	0.5	383	3	7830.484	23.9	1.6	48.887	166.822	3.9	40.5
21	0.1	303	1.5	5199.132	25	0.9	58.201	239.084	5.8	40.2
37	25	373	10	7385.051	25.9	6	50.51	342.779	9.3	2.4
37	10	319	11	5762.308	24.6	1.1	55.29	467.933	7.9	14.9
37	5	268	8.6	4475.339	26.1	1	59.975	526.967	6.9	22.4
37	1	183	4.8	2584.46	28.9	1.2	70.854	529.718	4.7	30.5
37	0.5	152	3.2	2058.192	28.9	1.6	73.648	547.601	3.8	31.5
37	0.1	113	1.6	1262.099	26.8	1.3	89.684	631.441	4.9	30.3
54	25	136	8.4	2066.465	33.2	9.3	65.925	415.987	7.1	18.2
54	10	120	7.6	1559.874	31.4	0.8	77.222	620.206	4.5	28.1
54	5	96	7.1	1174.072	30.6	1.5	82.168	709.648	4	30.6
54	1	65	5.2	659.145	28.6	2.6	98.148	734.073	4.3	30
54	0.5	59	3.8	539.239	26.4	3.4	108.816	767.766	5.2	26.9
54	0.1	46	1.7	366.955	21.3	3.9	125.853	855.931	7.6	19

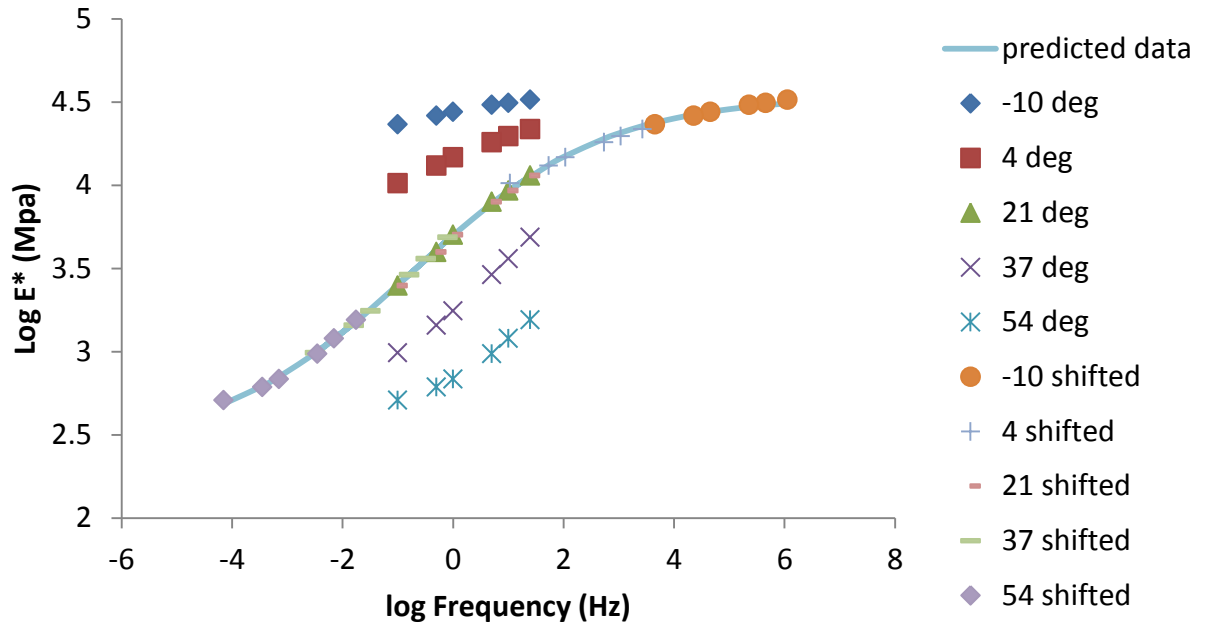Figure B. 9: Master curve for sample 5 (SP-III with PG 64-22 binder)
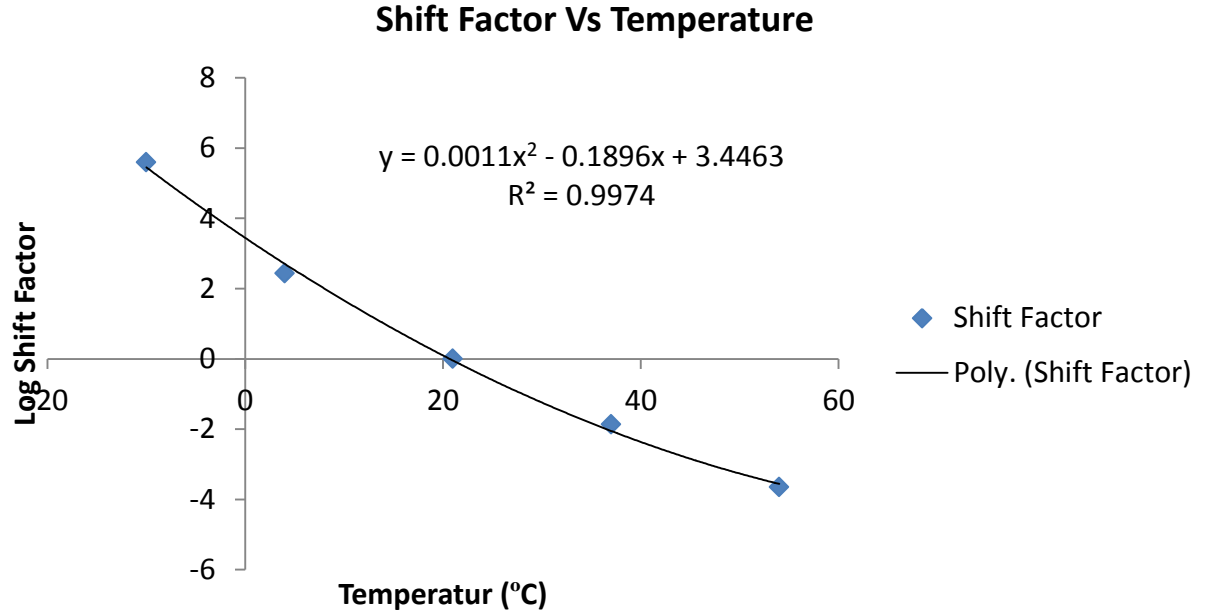
Figure B. 10: Shift factor for sample 5 (SP-III with PG 64-22 binder)

263

Table B. 6: *E** test results for Sample 6 (SP-III with PG 64-22 binder)

Temperature	Frequency	Stress		Dynamic Modulus	Phase Angle		Strain			
		Amplitude (P-P)	SE			UC	(P-P) Recoverable	Permanent	SE	UC
(deg C)	(Hz)	(kPa)	(%)	(MPa)	(deg)	(deg)	(micro e)	(micro e)	(%)	(%)
-10	25	1684	6.1	39516.027	8.9	0.4	42.61	37.892	8.1	21.3
-10	10	1636	6.9	39410.977	5.5	0.4	41.512	11.03	7.6	23.2
-10	5	1589	5.1	38824.109	4.7	0.1	40.929	12.448	7.1	23.1
-10	1	1424	1.4	34941.195	7.1	0.8	40.746	13.37	5.5	24
-10	0.5	1387	0.8	34042.211	6.8	0	40.75	15.708	6.8	22.6
-10	0.1	1218	0.5	31414.158	7	0	38.766	23.558	6.7	24.9
4	25	1506	6.2	24130.764	12.2	2.7	62.427	93.1	8.9	21.6
4	10	1449	7.2	22428.479	9.3	0.1	64.608	44.845	8.5	12.9
4	5	1356	5.6	20991.328	9.7	0.5	64.589	45.512	6.4	13.2
4	1	1144	1.9	17791.613	11.2	0	64.308	45.277	4.5	13.2
4	0.5	1065	1.1	16397.324	12.3	0.5	64.972	51.53	3	10.1
4	0.1	838	0.5	13484.795	14.6	0.6	62.139	88.915	3.5	8.3
21	25	664	6.7	11463.028	22.7	6.9	57.959	210.758	11	23.7
21	10	578	6.9	11011.873	17.3	1	52.475	265.408	6.7	33.4
21	5	500	5.9	9854.926	17.9	0.6	50.765	299.03	6.4	33.5
21	1	348	3	7012.647	21.8	1.9	49.695	298.292	5.3	36.7
21	0.5	282	2	5800.085	24.3	0.4	48.667	317.822	5.1	36.5
21	0.1	194	0.7	3820.879	26.8	1.5	50.789	394.336	3.8	39
37	25	320	7.7	5212.354	31.8	14.9	61.46	363.564	15	30.3
37	10	275	6.6	4033.591	26.5	3.4	68.189	522.086	8.3	45.5
37	5	228	5.4	3302.319	27.8	3	68.925	588.309	7.8	45.2
37	1	135	2.5	1894.822	30.3	3.9	71.114	573.641	5.8	47.7
37	0.5	107	1.6	1494.127	30.6	3.7	71.339	585.409	4.9	49.3
37	0.1	65	1	898.829	28.8	2.3	71.922	625.897	4.8	53.6
54	25	112	7.1	1852.333	45.5	25.5	60.432	255.664	14	9.3
54	10	80	6.6	1358.079	32.2	7.3	59.113	348.747	8.9	19
54	5	61	5.3	1034.453	31.1	7.5	59.117	377.314	9.1	24.8
54	1	34	3.1	564.193	27.3	8.6	59.62	366.493	8.8	46.2
54	0.5	28	3.3	471.387	23.6	8.5	59.281	373.442	13	57.9
54	0.1	23	2.5	318.732	19	4.8	71.133	410.3	7.3	68.8

264

Figure B. 11: Master curve for sample 6 (SP-III with PG 64-22 binder)

$$y = 0.0015x^2 - 0.1996x + 3.7002$$
$$R^2 = 0.9985$$

Figure B. 12: Shift factor for sample 6 (SP-III with PG 64-22 binder)

265

APPENDIX C

Dynamic Modulus Test Results for SP-II with PG 64-22 Binder

Table C. 1: E* test results for Sample 1 (SP-II with PG 64-22 binder)

Temperature	Frequency	Stress Amplitude (P-P)	SE	Dynamic Modulus	Phase Angle	UC	Strain (P-P) Recoverable	Permanent	SE	UC
(deg C)	(Hz)	(kPa)	(%)	(MPa)	(deg)	(deg)	(micro e)	(micro e)	(%)	(%)
-10	25	2078	5.6	35496.758	7.3	1.3	58.541	56.55	8.5	36.2
-10	10	2042	5.6	33913.875	5.4	2.1	60.222	13.497	7.7	34
-10	5	1982	4.7	32930.559	5.4	2	60.196	13.227	5.7	34.1
-10	1	1732	1.4	30479.164	6	2.6	56.811	12.795	4.7	35.9
-10	0.5	1743	0.7	28896.313	7	2.7	60.329	14.955	2.7	36.9
-10	0.1	1561	0.5	27275.375	7.5	2.6	57.228	22.703	3.3	35.1
4	25	1508	6.4	23246.865	10	0.3	64.869	107.336	7.3	22.2
4	10	1376	6.4	21961.838	8.5	1.8	62.634	53.261	7.1	21.3
4	5	1301	5.4	20698	8.9	1.5	62.858	58.107	5.9	21.3
4	1	1082	1.9	17775.93	10.2	0.7	60.858	58.883	7.7	21.1
4	0.5	977	1.1	16000.103	13.2	3	61.067	65.299	2.8	25.2
4	0.1	831	0.5	13364.011	14.6	1.7	62.172	105.128	3.1	25.4
21	25	856	6.4	15431.851	18.8	2.8	55.467	305.593	7.4	30.6
21	10	723	7.3	13307.329	18.4	3.2	54.358	346.984	7.1	23.9
21	5	625	6.5	11741.616	20	3.3	53.215	374.976	5.6	25.9
21	1	413	3.4	8275.877	24.9	3.4	49.889	363.451	4.2	27.7
21	0.5	348	2.4	7028.054	25.9	2.7	49.504	373.565	4.6	27
21	0.1	225	0.9	4524.876	28.5	2.8	49.807	426.507	4.2	26.1
37	25	499	7.2	7437.835	25.6	1.1	67.04	310.707	6.3	41.6
37	10	397	9	5847.632	25.6	1	67.903	354.776	5.7	38.2
37	5	295	8.4	4619.726	27.6	0.7	63.84	348.035	5.3	37.5
37	1	178	4.1	2600.065	31.4	0.2	68.319	311.343	4.8	33
37	0.5	140	2.9	2030.515	31.7	0.3	68.99	299.929	5	30.4
37	0.1	87	1.4	1197.621	30.7	1.1	72.597	322.399	4.4	27.4
54	25	109	8.4	2309.902	33.4	5.6	47.291	182.05	6	55.3
54	10	88	7.7	1673.724	29.7	6.2	52.38	231.082	5	43.9
54	5	75	7	1312.287	28.5	5.6	57.232	250.212	4.7	38.5
54	1	48	4	819.836	24.5	4.8	58.821	250.634	4.5	29.1
54	0.5	42	2.9	682.787	23.5	3.6	62.182	254.361	3.8	26.2
54	0.1	34	1.4	514.518	17.7	3.2	66.433	274.787	5	19.3

267
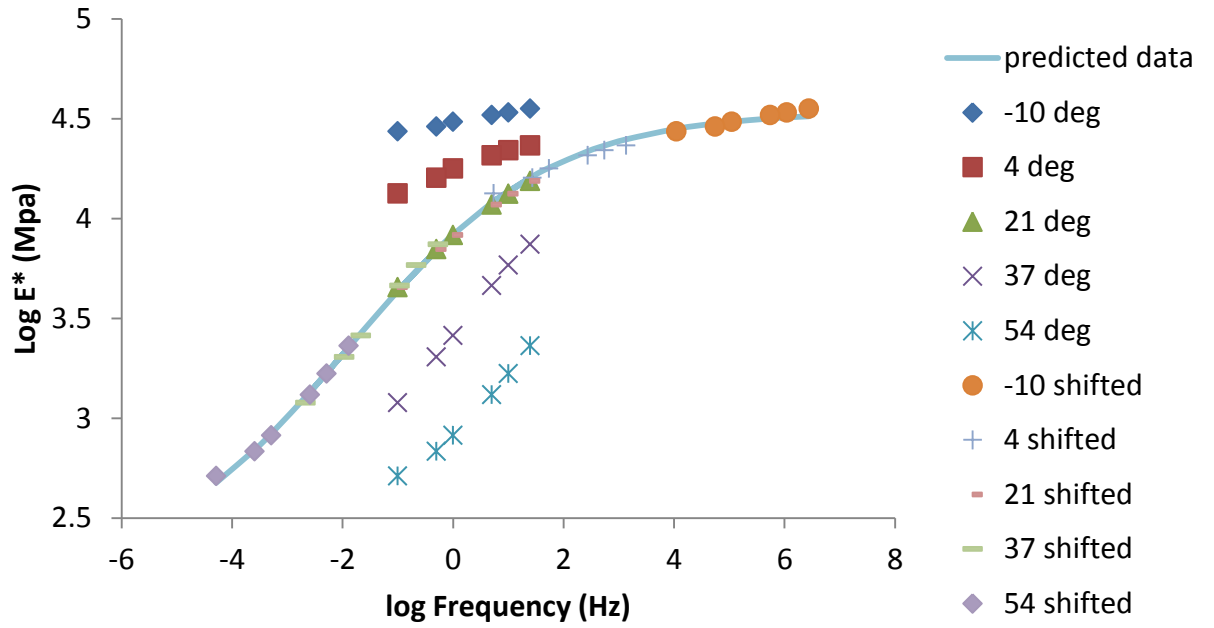
Figure C. 1: Master curve for sample 1 (SP-II with PG 64-22 binder)

$$y = 0.0011x^2 - 0.1719x + 2.9485$$
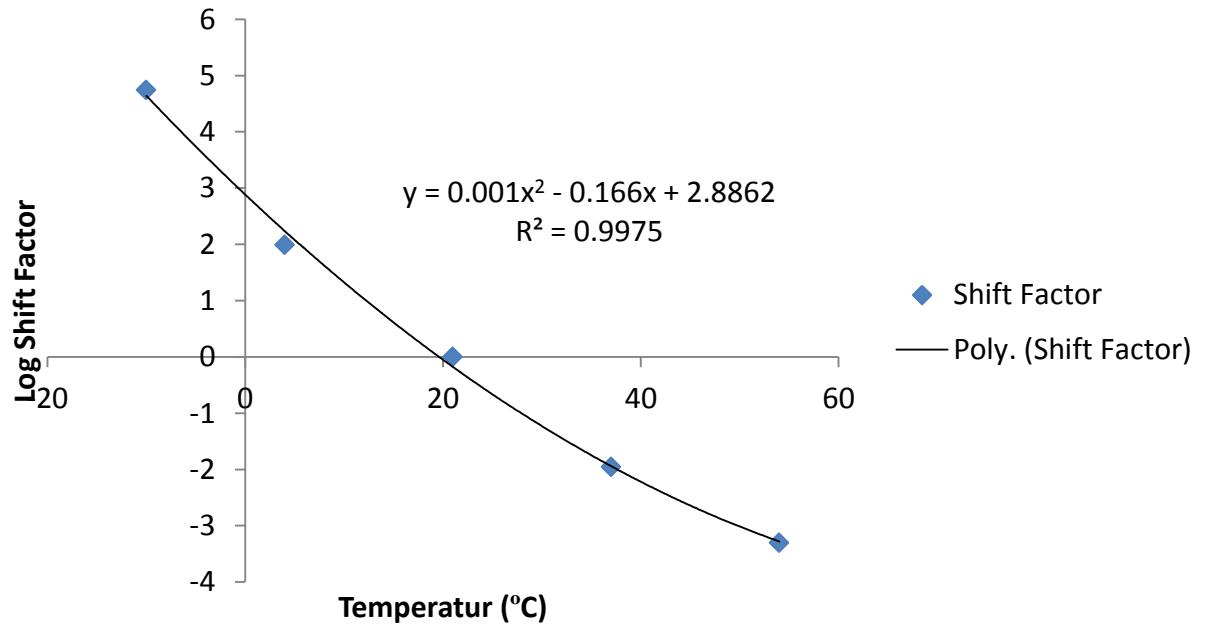$$R^2 = 0.9885$$

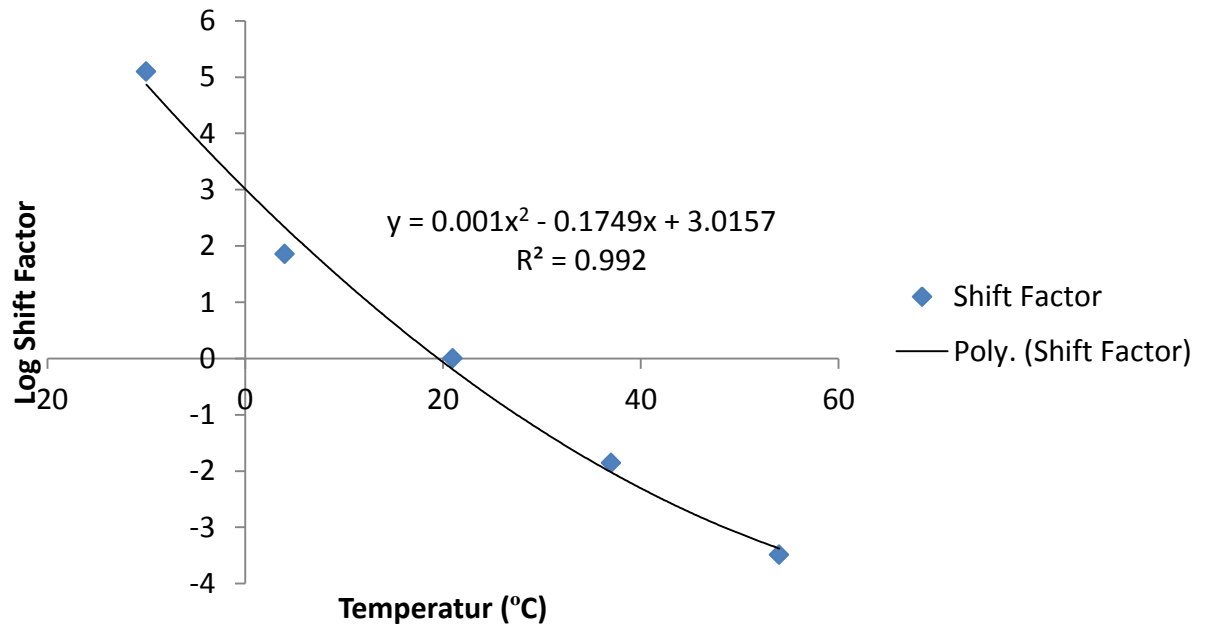Figure C. 2: Shift factor for sample 1 (SP-II with PG 64-22 binder)

Table C. 2: *E** test results for Sample 2 (SP-II with PG 64-22 binder)

| Temperature | Frequency | Stress | | | Phase Angle | | Strain | | | |
| | | Amplitude (P-P) | SE | Dynamic Modulus | | UC | (P-P) Recoverable | Permanent | SE | UC |
(deg C)	(Hz)	(kPa)	(%)	(MPa)	(deg)	(deg)	(micro e)	(micro e)	(%)	(%)
-10	25	2038	6.1	36369.063	7.3	2	56.043	61.216	10	7.1
-10	10	2067	6.1	35345.848	6.2	1.7	58.487	22.472	8	7.7
-10	5	2011	5.2	34335.277	6.1	1.8	58.564	25.55	6.7	7.7
-10	1	1804	1.5	32015.998	6.1	2.1	56.339	28.728	8	4.4
-10	0.5	1697	0.9	30246.063	8	2.2	56.119	30.371	4.3	3.2
-10	0.1	1543	0.5	27514.568	8.5	2.1	56.093	43.954	3.6	0.4
4	25	1521	6.3	24786.035	10.7	3.6	61.382	91.459	9.5	0.6
4	10	1490	6.5	23750.865	9	0.2	62.729	35.671	8.7	9.8
4	5	1420	5.2	22707.852	9	0.1	62.537	35.125	8.5	9.9
4	1	1201	1.7	19412.52	11.4	0.5	61.883	33.095	5	13.6
4	0.5	1103	1	17873.082	12.1	1	61.714	37.145	5.8	15.8
4	0.1	994	0.4	14309.274	15.3	0.2	69.443	82.434	3.9	17.2
21	25	855	7.3	12127.919	20	3.1	70.486	193.465	11	3
21	10	723	7.5	12137.903	17.5	0.3	59.534	161.287	7.7	28.9
21	5	626	6.8	10871.323	18.4	0.7	57.595	153.848	7.7	30.5
21	1	412	3.8	7686.097	23	0.4	53.6	124.476	4.2	30.6
21	0.5	348	2.5	6540.138	24.2	0.1	53.134	121.11	3.4	31.2
21	0.1	225	0.8	4174.866	27.3	0.2	53.915	154.915	3.1	32.1
37	25	485	8.9	7589.415	26.9	1.3	63.948	399.819	10	16.4
37	10	427	9.6	5981.912	26.5	2.2	71.301	498.915	7.8	22.8
37	5	364	9.1	4887.654	28	2.5	74.414	531.908	7.6	27.1
37	1	242	4.4	2706.521	31	2.2	89.236	514.193	6.7	36.7
37	0.5	200	3.2	2152.753	31.5	1.8	92.881	520.457	6	40.8
37	0.1	149	1.4	1342.989	30.3	0.5	110.685	606.569	5.7	44.2
54	25	137	9.1	2378.366	33.3	1.6	57.491	207.035	6.8	32.5
54	10	113	9.2	1769.989	30.2	1.1	64.014	262.814	6	25.5
54	5	97	8.7	1410.177	29.4	0.8	68.554	284.598	6	25.1
54	1	62	5.8	828.981	28.5	1	74.867	282.276	5.3	32.2
54	0.5	54	4.3	702.35	27	1	77.488	288.831	5.6	36.1
54	0.1	42	2.1	515.047	22.5	0.8	81.784	318.995	6.3	47.2

269
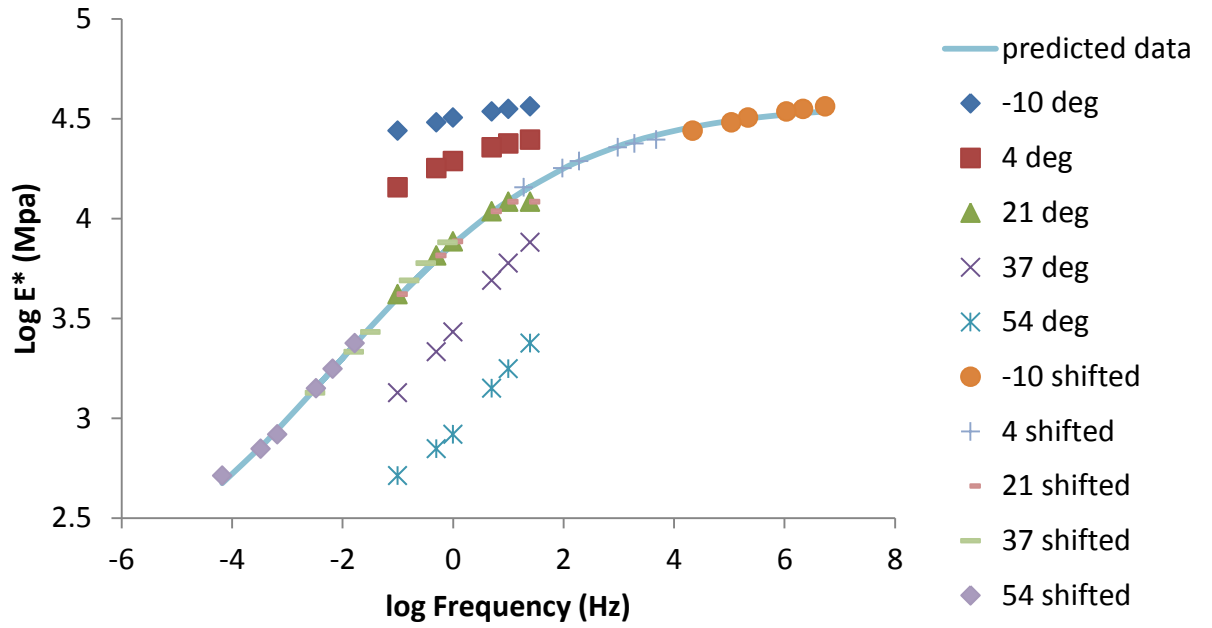
Figure C. 3: Master curve for sample 2 (SP-II with PG 64-22 binder)

$y = 0.0011x^2 - 0.1789x + 3.2716$
$R^2 = 0.9953$
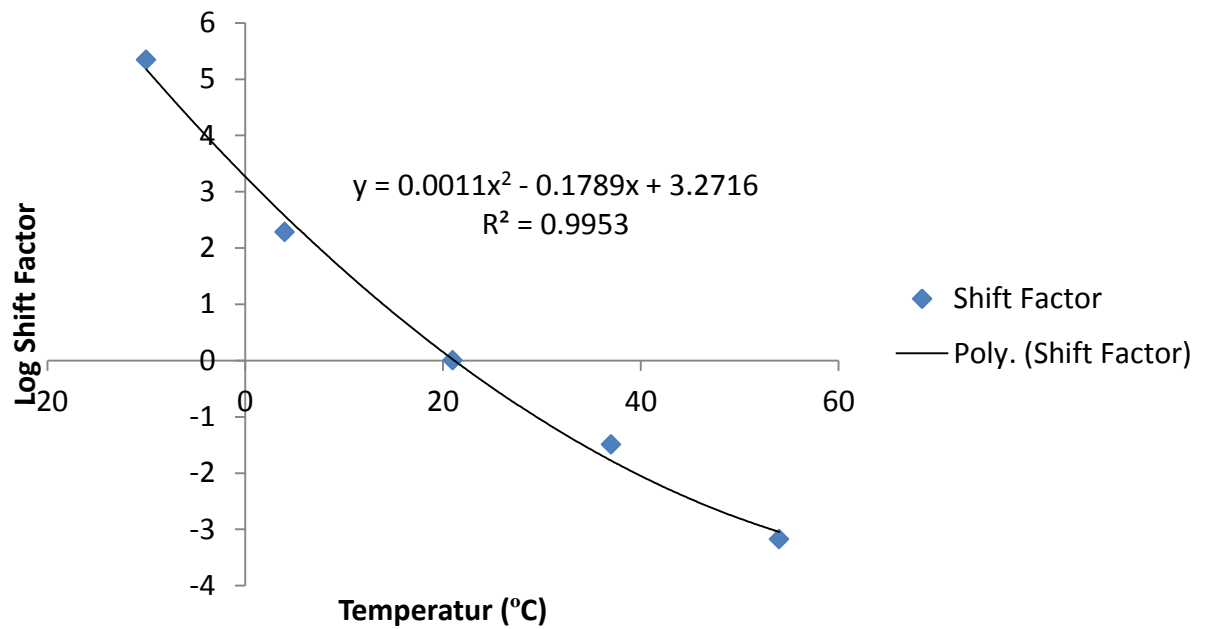
Figure C. 4: Shift factor for sample 2 (SP-II with PG 64-22 binder)

Table C. 3: *E** test results for Sample 3 (SP-II with PG 64-22 binder)

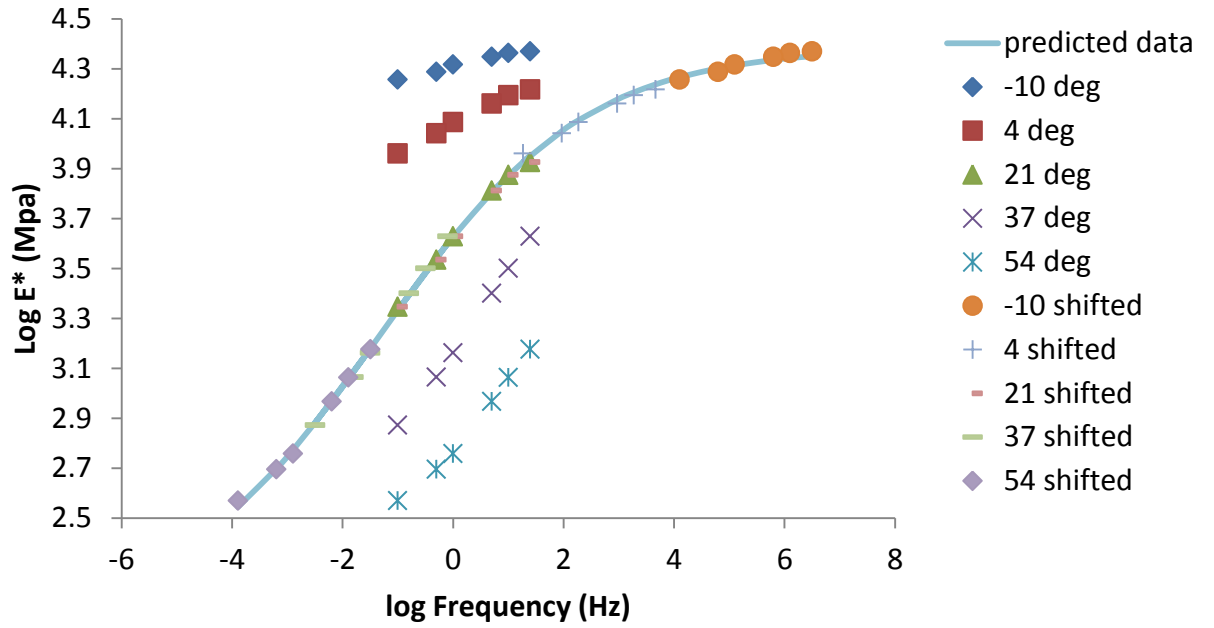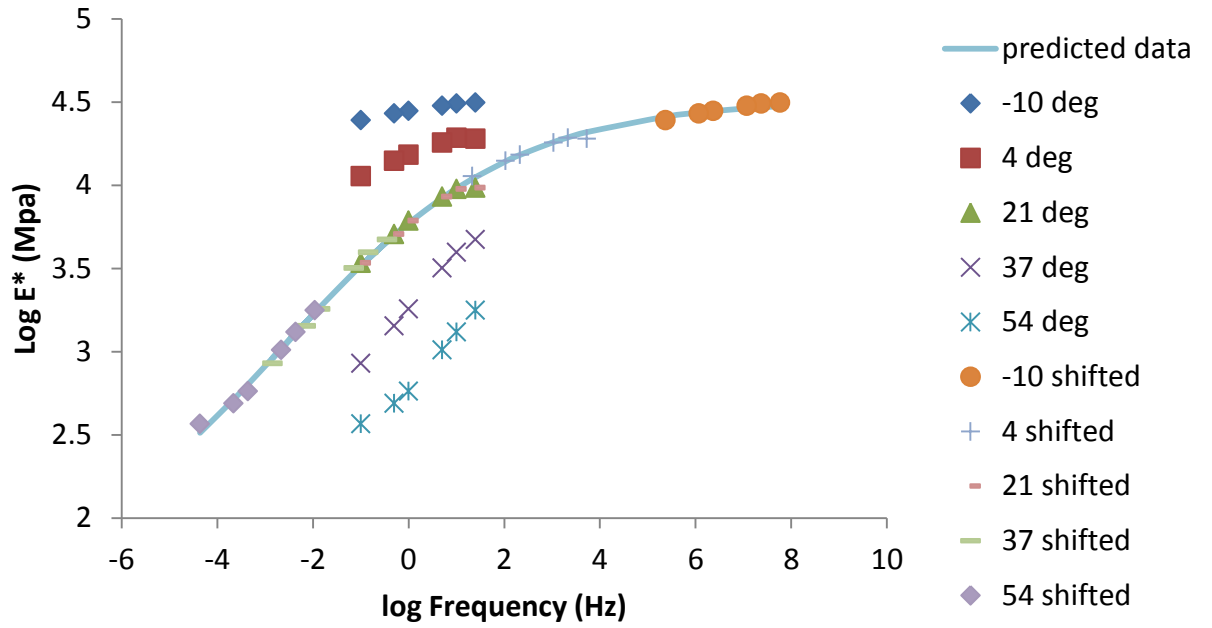| Temperature | Frequency | Stress | | | Phase Angle | | Strain | | | |
		Amplitude (P-P)	SE	Dynamic Modulus		UC	(P-P) Recoverable	Permanent	SE	UC
(deg C)	(Hz)	(kPa)	(%)	(MPa)	(deg)	(deg)	(micro e)	(micro e)	(%)	(%)
-10	25	2479	5.7	34573.656	5.5	0.7	71.714	86.201	23	15
-10	10	2435	5	33187.059	5.9	0.1	73.366	17.756	11	20.8
-10	5	2333	4.6	31952.471	6	1	73.027	16.391	12	19.4
-10	1	2052	1.1	29044.682	6.9	0.1	70.657	15.813	11	13.1
-10	0.5	1984	0.6	27750.891	7	1.1	71.507	18.27	12	11.3
-10	0.1	1742	0.4	24475.203	8.6	0.2	71.19	37.512	11	3.3
4	25	1598	8.1	31442.223	9.4	1.4	50.83	77.984	12	14.7
4	10	1586	7.8	28853.557	9	0.8	54.952	35.017	10	17.1
4	5	1505	6.6	27215.047	9.3	1.1	55.292	38.321	8.7	15.9
4	1	1259	2.7	23551.484	11.3	1.7	53.455	36.858	6.4	11
4	0.5	1137	1.6	22387.742	11.7	1.3	50.799	38.163	3.5	12.1
4	0.1	964	0.7	18269.055	14.1	1	52.779	70.114	3.3	6.9
21	25	1025	7.9	17994.422	15.5	1.5	56.95	251.191	12	6.3
21	10	952	7.7	15031.265	16.6	0.3	63.317	260.974	9.5	5.5
21	5	843	7.1	13415.535	17.6	0.4	62.813	285.964	8.5	6
21	1	593	3.9	10171.664	21.7	0.4	58.284	278.22	5.9	8.3
21	0.5	495	2.8	8995.204	23.1	0.5	55.027	290.251	5.7	11.1
21	0.1	341	1.5	6375.208	26.2	0.5	53.494	355.567	5.8	1.8
37	25	527	11	6204.32	25.7	3.1	84.889	347.693	14	16.3
37	10	426	11	5025.318	23.7	0.7	84.792	417.214	11	17.3
37	5	343	12	4218.61	24.8	0.7	81.292	432.946	10	18.5
37	1	223	8.2	2636.639	28	1.9	84.761	397.499	8.7	17.7
37	0.5	182	6.4	2178.816	28.8	2.6	83.528	398.814	7.4	13.2
37	0.1	116	2.7	1421.049	28.3	3.9	81.771	443.279	5.8	15.3
54	25	202	13	2388.001	30	3.3	84.564	382.143	20	11
54	10	164	12	1730.44	28.6	3.6	94.774	543.447	11	3
54	5	137	11	1395.827	28	3.6	98.056	621.081	9.1	3
54	1	87	7.7	855.588	27.2	3.7	101.416	625.51	7	18.2
54	0.5	79	5.5	715.444	25.7	3.6	110.018	647.736	5.6	24.7
54	0.1	59	2.4	490.544	22.1	1.6	119.715	713.906	4.8	38.1

Figure C. 5: Master curve for sample 3 (SP-II with PG 64-22 binder)
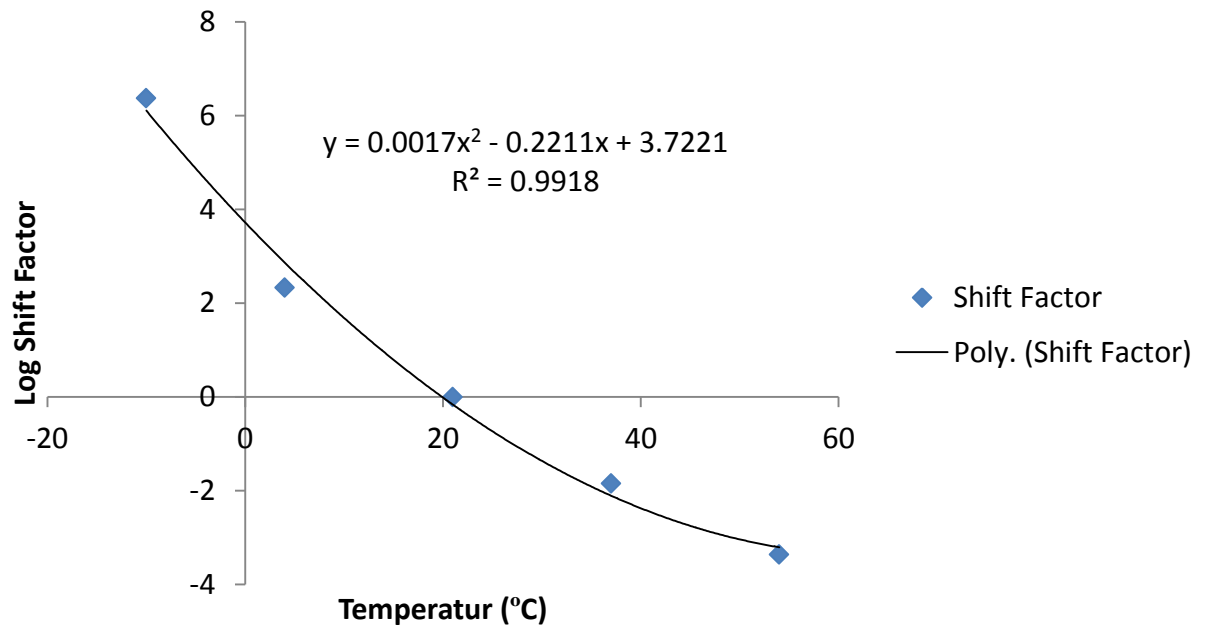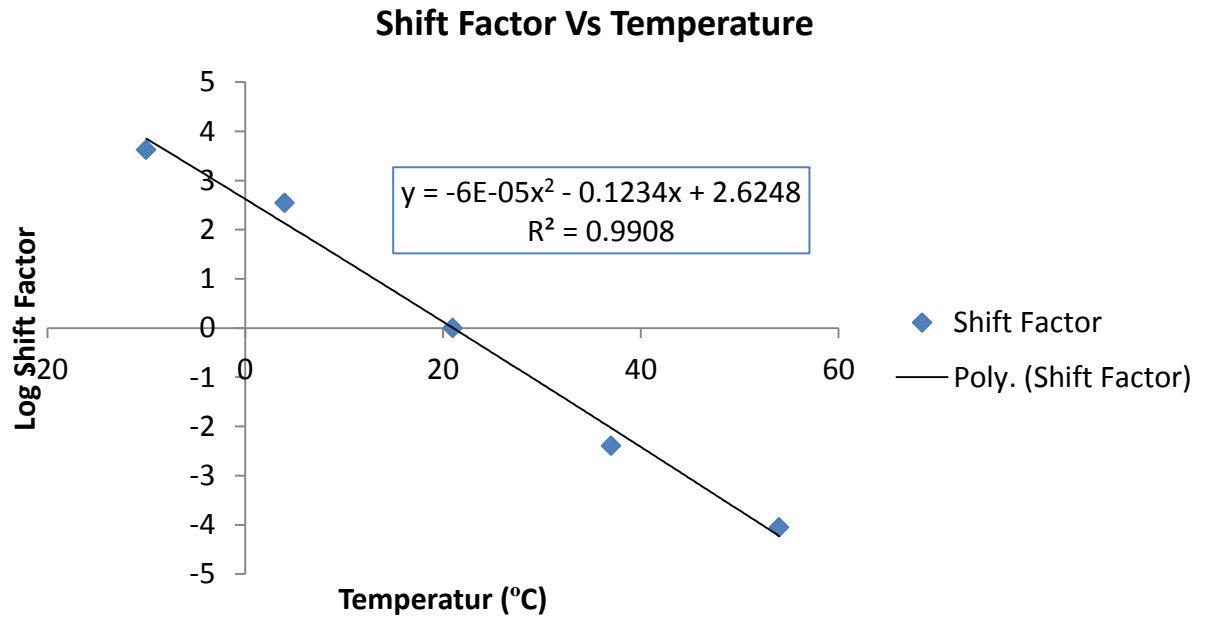

Figure C. 6: Shift factor for sample 3 (SP-II with PG 64-22 binder)

Table C. 4: *E** test results for Sample 4 (SP-II with PG 64-22 binder)

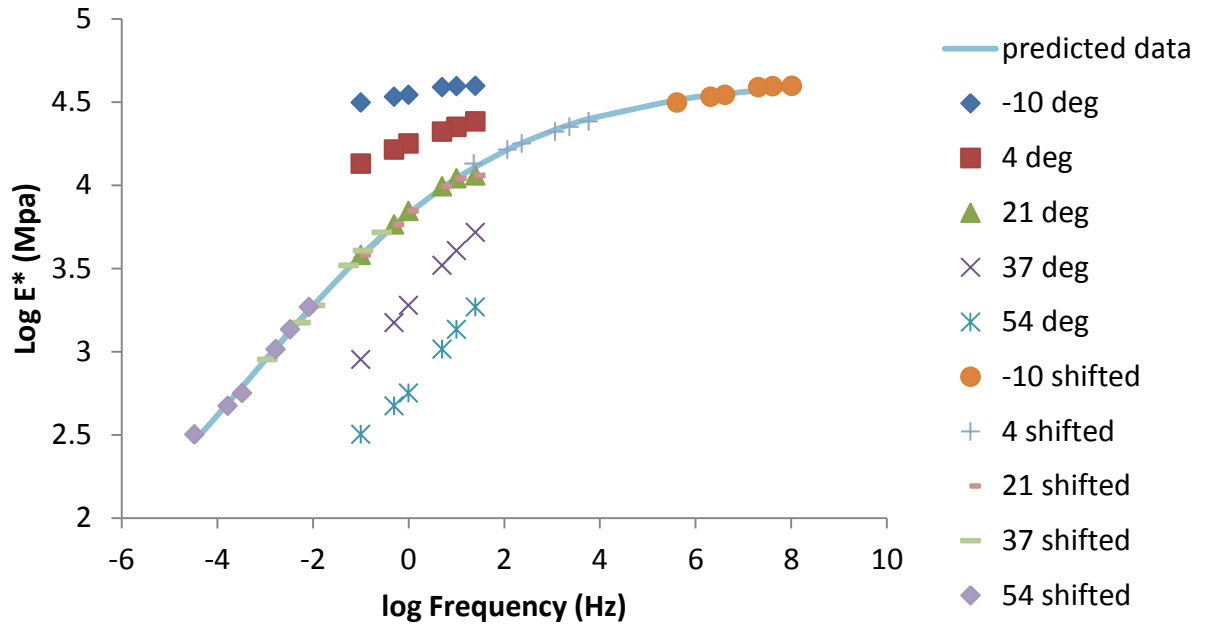| Temperature	Frequency	Stress Amplitude (P-P)	SE	Dynamic Modulus	Phase Angle	UC	Strain (P-P) Recoverable	Permanent	SE	UC
(deg C)	(Hz)	(kPa)	(%)	(MPa)	(deg)	(deg)	(micro e)	(micro e)	(%)	(%)
-10	25	1887	7.2	33972.43	9.4	5.1	55.555	59.167	9	14.3
-10	10	1902	6.8	33861.215	6.2	1.3	56.169	19.538	8.6	19.2
-10	5	1839	6	32843.027	6.2	1.3	56.001	18.243	7.4	19.1
-10	1	1619	2.2	30343.51	6.6	1	53.372	17.318	4.7	17.4
-10	0.5	1530	1.3	28768.539	7.2	0.9	53.184	18.294	4.2	13
-10	0.1	1413	0.5	26568.941	8.5	2.5	53.201	29.325	5.8	15.5
4	25	1125	8.4	20015.885	8.9	0.1	56.216	67.392	10	5.3
4	10	1105	8.4	18820.432	8.5	0.5	58.736	39.119	8.3	1.9
4	5	1051	7.3	17770.1	8.7	0.4	59.148	44.233	7.7	0.7
4	1	885	3.1	15128.261	10.6	0.4	58.521	43.869	5.6	2.5
4	0.5	800	1.9	13955.012	10.9	0.4	57.308	47.224	6.3	3.2
4	0.1	681	0.8	11559.654	12.7	0.8	58.869	79.411	5.1	7.4
21	25	721	8.5	11983.729	13.8	3.6	60.192	192.87	12	23.2
21	10	610	8.1	9832.118	16.4	0.8	62.022	203.279	7.8	8.1
21	5	536	7.7	8796.159	17.3	1.2	60.94	212.099	7.9	4.4
21	1	381	5	6343.747	21	1.3	59.996	192.696	5.2	2.7
21	0.5	326	3.5	5378.944	22.5	1.2	60.673	199.908	4.2	6
21	0.1	213	1.6	3517.992	24.9	0.1	60.473	267.376	5.2	12.7
37	25	450	9.2	7204.163	23.6	2.4	62.5	274.341	8.2	12.9
37	10	346	9.8	5762.231	23.3	2	60.062	346.43	6	14.6
37	5	281	8.8	4762.981	24.4	2	59.024	388.28	5.6	13.6
37	1	183	5	2890.281	26.9	2.3	63.212	385.7	4.6	9
37	0.5	152	3.4	2378.358	27.4	2.2	63.862	400.287	4.4	7.1
37	0.1	101	1.4	1547.319	26.6	2.3	65.293	447.842	3.6	3
54	25	121	10	2009.607	32.2	0.4	60.246	113.792	8	17.9
54	10	90	9	1489.218	29.5	2.1	60.676	170.54	5.8	22.2
54	5	70	8.1	1147.843	28.7	2	60.769	183.257	6.2	21.2
54	1	40	4.8	691.214	27	2.7	58.543	174.755	4.5	19.6
54	0.5	33	3.8	575.674	25.8	2.1	57.157	175.359	4	20.1
54	0.1	22	3	406.99	21.8	4	55.153	194.022	4.9	20.3

273

Figure C. 7: Master curve for sample 4 (SP-II with PG 64-22 binder)
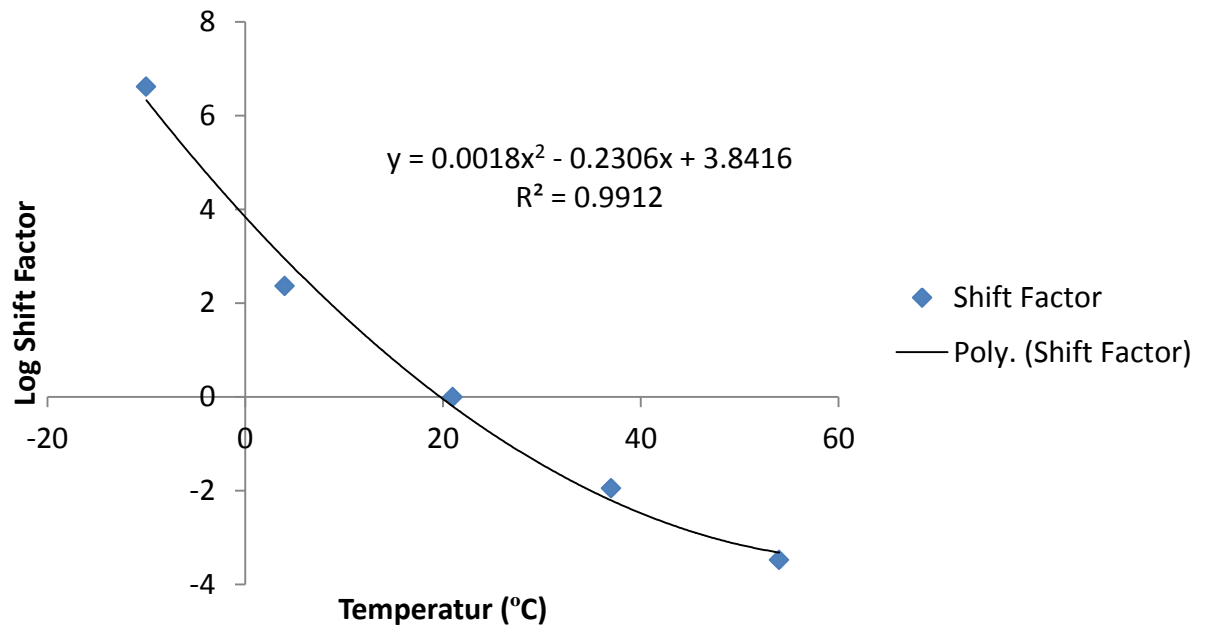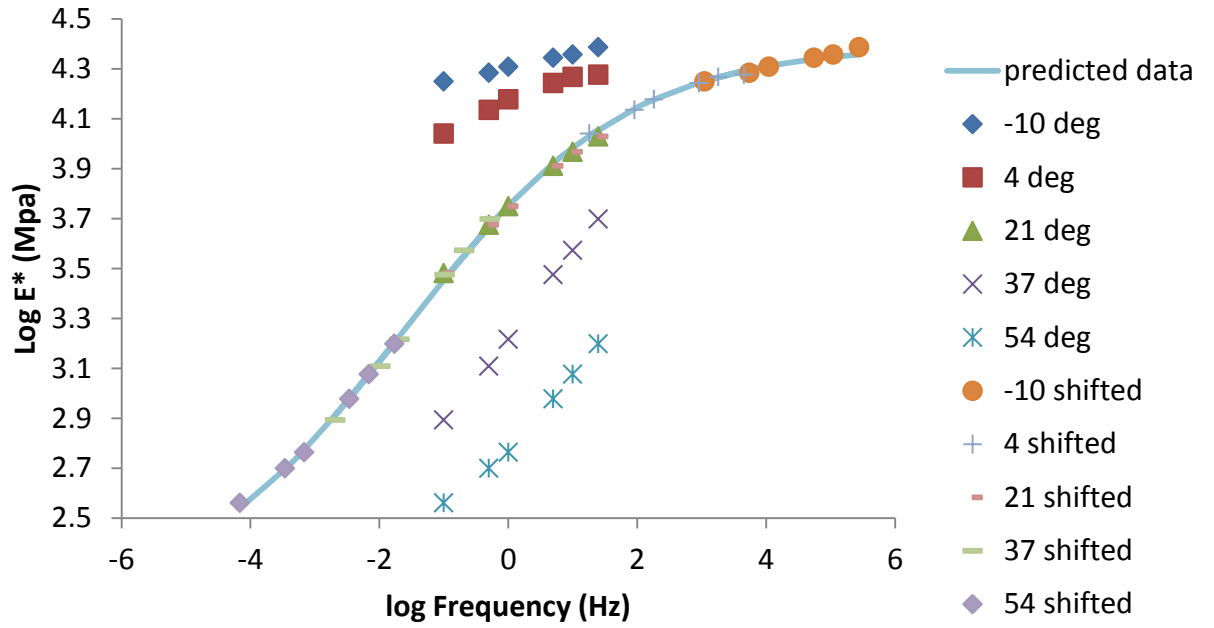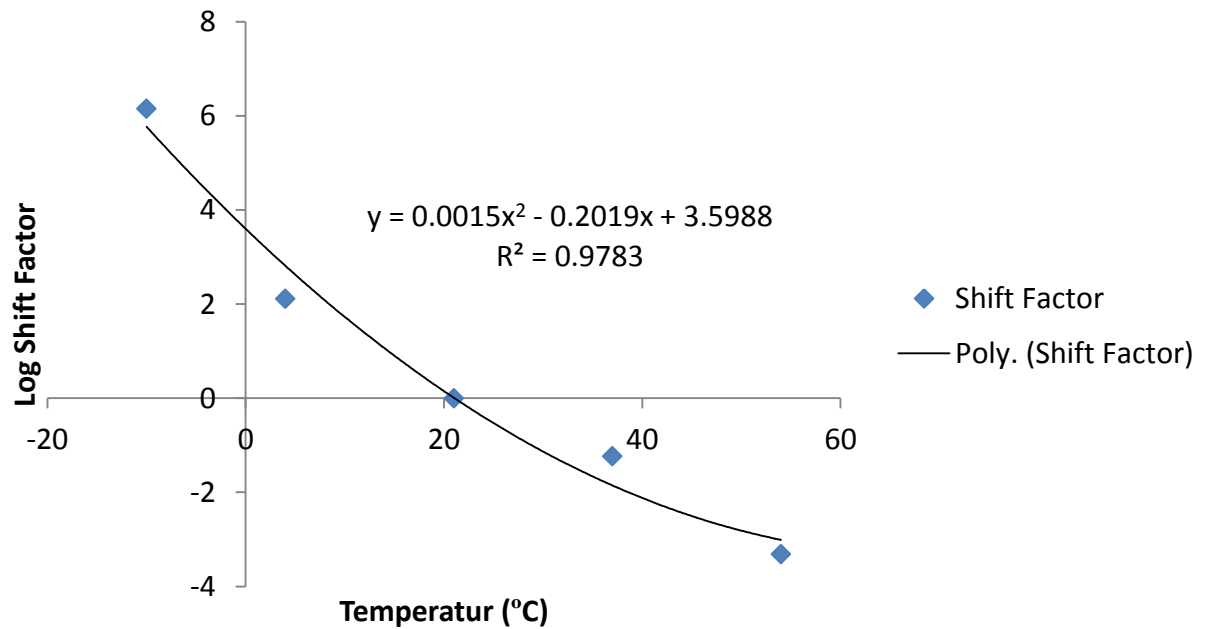

Figure C. 8: Shift factor for sample 4 (SP-II with PG 64-22 binder)

274

Table C. 5: *E** test results for Sample 5 (SP-II with PG 64-22 binder)

Temperature	Frequency	Stress		Dynamic Modulus	Phase Angle		Strain			
		Amplitude (P-P)	SE			UC	(P-P) Recoverable	Permanent	SE	UC
(deg C)	(Hz)	(kPa)	(%)	(MPa)	(deg)	(deg)	(micro e)	(micro e)	(%)	(%)
-10	25	1875	6.9	33439.43	6.7	1.9	56.085	51.823	9.9	13
-10	10	1886	6.7	33413.246	5.1	0.2	56.445	11.296	6.5	18.1
-10	5	1820	5.4	32511.082	4.9	0.1	55.969	9.707	6.3	19.3
-10	1	1613	1.9	29800.637	5.6	0.2	54.124	8.388	4.7	22.3
-10	0.5	1527	1	28775.555	4.4	1.5	53.063	9.357	5.7	23
-10	0.1	1412	0.5	26145.514	6.6	0.1	54.003	18.588	4.6	24.3
4	25	1646	7.1	24721.539	9.4	0.2	66.585	108.927	6.3	14.5
4	10	1499	7.6	23427.918	8.6	0.5	63.979	41.457	6.5	19.1
4	5	1418	6.4	22134.037	8.8	0.4	64.065	40.604	5.8	19.9
4	1	1187	2.6	18799.396	10	0.6	63.156	39.566	5.8	20.5
4	0.5	1072	1.6	17219.402	11.2	0.2	62.282	42.726	3.8	18
4	0.1	912	0.6	14186.721	13.2	0.1	64.263	74.565	3.9	18.3
21	25	844	7.8	13929.848	15.1	0.9	60.566	158.88	8.8	8.6
21	10	754	7.6	12212.933	15.5	0.3	61.776	161.313	6	13.2
21	5	675	6.9	10855.43	16.6	0.4	62.211	167.51	5.4	12.1
21	1	477	3.7	7835.529	19.8	0.4	60.82	151.398	4.3	6.2
21	0.5	408	2.8	6802.162	21.1	0.1	59.912	160.693	3.9	7.8
21	0.1	275	0.9	4582.961	23.1	0.4	60.024	215.225	3.6	6.9
37	25	450	9.2	7204.163	23.6	2.4	62.5	274.341	8.2	12.9
37	10	346	9.8	5762.231	23.3	2	60.062	346.43	6	14.6
37	5	281	8.8	4762.981	24.4	2	59.024	388.28	5.6	13.6
37	1	183	5	2890.281	26.9	2.3	63.212	385.7	4.6	9
37	0.5	152	3.4	2378.358	27.4	2.2	63.862	400.287	4.4	7.1
37	0.1	101	1.4	1547.319	26.6	2.3	65.293	447.842	3.6	3
54	25	141	9.6	2408.435	30.9	2.3	58.427	187.687	7.3	6
54	10	114	9	1836.391	28.7	1.1	61.885	236.423	6.4	0.7
54	5	93	8.2	1475.662	28.2	1.3	62.788	247.882	6	3.5
54	1	57	5.2	907.126	27.6	2.1	62.463	236.64	4.8	10.5
54	0.5	47	3.4	766.731	26.6	2.8	61.267	233.877	3.7	11.5
54	0.1	35	1.8	554.261	23.4	4.3	63.029	248.731	4.3	19.2

275
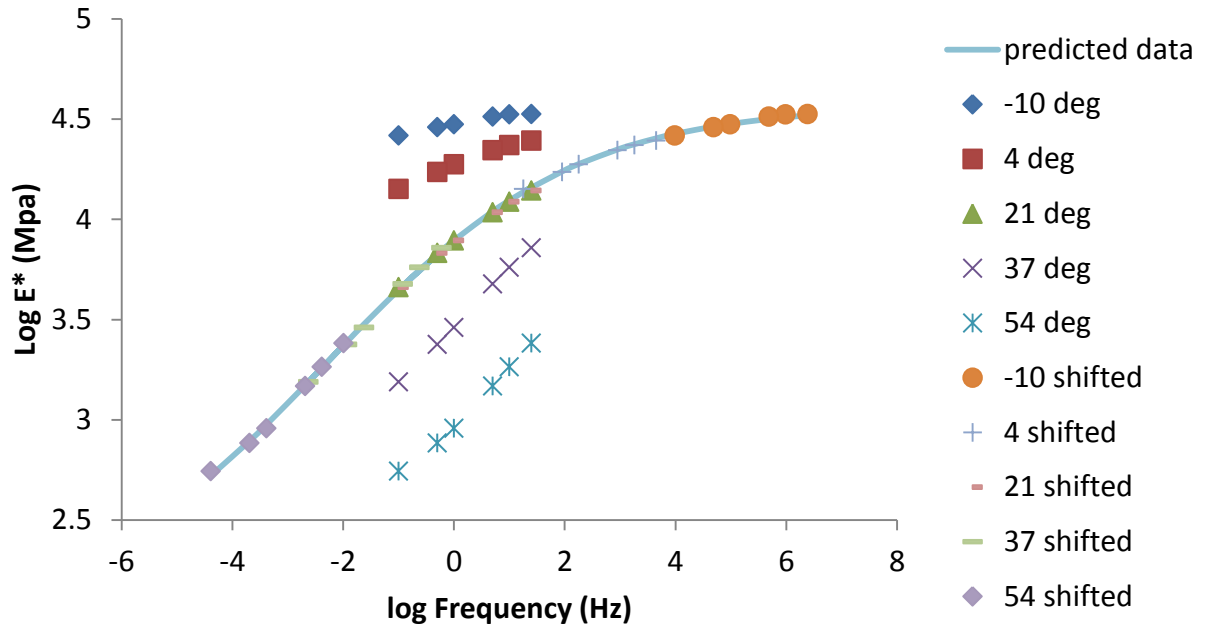
Figure C. 9: Master curve for sample 5 (SP-II with PG 64-22 binder)

$y = 0.0009x^2 - 0.1664x + 3.1193$
$R^2 = 0.9975$

Figure C. 10: Shift factor for sample 5 (SP-II with PG 64-22 binder)

276

Table C. 6: *E** test results for Sample 6 (SP-II with PG 64-22 binder)

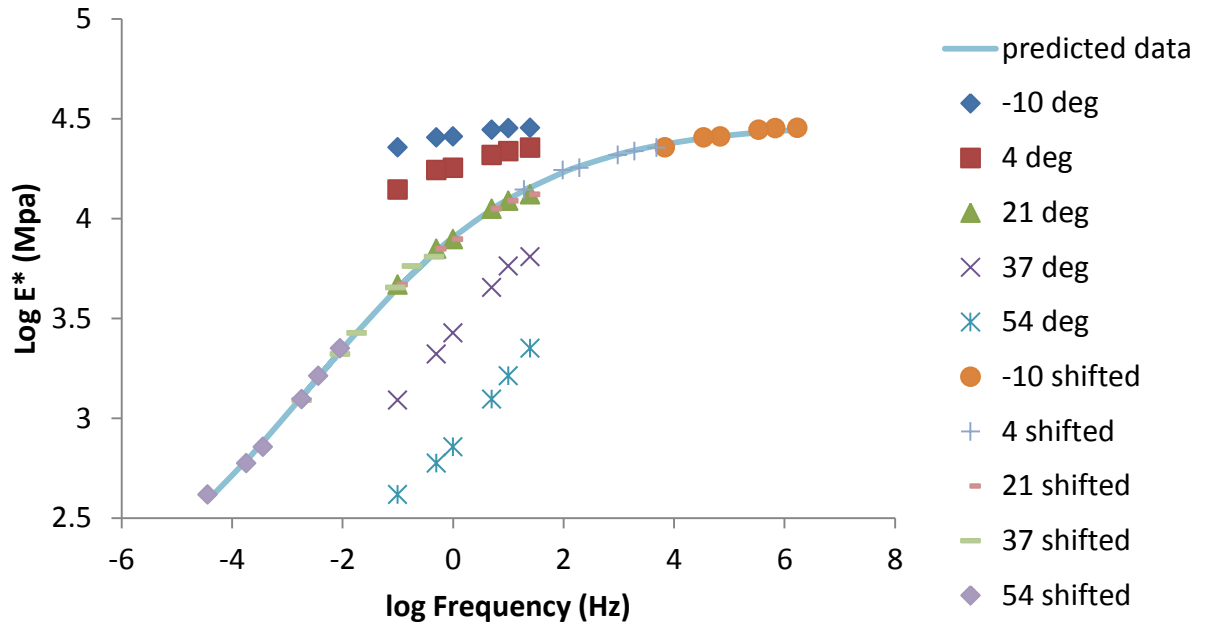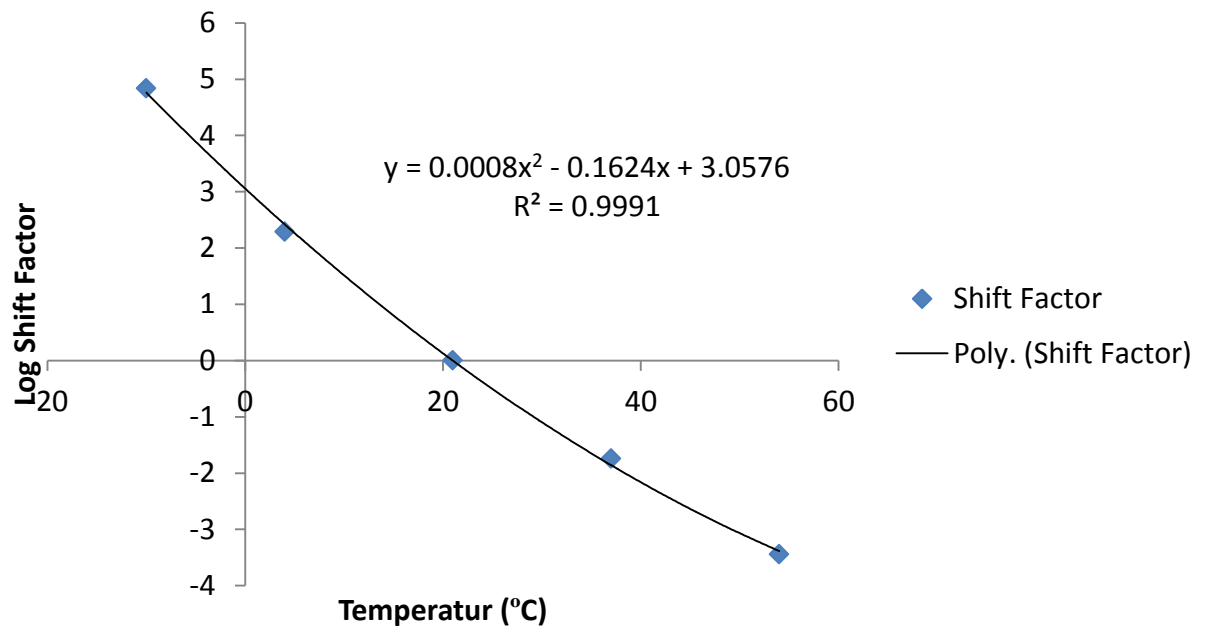| Temperature	Frequency	Stress		Dynamic Modulus	Phase Angle		Strain			
		Amplitude (P-P)	SE			UC	(P-P) Recoverable	Permanent	SE	UC
(deg C)	(Hz)	(kPa)	(%)	(MPa)	(deg)	(deg)	(micro e)	(micro e)	(%)	(%)
-10	25	1745	6.4	29015.891	7	0.2	60.144	33.169	12	19.9
-10	10	1698	6.3	27568.977	5.6	1.2	61.606	4.417	9.1	8.8
-10	5	1622	5.3	26854.023	5.2	1.8	60.392	-10.451	7.6	6.4
-10	1	1461	1.6	24833.041	5.7	1.9	58.836	-16.993	4.8	6.4
-10	0.5	1335	0.9	24290.967	6.3	1.6	54.963	-11.164	4.9	8.7
-10	0.1	1227	0.4	21284.256	7.6	1.4	57.636	-1.926	4.7	5.7
4	25	942	9.2	17343.375	9.3	0.4	54.295	33.88	11	3.3
4	10	832	9.5	16111.846	9.1	0.6	51.663	17.384	9.6	1
4	5	778	8.5	15249.849	9.4	0.7	51.008	16.156	8.4	1.4
4	1	712	4.1	13103.287	10.1	0.1	54.314	15.273	6	2.1
4	0.5	604	2.8	12133.614	11.4	1.3	49.793	17.226	3	4.6
4	0.1	499	1.1	10161.441	12.9	0.6	49.09	37.761	2.6	3.9
21	25	672	9.7	9523.605	14.7	1.5	70.552	163.279	15	16.4
21	10	605	9.7	8150.564	15.8	0.2	74.203	179.549	8.7	10.6
21	5	536	9.1	7279.357	16.8	0.2	73.634	193.177	8	9.4
21	1	376	6.4	5319.224	20.1	0.5	70.629	178.546	5.5	13.4
21	0.5	325	4.3	4572.022	21.5	0.3	71.155	192.086	4	14.9
21	0.1	226	1.5	3120.064	23.7	0.6	72.497	273.505	3	15.4
37	25	303	10	4503.634	22.3	4.1	67.386	298.372	15	11.5
37	10	252	10	3500.4	23.5	0.5	72.015	382.682	8.5	11.3
37	5	208	10	2888.458	24.7	0.6	72.116	413.889	8.7	8.9
37	1	127	8	1773.825	27.7	0.8	71.833	395.473	7.1	10.6
37	0.5	103	5.9	1444.666	28.3	1.4	71.329	403.658	6.3	10.4
37	0.1	65	2.3	912.941	27.9	2	70.839	453.616	4.6	12.6
54	25	102	11	1635.277	30.7	0.1	62.472	287.448	8.8	11.6
54	10	76	8.9	1290.741	27.7	2.6	59.013	386.887	6.2	0.6
54	5	65	7.4	1048.568	26.6	2.5	62.011	437.416	5.7	2.7
54	1	33	4.9	635.182	25	1.9	51.977	436.915	5	3
54	0.5	31	5	535.703	23.7	2.7	57.12	449.24	4	1.6
54	0.1	27	4.6	391.945	19.7	2.3	68.03	500.66	4.4	1.8

277
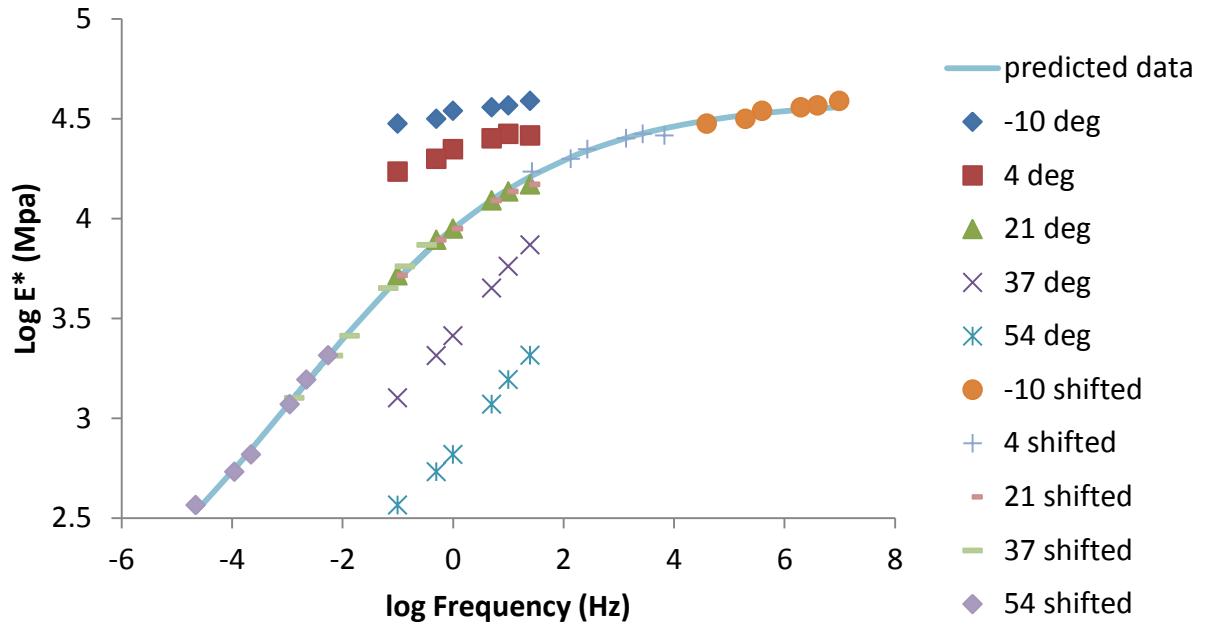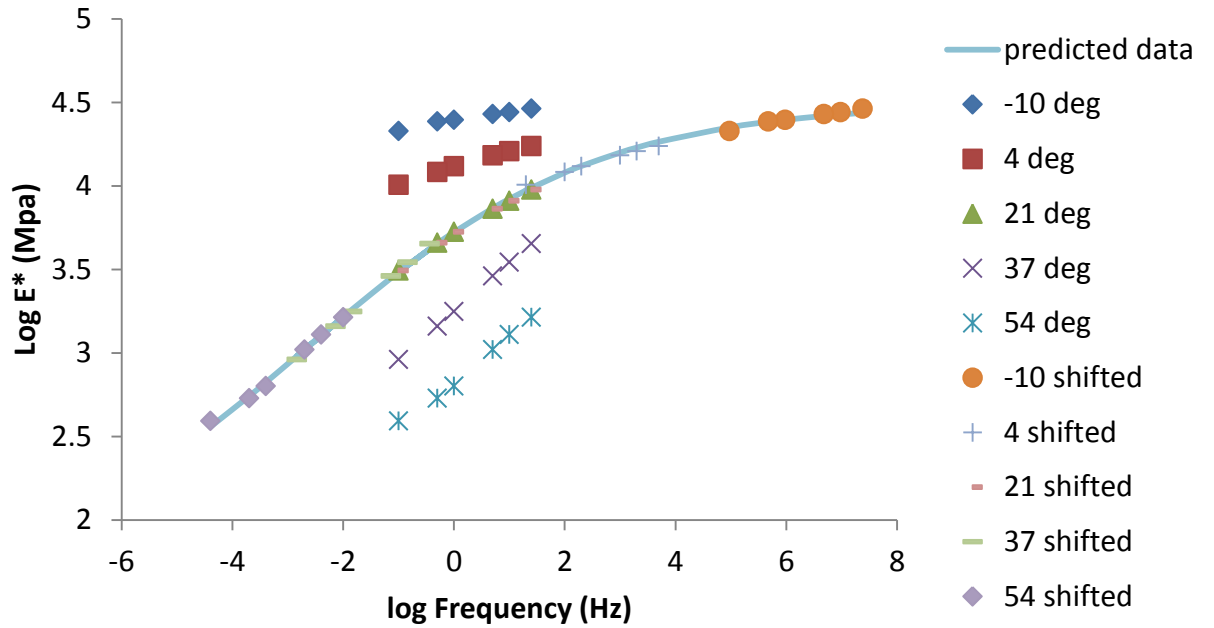
Figure C. 11: Master curve for sample 6 (SP-II with PG 64-22 binder)

Figure C. 12: Shift factor for sample 6 (SP-II with PG 64-22 binder)

278

APPENDIX D

Dynamic Modulus Test Results for SP-II with PG 70-22 Binder

Table D. 1: E* test results for Sample 1 (SP-II with PG 70-22 binder)

Temperature	Frequency	Stress		Dynamic Modulus	Phase Angle		Strain			
		Amplitude (P-P)	SE			UC	(P-P) Recoverable	Permanent	SE	UC
(deg C)	(Hz)	(kPa)	(%)	(MPa)	(deg)	(deg)	(micro e)	(micro e)	(%)	(%)
-10	25	1309	5.8	22393.246	9.9	1.5	58.435	35.645	8.4	14.2
-10	10	1334	5.9	22022.662	6.9	1.3	60.57	8.519	8.3	10.4
-10	5	1307	4.6	21429.338	6.4	1	60.998	7.7	7.4	10.1
-10	1	1181	1.4	19482.635	7.7	2.4	60.599	6.355	4.7	7.3
-10	0.5	1126	0.9	18753.098	9	3.5	60.033	7.1	5.7	7.9
-10	0.1	1037	0.5	16745.855	9.5	2.2	61.901	20.585	5	7.2
4	25	837	6.3	14776.076	11.4	1.5	56.626	54.003	8.1	6.3
4	10	755	6.7	13962.789	10.1	0.2	54.063	51.347	8.6	2.9
4	5	708	5.7	13052.636	10.5	0.2	54.236	55.71	7.4	2.2
4	1	591	2.5	11001.224	12.3	0.7	53.702	56.753	6	3.7
4	0.5	535	1.5	10042.3	13.4	0.2	53.282	62.565	4.5	3.6
4	0.1	456	0.7	8173.402	15.9	0.6	55.768	102.081	4.8	11.8
21	25	672	9.7	9523.605	14.7	1.5	70.552	163.279	15	16.4
21	10	605	9.7	8150.564	15.8	0.2	74.203	179.549	8.7	10.6
21	5	536	9.1	7279.357	16.8	0.2	73.634	193.177	8	9.4
21	1	376	6.4	5319.224	20.1	0.5	70.629	178.546	5.5	13.4
21	0.5	325	4.3	4572.022	21.5	0.3	71.155	192.086	4	14.9
21	0.1	226	1.5	3120.064	23.7	0.6	72.497	273.505	3	15.4
37	25	206	6.9	3457.687	26.2	0.3	59.721	192.878	6.3	43.1
37	10	165	5.7	2738.074	25.6	2.3	60.443	283.361	4.1	33.8
37	5	136	4.7	2244.93	26.7	1.7	60.545	309.935	4.1	27.7
37	1	77	2.3	1294.376	28.5	0.9	59.393	296.506	3.4	15.9
37	0.5	62	1.4	1045.145	28.5	0.7	59.664	306.558	3.5	11.7
37	0.1	39	1.7	671.566	26.8	0.3	57.787	347.994	3.8	3.7
54	25	87	7.1	1345.157	29.8	3.5	64.617	154.001	6.8	27.9
54	10	68	6.3	1024.803	26.1	2.1	66.766	231.246	6.9	22.3
54	5	53	5.1	828.984	25.7	1.9	63.447	254.506	4	26.6
54	1	31	4.7	532.754	22.8	2.2	59.069	251.941	4.8	34.9
54	0.5	27	3.9	453.839	21.8	2	60.369	260.976	6	36.2
54	0.1	21	4.2	346.742	17.9	1.8	60.601	294.036	5.4	43.7

280
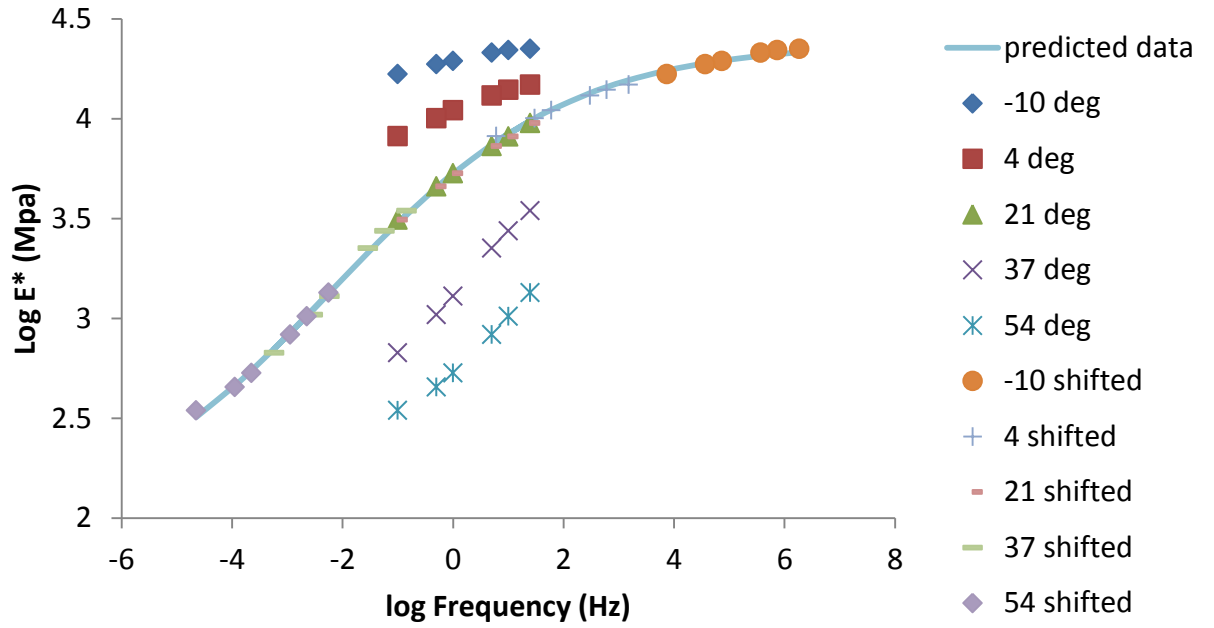
Figure D. 1: Master curve for sample 1 (SP-II with PG 70-22 binder)


$y = 0.001x^2 - 0.1726x + 2.8719$

$R^2 = 0.9931$
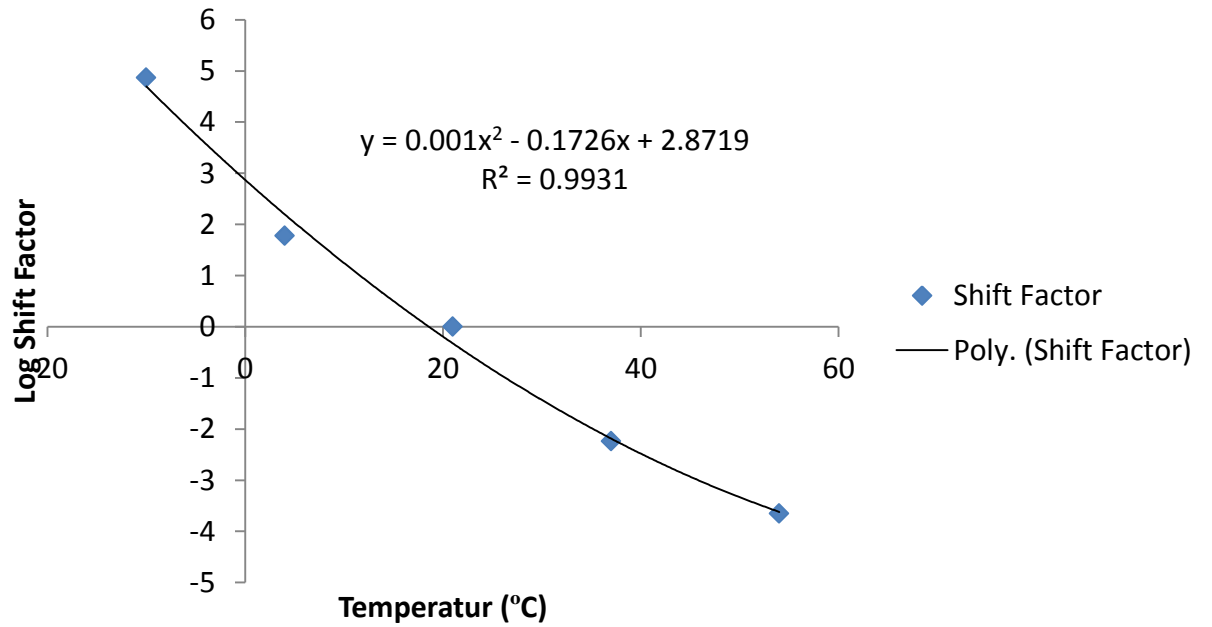
Figure D. 2: Shift factor for sample 1 (SP-II with PG 70-22 binder)

281

Table D. 2: *E** test results for Sample 2 (SP-II with PG 70-22 binder)

Temperature	Frequency	Stress		Dynamic Modulus	Phase Angle		Strain			
		Amplitude (P-P)	SE			UC	(P-P) Recoverable	Permanent	SE	UC
(deg C)	(Hz)	(kPa)	(%)	(MPa)	(deg)	(deg)	(micro e)	(micro e)	(%)	(%)
-10	25	2293	5.4	25258.293	7	0.4	90.778	100.005	7	19.6
-10	10	2255	5.3	24166.85	5.1	0.6	93.328	28.164	6.3	16.7
-10	5	2186	4.8	23551.881	4.8	0.4	92.797	28.869	5.8	16.6
-10	1	1906	1.3	21527.123	5.1	0.1	88.549	27.505	3.8	18
-10	0.5	1734	0.7	21126.848	4.6	0.6	82.072	29.139	3.1	17.3
-10	0.1	1574	0.5	18821.896	6.8	0.5	83.608	47.255	5	18.6
4	25	904	9.1	13652.99	6.7	5.8	66.232	38.866	15	20.6
4	10	816	10	15243.325	8.4	0.3	53.556	28.526	11	12.9
4	5	769	9.2	14473.225	8.3	0.1	53.158	26.487	9.3	12.2
4	1	652	4.7	12188.368	9.6	0.2	53.522	28.616	9.1	10.6
4	0.5	586	3.2	11317.236	6.8	1.2	51.805	31.219	8	10.1
4	0.1	497	1.2	9888.192	12.6	0	50.3	52.529	8.6	5
21	25	863	7.9	9231.69	15.9	1.5	93.506	279.318	6.9	42
21	10	729	8.9	8468.601	15.2	0.1	86.084	283.014	7.2	34.1
21	5	630	8.2	7608.027	16	0.6	82.865	300.203	8.5	32.7
21	1	432	4.6	5456.587	18.4	1.3	79.249	285.252	6.7	23.4
21	0.5	382	2.9	4716.106	20.2	0.4	81.073	298.301	4.8	19.9
21	0.1	304	1.4	3431.923	22.7	0.3	88.643	402.179	5.9	13.2
37	25	370	14	4328.697	24.5	12.9	85.392	397.899	17	0.2
37	10	319	11	4297.676	20.9	1.1	74.205	560.796	6.9	9.9
37	5	271	8.1	3436.286	22.5	0.8	78.936	635.377	5.9	10.4
37	1	183	4.8	2123.081	26	2	86.366	636.383	5.3	6.6
37	0.5	152	3.6	1720.912	26.7	2.7	88.14	661.869	4.1	2.2
37	0.1	113	2.2	1119.979	25.8	3.1	100.891	781.356	5.1	9.4
54	25	137	8.2	1918.862	31.5	5.4	71.487	357.352	6.6	13
54	10	121	7.4	1502.492	29.4	2.7	80.33	569.945	4.3	20.7
54	5	97	6.7	1187.823	29.3	3.4	81.598	665.377	4	22.8
54	1	65	4.8	715.493	29	3.5	91.259	691.578	5.4	23.1
54	0.5	58	3.5	622.655	28.2	4.6	93.595	729.052	5.7	26.1
54	0.1	46	1.7	435.285	25.1	5.1	106.44	829.028	7.8	24

282
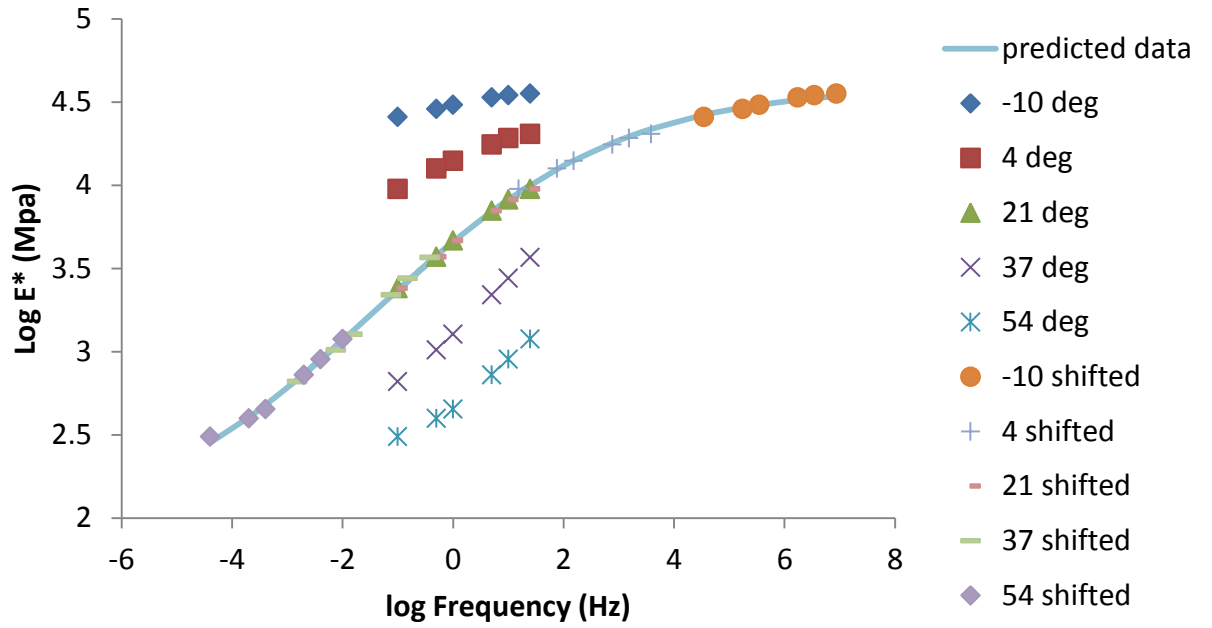
Figure D. 3: Master curve for sample 2 (SP-II with PG 70-22 binder)

$$y = 0.0013x^2 - 0.1905x + 3.3181$$
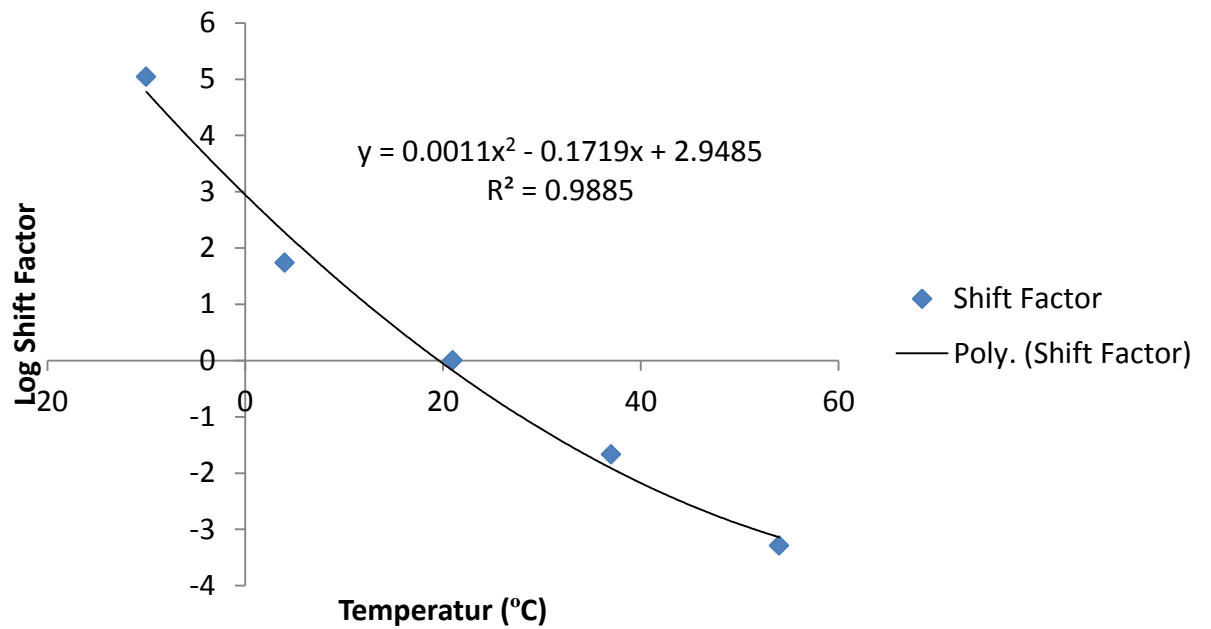$$R^2 = 0.9949$$

Figure D. 4: Shift factor for sample 2 (SP-II with PG 70-22 binder)

Table D. 3: *E** test results for Sample 3 (SP-II with PG 70-22 binder)

Temperature	Frequency	Stress		Dynamic Modulus	Phase Angle		Strain			
		Amplitude (P-P)	SE			UC	(P-P) Recoverable	Permanent	SE	UC
(deg C)	(Hz)	(kPa)	(%)	(MPa)	(deg)	(deg)	(micro e)	(micro e)	(%)	(%)
-10	25	2030	5.2	35461.676	10.4	2.8	57.243	68.967	13	14.4
-10	10	2100	4.7	34736.535	8.2	2.9	60.459	22.957	9.3	9.3
-10	5	2034	3.8	33632.422	8	3.1	60.481	23.367	7.8	6.7
-10	1	1734	1	30427.633	9.1	3.4	56.999	22.515	6.5	1
-10	0.5	1663	0.6	28684.082	9.4	3.3	57.981	24.997	6.2	5.3
-10	0.1	1462	0.4	25689.592	11	3.4	56.893	44.367	6.1	8.8
4	25	1654	5.4	20311.299	15.5	2.3	81.414	223.152	11	7.5
4	10	1503	5.3	19208.438	13.5	2.3	78.262	142.399	7.7	6.7
4	5	1416	4.2	17549.875	14.1	2.5	80.657	155.691	6.3	3
4	1	1181	1.2	14042.968	16.8	2.4	84.107	159.672	4.9	5.6
4	0.5	1069	0.7	12625.292	17.9	2.7	84.651	176.166	4	8.4
4	0.1	913	0.4	9496.972	21.3	2.3	96.088	276.243	2.5	6.9
21	25	627	6.1	9485.652	27.7	1.6	66.068	319.316	14	14.7
21	10	529	7.3	8204.207	21.2	0.1	64.418	393.351	7.4	7.7
21	5	457	6.4	7040.788	22.4	0.3	64.946	433.399	5.6	7.7
21	1	324	3.1	4657.685	26.4	0.7	69.574	423.541	4.3	5.3
21	0.5	279	1.4	3723.819	27.9	0.1	74.865	449.912	4.1	1.8
21	0.1	185	0.7	2405.771	30.1	0.3	76.728	546.803	3.1	6
37	25	207	6.5	3687.917	30.2	11.1	56.165	217.873	11	40.8
37	10	164	6.2	2763.598	28.6	1	59.517	295.966	6.5	28.9
37	5	135	5.4	2191.872	29	1	61.724	318.496	6.1	25.3
37	1	77	2	1273.728	30	0.3	60.633	301.766	3.5	12.4
37	0.5	63	1.5	1026.285	29.5	0.1	60.97	310.802	3.1	8.3
37	0.1	39	1.4	661.555	26.6	0.6	58.975	348.957	3	0.8
54	25	71	6.3	1191.62	32.6	1.7	59.274	254.294	6.3	33.3
54	10	50	4.6	900.586	29.1	2.3	55.615	310.819	3.8	17.7
54	5	39	3.6	724.882	27.1	2	54.323	331.515	3.6	12.1
54	1	24	2.7	451.474	23.5	1.4	52.978	335.279	4.8	1.8
54	0.5	18	3.1	397.848	20.7	1	45.77	338.627	4.1	2.6
54	0.1	15	2.9	308.37	16.8	0.1	49.54	361.393	6.5	6.7

284
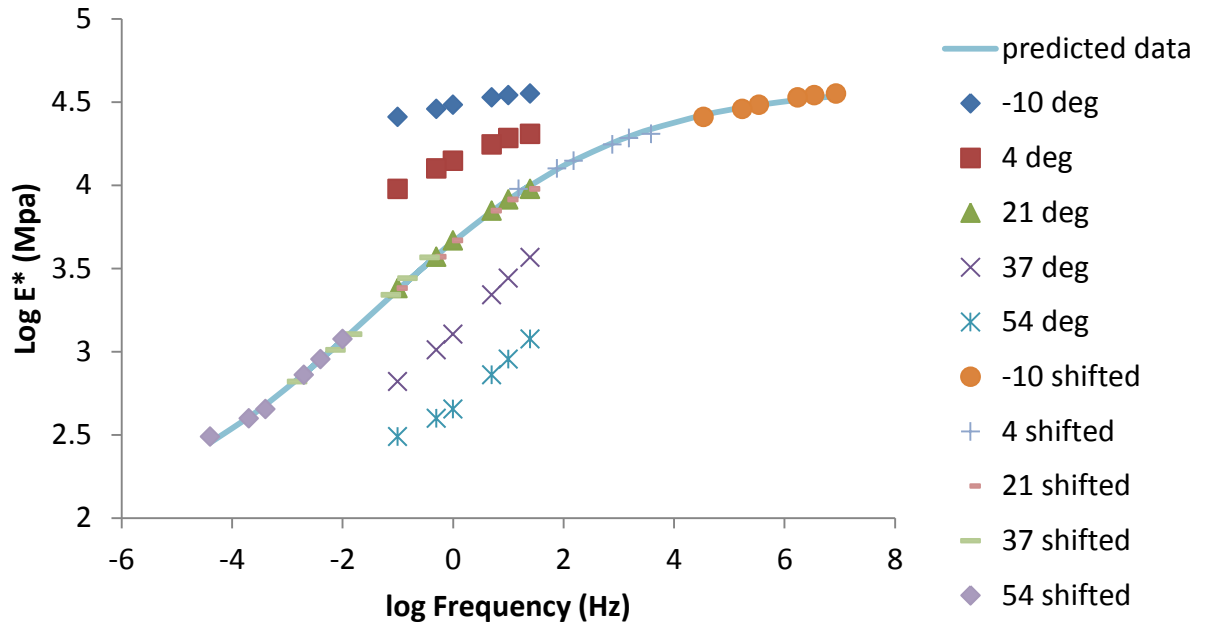
Figure D. 5: Master curve for sample 3 (SP-II with PG 70-22 binder)



$$y = 0.0013x^2 - 0.1904x + 3.3163$$
$$R^2 = 0.9949$$

Figure D. 6: Shift factor for sample 3 (SP-II with PG 70-22 binder)

285

Table D. 4: *E** test results for Sample 4 (SP-II with PG 70-22 binder)

Temperature	Frequency	Stress		Dynamic Modulus	Phase Angle		Strain			
		Amplitude (P-P)	SE			UC	(P-P) Recoverable	Permanent	SE	UC
(deg C)	(Hz)	(kPa)	(%)	(MPa)	(deg)	(deg)	(micro e)	(micro e)	(%)	(%)
-10	25	1303	6	23630.602	8.7	4.1	55.156	43.798	11	23
-10	10	1324	5.8	22770.619	7.1	0.7	58.153	18.703	8.4	26.2
-10	5	1306	4.7	22154.896	6.9	0.5	58.946	19.698	8.6	26.3
-10	1	1181	1.4	20257.17	7.2	0.1	58.279	20.874	8.2	26.5
-10	0.5	1126	0.8	19101.023	7.3	1.1	58.972	23.866	5.7	24
-10	0.1	1038	0.5	17075.572	9.3	0.3	60.796	41.42	4.2	26.5
4	25	839	6.4	14779.32	11.3	5.2	56.762	64.47	10	28.1
4	10	750	6.4	14028.559	10.6	1.7	53.467	64.522	6.8	26.6
4	5	704	5.5	13311.586	10.7	1.3	52.891	70.3	5.9	26.1
4	1	593	2.3	11103.771	12.9	1.9	53.364	72.029	3.2	22.5
4	0.5	535	1.5	10221.488	13.7	3	52.371	78.738	3.3	20.6
4	0.1	456	0.7	8304.708	16.3	2.4	54.911	121.379	3.3	13.5
21	25	541	6.8	8869.354	25.2	4	60.945	202.226	12	3.6
21	10	506	7.5	8312.87	18.9	2.8	60.816	276.14	6.8	1
21	5	436	6.9	7336.928	20	3.3	59.387	301.378	5.4	5.6
21	1	278	2.8	4810.072	23.8	5.1	57.788	279.822	3.5	25.4
21	0.5	234	1.9	4035.469	25.8	6.3	57.937	288.888	3.8	18.2
21	0.1	156	1.1	2696.693	28.4	8	57.878	351.739	3.2	0.1
37	25	283	7.1	4425.193	29.4	8.7	64.019	187.466	8.2	26.5
37	10	230	7	3581.793	26.2	7	64.168	217.801	6	19.4
37	5	184	6.3	2885.143	26.8	7.7	63.765	217.768	6.3	10
37	1	109	3.1	1734.764	27.7	9.8	62.693	196.071	5.1	15.4
37	0.5	86	2	1414.211	26.5	10.9	61.012	196.045	4.1	29.2
37	0.1	55	1.4	915.261	21.6	12.5	60.546	223.873	6.4	61.3
54	25	71	7.7	1743.423	30.2	3.4	40.897	99.511	6.2	7.8
54	10	51	6.2	1346.024	27.3	3.2	38.021	116.195	7.7	8.7
54	5	41	5.8	1069.521	25.3	3.3	38.031	122.194	5.7	16
54	1	24	3.7	714.917	21.4	3.5	33.618	122.258	5.8	32.9
54	0.5	18	3.4	615.903	19.4	3.8	29.846	125.62	5.1	36.2
54	0.1	15	3	485.561	14.9	2.9	31.365	141.025	5.4	43.8

286
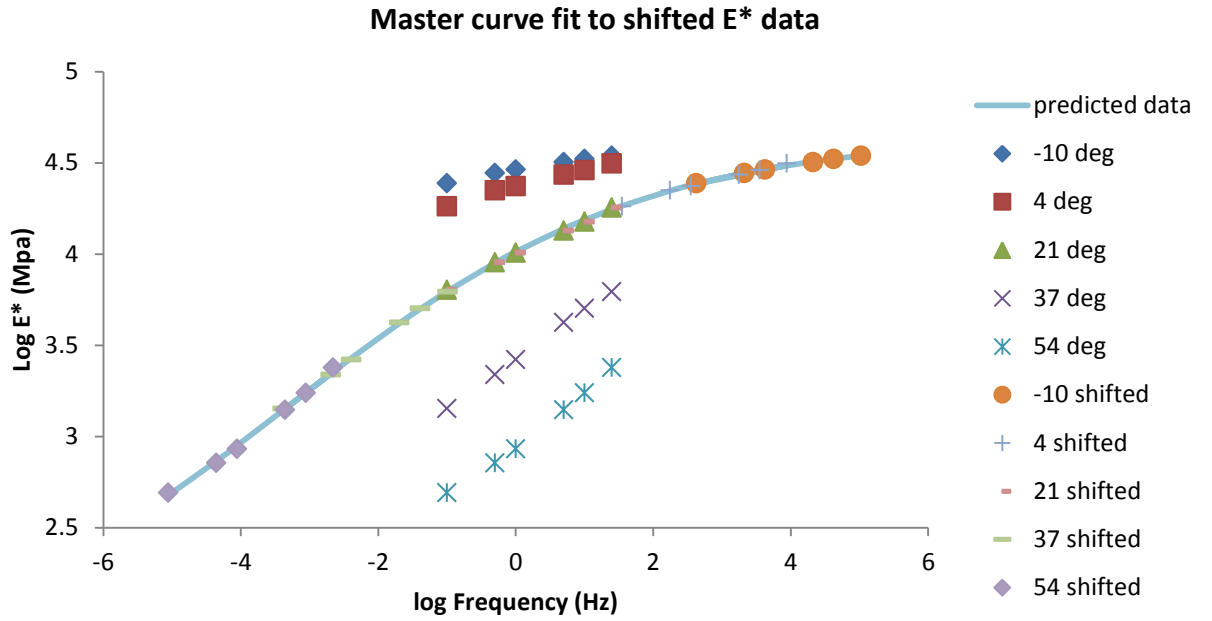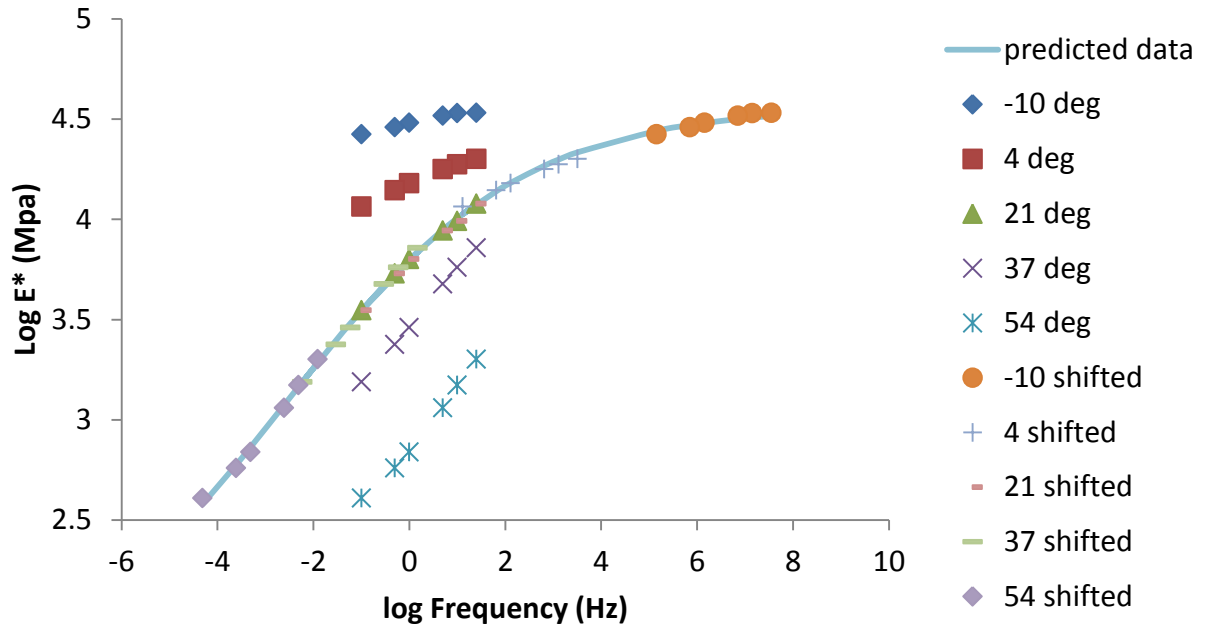
Figure D. 7: Master curve for sample 4 (SP-II with PG 70-22 binder)

Figure D. 8: Shift factor for sample 4 (SP-II with PG 70-22 binder)

287

www.manaraa.com

Table D. 5: *E** test results for Sample 5 (SP-II with PG 70-22 binder)

Temperature	Frequency	Stress		Dynamic Modulus	Phase Angle		Strain			
		Amplitude (P-P)	SE			UC	(P-P) Recoverable	Permanent	SE	UC
(deg C)	(Hz)	(kPa)	(%)	(MPa)	(deg)	(deg)	(micro e)	(micro e)	(%)	(%)
-10	25	2294	6.3	29461.037	9.3	2	77.859	79.036	7.7	27.9
-10	10	2248	6	28249.523	4.7	0.7	79.566	18.938	6.9	21
-10	5	2189	5.4	27618.645	4.5	0.7	79.243	18.577	6.8	19.6
-10	1	1910	1.7	25694.252	5.4	0.9	74.333	15.1	4.1	19.8
-10	0.5	1735	1	24770.588	3.9	0.3	70.027	16.195	4.1	20
-10	0.1	1574	0.5	23076.516	5.2	0.8	68.213	27.921	6.3	20.6
4	25	1269	7.9	21310.27	2.3	7.4	59.562	55.535	11	44.1
4	10	1333	7.7	22349.805	7.2	0.6	59.66	32.521	9.7	29.6
4	5	1306	6.4	21095.498	7.3	0.3	61.9	34.254	7.1	29.2
4	1	1115	2.8	18714.902	8.6	0.4	59.572	35.232	6.3	26.9
4	0.5	999	1.8	17643.465	10.2	0.1	56.633	37.837	4.8	24.5
4	0.1	860	0.7	15234.109	11.1	0.3	56.423	58.152	6.2	20.3
21	25	864	8.9	14017.16	11	8.2	61.658	90.759	22	47.8
21	10	738	8.7	12668.365	13.6	1.4	58.234	70.106	9.5	17
21	5	638	8.4	11794.512	14.5	1.1	54.106	65.132	9.5	15.1
21	1	436	4.8	8935.9	19.3	0	48.765	49.133	10	12.4
21	0.5	384	3.2	8444.93	17.4	2.1	45.524	52.787	6	7.1
21	0.1	304	1.3	5990.656	20.9	1.1	50.784	94.169	5	3.6
37	25	373	13	7376.699	26.4	10.1	50.616	173.983	21	4.5
37	10	321	11	7476.621	19.1	2	42.936	245.694	8.9	4.2
37	5	270	8.2	6294.983	19.9	2.5	42.96	272.439	8.6	9.9
37	1	183	4.9	4136.012	23.6	2.8	44.277	262.082	6.9	20.8
37	0.5	152	3.8	3437.292	25.7	2	44.299	272.424	6.1	21.7
37	0.1	112	1.9	2325.957	27.1	2.6	48.185	342.888	5.2	24.9
54	25	228	8.4	3754.338	28.4	6.4	60.608	367.061	8.6	3
54	10	204	8.3	3049.85	24.5	3	66.783	570.796	7	6
54	5	161	7.5	2527.257	25.7	2.7	63.866	641.863	6.2	8.5
54	1	109	5.6	1484.48	27.5	3.4	73.585	652.611	4.9	1.3
54	0.5	99	4.1	1269.382	27.7	4	77.8	693.33	6.4	2.7
54	0.1	78	1.7	897.949	25.8	3.9	87.349	820.33	8.6	6.8

288

Figure D. 9: Master curve for sample 5 (SP-II with PG 70-22 binder)

$y = 0.001x^2 - 0.1731x + 3.2678$
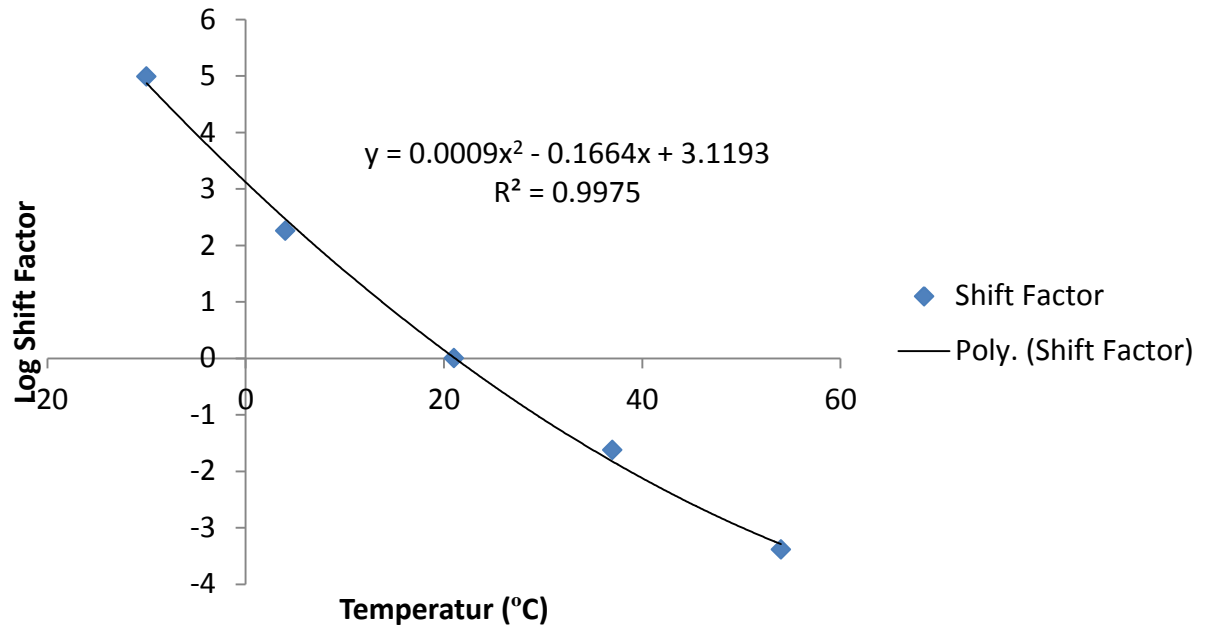$R^2 = 0.9994$

Figure D. 10: Shift factor for sample 5 (SP-II with PG 70-22 binder)

289

Table D. 6: E^* test results for Sample 6 (SP-II with PG 70-22 binder)

Temperature	Frequency	Stress		Dynamic Modulus	Phase Angle		Strain			
		Amplitude (P-P)	SE			UC	(P-P) Recoverable	Permanent	SE	UC
(deg C)	(Hz)	(kPa)	(%)	(MPa)	(deg)	(deg)	(micro e)	(micro e)	(%)	(%)
-10	25	2298	6.2	33331.75	4.7	1	68.929	74.001	11	19.7
-10	10	2254	6.3	32001.172	5.7	0.9	70.446	14.833	9	12.3
-10	5	2192	5.4	30705.807	6.2	1.4	71.375	14.831	8.2	13.4
-10	1	1909	1.7	29331.199	6	1.7	65.078	13.881	6.2	12.8
-10	0.5	1733	1	26629.072	6.8	1	65.068	14.763	5.8	15.6
-10	0.1	1574	0.5	25160.848	7.8	1.2	62.54	25.96	5.7	14.4
4	25	1266	8.9	18566.732	10.1	2.5	68.193	100.22	10	2
4	10	1326	9	17287.932	9.5	1.6	76.705	66.962	11	6.1
4	5	1307	7.7	16042.076	10	1.2	81.449	73.844	8.8	6.9
4	1	1117	3.5	13465.104	11.5	1.9	82.944	74.867	6	0.7
4	0.5	1001	2.3	12531.27	13.7	2.1	79.842	82.75	4.7	3.2
4	0.1	860	0.9	9997.458	15.2	2.8	86.035	140.225	4.2	7.9
21	25	860	9.5	13111.93	22.3	4.8	65.566	306.371	34	25.6
21	10	731	8.9	10558.581	18.2	0.2	69.269	339.97	11	21.3
21	5	629	8.1	9235.335	19.1	0.1	68.123	371.019	9.1	20.9
21	1	433	4.8	6917.416	21.9	0.6	62.609	354.494	7.2	22
21	0.5	383	3.3	5858.501	25.5	2.8	65.409	367.747	4.7	19.1
21	0.1	305	1.6	3950.138	26.7	1.8	77.142	468.614	4	16
37	25	378	13	5492.263	23.2	9	68.797	357.979	20	21.9
37	10	323	11	4713.86	24.6	1	68.503	486.454	8.9	18.3
37	5	270	9	3693.346	25.7	0.5	73.047	536.667	8.5	14.9
37	1	182	5.5	2232.767	28.8	0.1	81.694	523.027	6.3	3.8
37	0.5	152	4.1	1792.959	29.1	0.4	84.923	532.893	4.8	2.3
37	0.1	113	1.8	1139.466	27	0.6	99.484	617.198	4.3	1.9
54	25	114	9	1736.376	33.2	11.6	65.785	121.472	13	25.8
54	10	95	8.3	1441.434	27.1	0.4	65.879	175.315	6.4	5.8
54	5	78	8	1169.751	26.1	0.9	66.966	202.065	6.6	4.2
54	1	53	6.7	696.871	24.4	1.7	76.175	204.421	5.3	9.3
54	0.5	49	5.4	600.584	22.4	1.9	81.634	220.213	5	6.8
54	0.1	41	2.8	449.943	18.5	2.1	90.75	256.086	6.1	6.7

290

Figure D. 11: Master curve for sample 6 (SP-II with PG 70-22 binder)
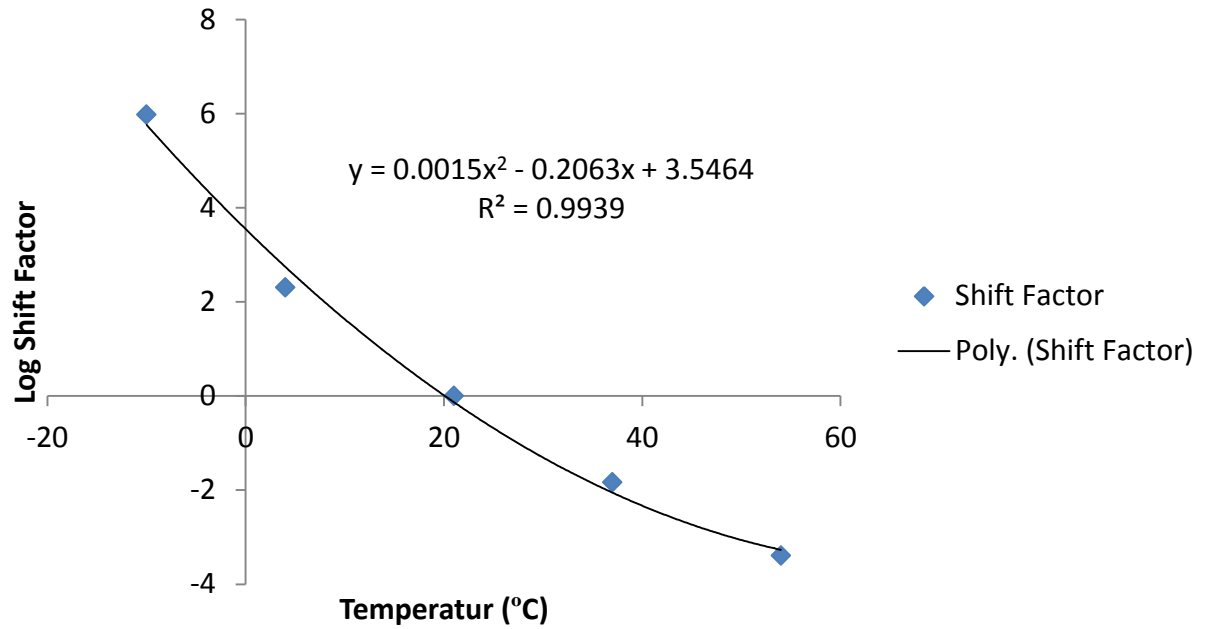

$y = 0.0013x^2 - 0.1896x + 3.1258$
$R^2 = 0.98$
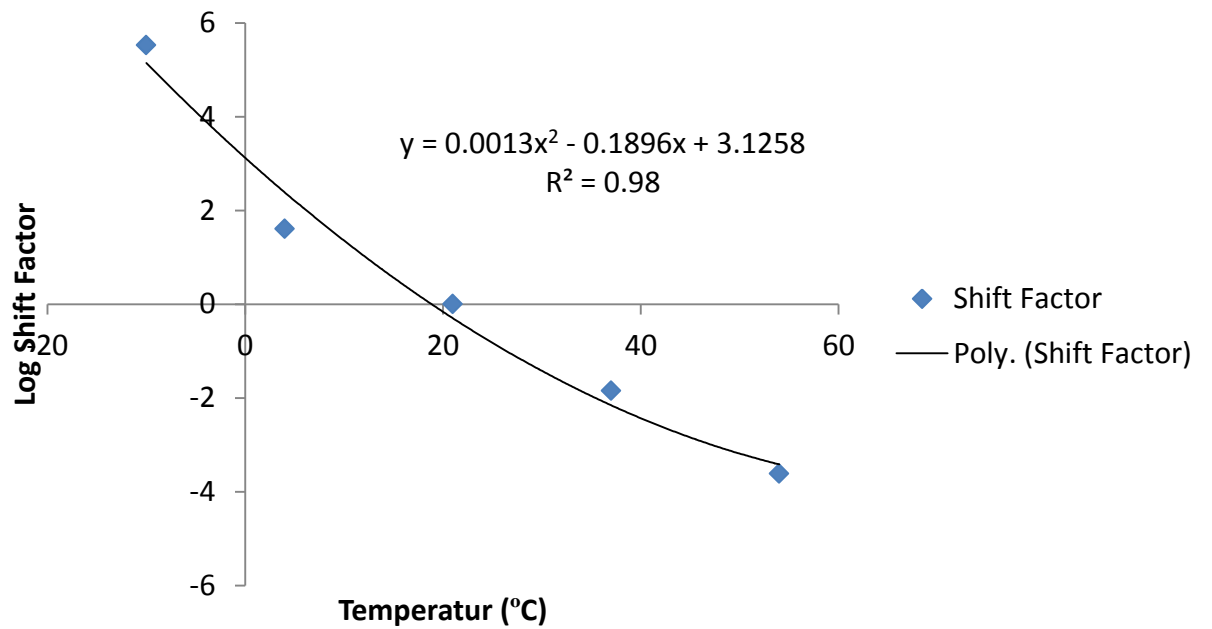
Figure D. 12: Shift factor for sample 6 (SP-II with PG 70-22 binder)

291

APPENDIX E

Dynamic Modulus Test Results for SP-IV with PG 70-22 Binder

Table E. 7: *E** test results for Sample 1 (SP-IV with PG 70-22 binder)

Temperature	Frequency	Stress		Dynamic Modulus	Phase Angle		Strain			
		Amplitude (P-P)	SE			UC	(P-P) Recoverable	Permanent	SE	UC
(deg C)	(Hz)	(kPa)	(%)	(MPa)	(deg)	(deg)	(micro e)	(micro e)	(%)	(%)
-10	25	1539	7.1	27403.5	12.1	1.7	56.1	62.5	13.5	15.8
-10	10	1552	7.7	27150.6	6.8	0.8	57.1	27.2	9.6	32.1
-10	5	1517	5.9	26043.9	6.7	1.2	58.2	26.7	9.0	33.1
-10	1	1364	1.8	23503.2	8.2	0.3	58.0	28.9	9.0	35.8
-10	0.5	1284	1.0	22032.2	6.9	1.0	58.3	31.9	5.1	36.7
-10	0.1	1166	0.5	19524.5	11.0	0.1	59.7	52.9	9.8	36.3
4	25	1113	8.1	19352.5	19.7	11.1	57.5	169.1	13.2	20.6
4	10	1024	8.3	17755.1	13.9	2.6	57.7	152.0	8.7	8.3
4	5	936	6.7	16204.3	14.6	2.5	57.8	169.1	6.9	6.6
4	1	715	2.9	12627.4	17.5	2.7	56.6	173.6	4.6	3.9
4	0.5	633	1.8	11057.0	21.3	4.7	57.2	191.1	7.5	1.8
4	0.1	448	0.9	8347.5	22.9	2.5	53.6	261.2	3.9	0.9
21	25	429	9.8	8068.7	23.7	1.9	53.2	404.6	11.5	23.3
21	10	356	11.2	6493.9	24.6	2.6	54.8	570.2	9.3	18.2
21	5	297	10.0	5331.0	26.3	3.0	55.7	655.6	8.1	14.6
21	1	202	5.1	3175.9	30.8	3.4	63.6	659.4	5.3	13.7
21	0.5	170	3.3	2589.5	32.4	4.1	65.7	703.7	4.5	14.4
21	0.1	112	1.2	1543.2	33.7	4.8	72.7	819.3	3.5	11.9
37	25	146	9.9	2484.5	36.7	0.4	58.7	460.0	8.2	1.9
37	10	124	9.8	1752.4	35.4	3.0	70.6	751.5	7.5	10.7
37	5	91	9.3	1343.2	35.9	3.5	68.0	846.9	7.4	11.5
37	1	53	5.7	703.8	35.2	4.4	75.4	852.8	5.9	13.9
37	0.5	41	4.1	555.1	34.2	5.0	73.0	864.2	4.7	10.5
37	0.1	25	1.8	364.5	29.6	6.3	67.7	886.7	4.9	2.9
54	25	28	6.7	534.709	35.3	6.2	52.074	310.572	7	19.3
54	10	23	5.4	401.472	29.9	0.1	56.448	434.176	4.8	1.2
54	5	19	5.8	329.095	27.6	0.8	56.339	468.307	9	0.7
54	1	11	6.2	220.836	20.7	0.5	51.886	466.481	11.6	2
54	0.5	10	8.2	195.123	18.7	0.7	51.153	469.821	9.3	1.2
54	0.1	8	9.8	153.339	16	0.7	52.708	486.686	14.8	3.2

293

Figure E. 13: Master curve for sample 1 (SP-IV with PG 70-22 binder)


$$y = 0.0006x^2 - 0.1573x + 3.0342$$
$$R^2 = 0.9994$$
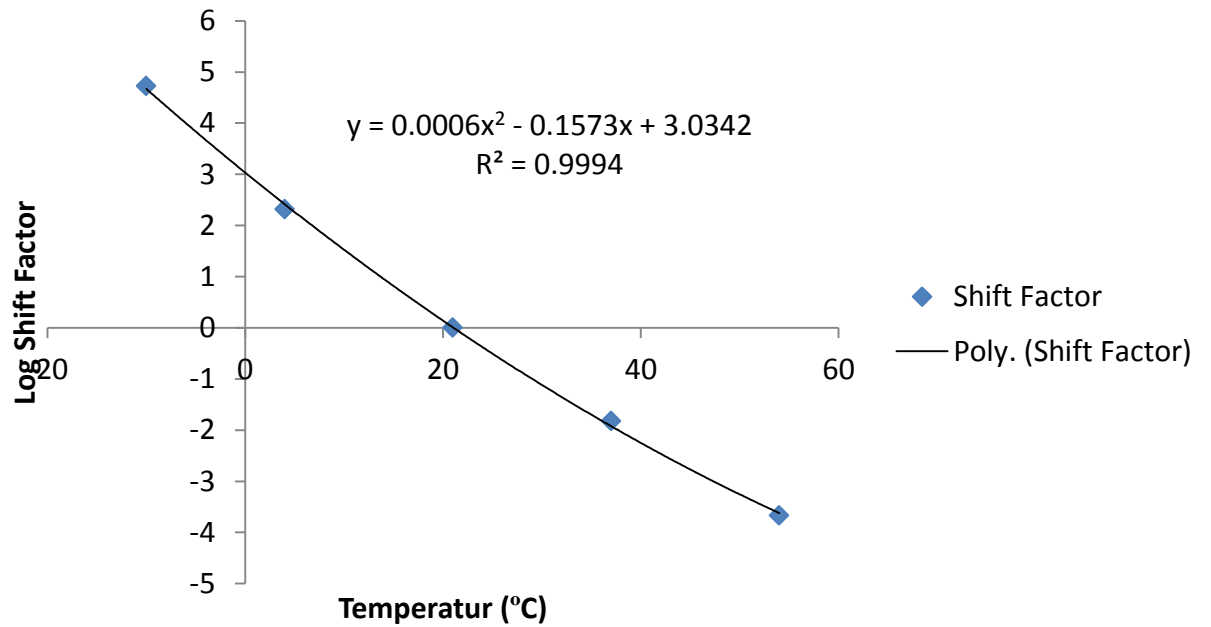
Figure E. 14: Shift factor for sample 1 (SP-IV with PG 70-22 binder)

Table E. 8: *E** test results for Sample 2 (SP-IV with PG 70-22 binder)

Temperature	Frequency	Stress		Dynamic Modulus	Phase Angle		Strain			
		Amplitude (P-P)	SE			UC	(P-P) Recoverable	Permanent	SE	UC
(deg C)	(Hz)	(kPa)	(%)	(MPa)	(deg)	(deg)	(micro e)	(micro e)	(%)	(%)
-10	25	1760	5.7	30858.7	6.0	1.7	57.0	57.8	6.9	29.9
-10	10	1782	5.7	29603.5	5.6	0.1	60.2	23.5	6.8	33.1
-10	5	1728	4.5	28745.9	5.4	0.3	60.1	16.4	5.5	33.5
-10	1	1557	1.2	26027.2	6.0	0.7	59.8	13.9	5.1	33.6
-10	0.5	1468	0.7	25135.9	7.3	0.3	58.4	18.0	4.1	35.7
-10	0.1	1335	0.4	21973.2	8.6	0.1	60.8	29.3	3.3	35.7
4	25	1113	7.7	18215.0	18.4	4.0	61.1	166.1	10.3	2.9
4	10	1027	7.8	16676.0	13.2	1.7	61.6	146.5	8.5	10.9
4	5	938	6.6	15346.3	13.9	1.2	61.1	164.2	6.6	11.3
4	1	715	2.9	12117.5	17.6	2.3	59.0	168.4	6.9	12.0
4	0.5	634	1.8	10977.4	17.4	1.1	57.7	183.8	4.0	10.0
4	0.1	448	1.0	8134.9	22.1	2.4	55.0	249.8	3.7	2.6
21	25	422	10.9	8268.7	29.4	1.4	51.1	485.7	35.0	22.1
21	10	358	10.6	7015.3	25.5	3.1	51.0	687.5	8.5	36.6
21	5	297	9.3	5772.3	27.0	3.3	51.5	786.6	6.7	32.2
21	1	202	4.5	3391.9	32.2	3.7	59.4	796.6	4.7	27.4
21	0.5	170	3.0	2709.9	33.5	3.5	62.8	841.1	3.8	27.8
21	0.1	112	1.1	1662.3	33.7	3.7	67.4	946.0	4.4	25.1
37	25	131	9.8	2284.8	33.6	1.8	57.5	382.8	8.2	2.0
37	10	110	9.4	1625.9	32.8	0.7	67.6	556.6	6.8	7.4
37	5	82	9.0	1227.7	32.9	0.8	67.0	608.9	6.9	13.5
37	1	47	5.7	642.6	31.7	0.6	73.7	604.9	5.0	20.8
37	0.5	37	4.4	505.5	29.9	0.7	72.6	610.5	3.9	23.7
37	0.1	21	2.2	316.1	24.0	1.2	67.5	624.7	3.5	22.8
54	25	41	9.2	592.4	28.1	34.3	68.5	196.4	10.7	42.0
54	10	32	7.4	494.1	31.1	3.6	65.4	296.2	5.8	13.9
54	5	27	6.8	417.7	27.0	3.2	65.8	340.8	4.2	3.2
54	1	18	4.9	320.0	19.3	0.8	55.6	336.0	4.2	18.1
54	0.5	15	4.4	301.0	16.6	0.9	51.4	334.0	3.6	25.2
54	0.1	11	2.9	265.1	10.4	0.6	42.2	330.5	5.1	39.6

295

Figure E. 15: Master curve for sample 2 (SP-IV with PG 70-22 binder)

$y = 0.0012x^2 - 0.1861x + 3.1787$
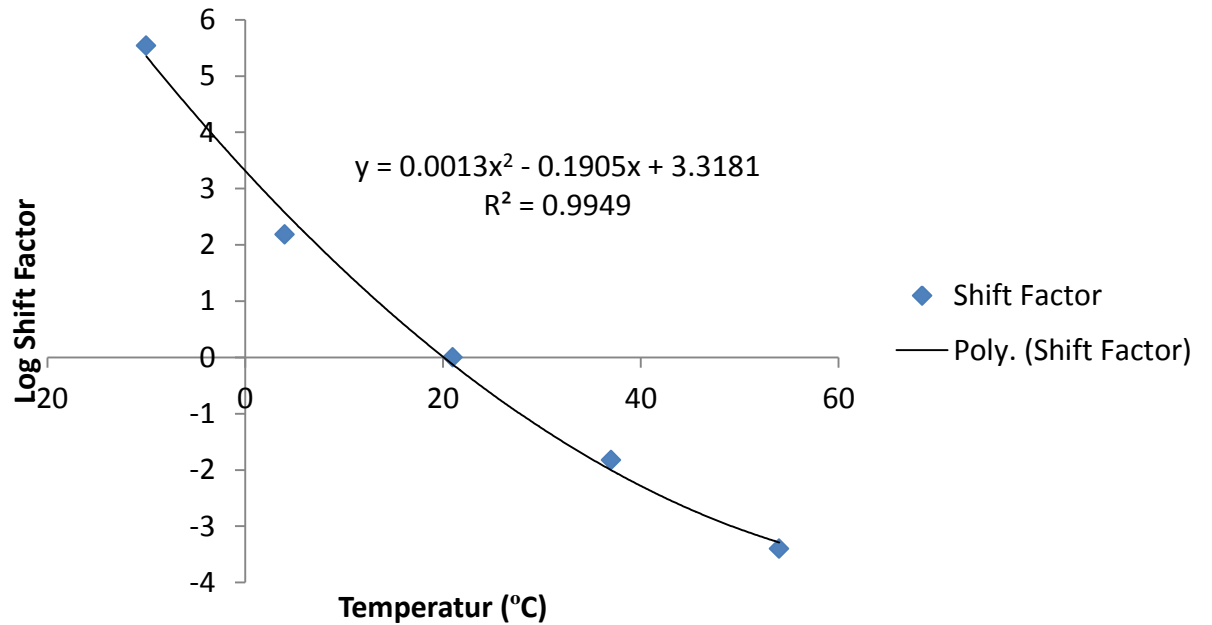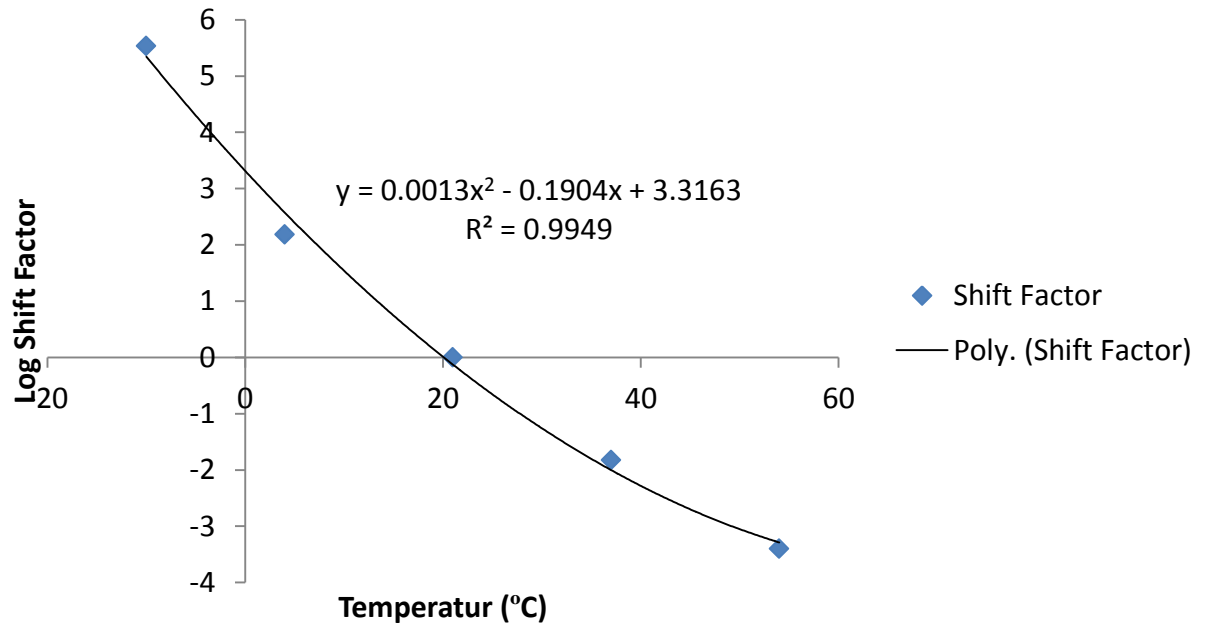$R^2 = 0.9948$
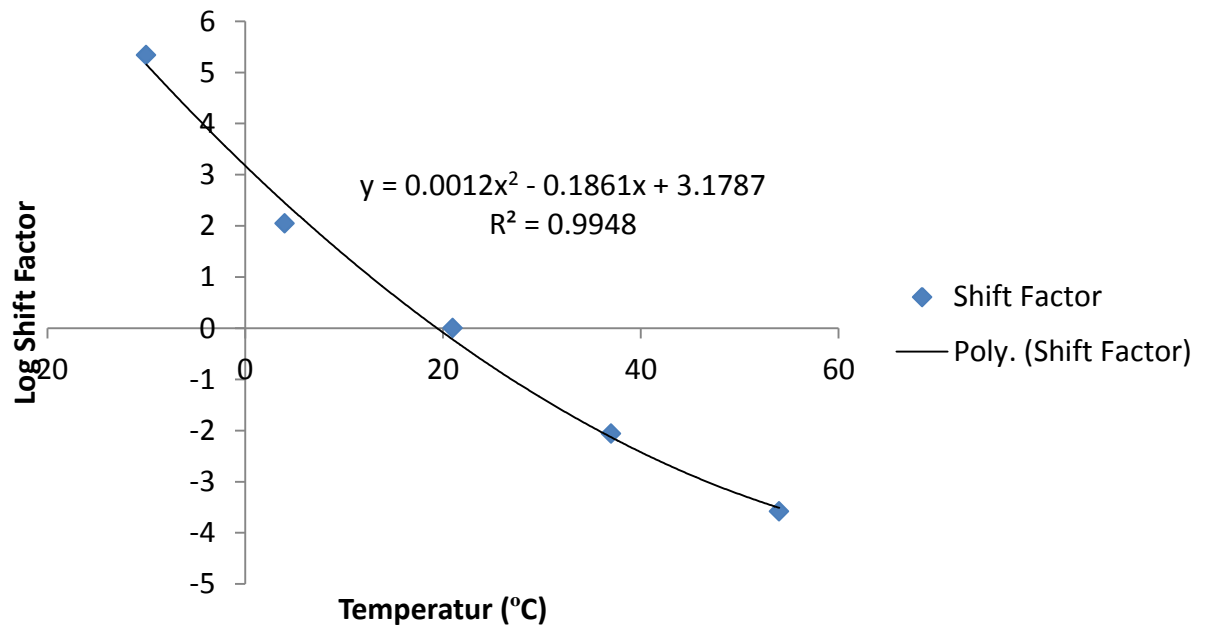
Figure E. 16: Shift factor for sample 2 (SP-IV with PG 70-22 binder)

296

Table E. 9: *E** test results for Sample 3 (SP-IV with PG 70-22 binder)

Temperature	Frequency	Stress		Dynamic Modulus	Phase Angle		Strain			
		Amplitude (P-P)	SE			UC	(P-P) Recoverable	Permanent	SE	UC
(deg C)	(Hz)	(kPa)	(%)	(MPa)	(deg)	(deg)	(micro e)	(micro e)	(%)	(%)
-10	25	2288	5.9	30190.744	5.8	1.1	75.793	79.415	8.8	18.9
-10	10	2188	6.1	29133.283	5.4	0.3	75.12	14.926	8.7	18.3
-10	5	2116	5.2	28118.191	5.2	0.5	75.271	13.198	9.4	17.4
-10	1	1858	1.6	25860.313	6.1	0.5	71.84	12.66	7.6	20
-10	0.5	1731	0.9	25818.975	6.6	0.3	67.057	13.633	5.2	18.7
-10	0.1	1604	0.5	22382.008	6.9	0.4	71.68	29.73	6.2	21.2
4	25	1469	6.5	21625.295	10.3	0.2	67.915	105.896	7.4	1.7
4	10	1365	7	20020.873	9.1	0.2	68.183	40.994	8.4	8.4
4	5	1281	6	18700.885	9.3	0.2	68.479	38.165	7.4	9.9
4	1	1072	2.3	15911.765	10.7	0	67.39	36.452	8.4	12.3
4	0.5	952	1.4	14191.255	11.6	0.1	67.101	42.252	4.2	15.3
4	0.1	785	0.5	11744.354	15.2	0.6	66.823	84.539	7.7	13.5
21	25	655	9.3	9905.348	19.3	2.3	66.118	317.902	13	8.8
21	10	550	9.5	8288.413	18.7	0.3	66.375	379.002	8.6	6
21	5	467	9.5	7255.802	20.1	0	64.315	416.217	7.8	6.2
21	1	303	5.5	4909.348	24.1	0.1	61.746	399.884	4.9	0.1
21	0.5	257	3.1	3999.884	25.7	0	64.319	420.825	3.6	1.1
21	0.1	169	1.3	2551.361	28.3	0.3	66.094	509.56	2.9	2.7
37	25	261	9.5	4214.005	26.6	7.1	62.027	413.907	19	14.3
37	10	218	9.7	3270.401	27.4	0.6	66.632	629.521	9.3	10.8
37	5	162	8.8	2577.224	28.1	0.1	62.724	680.179	7.1	9.2
37	1	96	5.6	1419.351	31.4	1.2	67.542	659.897	8.1	1.9
37	0.5	76	3.9	1126.01	31.2	0.5	67.113	674.609	5	3.8
37	0.1	43	2.7	658.969	29	0.2	65.315	722.468	4	8.5
54	25	71	9.3	1298.131	34.3	1.3	54.908	339.206	7.6	2.4
54	10	59	7.8	936.152	31.3	0.9	63.199	500.488	5.2	1.1
54	5	49	6.7	724.029	29.8	0.9	67.219	563.521	5.4	0.9
54	1	32	5.6	428.028	27.2	0.9	74.435	573.882	4.7	4.3
54	0.5	28	4.2	358.361	24.7	0.7	78.344	595.17	4.8	3.4
54	0.1	23	3.3	265.662	19.6	0.1	86.741	648.351	7.4	2.5

297

Figure E. 17: Master curve for Sample 3 (SP-IV with PG 70-22 binder)

$y = 0.0011x^2 - 0.1787x + 3.3405$
$R^2 = 0.9991$
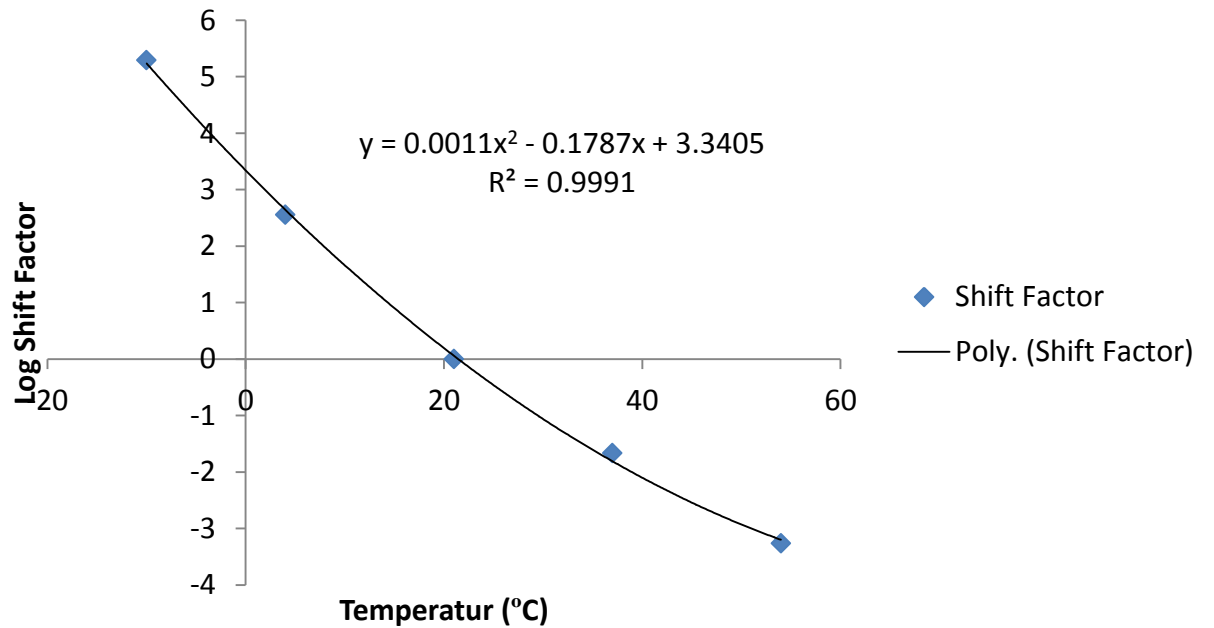
Figure E. 18: Shift factor for Sample 3 (SP-IV with PG 70-22 binder)

Table E. 10: *E** test results for Sample 4 (SP-IV with PG 70-22 binder)

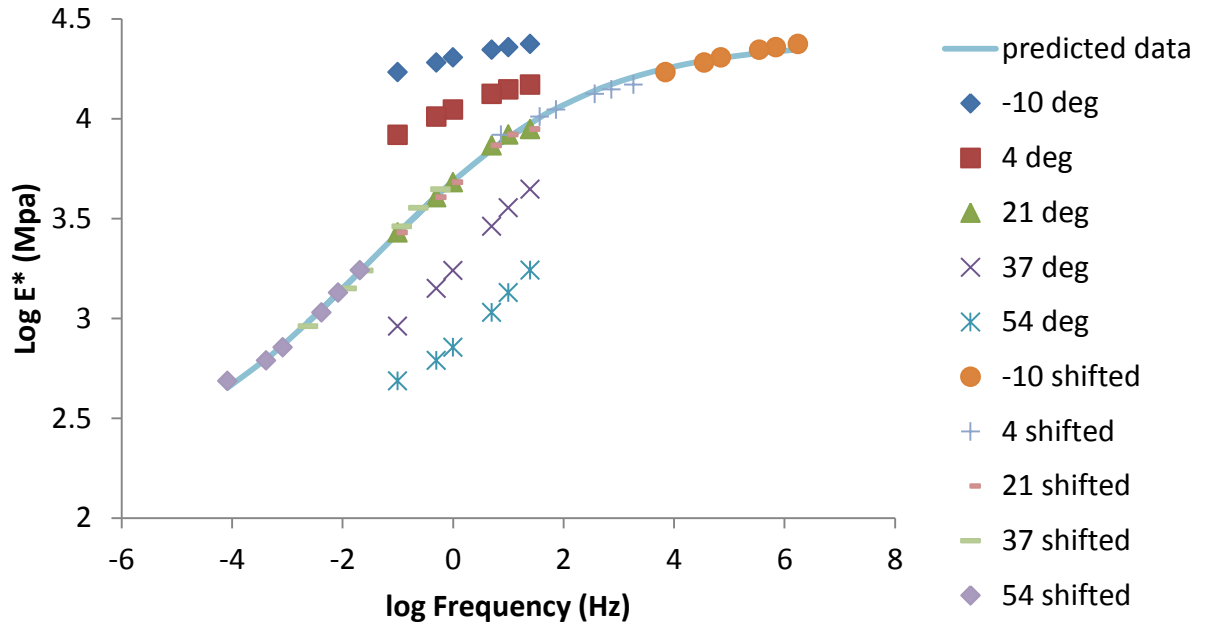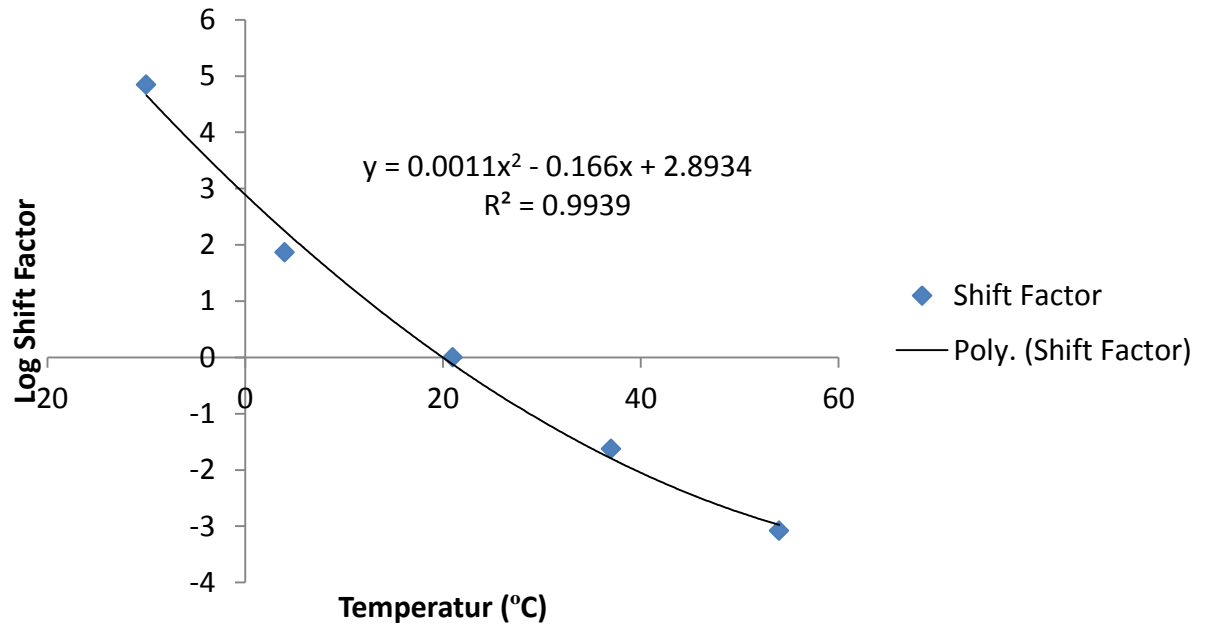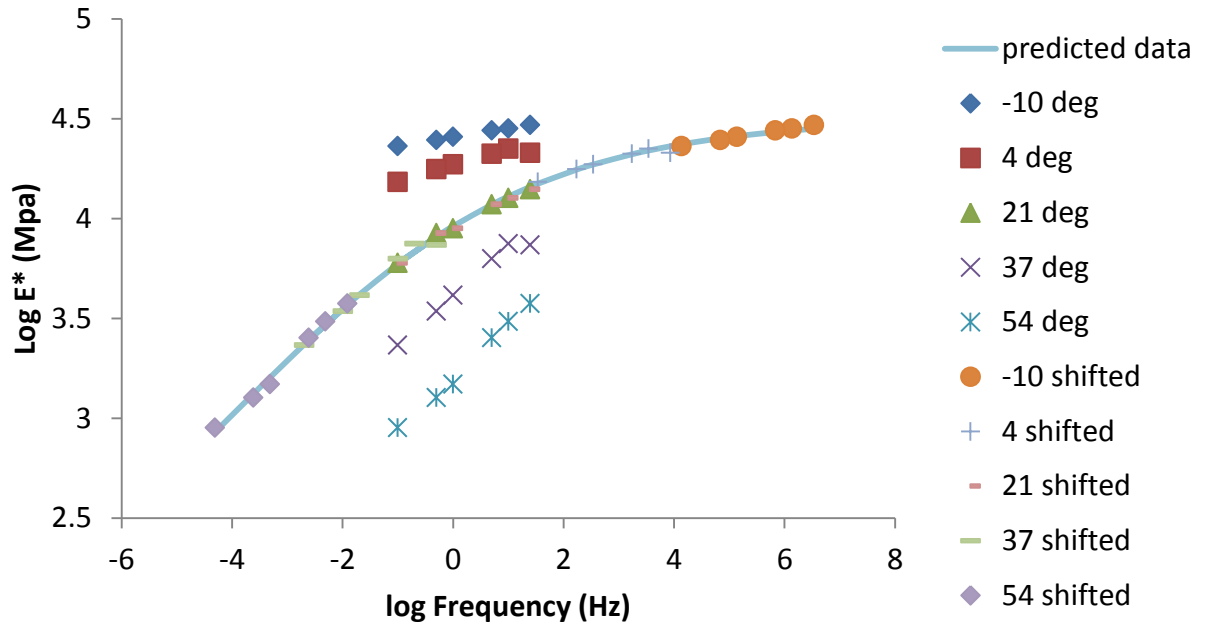| Temperature	Frequency	Stress		Dynamic Modulus	Phase Angle		Strain			
		Amplitude (P-P)	SE			UC	(P-P) Recoverable	Permanent	SE	UC
(deg C)	(Hz)	(kPa)	(%)	(MPa)	(deg)	(deg)	(micro e)	(micro e)	(%)	(%)
-10	25	2284	6.1	27870.521	8.2	6	81.941	95.201	7.3	5.2
-10	10	2182	6.1	26863.889	5.4	0	81.239	28.557	7.6	2.5
-10	5	2125	5.4	26322.541	5	0.2	80.714	26.048	6.6	1.2
-10	1	1860	1.7	24133.479	5.5	0.6	77.062	25.203	6.3	1
-10	0.5	1733	0.9	22164.762	6.4	0.1	78.181	26.649	4.5	1.8
-10	0.1	1605	0.4	20529.926	7.9	0.3	78.177	41.239	6	0.3
4	25	1473	7	20316.455	9.8	3.3	72.499	144.386	7.5	32.3
4	10	1367	7.8	18166.545	10	0.7	75.256	80.528	8.5	21.9
4	5	1279	6.7	17364.184	9.4	0.1	73.665	82.893	13	22.8
4	1	1073	2.6	14095.119	13.3	1.5	76.123	85.158	4.4	18.8
4	0.5	952	1.6	13090.8	13.9	1.5	72.694	92.668	4.7	19.2
4	0.1	784	0.6	10328.222	15.7	1.2	75.924	145.136	4.4	19.1
21	25	585	9.1	9268.237	17.9	2.4	63.172	237.591	8.4	2.4
21	10	492	10	7775.177	18.4	0.6	63.325	305.267	9.6	3.5
21	5	418	10	6926.833	19.6	0.7	60.413	336.126	8.6	3.3
21	1	274	5	4546.571	23.5	1	60.358	322.434	5.2	9.1
21	0.5	231	3.3	3849.597	25	0.8	60.12	338.254	4.6	9.9
21	0.1	153	1.2	2528.231	27.8	0.6	60.589	411.707	3.3	10.8
37	25	219	9.6	3357.617	28.1	2	65.172	559.408	9.3	16.3
37	10	183	9.6	2587.447	27.5	0.5	70.612	804.307	7.2	7.3
37	5	137	8.7	2067.036	28.6	0.9	66.126	867.508	6.3	7.7
37	1	79	5.8	1142.5	31.1	1	69.239	853.743	4.8	6.7
37	0.5	62	4	899.356	30.9	1.2	68.855	868.386	4.7	6
37	0.1	36	2.7	522.808	29.2	1.2	68.292	916.359	3.8	4.7
54	25	55	8.5	937.895	36.2	8	59.013	96.009	8.6	11.4
54	10	45	6.8	689.88	32.4	2.5	65.924	145.164	7.7	2.5
54	5	36	5.3	539.367	31.3	3.7	67.517	159.838	6.2	4.1
54	1	24	3.9	310.104	27.8	3.3	76.478	157.602	7.2	10.6
54	0.5	22	3.7	256.901	25.3	3	85.14	168.054	4.8	13.5
54	0.1	18	2.6	181.758	19.8	2.5	96.953	209.564	5.2	20.3

299

Figure E. 19: Master curve for Sample 4 (SP-IV with PG 70-22 binder)
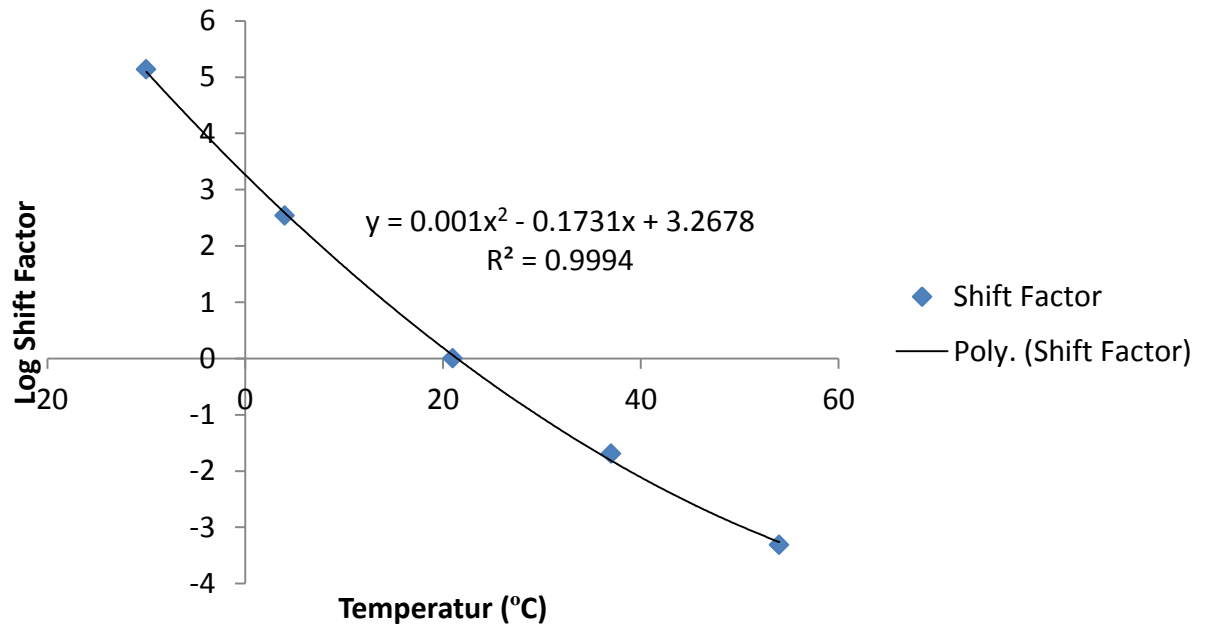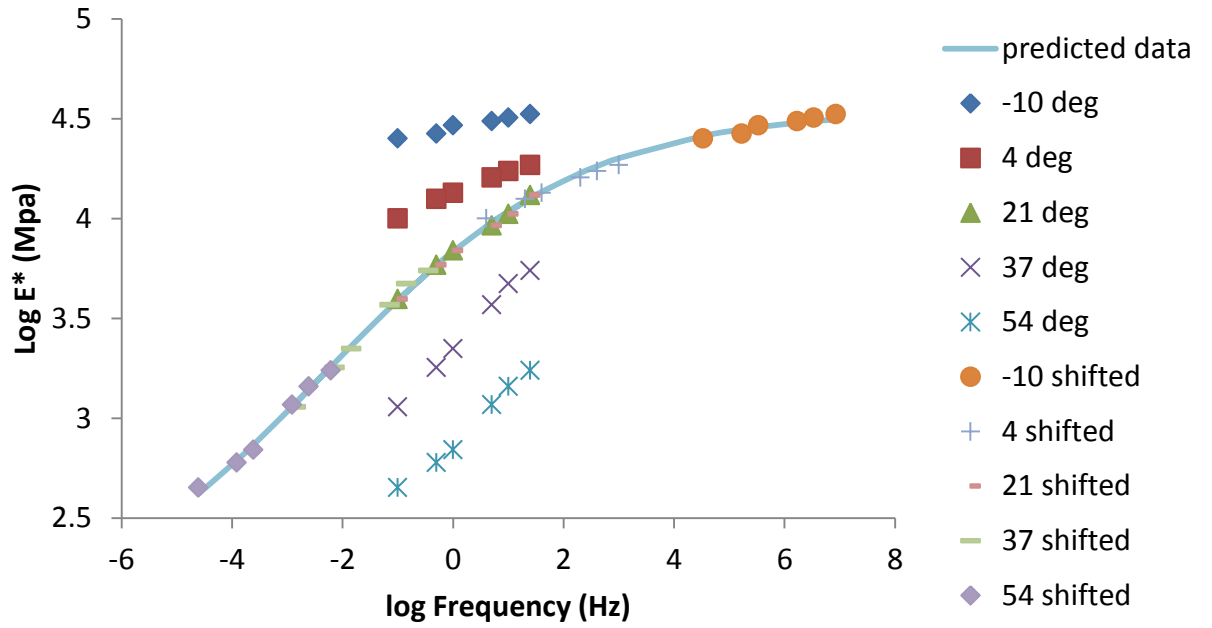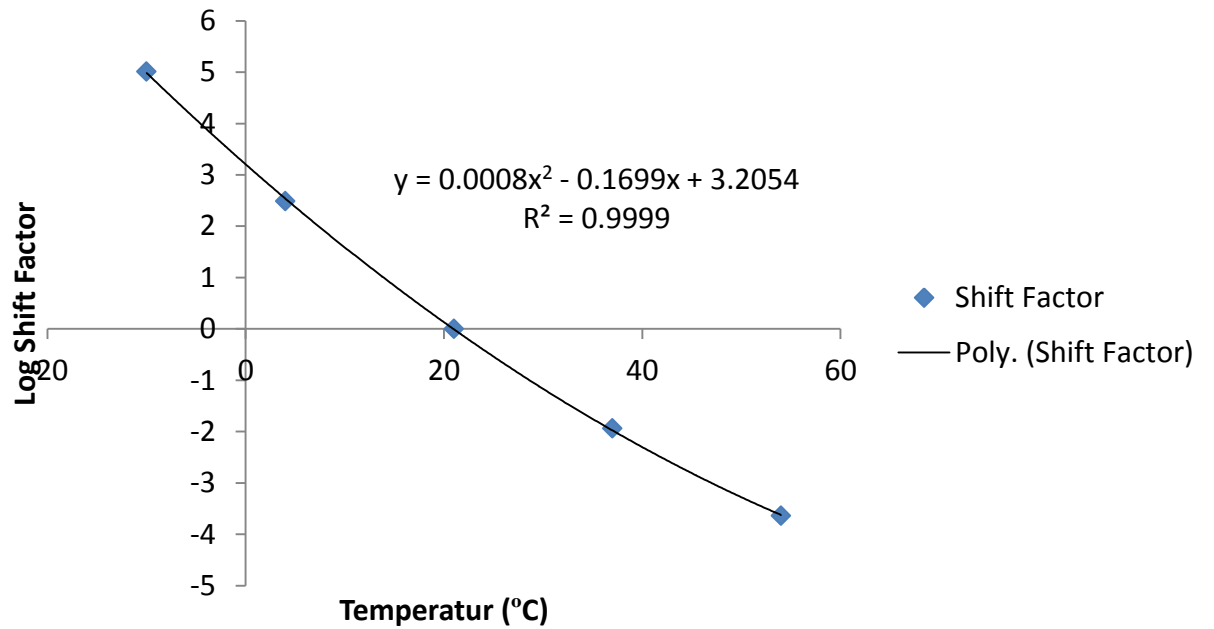

Figure E. 20: Shift factor for Sample 4 (SP-IV with PG 70-22 binder)

300

Table E. 11: *E** test results for Sample 5 (SP-IV with PG 70-22 binder)

Temperature	Frequency	Stress		Dynamic Modulus	Phase Angle		Strain			
		Amplitude (P-P)	SE			UC	(P-P) Recoverable	Permanent	SE	UC
(deg C)	(Hz)	(kPa)	(%)	(MPa)	(deg)	(deg)	(micro e)	(micro e)	(%)	(%)
-10	25	1539.0	5.5	24367.8	5.7	0.8	63.1	70.0	6.1	17.3
-10	10	1554.0	5.3	23665.4	5.6	0.2	65.7	30.4	5.6	24.3
-10	5	1506.0	4.2	22811.3	5.8	0.2	66.0	34.2	4.7	24.3
-10	1	1357.0	1.2	20487.9	7.0	0.3	66.2	33.3	4.4	24.8
-10	0.5	1281.0	0.7	19221.9	7.1	0.1	66.6	35.7	6.0	22.7
-10	0.1	1166.0	0.4	17009.3	8.3	0.1	68.5	59.4	6.6	23.3
4	25	1217.0	7.0	19924.6	14.3	2.0	61.1	185.7	6.8	0.7
4	10	1191.0	7.6	18009.6	13.5	2.7	66.1	157.1	7.5	8.3
4	5	1136.0	6.3	16418.0	14.2	2.9	69.2	178.4	6.2	8.6
4	1	963.0	2.3	12831.3	16.8	2.8	75.0	189.2	4.2	7.3
4	0.5	885.0	1.3	11478.9	19.7	3.5	77.1	217.9	3.0	7.3
4	0.1	796.0	0.7	8169.4	23.4	3.4	97.5	376.0	3.2	6.1
21	25	430.0	9.9	7528.9	25.6	0.9	57.1	389.0	21.0	27.2
21	10	357.0	10.2	6115.1	24.0	0.4	58.3	549.8	8.1	27.8
21	5	297.0	9.2	4965.0	25.4	0.5	59.8	628.8	5.8	27.8
21	1	202.0	4.6	2873.1	30.2	1.1	70.3	625.4	4.4	27.7
21	0.5	170.0	3.1	2268.7	31.7	1.2	75.1	664.1	3.5	26.2
21	0.1	112.0	1.1	1309.1	32.1	1.4	85.5	778.0	3.9	22.9
37	25	133.0	9.9	2197.8	33.9	0.7	60.3	557.9	8.2	25.7
37	10	110.0	9.6	1521.4	33.1	0.7	72.6	805.3	7.0	19.3
37	5	83.0	9.3	1133.4	33.2	0.8	72.9	882.3	6.8	20.5
37	1	47.0	6.0	592.6	31.3	1.8	79.9	879.3	5.2	27.9
37	0.5	37.0	4.3	463.0	29.6	1.7	79.9	887.4	4.4	30.6
37	0.1	22.0	2.0	284.6	23.6	1.4	75.9	906.6	3.6	39.8
54	25	41.0	9.4	469.2	30.9	31.4	86.4	539.6	11.4	39.5
54	10	33.0	7.7	378.7	28.3	0.7	86.4	735.0	6.3	31.3
54	5	28.0	7.4	305.4	26.0	0.2	91.7	827.1	5.1	30.6
54	1	18.0	5.4	208.4	19.7	0.0	85.4	836.2	6.6	37.6
54	0.5	15.0	4.3	184.0	18.2	0.2	83.6	850.0	5.3	35.3
54	0.1	11.0	3.2	150.0	13.0	0.4	74.5	873.7	7.1	34.9

301

Figure E. 21: Master curve for Sample 5 (SP-IV with PG 70-22 binder)

$$y = 0.0004x^2 - 0.139x + 2.8196$$
$$R^2 = 0.9992$$

Figure E. 22: Shift factor for Sample 5 (SP-IV with PG 70-22 binder)

302

Table E. 12: *E** test results for Sample 6 (SP-IV with PG 70-22 binder)

Temperature	Frequency	Stress		Dynamic Modulus	Phase Angle		Strain			
		Amplitude (P-P)	SE			UC	(P-P) Recoverable	Permanent	SE	UC
(deg C)	(Hz)	(kPa)	(%)	(MPa)	(deg)	(deg)	(micro e)	(micro e)	(%)	(%)
-10	25	2289.0	6.4	38885.2	6.0	1.0	58.9	63.6	8.5	11.3
-10	10	2189.0	6.5	37536.6	5.1	0.4	58.3	13.8	8.6	5.8
-10	5	2121.0	5.6	36217.8	5.2	0.0	58.6	19.1	7.6	5.6
-10	1	1858.0	1.7	32822.5	7.1	0.4	56.6	20.6	10.6	4.6
-10	0.5	1732.0	1.0	33693.9	4.1	2.3	51.4	17.8	8.8	9.0
-10	0.1	1604.0	0.5	28712.2	7.5	0.4	55.9	24.9	7.3	5.8
4	25	1473.0	7.4	27304.4	7.6	2.2	53.9	98.5	10.6	29.5
4	10	1361.0	7.7	24327.9	9.5	0.1	55.9	51.1	10.0	39.7
4	5	1275.0	6.5	22900.6	9.8	0.2	55.7	52.4	8.3	41.1
4	1	1073.0	2.6	19680.2	11.7	0.0	54.5	52.4	5.8	43.6
4	0.5	952.0	1.6	17955.7	9.5	0.9	53.0	56.0	5.6	45.8
4	0.1	784.0	0.6	14465.5	14.9	0.1	54.2	91.8	4.8	47.3
21	25	782.0	7.7	12364.9	17.8	1.0	63.3	296.0	8.0	11.8
21	10	658.0	8.3	10328.6	18.1	0.8	63.7	361.5	8.4	21.2
21	5	565.0	8.3	9085.9	19.1	1.3	62.2	403.3	8.2	21.4
21	1	367.0	5.1	6329.9	22.4	1.0	58.0	415.2	6.7	28.8
21	0.5	308.0	3.4	5340.4	24.9	1.4	57.7	464.1	5.0	29.4
21	0.1	202.0	1.4	3277.9	28.3	1.4	61.7	537.4	3.5	31.9
37	25	263.0	9.2	4372.4	27.4	2.0	60.2	611.3	8.5	9.2
37	10	220.0	9.7	3341.2	27.4	1.4	65.7	873.1	7.8	0.1
37	5	162.0	8.8	2672.5	28.5	1.3	60.7	938.0	6.8	1.2
37	1	95.0	5.7	1520.2	31.6	1.4	62.7	918.5	5.4	9.4
37	0.5	75.0	4.0	1196.0	31.9	1.8	62.7	930.7	4.6	13.7
37	0.1	45.0	1.9	709.3	30.0	1.3	62.9	968.6	3.4	18.0
54	25	70.0	9.9	1292.0	34.5	7.1	54.4	156.1	9.3	0.8
54	10	59.0	8.1	940.7	31.3	0.4	62.2	272.7	8.3	10.6
54	5	48.0	6.9	720.0	30.5	0.0	66.7	311.6	7.5	4.7
54	1	31.0	6.1	425.5	28.3	0.9	73.5	311.5	7.6	0.0
54	0.5	29.0	5.0	356.7	25.8	0.8	80.6	321.1	5.5	0.8
54	0.1	22.0	4.3	255.9	20.7	1.2	87.1	369.5	6.1	1.4

303
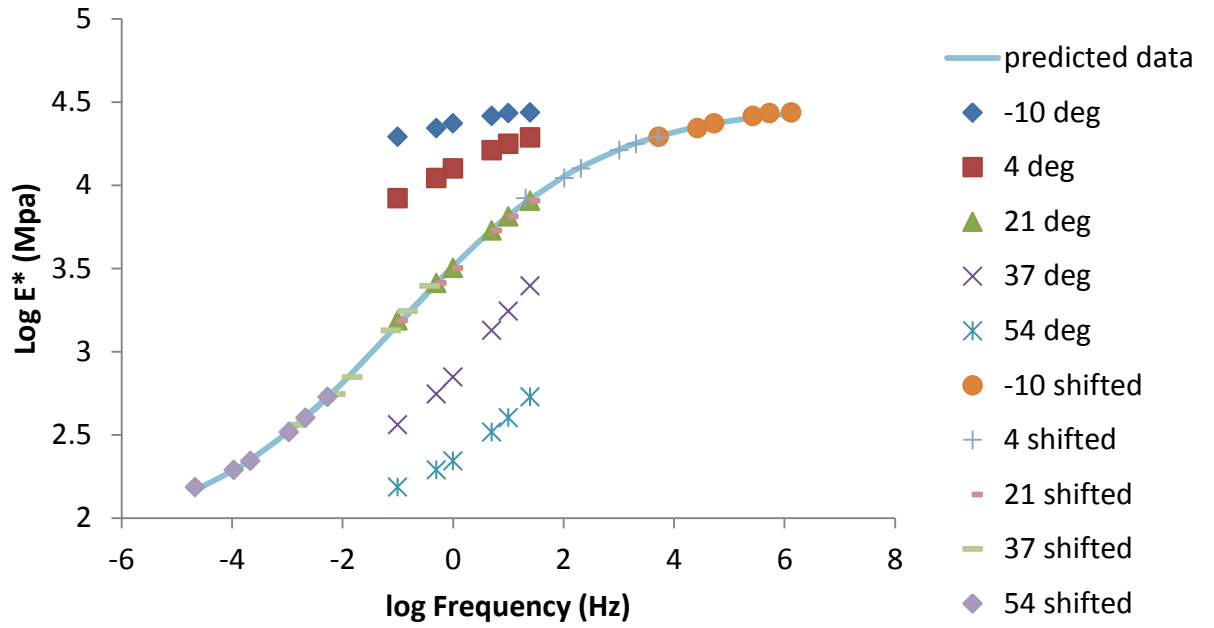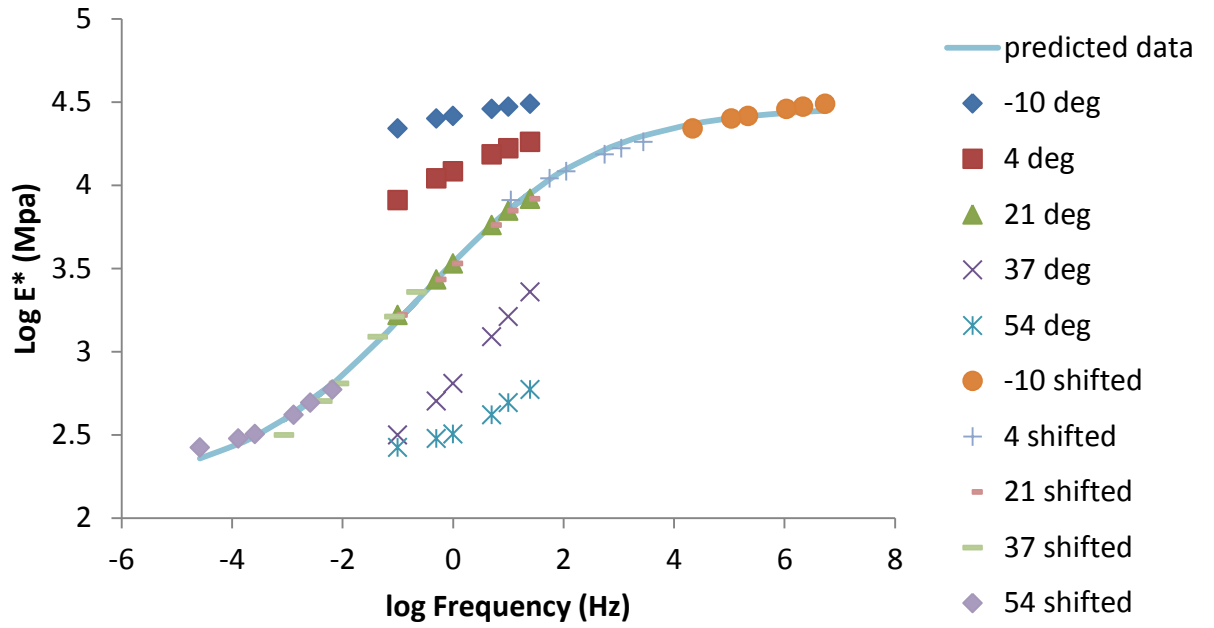
Figure E. 23: Master curve for Sample 6 (SP-IV with PG 70-22 binder)
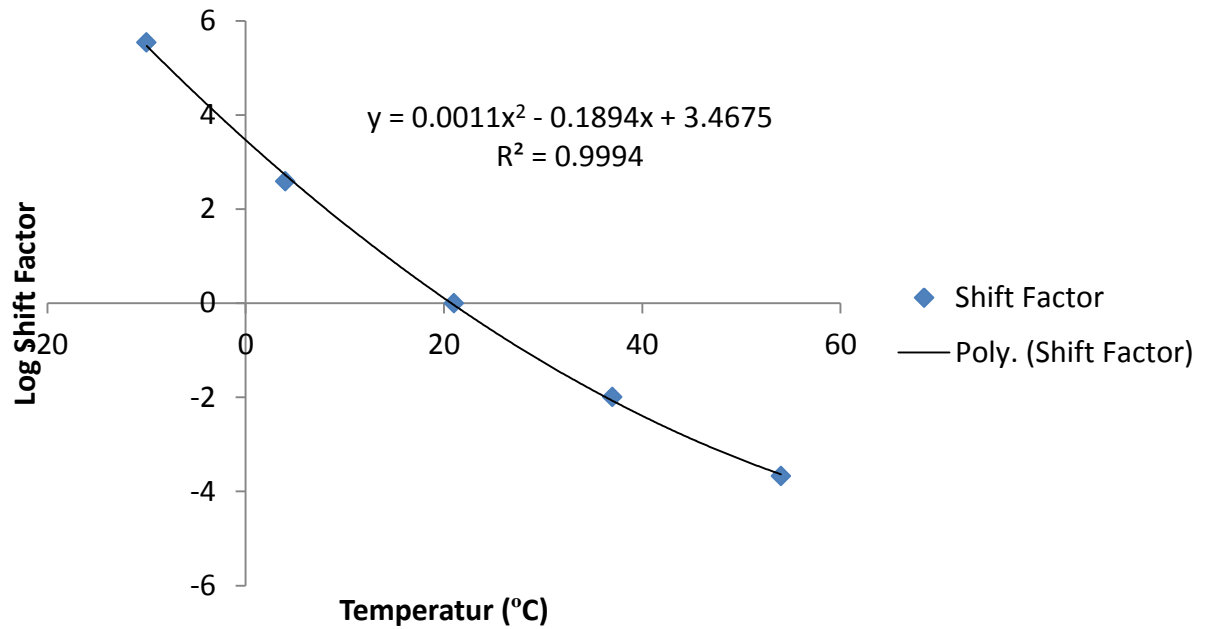
Figure E. 24: Shift factor for Sample 6 (SP-IV with PG 70-22 binder)

304

APPENDIX F

AMEC Laboratory Dynamic Modulus Test Results

FOR

SP-II WITH PG 64-22 BINDER

SP-II WITH PG 70-22 BINDER

SP-III WITH PG 64-22 BINDER

SP-III WITH PG 70-22 BINDER

SP-IV WITH PG 70-22 BINDER

MIXES

SP-II WITH PG 64-22 BINDER - Samples

Table F. 13: *E** test results for Sample 1 (SP-II with PG 64-22 binder)

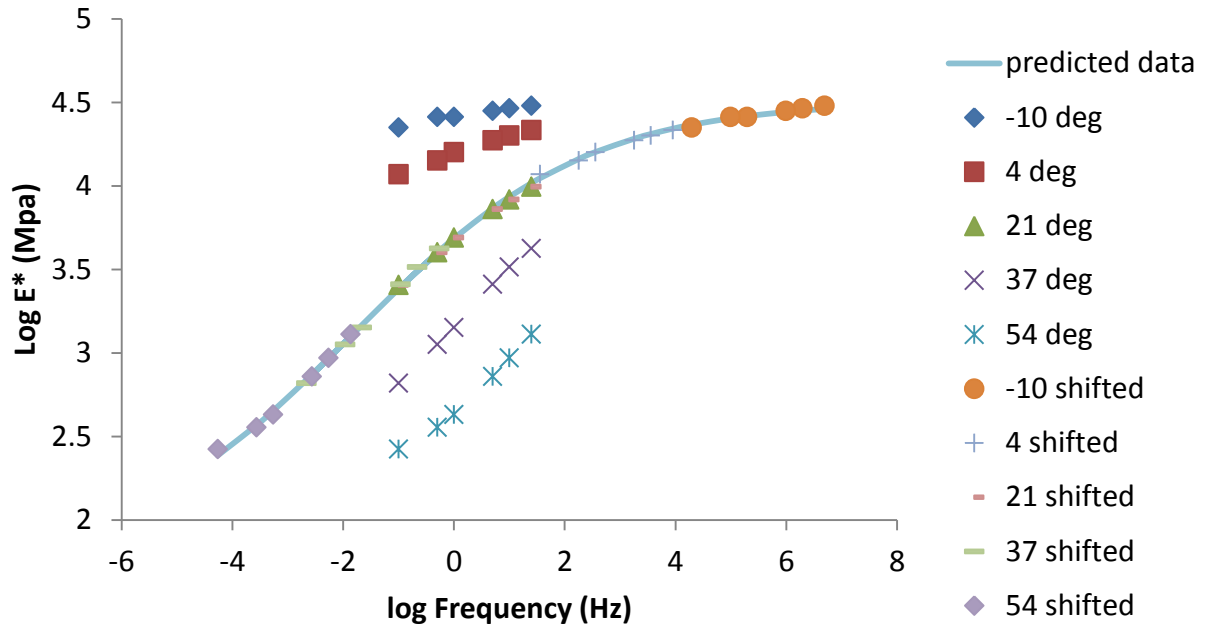| Temperature	Frequency	Stress		Dynamic Modulus	Phase Angle		Strain			
		Amplitude (P-P)	SE			UC	(P-P) Recoverable	Permanent	SE	UC
(deg C)	(Hz)	(kPa)	(%)	(MPa)	(deg)	(deg)	(micro e)	(micro e)	(%)	(%)
-10	25	1439.5	6.6	30474.2	5.3	1.6	47.237	-9.148	14	47.1
-10	10	1356.1	4.2	29670.5	4.8	0.9	45.705	-15.7	8	38.9
-10	5	1255.8	2.1	28941.1	4.3	0.6	43.39	-18.674	7.1	38.7
-10	1	1110	0.4	26219.3	5.4	0.3	42.335	-20.688	5.8	39.5
-10	0.5	1050.7	0.3	25208.1	5.5	0.6	41.682	-21.056	6	40.3
-10	0.1	908.4	0.2	23361.1	5.9	0.2	38.885	-16.345	5.7	42.2
4	25	1212.7	6	23668.0	8.7	2.1	51.237	15.442	9.6	53.1
4	10	1089.9	4	22520.6	9.2	2	48.397	15.315	7.7	48.5
4	5	976.8	2.1	21126.1	9.8	2.3	46.236	14.051	7.4	48.2
4	1	880.2	0.4	18292.3	10.2	1.8	48.12	12.294	7	49.2
4	0.5	799.9	0.3	17108.3	11.8	1.6	46.753	13.59	9	50
4	0.1	697.9	0.2	14392.7	13.5	2.2	48.491	34.858	6.6	47.7
21	25	653.6	5.7	14062.2	13.1	1.3	46.476	108.367	7.2	47.1
21	10	591.5	3.9	12427.5	14	0.5	47.6	142.111	5.6	44.6
21	5	529.8	2.2	11170.3	14.8	0.5	47.427	151.444	4.7	43.8
21	1	378.7	0.5	8415.5	18.1	0.8	44.997	141.069	4.8	45.7
21	0.5	318.3	0.4	7377.7	19.6	0.5	43.145	142.645	5.7	45.7
21	0.1	237.7	0.2	5210.6	22.8	1.2	45.611	184.179	3.3	43.8
37	25	329.9	5.6	6188.3	22.7	3.6	53.312	337.727	6.7	32.4
37	10	273.5	4.4	5056.8	24.2	2.6	54.095	429.362	6.2	29.1
37	5	224.7	2.8	4270.5	25.3	2.7	52.622	448.156	4.2	27.9
37	1	148.4	0.8	2715.2	28.7	2.5	54.648	423.158	4.5	27.7
37	0.5	108.7	0.8	2206.1	30.2	2	49.26	412.945	3.8	28.3
37	0.1	68.9	0.6	1420.3	30.7	2.1	48.5	444.599	5	28.8
54	25	127.7	6	2448.0	28.1	3.6	52.179	575.348	7.2	16.4
54	10	100.3	4.9	1842.1	27.7	2	54.438	714.831	5.9	14.3
54	5	84.6	3.3	1479.8	27.6	1.3	57.176	769.609	4.7	12.2
54	1	48.7	1.1	855.5	27.9	0.1	56.981	757.162	4.1	6.7
54	0.5	39	0.8	689.8	27.1	0.2	56.6	759.398	3.6	5.1
54	0.1	29.3	1.3	447.9	24.5	0.3	65.461	795.26	4.5	5.4
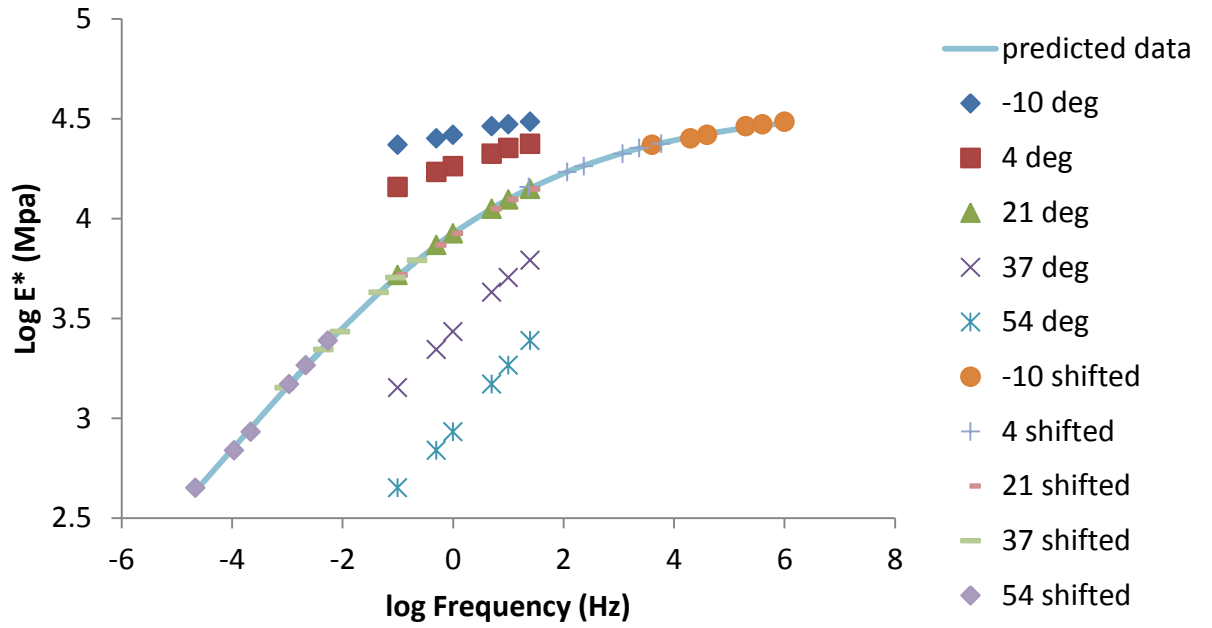
Figure F. 25: Master curve for Sample 1 (SP-II with PG 64-22 binder)
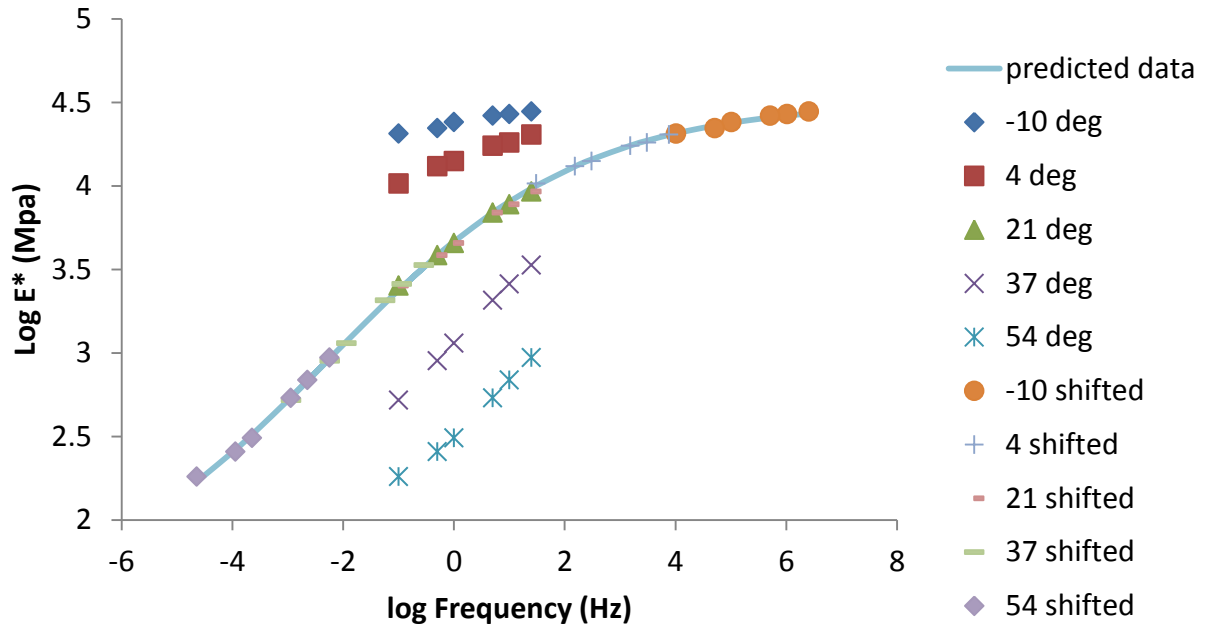

Figure F. 26: Shift factor for Sample 1 (SP-II with PG 64-22 binder)

307

www.manaraa.com

Table F. 14: *E** test results for Sample 2 (SP-II with PG 64-22 binder)

Temperature	Frequency	Stress		Dynamic Modulus	Phase Angle		Strain			
		Amplitude (P-P)	SE			UC	(P-P) Recoverable	Permanent	SE	UC
(deg C)	(Hz)	(kPa)	(%)	(MPa)	(deg)	(deg)	(micro e)	(micro e)	(%)	(%)
-10	25	1174.3	5.9	21325.5	3.9	0.8	55.066	-40.377	13	85.2
-10	10	1113	3.8	21173.8	3.7	0.3	52.563	-52.739	8.3	85.1
-10	5	1057.5	2	20462.5	4.2	0.2	51.68	-57.884	7.2	84.4
-10	1	949.7	0.4	19009.1	4.9	1.3	49.962	-61.702	7.7	86.3
-10	0.5	900.1	0.3	18523.2	124.1	207	48.593	-63.3	6.3	88.1
-10	0.1	818.5	0.2	17017.7	5.3	0.4	48.098	-58.066	6.3	88.5
4	25	914.6	5.9	17416.6	7.6	2.3	52.513	-36.468	7.1	45
4	10	844	4.1	16502.7	7.9	1	51.145	-50.547	5.7	42.9
4	5	797.6	2.2	15718.6	8.1	0.7	50.743	-52.623	5.6	42.9
4	1	699.6	0.5	13679.6	9.2	0.8	51.145	-55.637	4.7	44.5
4	0.5	649.8	0.4	12836.4	10.4	0.5	50.619	-54.446	4	44.2
4	0.1	547	0.3	10844.0	11.9	0.5	50.447	-33.017	4	42.2
21	25	539.8	5.7	11019.3	13.3	1.9	48.989	165.104	6.2	1.6
21	10	497.6	4.2	9851.8	14.3	0.6	50.506	224.924	4.9	2
21	5	439.3	2.3	8888.1	15.5	0.1	49.422	258.529	4.4	0.5
21	1	338.4	0.5	6531.5	19.1	0.4	51.815	314.903	4.4	1.5
21	0.5	298	0.4	5493.2	20.5	0.9	54.25	383.798	4.1	2.7
21	0.1	208.1	0.2	3564.9	24.8	0.5	58.388	476.701	3.8	5
37	25	299.1	5.7	5663.2	20.1	0.1	52.821	459.606	6.6	21.9
37	10	245	4.5	4586.3	21.7	0.5	53.428	581.537	4.6	21.2
37	5	195	3.1	3779.7	23.3	0.5	51.603	611.742	4.8	22.1
37	1	128.9	0.8	2313.5	26.6	0.9	55.702	598.556	3.9	26.4
37	0.5	88.9	0.6	1826.2	28.5	1.1	48.689	593.153	3.7	30.2
37	0.1	49.2	0.5	1087.0	28.8	1.1	45.241	619.495	3.8	32
54	25	128.8	6.1	2425.5	27.6	0.5	53.091	505.021	6.4	10.5
54	10	102.3	5.2	1781.9	28.5	0.2	57.39	659.034	5	10.2
54	5	85.5	3.9	1400.8	28.9	0.3	61.059	727.464	5.1	8.9
54	1	53.9	1.4	769.8	29	1.1	69.957	725.481	4.5	12.5
54	0.5	39.1	1	588.7	28.7	1.2	66.409	721.448	4.8	13.6
54	0.1	27.4	1.3	361.9	25.3	2.3	75.573	753.168	4.8	16.5

308

Figure F. 27: Master curve for Sample 2 (SP-II with PG 64-22 binder)

$$y = 0.0008x^2 - 0.1493x + 2.7941$$
$$R^2 = 0.9999$$

Figure F. 28: Shift factor for Sample 2 (SP-II with PG 64-22 binder)

309

SP-II WITH PG 70-22 BINDER - Samples

Table F. 15: *E** test results for Sample 1 (SP-II with PG 70-22 binder)

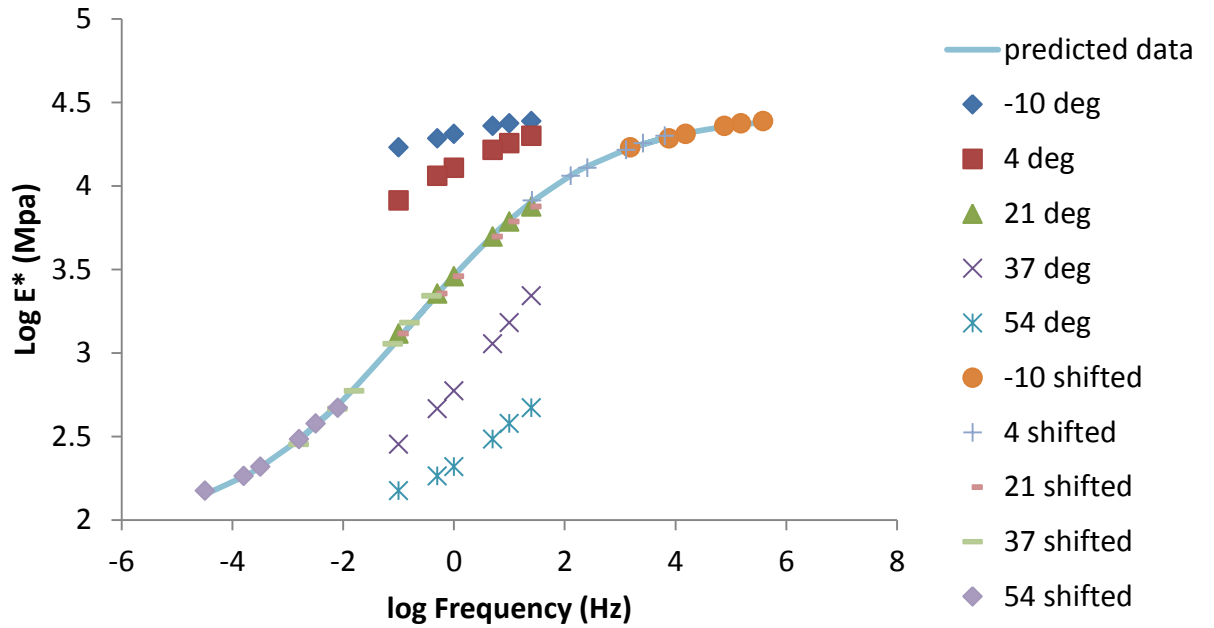| Temperature	Frequency	Stress		Dynamic Modulus	Phase Angle		Strain			
		Amplitude (P-P)	SE			UC	(P-P) Recoverable	Permanent	SE	UC
(deg C)	(Hz)	(kPa)	(%)	(MPa)	(deg)	(deg)	(micro e)	(micro e)	(%)	(%)
-10	25	1171.6	6	29126.2	5.6	2.7	40.226	-49.751	11	16
-10	10	1111.7	3.9	28092.4	5.9	2.4	39.574	-64.516	9.6	13.9
-10	5	1054.2	2	27174.7	6	1.3	38.794	-70.332	8.9	15.7
-10	1	950.1	0.4	24946.3	6.3	2.1	38.085	-74.961	9.5	18.4
-10	0.5	900	0.3	24080.6	7.5	1	37.373	-76.597	8.3	20.3
-10	0.1	818.5	0.2	21588.8	7.6	0.6	37.915	-70.64	8.8	22.8
4	25	1220.4	6	21289.1	7.7	0.6	57.324	17.179	7.9	25.8
4	10	1091.1	3.8	19857.9	8.2	0.4	54.946	24.681	5.4	27.1
4	5	1005.9	2	18726.2	9.2	0.3	53.715	29.41	4	27.5
4	1	899.7	0.4	15868.7	10.6	0.9	56.695	30.767	4.2	28.1
4	0.5	819.2	0.3	14628.3	11.8	1	56.002	36.19	3.3	28.9
4	0.1	717.9	0.2	11939.7	14.1	1.5	60.127	76.26	3.6	33
21	25	608.5	5.4	11077.8	16.5	1	54.927	217.436	8.2	51.6
21	10	541.9	3.7	9564.1	17.2	0.3	56.663	297.255	6.2	49.5
21	5	481	2.2	8488.4	18.2	0.4	56.66	328.063	5.1	49.7
21	1	348.3	0.5	5869.7	22.4	0.6	59.333	322.72	4	51.3
21	0.5	298.3	0.4	5019.9	23.7	0.4	59.419	335.784	4.6	52.1
21	0.1	217.7	0.2	3421.2	26.7	0.8	63.638	412.048	4.4	51.4
37	25	329.8	5.6	4624.7	23.4	0.7	71.31	733.518	5.5	26.4
37	10	272.5	4.1	3646.6	24.5	0.7	74.737	893.987	4.1	24.7
37	5	222.3	2.5	2982.8	25.4	1.1	74.526	933.179	4.1	25.2
37	1	147.8	0.7	1717.8	27.9	1.8	86.047	911.834	3.7	28.3
37	0.5	108.3	0.6	1325.4	28.5	2	81.703	905.267	4.5	31.8
37	0.1	68.8	0.4	807.2	27.2	1.5	85.29	952.352	4.2	35.9
54	25	108	5.9	1748.3	29.6	1.6	61.792	322.677	5.5	17.6
54	10	85.1	4.3	1283.5	28.1	0.3	66.311	377.081	4.9	16.3
54	5	69.8	3.2	1008.9	27.5	0.7	69.224	377.141	4.5	16.1
54	1	38.7	1.4	587.5	26.2	1.3	65.825	349.997	4.9	16.8
54	0.5	29.1	1.2	477.3	25.3	1.9	60.959	332.135	4.1	17
54	0.1	23.3	1.6	341.2	20.8	1.8	68.347	326.619	5	17.7

310

Figure F. 29: Master curve for Sample 1 (SP-II with PG 70-22 binder)
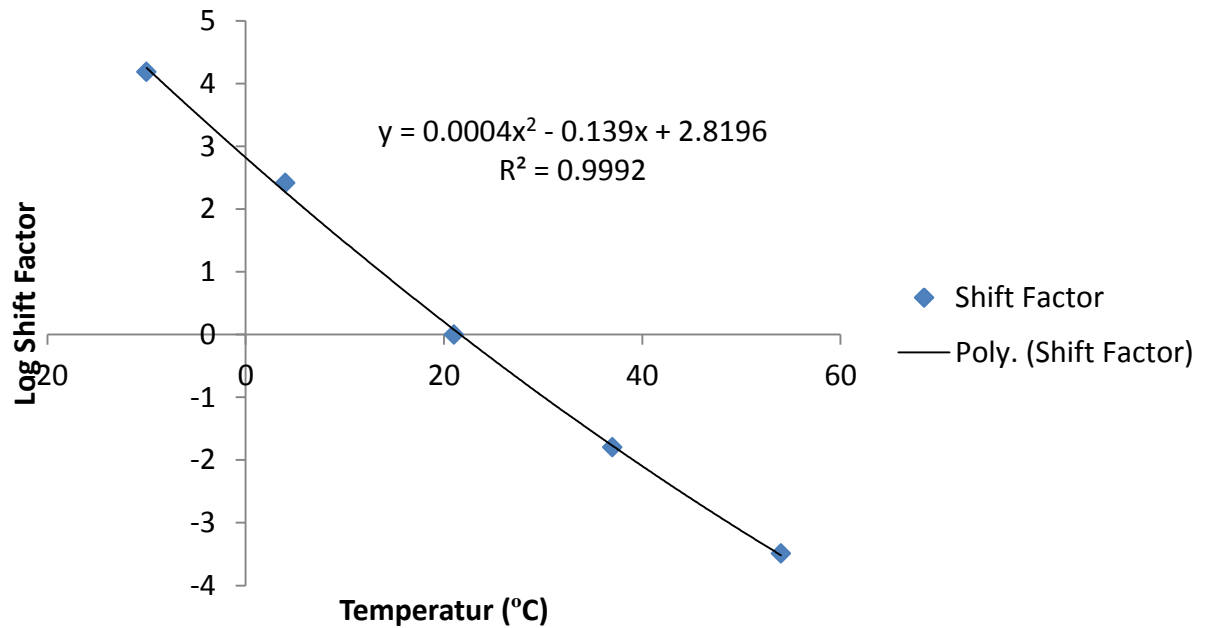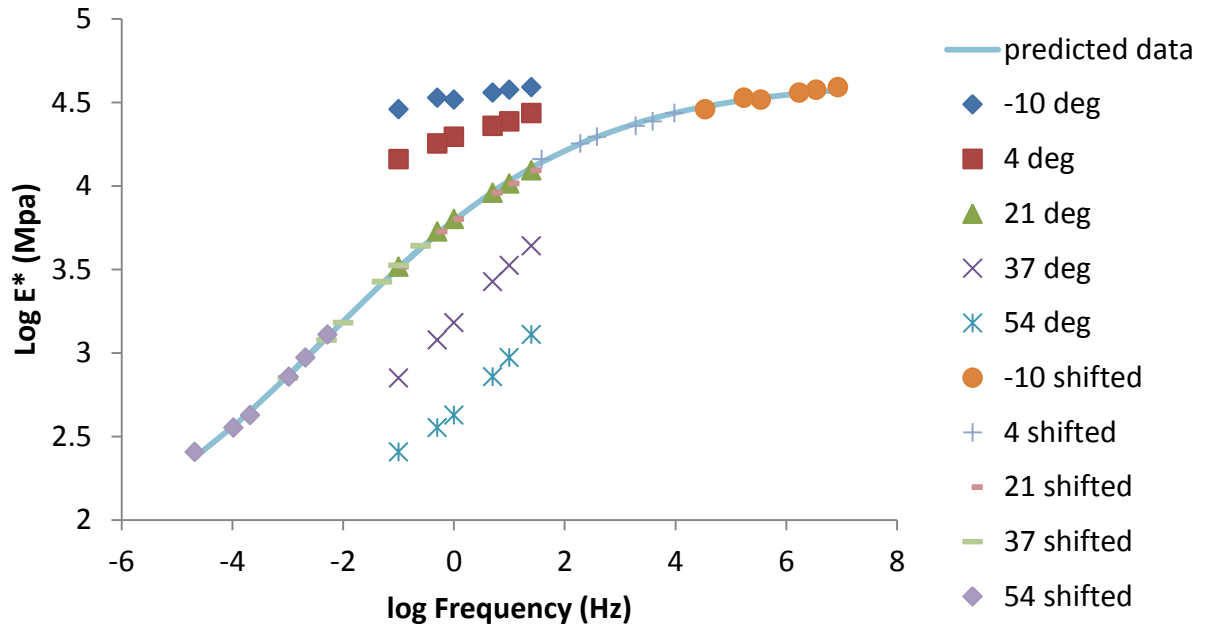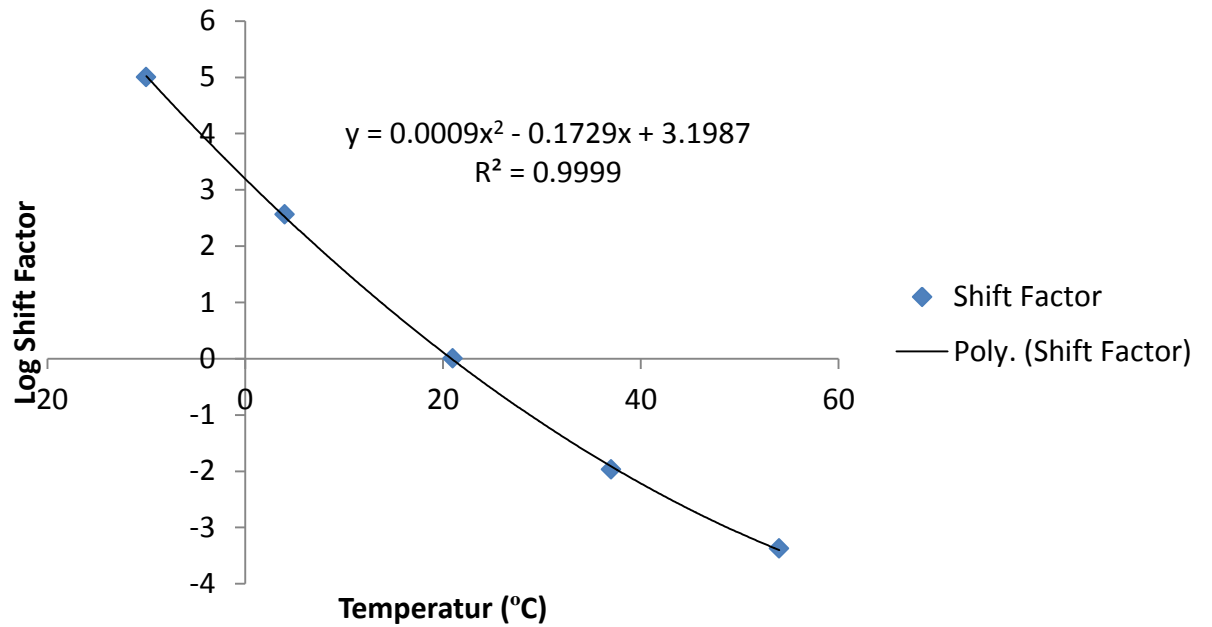

Figure F. 30: Shift factor for Sample 1 (SP-II with PG 70-22 binder)

311

Table F. 16: *E** test results for Sample 2 (SP-II with PG 70-22 binder)

Temperature	Frequency	Stress		Dynamic Modulus	Phase Angle		Strain			
		Amplitude (P-P)	SE			UC	(P-P) Recoverable	Permanent	SE	UC
(deg C)	(Hz)	(kPa)	(%)	(MPa)	(deg)	(deg)	(micro e)	(micro e)	(%)	(%)
-10	25	1443.2	6.9	29189.7	20.4	27.3	49.441	-27.301	29	124
-10	10	1357.3	4.8	28277.5	7.1	3.9	48	-39.721	19	120
-10	5	1260.1	2.7	27560.8	6.2	2.4	45.72	-38.842	21	122
-10	1	1153.3	0.7	25176.0	7.7	2.1	45.811	-32.899	21	125
-10	0.5	1101.2	0.4	24459.2	126.5	204.8	45.021	-38.626	25	127
-10	0.1	998.3	0.2	21753.6	8.6	2.6	45.892	-31.187	26	125
4	25	1279.4	6.1	20443.2	8.6	1.4	62.581	2.14	8.6	31.9
4	10	1153.2	3.9	18650.0	8.3	0.5	61.834	-2.274	6	28.6
4	5	1066.5	2	17227.4	9.4	0.2	61.906	-5.039	4.4	27.7
4	1	959.4	0.4	14522.8	10.9	0.2	66.061	-9.946	3	27.5
4	0.5	880.1	0.3	13310.4	11.9	0.2	66.125	-9.61	2.9	26.9
4	0.1	777.9	0.2	10729.4	14.5	0.3	72.503	29.748	2.9	23.4
21	25	621.6	5.8	11694.0	14.9	2	53.159	141.616	6.7	15.8
21	10	560.3	4.2	10118.2	15.9	2.2	55.376	189.511	5.8	18.6
21	5	500.1	2.4	9070.1	17	2.3	55.134	204.915	4.9	20.9
21	1	348.2	0.5	6699.4	20.5	2.9	51.978	192.903	3.1	21.7
21	0.5	297.9	0.4	5847.9	22	2.4	50.95	199.512	3.6	22.9
21	0.1	218.1	0.2	4141.3	24.6	3.2	52.656	270.133	4.6	25.2
37	25	298.9	5.7	5060.3	21.9	1.2	59.06	404.828	5.9	32.5
37	10	253.9	4.3	4049.4	22.7	0.4	62.697	519.682	4.7	27.5
37	5	193	2.9	3329.5	24.3	0.7	57.981	521.841	4.2	29.9
37	1	113.6	0.8	1966.0	28.9	1.5	57.765	469.87	3.5	38.4
37	0.5	88.8	0.6	1560.3	29.9	1.8	56.89	457.025	5.7	41.7
37	0.1	54.1	0.5	949.6	30.3	2.7	56.923	480.744	5.7	43
54	25	128.3	6.1	2293.7	28.1	1.2	55.955	406.434	6.1	36.1
54	10	100.6	4.6	1715.8	28	1	58.605	510.425	5.4	35.3
54	5	79.1	3.2	1357.2	28.4	1.3	58.302	535.748	6.6	36.1
54	1	40.9	1.1	765.0	28.8	1.3	53.403	509.695	3.9	40.5
54	0.5	31.1	1	620.9	27.8	1.4	50.134	502.976	4.3	43.4
54	0.1	21.4	1.5	410.9	23.9	1.9	52.002	518.524	4.7	46.4

Figure F. 31: Master curve for Sample 2 (SP-II with PG 70-22 binder)

$y = 0.0011x^2 - 0.1725x + 2.9512$
$R^2 = 0.9975$

Figure F. 32: Shift factor for Sample 2 (SP-II with PG 70-22 binder)

313

SP-III WITH PG 64-22 BINDER - Samples

Table F. 17: *E** test results for Sample 1 (SP-III with PG 64-22 binder)

Temperature	Frequency	Stress		Dynamic Modulus	Phase Angle		Strain			
		Amplitude (P-P)	SE			UC	(P-P) Recoverable	Permanent	SE	UC
(deg C)	(Hz)	(kPa)	(%)	(MPa)	(deg)	(deg)	(micro e)	(micro e)	(%)	(%)
-10	25	1437.4	6.5	28409.1	7.7	7.5	50.595	-59.154	30	93.1
-10	10	1356.8	4.6	27961.9	5.5	2.1	48.523	-78.339	18	89.8
-10	5	1256.5	2.5	27220.4	3.4	2.1	46.161	-87.045	18	91.1
-10	1	1150.2	0.5	24882.2	8.2	5.8	46.225	-92.074	35	91.1
-10	0.5	1080.8	0.3	24542.8	6.8	2.1	44.037	-94.534	26	95
-10	0.1	948.2	0.2	21918.7	11.9	9.7	43.26	-89.287	54	94.3
4	25	1226.6	6.1	23386.3	7.4	3	52.448	-2.94	9.5	79.2
4	10	1092.5	4.1	22811.8	7.9	1.8	47.891	-6.165	6.9	76.1
4	5	1007.7	2.2	21770.6	9.1	1.6	46.285	-6.732	6.9	74.9
4	1	899.5	0.4	18826.3	9.9	2.2	47.781	-8.684	4.9	76
4	0.5	819.4	0.3	17553.8	11.3	2	46.68	-6.276	5.7	76.2
4	0.1	718.1	0.2	14845.2	13.4	2	48.37	19.961	5.7	74
21	25	814.3	6	15647.4	13.1	1.3	52.039	204.909	7.1	36.3
21	10	755.2	4.4	13590.4	14.7	0.7	55.566	262.581	5.9	35.2
21	5	690.4	2.5	12137.0	15.8	0.7	56.88	281.725	5.6	33
21	1	589.7	0.5	8842.9	19.5	1.3	66.691	288.311	3.6	34.5
21	0.5	529.8	0.4	7543.1	21.1	1.2	70.241	309.799	4.2	33.9
21	0.1	387.1	0.3	5130.8	24.5	1.4	75.438	406.191	3.8	34.1
37	25	357.7	5.9	6872.4	22.4	0.4	52.05	444.668	6.9	13.2
37	10	282.9	4.7	5446.4	24.2	0.3	51.936	554.327	6.1	13.9
37	5	235.2	2.9	4488.4	26	0.6	52.403	584.668	4.9	12.9
37	1	138.4	0.8	2649.9	29.7	1.4	52.23	545.3	4.5	17.9
37	0.5	98.7	0.6	2058.5	30.9	1.6	47.938	529.125	5	21.6
37	0.1	69	0.4	1201.9	30.9	2.3	57.404	566.399	4.2	24.2
54	25	127.8	6.2	2535.3	32.1	1.6	50.402	379.599	6.8	6.5
54	10	99.8	4.8	1778.0	32.2	1.5	56.119	462.267	5.4	6.1
54	5	84.2	3.3	1366.9	32.2	1.4	61.61	494.06	4.7	6
54	1	48.6	1.2	727.6	31.7	1.8	66.822	461.204	4	3.9
54	0.5	39	0.8	573.3	30.5	1.7	67.983	444.271	4	4.3
54	0.1	27.3	0.8	359.0	25.8	1.7	76.159	449.279	4.5	4.8

314

Figure F. 33: Master curve for Sample 1 (SP-III with PG 64-22 binder)

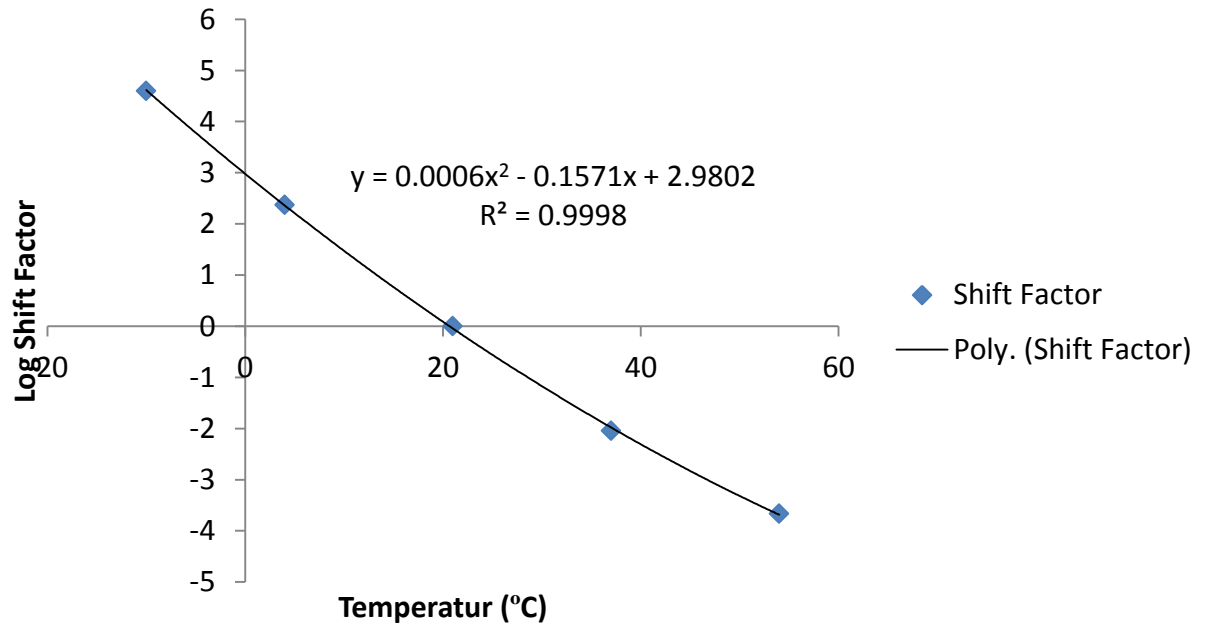$$y = 0.0004x^2 - 0.1354x + 2.6302$$
$$R^2 = 0.9996$$
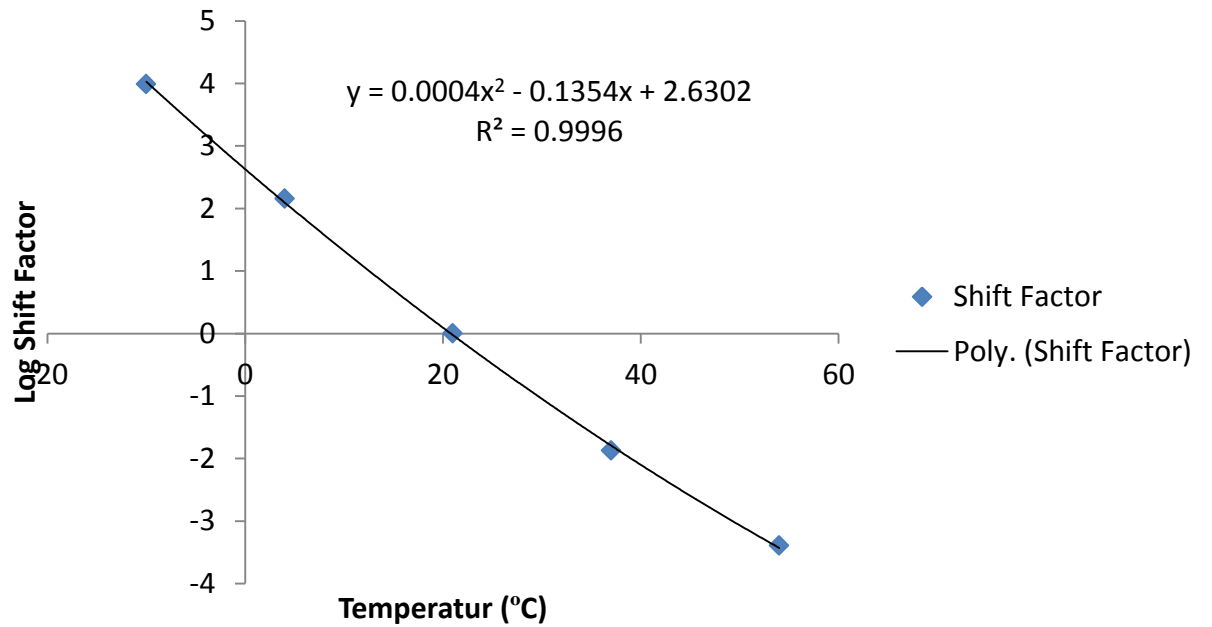
Figure F. 34: Shift factor for Sample 1 (SP-III with PG 64-22 binder)

Table F. 18: *E** test results for Sample 2 (SP-III with PG 64-22 binder)

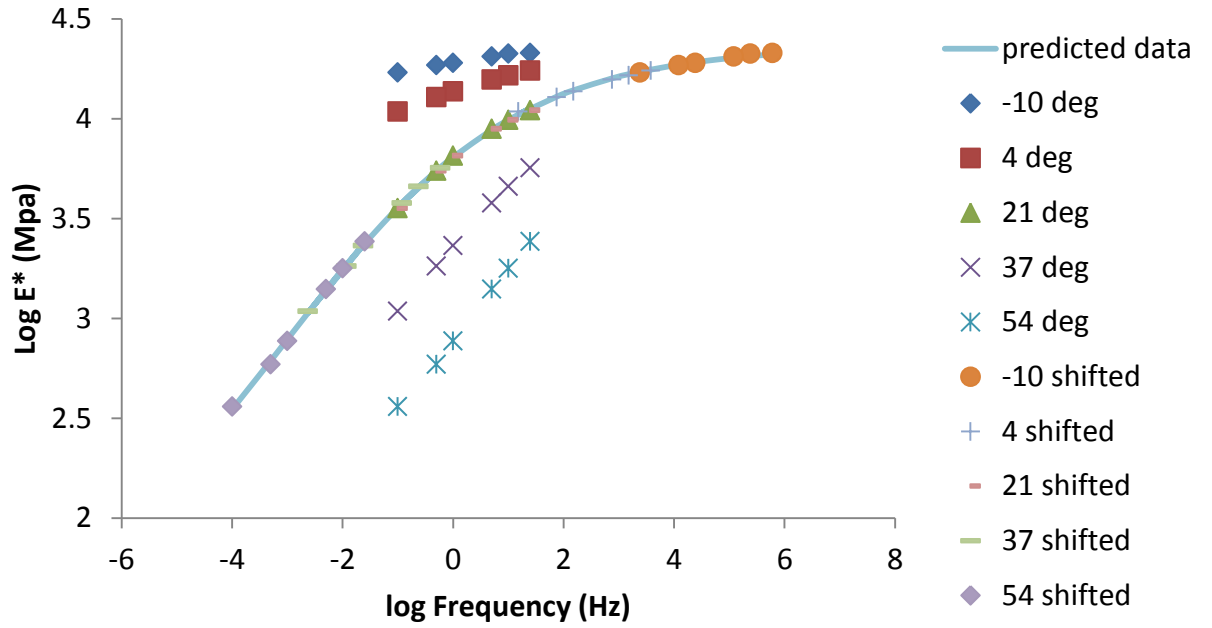| Temperature | Frequency | Stress | | Dynamic Modulus | Phase Angle | | Strain | | | |
		Amplitude (P-P)	SE			UC	(P-P) Recoverable	Permanent	SE	UC
(deg C)	(Hz)	(kPa)	(%)	(MPa)	(deg)	(deg)	(micro e)	(micro e)	(%)	(%)
-10	25	1435.7	6.5	48110.0	7.5	4	29.843	-57.701	26	100
-10	10	1359.5	4.7	46624.2	5.5	1.7	29.16	-71.607	20	90.8
-10	5	1258.6	2.6	45764.7	6.1	3.1	27.501	-75.745	25	92
-10	1	1150	0.5	42565.3	7.1	3.2	27.018	-77.894	23	98.6
-10	0.5	1099.9	0.4	41863.6	125.5	205.5	26.274	-77.925	20	102
-10	0.1	999	0.2	37570.8	6.2	0.6	26.59	-72.746	20	103
4	25	1443.3	7.1	32572.3	14.7	8.7	44.311	-54.551	41	125
4	10	1364.6	5.3	30817.2	7.3	0.3	44.279	-61.548	24	112
4	5	1269.8	3.3	28910.8	9	1.7	43.921	-63.535	25	108
4	1	1152.2	0.7	24786.8	10.1	1.3	46.483	-63.559	28	113
4	0.5	1111.4	0.5	22856.3	12.1	2	48.625	-57.393	28	112
4	0.1	998.2	0.2	18379.3	13.1	0.9	54.31	-26.329	29	111
21	25	1121.6	5.9	20012.9	15.1	4.1	56.043	187.582	6.5	36.1
21	10	1027.4	3.8	17146.4	16.6	3.4	59.919	269.093	4.6	37.8
21	5	947.2	2	15061.3	17.7	3.7	62.887	317.096	4.7	38.6
21	1	799.4	0.4	10870.7	22.2	3.4	73.538	338.906	4.2	38.5
21	0.5	708.8	0.4	9344.7	23.3	3.2	75.855	377.709	2.6	37.7
21	0.1	627.2	0.3	6354.1	27.2	3	98.716	576.722	3.6	36.2
37	25	452.4	5.9	8562.7	22.2	1.3	52.83	501.039	6.7	43.8
37	10	377.5	4.6	6906.3	23.8	0.7	54.667	591.8	5.9	44.8
37	5	328.2	3.1	5712.4	25.7	0.8	57.445	646.667	4.9	45.5
37	1	218.2	0.8	3435.7	29.5	1.5	63.508	618.597	3.9	47
37	0.5	173.3	0.6	2733.6	30.2	1.8	63.392	602.821	4.6	47.8
37	0.1	88.8	0.7	1554.8	30.9	3.1	57.139	590.014	5.5	54.2
54	25	147.5	6.6	2897.9	32.8	0.6	50.885	573.531	8.5	27
54	10	114.7	5.5	2062.4	32.9	1.5	55.596	687.403	7.2	26.7
54	5	95.3	3.9	1570.2	33.1	1.9	60.697	695.075	6.4	27.5
54	1	63.3	1.2	855.4	32.3	1.5	73.973	653.607	6	27.9
54	0.5	53.7	0.8	667.7	31.5	0.8	80.417	643.854	5.8	27.4
54	0.1	34.2	1.2	404.6	27.6	0.9	84.422	656.19	6.3	28.4

316

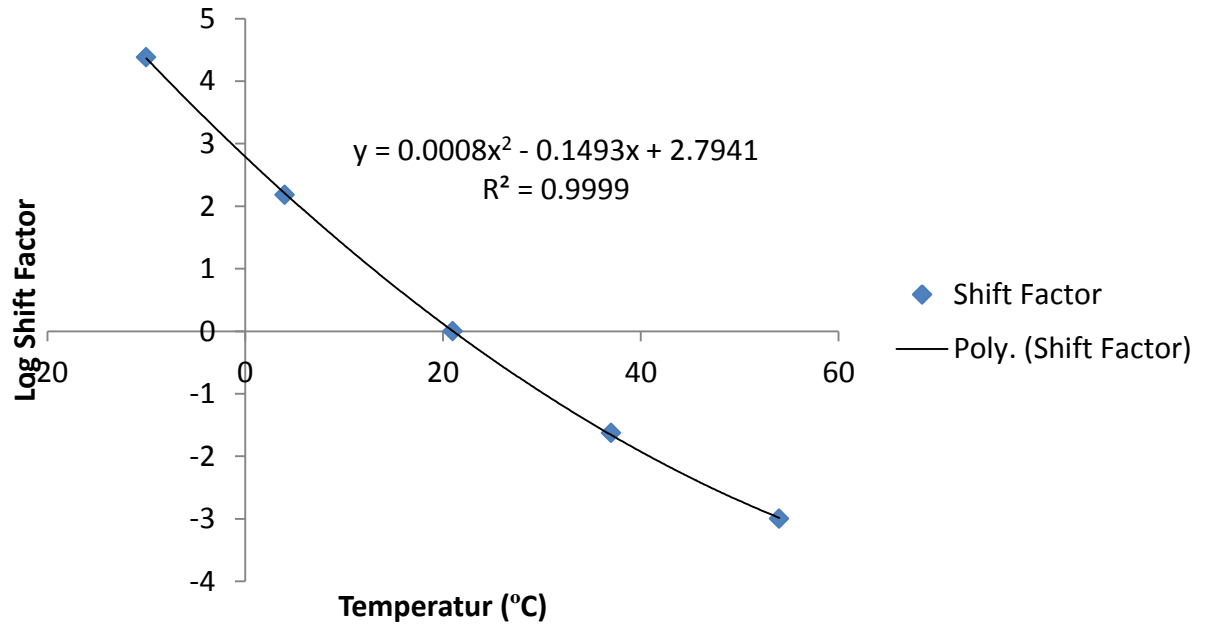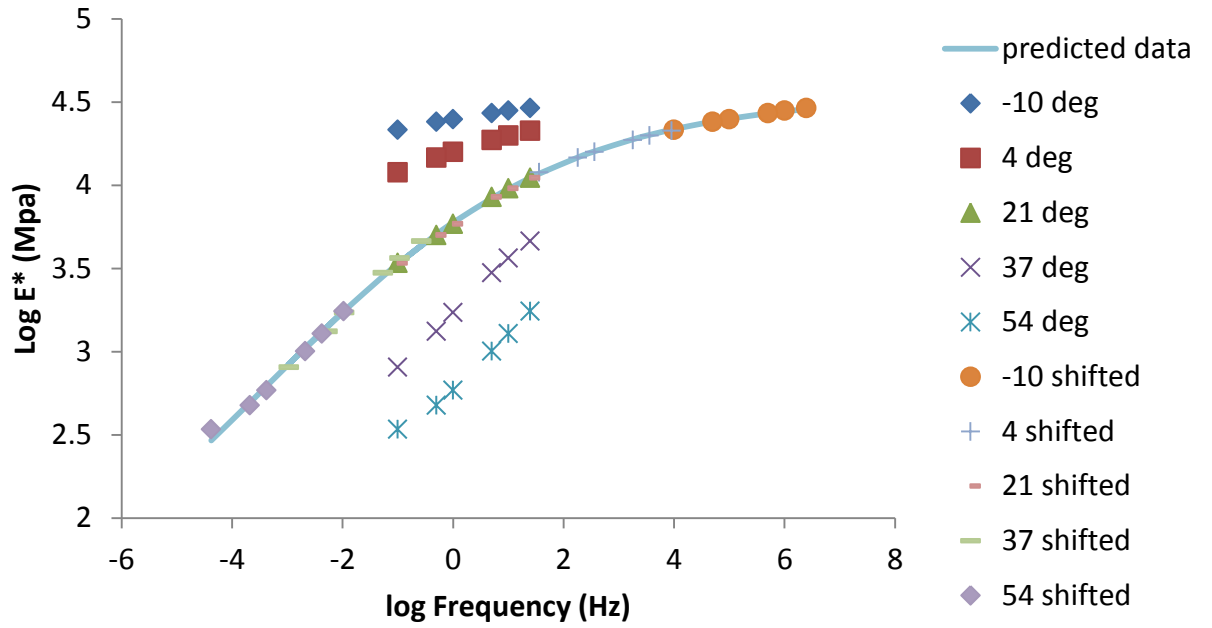Figure F. 35: Master curve for Sample 2 (SP-III with PG 64-22 binder)
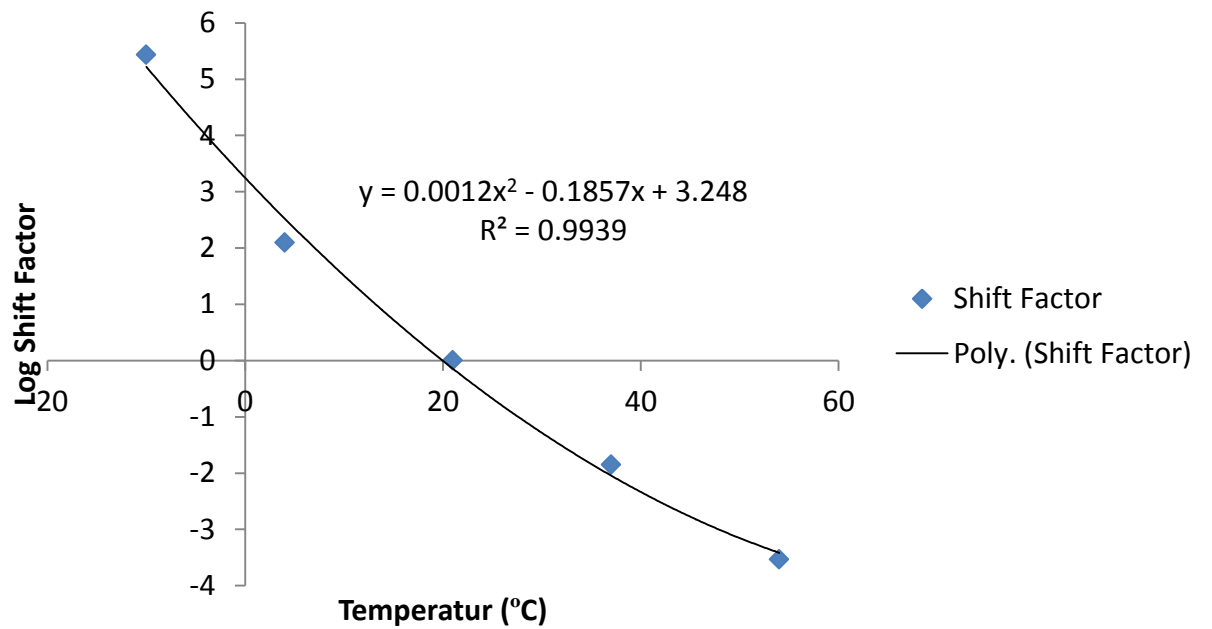
Figure F. 36: Shift factor for Sample 2 (SP-III with PG 64-22 binder)

317

SP-III WITH PG 70-22 BINDER - Samples

Table F. 19: *E** test results for Sample 1 (SP-III with PG 70-22 binder)

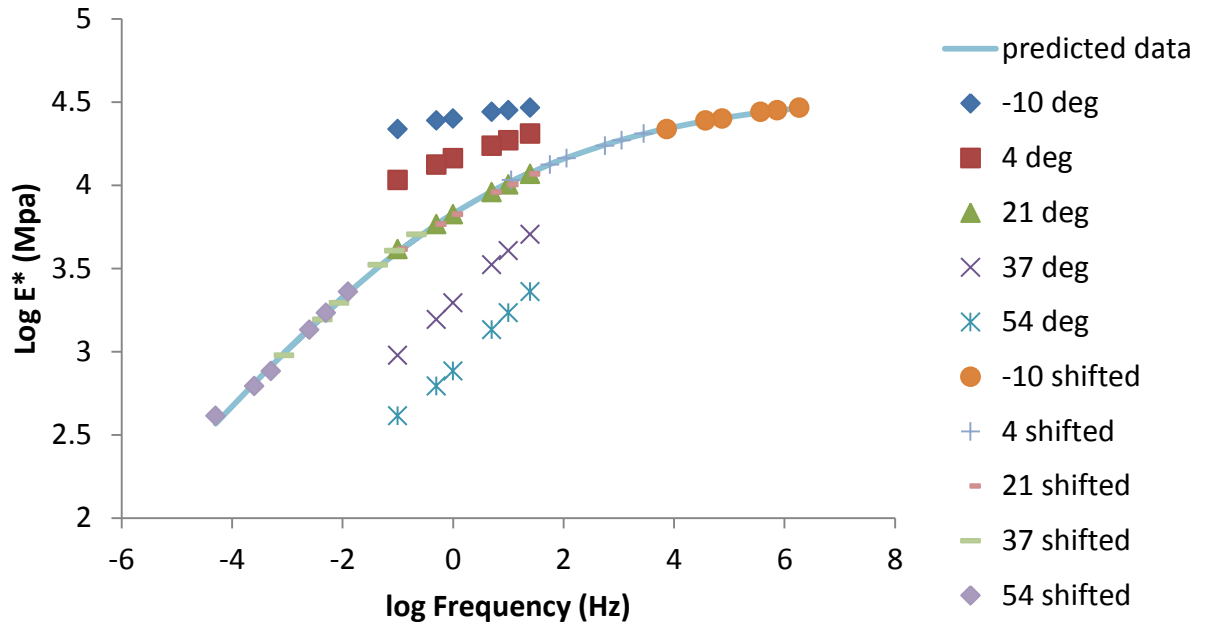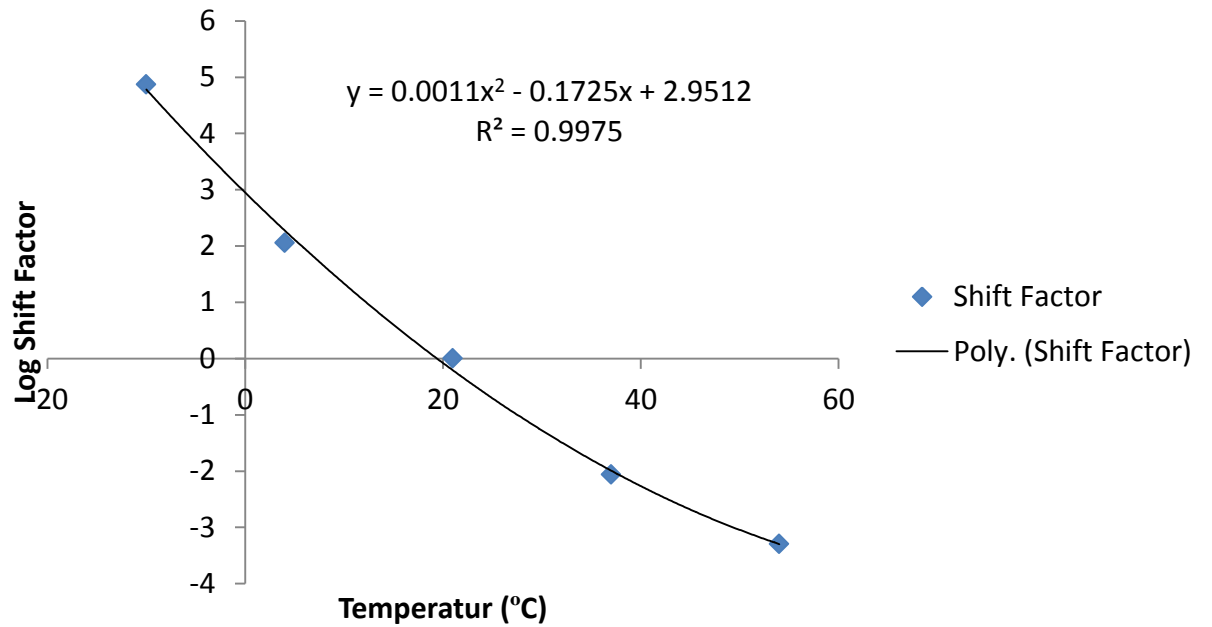| Temperature	Frequency	Stress		Dynamic Modulus	Phase Angle		Strain			
		Amplitude (P-P)	SE			UC	(P-P) Recoverable	Permanent	SE	UC
(deg C)	(Hz)	(kPa)	(%)	(MPa)	(deg)	(deg)	(micro e)	(micro e)	(%)	(%)
-10	25	1171	5.7	28726.0	8.6	4	40.764	-47.598	7.2	20.4
-10	10	1113.1	3.6	28241.1	8.7	4.1	39.414	-68.569	5	20.5
-10	5	1056.6	1.8	27029.0	9.1	4.5	39.09	-78.544	5.5	20.4
-10	1	950.6	0.3	23942.1	9.4	4	39.703	-85.025	5.5	19.6
-10	0.5	899.9	0.3	22940.9	9.8	4.1	39.226	-86.559	5.4	20.2
-10	0.1	818.5	0.2	19830.6	11.3	3.3	41.275	-75.716	4.2	19.8
4	25	1068.4	5.8	19615.5	9.7	2.1	54.467	31.466	7.1	39.2
4	10	1003.6	3.6	18102.7	10.4	1.1	55.437	40.352	4.4	38.4
4	5	948.3	1.9	16806.7	11	1.2	56.422	46.336	4	38
4	1	859.5	0.4	13748.5	13.2	0.6	62.516	48.377	2.7	38.1
4	0.5	800	0.3	12423.1	14.6	0.7	64.395	58.375	2.6	38.2
4	0.1	707.8	0.2	9579.6	17.2	0.7	73.886	126.194	2.6	38
21	25	551	5.7	9534.8	17.7	2.1	57.785	344.397	6.1	41.9
21	10	492.4	3.9	8227.2	18.4	1	59.852	448.857	5.3	38.9
21	5	430.9	2.5	7180.5	20	1.3	60.005	485.857	4.5	37.6
21	1	328.6	0.6	4874.5	23.7	0.8	67.41	487.864	3.7	38.5
21	0.5	288.3	0.4	4121.4	24.6	0.4	69.962	508.554	5.2	39.1
21	0.1	197.8	0.3	2722.7	27.5	1.7	72.661	588.604	4.7	43.6
37	25	298.7	5.6	3863.1	26	3.6	77.311	930.954	5.7	7.9
37	10	244.5	4.3	2919.8	26.7	2.6	83.734	1074.152	4.2	10.5
37	5	193.6	3.1	2321.5	27.9	2.6	83.388	1101.466	4.2	11.9
37	1	128.1	0.9	1315.3	29.8	2.7	97.428	1073.225	3.8	14.9
37	0.5	88.5	0.7	1004.8	30.7	2.7	88.103	1053.952	4	15.6
37	0.1	49.1	0.5	591.6	29	2.5	82.937	1072.005	3.9	17.8
54	25	108.1	5.9	1352.1	33.2	4.5	79.954	634.408	5.4	7.9
54	10	79.7	4.6	968.8	31.9	3.3	82.32	698.325	4.2	6.9
54	5	64.5	3.7	764.8	31.2	2.9	84.392	712.556	4.7	8.2
54	1	33.7	1.6	430.0	29.8	1.6	78.435	688.969	4.6	10.6
54	0.5	24.2	1.3	352.8	28.2	0.8	68.541	678.366	4.2	14.8
54	0.1	17.4	1.2	257.5	22.8	2.3	67.425	689.667	4.8	26.1

318
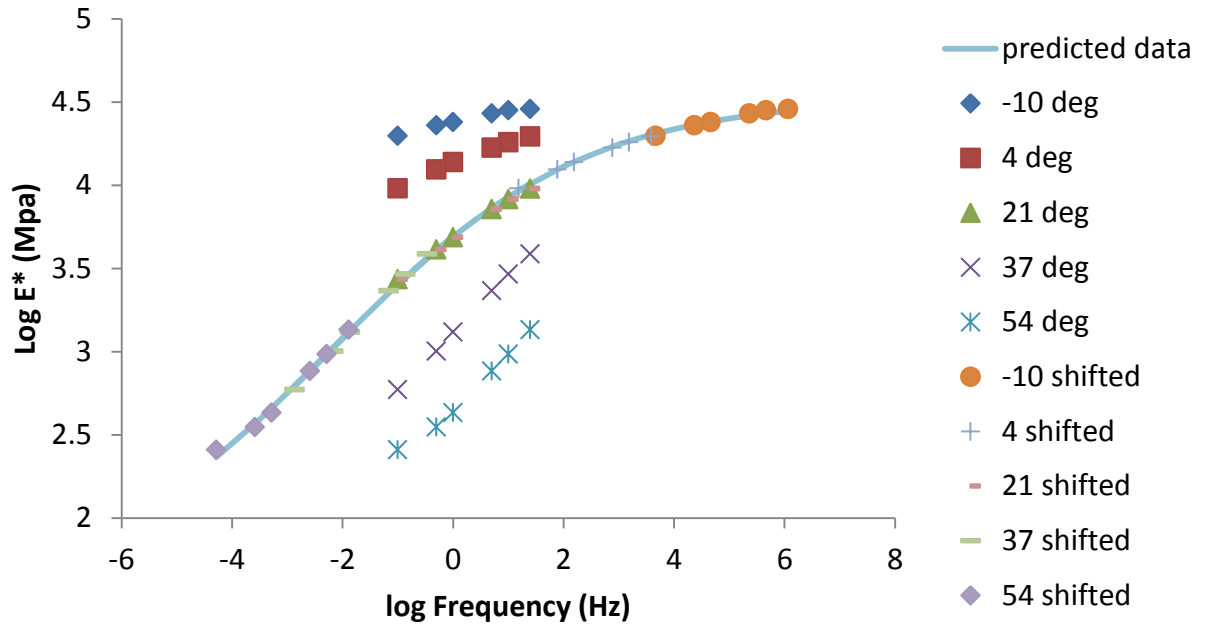
Figure F. 37: Master curve for Sample 1 (SP-III with PG 70-22 binder)

Figure F. 38: Shift factor for Sample 1 (SP-III with PG 70-22 binder)

319

Table F. 20: *E** test results for Sample 2 (SP-III with PG 70-22 binder)

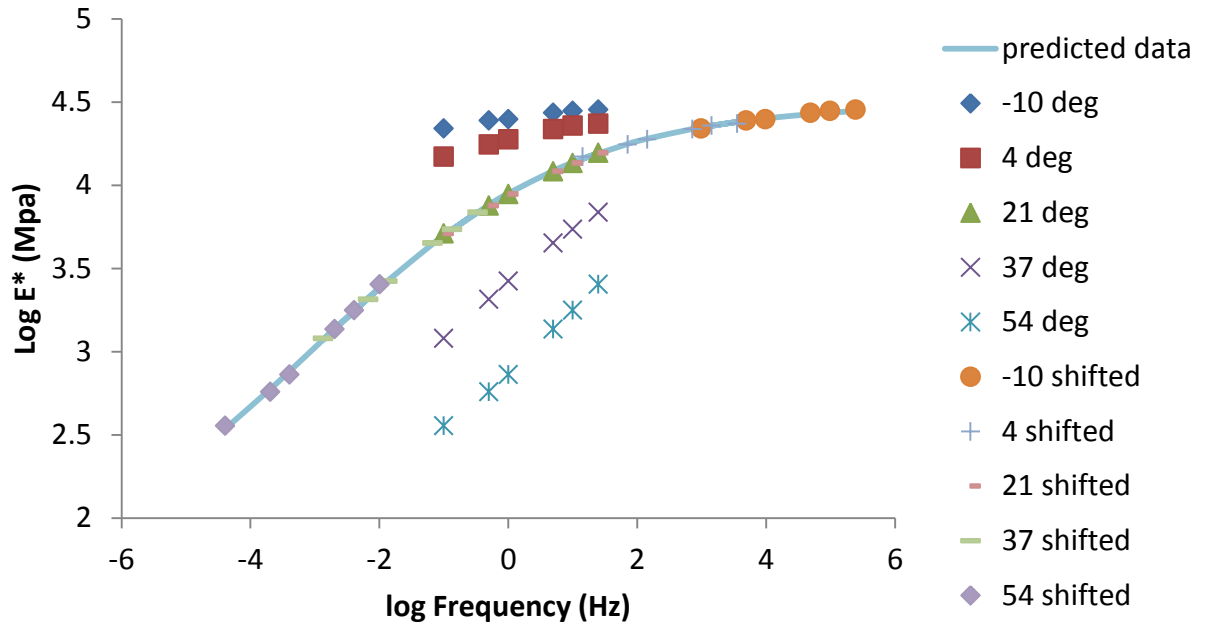| Temperature | Frequency | Stress | | Dynamic Modulus | Phase Angle | | Strain | | | |
		Amplitude (P-P)	SE			UC	(P-P) Recoverable	Permanent	SE	UC
(deg C)	(Hz)	(kPa)	(%)	(MPa)	(deg)	(deg)	(micro e)	(micro e)	(%)	(%)
-10	25	1430	6.1	35672.0	9.5	6.6	40.087	-7.789	33	85
-10	10	1350.6	3.8	33370.5	11.3	9.4	40.473	-14.475	44	81.8
-10	5	1253	1.9	32080.2	5.6	0.8	39.059	-15.641	24	82.3
-10	1	1110	0.3	29025.4	7.2	0.7	38.244	-16.311	32	82.8
-10	0.5	1050.6	0.3	27775.0	7.9	1.3	37.827	-15.11	25	83.4
-10	0.1	908.1	0.2	24208.3	10.9	4.3	37.511	-4.404	21	82.5
4	25	1122.7	5.9	24090.7	10.2	1.7	46.603	7.234	8.3	24.8
4	10	1054.9	3.7	21081.1	10.9	0.3	50.042	15.783	5.5	33.5
4	5	978	2	19405.8	11.9	0.5	50.398	19.402	4	34.8
4	1	880.2	0.4	15706.3	14.4	0.8	56.043	20.862	3.6	33.2
4	0.5	799.8	0.3	14226.4	14.9	0.3	56.219	30.045	5.6	33
4	0.1	697.7	0.2	10860.1	18.4	0.9	64.247	93.445	3.6	33.9
21	25	651.6	5.6	13026.0	18.7	4	50.026	319.127	6.8	39.5
21	10	591.4	3.8	10642.5	20.3	3.7	55.566	428.324	7	39.3
21	5	531	2.1	9067.9	21.9	3.5	58.554	478.221	5.1	40.9
21	1	399.9	0.5	6029.9	26.2	3.6	66.314	483.459	4.3	47.2
21	0.5	348.5	0.4	5004.9	27.1	3.8	69.641	505.711	5	48.6
21	0.1	267.3	0.3	3248.4	28.6	3.2	82.277	608.073	4.8	48.8
37	25	327.4	5.8	5440.0	29.3	3.7	60.183	833.293	7	59
37	10	270.7	4.5	4026.2	30.5	5.4	67.232	973.982	6.4	60.4
37	5	222.7	2.8	3192.1	31	5.4	69.764	1004.743	7.8	62.5
37	1	148.3	0.9	1784.5	32.8	4.5	83.081	979.693	7.2	63.5
37	0.5	108	0.6	1409.2	33	3.3	76.656	965.443	6	65.9
37	0.1	68.8	0.4	911.3	29.4	1.7	75.506	985.886	6	63.4
54	25	127.2	6.7	1624.4	35.5	2.4	78.317	569.412	7.1	58.7
54	10	99.1	5.8	1199.8	32.9	3.5	82.579	653.613	6.2	56.7
54	5	84.1	4.5	951.9	32	2.6	88.392	670.411	6.4	53.7
54	1	52.7	1.8	568.6	30.1	1.9	92.632	646.21	7.5	51.3
54	0.5	38.7	1.1	466.9	29	2.2	82.807	626.121	6.7	49.1
54	0.1	27.2	0.8	370.5	24.1	3.1	73.39	608.726	5.8	41.4

320
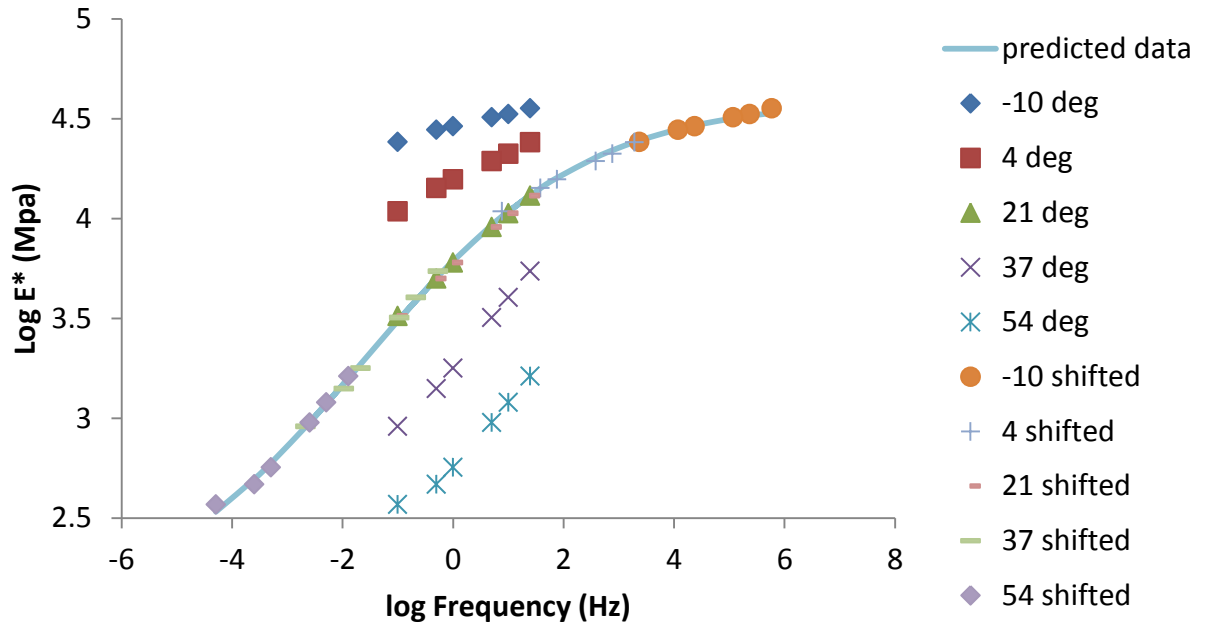
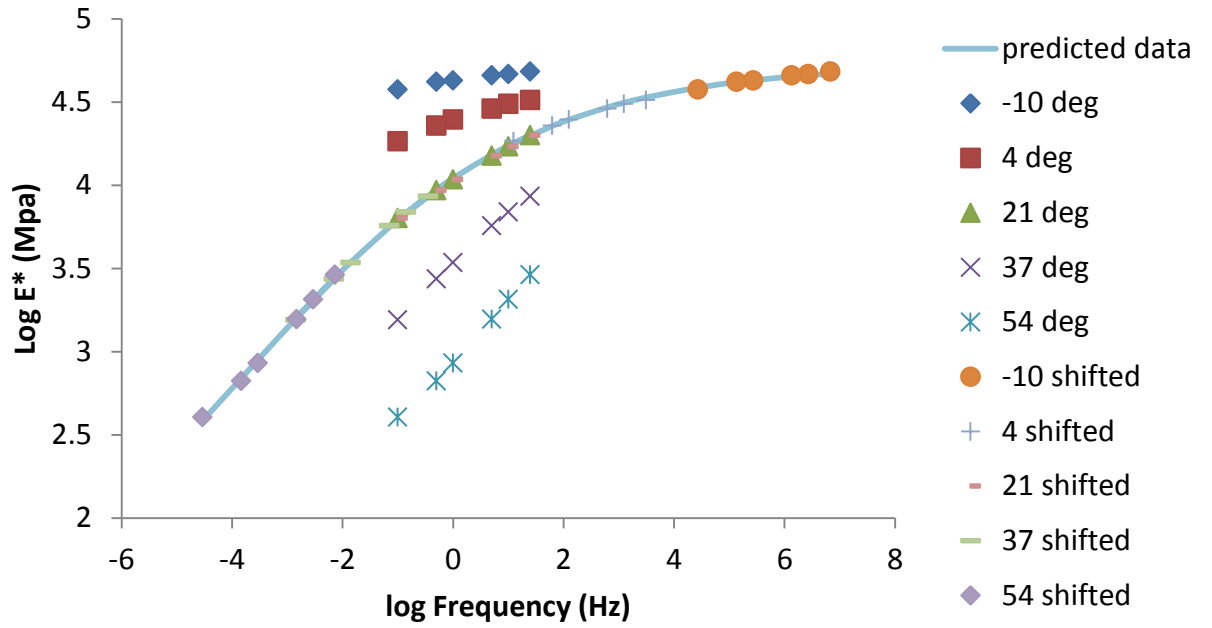Figure F. 39: Master curve for Sample 2 (SP-III with PG 70-22 binder)

Figure F. 40: Shift factor for Sample 2 (SP-III with PG 70-22 binder)

321

Table F. 21: *E** test results for Sample 3 (SP-III with PG 70-22 binder)

Temperature	Frequency	Stress		Dynamic Modulus	Phase Angle		Strain			
		Amplitude (P-P)	SE			UC	(P-P) Recoverable	Permanent	SE	UC
(deg C)	(Hz)	(kPa)	(%)	(MPa)	(deg)	(deg)	(micro e)	(micro e)	(%)	(%)
-10	25	1173.6	5.9	18871.2	5.9	0.8	62.189	-18.957	6.8	16.3
-10	10	1113.1	3.8	18102.3	6.2	0.4	61.487	-24.079	4.8	14.4
-10	5	1055.2	1.9	17521.9	6.2	0.5	60.223	-16.127	3.8	14.8
-10	1	950.4	0.4	15841.3	7.4	0.4	59.995	-4.38	3.7	16
-10	0.5	900.2	0.3	15124.2	7.7	0.3	59.518	6.165	3.3	15.5
-10	0.1	818.6	0.2	13534.8	8.5	0.7	60.481	28.431	3.6	14.6
4	25	913.3	5.8	13693.5	9.2	0.3	66.693	29.305	5.7	9.3
4	10	844.6	3.7	12908.0	10.3	0.6	65.431	40.105	3.9	8.2
4	5	797.5	2	12057.7	11	0.7	66.138	40.177	3.4	9.3
4	1	699.1	0.4	9860.7	13.2	1	70.901	37.635	3.4	10.1
4	0.5	649.5	0.3	9000.4	14.6	1	72.161	47.584	3.5	11.1
4	0.1	548.2	0.2	7097.3	17.2	1.2	77.246	118.17	4.5	13.5
21	25	518.8	5.6	8128.2	17.2	0.4	63.829	334.237	5.6	18
21	10	459.9	3.4	7011.6	18.5	0.9	65.591	410.852	4.1	18.2
21	5	399.5	2.1	5954.8	20.2	1.2	67.09	490.916	3.2	17.7
21	1	278.6	0.5	3902.4	24.9	1.8	71.396	474.193	2.9	16.5
21	0.5	247.5	0.4	3212.7	26.3	1.4	77.028	496.673	3.8	16.1
21	0.1	158.2	0.3	2075.7	28.4	1.8	76.195	568.377	3.3	16
37	25	220.4	5.6	3096.7	27.6	0.4	71.163	443.457	5.4	21.6
37	10	163.6	4.4	2310.0	28.8	0.9	70.821	469.686	3.9	17.5
37	5	121.4	3.5	1797.9	30	0.9	67.532	446.732	4.2	16
37	1	68.6	1.2	985.5	31.7	0.7	69.64	400.174	3.1	9.3
37	0.5	48.9	0.9	769.7	31.3	0.9	63.59	377.459	3.2	6.3
37	0.1	29.3	0.8	473.1	28.1	2.1	61.88	378.396	4.2	8.7
54	25	78.8	5.9	1009.0	31.1	2.3	78.144	141.032	5.6	27.1
54	10	59.5	4.8	736.1	28.3	2.5	80.876	150.366	3.6	13.1
54	5	43.9	4.1	575.3	27.3	2.6	76.375	140.191	3.8	10.5
54	1	23.8	2.1	346.0	24.3	2.2	68.794	118.479	4.5	7.8
54	0.5	19.2	1.9	288.3	22.8	2.1	66.472	94.361	4.2	7.4
54	0.1	14.4	1.3	212.8	18.4	1.7	67.72	73.424	5.4	7.9

322
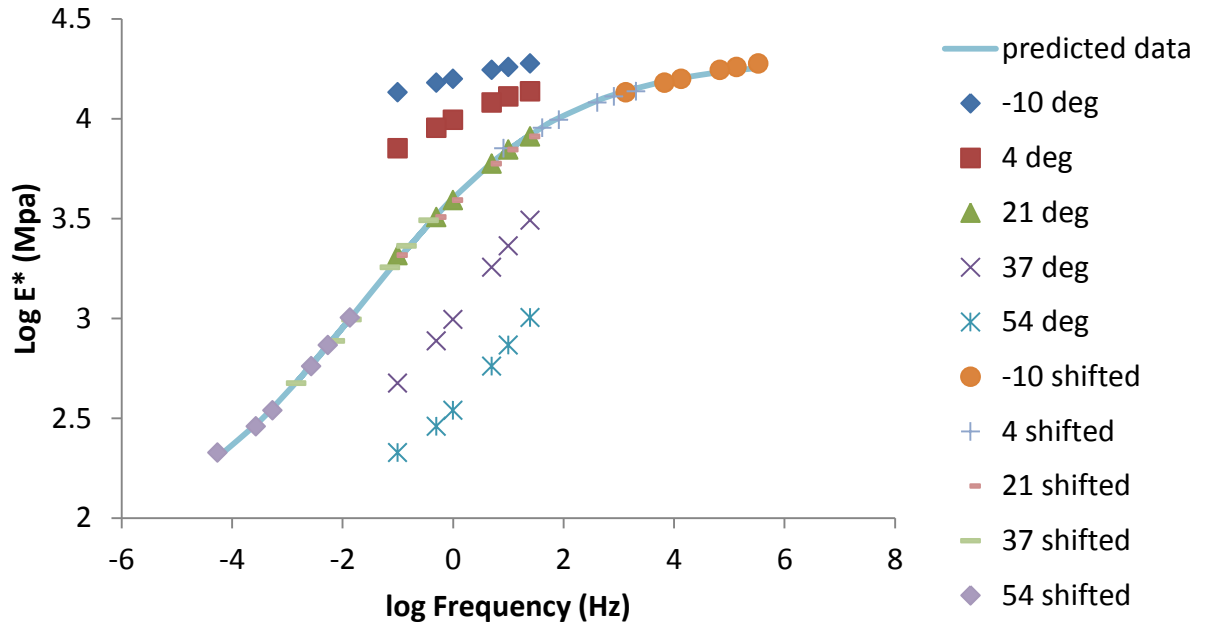
Figure F. 41: Master curve for Sample 3 (SP-III with PG 70-22 binder)

$$y = 0.0006x^2 - 0.1419x + 2.5984$$
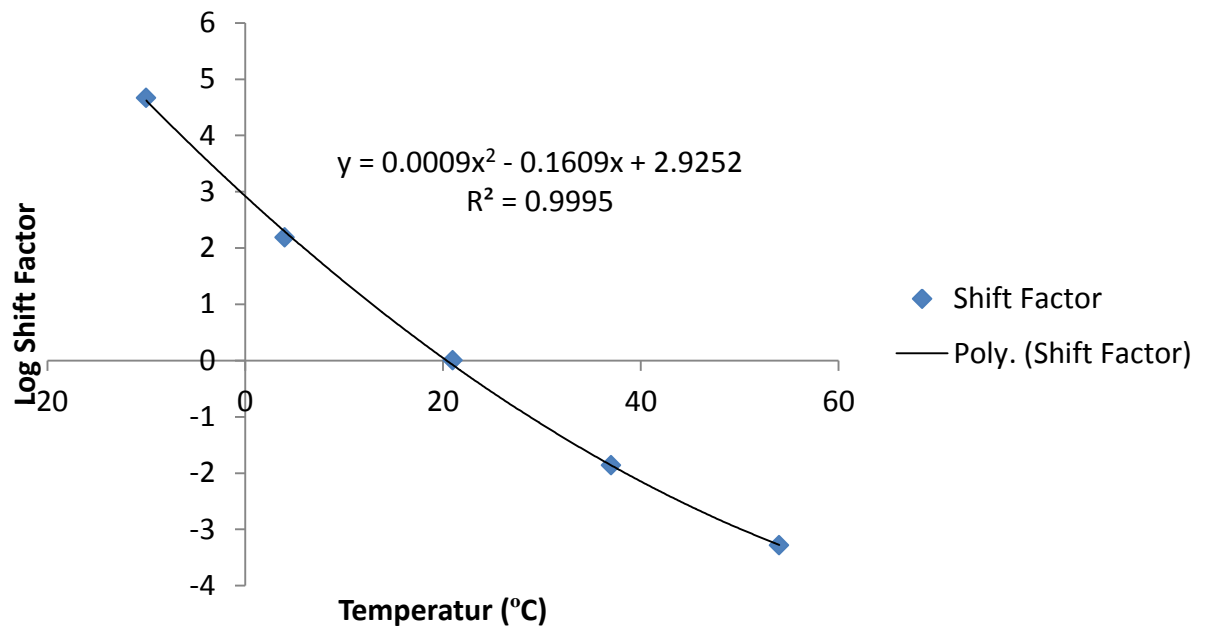$$R^2 = 0.9991$$

Figure F. 42: Shift factor for Sample 3 (SP-III with PG 70-22 binder)

Table F. 22: *E** test results for Sample 4 (SP-III with PG 70-22 binder)

Temperature	Frequency	Stress		Dynamic Modulus	Phase Angle		Strain			
		Amplitude (P-P)	SE			UC	(P-P) Recoverable	Permanent	SE	UC
(deg C)	(Hz)	(kPa)	(%)	(MPa)	(deg)	(deg)	(micro e)	(micro e)	(%)	(%)
-10	25	1175.0	5.9	16488.0	5.6	0.9	71.3	-82.3	6.1	4.4
-10	10	1113.4	3.7	16338.1	6.2	0.6	68.1	-120.8	3.3	2.7
-10	5	1056.2	1.9	15982.5	6.3	0.7	66.1	-143.5	2.7	2.6
-10	1	950.4	0.4	14531.8	7.3	0.9	65.4	-158.7	2.6	3.9
-10	0.5	900.0	0.3	14045.5	7.3	1.1	64.1	-167.4	3.2	4.6
-10	0.1	818.4	0.2	12851.1	8.2	0.9	63.7	-160.7	2.8	5.0
4	25	910.8	5.7	13161.1	8.7	0.8	69.2	0.8	5.5	10.9
4	10	845.1	3.6	12513.8	9.3	0.3	67.5	1.1	3.9	10.3
4	5	798.7	1.9	11795.1	10.0	0.7	67.7	4.6	3.1	9.8
4	1	700.0	0.4	9794.9	12.3	0.9	71.5	4.6	3.2	9.1
4	0.5	649.5	0.3	9013.0	13.4	0.8	72.1	14.1	3.3	8.8
4	0.1	548.1	0.2	7390.5	15.8	1.0	74.2	75.1	3.2	7.4
21	25	523.6	5.7	8808.1	15.4	1.1	59.4	252.4	6.2	22.6
21	10	461.5	3.8	7887.3	16.6	0.4	58.5	325.8	4.4	19.8
21	5	398.9	2.4	6761.6	18.0	0.4	59.0	338.0	4.7	17.4
21	1	248.3	0.6	4410.4	22.8	0.4	56.3	312.9	5.2	26.8
21	0.5	208.3	0.5	3696.6	23.4	0.6	56.4	317.3	5.9	29.6
21	0.1	148.3	0.2	2448.1	26.5	0.4	60.6	380.8	5.0	34.4
37	25	281.3	5.6	4240.8	24.5	2.0	66.3	739.9	5.8	18.5
37	10	216.0	4.2	3261.6	25.7	0.9	66.2	850.2	4.4	17.6
37	5	162.0	3.1	2580.5	27.1	0.9	62.8	855.3	3.9	17.6
37	1	88.6	1.0	1373.6	31.1	1.7	64.5	799.9	3.9	23.2
37	0.5	68.8	0.7	1068.8	31.3	1.9	64.3	789.4	3.7	24.9
37	0.1	39.2	0.6	618.2	30.5	2.3	63.4	813.4	3.7	26.3
54	25	109.9	6.0	1511.7	30.1	2.8	72.7	364.6	5.9	21.5
54	10	80.4	4.7	1085.0	28.8	2.9	74.1	397.5	4.4	14.6
54	5	64.9	4.0	851.0	28.0	3.0	76.3	393.2	4.6	14.4
54	1	33.8	1.9	478.1	26.9	3.0	70.6	356.7	4.8	13.4
54	0.5	24.2	1.4	382.4	26.0	3.3	63.2	337.3	3.9	13.2
54	0.1	17.4	1.0	265.8	21.7	3.0	65.3	341.5	3.9	14.5

Figure F. 43: Master curve for Sample 4 (SP-III with PG 70-22 binder)

$y = 0.0006x^2 - 0.1333x + 2.4332$
$R^2 = 0.9987$
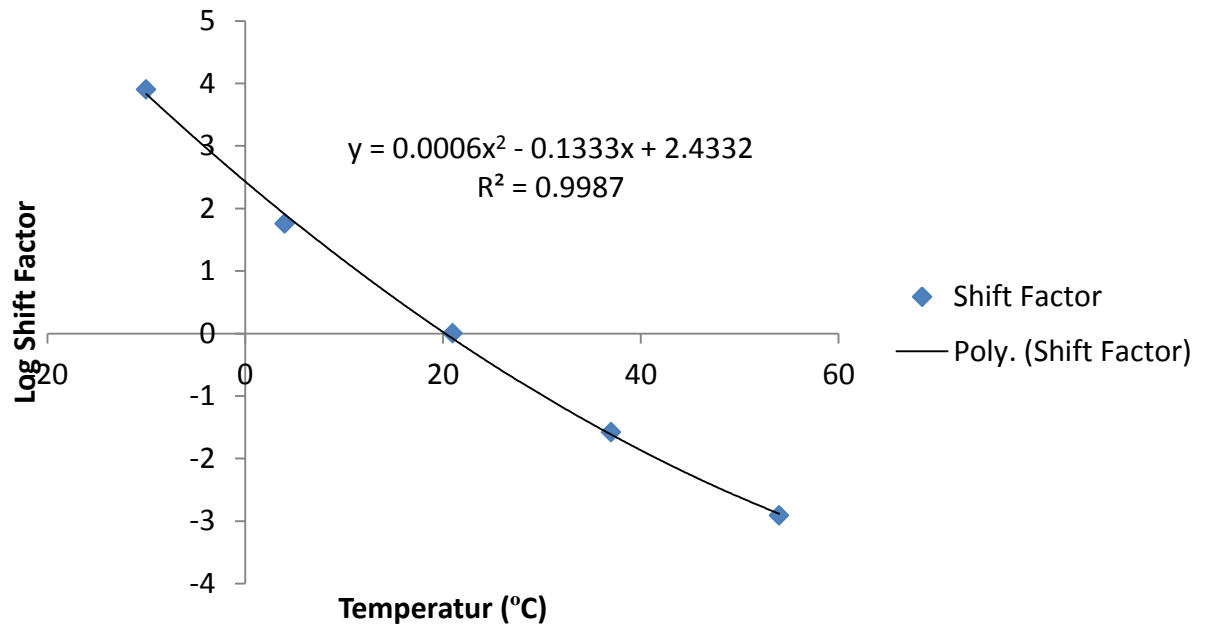
Figure F. 44: Shift factor for Sample 4 (SP-III with PG 70-22 binder)

SP-IV WITH PG 70-22 BINDER - Samples

Table F. 23: *E** test results for Sample 1 (SP-IV with PG 70-22 binder)

Temperature	Frequency	Stress		Dynamic Modulus	Phase Angle		Strain			
		Amplitude (P-P)	SE			UC	(P-P) Recoverable	Permanent	SE	UC
(deg C)	(Hz)	(kPa)	(%)	(MPa)	(deg)	(deg)	(micro e)	(micro e)	(%)	(%)
-10	25	1172.7	5.8	33728.5	7.1	2.1	34.8	-41.6	9.1	40.7
-10	10	1115.8	3.7	32000.4	6.4	1.0	34.9	-57.3	6.1	35.0
-10	5	1056.5	1.9	30637.3	6.8	1.1	34.5	-62.7	5.0	35.0
-10	1	950.5	0.4	27276.1	8.1	0.9	34.8	-67.4	3.6	35.7
-10	0.5	900.0	0.3	25772.9	8.7	0.9	34.9	-68.4	3.8	34.3
-10	0.1	818.5	0.2	22499.7	10.1	1.4	36.4	-59.1	3.9	31.7
4	25	1125.4	6.0	16449.9	10.1	3.0	68.4	73.0	7.9	33.8
4	10	1059.1	3.7	15180.2	10.5	0.7	69.8	101.5	4.8	27.1
4	5	1006.5	1.9	14076.1	11.2	0.4	71.5	118.5	4.1	25.0
4	1	859.6	0.4	11427.0	14.0	0.9	75.2	123.6	3.5	26.6
4	0.5	789.9	0.3	10291.1	15.1	0.5	76.8	142.9	3.4	26.5
4	0.1	697.3	0.3	7733.7	18.8	0.9	90.2	253.0	3.1	24.0
21	25	599.9	5.5	8979.3	18.4	1.1	66.8	650.3	5.9	15.3
21	10	541.2	3.4	7500.2	20.3	0.8	72.2	920.6	3.7	14.8
21	5	489.4	1.9	6389.9	22.1	0.8	76.6	1073.2	3.4	13.8
21	1	389.1	0.4	4140.4	26.9	1.3	94.0	1141.9	2.9	10.8
21	0.5	338.1	0.4	3375.5	28.5	1.2	100.2	1236.3	2.6	9.1
21	0.1	257.5	0.2	2015.8	30.9	1.0	127.7	1532.4	2.8	7.4
37	25	189.9	5.6	2829.8	30.4	1.7	67.1	861.0	5.6	5.7
37	10	131.0	4.3	1993.1	31.9	0.6	65.7	978.2	5.0	8.0
37	5	89.9	3.1	1464.4	33.3	1.0	61.4	988.2	3.7	10.2
37	1	53.3	1.2	759.3	34.0	1.8	70.2	956.6	3.2	10.0
37	0.5	38.9	0.9	567.2	33.3	2.5	68.5	934.2	3.6	10.1
37	0.1	19.3	1.0	314.1	29.5	2.5	61.5	916.7	3.5	6.7
54	25	73.0	5.6	858.4	35.6	2.4	85.0	973.3	5.1	3.9
54	10	49.3	4.4	567.8	34.3	1.0	86.8	1048.4	4.2	4.0
54	5	38.5	3.9	431.1	33.1	2.0	89.4	1037.5	3.9	6.5
54	1	18.6	2.3	234.1	30.2	3.3	79.4	940.2	4.2	17.8
54	0.5	16.1	1.8	198.4	27.3	3.6	81.2	881.3	5.5	25.1
54	0.1	11.4	2.5	149.8	19.4	1.8	76.2	811.3	5.3	44.7

326

Figure F. 45: Master curve for Sample 1 (SP-IV with PG 70-22 binder)

$$y = 0.0014x^2 - 0.1935x + 3.1378$$
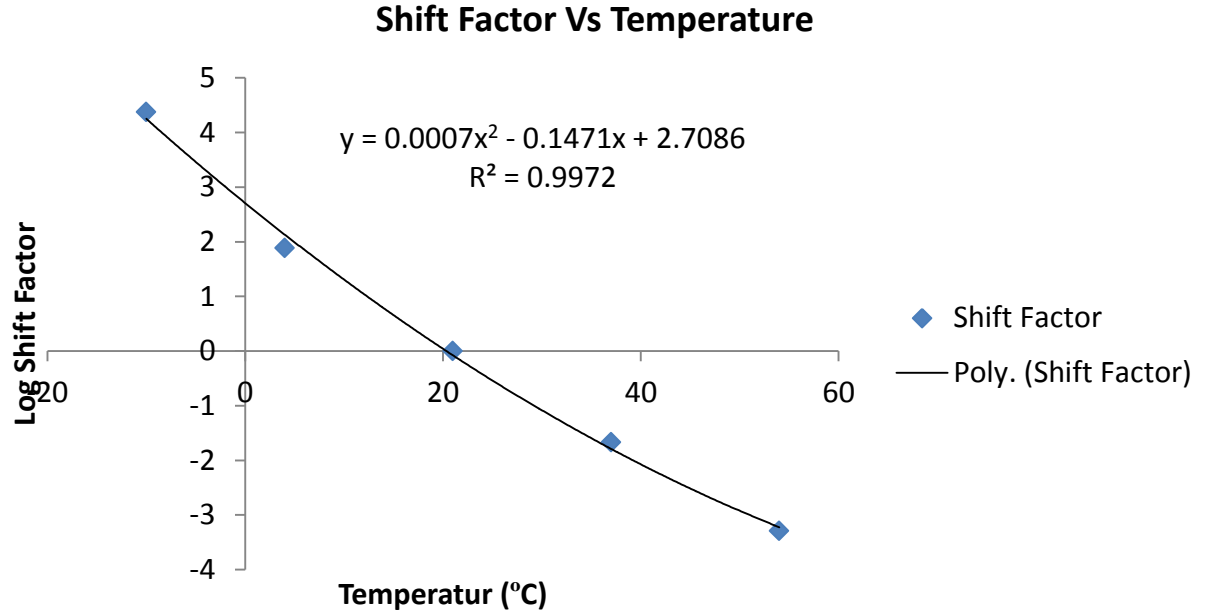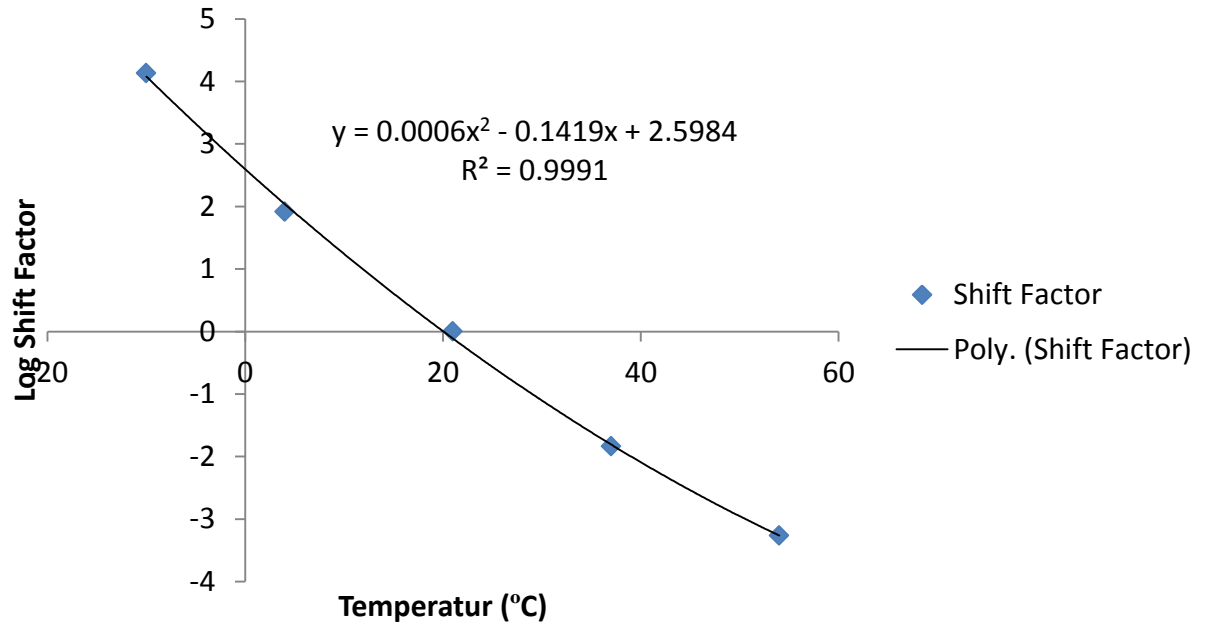$$R^2 = 0.9892$$
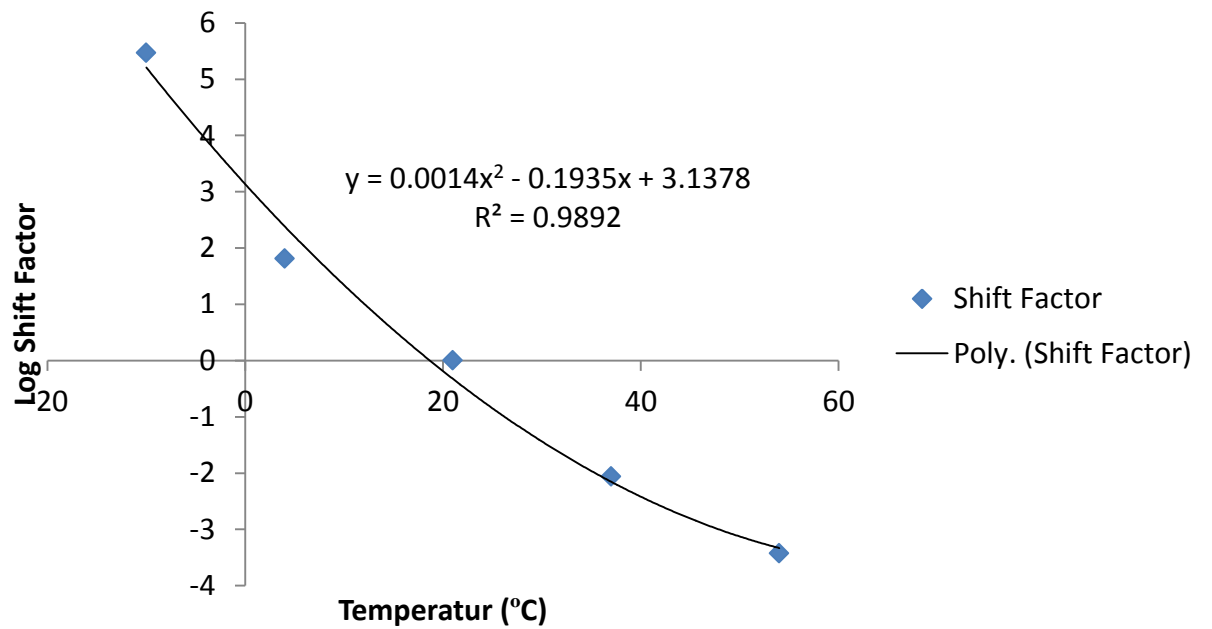
Figure F. 46: Shift factor for Sample 1 (SP-IV with PG 70-22 binder)

327

Table F. 24: *E** test results for Sample 2 (SP-IV with PG 70-22 binder)

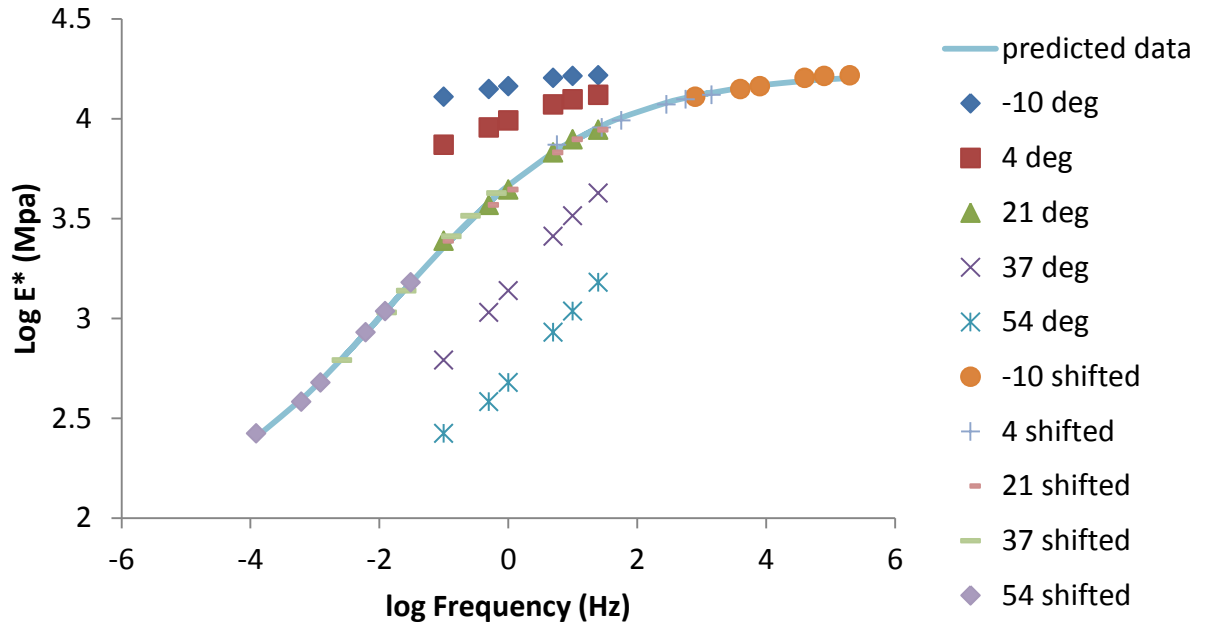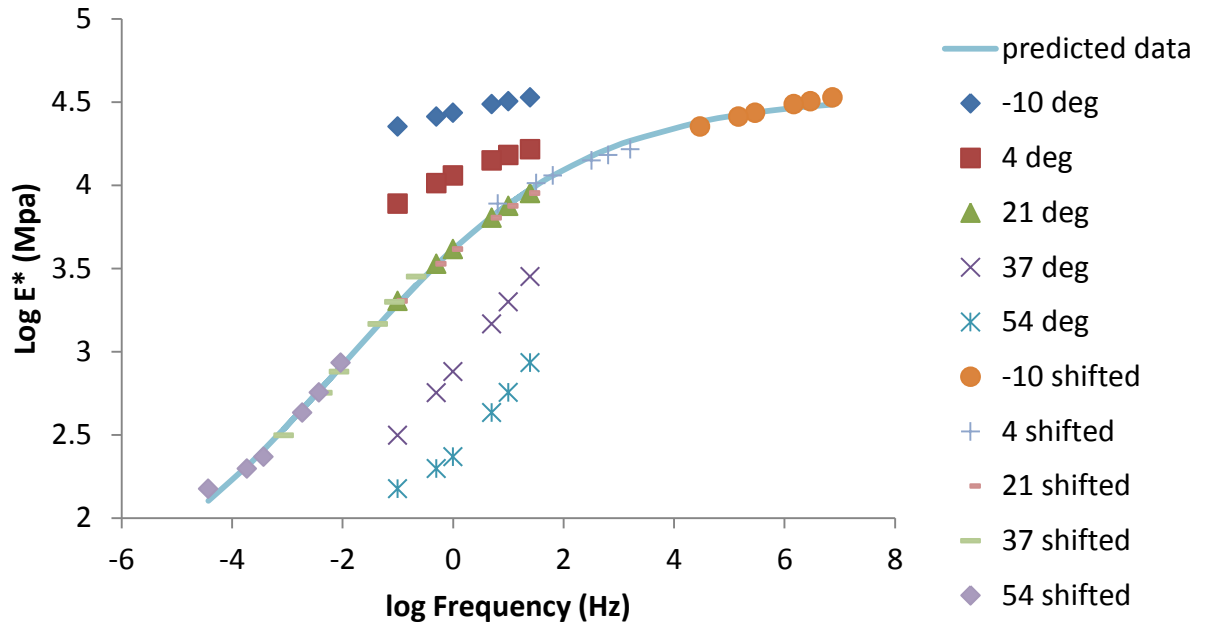| Temperature | Frequency | Stress | | Dynamic Modulus | Phase Angle | | Strain | | | |
		Amplitude (P-P)	SE			UC	(P-P) Recoverable	Permanent	SE	UC
(deg C)	(Hz)	(kPa)	(%)	(MPa)	(deg)	(deg)	(micro e)	(micro e)	(%)	(%)
-10	25	1172.5	5.8	22379.3	5.7	1.7	52.4	-40.6	6.6	20.9
-10	10	1114.1	3.6	21593.3	6.0	1.6	51.6	-57.4	4.6	19.6
-10	5	1056.5	1.7	20746.7	6.4	1.6	50.9	-65.4	4.0	19.0
-10	1	949.8	0.3	18551.5	7.3	1.2	51.2	-71.9	3.8	16.7
-10	0.5	900.0	0.3	17584.0	7.7	1.5	51.2	-73.6	2.5	16.0
-10	0.1	818.4	0.2	15389.6	9.4	1.7	53.2	-60.6	2.7	16.5
4	25	965.8	5.8	15585.6	10.0	2.2	62.0	40.3	7.8	27.9
4	10	910.2	3.6	14349.4	10.6	1.1	63.4	57.8	5.2	24.4
4	5	859.8	1.9	13312.4	11.4	1.2	64.6	69.7	4.4	22.9
4	1	779.7	0.4	10628.7	14.5	1.6	73.4	76.7	3.7	19.9
4	0.5	728.9	0.3	9612.0	15.8	1.8	75.8	95.2	3.1	18.5
4	0.1	638.0	0.2	7306.1	19.0	1.3	87.3	201.3	2.5	15.5
21	25	548.2	5.5	8454.8	18.1	2.1	64.8	596.3	6.2	16.4
21	10	488.7	3.6	7248.7	19.6	1.7	67.4	837.7	4.8	14.7
21	5	429.7	2.0	6262.9	21.8	1.9	68.6	954.3	3.6	14.5
21	1	298.6	0.5	4086.9	26.6	1.6	73.1	974.3	3.0	13.1
21	0.5	258.5	0.4	3369.7	27.6	1.8	76.7	1024.9	5.2	12.9
21	0.1	168.0	0.3	2036.7	30.9	1.3	82.5	1157.1	3.9	9.8
37	25	199.8	5.6	2919.3	31.5	5.1	68.4	931.1	5.4	12.7
37	10	140.6	4.1	2083.0	32.8	3.6	67.5	1068.6	4.2	8.0
37	5	110.2	2.9	1564.8	34.2	3.5	70.4	1120.0	3.8	5.4
37	1	58.3	0.9	785.0	35.9	3.1	74.2	1083.6	3.2	4.5
37	0.5	43.8	0.8	594.1	35.1	3.0	73.7	1073.2	3.5	4.3
37	0.1	24.2	1.0	332.3	31.4	2.9	72.9	1083.0	4.0	0.6
54	25	77.5	5.6	823.7	37.7	4.4	94.1	736.0	5.7	13.2
54	10	58.7	4.3	544.1	35.3	2.9	108.0	890.4	4.1	7.1
54	5	43.7	3.9	396.9	34.2	2.7	110.2	913.3	4.1	5.8
54	1	23.3	3.4	210.6	30.7	3.0	110.4	856.5	5.5	8.1
54	0.5	19.0	1.9	171.2	28.3	3.1	110.7	814.1	4.8	10.6
54	0.1	14.3	1.6	120.2	22.2	3.4	119.0	792.7	6.0	15.2
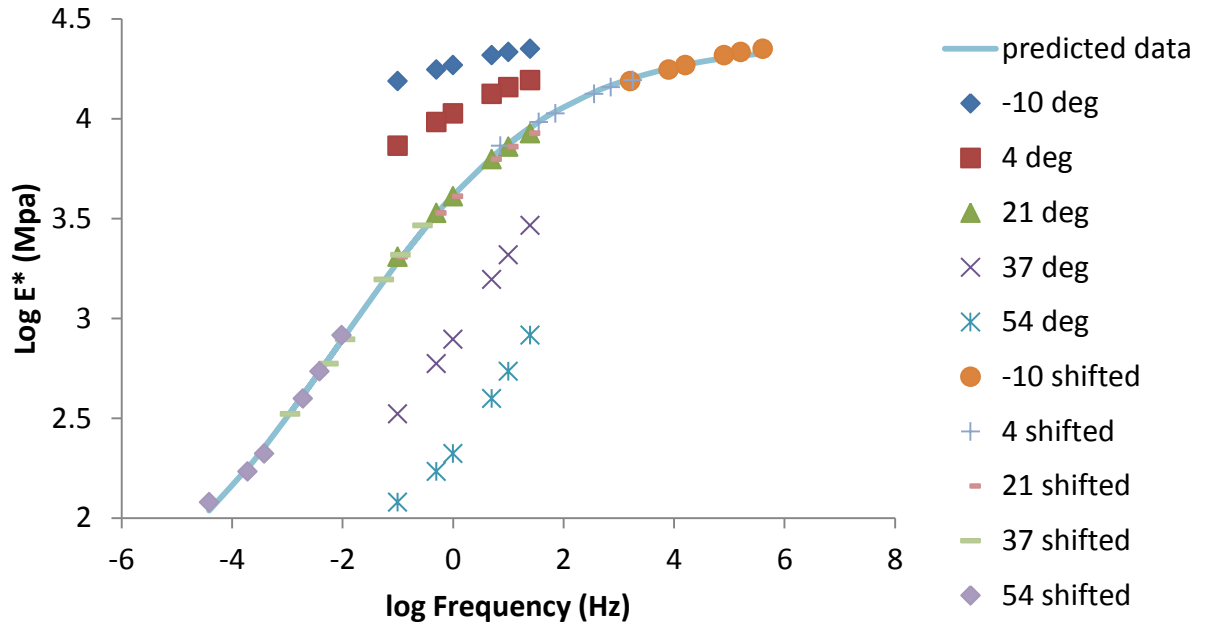
Figure F. 47: Master curve for Sample 2 (SP-IV with PG 70-22 binder)
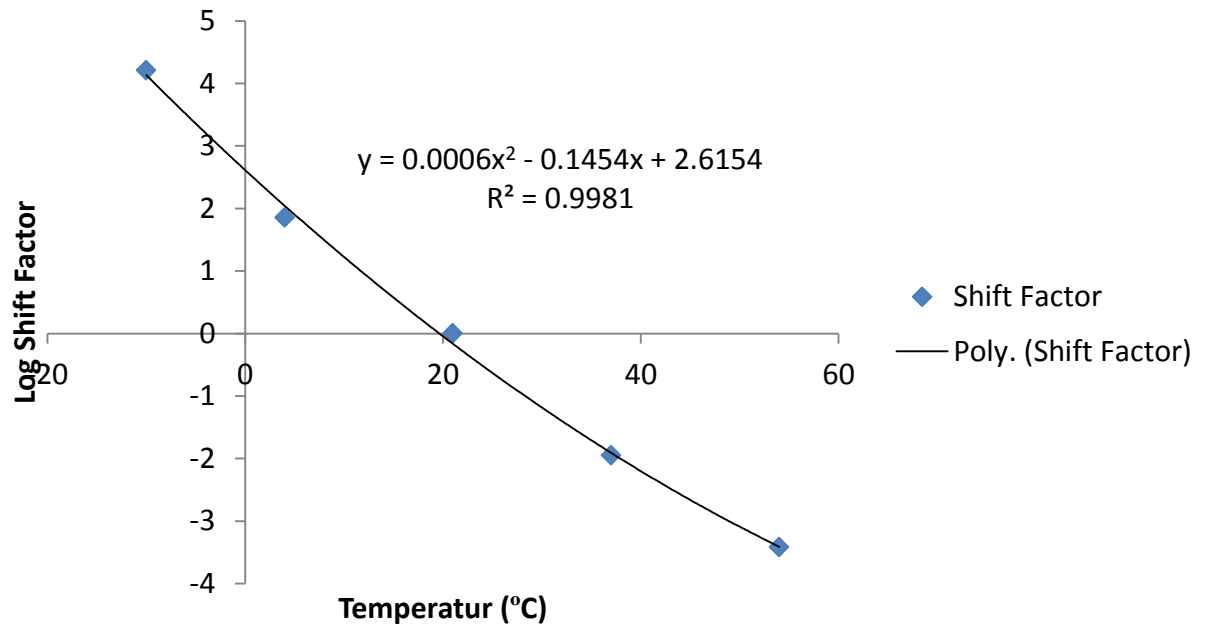
Figure F. 48: Shift factor for Sample 2 (SP-IV with PG 70-22 binder)

329

APPENDIX G

Dynamic Shear Modulus Test Results for PG 64-22 and PG 70-22 Binders

Table G. 25: DSR test result PG 64-22 at 54 ºC

Meas. Pts.	Binder Grade	Temperature ºC	Angular Frequency [rad/s]	Storage Modulus [Pa]	Loss Modulus [Pa]	Phase Angle [°]
1		54.44	5.00E+02	1.35E+05	3.30E+05	67.84
2		54.44	3.97E+02	1.10E+05	2.77E+05	68.3
3		54.44	3.16E+02	9.07E+04	2.33E+05	68.77
4		54.44	2.51E+02	7.42E+04	1.96E+05	69.27
5		54.44	1.99E+02	6.06E+04	1.64E+05	69.76
6		54.44	1.58E+02	4.93E+04	1.38E+05	70.26
7		54.44	1.26E+02	4.02E+04	1.15E+05	70.76
8		54.44	9.98E+01	3.27E+04	9.65E+04	71.26
9		54.44	7.92E+01	2.65E+04	8.05E+04	71.77
10		54.44	6.30E+01	2.14E+04	6.69E+04	72.29
11		54.44	5.00E+01	1.72E+04	5.58E+04	72.82
12		54.44	3.97E+01	1.39E+04	4.65E+04	73.35
13		54.44	3.16E+01	1.12E+04	3.88E+04	73.92
14		54.44	2.51E+01	8.91E+03	3.21E+04	74.48
15	PG 64-22	54.44	1.99E+01	7.05E+03	2.64E+04	75.06
16		54.44	1.58E+01	5.61E+03	2.19E+04	75.64
17		54.44	1.26E+01	4.49E+03	1.83E+04	76.21
18		54.44	9.98E+00	3.55E+03	1.51E+04	76.81
19		54.44	7.92E+00	2.78E+03	1.25E+04	77.43
20		54.44	6.30E+00	2.16E+03	1.02E+04	78.08
21		54.44	5.00E+00	1.67E+03	8.38E+03	78.72
22		54.44	3.97E+00	1.29E+03	6.85E+03	79.37
23		54.44	3.16E+00	9.89E+02	5.61E+03	80
24		54.44	2.51E+00	7.49E+02	4.55E+03	80.66
25		54.44	1.99E+00	5.62E+02	3.68E+03	81.31
26.		54.44	1.58E+00	4.27E+02	2.99E+03	81.89
27		54.44	1.26E+00	3.22E+02	2.43E+03	82.47
28		54.44	9.98E-01	2.39E+02	1.97E+03	83.08
29		54.44	7.92E-01	1.78E+02	1.60E+03	83.66
30		54.44	6.30E-01	1.30E+02	1.28E+03	84.2
31		54.44	5.00E-01	9.58E+01	1.04E+03	84.72

Table G. 26: DSR test result PG 64-22 at 46 ºC

Meas. Pts.	Binder Grade	Temperature ºC	Angular Frequency [rad/s]	Storage Modulus [Pa]	Loss Modulus [Pa]	Phase Angle [°]
1		46.11	5.00E+02	4.45E+05	8.57E+05	62.55
2		46.11	3.97E+02	3.69E+05	7.30E+05	63.17
3		46.11	3.16E+02	3.06E+05	6.21E+05	63.74
4		46.11	2.51E+02	2.55E+05	5.29E+05	64.31
5		46.11	1.99E+02	2.12E+05	4.51E+05	64.86
6		46.11	1.58E+02	1.75E+05	3.83E+05	65.4
7		46.11	1.26E+02	1.45E+05	3.25E+05	65.93
8		46.11	9.98E+01	1.20E+05	2.75E+05	66.45
9		46.11	7.92E+01	9.90E+04	2.33E+05	66.95
10		46.11	6.30E+01	8.16E+04	1.97E+05	67.45
11		46.11	5.00E+01	6.74E+04	1.66E+05	67.94
12		46.11	3.97E+01	5.56E+04	1.41E+05	68.43
13		46.11	3.16E+01	4.54E+04	1.18E+05	68.94
14		46.11	2.51E+01	3.72E+04	9.93E+04	69.44
15		46.11	1.99E+01	3.06E+04	8.37E+04	69.94
16	PG 64-22	46.11	1.58E+01	2.49E+04	7.02E+04	70.47
17		46.11	1.26E+01	2.02E+04	5.86E+04	71.02
18		46.11	9.98E+00	1.63E+04	4.91E+04	71.58
19		46.11	7.92E+00	1.32E+04	4.10E+04	72.15
20		46.11	6.30E+00	1.06E+04	3.41E+04	72.75
21		46.11	5.00E+00	8.51E+03	2.85E+04	73.35
22		46.11	3.97E+00	6.78E+03	2.36E+04	73.99
23		46.11	3.16E+00	5.40E+03	1.96E+04	74.62
24		46.11	2.51E+00	4.28E+03	1.63E+04	75.28
25		46.11	1.99E+00	3.36E+03	1.34E+04	75.96
26.		46.11	1.58E+00	2.64E+03	1.11E+04	76.64
27		46.11	1.26E+00	2.06E+03	9.13E+03	77.32
28		46.11	9.98E-01	1.58E+03	7.48E+03	78.04
29		46.11	7.92E-01	1.23E+03	6.14E+03	78.72
30		46.11	6.30E-01	9.48E+02	5.07E+03	79.4
31		46.11	5.00E-01	7.26E+02	4.15E+03	80.09

332

Table G. 27: DSR test result PG 64-22 at 37 ℃

Meas. Pts.	Binder Grade	Temperature ℃	Angular Frequency [rad/s]	Storage Modulus [Pa]	Loss Modulus [Pa]	Phase Angle [°]
1		37.78	5.00E+02	1.52E+06	2.66E+06	60.34
2		37.78	3.97E+02	1.33E+06	2.26E+06	59.45
3		37.78	3.16E+02	1.14E+06	1.94E+06	59.6
4		37.78	2.51E+02	9.85E+05	1.69E+06	59.68
5		37.78	1.99E+02	8.41E+05	1.46E+06	60.02
6		37.78	1.58E+02	7.11E+05	1.25E+06	60.45
7		37.78	1.26E+02	5.98E+05	1.08E+06	60.96
8		37.78	9.98E+01	5.01E+05	9.23E+05	61.51
9		37.78	7.92E+01	4.16E+05	7.91E+05	62.26
10		37.78	6.30E+01	3.52E+05	6.77E+05	62.54
11		37.78	5.00E+01	2.96E+05	5.82E+05	63.01
12		37.78	3.97E+01	2.50E+05	5.00E+05	63.48
13		37.78	3.16E+01	2.08E+05	4.26E+05	63.98
14		37.78	2.51E+01	1.74E+05	3.64E+05	64.46
15	PG 64-22	37.78	1.99E+01	1.45E+05	3.10E+05	64.93
16		37.78	1.58E+01	1.21E+05	2.64E+05	65.43
17		37.78	1.26E+01	9.99E+04	2.24E+05	65.93
18		37.78	9.98E+00	8.29E+04	1.90E+05	66.4
19		37.78	7.92E+00	6.85E+04	1.61E+05	66.9
20		37.78	6.30E+00	5.63E+04	1.35E+05	67.42
21		37.78	5.00E+00	4.65E+04	1.15E+05	67.93
22		37.78	3.97E+00	3.84E+04	9.71E+04	68.44
23		37.78	3.16E+00	3.14E+04	8.18E+04	68.99
24		37.78	2.51E+00	2.55E+04	6.86E+04	69.56
25		37.78	1.99E+00	2.09E+04	5.78E+04	70.14
26		37.78	1.58E+00	1.69E+04	4.83E+04	70.73
27		37.78	1.26E+00	1.37E+04	4.04E+04	71.33
28		37.78	9.98E-01	1.10E+04	3.38E+04	71.99
29		37.78	7.92E-01	8.84E+03	2.83E+04	72.64
30		37.78	6.30E-01	7.11E+03	2.37E+04	73.27
31		37.78	5.00E-01	5.66E+03	1.96E+04	73.93

333

Table G. 28: DSR test result PG 64-22 at 29 ℃

Meas. Pts.	Binder Grade	Temperature ℃	Angular Frequency [rad/s]	Storage Modulus [Pa]	Loss Modulus [Pa]	Phase Angle [°]
1		29.44	5.00E+02	5.53E+06	6.89E+06	51.25
2		29.44	3.97E+02	4.84E+06	6.06E+06	51.42
3		29.44	3.16E+02	4.19E+06	5.35E+06	51.95
4		29.44	2.51E+02	3.62E+06	4.71E+06	52.46
5		29.44	1.99E+02	3.12E+06	4.15E+06	53.04
6		29.44	1.58E+02	2.67E+06	3.66E+06	53.87
7		29.44	1.26E+02	2.31E+06	3.21E+06	54.26
8		29.44	9.98E+01	1.98E+06	2.82E+06	54.86
9		29.44	7.92E+01	1.70E+06	2.47E+06	55.48
10		29.44	6.30E+01	1.45E+06	2.16E+06	56.11
11		29.44	5.00E+01	1.24E+06	1.90E+06	56.9
12		29.44	3.97E+01	1.06E+06	1.65E+06	57.35
13		29.44	3.16E+01	9.01E+05	1.43E+06	57.83
14		29.44	2.51E+01	7.66E+05	1.24E+06	58.34
15	PG 64-22	29.44	1.99E+01	6.49E+05	1.08E+06	58.88
16		29.44	1.58E+01	5.49E+05	9.29E+05	59.41
17		29.44	1.26E+01	4.65E+05	8.03E+05	59.93
18		29.44	9.98E+00	3.93E+05	6.94E+05	60.45
19		29.44	7.92E+00	3.36E+05	6.04E+05	60.92
20		29.44	6.30E+00	2.85E+05	5.23E+05	61.4
21		29.44	5.00E+00	2.39E+05	4.48E+05	61.92
22		29.44	3.97E+00	2.00E+05	3.83E+05	62.45
23		29.44	3.16E+00	1.68E+05	3.28E+05	62.93
24		29.44	2.51E+00	1.41E+05	2.81E+05	63.45
25		29.44	1.99E+00	1.16E+05	2.38E+05	63.97
26		29.44	1.58E+00	9.65E+04	2.02E+05	64.51
27		29.44	1.26E+00	8.05E+04	1.73E+05	65.02
28		29.44	9.98E-01	6.74E+04	1.48E+05	65.53
29		29.44	7.92E-01	5.56E+04	1.25E+05	66.05
30		29.44	6.30E-01	4.60E+04	1.07E+05	66.62
31		29.44	5.00E-01	3.85E+04	9.14E+04	67.15

334

Table G. 29: DSR test result PG 64-22 at 21 ºC

Meas. Pts.	Binder Grade	Temperature ºC	Angular Frequency [rad/s]	Storage Modulus [Pa]	Loss Modulus [Pa]	Phase Angle [°]
1		21.11	5.00E+02	1.79E+07	1.64E+07	42.5
2		21.11	3.97E+02	1.59E+07	1.49E+07	43.06
3		21.11	3.16E+02	1.41E+07	1.35E+07	43.69
4		21.11	2.51E+02	1.23E+07	1.22E+07	44.8
5		21.11	1.99E+02	1.11E+07	1.10E+07	44.94
6		21.11	1.58E+02	9.70E+06	1.00E+07	45.92
7		21.11	1.26E+02	8.55E+06	9.02E+06	46.51
8		21.11	9.98E+01	7.54E+06	8.07E+06	46.95
9		21.11	7.92E+01	6.62E+06	7.23E+06	47.52
10		21.11	6.30E+01	5.82E+06	6.49E+06	48.14
11		21.11	5.00E+01	5.10E+06	5.82E+06	48.75
12		21.11	3.97E+01	4.47E+06	5.21E+06	49.37
13		21.11	3.16E+01	3.90E+06	4.65E+06	49.99
14		21.11	2.51E+01	3.40E+06	4.14E+06	50.6
15	PG 64-22	21.11	1.99E+01	2.96E+06	3.68E+06	51.22
16		21.11	1.58E+01	2.57E+06	3.26E+06	51.83
17		21.11	1.26E+01	2.22E+06	2.88E+06	52.44
18		21.11	9.98E+00	1.92E+06	2.55E+06	53.05
19		21.11	7.92E+00	1.65E+06	2.24E+06	53.65
20		21.11	6.30E+00	1.42E+06	1.97E+06	54.25
21		21.11	5.00E+00	1.21E+06	1.73E+06	54.85
22		21.11	3.97E+00	1.04E+06	1.50E+06	55.47
23		21.11	3.16E+00	8.79E+05	1.31E+06	56.06
24		21.11	2.51E+00	7.53E+05	1.14E+06	56.64
25		21.11	1.99E+00	6.46E+05	1.00E+06	57.16
26.		21.11	1.58E+00	5.51E+05	8.73E+05	57.73
27		21.11	1.26E+00	4.69E+05	7.58E+05	58.28
28		21.11	9.98E-01	3.96E+05	6.55E+05	58.85
29		21.11	7.92E-01	3.36E+05	5.68E+05	59.36
30		21.11	6.30E-01	2.84E+05	4.90E+05	59.95
31		21.11	5.00E-01	2.40E+05	4.25E+05	60.49

Table G. 30: DSR test result PG 64-22 at 12 ºC

Meas. Pts.	Binder Grade	Temperature ºC	Angular Frequency [rad/s]	Storage Modulus [Pa]	Loss Modulus [Pa]	Phase Angle [°]
1		12.78	5.00E+02	4.94E+07	3.33E+07	33.94
2		12.78	3.97E+02	4.51E+07	3.11E+07	34.55
3		12.78	3.16E+02	4.12E+07	2.90E+07	35.17
4		12.78	2.51E+02	3.75E+07	2.70E+07	35.81
5		12.78	1.99E+02	3.39E+07	2.51E+07	36.56
6		12.78	1.58E+02	3.08E+07	2.33E+07	37.13
7		12.78	1.26E+02	2.79E+07	2.16E+07	37.72
8		12.78	9.98E+01	2.51E+07	1.99E+07	38.36
9		12.78	7.92E+01	2.27E+07	1.83E+07	39
10		12.78	6.30E+01	2.03E+07	1.69E+07	39.65
11		12.78	5.00E+01	1.83E+07	1.55E+07	40.27
12		12.78	3.97E+01	1.64E+07	1.42E+07	40.9
13		12.78	3.16E+01	1.47E+07	1.30E+07	41.52
14		12.78	2.51E+01	1.31E+07	1.19E+07	42.14
15	PG 64-22	12.78	1.99E+01	1.17E+07	1.08E+07	42.76
16		12.78	1.58E+01	1.04E+07	9.83E+06	43.4
17		12.78	1.26E+01	9.21E+06	8.91E+06	44.04
18		12.78	9.98E+00	8.16E+06	8.07E+06	44.68
19		12.78	7.92E+00	7.23E+06	7.31E+06	45.3
20		12.78	6.30E+00	6.37E+06	6.58E+06	45.94
21		12.78	5.00E+00	5.61E+06	5.93E+06	46.57
22		12.78	3.97E+00	4.94E+06	5.33E+06	47.2
23		12.78	3.16E+00	4.34E+06	4.79E+06	47.84
24		12.78	2.51E+00	3.80E+06	4.29E+06	48.46
25		12.78	1.99E+00	3.31E+06	3.82E+06	49.12
26		12.78	1.58E+00	2.89E+06	3.41E+06	49.73
27		12.78	1.26E+00	2.52E+06	3.04E+06	50.34
28		12.78	9.98E-01	2.19E+06	2.70E+06	51
29		12.78	7.92E-01	1.90E+06	2.40E+06	51.63
30		12.78	6.30E-01	1.65E+06	2.13E+06	52.24
31		12.78	5.00E-01	1.43E+06	1.89E+06	52.84

336

Table G. 31: DSR test result PG 64-22 at 10ºF

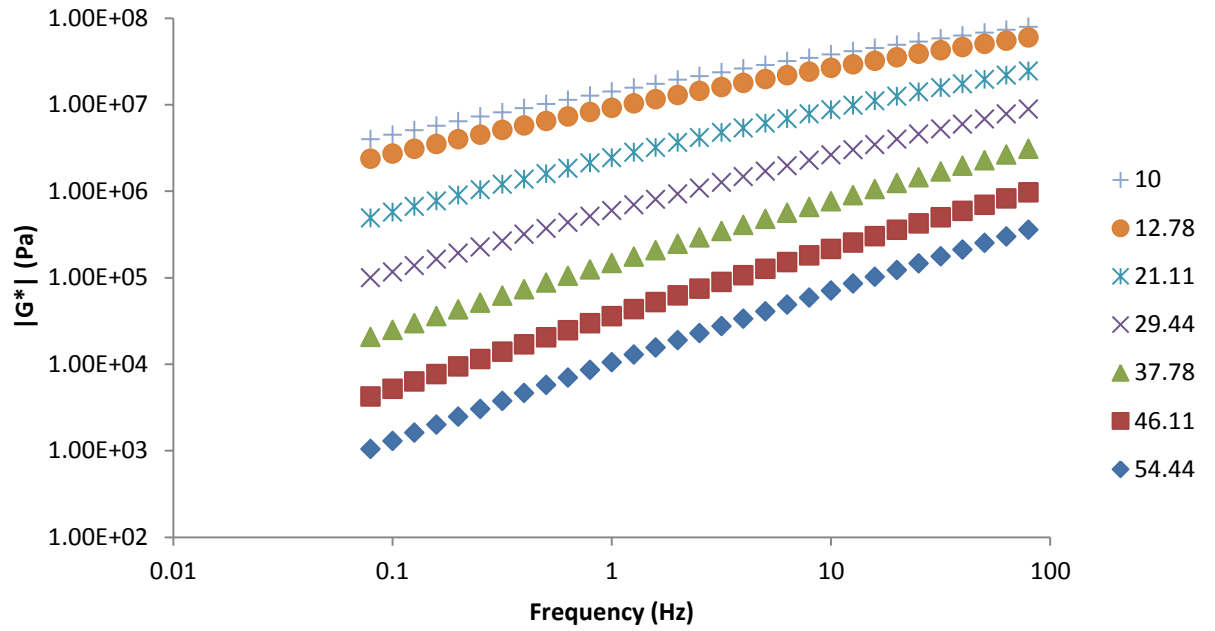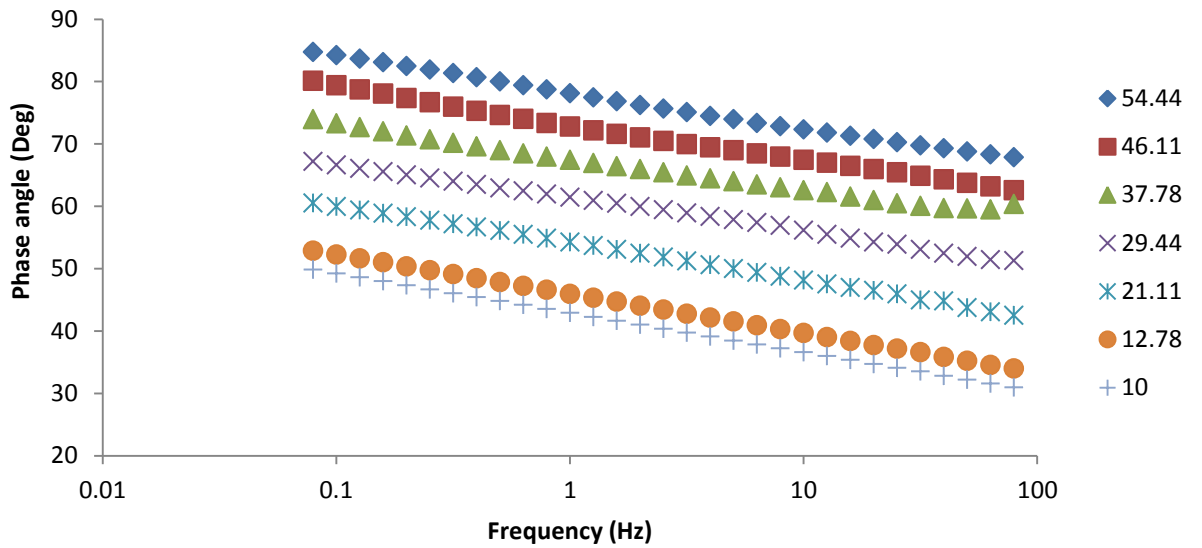| Meas. Pts.	Binder Grade	Temperature ºC	Angular Frequency [rad/s]	Storage Modulus [Pa]	Loss Modulus [Pa]	Phase Angle [°]
1		10	5.00E+02	6.77E+07	4.06E+07	30.93
2		10	3.97E+02	6.23E+07	3.82E+07	31.55
3		10	3.16E+02	5.74E+07	3.61E+07	32.16
4		10	2.51E+02	5.27E+07	3.39E+07	32.79
5		10	1.99E+02	4.82E+07	3.19E+07	33.49
6		10	1.58E+02	4.41E+07	2.98E+07	34.06
7		10	1.26E+02	4.03E+07	2.79E+07	34.69
8		10	9.98E+01	3.67E+07	2.60E+07	35.33
9		10	7.92E+01	3.34E+07	2.42E+07	35.95
10		10	6.30E+01	3.03E+07	2.25E+07	36.58
11		10	5.00E+01	2.75E+07	2.09E+07	37.19
12		10	3.97E+01	2.50E+07	1.94E+07	37.8
13		10	3.16E+01	2.25E+07	1.78E+07	38.43
14		10	2.51E+01	2.02E+07	1.64E+07	39.08
15	PG 64-22	10	1.99E+01	1.81E+07	1.50E+07	39.72
16		10	1.58E+01	1.62E+07	1.38E+07	40.35
17		10	1.26E+01	1.46E+07	1.26E+07	40.97
18		10	9.98E+00	1.30E+07	1.15E+07	41.6
19		10	7.92E+00	1.16E+07	1.05E+07	42.23
20		10	6.30E+00	1.03E+07	9.56E+06	42.88
21		10	5.00E+00	9.15E+06	8.69E+06	43.51
22		10	3.97E+00	8.10E+06	7.86E+06	44.15
23		10	3.16E+00	7.19E+06	7.14E+06	44.78
24		10	2.51E+00	6.38E+06	6.46E+06	45.39
25		10	1.99E+00	5.64E+06	5.84E+06	46.01
26		10	1.58E+00	4.96E+06	5.26E+06	46.66
27		10	1.26E+00	4.35E+06	4.71E+06	47.31
28		10	9.98E-01	3.81E+06	4.22E+06	47.95
29		10	7.92E-01	3.33E+06	3.77E+06	48.61
30		10	6.30E-01	2.93E+06	3.39E+06	49.21
31		10	5.00E-01	2.55E+06	3.03E+06	49.84

337

Figure G. 49: $|G^*|$ test results PG 64-22

Figure G. 50: Phase angle test results PG 64-22
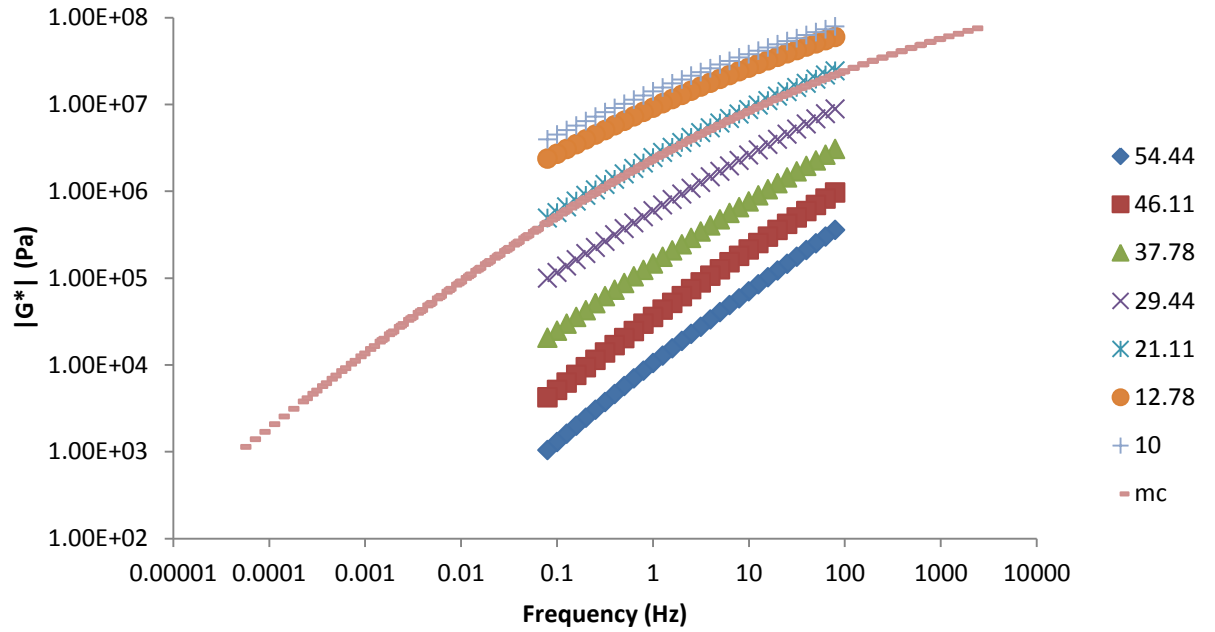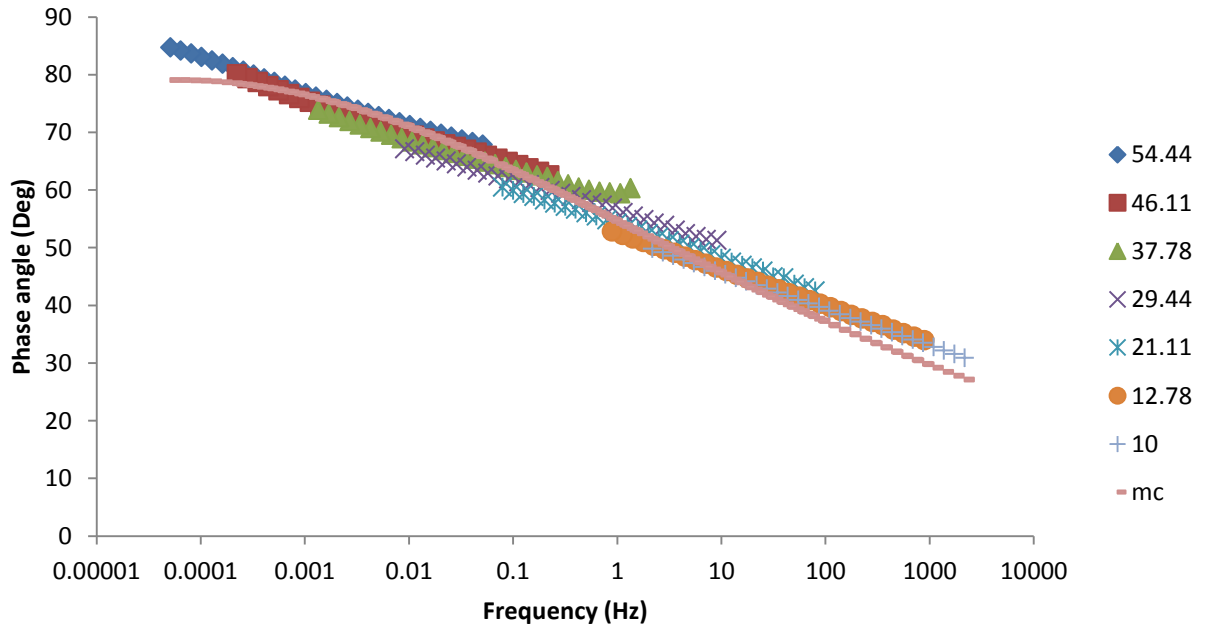
Figure G. 51: *G** mastercurve for PG 64-22

Figure G. 52: Phase angle mastercurve for PG 64-22

339

Table G. 32: DSR test result PG 70-22 at 54 ºC

Meas. Pts.	Binder Grade	Temperature ºC	Angular Frequency [rad/s]	Storage Modulus [Pa]	Loss Modulus [Pa]	Phase Angle [°]
1		54.44	5.00E+02	6.78E+04	1.58E+05	66.81
2		54.44	3.97E+02	5.69E+04	1.33E+05	66.78
3		54.44	3.16E+02	4.74E+04	1.11E+05	66.89
4		54.44	2.51E+02	3.96E+04	9.29E+04	66.9
5		54.44	1.99E+02	3.31E+04	7.79E+04	66.96
6		54.44	1.58E+02	2.78E+04	6.54E+04	67
7		54.44	1.26E+02	2.33E+04	5.51E+04	67.07
8		54.44	9.98E+01	1.92E+04	4.68E+04	67.66
9		54.44	7.92E+01	1.63E+04	3.94E+04	67.54
10		54.44	6.30E+01	1.39E+04	3.33E+04	67.36
11		54.44	5.00E+01	1.18E+04	2.79E+04	67.12
12		54.44	3.97E+01	1.00E+04	2.35E+04	66.96
13		54.44	3.16E+01	8.46E+03	1.98E+04	66.85
14		54.44	2.51E+01	7.13E+03	1.66E+04	66.76
15	PG 70-22	54.44	1.99E+01	6.02E+03	1.40E+04	66.75
16		54.44	1.58E+01	5.08E+03	1.18E+04	66.77
17		54.44	1.26E+01	4.28E+03	9.98E+03	66.8
18		54.44	9.98E+00	3.61E+03	8.44E+03	66.86
19		54.44	7.92E+00	3.03E+03	7.11E+03	66.95
20		54.44	6.30E+00	2.54E+03	6.00E+03	67.05
21		54.44	5.00E+00	2.14E+03	5.08E+03	67.18
22		54.44	3.97E+00	1.78E+03	4.27E+03	67.36
23		54.44	3.16E+00	1.49E+03	3.61E+03	67.54
24		54.44	2.51E+00	1.25E+03	3.05E+03	67.78
25		54.44	1.99E+00	1.04E+03	2.57E+03	68.01
26		54.44	1.58E+00	8.60E+02	2.16E+03	68.33
27		54.44	1.26E+00	7.14E+02	1.83E+03	68.65
28		54.44	9.98E-01	5.90E+02	1.54E+03	68.99
29		54.44	7.92E-01	4.88E+02	1.29E+03	69.34
30		54.44	6.30E-01	4.00E+02	1.09E+03	69.8
31		54.44	5.00E-01	3.26E+02	9.10E+02	70.27

340

Table G. 33: DSR test result PG 70-22 at 46 ºC

Meas. Pts.	Binder Grade	Temperature	Angular Frequency	Storage Modulus	Loss Modulus	Phase Angle
		ºC	[rad/s]	[Pa]	[Pa]	[°]
1		46.11	5.00E+02	1.83E+05	4.05E+05	65.65
2		46.11	3.97E+02	1.55E+05	3.42E+05	65.65
3		46.11	3.16E+02	1.30E+05	2.89E+05	65.7
4		46.11	2.51E+02	1.10E+05	2.43E+05	65.74
5		46.11	1.99E+02	9.27E+04	2.06E+05	65.79
6		46.11	1.58E+02	7.82E+04	1.74E+05	65.82
7		46.11	1.26E+02	6.59E+04	1.47E+05	65.83
8		46.11	9.98E+01	5.56E+04	1.24E+05	65.84
9		46.11	7.92E+01	4.70E+04	1.05E+05	65.83
10		46.11	6.30E+01	3.98E+04	8.85E+04	65.8
11		46.11	5.00E+01	3.37E+04	7.49E+04	65.76
12		46.11	3.97E+01	2.85E+04	6.31E+04	65.71
13		46.11	3.16E+01	2.41E+04	5.33E+04	65.66
14		46.11	2.51E+01	2.05E+04	4.52E+04	65.63
15	PG 70-22	46.11	1.99E+01	1.73E+04	3.81E+04	65.55
16		46.11	1.58E+01	1.46E+04	3.21E+04	65.5
17		46.11	1.26E+01	1.24E+04	2.72E+04	65.45
18		46.11	9.98E+00	1.05E+04	2.30E+04	65.41
19		46.11	7.92E+00	8.89E+03	1.94E+04	65.39
20		46.11	6.30E+00	7.53E+03	1.64E+04	65.38
21		46.11	5.00E+00	6.39E+03	1.39E+04	65.38
22		46.11	3.97E+00	5.40E+03	1.18E+04	65.4
23		46.11	3.16E+00	4.55E+03	9.96E+03	65.43
24		46.11	2.51E+00	3.83E+03	8.41E+03	65.5
25		46.11	1.99E+00	3.25E+03	7.14E+03	65.57
26.		46.11	1.58E+00	2.74E+03	6.06E+03	65.69
27		46.11	1.26E+00	2.32E+03	5.15E+03	65.81
28		46.11	9.98E-01	1.95E+03	4.37E+03	65.92
29		46.11	7.92E-01	1.64E+03	3.71E+03	66.08
30		46.11	6.30E-01	1.38E+03	3.14E+03	66.32
31		46.11	5.00E-01	1.15E+03	2.65E+03	66.58

341

Table G. 34: DSR test result PG 70-22 at 37 ºC

Meas. Pts.	Binder Grade	Temperature ºC	Angular Frequency [rad/s]	Storage Modulus [Pa]	Loss Modulus [Pa]	Phase Angle [°]
1		37.78	5.00E+02	5.84E+05	1.40E+06	67.3
2		37.78	3.97E+02	5.56E+05	1.17E+06	64.55
3		37.78	3.16E+02	4.79E+05	9.84E+05	64.04
4		37.78	2.51E+02	4.14E+05	8.29E+05	63.47
5		37.78	1.99E+02	3.53E+05	7.01E+05	63.3
6		37.78	1.58E+02	2.99E+05	5.95E+05	63.31
7		37.78	1.26E+02	2.55E+05	5.09E+05	63.37
8		37.78	9.98E+01	2.15E+05	4.31E+05	63.53
9		37.78	7.92E+01	1.83E+05	3.70E+05	63.67
10		37.78	6.30E+01	1.55E+05	3.15E+05	63.83
11		37.78	5.00E+01	1.31E+05	2.68E+05	63.92
12		37.78	3.97E+01	1.10E+05	2.27E+05	64.01
13		37.78	3.16E+01	9.31E+04	1.92E+05	64.09
14		37.78	2.51E+01	7.89E+04	1.63E+05	64.14
15	PG 70-22	37.78	1.99E+01	6.68E+04	1.38E+05	64.17
16		37.78	1.58E+01	5.65E+04	1.17E+05	64.2
17		37.78	1.26E+01	4.78E+04	9.89E+04	64.22
18		37.78	9.98E+00	4.06E+04	8.40E+04	64.2
19		37.78	7.92E+00	3.44E+04	7.10E+04	64.17
20		37.78	6.30E+00	2.93E+04	6.03E+04	64.13
21		37.78	5.00E+00	2.49E+04	5.13E+04	64.09
22		37.78	3.97E+00	2.13E+04	4.37E+04	64.05
23		37.78	3.16E+00	1.80E+04	3.70E+04	64.02
24		37.78	2.51E+00	1.51E+04	3.10E+04	64.01
25		37.78	1.99E+00	1.28E+04	2.62E+04	63.98
26.		37.78	1.58E+00	1.09E+04	2.23E+04	63.94
27		37.78	1.26E+00	9.37E+03	1.91E+04	63.92
28		37.78	9.98E-01	8.05E+03	1.64E+04	63.93
29		37.78	7.92E-01	6.88E+03	1.41E+04	63.92
30		37.78	6.30E-01	5.85E+03	1.20E+04	63.95
31		37.78	5.00E-01	4.87E+03	1.00E+04	64.04

Table G. 35: DSR test result PG 70-22 at 29 ºC

Meas. Pts.	Binder Grade	Temperature ºC	Angular Frequency [rad/s]	Storage Modulus [Pa]	Loss Modulus [Pa]	Phase Angle [°]
1		29.44	5.00E+02	2.38E+06	3.76E+06	57.69
2		29.44	3.97E+02	2.10E+06	3.25E+06	57.13
3		29.44	3.16E+02	1.80E+06	2.81E+06	57.37
4		29.44	2.51E+02	1.55E+06	2.44E+06	57.56
5		29.44	1.99E+02	1.33E+06	2.12E+06	57.88
6		29.44	1.58E+02	1.13E+06	1.83E+06	58.29
7		29.44	1.26E+02	9.61E+05	1.58E+06	58.71
8		29.44	9.98E+01	8.11E+05	1.37E+06	59.35
9		29.44	7.92E+01	6.92E+05	1.18E+06	59.52
10		29.44	6.30E+01	5.87E+05	1.01E+06	59.89
11		29.44	5.00E+01	5.00E+05	8.73E+05	60.23
12		29.44	3.97E+01	4.25E+05	7.52E+05	60.55
13		29.44	3.16E+01	3.60E+05	6.45E+05	60.85
14		29.44	2.51E+01	3.05E+05	5.52E+05	61.12
15	PG 70-22	29.44	1.99E+01	2.59E+05	4.75E+05	61.36
16		29.44	1.58E+01	2.20E+05	4.06E+05	61.59
17		29.44	1.26E+01	1.86E+05	3.46E+05	61.77
18		29.44	9.98E+00	1.58E+05	2.96E+05	61.93
19		29.44	7.92E+00	1.34E+05	2.52E+05	62.07
20		29.44	6.30E+00	1.14E+05	2.15E+05	62.19
21		29.44	5.00E+00	9.67E+04	1.84E+05	62.28
22		29.44	3.97E+00	8.23E+04	1.57E+05	62.34
23		29.44	3.16E+00	7.00E+04	1.34E+05	62.41
24		29.44	2.51E+00	5.94E+04	1.14E+05	62.45
25		29.44	1.99E+00	5.07E+04	9.73E+04	62.48
26		29.44	1.58E+00	4.33E+04	8.31E+04	62.48
27		29.44	1.26E+00	3.68E+04	7.08E+04	62.5
28		29.44	9.98E-01	3.20E+04	6.14E+04	62.48
29		29.44	7.92E-01	2.70E+04	5.18E+04	62.48
30		29.44	6.30E-01	2.27E+04	4.35E+04	62.44
31		29.44	5.00E-01	1.93E+04	3.70E+04	62.42

343

Table G. 36: DSR test result PG 70-22 at 21 ℃

Meas. Pts.	Binder Grade	Temperature ℃	Angular Frequency [rad/s]	Storage Modulus [Pa]	Loss Modulus [Pa]	Phase Angle [°]
1		21.11	5.00E+02	8.39E+06	9.64E+06	48.95
2		21.11	3.97E+02	7.43E+06	8.62E+06	49.24
3		21.11	3.16E+02	6.49E+06	7.68E+06	49.78
4		21.11	2.51E+02	5.66E+06	6.82E+06	50.32
5		21.11	1.99E+02	4.94E+06	6.08E+06	50.93
6		21.11	1.58E+02	4.30E+06	5.40E+06	51.48
7		21.11	1.26E+02	3.73E+06	4.78E+06	52.04
8		21.11	9.98E+01	3.22E+06	4.23E+06	52.67
9		21.11	7.92E+01	2.77E+06	3.75E+06	53.58
10		21.11	6.30E+01	2.40E+06	3.31E+06	54.04
11		21.11	5.00E+01	2.08E+06	2.91E+06	54.45
12		21.11	3.97E+01	1.79E+06	2.54E+06	54.89
13		21.11	3.16E+01	1.53E+06	2.22E+06	55.36
14		21.11	2.51E+01	1.32E+06	1.94E+06	55.82
15	PG 70-22	21.11	1.99E+01	1.12E+06	1.68E+06	56.29
16		21.11	1.58E+01	9.55E+05	1.46E+06	56.77
17		21.11	1.26E+01	8.09E+05	1.26E+06	57.23
18		21.11	9.98E+00	6.86E+05	1.08E+06	57.67
19		21.11	7.92E+00	5.88E+05	9.42E+05	58.04
20		21.11	6.30E+00	5.04E+05	8.19E+05	58.39
21		21.11	5.00E+00	4.30E+05	7.07E+05	58.73
22		21.11	3.97E+00	3.64E+05	6.07E+05	59.06
23		21.11	3.16E+00	3.08E+05	5.20E+05	59.38
24		21.11	2.51E+00	2.64E+05	4.51E+05	59.63
25		21.11	1.99E+00	2.28E+05	3.92E+05	59.86
26		21.11	1.58E+00	1.95E+05	3.38E+05	60.04
27		21.11	1.26E+00	1.66E+05	2.91E+05	60.22
28		21.11	9.98E-01	1.42E+05	2.50E+05	60.43
29		21.11	7.92E-01	1.22E+05	2.16E+05	60.59
30		21.11	6.30E-01	1.03E+05	1.83E+05	60.7
31		21.11	5.00E-01	8.72E+04	1.56E+05	60.82

344

Table G. 37: DSR test result PG 70-22 at 12 ºC

Meas. Pts.	Binder Grade	Temperature ºC	Angular Frequency [rad/s]	Storage Modulus [Pa]	Loss Modulus [Pa]	Phase Angle [°]
1		12.78	5.00E+02	2.74E+07	2.27E+07	39.65
2		12.78	3.97E+02	2.46E+07	2.08E+07	40.29
3		12.78	3.16E+02	2.19E+07	1.91E+07	41.06
4		12.78	2.51E+02	1.96E+07	1.74E+07	41.58
5		12.78	1.99E+02	1.75E+07	1.59E+07	42.28
6		12.78	1.58E+02	1.56E+07	1.45E+07	43.07
7		12.78	1.26E+02	1.39E+07	1.32E+07	43.54
8		12.78	9.98E+01	1.23E+07	1.20E+07	44.15
9		12.78	7.92E+01	1.09E+07	1.08E+07	44.77
10		12.78	6.30E+01	9.72E+06	9.84E+06	45.37
11		12.78	5.00E+01	8.62E+06	8.92E+06	45.97
12		12.78	3.97E+01	7.63E+06	8.06E+06	46.56
13		12.78	3.16E+01	6.69E+06	7.22E+06	47.2
14		12.78	2.51E+01	5.84E+06	6.45E+06	47.84
15	PG 70-22	12.78	1.99E+01	5.09E+06	5.75E+06	48.47
16		12.78	1.58E+01	4.46E+06	5.14E+06	49.06
17		12.78	1.26E+01	3.90E+06	4.59E+06	49.64
18		12.78	9.98E+00	3.39E+06	4.08E+06	50.24
19		12.78	7.92E+00	2.96E+06	3.63E+06	50.8
20		12.78	6.30E+00	2.56E+06	3.20E+06	51.38
21		12.78	5.00E+00	2.21E+06	2.82E+06	51.95
22		12.78	3.97E+00	1.90E+06	2.48E+06	52.52
23		12.78	3.16E+00	1.64E+06	2.18E+06	53.04
24		12.78	2.51E+00	1.43E+06	1.93E+06	53.55
25		12.78	1.99E+00	1.24E+06	1.71E+06	53.99
26		12.78	1.58E+00	1.06E+06	1.49E+06	54.51
27		12.78	1.26E+00	9.08E+05	1.30E+06	55
28		12.78	9.98E-01	7.89E+05	1.14E+06	55.41
29		12.78	7.92E-01	6.70E+05	9.88E+05	55.83
30		12.78	6.30E-01	5.75E+05	8.62E+05	56.3
31		12.78	5.00E-01	4.97E+05	7.56E+05	56.69

345

Table G. 38: DSR test result PG 70-22 at 10 ℃

Meas. Pts.	Binder Grade	Temperature ℃	Angular Frequency [rad/s]	Storage Modulus [Pa]	Loss Modulus [Pa]	Phase Angle [°]
1		10	5.00E+02	3.84E+07	2.87E+07	36.76
2		10	3.97E+02	3.47E+07	2.66E+07	37.42
3		10	3.16E+02	3.14E+07	2.46E+07	38.03
4		10	2.51E+02	2.83E+07	2.27E+07	38.69
5		10	1.99E+02	2.54E+07	2.09E+07	39.52
6		10	1.58E+02	2.29E+07	1.93E+07	40.13
7		10	1.26E+02	2.05E+07	1.76E+07	40.65
8		10	9.98E+01	1.85E+07	1.62E+07	41.27
9		10	7.92E+01	1.65E+07	1.48E+07	41.92
10		10	6.30E+01	1.47E+07	1.35E+07	42.56
11		10	5.00E+01	1.31E+07	1.23E+07	43.2
12		10	3.97E+01	1.16E+07	1.12E+07	43.83
13		10	3.16E+01	1.03E+07	1.01E+07	44.47
14		10	2.51E+01	9.10E+06	9.13E+06	45.11
15	PG 70-22	10	1.99E+01	8.05E+06	8.25E+06	45.72
16		10	1.58E+01	7.08E+06	7.43E+06	46.35
17		10	1.26E+01	6.23E+06	6.68E+06	46.97
18		10	9.98E+00	5.48E+06	6.00E+06	47.58
19		10	7.92E+00	4.80E+06	5.36E+06	48.19
20		10	6.30E+00	4.20E+06	4.80E+06	48.78
21		10	5.00E+00	3.69E+06	4.29E+06	49.35
22		10	3.97E+00	3.21E+06	3.82E+06	49.94
23		10	3.16E+00	2.79E+06	3.39E+06	50.51
24		10	2.51E+00	2.42E+06	3.00E+06	51.1
25		10	1.99E+00	2.10E+06	2.66E+06	51.64
26.		10	1.58E+00	1.82E+06	2.34E+06	52.18
27		10	1.26E+00	1.58E+06	2.07E+06	52.7
28		10	9.98E-01	1.36E+06	1.82E+06	53.24
29		10	7.92E-01	1.18E+06	1.60E+06	53.75
30		10	6.30E-01	1.02E+06	1.42E+06	54.23
31		10	5.00E-01	8.78E+05	1.24E+06	54.7

346

www.manaraa.com
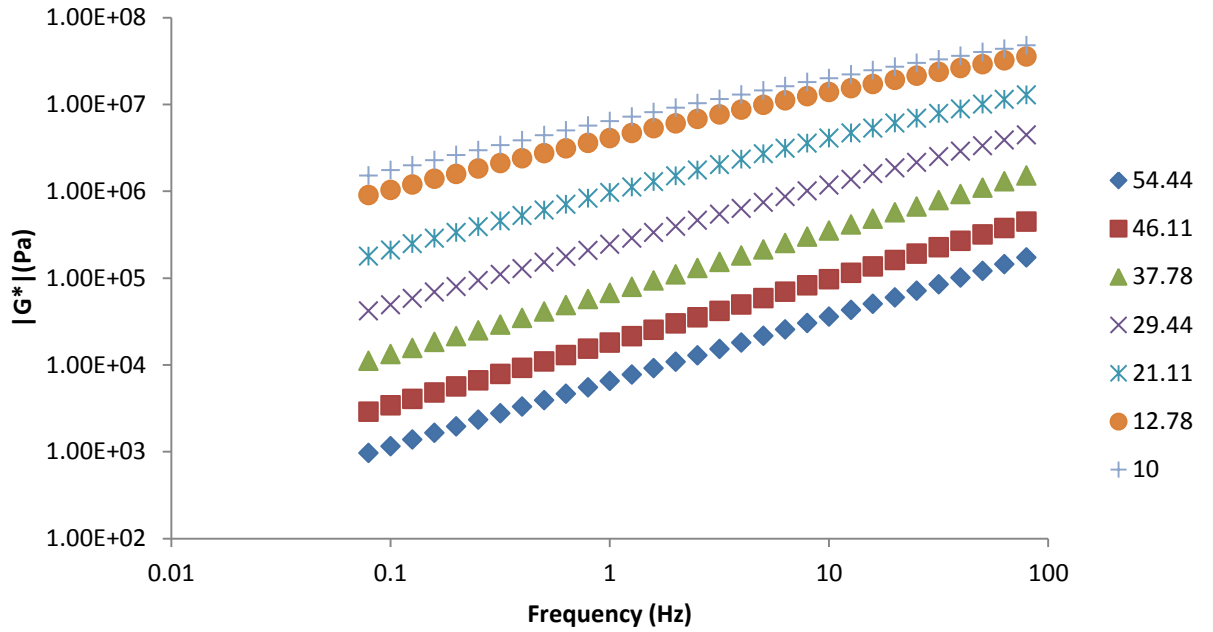
Figure G. 53: *G** test result for PG 70-22
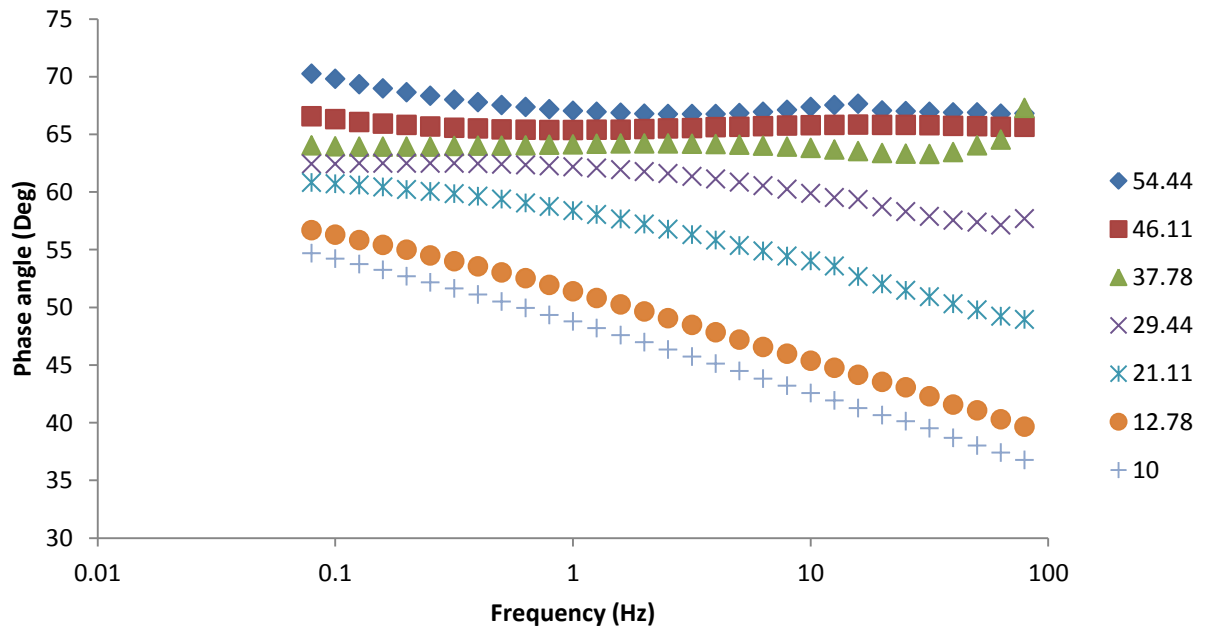
Figure G. 54: phase angle result for PG 70-22

347
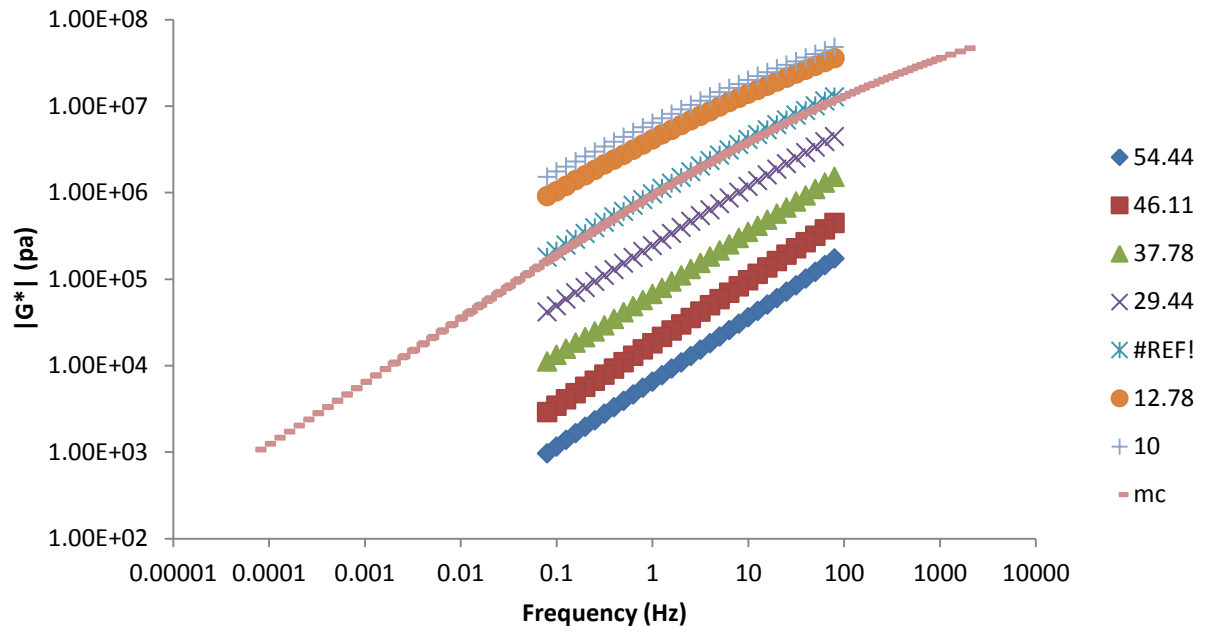
Figure G. 55: *G** mastercurve PG 70-22
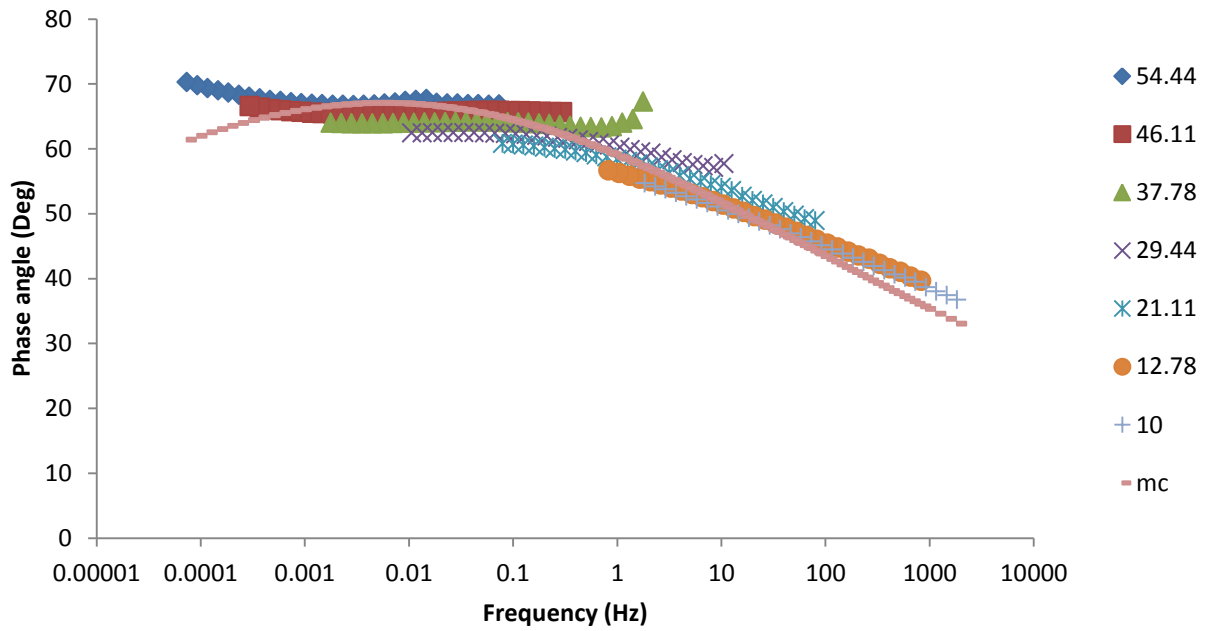
Figure G. 56: Phase angle mastercurve for PG 70-22

348

APPENDIX H

Critical Evaluation of AASHTO TP-62 Load Specification on the Criteria of Meeting Linear Viscoelastic (LVE) Requirements

Critical Evaluation of AASHTO TP-62 Load Specification on the Criteria of Meeting Linear Viscoelastic (LVE) Requirements

Mekdim T. Weldegiorgis[1] and Rafiqul A. Tarefder[2]

Abstract: In this study, linear viscoelastic (LVE) limits for an asphalt mixture is determined using dynamic modulus testing. Stress sweep dynamic modulus testing is conducted on 100 mm cylindrical samples at different frequencies. Superposition principle, proportionality principle and 5% stiffness reduction limit are implemented to determine the linear viscoelastic limits for stress and strain. All applied principles consistently showed that the stress and strain linearity limits for the studied mix are 155, 414, 506, 772, 470, 462 kPa and 55, 69, 84, 99, 36, 50 micro-strain each for loading frequency of 0.1, 0.5, 1, 5, 10, 25 Hz respectively. The AASHTO TP-62 limiting stress and strain values are 150 micro-strains and 700 kPa, which are considerably higher than the results found in this study. This indicates that there is a significant chance of conducting the dynamic modulus test outside the LVE region. Investigation on the effect of the stress sweep on the phase angle of the mix showed that the phase angle is not dependent on stress. However, the softening rate at which the dynamic modulus decreases is found to be approximately the same over the entire stress sweep range, which indicates the dependency of dynamic modulus on stress.

CE Database subject headings: Dynamic Tests; Asphalt Pavements; Mixtures; Viscoelasticity; Material properties.

Author keywords: Linear Viscoelasticity; Asphalt Concrete; Superpave Mix; Dynamic Modulus

[1] Department of Civil Engineering, Graduate Research Assistant, University of New Mexico, Albuquerque, NM 87106, USA (mteshome@unm.edu)

[2] Department of Civil Engineering, Associate Professor and Regents' Lecturer, University of New Mexico, Albuquerque, NM 87106, USA (Tarefder@unm.edu)

Introduction

Linear viscoelasticity is a major assumption in the analysis of dynamic modulus test results. Dynamic modulus is defined as the ratio of maximum amplitude of stress to maximum amplitude of recoverable strain. In this definition, the effect of unrecovered strain is completely disregarded and assumes the test is conducted in the linear viscoelastic (LVE) range. Permanent deformation is assumed to have no significant effect on the measured dynamic modulus in the LVE range. The decomposition of complex modulus into the storage modulus and loss modulus components using the phase angle also assumes linear viscoelasticity. In addition, the application of time-temperature superposition in the development procedure of the dynamic modulus master curve is dependent on the assumption that asphalt concrete (AC) is a thermo-rheologically simple material and behaves as a LVE material within the LVE range.

There are different methods to determine the LVE limit of AC. Anderson et al. (1994) determined the LVE range for pure asphalt binders by arbitrarily assuming that asphalt will behave in a LVE manner if the reduction in the dynamic modulus is less than 5% of the initial (reference) modulus. Airey et al. (2003) adopted this same definition to determine the LVE range of both asphalt binder as well as AC. This definition, referred as "5% stiffness reduction principle" here after, requires conducting strain or stress sweep tests to determine the LVE limit. The dynamic moduli with an incremental strain or stress level are then computed and the strain or stress at which the dynamic modulus is reduced by more than 5% is taken to be the maximum possible strain or stress to which the hot mix asphalt (HMA) concrete can be exposed to without exceeding the LVE range. Another method for determining the viscoelastic range of AC is to check for the validity of superposition and proportionality principles (Mehta and Christensen 2000). The principle of proportionality requires the material response to change in the same proportion as the change in a trigger. For a stress controlled test, the trigger is stress and the material response is strain. For the superposition principle to be valid, the sum of the material responses resulting from two triggers should be the same as the response resulting from the sum of the triggers (Schapery 1974, Mehta and Christensen 2000).

Numerous studies have been done to determine the LVE range of asphalt mixtures. However, the LVE ranges determined show a wide variation. In the 1960s, Pell (1962), Pell and Taylor (1969), Sayegh (1967), Gardner and Skok (1967), and Taylor (1968) all investigated the behavior of AC under varying strain levels and reported maximum strain linearity limits ranging from 20 micro-strain up to 200 micro-strain. Specifically, Sayegh (1967) conducted laboratory testing and found 20 micro-strain as a limit, Gardner and Skok (1967) conducted repeated compressive load tests and found 100 micro-strain to be the LVE limit and Taylor (1968) applied dynamic loading and found 200 micro-strain to be the maximum bulk strain AC can sustain without exceeding the LVE range. (DoubBaneh E 1995, Benedetto and Roche 1998) also state that the modulus of AC decreases substantially for tension compression tests performed in strain levels between

351

30 to 80 micro-strain. While these studies show the existence of a strain dependent LVE range, the applicability of the determined strain limits to Superpave asphalt mixtures remains questionable since these studies were performed on penetration grade bitumen mixtures.

Recently, Airey et al. (2003) and Airey et al. (2004) conducted a strain controlled test on AC to determine the LVE range of AC and they found that LVE strain criterion for the asphalt mixes is in the order of 100 micro-strain which is consistent with previous findings by Pell and Taylor (1969). For this study, a stress sweep test is conducted using a purpose built dynamic modulus testing equipment to observe the change in the dynamic modulus with increasing stress levels. However, this study is also conducted on penetration grade binders and the asphalt mixture types used are dense bitumen macadam and hot rolled asphalt. In addition, the number of cycles adopted to determine the dynamic modulus is limited to 30.

Different attempts are made to explain the cause of AC nonlinearity. Physical nonlinearity such as granular microstructure change and rearrangement, during loading, is one of the proposed causes of AC nonlinearity. The other is geometric nonlinearity, which are basically different defects in AC such as air voids and cracks. Air voids and cracks in AC result in non-uniform stress distribution which is the cause for different rates of micro crack propagation (Benedetto and Roche 1998, Hasrzyniski 1966, Linder 1977, Bazin and Saunier 1967).

The AASHTO TP-62 dynamic modulus testing procedure requires maintaining strain levels between 50 and 150 micro-strain to meet the small strain requirement of the LVE range. In addition, for stress controlled dynamic modulus testing, the standard recommends conducting tests in stress ranges presented in Table 1. The numbers of cycles for conducting dynamic modulus testing according to AASHTO TP-62 standard are also presented in Table 1. It can be observed from Table 1 that the number of cycles for testing dynamic modulus can be as high as 200 cycles. The assumption that asphalt behaves as a LVE material for small strain levels is not entirely resulting from a pure linear behavior, rather, it is an arbitrary assumption that within this limit even if the asphalt mix shows nonlinearity the change in the dynamic modulus is very small and not significant. If one considers the fact that asphalt mixes actually behave to some extent in a nonlinear fashion, the effect of number of cycles becomes significant enough for further study. Moreover, the stress ranges recommended in AASHTO TP-62 are found to result in strain levels beyond 150 micro-strain by (Mohamed and Zeghal 2007). In a similar study, Osman et al. (2007) also concluded that the AASHTO TP-62 recommended stress ranges are excessive for testing at hotter temperatures and/ or lower frequencies. However, the mixes used for these studies are prepared predominantly using Marshall

352

Mix design methods and only limited samples are prepared using Superpave mix design procedure.

Considering that there is considerable difference in the number of cycles specified by AASHTO TP-62 dynamic modulus testing procedure, and the number of cycles used in previous LVE range studies, and the difference in the materials used for current pavement construction, and the materials used for the LVE range determination, it is thought important to check if the Superpave mixes at hand exhibit the LVE behavior under the AASHTO TP-62 recommended testing conditions. Therefore, the main goal of this study is to verify if the LVE range of a selected mix under the AASHTO TP-62 recommended loading amplitudes and cycles.

Objective

The objectives of this study are to verify whether an asphalt mix remains in the LVE range when dynamic modulus tests are conducted using the AASHTO TP-62 recommended testing stress ranges and number of cycles. In this study, the AASHTO TP-62 recommended stress ranges will be assessed on the conditions of maintaining LVE requirement using stress sweep dynamic modulus testing. The Dynamic modulus data collected from each stress sweep test will be analyzed for LVE range using 5% stiffness reduction principle, proportionality principle and superposition principles. All LVE limits determined using the three methods will be compared with each other for validation of results. The LVE ranges will be determined for the testing stress and recoverable strains. In addition to this, the cumulative permanent strain corresponding to the LVE limits will be identified. Then, stress, recoverable and permanent strains will be compared with the AASHTO TP-62 recommendations. In addition, the relationship between phase angle and LVE limits will be investigated.

Material

SP-III HMA mix is collected from an actual construction site with aim of collecting Superpave HMA mixes that are widely used in the design and construction of roads in the state of New Mexico. The SP-III mix is prepared in the mixing plant and sampling was performed from windrows of an actual pavement construction as per the requirements of AASHTO T-168. The binder grade of PG 70-22 and an aggregate composition with nominal maximum aggregate size of 19 mm is used for the mix. Theoretical maximum gravity test, asphalt content test and sieve analysis test are conducted on the sample collected as per the requirements of AASHTO T-209, T-308 and T-27. The aggregate distribution analysis results are presented in a 0.45 powers Gradation Chart in Fig. 1. Asphalt content test is performed by ignition method and the average asphalt content was found to be 4.5%. Table 2 shows asphalt content test results. The theoretical maximum

353

specific gravity of the mix is determined using mass determination in air method. Three replicate tests were conducted and the results are presented in Table 3.

Sample Fabrication

Specimen compaction is performed using a Gyratory compaction machine. The sample size for compaction is 150 mm in diameter and 170 mm in height. The compaction temperature used to achieve a viscosity of 280±30 centipoise is 155 °C. Several trial gyratory specimens are prepared to achieve a target air void of 4.0±0.5% for the inside core. Compacted samples are cooled off for about 16 hrs to gain strength and using a core drilling machine, a 100 mm diameter sample is cored out of the 150 mm diameter sample. Afterward, the ends of the 100 mm sample are trimmed off using the laboratory diamond edged wet saw to reduce the height of the specimen to 150 mm and a produce smooth and perpendicular surface. The bulk specific gravity of the final 100 mm samples is determined according to the AASHTO T-166 to determine the air voids in the sample. The bulk specific gravity and air voids of all samples utilized in this study are presented in Table 4.

In addition to the desired air void, samples prepared for dynamic modulus need to meet geometry requirements. Geometric parameters mentioned to be checked in the AASHTO TP-62 provisional standard are sample diameter, height, end perpendicularity and waviness. The diameters of each specimen at the middle, top and bottom sections along two axes 90 degrees apart are recorded. The means and standard deviations of the recorded diameters are calculated and compared with the AASHTO TP 62 requirements. The ends of all samples are also checked for perpendicularity and waviness requirements right before testing. Perpendicularity is checked at two perpendicular axes of both top and bottom ends by using the rock flatness gauge and using a straightedge and feeler gauge checks waviness. Then, linear variable differential transducer (LVDT) mounting buttons are glued to the specimen using five minute epoxy. The gauge length is maintained to be 100 mm and the Automatic Positioning Fixture is used to fix LVDT mounting buttons 50 mm away from the mid height of the specimen. In addition, end treatments are used instead of capping between specimen ends and platens.

Test Apparatus

In this study a Servo-Hydraulic testing system (GCTS ATM-025) presented in Fig. 2 is utilized for dynamic modulus testing. The machine is capable of producing controlled haversine compressive loading up to 100 Hz frequency. The top actuator has a dynamic load capacity of 25kN with stock of 100 mm. The system is equipped with an environmental chamber capable of controlling temperature over the range of -30 °C to +150 °C with an accuracy of ±0.5 °C. Spring loaded LVDTs with a range of ± 0.5 mm and resolution of 0.0025 mm are used for measuring specimen deformation.

Test Matrix

354

Dynamic modulus laboratory test is conducted as per the requirements of AASHTO TP62. However; a wider stress range is utilized for testing. As a starting point, the minimum stress amplitude is chosen as half of the standard minimum recommendation that is 175 kPa for testing at 21 ºC. However, this stress level was found too high for 0.1 Hz stress sweep testing which led to further reduction of the initial testing stress to 60 kPa for this particular testing frequency. The stress sweep test is conducted by increasing the maximum peak to peak stress amplitude at 10% increments until the modulus decreased substantially. The stress sweep test is performed only at 21 ºC and six loading frequencies (25, 10, 5, 1, 0.5, 0.1 Hz) with corresponding cycles of 200, 200, 100, 20, 15, and 15. The adopted test matrix is presented in Table 5.

Results and Discussion

The stress sweep test data is first studied to determine the trend of dynamic modulus with increasing stress amplitude. Then, the LVE limit of the AC is determined and verified using the three principles described above. The first principle adopted, as implemented in SHARP -A- 369 project, is to consider AC as LVE material as long as the dynamic modulus does not decrease by more than 5%. The second and third principles are proportionality and superposition principles which are implemented for determining the LVE limit of AC by Mehta and Christensen (2000). Proportionality and superposition principles are applied to check how well the 5% stiffness reduction principle identifies LVE stress limit. Finally, the results are compared with current AASHTO TP-62 recommended strain and stress limits. The trend of phase angle with increasing stress amplitude is also investigated.

Data collection is set up to collect one hundred data points per wave form for the last five cycles of each dynamic modulus test. Time, axial force and axial deformation of the two LVDTs collected for the last five cycles of each stress sweep are used for dynamic modulus determination. Dynamic modulus is determined as the average of the dynamic modulus of the last five cycles. For each cycle the dynamic modulus is determined as the ratio of the maximum stress amplitude to the maximum recoverable strain amplitude. The displacements of each of the LVDTs are divided by the axial gauge length to get the actual axial strain on two sides of the specimen that are 180 degrees apart. The strains are calculated for each displacement data collected and a sine curve is fitted for which the amplitude is determined. Dynamic modulus is determined using the average amplitude of the two strain curves. In a similar fashion time, verses stress curves are determined for the actual stress applied. The actual stress is determined by dividing the 100 axial force data points collected for each cycle by the calculated area of the specimen.

Dynamic modulus , $|E^*|$, trend with increasing amplitude of stress and 5% stiffness loss requirement

In the LVE range, the dynamic modulus is assumed to be independent of stress. This requirement is checked for the AASHTO recommended load rage at test temperature of 21 ℃. For testing at 21 degree centigrade, the AASHTO recommended testing stress range is 350kPa to 700kPa. For this study though, the stress range used has a minimum and maximum bound of 60, 175, 175, 428, 197, 175 kPa and 1075, 605, 817, 2427, 1233, 997 kPa for the testing frequencies of 0.1, 0.5, 5, 10 and 25 Hz respectively. For all testing frequencies, the dynamic modulus showed a steadily decreasing trend.

Fig. 3 presents the normalized dynamic modulus with increasing stress amplitude for the six test frequencies at 21 °C. It can be observed that the dynamic modulus always decreases no matter how small the stress. Moreover, the slope of the normalized dynamic modulus verses stress curve is more or less constant for all testing frequencies. This trend indicates that the dynamic modulus is dependent on stress amplitude even at small stress levels and the softening rate is constant and independent of testing frequency.

Fig. 4 shows the trend of dynamic modulus as the applied stress is gradually increased for the six testing frequencies (0.1, 0.5, 1, 5, 10 and 25 Hz). There are two ordinates for each abscissa in the plots. The abscissa is always dedicated to stress and the ordinates are dedicated to dynamic modulus on the left and recoverable strain on the right. The two horizontal lines indicate 95% and 105% of the initial (reference) dynamic modulus. Each point on the dynamic modulus series represents the dynamic modulus obtained at the applied stress level presented on the horizontal axis. Each point on the (p-p) recoverable series represents the amount of peak recoverable strain measured for the applied stress amplitude.

Fig. 4(a) shows the dynamic modulus stress sweep test results at 0.1 Hz. It can be observed that the dynamic modulus decreases more or less at a constant slope with increasing stress amplitude, and recoverable strain also increases with increased stress. The initial stress for the stress sweep test is 60 kPa and the initial (reference) dynamic modulus at this stress is 2928 MPa. The strain recorded at the initial and final stresses (60 kPa and 1075 kPa) are 20 and 460 micro-strain. Stress sweep test is conducted at an increment of 10% until a maximum stress of 1075 kPa is reached. At this stress the dynamic modulus has decreased to 2334 MPa. The dynamic modulus at this frequency remained within the ±5% band for a stress range between 60 and 155 kPa. Corresponding strain levels for the ±5% band are observed to be 20 and 55 micro-strain. A strain of 50 micro-strain is observed for stress amplitude of 141 kPa and 150 micro-strain is reached at a stress amplitude of 412 kPa. The average slope of the dynamic modulus (softening rate) at this frequency is determined from a linear fit to be -0.6. All in all, it can be concluded that at 0.1 Hz loading frequency the AC experiences softening as the stress increases.

Fig. 4(b) shows the change in the dynamic modulus at a testing frequency of 0.5 Hz. Similar to the 0.1 Hz results, at this frequency also, decreasing and increasing trends for

356

dynamic modulus and recoverable strain are observed as the testing stress is increased. The stress range for the stress sweep test is from 175 kPa to 605 kPa with a 10% increment. Corresponding maximum and minimum dynamic moduli are 6321 and 5386 MPa. Observed peak strains range from 27 to 112 micro-strain. 5% of the dynamic modulus is lost when the strain level reached 69 micro-strain and when the stress was 414 kPa. Stress levels for 50 micro-strain are determined to be 310 kPa and the average softening rate is found to be -2.2.

Fig. 4(c) shows the stress sweep test result at a test frequency of 1 Hz. Here the dynamic modulus shows a constant trend for a stress range between 200 kPa and 400 kPa, however, the recoverable strain shows a continuous increase with increasing stress. The dynamic modulus shows a decreasing trend when the stress is increased beyond 400 kPa but remains within the ±5% range until 550 kPa and 95 micro-strain is reached. The stress sweep range is from 175 to 817 kPa. The maximum dynamic modulus observed at the minimum stress is 6286 MPa and the minimum dynamic modulus at maximum stress is 5501 MPa. The observed strain range is from 27 micro-strain to 148 micro-strain. Stresses corresponding to 50 and 150 micro-strain are approximately 311 and 817 kPa. The average softening rate is determined to be -1.7.

Fig. 4(d) shows the change in dynamic modulus with increasing applied stress at a testing frequency of 5 Hz. At this frequency, also, the dynamic modulus shows a decreasing trend accompanied with an increasing trend of recoverable strain as the applied stress increases. The rate at which the dynamic modulus decreases is determined to be -1.3. The maximum dynamic modulus at this frequency is 8152 MPa and the minimum dynamic modulus is 5782 MPa. The dynamic modulus did not change by more than 5% until the stress and strain reached 772 kPa and 99 micro-strain. The dynamic modulus stress sweep test is performed for a stress range of 428 to 2427 kPa. The maximum and minimum corresponding strains are 52 to 419 micro-strains. Stress at 50 and 150 micro-strains are observed to be approximately 428 and 1120 kPa.

Fig. 4(e) shows the change in dynamic modulus at a test temperature of 21 ℃ and testing frequency of 10 Hz. Similar to the stress sweep test done at 1 Hz, the dynamic modulus shows a constant trend for testing between 200 kPa and 350 kPa. Then, the dynamic modulus decreases with a constant rate of -3.7 as the applied stress is increased at an increment of 10%. The strain, however, shows an increasing trend with increasing stress. The 5% decrease in dynamic modulus is observed at 470 kPa and 36 micro-strain. The stress sweep range is 197 to 1233 kPa and the observed strain range is 14 to 119 micro-strain. Corresponding maximum and minimum dynamic moduli are found to be 13593 and 10301 MPa. Stress corresponding to 50 micro-strain is found to be 629 kPa.

Fig. 4(f) presents the change in the dynamic modulus with at a stress sweep testing frequency of 25 Hz. Here, also, the dynamic modulus decreased, as the testing stress is increased and the recoverable strain increased. The average softening rate at which the

357

dynamic modulus decreased is found to be -1.8. The dynamic modulus reduced to 95% of the initial value at the stress level of 462 kPa and a strain level of 50 micro-strain. The stress sweep range is from 177 to 997 kPa and the resulting strain range is 18 to 119 micro-strain. The maximum and the minimum dynamic moduli observed are 9700 MPa and 8363 MPa.

The stress corresponding to the 95% dynamic modulus values can be extracted and summarized from the normalized dynamic modulus verses the applied stress plot presented in Fig. 3 or from the dynamic modulus trend plots presented in Fig. 4. Accordingly, the stresses and strains (recoverable and cumulative permanent) corresponding to the 95% of initial dynamic modulus are summarized in Table 6. The results indicate that 155, 414, 506, 772, 470, 462 kPa and 55, 69, 84, 99, 36, 50 micro-strain are stress and strains at the boundary of linear and nonlinear viscoelastic response for the mix at 0.1, 0.5, 1.0, 5, 10 and 25 Hz testing frequencies. The corresponding permanent strains are also found to be 253, 667, 737, 1018, 169 and 917 micro-strains. From these results, it can be observed that the LVE limit stress and strains corresponding to the 95% of maximum E^* value is very close to the minimum recommended testing stress and strains in the AASHTO TP-62 standard. In addition, the percentage loss in the dynamic modulus is found to increase beyond the recommended 5% even if the testing load is maintained with in the AASHTO recommended load range. This indicates that the load ranges recommended in the AASHTO test procedure are high and can result in nonlinear viscoelastic response of the AC.

With regards to the softening rate of the dynamic modulus with increasing stress, the limited data collected shows an increasing softening trend with increasing frequency as shown in Fig. 5. As can be seen form the plot, a very weak power fit shows an increasing trend for the softening rate. However, further research is required to determine typical softening rate of asphalt concrete.

Proportionality

The law of proportionality requires a material response to change in equal proportion to an increase of an input (Mehta and Christensen 2000, Schapery 1974). The study here is based on a stress controlled test. In a stress controlled test the input is the stress and the response is the deformation or the strain. Therefore, the proportionality principle is applied by taking the stress as an input and the strain as a response. The proportionality constant for this study is 110% since the stress sweep test was conducted in increments of 10%. This can be represented by Eq. (4) as follows:

$$\varepsilon_2 = R\{c\sigma_1\} = cR\{\sigma_1\} \qquad (4)$$

$$= c\varepsilon_1$$

358

where: c = Constant=1.1; σ = input; R{σ} = response = strain

To determine the validity of the proportionality principle, the strain increments for each stress sweep test are computed and compared with the constant stress increment of 10%. Furthermore, stress sweep test results are divided in to two parts based on the 5% stiffness reduction principle for validation of the LVE limits determined earlier. To access the significance of variation in between the stress and strain increments, the student's t-test is performed. The null hypothesis: stress increment and strain increment are equal and the alternative hypothesis: stress and strain increments are not equal are tested at the significance level of 5% using the t-test.

Fig. 6 shows the applied stress increment factors and experimentally observed strain increments for each 21 ℃ stress sweep tests conducted at the six frequencies (0.1, 0.5, 1, 5, 10 and 25 Hz). There are six plots in Fig. 6 for each frequency. The ordinate on the left side of each plot shows the applied stress increment and the ordinate on the right side shows the observed strain increments for corresponding applied stress increments. Different series are also used for to represent stress and strain data below and above the 95% of the initial (reference) dynamic modulus (E_o^*).

Fig. 6 (a) shows the stress and strain increments at 0.1 Hz. The applied stress increment factor is fixed to 10%, but due to machine compliance there is slight variation. The actual applied increment factors have an average value of 10% with a standard deviation of 1% for the 30 incremental tests performed. The maximum and minimum applied incremental stresses are observed to be 12% and 8%. The resulting incremental strains average to 11% with a standard deviation of 1%. The range for the incremental strains is from 13% to 8%. This indicates a variation between the stress and strain incremental constants. Statistical t-test performed on the entire data confirms the variation as well. However, the proportionality principle is not expected to be valid over the entire stress sweep data. Rather, it is expected to be valid for the part of stress sweep data that is associated with dynamic modulus greater than 95% of E_{ref}^*. Therefore, two separate t-tests are conducted on stress and strain incremental values taking the 95% of E_{ref}^* as a delineator for linear and nonlinear viscoelastic response. The significance level adopted is 95%. The result as presented in Table 7 indicates that the average of incremental stress and incremental strains are equal to each other when the dynamic modulus is greater than 95% of E_{ref}^* and are significantly different when the dynamic modulus has decreased by more than 5%. This confirms that stress and strain incremental values are equal and subsequently the proportionality requirement is satisfied when the 5% stiffness reduction principle is applied to identify the LVE limit.

Fig. 6 (b) shows the proportionality requirement analysis for the dynamic modulus stress sweep test at 21 ℃ and 0.5 Hz. The average value of the stress incremental value is observed to be 10% with a standard deviation of 0%, while strain increments have an average of 11% with a standard deviation of 2%. This indicates variation between stress

359

and strain increments as well. The results of the t-tests conducted for the linear and nonlinear viscoelastic parts are presented in Table 8. The P-value for the data set having dynamic modulus above 95% of E^*_{ref} (LVE part) is found to be 0.13 which indicates that the stress and strain increments are equal at 95% significance level. However, for the data set having dynamic modulus below 95% of E^*_{ref}, the P-value is found to be 0.0002 indicating that the stress and strain increments are not equal. This confirms that the 95% boundary point is indeed a good delineator for linear and nonlinear viscoelastic properties and the proportionality requirement is violated when the AC dynamic modulus has decreased by more than 5% at 5 Hz stress sweep testing as well.

Similarly, Fig. 6 (c) shows the stress sweep test conducted to study LVE properties of the AC at 21 ℃ and 1 Hz. Here the applied stress increments have an average of 10% with a standard deviation of 0% which indicates a very good machine compliance. The strain increments averaged 11% with 1% standard deviation. The range of applied stress increments and resulting strain increments are observed to be in between 10% - 11% and 7% - 13% respectively. Based on the above observation it is clear that there is some variation between the stress and strain increments. The two tailed student's t-test performed to decide the significance of the difference between the stress and strain increments at $\alpha = 0.5$ is presented in Table 9. The p-value for the t-test is found to be 0.38 for a data set having dynamic modulus greater than 95% of the original dynamic modulus which indicates that there is no significant difference between the stress and strain increments. However, the P-value for the stress and strain increments is 0.0 for the part having dynamic modulus less than 95% of the original dynamic modulus, which indicates a significant difference. Here, again the proportionality requirement is found to be satisfied when the dynamic modulus have not decreased by more than 5% and it is violated when the dynamic modulus is below 95% of the initial value. This indicates that the dynamic modulus is behaving nonlinearly after the dynamic modulus is less than 95% of the initial value.

Fig. 6 (d) shows the proportionality test for the stress sweep test results at 21 ℃ and 5 Hz. The average stress and strain increments are found to be 10% and 12% each with a standard deviation of 0% and 2% respectively. The range of stress increments is between 10% to 11% while the range for strains is between 10% to 17%. As can be seen in Table 10, the two tailed t-tests resulted in a P-value of 0.007 and 0.05 for the dynamic modulus above and below 95% of reference E^*. This indicates significant difference between the stress and strain increments in both ranges indicating nonlinear viscoelastic behavior even when the dynamic modulus has not decreased by more than a 5%. This indicates the drawback of 5% stiffness reduction principle at high stress levels. Based on the proportionality principle, here, even if the dynamic modulus did not decrease by more than 5%, the initial testing stress level is high enough to cause a nonlinear response. This indicates that 5% stiffness reduction principle may not be a sufficient indicator of

linearity and needs to be supported with additional methods like the proportionality principle for indicating nonlinear viscoelastic behavior at a higher stress level.

Fig. 6 (e) shows applied stress increments and associated strain increments for the stress sweep test conducted at 21 ºC and 10 Hz. Here, the overall average of the stress increments is found to be 10% ± 1% and the average for strain is found to be 12% ±2%. The maximum and minimum stress increments are 12% and 6% and maximum and minimum of strain increments are 14% and 7%. The t-test conducted for linear and nonlinear viscoelastic responses are presented in Table 11. A P-value of 0.53 is observed for increments associated with the dynamic modulus greater than 95% of reference E^* and P-value 0.0 is found for the data section with less than 95% of the initial dynamic modulus. This indicates the stress and strain increments are equal at the 95% significance level when the dynamic modulus is above 95% and not equal to each other when the dynamic modulus is below 95%. This shows that the AC is behaving as a LVE material when the dynamic modulus is above 95% and it is violating the proportionality requirement when the dynamic modulus is below 95% suggesting nonlinear viscoelastic behavior.

Fig. 6 (f) also shows the for the proportionality requirement for the stress sweep test at 21 ºC and 25 Hz. The results observed are consistent with results at other frequencies. The average for applied stress increments is 10% ± 1% and the average resulting strain increment is found to be 11% ± 2%. The range for the stress increments is 8% to 12% while the range for strain increments is 6% to 13%. Since the dynamic modulus is found to decrease below 95% of the initial value, two separate t-tests are conducted for the two classes as presented in Table 12. The P-value for the stress and strain increments associated with dynamic modulus greater that 95% of E^*_{ref} is 0.46 indicating that the average stress increments are equal to the average strain increments. The P-value associated to the stress and strain increments having dynamic modulus below 95% of of E^*_{ref} is 0.006. This indicates that there is a significant difference between the stress and strain increments at a 95% significance level. In other words, the proportionality requirement is satisfied for the stress sweep test having dynamic modulus above 95% of the initial value and it is not satisfied when the dynamic modulus is reduced by more than 5% suggesting linear and nonlinear viscoelastic behaviors respectively.

In general, the proportionality requirement is found to be valid when the dynamic modulus is kept above 95% of the initial dynamic modulus and it is found to be not satisfied when the dynamic modulus decreases by more than 5%. This indicates that the 95% percent requirement is a good indicator of LVE behavior.

Superposition

The validly of the LVE range determined as the region having dynamic modulus greater than 95% of the initial stiffness is also checked by applying the superposition principle.

361

The law of superposition is satisfied when the response for two independent inputs applied at different times is equal to the sum of the responses obtained when the inputs are applied separately. As mentioned before, this study is based on a stress controlled test. Therefore, stress is the input and the resulting strain is considered as a response. The superposition principle as applied to this specific situation can be represented by Eq. (5) as follows:

$$\varepsilon_c = R\{\sigma_a + \sigma_b\} = R\{\sigma_a\} + R\{\sigma_b\} = \varepsilon_a + \varepsilon_b \qquad (5)$$

where: σ_a, σ_b = Different input stresses; $R\{\sigma_i\}$ = strain response $= \varepsilon_i$

The stress sweep dynamic modulus test data collected with 10% stress increments is used for superposition analysis as well. Superposition principle is applied by determining the stress and strain relationship. The strain-stress relationship is observed to have two different trends when the dynamic modulus is greater than and less than 95% of the initial value. Two different linear fits are developed for the two observed trends. These trend fits are used to perform the superposition analysis. To avoid the problem of extrapolation, all analysis is performed within the range of the test data collected. Fig. 7 presents superposition analysis results based on the trend observed for the stress sweep test conducted at 21 ˚C and six frequencies (0.1, 0.5, 1, 5, 10, 25 Hz).

Fig. 7 (a), (b) and (c) show a graphical representation of the superposition analysis performed on the stress sweep test data conducted at 25, 10 and 5 Hz. The plots have two horizontal axes and two vertical axes. Both vertical axes are observed strains responses and both horizontal axes are applied stress amplitudes; however, the ranges are different. The ordinates on the left labeled as "stress in LVE range" are showing the strain data that has dynamic modulus above 95% of the initial value and the second ordinate on the right labeled "stress above LVE range" is showing part of the strain values that are associated with the dynamic modulus less than 95% of the reference value. The stress axes are also designated as in LVE range and above LVE range considering whether the dynamic modulus is above 95% of the initial value or not. There are basically two strain series presented in the plots. Series labeled as "$\varepsilon\{\sigma_1\} + \varepsilon\{\sigma_2\}$" presents the sum of strain values found by applying two different stresses at different times and the series labeled as "$\varepsilon\{\sigma_1 + \sigma_2\}$" gives the strain values found by applying the sum of the stresses at once. The superposition principle is valid if these strains are equal and not valid if there are significant differences between the two strain series.

From Fig. 7 (a) it is possible to observe that the sum of the output strains computed for two different stress levels separately and the strain computed for the sum of the two independent stresses are overlapping with each other when the dynamic modulus is above 95% of the initial dynamic modulus and the strains show very wide difference when the dynamic modulus is less than 95% of the initial dynamic modulus. This is a consistent

362

result with analysis found using the proportionality principle and it is a confirmation of the accuracy of the 95% limit for the LVE range. Fig. 7 (b) and (c) also show similar superposition analysis on the stress sweep test data at 10 and 5Hz. The results indicate that the superposition principle is valid for the stress and strain amplitudes resulting in dynamic modulus reduction less than 5% as the strains resulting from two independent stresses and the strain resulting from the sum of the two stresses are overlapping within the this region. On the other hand when the dynamic modulus is less than 95% of the reference dynamic modulus, the strains are distinctively different. This confirms the LVE region for the 10 Hz and 5 Hz stress sweep tests.

Fig. 7 (d), (e) and (f) also show superposition analysis at 1, 0.5 and 0.1 Hz. The plots are showing the superposition analysis performed with an emphasis on the point at which the strain trends start to deviate. It can be observed from theses plots that the point at which the superposition principle fails to be valid have similar stress and strain values at which the dynamic modulus decreases by 5%. Moreover, it can be observed that the differences between the strains keep increasing as the input stress are increased beyond the LVE limit. These results also confirm the validity of the 5% dynamic modulus reduction limit for delineating the linear and nonlinear viscoelastic regions.

Overall, for the stress sweep tests conducted at six different frequencies (0.1, 0.5, 1, 5, 10 and 25 Hz), the superposition principle is found to give overlapping/equal strain outputs for stresses resulting in dynamic modulus above 95% of the reference dynamic modulus and it is found to confirm the nonlinear viscoelastic response when the dynamic modulus decreases by more than 5%. This is consistent with the results found from the proportionality principle analysis and it also indicates that the 95% requirement is a good indicator of the LVE behavior limit.

Recommended Testing Stresses of AASHTO TP-62 Test Standard

The AASHTO TP-62 recommends different stress levels for different temperatures as shown in Table 1. The recommended testing stress range at 21 °C is from 350 kPa to 700 kPa. This study focuses on evaluation of the stress range specified in the AASHTO TP-62 requirement on the criteria of LVE behavior. The study is based on the stress sweep test over a wide range. The LVE range is determined using three principles for a stress range that is wider than specified in the AASHTO- TP 62 dynamic modulus test standard. For all stress sweep tests, the numbers of cycles as specified in the AASHTO TP-62 are applied.

The maximum stresses that can be applied to maintain the AC response as a LVE material are determined to be 155, 414, 506, 772, 470, 462 kPa for stress sweep testing at 0.1, 0.5, 1, 5, 10 and 25 Hz with respective testing cycles of 200, 200, 100, 20, 15, 15. A comparison of these results with the AASHTO TP 62 recommended dynamic modulus

363

testing stresses is presented in Fig. 8 (a). It can be observed from the plot that LVE stress limits are within the AASHTO specified stress range (350-700 kPa) except for the 155 kPa observed for 0.1 Hz testing and 772 kPa observed for 5 Hz testing. However, it is important to note that even if the observed results are within the specified testing stresses, the LVE limits determined in this study are mostly below half of the range specified. This indicates there is more than a 50% chance to assume LVE response while in fact the dynamic modulus testing results in nonlinear viscoelastic behavior.

Recoverable Stain limits of AASHTO TP-62 Test Standard

In addition to the stress range recommendation, the AASHTO TP-62 test standard requires dynamic modulus tests to be conducted at recoverable strain levels between 50 and 150 micro-strains. Under this strain limit ACs is assumed to behave as a LVE material. This range is set considering previous research studies conducted to determine the LVE range of AC. However, the number of studies conducted using dynamic modulus testing is limited. Moreover, the studies conducted using dynamic modulus typically use thirty cycles to conduct the strain amplitude sweep test which is considerably lower than the number of cycles specified in the AASHTO TP-62 standard. Other studies which are based on creep and relaxation tests are also available, but these testing methods do not consider the dynamic loading nature of dynamic modulus test.

The limit for the LVE range is determined using 5% reduction principle, proportion principle and superposition principle and the maximum strains are determined to be 55, 69, 84, 99, 36, 50 micro-strain for stress sweep testing at 0.1, 0.5, 1, 5, 10 and 25 Hz with respective testing cycles of 200, 200, 100, 20, 15, 15 at 21 °C. A comparison of these results with the AASHTO specified strain range is presented in Fig. 8 (b). It can be observed that maximum strain limits for the LVE range are within the AASHTO specified range except for the 36 micro-strain found at 10 Hz. However, dynamic modulus tests that result in strain levels above these LVE limits produce a nonlinear response. For this specific study, all of the LVE limits are found to be less than 100 micro-strain which is the median of the AASHTO TP-62 specified range. This indicates that there is more than 50% chance for the test to be in nonlinear range if the test is conducted following AASHTO specification only.

Permanent Strain and LVE Range

The LVE range analysis methods (5% stiffness reduction, proportionality and superposition principles) do not consider permanent accumulated strain on the sample. However, there is a critical amount of cumulative permanent strain under which AC is expected to behave as a LVE material. This cumulative permanent strain is specified as 1500 micro-strain in AASHTO TP-62 specification.

364

Fig. 9 shows the increasing trend of cumulative permanent strains at the end of each stress cycle for stress sweep test at 21 °C and six frequencies. Permanent strain corresponding to 95% of the reference dynamic modulus is found to be 253, 667, 737, 1018, 170 and 917 micro-strain for stress sweep testes conducted at 0.1, 0.5, 1, 5, 10 and 25 Hz. In all frequency cases the cumulative permanent strain at the LVE limit is found to be below 1500 micro-strain. A comparison of the AASHTO specification for permanent strain limit and the maximum cumulative strains at the LVE limits determined in this study is presented in Fig. 8 (c). It can be observed from Fig. 8 (c) that the cumulative permanent strains are much lower than the AASHTO specification. This again indicates that the AASHTO specification for permanent strain is too high and may allow for nonlinear response of AC.

Phase Angle and LVE Range

In addition to the stress and strain relationship, the phase-angle is another important material property for viscoelastic materials. The change in phase angle with increasing stress is shown in Fig. 10. It can be observed that the phase angle is not varying significantly with increasing amplitude of stress for all testing frequencies at 21 °C. The range of the phase angles are determined to be 1.4, 2.4, 1.3, 1.2, 1.4 and 3.4 for the entire stress sweep tests at the frequency of 25, 10, 5, 1, 0.5, 0.1 Hz respectively. This indicates that there is no relationship between the LVE and the phase angle. In addition, it indicates that even if the material behavior changes from linear to nonlinear viscoelastic the viscosity of the material does not change. Therefore, stress does not have significant effect on viscosity of AC.

Conclusions

In this study, the LVE limit for a typical 19 mm New Mexico mix at 21 ºC is determined. Three well-known principles (5% stiffness reduction principle, proportionality principle and superposition principle) are used to determine counter check and confirm the LVE limits of the mix. Then, the stress and strain limits specified in the AASHTO TP-62 testing standard for LVE property are compared with the results found from this study. The effect of stress sweep on the phase angle is also investigated.

Based on this study, the following conclusions and recommendations can be made on the LVE limits of the asphalt mix studied:

- LVE limits determined using 5% stiffness reduction principle, proportionality principle and superposition principle are found to be consistent and supportive with each other. Therefore, taking the minimum limit of the LVE range as

365

95% E^*_{ref} is found to be a good method to determine the LVE range of AC. However, caution is required for at high stresses.

- The stress LVE limits for the mix are determined to be 155, 414, 506, 772, 470, 462 kPa at 0.1, 0.5, 1.0, 5, 10, 25 Hz respectively.

- The recoverable strain LVE limits of the mix are determined to be 55, 69, 84, 99, 36, 50 micro-strain 0.1, 0.5, 1.0, 5, 10, 25 Hz respectively.

- The permanent strain LVE limits for the mix are determined to be 253, 667, 737, 1018, 169, 917 micro-strain at 0.1, 0.5, 1.0, 5, 10 and 25 Hz respectively.

- Comparison of AASHTO TP-62 recommended stress and strain ranges with LVE limits determined the mix indicates that the AASHTO recommended stress and strain levels are too high and may result in a nonlinear viscoelastic response.

- The maximum cumulative permanent strain recommended in the AASHTO TP-62 is found to be very high compared with the values corresponding to 95% E^*_{ref} found in this research.

- Observation on the trend of the phase angle with increasing stress indicates that the phase angle is not significantly affected with increasing stress.

Reference

AASHTO Standard T 27 (2011). "Standard Method of Test for Sieve Analysis of Fine and Coarse Aggregate." American Association of State Highway and Transportation Officials, Washington, DC 20001, www.transportation.org

AASHTO Standard T 166 (2011). "Standard Method of Test for Bulk Specific Gravity (Gmb) of Compacted Hot Mix Asphalt (HMA) Using Saturated Surface-Dry Specimens." American Association of State Highway and Transportation Officials, Washington, DC 20001, www.transportation.org

AASHTO Standard T 168 (2011). "Standard Method of Test for Sampling Bituminous Paving Mixtures." American Association of State Highway and Transportation Officials, Washington, DC 20001, www.transportation.org

AASHTO Standard T 209 (2011). "Standard Method of Test for Theoretical Maximum Specific Gravity (Gmm) and Density of Hot Mix Asphalt (HMA)." American Association of State Highway and Transportation Officials, Washington, DC 20001, www.transportation.org

AASHTO Standard T 308 (2011). "Standard Method of Test for Determining the Asphalt Binder Content of Hot Mix Asphalt (HMA) by the Ignition Method." American Association of State Highway and Transportation Officials, Washington, DC 20001, www.transportation.org

AASHTO Standard TP 62 (2011). "Standard Method of Test for Determining Dynamic Modulus of Hot Mix Asphalt (HMA)." American Association of State Highway and Transportation Officials, Washington, DC 20001, www.transportation.org

Airey, G., Rahimzadeh, B, and Collop, A. (2003). "Viscoelastic linearity limits for bituminous materials." *Materials and Structures*, 36(December), 643–647.

Airey, G., Rahimzadeh, Behzad, and Collop, A. (2004). "Linear rheological behavior of bituminous paving materials." *Materials in Civil Engineering*, (June), 212–220.

Anderson, D., Christensen, D., and Bahia, H. (1994). *Binder Characterization and Evaluation. Volume 3: Physical Characterization*.

Bazin, P., and Saunier, J. B. (1967). "Deformibility, fatigue and healing properties of asphalt mixes." *Proceeding of the second Internationla Conference on the structural Design of Asphalt pavements*, Ann Arbour, MI.

Benedetto, H. di, and Roche, C. de la. (1998). "State of the Art on Stiffness Modulus and fatgue of Bituminous Mixtures." *Bitumionus Binders and Mixes; State of the art and interlaboratory tests on Mechanical Behaviour and Mix design; Report of RILEM Technical Committee 152-PBM; Performance of Bituminous Materials*, L. Franken, ed., E & Fn Spon, Brussels, 137–180.

DoubBaneh E. (1995). "Comportmentmecanique des enrobes bitumineux des petites aux grandes deformations." Institut National des Sciences Appliquees de Lyon, ENTPE.

Gardner, L. J., and Skok, E. L. (1967). "Use of Viscoelastic Concepts to Evaluate Laboratory Test results and Field Performance of Some Minnesota Asphalt Mixtures." *2nd Int. Conf. Structural Design of Asphalt Pavements, Session IV*, Ann Arbor, MI.

Hasrzyniski F. (1966). "Etude de la rheologie d'un bitume modeifie par des polymeres et prevision du comportement mecanique des melanges avec fines, sables et graviers." Universite de ParisNord.

Linder R. (1977). "Application de l'essi de traction directe aux enrobes bitumineux." *Bulletin de Liason des laboratories des ponts et Chaussees*, No Special, 225–274.

Mehta, Y., and Christensen, D. (2000). "Determination of the Linear Viscoelastic Limits of Asphalt Concrete at Low and Intermediate Temperatures." *... of Asphalt Paving Technologists Proc*.

Mohamed, E. Hussein H., and Zeghal, M. (2007). "Testing technique to maintain asphalt concrete within the visco-elastic response." 1–6.

Osman, A., Adam, Y., Zeghal, M., and Maadani, O. (2007). "Control over strain in the dynamic modulus test." 1–25.

Pell, P. S. (1962). "Discussion." *Int. Conf. Structural Design of Asphalt Pavements, Session IV*, Ann Arbor, MI.

Pell, P. S., and Taylor, I. F. (1969). "Asphaltic road materials in fagiue." *Assoc. Asphalt Paving Technol.*, 38.

Sayegh, G. (1967). "Determination of the viscoelastic properties of bituminous concrete by longitudinal vibrations." *British Rheology Society Conf.*, London.

Schapery, R. A. (1974). "Viscoealstic Behavior and Analysis of Composite Materials." *Mechanics of Composite Materials*, 2(Sedeckyj), 86–168.

Taylor, I. F. (1968). "Asphaltic road materials in fatigue." Univ. of Nottingham.

List of Tables and Figures

Fig. 29. Cumulative Permanent strain and $|E^*|$ trend for stress sweep test (SST)

Fig. 10. Phase angle and $|E^*|$ trend for stress sweep test (SST)

Table 3. AASHTO Recommended Stress Ranges, Frequencies and Number of Cycles

Stress Depending on Temperatures	
Temperature	Recommended Stress Range
(ºC)	(kPa)
-10	1400-2800
4	700-1400
21	350-700
37	140-250
54	35-70
Number of Cycles Depending on Test Frequencies	
Frequency	Recommended Cycles
(Hz)	(No)
25	200
10	200
5	100
1	20
0.5	15
0.1	15

371

Table 4. Asphalt Content Test Results

Core No.	Sample wt. (gm)	Wt. loss (gm)	Percent Loss (%)	Calibrated Asphalt Content (%)	Average AC (%)
1	1306	75.3	5.77	4.44	4.5
2	1423	85	5.97	4.67	
3	1329	75.6	5.69	4.36	

Table 5. Theoretical Maximum Specific Gravity Test,(G_{mm})

Specimen No.	Wt. of Sample in air (gm)	Wt. of Flask with water (gm)	Wt. of flask with water and Sample (gm)	G_{mm}	Average G_{mm}
1	2577.9	5513.2	7026.1	2.421	2.417
2	3007.2	5508.1	7268.4	2.412	
3	2943.4	5508.1	7232.6	2.415	

Table 6. Bulk Specific Gravity Test, (G_{mb})

Specimen No	Wt. of Sample in air (gm)	Wt. of Sample in water (gm)	Wt. Surface Dry (gm)	Bulk Specific Gravity (G_{mb})	Air Void (%)
1	2825.4	1617	2830.7	2.328	3.7
2	2779.2	1581.5	2783.4	2.312	4.3
3	2779.6	1582	2783.7	2.313	4.3
4	2814.7	1606.4	2820.4	2.319	4.1
5	2816.5	1605.3	2821.2	2.316	4.2
6	2719.1	1540.7	2724.4	2.297	5.0

Table 7. Test Matrix

Test Parameters	values
Temperature (°C)	21
Stress (kPa)	60 – 1400 @ 10% increment
Frequency (Hz)	25, 10, 5, 1, 0.5, 0.1
Cycles (No)	200, 200, 100, 20, 15, 15

375

Table 8. Stress and Strain at 95% of $|E^*|_{ref}$ for 21ºC

Temperature (ºC)	Frequency (Hz)	Stress at 95% of maximum dynamic modulus $|E^*|_{ref}$ (kPa)	Recoverable Strain at 95% of maximum dynamic modulus $|E^*|_{ref}$ ($\mu\varepsilon$)	Cumulative Permanent Strain at 95% of maximum dynamic modulus $|E^*|_{ref}$ ($\mu\varepsilon$)
21	0.1	155	55	253
21	0.5	414	69	667
21	1	506	84	737
21	5	772	99	1018
21	10	470	36	170
21	25	462	50	917
AASHTO TP-62 Recommended testing limits		350-700	100-150	Max of 1500

Table 9. t-Test: Two-Sample Assuming Unequal Variances for Stress Sweep Test at 0.1 Hz

	Stress increment for $E_n^*>95\%E_o^*$	Strain increment for $E_n^*>95\%E_o^*$	Stress increment for $E_n^*<95\%E_o^*$	Strain increment for $E_n^*<95\%E_o^*$
Mean	1.100363	1.105593	1.101407	1.112264
Variance	6.19E-05	7.25E-05	3.81E-05	8.6E-05
Observations	12	12	18	18
Hypothesized Mean Difference	0		0	
df	22		30	
t Stat	-1.56236		-4.13442	
P(T<=t) one-tail	0.066238		0.000132	
t Critical one-tail	1.717144		1.697261	
P(T<=t) two-tail	0.132475		0.000264	
t Critical two-tail	2.073873		2.042272	

Table 10. t-Test: Two-Sample Assuming Unequal Variances for Stress Sweep Test at 0.5 Hz

	Stress increment for $E_n^*>95\%E_o^*$	*Strain increment for $E_n^*>95\%E_o^*$*	*Stress increment for $E_n^*<95\%E_o^*$*	*Strain increment for $E_n^*<95\%E_o^*$*
Mean	1.099958	1.104944	1.100387	1.128123
Variance	1.3E-05	0.000117	4.35E-06	7.51E-05
Observations	8	8	5	5
Hypothesized Mean Difference	0		0	
df	9		4	
t Stat	-1.23655		-6.95856	
P(T<=t) one-tail	0.123775		0.001121	
t Critical one-tail	1.833113		2.131847	
P(T<=t) two-tail	0.247551		0.002241	
t Critical two-tail	2.262157		2.776445	

378

Table 11. t-Test: Two-Sample Assuming Unequal Variances for Stress Sweep Test at 1 Hz

	Stress increment for $E_n^*>95\%E_o^*$	*Strain increment for $E_n^*>95\%E_o^*$*	*Stress increment for $E_n^*<95\%E_o^*$*	*Strain increment for $E_n^*<95\%E_o^*$*
Mean	1.101341	1.105773	1.100563	1.12057
Variance	1.61E-05	0.000242	4.44E-06	2.77E-06
Observations	11	11	5	5
Hypothesized Mean Difference	0		0	
df	11		8	
t Stat	-0.91437		-16.6647	
P(T<=t) one-tail	0.190064		8.5E-08	
t Critical one-tail	1.795885		1.859548	
P(T<=t) two-tail	0.380127		1.7E-07	
t Critical two-tail	2.200985		2.306004	

379

Table 12. t-Test: Two-Sample Assuming Unequal Variances for Stress Sweep Test at 5 Hz

	Stress increment for $E_n^*>95\%E_o^*$	Strain increment for $E_n^*>95\%E_o^*$	Stress increment for $E_n^*<95\%E_o^*$	Strain increment for $E_n^*<95\%E_o^*$
Mean	1.103307	1.112448	1.099711	1.127614
Variance	5.47E-06	3.18E-05	4.87E-06	0.000403
Observations	6	6	9	8
Hypothesized Mean Difference	0		0	
df	7		7	
t Stat	-3.66875		-3.90886	
P(T<=t) one-tail	0.003989		0.002916	
t Critical one-tail	1.894579		1.894579	
P(T<=t) two-tail	0.007977		0.005832	
t Critical two-tail	2.364624		2.364624	

380

Table 13. t-Test: Two-Sample Assuming Unequal Variances for Stress Sweep Test at 10 Hz

	Stress increment for $E_n^*>95\%E_o^*$	Strain increment for $E_n^*>95\%E_o^*$	Stress increment for $E_n^*<95\%E_o^*$	Strain increment for $E_n^*<95\%E_o^*$
Mean	1.101552	1.107327	1.101257	1.126874
Variance	0.000285	0.00047	1.34E-05	3.75E-05
Observations	9	9	10	10
Hypothesized Mean Difference	0		0	
df	15		15	
t Stat	-0.63035		-11.3539	
P(T<=t) one-tail	0.268976		4.59E-09	
t Critical one-tail	1.75305		1.75305	
P(T<=t) two-tail	0.537952		9.17E-09	
t Critical two-tail	2.13145		2.13145	

Table 14. t-Test: Two-Sample Assuming Unequal Variances for Stress Sweep Test at 25 Hz

	Stress increment for $E_n^*>95\%E_o^*$	*Strain increment for $E_n^*>95\%E_o^*$*	*Stress increment for $E_n^*<95\%E_o^*$*	*Strain increment for $E_n^*<95\%E_o^*$*
Mean	1.100763	1.106769	1.100927	1.114389
Variance	0.000168	0.000461	1.17E-05	9.87E-05
Observations	10	10	8	8
Hypothesized Mean Difference	0		0	
df	15		9	
t Stat	-0.75782		-3.6253	
P(T<=t) one-tail	0.23015		0.002763	
t Critical one-tail	1.75305		1.833113	
P(T<=t) two-tail	0.4603		0.005526	
t Critical two-tail	2.13145		2.262157	
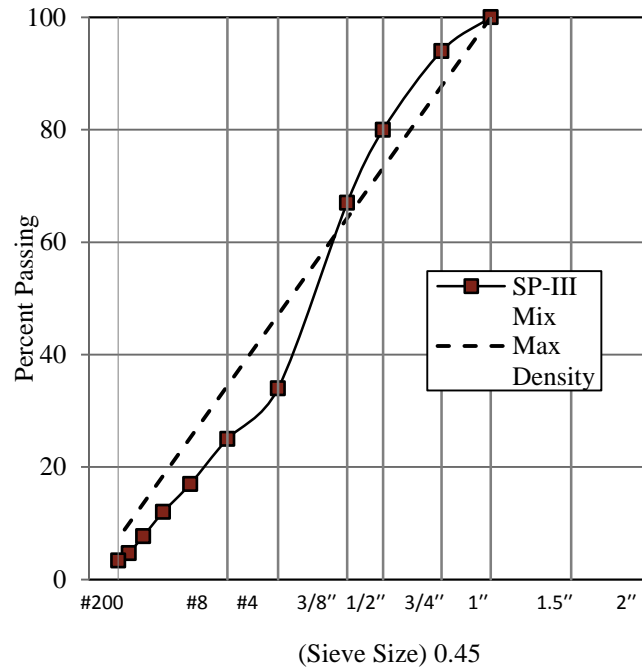
Fig. 1. 0.45 Power Aggregate Gradation Curve for SP-III Asphalt Mix

383
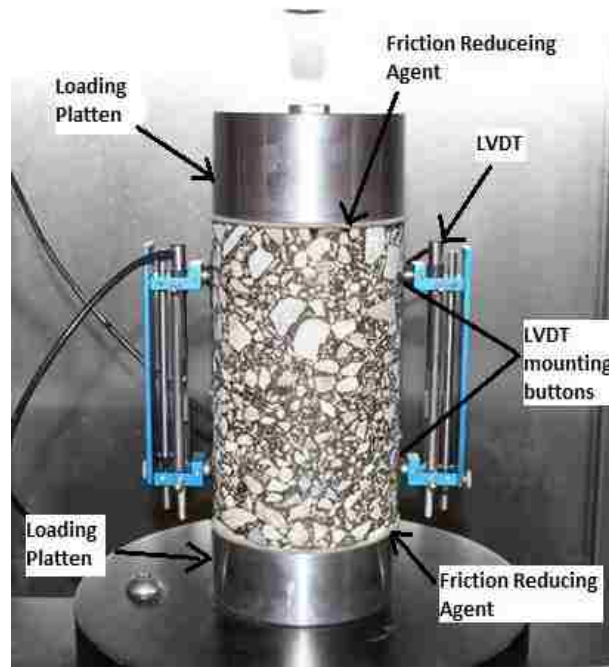
Fig. 2. Dynamic Modulus Test Specimen Set Up
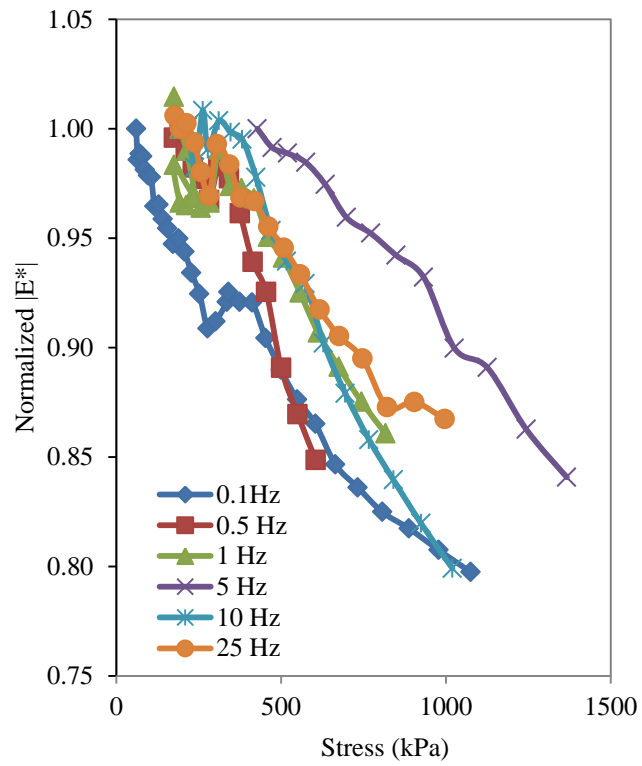
Fig. 3. Normalized Dynamic Modulus for Stress Sweep test at 21 °C
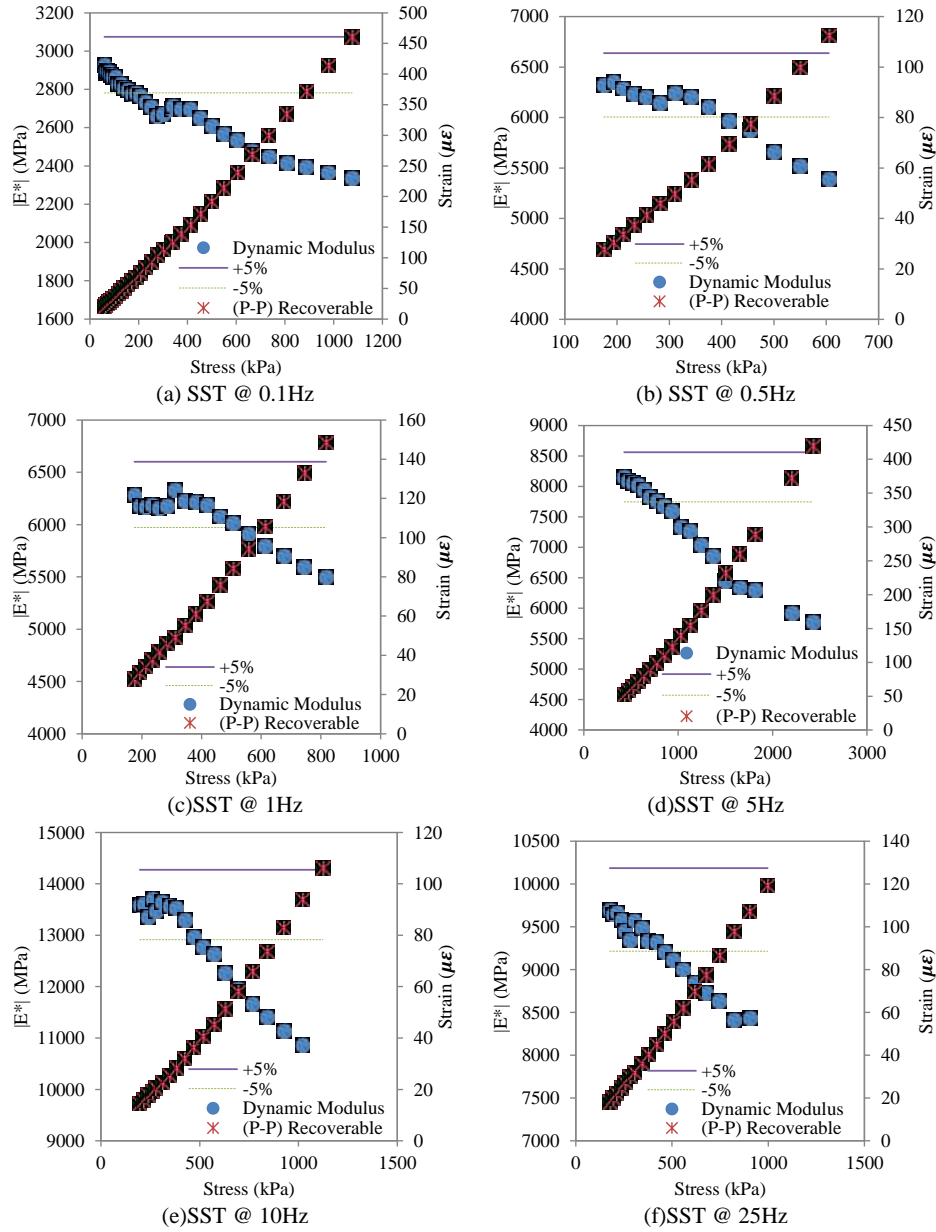
Fig. 4. 5% stiffness loss requirement analysis for stress sweep test (SST)

386
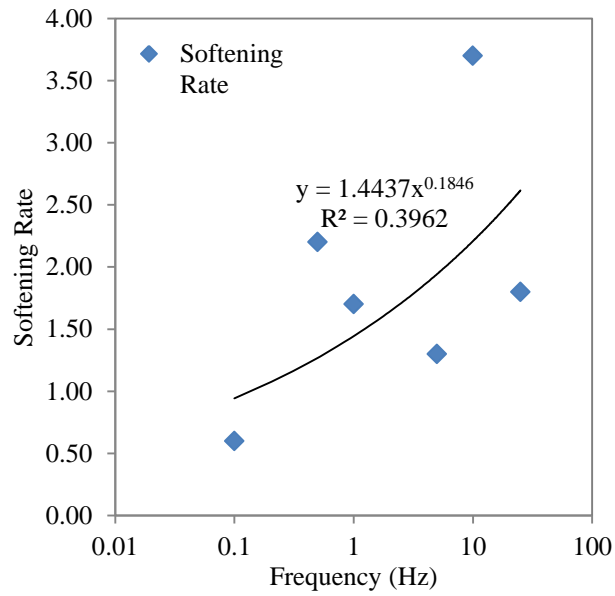
Fig. 5. Softening Rate Trend with testing Test Frequency

(a) SST @ 0.1 Hz

(b) SST @ 0.5 Hz

(c) SST @ 1.0 Hz

(d) SST @ 5Hz
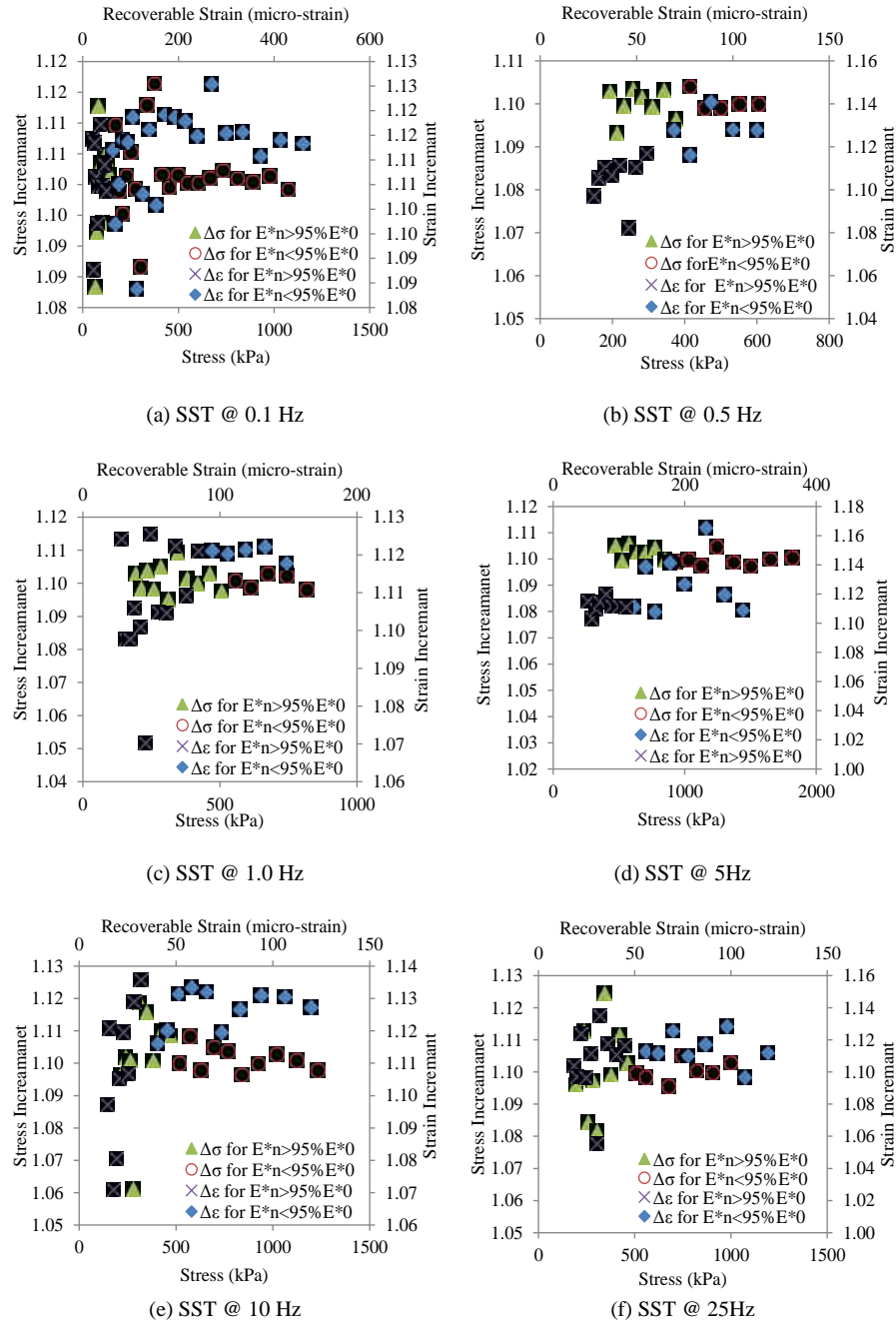
(e) SST @ 10 Hz

(f) SST @ 25Hz

Fig. 6. Proportionality Requirement analysis for stress sweep test (SST)
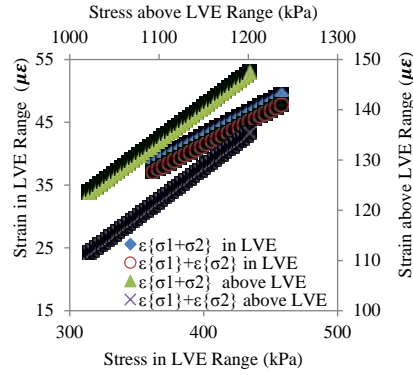
Fig. 7. Superposition Requirement analysis for stress sweep test (SST)

ال_ازة للاستشارات

(a)

(b)

(c)

Fig. 8. Stress and strain at 95% of $|E^*|_{ref}$

390

(a)SST @ 25Hz

(b)SST @ 10Hz

(c)SST @ 5Hz

(d) SST @ 1Hz

(e)SST @ 10Hz

(f)SST @ 25Hz

Fig. 9. Cumulative Permanent strain and $|\mathbf{E}^*|$ trend for stress sweep test (SST)

(a) SST @ 25Hz

(b) SST @ 10Hz

(c) SST @ 5Hz

(d) SST @ 1Hz

(e)SST @ 10Hz

(f)SST @ 25Hz
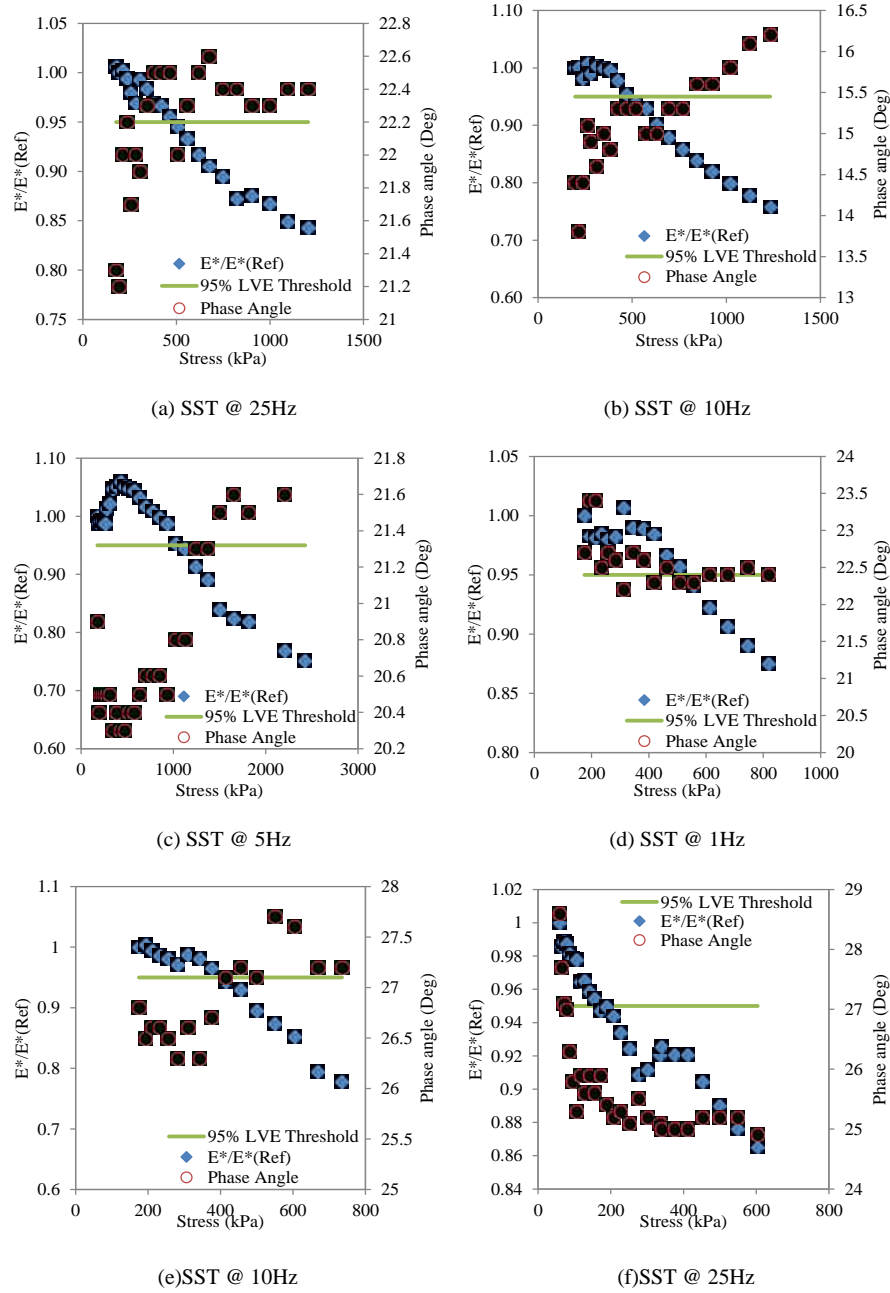
Fig. 10. Phase angle and $|E^*|$ trend for stress sweep test (SST)

APPENDIX I

Characterization of Asphalt Mastic and Aggregate Phases for Moisture Damage

Characterization of Asphalt Mastic and Aggregate Phases for Moisture Damage

Name: Faisal, Hasan M.
Affiliation: Graduate Research Assistant
                Civil Engineering Department
                The University of New Mexico
Address: MSC01-1070
                Albuquerque, New Mexico, NM 87131-0001
Telephone: (505) 730-1793
Fax: (505) 277-1988
E-mail: hfaisal@unm.edu

Name: Tarefder, Rafiqul A.
Affiliation: Associate Professor
                Civil Engineering Department
                The University of New Mexico
Address: MSC01-1070
                Albuquerque, New Mexico, NM 87131-0001
Telephone: (505) 277-6083
Fax: (505) 277-1988
E-mail: tarefder@unm.edu

Name: Weldegiorgis, Mekdim T.
Affiliation: Graduate Research Assistant
                Civil Engineering Department
                The University of New Mexico
Address: MSC01-1070
                Albuquerque, New Mexico, NM 87131-0001
Telephone: (505) 515-6879
Fax: (505) 277-1988
E-mail: mteshome@unm.edu

Total Number of Words: 3856 + (15 x 250) = 7606

Submission Date: August 1st 2013

ABSTRACT

Traditional microscale testing cannot be performed on asphalt binder, mastic or aggregate while they are an integral part of asphalt concrete (AC). A recently developed nanoindentation test has created an opportunity to characterize mastic and asphalt binder while they reside in AC. In the study, laboratory nanoindentation testing is carried out to characterize moisture-induced damage in different phases of AC. A Moisture Induced Sensitivity Testing (MIST) device is utilized for moisture conditioning of AC. In the MIST device, an AC sample is fully submerged under water and all around cyclic pressure is applied through the pore walls inside the AC sample. In this study, a Berkovich nanoindenter is used with an extended dwell time of 200 seconds and fast unloading rate of 0.02 mN/sec. to minimize viscous effect of asphalt on test results. Hundreds of indentations are done on each moisture damage conditioned and unconditioned sample to cover mastic, aggregate and matrix of AC. Indentation load-displacement curve is analyzed by Oliver-Pharr method to obtain elastic modulus and hardness. While comparing wet and dry samples indentation test results, it is seen that modulus and hardness of aggregate phase reduces significantly due to water action. Modulus of the wet mastic reduces to 60% of dry mastic modulus. Overall moisture conditioning reduces modulus of AC by 70%. In addition, the creep response of mastic phase is modeled by a viscoelastic Burger model. The creep compliance value of wet mastic is 42% higher than that of dry mastic.

395

INTRODUCTION

Asphalt concrete (AC) is created by mixing asphalt binder with aggregate. Aggregate can be divided into two classes: coarse aggregate and fines. Coarse aggregate is defined as aggregate materials that are retained on a #200 sieve (75 microns). In hot mix asphalt (HMA), asphalt binder creates a coating or film around the coarse aggregate. Fines are defined as aggregate materials that pass through a #200 sieve. Fines are believed to be trapped inside an asphalt film or mixed with asphalt binder, creating a composite material called mastic, whereas matrix is defined as the mixture of asphalt binder and fine aggregates retained on a #200 sieve. Thus, AC can be defined by four constituents: asphalt film binder, mastic, matrix and coarse aggregate (Figure 1).

All these phases play major roles in governing moisture-induced damage performance of AC. Researchers have performed various tests on mastic and asphalt binder at microscale to understand the macroscale behavior of AC (*1-9*). However, test methods developed and performed on mastic and binders, to this day, are mostly rheological tests. Very few studies have been conducted on the compression stiffness and hardness of mastic and binder, rather than shear stiffness (*10-15*). The existing tests used in the asphalt area cannot be performed on mastic and matrix while they are an integral part of AC. Rather; the tests developed by Superpave effort are performed on the bulk asphalt binder and mastic separately. Nanoindentation has created an opportunity to characterize mastic and asphalt binder while they are parts of AC.
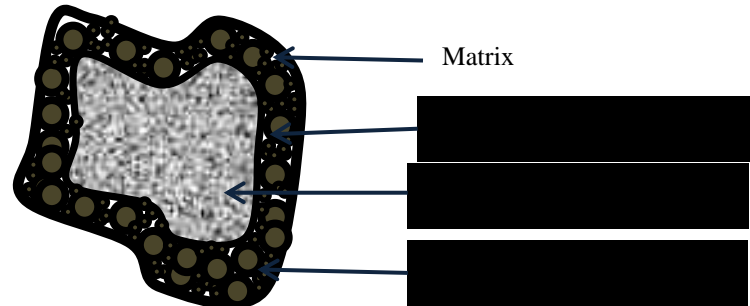

FIGURE 1 Asphalt constituents in asphalt concrete (AC).

To date, numerous test methods have been developed and used to predict moisture damage in AC (*1, 16, 17, 18*). In the last two decades, there have been significant improvements in moisture damage test methods and understanding the micro-to-macro scale behavior of AC. There exists evidence that moisture damage in AC is caused by primarily two mechanisms: loss of adhesion and loss of cohesion. Loss of adhesion breaks and weakens the asphalt-aggregate or mastic-aggregate interface. Loss of cohesion is the softening of mastic and asphalt binder. Of course, the aggregate itself can be softened due to moisture action. Therefore, it is evident that moisture damage in AC is a phenomena that is affected by the moisture interaction at different phases of AC. A

396

fundamental study to characterize stiffness and hardness of different phases of AC before and after moisture conditioning, such as this, can be useful for understanding moisture-induced damage is AC.

In a nanoindentation test, a sharp indenter is loaded to indent an asphalt sample surface and the displacement of the indenter is measured as a function of the load. Load, displacement and time data are recorded when the indenter indents and retracts. Modulus of elasticity (E), hardness (H), and brittleness of a material are determined from the load-displacement data. Though the properties of hard materials such as metals and polymeric composites are commonly determined by nanoindenter, mastic, aggregate or asphalt binder (film) have not tested because they are soft. This study takes the challenge of indenting soft, viscous materials such as the different phases of AC subjected to wet conditioning.

The introduction of nanoindentation in the field of asphalt researchers is rather limited (*10-15*). Asphalt is known to be a viscoelastic material that exhibits creep behavior. Tarefder et al. developed a range of indentation derived elastic modulus and hardness values of aged asphalt (*10*). Jager et al. studies the thermal effects on the mechanical properties of the asphalt binder (*8*). However, no research has been attempted to characterize moisture-induced damage in different phases of AC yet.

PRELIMINARIES OF NANOINDENTATION TEST

As mentioned previously, modulus of elasticity of the sample is determined from the load-displacement data. A typical load-displacement curve from a nanoindentation test is shown in Figure 2(a). A sitting load is typically applied initially to facilitate contact between the tip and sample surface. Next, the load is increased gradually from point *a* to *b*. The tip is unloaded at the maximum load point *b*. The unloading path is assumed to be elastic for most of the elastoplastic material. The unloading curve does not come back to point *a* due to plastic deformation in elastoplastic materials. The slope of the unloading curve at point *b* is usually equal to the slope of the loading curve at point *a*.

397
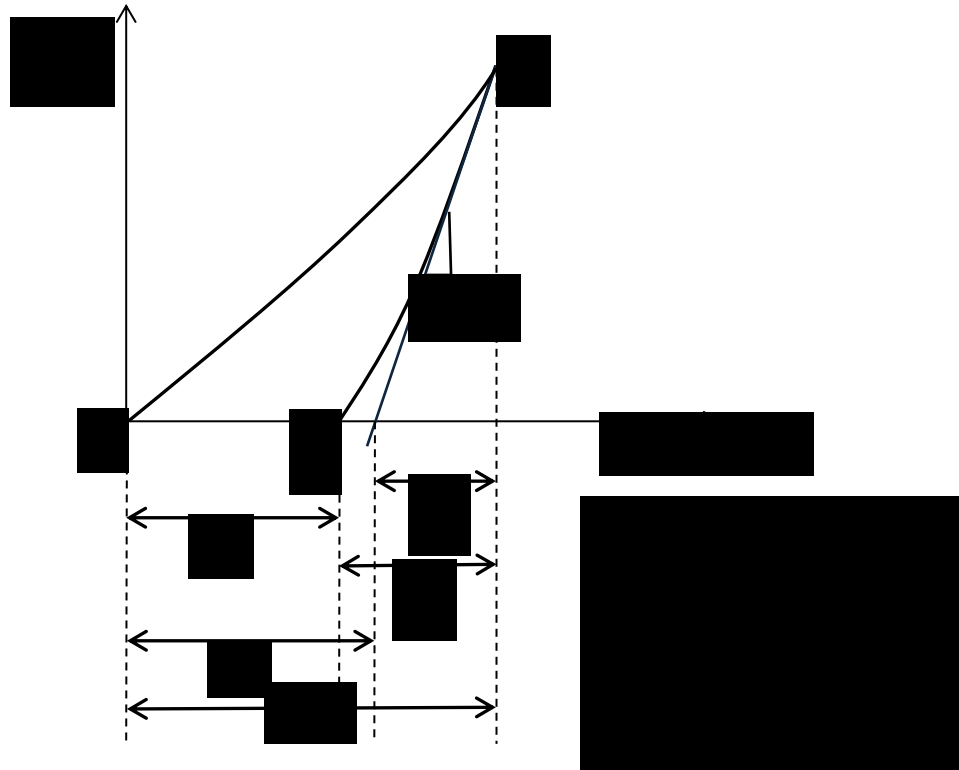
(a) Load −Displacement Curve
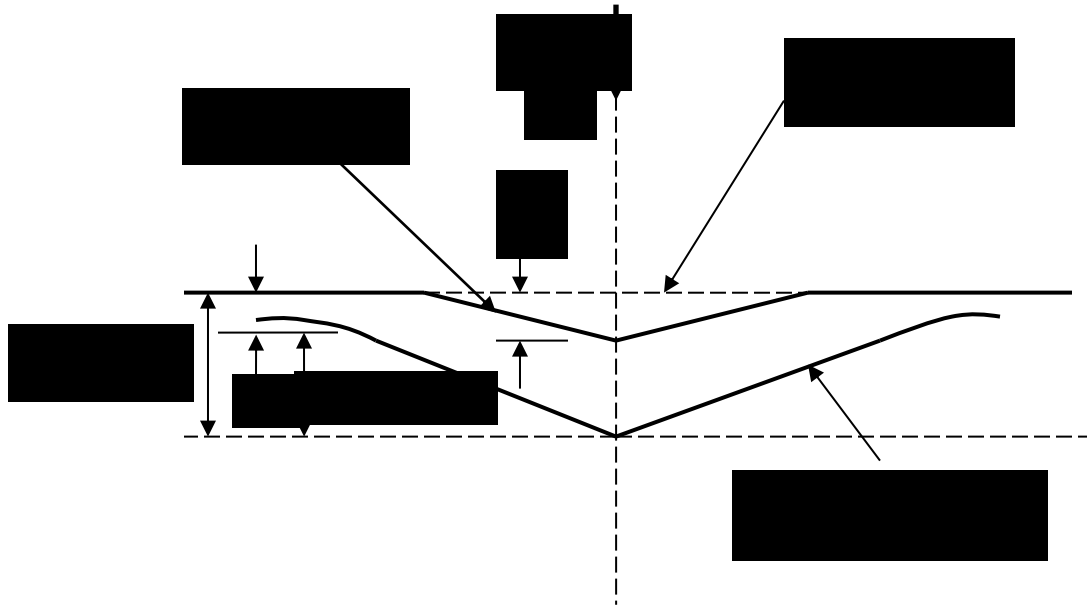
(b) Indentation Depth

FIGURE 2 Schematic of the Indentation Test.

Figure 2(b) shows the surface profile as a function of the penetration depth during loading and unloading. Here, h_{max} is the total depth of indentation at a maximum load, h_p is the total depth of indentation that is unrecovered, h_s is the depth of the surface at the

perimeter of the indenter contact and h_c is the vertical depth along which the contact is made between the indenter and the sample. Therefore:

$$h_c = h_{max} - h_s \tag{1}$$

The depth of impression that is recovered is:

$$h_e = h_{max} - h_p \tag{2}$$

Oliver-Pharr Method

Oliver-Pharr method is the most widely used method for determining stiffness and hardness values from load-displacement data of an indentation test. According to the Oliver-Pharr method elastic modulus of an indented sample can be inferred from the following equation (*19*):

$$\frac{dP}{dh} = 2E^* \sqrt{Rh} = 2E^* a \tag{3}$$

where R = indenter radius, a = contact radius, P = load, h = indentation depth, E^* = is the combined elastic modulus of the material and the indenter.

The projected area at the maximum load can be defined as: $A = \pi a^2$. Therefore,

$$S = \frac{dP}{dh} = \frac{2}{\sqrt{\pi}} E^* \sqrt{A} \tag{4}$$

where S is the unloading stiffness or slope of the unloading curve.

$$E^* = \frac{\sqrt{\pi}}{2\sqrt{A}} (S) \tag{5}$$

How to Find S: Oliver and Pharr uses a power law function to fit the unloading path of the load-displacement curve (*19*). The power law function used by Oliver-Pharr is shown in Eq. (6):

$$P = \alpha (h - h_f)^m \tag{6}$$

where h is depth of penetration, h_f is plastic depth, α and m are curve fitting parameters related to tip geometry. m is equal to 1 for flat ended cylindrical tip, m is 1.5 for spherical tip, and m is 2 for conical tip (Berkovich tip). Slope is measured by differentiation in the above Eq. (6) at onset of unloading.

How to Find A: Oliver and Pharr defined the projected area A as a function of h_c defined in Eq. (1). Oliver and Pharr extrapolated the tangent line to the unloading curve at the maximum loading point down to zero loads. This yields an intercept value for depth which estimates the h_s by:

$$h_s = \varepsilon \frac{P_{max}}{S} \tag{7}$$

Therefore,

$$h_c = h_{max} - \varepsilon \frac{P_{max}}{S} \tag{8}$$

where ε is a geometric constant. $\varepsilon = 0.72$ for conical tip, $\varepsilon = 0.75$ for Berkovich tip, and $\varepsilon = 0.72$ for spherical tip. The project area is measured by:

$$A = \pi a^2 = \pi (R h_c) \tag{9}$$

where R is known and h_c is calculated using the above Eq. (9).

399

*How to Find E:*Timoshenko and Goodier (*19*) found the reduced elastic modulus, *E** is related to the modulus of the indenter and the specimen, and given by Eq. (10):

$$\frac{1}{E*} = \frac{1-v^2}{E} + \frac{1-v_i^2}{E_i} \tag{10}$$

where *E* is Young's modulus of the material, *v* is Poisson's ratio of the material, E_i is Young's modulus of the indenter and v_i is Poisson's ratio of the indenter, *E** is the reduced modulus. One can find the elastic modulus of the sample, *E* using Eq. (10).

How to Find Hardness, H: Hardness, *H,* is defined by the maximum load divided by the projected area:

$$H = \frac{P_{max}}{A} \tag{11}$$

where P_{max} is peak load and *A* is projected area of contact at the peak load. The unit of hardness is given in N/m^2 or Pa.

SAMPLE PREPARATION AND MOISTURE CONDITIONING

Sample Preparation

A Superpave (SP) SP-IV (nominal maximum aggregate size 12.5 mm, PG 64-22 binder) mix was collected from a local plant in cooperation with New Mexico Department of Transportation (NMDOT). Mix was compacted by a Superpave gyratory compactor in the binder laboratory at the University of New Mexico (UNM).

Figure 3 shows the gyratory compacted sample being extracted from the compaction mold. The dimension of the gyratory compacted sample is 150 mm in diameter and 170 mm in height. Coring was performed to prepare nanoindentation sample from the middle part of the gyratory sample. Middle part of the gyratory compacted sample is used because this part has the most uniform air void distribution. The required sample size to conduct nanoindentation test can be as small as a few millimeters. In this study, a 25 mm diameter sample was used.

(a) Gyratory Compactor   (b) Coring of Sample

FIGURE 3 Sample Compaction

Next, the 25 mm diameter sample was polished to produce a smooth surface. Surface smoothness is a crucial for nanoindentation test since the contact area of the manoindenter is measured indirectly from the depth of penetration (*10*). Polishing of nanoindentation sample is performed using water cooled polishing machine. To produce a smooth surface without dislodging any small aggregate form the 25 mm diameter sample, a sequence of water resistant silicon carbide polishing papers with decreasing abrasiveness are utilized. The set of polishing papers are 100, 200, 400, 600, 800, 1,200 and 1,500 grit sizes each for duration of 150 seconds. Then the polished nanoindentation sample is washed to remove dust particles. Ideally, one can argue that moisture damage has occurred on the sample surface during polishing. Therefore, such sample is not appropriate for a moisture damage study. The fact is that both the dry and wet conditioned samples are subjected to polishing, which is required for the indentation tip to locate the surface during testing. Therefore, it can be counter argued that both samples are subjected to the same damage during polishing, however, the difference lies between them due to wet and dry conditioning, as described in the next section.

Figure 4 shows the sample that was indented. The sample surface is marked by an ink pen to show mastic and aggregate. In the study, a specific area (1cm^2) covering aggregate and mastic phases were defined for nanoindentation testing visually.
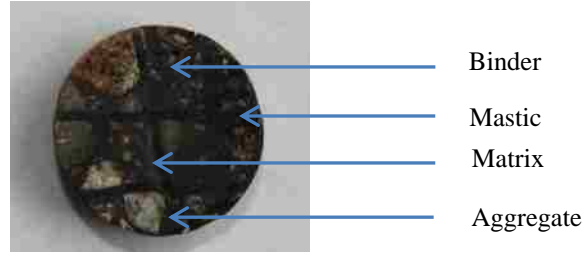
401

FIGURE 4 Nanoindentation Sample.

Moisture Conditioning Using MIST

Moisture Induced Sensitivity Testing (MIST) moisture conditioning was performed first by placing the sample in the MIST chamber and submerging it fully under water as shown in Figure 5. The MIST chamber was then closed and pressure cycles were applied to push and pull water into and out of the sample. According to the manufacturer of the MIST (InstroTek, Inc.), this simulates the action of a car tire as it produces pressure in a roadway while on top of the AC sample, and releases pressure when away from it (*20*). After placing the sample in the MIST chamber, the chamber is tightly secured with a stainless steel cover and bolts. The temperature of the specimen and chamber water was raised to 60 °C. A total of 10500 cycles at 275 kPa pressure is applied. The total time for stabilizing the temperature and applying pressure cycles was about 10 hours. The MIST conditioned sample was then oven dried overnight before testing.

FIGURE 5 Moisture Induced Sensitivity Tester (MIST).

Nanoindentation Testing

The nanoindenter device at the UNM nano test laboratory was used for indentation. Figure 6 shows the nanoindentation test setup with the Berkovich indenter tip and sample indenting in AC. In the nanoindentation test, the AC sample was mounted on a polymer substrate and the sample substrate system held by a sample stub. The pendulum in the system was used to adjust the bridge box output for the Berkovich indenter tip.
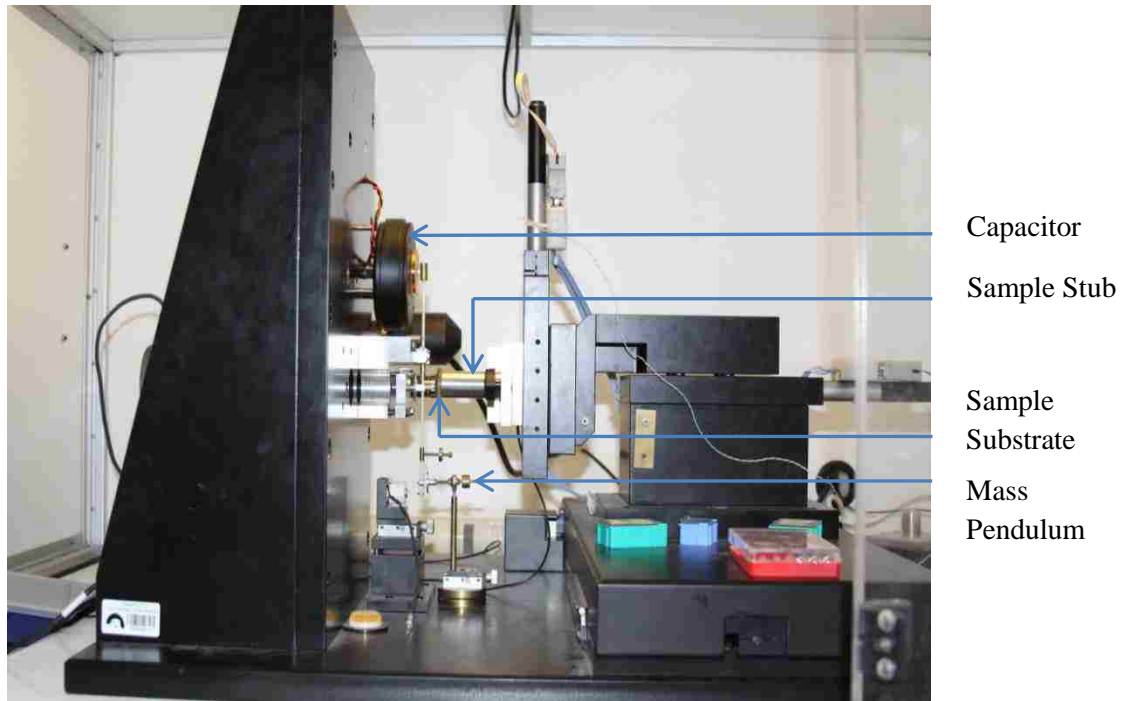
FIGURE 6 Nanoindentation test setup for AC.

In the previous study of the authors, both spherical and Berkovich tips were used on asphalt (*11, 12*). However, their study concluded that the Berkovich tips are more suitable than the spherical tips for asphalt binder testing. Spherical tips tend to adhere to the unaged asphalt sample surface at room temperature. As a result, system compliance can be lost during indentation on asphalt. Based on the previous experience, a Berkovich tip was used in the current study. A Berkovich tip consists of three-sided pyramidal Berkovich tip with a semiangle of 65.27°. It has sharp and well-defined (pyramid defined by face angle 65.3°) tip geometry.

In this study, a maximum load of 0.51 mN was applied with an unloading rate of 0.02 mN/sec. A sitting load of 0.01 mN was used for all the samples. A creep time of 200 seconds was applied after reaching the maximum load. The viscous effects of the test results are reduced by using a fast unloading rate and applying an extended dwell time. Tarefder and Faisal have shown that a dwell time of 100-200 seconds (long) can minimize the viscous effect of asphalt (*11*). Based on the previous study by the authors, a loading rate of 0.02 mN/sec. and a dwell time of 200 seconds were chosen for the nanoindentation test of AC in this study (17). Each phase of the AC sample was indented at 100 locations to deal with the variability of nanoindentation results due to material heterogeneity in the asphalt mastic or matrix.

RESULTS AND DISCUSSIONS

Figure 7(a) shows the load-displacement curves obtained from the indentation tests on the dry and wet conditioned AC sample. It can be seen that the load-displacement curves widely ranged with displacements from 20 nm to 6300 nm of displacement for same load of 0.51.

403
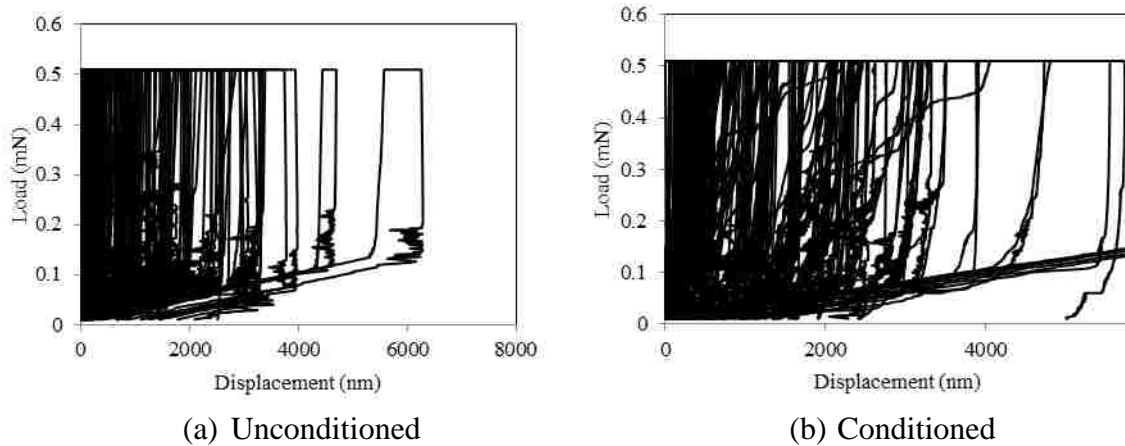
(a) Unconditioned   (b) Conditioned

FIGURE 7 Nanoindentation load-displacement curves for unconditioned AC sample.

Ideally one should use a nano-positioner (add-on to the indenter) to locate the phases of a sample that is indented. Due to the lack of such nano-positioner, this study conducts a number of indentations on a certain area to cover different phases. Phase specific indentation data are separated based on materials softness and indentation depth. Ideally for a constant load, indentation depth is higher in the soft material part than in the hard material part. It is known that mastic is softer than aggregate phase. This study makes the following assumptions based on the findings from the previous study (*12*): For maximum nanoindentation load of 0.51 mN and a dwell time of 200 seconds, (i) if the indentation depth remains within 500 nm, the indented phase is defined as the aggregate phase of AC, (ii) if the indentation depth remains between 500 nm to 1500 nm for AC, the indented phase is defined as the matrix phase of AC and (iii) if the indentation depth is higher than 1500 nm for AC, the indented phase is defined as the mastic phase of AC.

Based on the above assumptions, test results presented in Figure 7(a) for dry sample is separated according to a specific phase and presented in five load-displacement curves for each phase in Figures 8(a) to 8(c). Figure 8(a) shows five nanoindentation load-displacement curves on the mastic phase of AC. In all the curves maximum displacement is higher than 1500 nm.
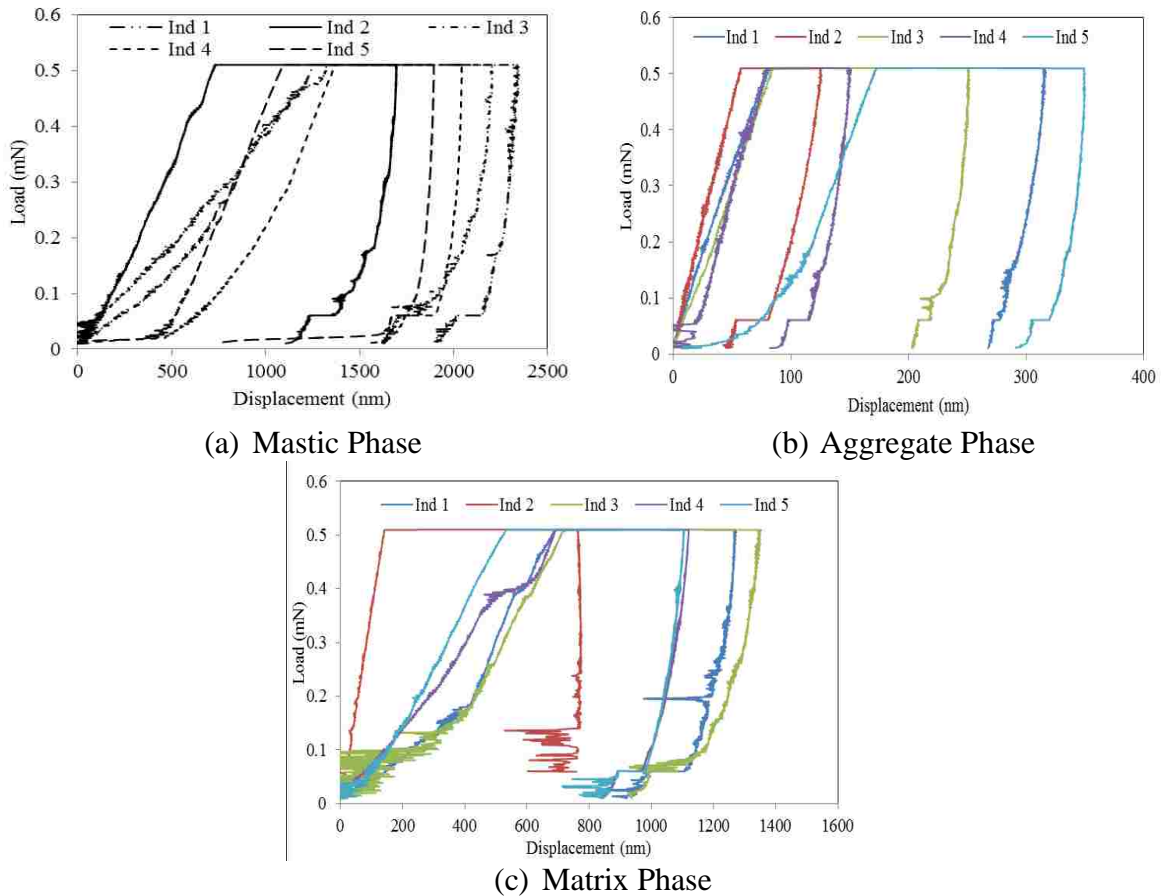
404

(a) Mastic Phase

(b) Aggregate Phase

(c) Matrix Phase

**FIGURE 8 Nanoindentation load-displacement curves for different phases
of AC.**

Figure 8(b) shows the load-displacement curves of the aggregate phase. Here the maximum displacement is limited to 500 nm. Figure 8(c) shows the load-displacement curves from the matrix phase. Apparently, the matrix phase shows some noise in the unloading curve. The indentations may have been affected by the small particle in matrix. While aggregate may act as elastic material, the binder or mastic in matrix might have acted as viscoelastic material and result in noisy unloading.

Oliver-Pharr method is utilized to determine the elastic modulus and hardness. Figure 9 shows a comparative analysis of the box plot for all nanoindentation (100 test data) modulus values. Clearly, a dry sample has higher mean and median of elastic modulus values than a wet AC sample. The average elastic modulus is 2.71 GPa for a wet sample and is 9.38 GPa for wet sample. Modulus decreases about 70% due to wet conditioning.
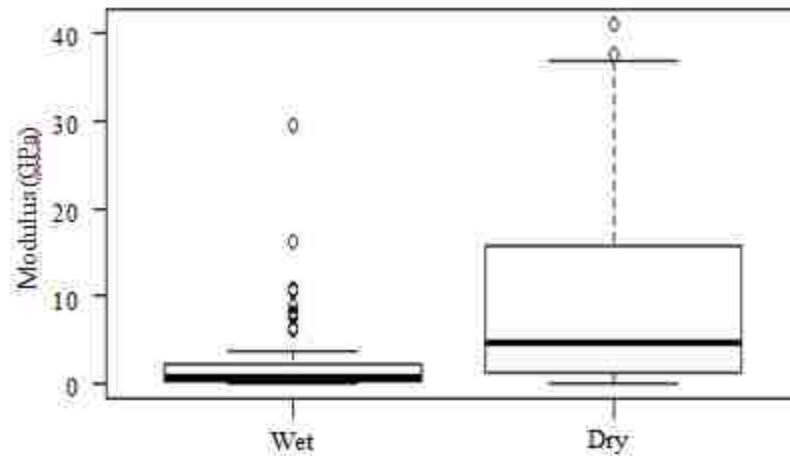
405

FIGURE 9 Wet vs. Dry Modulus (Average of all tests).

Wet vs. Dry Modulus and Hardness of Mastic
Figure 10(a) compares the modulus mastic of phases of dry to wet samples. Average modulus of wet mastic is 0.43 GPa, whereas average modulus of the dry mastic is 1.02 GPa. Moisture damage causes approximately 60% modulus reduction in the mastic phase. Surprisingly, the hardness values of dry and wet conditioned mastics are the same (approximately 4 MPa), as shown in Figure 10(b). The indented area might not change for the same load to create the same hardness for wet and dry condition.
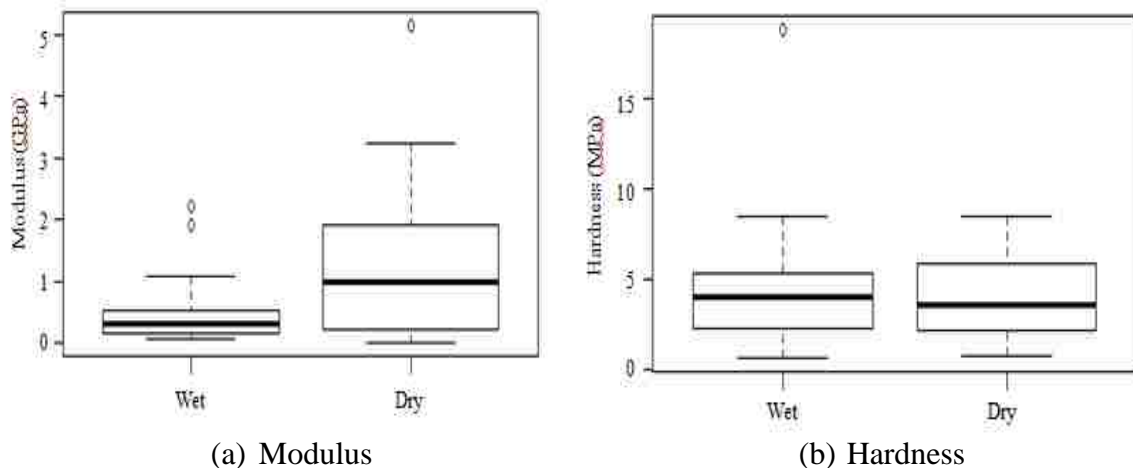
(a) Modulus   (b) Hardness
FIGURE 10 Moisture damage characterizations for mastic phase of AC.

Wet vs. Dry Modulus and Hardness of Matrix
Figure 11(a) compares the average elastic modulus of the moisture conditioned matrix phase to that of dry matrix. The average value of modulus is 1.26 GPa for wet matrix and 3.0 GPa for dry matrix. There is a 58% reduction in modulus in the matrix phase of AC due to moisture damage. Unlike the mastic phase, hardness of the matrix phase reduces by 24% form 24.9 MPa (in the dry phase) to 18.91 MPa (in wet phase), as shown in Figure 11(b).
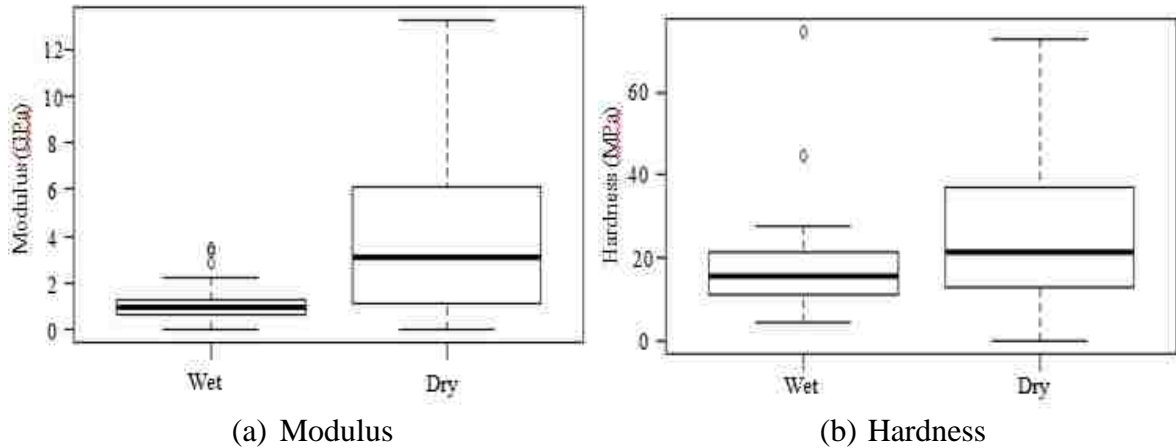
406

(a) Modulus   (b) Hardness

FIGURE 11 Moisture damage characterizations for matrix phase of AC.

Wet vs. Dry Modulus and Hardness of Aggregate

Figure 12(a) shows that the average modulus of the aggregate phase is 8 GPa under wet conditioning and 24 GPa under dry conditioning. Moisture damage reduces 67% of its original modulus. From Figure 12(b), it can be seen that hardness reduces 74% in the aggregate phase from 1247 MPa in dry to 324 MPa in the wet phase.
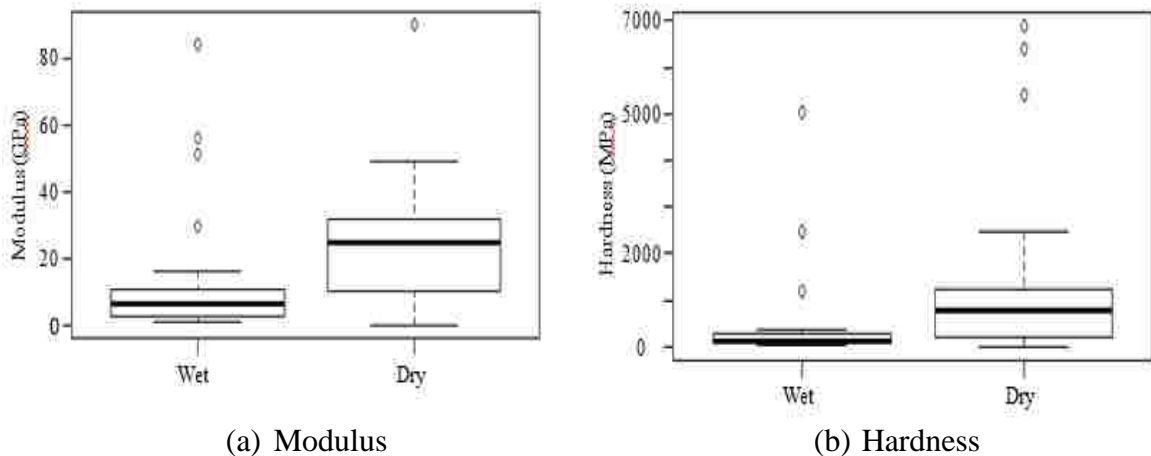

(a) Modulus   (b) Hardness

FIGURE 12 Moisture damage characterizations for aggregate phase of AC.

WET VS. DRY CREEP BEHAVIOR OF MASTIC

In the previous analysis in this paper, all phases are considered elastic and analyzed by the Oliver-Pharr method. While the idealization of aggregate and matrix by elastic behavior may be acceptable, one can always argue that the mastic phase should be characterized as viscoelastic material. To this end, the load-displacement curve of the mastic phase is modeled with a linear viscoelastic Burger model. In essence, consider the dwell time portion of the load-displacement curve, which represents the creep behavior of the mastic phase.

Burger Model

407

Figure 13 shows a four element Burger model, which was found to be the most suitable model for asphalt in a previous study by the authors (*13*).
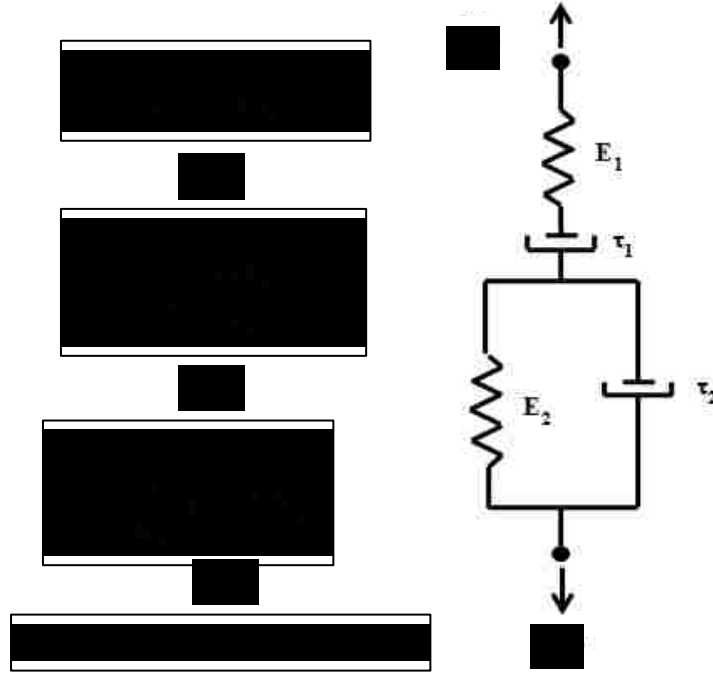

FIGURE 13 Burger Model.

The final form of the Burger model can be found in Tarefder and Faisal (*11*) and is given below:

$$h^2 = \frac{2}{\pi} P_0 \cot \psi [\frac{1}{E_1} + \frac{1}{E_2}[1 - e^{(-t/\tau_2)} + \frac{t}{\eta_1}]] \tag{12}$$

where P_0 = indentation load

h = displacement due to applied load in a material

E' = elastic modulus of indented material

v = Poisson's ratio of the material

ψ = include half angle of Berkovich indenter.

For the known value of (h, P_0 and t) from an indentation test, the values of E_1, E_2, τ_1 and τ_2 can be obtained from the simplified Eq (13).

$$h^2(t) = A_1 + A_2(1 - e^{-t/\tau_2}) + A_3 t \tag{13}$$

where $A_1 = \frac{2}{\pi} P_0 \cot \psi \frac{1}{E_1}$ and $A_2 = \frac{2}{\pi} P_0 \cot \psi \frac{1}{E_2}$ and $A_3 = \frac{2}{\pi} P_0 \cot \psi \frac{E_1 t}{\tau_2}$.

In this study, Eq (13) is fitted to laboratory data to find A_1, A_2 and A_3. A nonlinear curve fitting algorithm is used in MATLAB to optimize those parameters.

Figure 14 compares model Eq. (13) data with laboratory. The optimized values of parameters are: E_1 = 1.378 GPa (dry sample), 1.242 GPa (wet sample); E_2 = 0.4087 GPa (dry sample), 0.0631 GPa (wet sample); τ_1 = 0.125 seconds (dry sample), 0.1742 (wet sample); and τ_2 = 5.565 seconds (dry sample), 7.899 (wet sample).

408

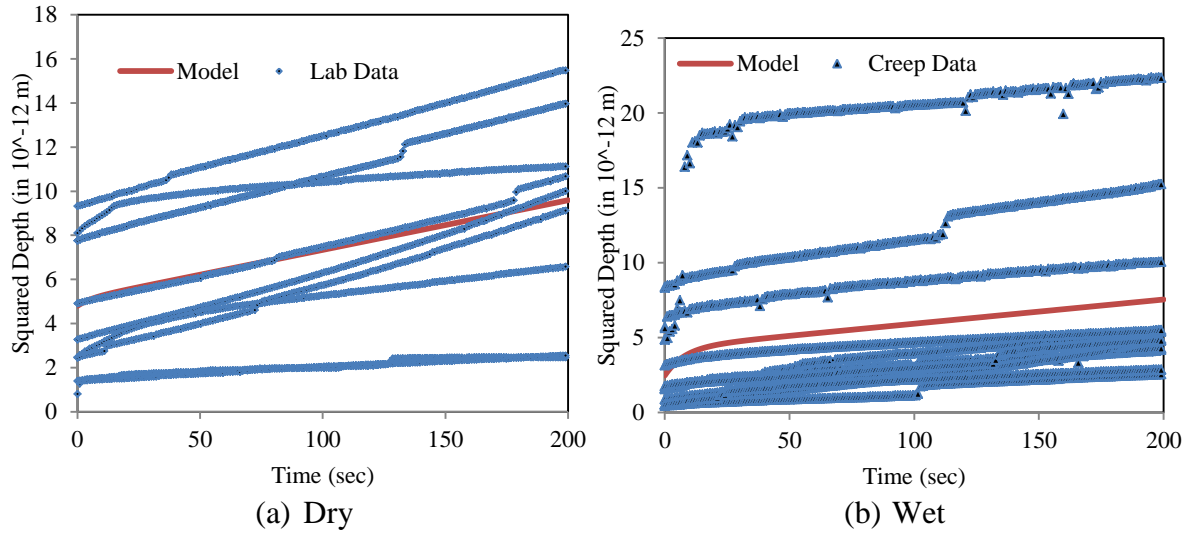(a) Dry   (b) Wet

FIGURE 14 Curve fitting of creep data of mastic phase of AC.

Using the Burger model parameters, creep compliance, $J(t)$ of the mastic is determined from the following Eq. (14):

$$J(t) = \frac{1}{E_1} + \frac{1}{E_2}[1 - e^{(-t/\tau_2)} + \frac{t}{\eta_1}]$$ (14)

Figure 15 shows that the creep compliance of wet conditioned mastic is 23.5 GPa^{-1}, whereas the creep compliance of dry mastic is 13.5 GPa^{-1}. Creep compliance of the wet sample is 42% higher than that of the dry mastic phase.
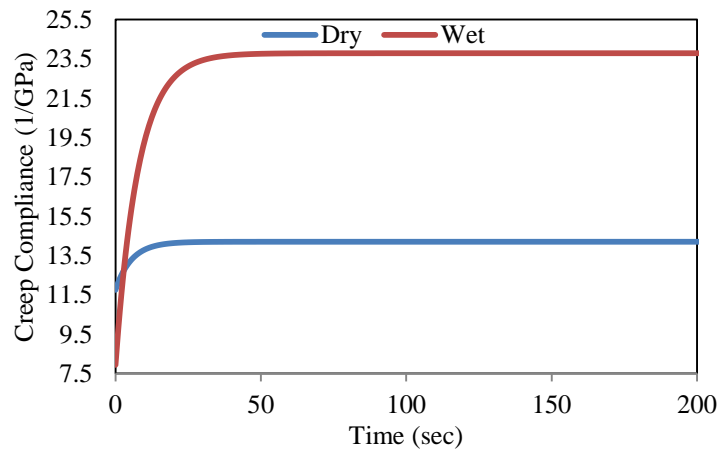

FIGURE 15 Creep compliance of Wet vs. Dry Mastic Phase.

CONCLUSIONS

In this study, nanoindentation tests are conducted on three phases of an asphalt sample under wet and dry conditioning. The load-displacement curves from nanoindentation tests are analyzed using Oliver-Phar method to determine elastic modulus and hardness. In addition, the nanoindentation creep response of the mastic phase is modeled using the Burger model to determine creep compliance values. Based on the findings of this study, the following conclusions can be made:

409

- The moduli of mastic, matrix and aggregate phase of an AC sample decreases by 60%, 58% and 67%, respectively, due to moisture-induced damage.
- Moisture reduces the overall indentation modulus of AC by approximately 70%. Modulus of mastic, matrix and aggregate are 1.02 GPa, 3 GPa, 24 GPa in dry samples and 0.43 GPa, 1.26 GPa, 8 GPa in wet samples.
- The hardness of the mastic, matrix and aggregate phases of the AC sample reduce by 0%, 24% and 74%, respectively, due to moisture induced damage. The hardness of the mastic, matrix and aggregate are 4 MPa, 24.9 MPa, 1247 MPa in dry samples and 4 MPa, 18.91 MPa, 324 MPa in wet samples.
- Creep compliance of the wet mastic is 42% higher than that of dry mastic.

ACKNOWLEDGEMENTS

410

REFERENCES

1. Raquel, M., R. Velasquez, and H. U. Bahia. Measuring the Effect of Moisture on Asphalt-Aggregate Bond with the Bitumen Bond Strength Test. *Transportation Research Record*, *2209*, Washington, D.C., 2011, pp. 70–81.

2. Huet, C. Etude, par une methode d'impedance, du compormement viscoelastique des materiaux hydrocarbones (Study of viscoelastic behavior of bituminous mixes by method of impedance). *Annales des Ponts et Chaussees*, Vol. 135, No.6, 1965, pp. 373–429.

3. Little, D. N., A. Letton, S. Prapnnachari, and Y. R. Kim. Rheological and rheo-optical characterization of asphalt cement and evaluation of relaxation properties. *Transportation Research Record*, *1436*, Washington, D.C., 1995, pp. 71–82.

4. Masad, E., N. Somadevan, H. U. Bahia, and S. Kose. Modeling and experimental measurements of strain distribution in asphalt mixes. *Journal of Transportation Engineering, ASCE*, Vol. 127, No. 6, 2001, pp. 477–485.

5. Buttlar, W. G., and Z. You. Discrete element modeling of asphalt concrete: Microfabric approach. *Transportation Research Record*, *1757*, Washington, D.C., 2001, pp. 111–118.

6. Guddati, M. N., Z. Feng, and Y. R. Kim. Toward a micromechanics-based procedure to characterize fatigue performance of asphalt concrete *Transportation Research Record*, *1789*, Washington, D.C., 2002, pp. 121–128.

7. Xu, Q., and M. Solaimania. Modelling linear viscoelastic properties of asphalt concrete by the Huet-Sayegh model. *International Journal of Pavement Engineering*, Vol. 10, No. 6, 2009, pp. 401–422.

8. Jager, A., R. Lackner, and K. Sangl. Microscale characterization of bitumen-back analysis of viscoelastic properties by means of nanoindentation. *International Journal of Material Research* (formerly Z. Metallkd.), Vol. 98, 2010, pp. 404–413.

9. Zofka, A., and D. Nener-Plante. Determination of Asphalt Binder Creep Compliance Using Depth-Sensing Indentation. *Experimental Mechanics*, Vol. 51, No. 8, 2011, pp. 1365–1377.

10. Tarefder, R. A., A. M. Zaman, and W. Uddin. Determining Hardness and Elastic Modulus of Asphalt by Nanoindentation. *Journal of Geomechanics, ASCE*, Vol. 10, No. 3, 2010, pp. 106–116.

11. Tarefder, R. and H. Faisal. Effects of Dwell Time and Loading Rate on the Nanoindentation Behavior of Asphaltic Materials. *Journal of Nanomechanics and Micromechanics, ASCE*, Vol. 3, No. 2, pp. 17–23.

12. Tarefder, R. A. and H. M. Faisal. Nanoindentation Characterization of Asphalt Concrete Aging. *Journal of Nanomechanics and Micromechanics, ASCE*, 2013, In press

13. Tarefder, R. A. and H. M. Faisal. Modeling Nanoindentation Creep Behavior of Asphalt Binder. *Advances in Civil Engineering Materials, ASTM*, 2013, In press.

14. Ossa, E. A., and A. C. Collop. Spherical indentation behavior of asphalt mixtures. *Journal of Material in Civil Engineering*, Vol. 19, No. 9, 2007, pp. 753–761.

15. Ossa, E. A., V. S. Deshpande, and D. Cebon. Spherical indentation behaviour of bitumen. *Acta Materialia*, Vol. 53, No. 11, 2005, pp. 3103–3113.

411

16. Wasiuddin, N. M., M. M. Zaman, and E. A. O'Rear. Effect of sasobit and asphamin on wettability and adhesion between asphalt binders and aggregates. *Transportation Research Record*, *2051*, Washington, D.C., 2008, pp. 80-89.

17. Tarefder, R. A., and Arifuzzaman, M. Nanoscale Evaluation of Moisture Damage in Polymer Modified Asphalts. *ASCE Journal of Materials in Civil Engineering*, Vol. 22, No. 7, 2010, pp 714-725.

18. Bahia, H. U., A. Hanz, K. Kanitpong, and H. Wen. Testing Methods to Determine Aggregate/Asphalt Adhesion Properties and Potential Moisture Damage. *WHRP 07-02, Wisconsin Highway Research Program*, Madison, Wisconsin, 2007.

19. Oliver, W. C., and G. M. Pharr. An improved technique for determining hardness and elastic modulus using load and displacement sensing indentation experiments. *Journal of Material Research*, Vol. 7, No. 6, 1992, pp. 1564–1583.

20. InstroTek, Inc. Raleigh, NC. The MIST. http://instrotek.com/material-testing/laboratory-products/mist/#!prettyPhoto. Accessed July 29th , 2013.